

**SECOND COORDINATION SPHERE PROMOTED CATALYSIS:
ORGANOMETALLIC HYDROGEN BOND DONORS FOR
ENANTIOSELECTIVE ORGANIC TRANSFORMATIONS**

A Dissertation

by

TATHAGATA MUKHERJEE

Submitted to the Office of Graduate and Professional Studies of
Texas A&M University
in partial fulfillment of the requirements for the degree of

DOCTOR OF PHILOSOPHY

Chair of Committee,	John A. Gladysz
Committee Members,	Daniel A. Singleton
	Karen L. Wooley
	Stephen T. Talcott
Head of Department,	Francois P. Gabbai

August 2015

Major Subject: Chemistry

Copyright 2015 Tathagata Mukherjee

ABSTRACT

This dissertation describes the development of 2-guanidinobenzimidazole (**GBI**) containing ruthenium based organometallic hydrogen bond donors and their applications in second coordination sphere promoted catalysis (SCSPC).

The *synperiplanar* triad arrangement of the NH donor (D) sites in **GBI** and derivatives are studied to establish that chelation preorganizes **GBI** in a DDD motif that is not an energy minimum with the free ligand.

Later the importance of preorganization is explored in reactions catalyzed by **GBI** and derivatives. Protonated or methylated BAr_f^- ($\text{B}(3,5\text{-C}_6\text{H}_3(\text{CF}_3)_2)_4$) salts of **GBI**, $\mathbf{1}^+ \text{BAr}_f^-$ (84%) and $\mathbf{2}^+ \text{BAr}_f^-$ (58%), are prepared along with the protonated salts of guanidine and 2-aminobenzimidazole, $\mathbf{3}^+ \text{BAr}_f^-$ (70%) and $\mathbf{4}^+ \text{BAr}_f^-$ (75%), respectively. Refluxing **GBI** and $(\eta^5\text{-C}_5\text{H}_5)\text{Ru}(\text{PPh}_3)_2(\text{Cl})$ in toluene forms the chelated complex $[(\eta^5\text{-C}_5\text{H}_5)\text{Ru}(\text{PPh}_3)(\mathbf{GBI})]^+ \text{Cl}^-$ ($\mathbf{8}^+ \text{Cl}^-$; 96%), which upon addition of CO forms $[(\eta^5\text{-C}_5\text{H}_5)\text{Ru}(\text{CO})(\mathbf{GBI})]^+ \text{Cl}^-$ ($\mathbf{9}^+ \text{Cl}^-$; 91%). Subsequent anion metathesis of $\mathbf{8}^+$ and $\mathbf{9}^+ \text{Cl}^-$ gives the respective PF_6^- and BAr_f^- salts (83-92%). $\mathbf{9}^+ \text{PF}_6^-$ can also be prepared from $[(\eta^5\text{-C}_5\text{H}_5)\text{Ru}(\text{CO})(\text{NCCH}_3)_2]^+ \text{PF}_6^-$ (81%). **GBI** and $\mathbf{9}^+ \text{Cl}^-$ (10 mol%, rt) are ineffective (48 h) for the condensations of 1-methylindole and *trans*- β -nitrostyrene (**6**). In contrast, salts $\mathbf{1-4}^+ \text{BAr}_f^-$ (25-95%, 1 h) and $\mathbf{8-9}^+ \text{X}^-$ (PF_6^- and BAr_f^-) are active catalysts (30-97%) under similar conditions.

Furthermore, **GBI** derivatives with a NHR group (**GBI-R**; R = **16a**, CH_2Ph ; **16b**, $(S_C)\text{-CH}(\text{CH}_3)\text{Ph}$; **16c**, $(R_C R_C)\text{-CH}(\text{CH}_2)_4\text{-CH-NMe}_2$; **16d**, $(R_C R_C)\text{-CH}(\text{CH}_2)_4\text{-CH-NCH}_2(\text{CH}_2)_3\text{CH}_2$) are prepared. Reactions with $[(\eta^5\text{-C}_5\text{H}_5)\text{Ru}(\text{CO})(\text{NCCH}_3)_2]^+ \text{PF}_6^-$ afford the chiral-at-metal chelates $[(\eta^5\text{-C}_5\text{H}_5)\text{Ru}(\text{CO})(\mathbf{GBI-R})]^+ \text{PF}_6^-$ (**18a-d** $^+ \text{PF}_6^-$, 39-77%). The Ru,C configurational diastereomers of **18c** $^+ \text{PF}_6^-$ separate upon alumina

chromatography ($R_{Ru}R_C R_C$, >99:01 diastereomer ratio (dr); $S_{Ru}R_C R_C$, <2:98 dr). Configurations are assigned by CD spectra, DFT calculations, and a crystal structure. Both ($S_{Ru}R_C R_C$)-**18c**⁺ PF₆⁻ and ($R_{Ru}R_C R_C$)-**18c**⁺ PF₆⁻ (1-10 mol%) catalyze Michael addition reactions between 1,3-dicarbonyl equivalents and **6** in high yields and enantioselectivities (90-99% ee). The free **GBI**-R ligand exhibits only modest activity. The chiral ruthenium center has little influence over the product configuration.

Finally, ruthenium **GBI** complexes bearing a bulky electron withdrawing pentaphenylcyclopentadienyl ligand are accessed by treating a CH₃CN suspension of (η^5 -C₅Ph₅)Ru(CO)₂(Br) with Me₃NO·2H₂O, **GBI**, and Ag⁺ PF₆⁻. Silica gel chromatography workups lead to [(η^5 -C₅Ph₅)Ru(CO)(**GBI**)]⁺ PF₆⁻ (**48**⁺ PF₆⁻; 70%), whereas with alumina [(η^5 -C₅Ph₅)Ru(CO)(**GBI**)]⁺ BAr_f⁻ (**48**⁺ BAr_f⁻; 69%) is obtained after anion metathesis. The neutral compound (η^5 -C₅Ph₅)Ru(CO)(**GBI**-H) (**49**; 72%) bearing a deprotonated **GBI** ligand (**GBI**-H) is obtained from **48**⁺ PF₆⁻ with K⁺ *t*-BuO⁻. These are characterized by NMR, other spectroscopic methods, and X-ray crystallography. Protonation of **49** with the axially chiral enantiopure phosphoric acid, (*P*)-Phos-H (HOP(=O)(*o*-C₁₀H₆O)₂), leads to (R_{Ru}/S_{Ru})-**48**⁺ (*P*)-Phos⁻ (92%) as a mixture of Ru,Axial configurational diastereomers. The diastereomer (S_{Ru})-**48**⁺ (*P*)-Phos⁻ (35%) can be isolated with >98:02 dr from cold toluene/hexane. Subsequent anion metathesis provides (S_{Ru})-**48**⁺ BAr_f⁻ (80%). The absolute configuration is assigned by CD spectroscopy. (S_{Ru})-**48**⁺ BAr_f⁻ (10 mol%) is an efficient catalyst for Friedel-Crafts alkylations and Michael addition reactions even under aerobic conditions. The addition of thiophenol to *trans*-3-cinnamoyloxazolidin-2-one is highly enantioselective (>99%). The neutral complex **49** is even capable of acting as a multifunctional catalyst and promotes Michael addition reaction of diethyl malonate and **6** in the absence of an external base.

DEDICATION

I dedicate this dissertation to my wife and dad. Both have played an immense role in my life. Especially, Neelanjana (wife) for listening to my complaints, supporting me in difficult times, and encouraging me each and every second. I am lucky to be your husband.

ACKNOWLEDGEMENTS

I would like to thank Dr. John A. Gladysz, for providing me the opportunity to work in his lab and explore new horizons in chemistry. He allowed me to pursue research with intellectual freedom and trusted me with my conclusions. These were most encouraging for a young scientist like me. His effort in teaching scientific organization and editing through this dissertation has been instrumental.

Furthermore, I would like to thank my committee members, Dr. Daniel A. Singleton, Dr. Karen L. Wooley, Dr. Stephen T. Talcott, and Dr. Janet Bluemel for taking their time to review this dissertation. Thanks to Dr. Nattamai Bhuvanesh for his crystallographic studies and Dr. Perez for the computational studies. Also thanks to Dr. Romo and Dr. Begley for allowing me to use their instruments, without which much of this dissertation would have been incomplete.

Thanks to Procter & Gamble (*P&G*), Dr. Zhang and his entire team for the internship opportunity, as it is the best thing happened to me during my PhD. Dr. Zhang at *P&G* is the best colleague till date and a superb advisor to work with.

The Gladysz group has been immensely helpful and each member has played a significant role in shaping me. Specifically, I would like to thank Soumik Biswas and Alexander Estrada for all the "chemical talks" over the coffee breaks and Sugam Kharel for being a tremendous colleague and a real friend in and out of the lab.

Thanks to my mother, brother, mother-in-law, and father-in-law for their encouragement. A special thanks to my wife, Neelanjana, for her patience and love. Finally, thanks to my dad for always being there.

NOMENCLATURE

δ	chemical shift in ppm
ϵ	molar extinction coefficient
ν	stretching mode (IR)
μ	micro ($\times 10^{-6}$)
$^{\circ}$	degree (angle)
$^{\circ}$	degree (temperature)
$[\theta]$	molar ellipticity
$\Delta\epsilon$	molar circular dichroism
β	beta position
Δ	Delta (right-handed, absolute stereo configuration of octahedral complex)
Λ	Lambda (left-handed, absolute stereo configuration of octahedral complex)
η^n	eta (hapticity), describes a ligand that coordinates through n contiguous atoms
$\{^1\text{H}\}$	proton decoupled
\AA	Angstrom
Anal.	analysis
Ar	aryl
BAMOL	1,1'-biaryl-2,2'-dimenthol
BINOL	1,1'-bi-2-naphthol

br	broad
Bu	butyl
Calcd	calculated
CD	circular dichroism
CH ₂ Cl ₂	dichloromethane
CH ₃ CN	acetonitrile
C ₆ H ₁₄	hexane
C ₅ H ₁₂	pentane
CH ₃ COCH ₃	acetone
CH ₃ C ₆ H ₅	toluene
CH ₃ COOH	glacial acetic acid
Cp [*]	pentamethylcyclopentadienyl
d	doublet (NMR)
d	days
dec	decomposition
dr	diastereomer ratio
DMSO	dimethylsulfoxide
ee	enantiomeric excess
en	ethylenediamine
Et	ethyl
Et ₃ N	triethylamine
EtOAc	ethyl acetate

EtOH	ethanol
equiv	equivalent
g	gram
h	hour
HPLC	high pressure liquid chromatography
Hz	hertz
<i>i</i>	ipso or iso
$^iJ_{jk}$	scalar coupling constant for coupling of nucleus j with nucleus k through i bonds
IR	infrared
kcal	kilocalorie
M	mol/Liter
M	metal
m	multiplet (NMR), medium (IR)
m	meta
Me	methyl
MeOH	methanol
min	minutes
mmol	millimole
mp	melting point
NMR	nuclear magnetic resonance
<i>o</i>	ortho

<i>p</i>	para
PF ₆ ⁻	hexafluorophosphate
Ph	phenyl
ppm	parts per million
Pr	propyl
q	quartet
R	organic group
rt	room temperature
s	singlet (NMR), strong (IR)
sep	septet (NMR)
t	triplet (NMR)
<i>t</i>	tertiary
TADDOL	$\alpha,\alpha,\alpha,\alpha$ -tetraaryl-1,3-dioxolane-4,5-dimethanol
temp	temperature
TLC	thin layer chromatography xxviii
UV	ultraviolet
v/v	volume/volume
vis	visible
vs	very strong
w	weak

TABLE OF CONTENTS

	Page
ABSTRACT	ii
DEDICATION	iv
ACKNOWLEDGEMENTS	v
NOMENCLATURE	vi
TABLE OF CONTENTS	x
LIST OF FIGURES	xii
LIST OF SCHEMES	xvii
LIST OF TABLES	xx
1. INTRODUCTION: SECOND COORDINATION SPHERE PROMOTED CATALYSIS	1
1.1 Hydrogen bonding and its applications	1
1.2 2-Guanidinobenzimidazole: an overlooked hydrogen bond donor	8
1.3 Preorganization and hydrogen bonding	15
1.4 Purpose of second coordination sphere promoted catalysis with GBI	19
2. MODIFICATION AND APPLICATION OF 2-GUANIDINOBENZIMIDAZOLE FOR SECOND COORDINATION SPHERE PROMOTED CATALYSIS	21
2.1 Introduction	21
2.2 Results	29
2.3 Discussion	51
2.4 Conclusion	58
2.5 Experimental section	59
3. EPIMERIC CHIRAL-AT-METAL RUTHENIUM COMPLEXES: SEPARATION AND APPLICATIONS	77

	Page
3.1 Introduction	77
3.2 Results	78
3.3 Discussion	103
3.4 Conclusion.....	108
3.5 Experimental section	109
4. ENANTIOPURE CHIRAL-AT-METAL RUTHENIUM COMPLEXES: SYNTHESES, RESOLUTION, AND APPLICATIONS IN SECOND COORDINATION SPHERE PROMOTED CATALYSIS	137
4.1 Introduction	137
4.2 Results	141
4.3 Discussion	171
4.4 Conclusion.....	177
4.5 Experimental section	179
5. SUMMARY AND CONCLUSION.....	198
5.1 Conclusion from this study	198
5.2 Beyond this study	200
REFERENCES.....	202
APPENDIX A	227
APPENDIX B	244
APPENDIX C	285

LIST OF FIGURES

FIGURE	Page
1.1 The 1:1 complex (I) of 1,2-bis(<i>m</i> -nitrophenyl)urea and <i>N,N</i> -dimethyl- <i>p</i> -nitroaniline with hydrogen bonding (highlighted in red).....	2
1.2 Left: representative, previously reported, DD type hydrogen bond donor catalysts (participating hydrogen atoms in red). Right: activation of carbonyl compounds by dual (chiral/achiral) hydrogen bond donors.....	3
1.3 Top: representative bifunctional hydrogen bond donors used in enantioselective catalysis. Bottom: transition state assemblies for the Michael addition of a dialkyl malonate to <i>trans</i> - β -nitrostyrene catalyzed by XII	4
1.4 Left: spectroscopically detected hydrogen bonding between cation (Cp [*]) ₂ OsH ⁺ and OPPh ₃ (XVI , top) and crystal structure of Et ₃ NH ⁺ Co(CO) ₄ ⁻ with hydrogen bonding highlighted in red (XVII , bottom). Middle: [Co(en) ₃] ₃ ⁺ trication (XVIII). Right: previously characterized 2:1 adduct of a rhenium ammonia complex and 18-crown-6 (XIX)	5
1.5 Proposed transition state assembly for a ketone hydrogenation catalyst of Noyori.....	7
1.6 Crystal structures of the constitutional isomers XXV (left) and XXVI (right) with intramolecular hydrogen bonding highlighted in red	11
1.7 Crystal structure of GBI 18-crown-6 ether cocrystal (XXVII , left), dimethyl GBI phthalimide cocrystal (XXIX , middle), and GBI phthalimide cocrystal (XXX , right) with hydrogen bonding distances < 2 Å (highlighted in red) and > 2 Å (highlighted in cyan)	13
1.8 Top: crystal structure of two neutral Zn(GBI)Cl ₂ molecules with intermolecular hydrogen bonding highlighted in red (XXXI , left), crystal structure of Cu[(GBI) ₂] ²⁺ 2ClO ₄ ⁻ ·H ₂ O with hydrogen bonding highlighted in red (XXXII , right). Bottom: self-association of two molecules of Ni(dimethyl GBI - H) ₂ with hydrogen bonding interactions highlighted in red	14

1.9	Left: preorganization of hydrogen bond donors to promote dual functionality (hydrogen bonding atoms highlighted in red). Middle: fragment that activates substrate via hydrogen bonding (hydrogen bonding atoms highlighted in red). Right: fragment that creates a compact transition state via hydrogen bonding (hydrogen bonding atom highlighted in red)	19
2.1	Representative crystallographically characterized adducts of urea hydrogen bond donors and Lewis bases.....	22
2.2	Top: preorganization of GBI through chelation. Middle: enantiomers derived by bonding to a ruthenium fragment with two different ligands. Bottom: modularity of the catalyst.....	28
2.3	Top: thermal ellipsoid diagram (50% probability level) of the molecular structure of $3^+ \text{BAR}_f^- \cdot \text{H}_2\text{O}$ and hydrogen bonding between the cation and H_2O molecule (highlighted in red). Bottom: thermal ellipsoid diagram (50% probability level) showing the structure of two independent molecules of $4^+ \text{BAR}_f^- \cdot \text{H}_2\text{O} \cdot (\text{CH}_2\text{Cl}_2)_{0.5}$ and hydrogen bonding between the cations and H_2O molecules (highlighted in red).....	33
2.4	Top: a bromide salt of diprotonated GBI. Bottom: thermal ellipsoid (50% probability level) of two molecules of $[1\text{-H}]^{2+} 2\text{Br}^- \cdot \text{H}_2\text{O}$. Key distances involving hydrogen bonds (Å): H1-O1 1.813, N1-O1 2.693(3), H2-Br1 2.415, N2-Br1 3.265(3), H3-Br2 2.331, N3-Br2 3.207(3), H4A-Br2 3.081, N4-Br2 3.759(3).....	36
2.5	^1H NMR spectra (rt, 500 Hz, CD_2Cl_2): $9^+ \text{BAR}_f^- \cdot 2\text{H}_2\text{O}$ (bottom); after addition of 0.5 equiv of 10a (middle); after addition of 1.0 equiv of 10a (top). Key downfield shifted NMR signals (δ , bottom, middle, top, $\Delta(\delta_{\text{top}} - \delta_{\text{bottom}})$): -NH 9.21, 9.53, 10.10, 0.89; -NH 8.19, 8.46, 8.69, 0.50; -NH 4.92, 5.02, 5.19, 0.27. Key upfield shifted NMR signals (δ , bottom, middle, top, $\Delta(\delta_{\text{top}} - \delta_{\text{bottom}})$): -NH 5.41, 5.37, 5.30, -0.11; H_2O 2.23, 2.14, 1.99, -0.24.....	45
2.6	^1H NMR spectra of 9^+Cl^- (300 MHz, CDCl_3) before (top) and after (below) the addition of CD_3OD (6 equiv).....	46
2.7	Rate profiles for the condensation of 5b (2.0 equiv) and 6 (1.0 equiv) with different catalysts (10 mol%, rt, selected reactions from Table 2.9): (♦) 9^+BAR_f^- (■) 9^+PF_6^- (◆) 8^+BAR_f^-	50

2.8	Left: proposed preorganization of 1^+ BAr_f^- (red), <i>synperiplanar</i> NH donor sites (D) (blue). Right: equilibrium involving 2^+ BAr_f^-	52
2.9	Thermal ellipsoid diagram (50% probability level) of the molecular structure of 8^+ $\text{BAr}_f^- \cdot \text{CH}_2\text{Cl}_2$ with the solvate molecule omitted.....	53
2.10	Topicities of indenyl protons in XLVIII and IL , and consequences for ^1H NMR spectra.....	55
2.11	^1H NMR spectra (rt, 300 MHz, CD_2Cl_2) of 9^+ BAr_f^- before (above) after addition of 1 equiv. of 6 (below), and some possible structures of the adduct 9^+ BAr_f^-	56
3.1	Top: GBI derivatives and their metal complexes. Bottom: Takemoto's famous thiourea based dual hydrogen bond donor bifunctional catalyst (left), conceptually analogous bifunctional GBI (right)	78
3.2	Top: thermal ellipsoid diagram (50% probability level) of the molecular structure of $(R_{\text{Ru}}R_{\text{C}}R_{\text{C}})\text{-18c}^+$ (Δ)- $\text{TRISPHAT}^- \cdot \text{CHCl}_3$ with the solvate molecule omitted. Bottom: alternative view of the cation. Key distances involving hydrogen bonds (\AA): H10-O3 2.23, N10-O3 3.030(6), H10-O5 2.40, N10-O5 3.078(6), H13-O5 2.29, N13-O5 3.072(6), N20-H13 2.21, N20-N13 2.721	88
3.3	Top: thermal ellipsoid diagram (50% probability level) of the molecular structure of $(R_{\text{Ru}}R_{\text{C}}R_{\text{C}}/S_{\text{Ru}}R_{\text{C}}R_{\text{C}})\text{-18c}^+$ (Δ/Λ)- $\text{TRISPHAT}^- \cdot (\text{Et}_2\text{O})_2$ with solvate molecules omitted. Bottom: alternative views of each diastereomeric cation. Key distances involving hydrogen bonds (\AA): $(S_{\text{Ru}}R_{\text{C}}R_{\text{C}})\text{-18c}^+$, H10-N20 1.72, N10-N20, 2.584; $(R_{\text{Ru}}R_{\text{C}}R_{\text{C}})\text{-18c}^+$, H10-N20 1.77, N10-N20, 2.609.....	91
3.4	CD spectra of $(R_{\text{Ru}}R_{\text{C}}R_{\text{C}})\text{-18c}^+$ PF_6^- (blue trace) and $(S_{\text{Ru}}R_{\text{C}}R_{\text{C}})\text{-18c}^+$ PF_6^- (red trace) in CH_3CN	92
3.5	Rate profiles for condensations of malonate esters (1.8 equiv) and 6 (1.0 equiv) with different catalysts under conditions similar to Table 3.4 (10 mol%, rt, ca. 25% more dilute). Data for dimethyl malonate: (■) $(S_{\text{Ru}}R_{\text{C}}R_{\text{C}})\text{-18c}^+$ PF_6^- ; (■) $(R_{\text{Ru}}R_{\text{C}}R_{\text{C}})\text{-18c}^+$ PF_6^- . Data for diethyl	

malonate: (▲) ($S_{Ru}R_C R_C$)- 18c ⁺ PF ₆ ⁻ ; (▲) ($R_{Ru}R_C R_C$)- 18c ⁺ PF ₆ ⁻ ; (▲) ($R_C R_C$)- 16c . Data for diisopropyl malonate: (◆) ($S_{Ru}R_C R_C$)- 18c ⁺ PF ₆ ⁻ ; (◆) ($R_{Ru}R_C R_C$)- 18c ⁺ PF ₆ ⁻ ; (◆) ($R_C R_C$)- 16c	98
3.6 Other chiral hydrogen bond donors that catalyze highly enantioselective additions to 6 by 10b (XII, LXVI-LXVIII) or 10a (LXIX).....	106
3.7 Transition state assemblies. Top: proposed models for additions of malonate esters to 6 catalyzed by the bifunctional thiourea XII . Bottom: analogous models for the bifunctional ruthenium catalysts used in this chapter	108
4.1 Specific aim of this chapter: does modification of the cyclopentadienyl ligand of 9 ⁺ X ⁻ to a pentaphenylcyclopentadienyl ligand lead to a more easily resolved cation and an effective enantioselective catalyst?	140
4.2 Partial NMR spectra (CD ₂ Cl ₂): (a) ¹ H (500 MHz), mixture of (R_{Ru})- 48 ⁺ (<i>P</i>)-Phos ⁻ and (S_{Ru})- 48 ⁺ (<i>P</i>)-Phos ⁻ ; (b) ¹ H (500 MHz), (S_{Ru})- 48 ⁺ (<i>P</i>)-Phos ⁻ as a toluene solvate per text and experimental section; (c) (inset) downfield NH signals for (a) and (b); (d) ¹³ C{ ¹ H} (125 MHz), mixture of (R_{Ru})- 48 ⁺ (<i>P</i>)-Phos ⁻ and (S_{Ru})- 48 ⁺ (<i>P</i>)-Phos ⁻ ; (e) ¹³ C{ ¹ H} (125 MHz), (S_{Ru})- 48 ⁺ (<i>P</i>)-Phos ⁻ as a toluene solvate per text and experimental section.....	150
4.3 (a) CD spectrum of (S_{Ru})- 48 ⁺ BAr _f ⁻ (red trace) in CH ₃ CN. (b) CD spectra of ($R_{Ru}R_C R_C$)- 18c ⁺ PF ₆ ⁻ (blue trace) and ($S_{Ru}R_C R_C$)- 18c ⁺ PF ₆ ⁻ (red trace) in CH ₃ CN	151
4.4 ¹³ C{ ¹ H} NMR spectra (125 MHz): 48 ⁺ BAr _f ⁻ in CD ₂ Cl ₂ (bottom, red), 48 ⁺ PF ₆ ⁻ in CD ₂ Cl ₂ (middle, green), 49 in CDCl ₃ /CD ₃ OD (top, blue), and insets showing the <i>i</i> -C _{Ph} , <i>o</i> -C _{Ph} , <i>m</i> -C _{Ph} , <i>p</i> -C _{Ph} , and CO signals	153
4.5 Thermal ellipsoid diagram (50% probability level) showing the structure of two molecules of 48 ⁺ PF ₆ ⁻ ·(C ₅ H ₁₂) _{1.5} with solvate molecules omitted and hydrogen bonding between cations and anions. Hydrogen bonding distances of < 2.5 (Å) (in red), 2.5 - 3.2 (Å) (in cyan), and 3.2 - 4.0 (Å) (in magenta)	156

4.6	Thermal ellipsoid diagram (50% probability level) showing the structure of 48 ⁺ BAr _f ⁻ ·H ₂ O and hydrogen bonding between cation and solvent. Hydrogen bonding distances of < 2.5 (Å) (in red) and 3.2 - 4.0 (Å) (in magenta).....	160
4.7	Overlay of the cations of 48 ⁺ PF ₆ ⁻ ·(C ₅ H ₁₂) _{1.5} (in red), and 48 ⁺ BAr _f ⁻ ·H ₂ O (in blue); key -NH groups are shown in white	161
4.8	Thermal ellipsoid diagram (50% probability level) showing the structure of 49	163
4.9	Overlay of the cations of 48 ⁺ PF ₆ ⁻ ·(C ₅ H ₁₂) _{1.5} (in red), and the neutral complex 49 (in green); key -NH groups are shown in white	163
4.10	¹ H NMR spectra (rt, 500 Hz, CD ₂ Cl ₂): 48 ⁺ BAr _f ⁻ ·4H ₂ O (bottom); after addition of 0.5 equiv of 10a (middle); after addition of 1.0 equiv of 10a (top). Key downfield shifted NMR signals (δ, bottom, middle, top, Δ(δ _{top} -δ _{bottom})): -NH 9.42 , 10.20 , 10.50 , 1.08; -NH 8.29 , 8.67 , 8.81 , 0.52; -NH 5.04 , 5.27 , 5.36 , 0.32. Key upfield shifted NMR signals (δ, bottom, middle, top, Δ(δ _{top} -δ _{bottom})): -NH 5.13 , 5.01 , 4.98 , -0.15; H ₂ O 1.77 , 1.66 , 1.61 , -0.16.....	165
4.11	Rationale behind choosing 50 as the hydrogen bond acceptor (top); two conformations around the C=C-C=O single bond are shown (middle); the <i>s-trans</i> conformation results in A ^{1,3} strain with a strain energy of ca. 4.5 kcal/mol (bottom, box). ¹⁷⁴	173
4.12	Transition state model for rationalizing the extremely high enantioselectivity.....	174
4.13	Representation of 52 as the hydrogen bond acceptor (top); two conformations around the C=C-C=O single bond are shown (middle); <i>s-trans</i> and <i>s-cis</i> conformations both encounter A ^{1,3} strain (bottom, box)...	174
4.14	Deprotonated neutral complex (LXXIX) capable of acting as a base and hydrogen bond donor	177
5.1	Transition state assemblies. Activation models for ruthenium based organometallic hydrogen bond donor catalysts described in this thesis	198

LIST OF SCHEMES

SCHEME	Page
1.1 Accelerated Claisen rearrangement in the presence of urea IIa	2
1.2 Hydrogen bonding induced self assembly of monodentate to bidentate ligands for metal complexes.....	7
1.3 Possible tautomers of GBI . Potential hydrogen bond donors (highlighted in blue) and hydrogen bond acceptors (highlighted in black). The benzimidazole and guanidine moieties are depicted in green and red	9
1.4 Representative deprotonations of GBI to give GBI_H and then metal complexes (XXIVa/b).....	10
1.5 Degenerate tautomeric (HN3/HN5) and conformational (C2-N2) equilibrium transposing the DAD triad of GBI	11
1.6 Representative prototropic equilibria involving the GBI ligand of a chelate complex.....	15
1.7 Preorganization effects in binding of Li ⁺ to cyclic polyether hosts.....	16
1.8 Example of a template synthesis by Stoddart.....	17
1.9 Synthesis of a rotaxane by the Gladysz group	18
1.10 Top: preorganizing GBI through chelation. Bottom: enantiomers derived by bonding to a metal fragment with two different ligands	20
2.1 Diels-Alder reactions catalyzed by thiourea derivatives, their relative rates, and proposed models (XLIIIa,b)	24
2.2 Top: possible tautomers of GBI . Potential hydrogen bond donors (highlighted in blue) and hydrogen bond acceptors (highlighted in black). The benzimidazole and guanidine moieties are depicted in green and red. Bottom: degenerate tautomeric (HN3/HN5) and conformational (C2-N2) equilibrium transposing the DAD triad of GBI	25

2.3	Correlation of catalytic activity and pK_a for a few thiourea based hydrogen bond donor catalysts.....	26
2.4	Chiral tin- GBI chelate complex catalyzed addition of nitrocyclohexane to 2-cyclohexen-1-one.....	27
2.5	Top: syntheses of cationic GBI derivatives 1^+ BAr_f^- and 2^+ BAr_f^- . Bottom: other relevant derivatives; cationic guanidine derivative, 3^+ BAr_f^- (red), cationic 2-aminobenzimidazole derivative, 4^+ BAr_f^- (blue).....	30
2.6	Syntheses of cyclopentadienyl ruthenium GBI complexes	41
2.7	Representative prototropic equilibria involving the GBI ligand of the chelate complex 9^+ X^-	47
2.8	Top: two step exchange of the achiral anion in 9^+ Cl^- by a chiral anion. Bottom: the cyclopentadienyl 1H NMR signal of 9^+ (<i>P</i>)-Phos $^-$ (CD_2Cl_2 , 500 MHz)	48
3.1	Synthesis of intermediate $13-H^+$ I^- and its use towards the syntheses of achiral/chiral substituted GBI ligands.....	80
3.2	Syntheses of ruthenium chelate complexes of substituted GBI ligands	82
3.3	Separation and epimerization of the diastereomers of $18c^+$ PF_6^-	83
3.4	Plausible pathway for the inversion of the ruthenium center in Scheme 3.3.....	85
4.1	Top: <i>P</i> and <i>M</i> descriptors for an axial chiral phosphoric acid. Bottom: resolution of a chiral amino acid using an enantiopure phosphoric acid ...	138
4.2	Resolution of neutral gold species using a silver salt of an enantiopure phosphoric acid ((<i>P</i>)- LXXIV)	139
4.3	Synthesis of a ruthenium pentaphenylcyclopentadienyl complex (42) from 2,3,4,5-tetraphenylcyclopentadienone (45)	142
4.4	Syntheses of pentaphenylcyclopentadienyl ruthenium GBI complexes....	143

4.5	Resolution of a chiral-at-metal ruthenium complex with enantiopure (<i>P</i>)- 12	148
4.6	Strategic aspects of the application of the neutral ruthenium complex 49 in catalysis	176

LIST OF TABLES

TABLE	Page
2.1 Summary of crystallographic data. ^a	32
2.2 Key bond lengths [Å], bond angles [°], and torsion angles [°] for 3 ⁺ BAr _f ⁻ ·H ₂ O. ^a	34
2.3 Key bond lengths [Å], bond angles [°], and torsion angles [°] for 4 ⁺ BAr _f ⁻ ·H ₂ O·(CH ₂ Cl ₂) _{0.5} . ^a	35
2.4 Key bond lengths [Å], bond angles [°], and torsion angles [°] for [1-H] ²⁺ 2Br ⁻ ·2H ₂ O. ^a	37
2.5 Friedel-Crafts alkylation of 5a by 6 . ^a	38
2.6 NH ¹ H NMR signals of 8-9 ⁺ X ⁻ (δ). ^a	42
2.7 ¹³ C{ ¹ H} NMR signals of the GBI ligand in 8-9 ⁺ X ⁻ (δ). ^a	42
2.8 C ₅ H ₅ ¹ H NMR signals of 8-9 ⁺ X ⁻ , ^a and IR ν _{CO} values (brackets) ^b for 9 ⁺ X ⁻	43
2.9 Friedel-Crafts alkylation of 5a or 5b by 6 . ^a	49
3.1 Epimerization data for the diastereomers of 18c ⁺ PF ₆ ⁻	86
3.2 Key bond lengths [Å], bond angles [°], and torsion angles [°] for (<i>R</i> _{Ru} <i>R</i> _C <i>R</i> _C)- 18c ⁺ (Δ)-TRISPHAT ⁻ ·CHCl ₃ and (<i>R</i> _{Ru} <i>R</i> _C <i>R</i> _C / <i>S</i> _{Ru} <i>R</i> _C <i>R</i> _C)- 18c ⁺ (Δ/Λ)-TRISPHAT ⁻ ·(Et ₂ O) ₂ . ^a	89
3.3 Friedel-Crafts alkylation of 5a or 5b with 6 catalyzed by (<i>S</i> _{Ru} <i>R</i> _C <i>R</i> _C)- 18c ⁺ PF ₆ ⁻ . ^{a,b}	94

3.4	Yields and ee values for the additions of dialkyl malonates to nitroalkenes catalyzed by the diastereomers of 18c ⁺ PF ₆ ⁻ . ^{a,b}	97
3.5	Yields and ee value for the additions of Michael donors to 6 catalyzed by 18c ⁺ PF ₆ ⁻ . ^{a,b}	99
3.6	Yields and ee values for the additions of 22 to dialkyl azodicarboxylates catalyzed by 18c ⁺ PF ₆ ⁻ . ^{a,b}	102
4.1	NH ¹ H NMR signals of 48 ⁺ X ⁻ and 49 (δ). ^a	144
4.2	¹³ C{ ¹ H} NMR signals of the GBI ligand in 48 ⁺ X ⁻ and 49 (δ). ^a	145
4.3	¹³ C{ ¹ H} NMR chemical shifts of the CO and pentaphenylcyclopentadienyl ligands (δ) of 48 ⁺ X ⁻ and 49 . ^a	146
4.4	¹³ C{ ¹ H} NMR chemical shifts of the CO ligand (δ) and IR ν _{CO} values (cm ⁻¹) for 48 ⁺ X ⁻ , 49 , 9 ⁺ X ⁻ , and 11 . ^a	147
4.5	Summary of crystallographic data. ^a	155
4.6	Key bond lengths [Å], bond angles [°], and torsion angles [°] for 48 ⁺ PF ₆ ⁻ ·(C ₅ H ₁₂) _{1.5} , 48 ⁺ BAr _f ⁻ ·H ₂ O, and 49 . ^{a,b}	157
4.7	Selected F···H, P···N, and F···N distances [Å] in 48 ⁺ PF ₆ ⁻ ·(C ₅ H ₁₂) _{1.5} . ^{a,b}	159
4.8	Selected O···H and O···N distances [Å] in 48 ⁺ BAr _f ⁻ ·H ₂ O. ^{a,b}	160
4.9	Yields and ee values for Friedel-Crafts alkylations ^a and Michael addition reactions ^b catalyzed by (S _{Ru})- 48 ⁺ BAr _f ⁻ . ^c	167
4.10	Yields and ee values for the additions of 28 to 50 or 52 catalyzed by (S _{Ru})- 48 ⁺ BAr _f ⁻ . ^{a,b}	169
4.11	Isolated yields for the addition of Michael donors to 6 catalyzed by 49 . ^{a,b}	170

1. INTRODUCTION: SECOND COORDINATION SPHERE PROMOTED CATALYSIS

1.1 Hydrogen bonding and its applications

Non-covalent interactions such as hydrogen bonding¹ play a crucial role in our existence. Two prominent examples out of many include the double helical structure of DNA² and the unique colligative properties of H₂O.^{1a} The strengths of hydrogen bonds span more than two orders of magnitude (0.2-40 kcal mol⁻¹)^{1b} and nature has ubiquitously exploited them for molecular recognition and tuning reactivity.³ The first mention of hydrogen bonding as some unexplained interaction dates back to 1913 when Moore and Winmill studied the ionization of aqueous solutions of primary, secondary, and tertiary amines and quaternary ammonium salts.⁴ Since then the understanding of hydrogen bonding has inspired chemists to apply these interactions for diverse purposes.⁵⁻⁹

1.1.1 Hydrogen bonding in Organocatalysis

From an application standpoint, hydrogen bonding has been explored as an architectural unit for supramolecular assembly and host-guest interactions.⁵⁻⁹ Macromolecules that mimic enzyme binding sites have shown the capability to catalyze numerous organic transformations aided by hydrogen bonding from peptidic NH or OH linkages.³ Later, Etter with her pioneering work on hydrogen bonding motifs of ureas in the solid state (Figure 1.1)¹⁰ and Curran with his solution studies with thioureas (Scheme 1.1)¹¹ laid the foundation for small molecule hydrogen bonding promoted

catalysis. These molecules are often termed as "organocatalysts".¹²

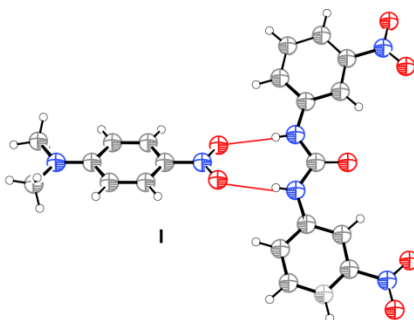
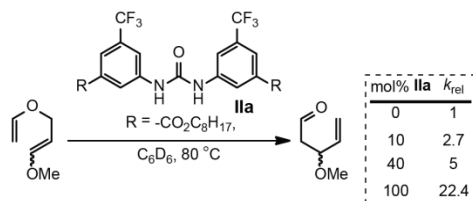


Figure 1.1 The 1:1 complex (I) of 1,2-bis(*m*-nitrophenyl)urea and *N,N*-dimethyl-*p*-nitroaniline with hydrogen bonding (highlighted in red).



Scheme 1.1 Accelerated Claisen rearrangement in the presence of urea IIa.

Soon, this new field of catalysis exploded with chiral molecules capable of hydrogen bond donation. A plethora of enantioselective and/or diastereoselective transformations were shown to take place with this new kind of catalytic activation. Though thiourea and urea derivatives (thiourea, **III**, urea, **II**)¹³ were the first to be developed, many other backbones like guanidine (**IV**), TADDOL (**V**), BAMOL (**VI**), BINOL (**VII**), amidinium ions (**VIII**), squaramide (**IX**), and silanediols (**X**) emerged soon thereafter.¹³⁻²⁰ Some representative catalysts are shown in Figure 1.2 (left). They can have one or more hydrogen bond donor sites. The systems shown in Figure 1.2 are the most typical. Achiral analogs can participate in a dual hydrogen bonding motif as

illustrated for ketones in **XIa** (Figure 1.2, right). These activate the carbonyl carbon towards nucleophilic attack. With a chiral catalyst and an unsymmetrical ketone, the host-guest interaction creates two diastereotopic C=O faces as illustrated in **XIb** (Figure 1.2, right). Subsequent reactions with nucleophiles can lead to enantioenriched products.

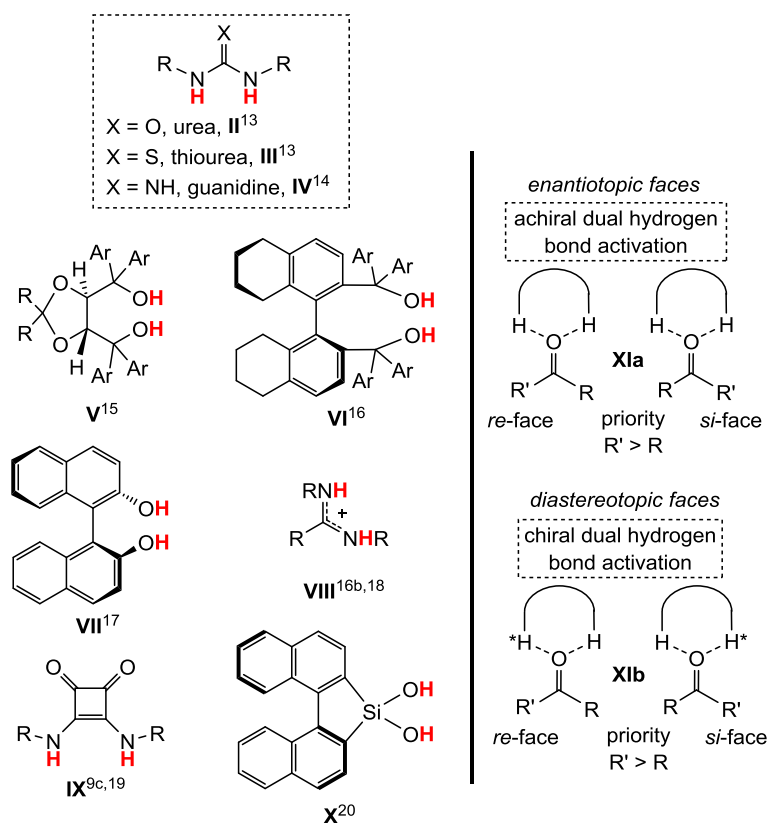


Figure 1.2 Left: representative, previously reported, DD type hydrogen bond donor catalysts (participating hydrogen atoms in red). Right: activation of carbonyl compounds by dual (chiral/achiral) hydrogen bond donors.

Enantiopure catalysts with auxiliary functionality have subsequently been developed. These new multifunctional hydrogen bond donors, **XII-XIV²¹⁻²³** (Figure 1.3, top), expanded the range of successfully catalyzed organic transformations. The Michael

addition reaction has seen particular emphasis. Plausible transition state assemblies for the **XII**-catalyzed addition of dialkyl malonates to *trans*- β -nitrostyrene have been shown in Figure 1.3 (bottom). The reason for the enantioenrichment was originally explained based on the model **XVa** (Figure 1.3, bottom box).^{21b} Computationally, **XVb** was subsequently proposed as a transition state assembly for a similar reaction.^{21c} This kind of system was first explored explicitly by Takemoto.^{8g,21} Subsequently, other types of NH containing bifunctional hydrogen bond donors were developed (selected examples include **XIII-XIV**, basic moiety **N**). All of these systems were extended to other types of asymmetric organic transformations.^{8g,13-19}

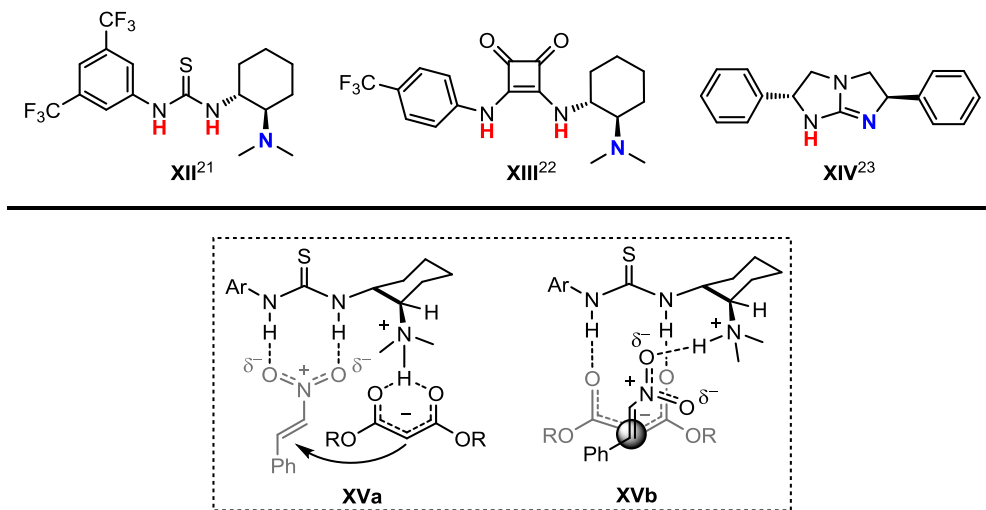


Figure 1.3 Top: representative bifunctional hydrogen bond donors used in enantioselective catalysis. Bottom: transition state assemblies for the Michael addition of a dialkyl malonate to *trans*- β -nitrostyrene catalyzed by **XII**.

1.1.2 Hydrogen bonding in the "Second Coordination Sphere"

Examples of hydrogen bonding in inorganic molecules include H₂O and NH₃.

Because H₂O is a liquid, periodic trends predict that H₂S should be a liquid. Similarly, periodic trends predict that PH₃ should have a higher boiling point than NH₃. In reality, H₂S is a gas and NH₃ has a higher boiling point than PH₃. Only hydrogen bonding interactions can explain these anomalies. These interactions are not present in H₂S and PH₃.

Hydrogen atoms directly linked to metals (M-H) can participate in hydrogen bonding. The M-H moiety usually acts as a hydrogen bond donor, as shown in **XVI** (Figure 1.4, left (top)).²⁴ Also the metal itself sometimes can act as a hydrogen bond acceptor as illustrated in **XVII** (Figure 1.4 left (bottom)).²⁵

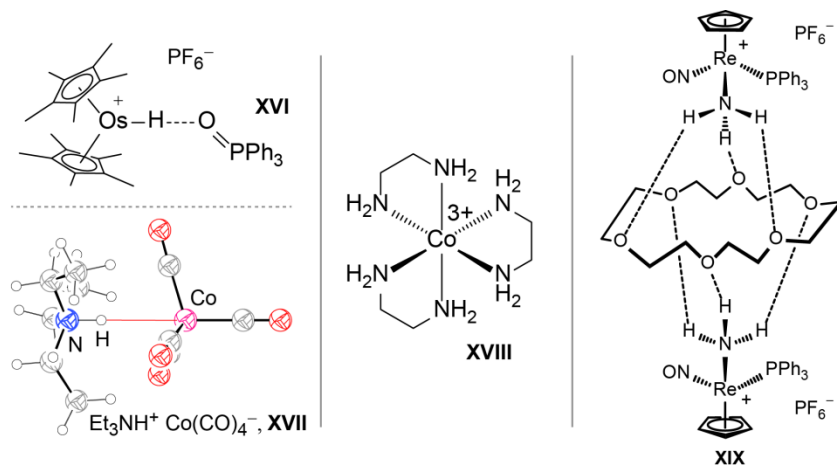


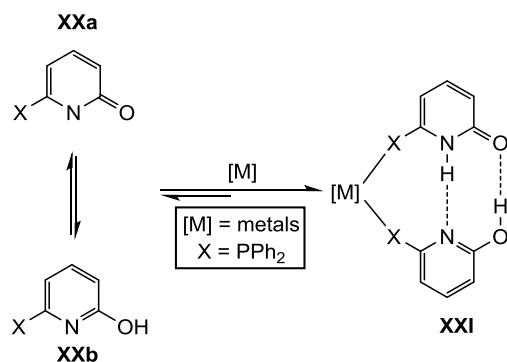
Figure 1.4 Left: spectroscopically detected hydrogen bonding between cation (Cp*)₂OsH⁺ and OPPh₃ (**XVI**, top) and crystal structure of Et₃NH⁺ Co(CO)₄⁻ with hydrogen bonding highlighted in red (**XVII**, bottom). Middle: [Co(en)₃]³⁺ trication (**XVIII**). Right: previously characterized 2:1 adduct of a rhenium ammonia complex and 18-crown-6 (**XIX**).

Similarly, hydrogen atoms not directly attached to the metal center (remote) can also participate in hydrogen bonding, either intermolecularly or intramolecularly. Numerous examples of such hydrogen bonding are evident in the crystal structures of

inorganic complexes. A simple and readily available cobalt trication,²⁶ $[\text{Co}(\text{en})_3]^{3+}$ with three 1,2-ethylenediamine ligands, **XVIII** (Figure 1.4, right), can be found in 115 crystal structures in the Cambridge Crystallographic Data Centre (survey on February 2015).²⁷ The trication is "chiral-at-metal" and can be separated into enantiomers using the tartrate anion. Hydrogen bonding plays an important role in the resolution.²⁸

In these systems, the hydrogen atoms attached to nitrogen atoms are a part of the second coordination sphere. These hydrogen atoms act as donors and bind to suitable heteroatoms either intermolecularly or intramolecularly. These bonding interactions also involve anions or solvent molecules, which are evident in their crystal structures.^{27b} Indeed, such interactions have been utilized in inorganic crystal engineering.²⁹ A variety of metal-ammonia complexes $[\text{L}_y\text{MNH}_3]^{z+}$ ($z = 0, 1$) have been found to afford stable adducts with crown ethers, both in solution and the solid state.^{30,31} One example is shown as **XIX** (Figure 1.4, right).³¹

Breit and Reek separately have shown (Scheme 1.2) that self-assembly of a monodentate ligand (**XX**) to a bidentate ligand can be achieved *in situ* with the aid of hydrogen bonding.^{32,33} This self assembled adduct behaves similarly to a chelating ligand and forms complexes of the type **XXI**. Similar covalently linked structures are difficult to obtain. Thus, the self-assembly approach simplifies ligand syntheses. An added benefit is the possibility of generating combinatorial libraries of bidentate ligands through the simple mixing of suitably functionalized monodentate precursors.^{32f,g}



Scheme 1.2 Hydrogen bonding induced self assembly of monodentate to bidentate ligands for metal complexes.

Reactions involving atoms directly connected to the metal center represent first coordination sphere interactions. Participating atoms remote from the metal center constitute second coordination sphere interactions. A classic example in which both first and second coordination sphere interactions are involved features Noyori's ketone hydrogenation catalyst (transition state assembly **XXII**, Figure 1.5, left).³⁴ Here, the ruthenium hydride moiety (Ru-H) is interacting with the carbonyl carbon in the first coordination sphere (Figure 1.5, right (blue)). A remote NH is interacting via hydrogen bonding to the carbonyl oxygen in the second coordination sphere (Figure 1.5, right (red)).

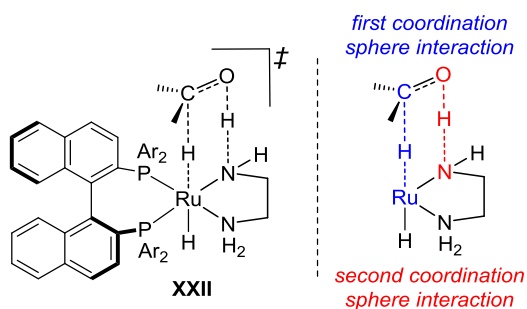


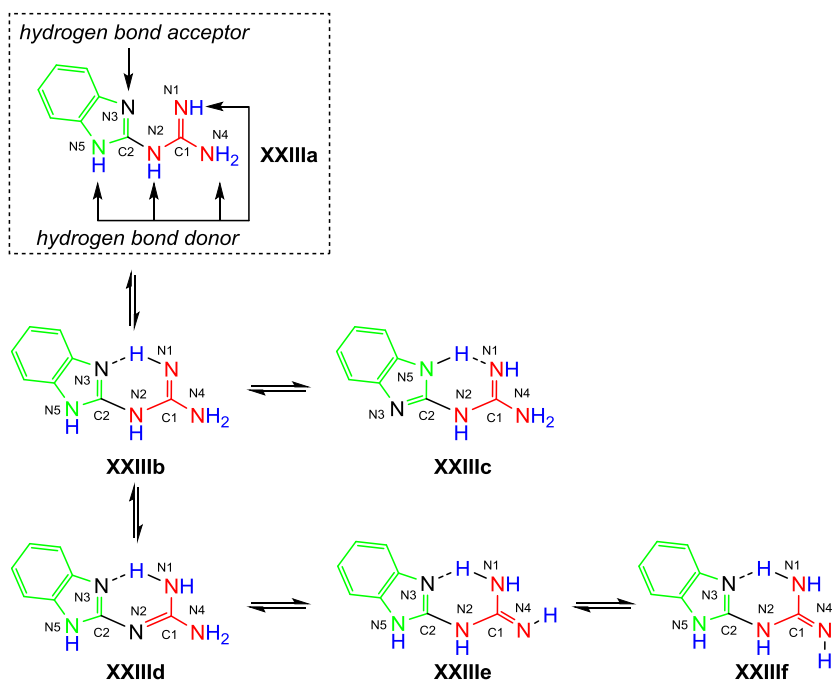
Figure 1.5 Proposed transition state assembly for a ketone hydrogenation catalyst of Noyori.

1.2 2-Guanidinobenzimidazole: an overlooked hydrogen bond donor

1.2.1 Why 2-Guanidinobenzimidazole?

An inexpensive and readily available nitrogen heterocycle, 2-guanidinobenzimidazole (**GBI**), has been extensively studied.³⁵ **GBI** has five N-H bonds (Scheme 1.3, blue) capable of hydrogen bonding as evident from the crystal structures of **GBI**, **GBI**/crown ether adducts, and **GBI**/aza crown ether adducts.^{36,37} Its structure has been thoroughly characterized both in solution³⁵ and in the solid state.³⁶⁻³⁸ As depicted in Scheme 1.3, it consists of guanidine (red) and benzimidazole (green) fragments. Like the constituent fragments, it also exhibits some biological activity.^{35c} Similar to **GBI**, various derivatives have also been studied both in solution and the solid state.^{35a,39}

The **GBI** molecule can in theory exist as a number of different tautomeric structures stabilized by intramolecular and intermolecular hydrogen bonding.^{35a,c} The tautomers **XXIIIa-f** are depicted in Scheme 1.3. The atom numbering system commonly employed is also illustrated. In most tautomers, N5, N2, and N4 feature N-H bonds.

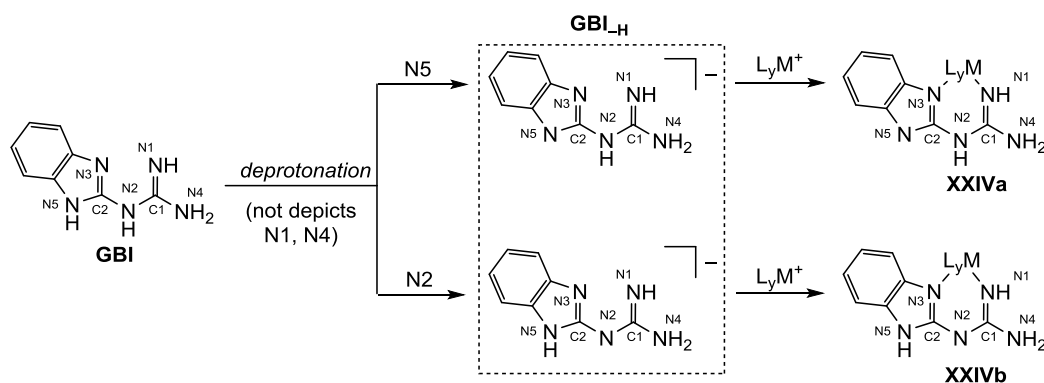


Scheme 1.3 Possible tautomers of **GBI**. Potential hydrogen bond donors (highlighted in blue) and hydrogen bond acceptors (highlighted in black). The benzimidazole and guanidine moieties are depicted in green and red.

Many planar nitrogen heterocycles with functionality arrays that can participate in hydrogen bond donor/acceptor host-guest interactions are known. It is common to indicate *synperiplanar* acceptor (A) and donor (D) sites of the heterocycle by a linear sequence of letters (e.g. DDADA). Complementary partners for host-guest interactions would have the opposite sequence of letters.

Some molecules can be self-complementary whereas others interact with complementary partners. The D and A sites in **GBI** are shown in Scheme 1.3. Having both donor and acceptor sites within the same molecule makes **GBI** interesting for solution and solid state studies. Furthermore, due to the five atom array **N1=C1-N2-C2=N3**, **GBI** can serve as a chelating ligand akin to acetylacetonate (acac). Many metal or main group element chelated complexes of **GBI** featuring six membered rings have been prepared and studied.^{35,39c,40}

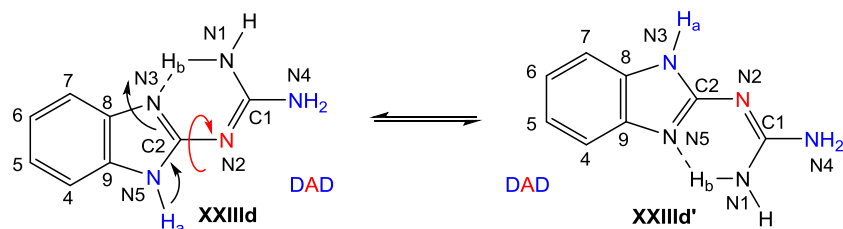
One would expect the five NH protons on **GBI** to exhibit comparable acidities, and several tautomers would be possible for the conjugate base **GBI_{-H}**.²⁶ Two such anions are depicted in Scheme 1.4, together with chelate complexes derived from a cationic metal fragment L_yM^+ (**XXIVa/b**).



Scheme 1.4 Representative deprotonations of **GBI** to give **GBI_{-H}** and then metal complexes (**XXIVa/b**).

1.2.2 **GBI** in solution and the solid state

GBI can exhibit different tautomeric forms stabilized by intramolecular and intermolecular hydrogen bonding.^{35a,c} Consider the tautomer **XXIII_d** from Scheme 1.3, which is believed to dominate in solution.^{35c} It is redrawn in Scheme 1.5 together with the degenerate structure **XXIII_{d'}**. These are interconvertible by a proton transfer from N5 to N3 and a subsequent 180° C2-N2 bond rotation. There are other C2-N2 rotamers, but those in Scheme 1.5 are distinguished by intramolecular hydrogen bonding. In these two structures **GBI** attains a DAD triad sequence.



Scheme 1.5 Degenerate tautomeric (HN3/HN5) and conformational (C2-N2) equilibrium transposing the DAD triad of **GBI**.

GBI and its derivative, *N*-1*H*-benzimidazol-2-yl-*N'*,*N''*-bis(isopropyl)guanidine, **XXV** (Figure 1.5, left), exhibit a N1-H1...N3 hydrogen bond (Figure 1.6, left (bottom)). Even when the symmetry between N1 and N4 is removed, as in the constitutional isomer *N'*-1*H*-benzimidazole-2-yl-*N,N*-bis(isopropyl)guanidine, **XXVI** (Figure 1.6, right), a similar N1-H1...N3 linkage is observed (Figure 1.6, right (bottom)).^{39b} In both the examples in Figure 1.6, the heterocycle presents a DA dyad sequence.^{39b} The hydrogen atom or lone pair on N4 does not exhibit a *synperiplanar* relationship to N2 lone pair, precluding a triad.

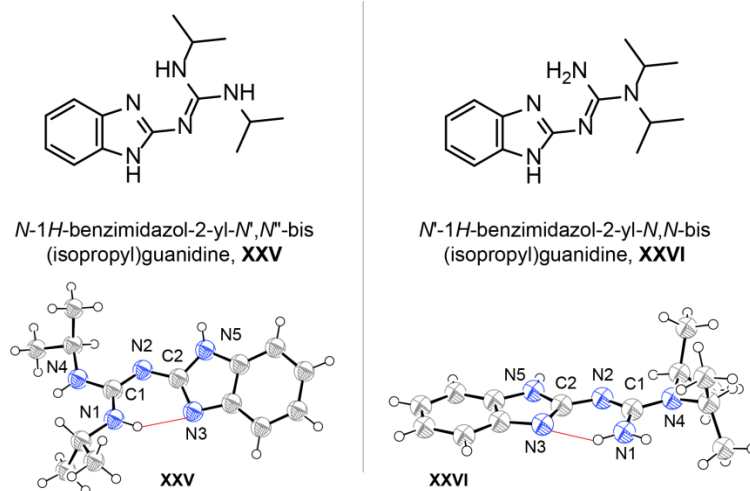


Figure 1.6 Crystal structures of the constitutional isomers **XXV** (left) and **XXVI** (right) with intramolecular hydrogen bonding highlighted in red.

Crystal structures of **GBI**/crown ether adducts^{37a} (Figure 1.7, left) and aza crown ether adducts^{37b} demonstrate that **GBI** molecules form both intramolecular and intermolecular hydrogen bonds. In the **GBI** 18-crown-6 ether complex (**XXVII**), **GBI** is perpendicular to the ether plane and the N4 NH₂ group points towards the cavity of the crown ether. Here, two of the NH units are hydrogen bonded to three oxygen atoms of the ether (cyan). The shortest hydrogen bond was seen in the case of the intramolecular interaction between N3 and H1 (red, < 2 Å). **GBI** exhibits a DAD triad.

In cases of **GBI**-phthalimide³⁸ and **GBI** (derivative)-phthalimide^{39c} complexes, two kinds of structures were obtained. A **GBI** derivative, *N*'-(5,6-dimethyl-1*H*-benzimidazol-2-yl)guanidine (dimethyl**GBI**; **XXVIII**), afforded the 1:1 adduct **XXIX** whereas **GBI** yielded **XXX** (Figure 1.7, middle and right).^{39c} Both of these structures are essentially planar with intramolecular hydrogen bonding between H1 and N3 of **GBI**. The only difference is in the intermolecular hydrogen bonding between N2 and the NH unit of phthalimide. The dimethyl**GBI** triad in **XXIX** exhibits a DAD motif, whereas phthalimide possesses a complementary ADA motif. In contrast, the **GBI** phthalimide adduct (**XXX**) exhibits a linear DDD-AAA arrangement, indicating the transfer of the phthalimide proton to **GBI**, forming a zwitterion. This also reflects the ability of **GBI** to act as a base. The hydrogen bonding distances in **XXX** are shorter than those in **XXIX**.

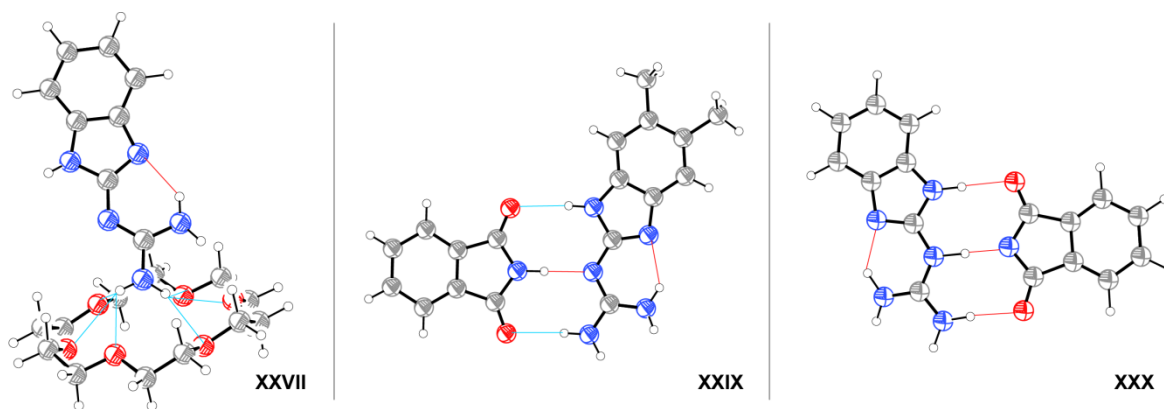


Figure 1.7 Crystal structure of **GBI** 18-crown-6 ether complex (**XXVII**, left), dimethyl**GBI** phthalimide complex (**XXIX**, middle), and **GBI** phthalimide complex (**XXX**, right) with hydrogen bonding distances < 2 Å (highlighted in red) and > 2 Å (highlighted in cyan).

1.2.3 Hydrogen bonding in the second coordination sphere of metal **GBI** complexes

The structures of metal **GBI** complexes have been investigated in solution by NMR and in the solid state by IR spectroscopy and X-ray crystallography.^{35,40a,d} Chelation can be clearly identified by the changes in the IR spectra.^{40a} Some representative neutral and cationic metal complexes of **GBI** are discussed below.

The neutral tetrahedral zinc complex, Zn(**GBI**)Cl₂ (**XXXI**), is seen to participate in intermolecular hydrogen bonding (Figure 1.8, top left).^{40d} The chloride ligand interacts with the H2 and H5 protons of the **GBI** ligand of an adjacent molecule. Similarly, in a hydrated copper salt Cu(**GBI**)²⁺ 2ClO₄⁻·H₂O (**XXXII**), the dication shows hydrogen bonding interactions with H₂O and one perchlorate anion (top right).⁴¹

In all of the examples above, the **GBI** ligand features a DDD triad, which is rare in studies of the free ligand. Thus, the metal can significantly alter the properties of the free ligand. The DDD arrangement can be compared to the DD motif seen in thioureas that have been used as hydrogen bond donor catalysts.^{13b} Similarly, metal **GBI** complexes can potentially act as hydrogen bond donor catalysts.

Interestingly, the crystal structure of a nickel complex (**XXXIII**) derived from deprotonated dimethyl**GBI** (dimethyl**GBI**_{-H})²⁶ revealed two independent structures within the unit cell.^{39c} One is derived from the loss of H5 forming a ADD triad while the other from the loss of H2 forming a DAD triad. The important feature is that two of the molecules with the ADD triad subsequently self assembled via hydrogen bonding as illustrated in Figure 1.8 (bottom). To complement each other, the molecules assemble head to tail leaving the N4 donor NH unbound.

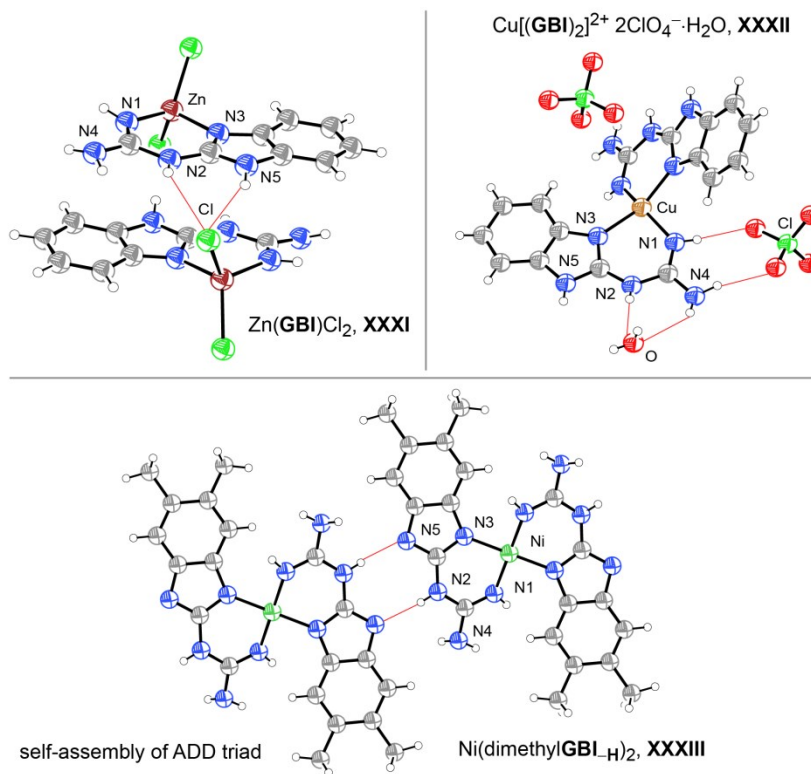
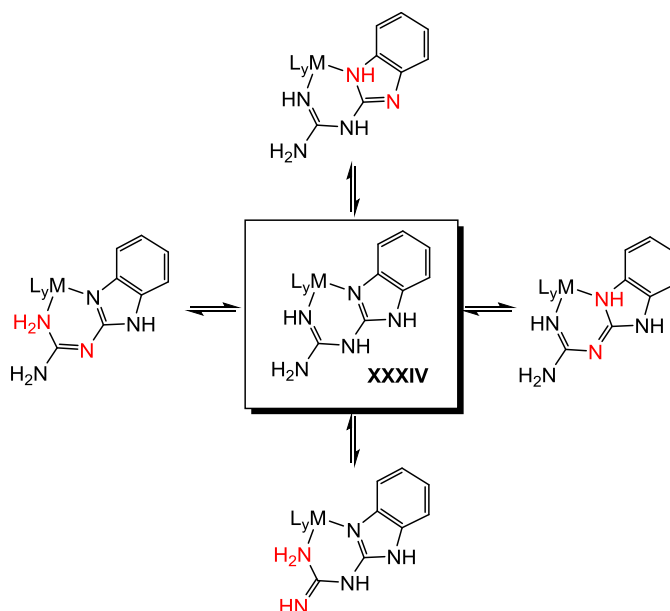


Figure 1.8 Top: crystal structure of two neutral $\text{Zn}(\text{GBI})\text{Cl}_2$ molecules with intermolecular hydrogen bonding highlighted in red (**XXXI**, left), crystal structure of $\text{Cu}[(\text{GBI})_2]^{2+} 2\text{ClO}_4^- \cdot \text{H}_2\text{O}$ with hydrogen bonding highlighted in red (**XXXII**, right). Bottom: self-association of two molecules of $\text{Ni}(\text{dimethylGBI-H})_2$ with hydrogen bonding interactions highlighted in red.

For both **GBI** and **GBI_H** adducts, several tautomers are always possible, any one of which – or as in **XXXIII**, any group of which – can crystallize. The most obvious possibilities for **GBI** complex tautomers are summarized in Scheme 1.6. The central structure, **XXXIV**, represents the motif found most often in the subsequent chapters.



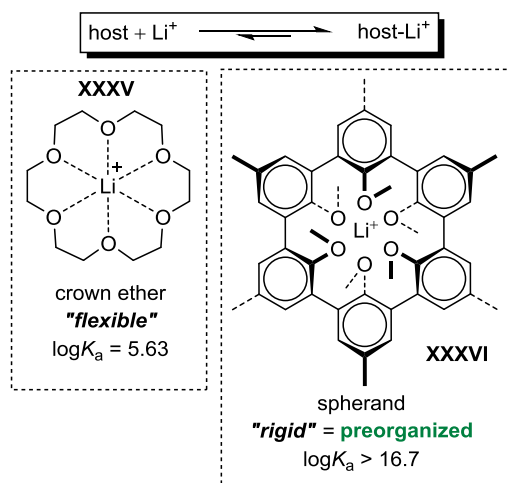
Scheme 1.6 Representative prototropic equilibria involving the **GBI** ligand of a chelate complex.

1.3 Preorganization and hydrogen bonding

1.3.1 Importance of preorganization and some applications

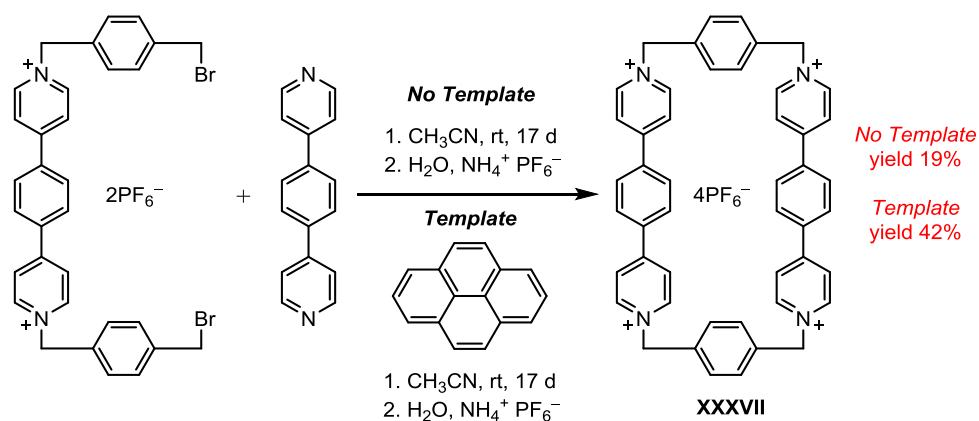
Preorganization is both an important concept and phenomenon in chemistry.⁴² The beneficial effect of preorganization with respect to binding affinities has been demonstrated by Cram for complexes of crown ethers and spherands with cations, as

illustrated for Li^+ in Scheme 1.7.⁴³ For both types of hosts, enhanced nucleophilicities are often observed for the counter anions associated with the cations. This reflects the diminished electrostatic and other interactions and represents one of the many applications of preorganization.



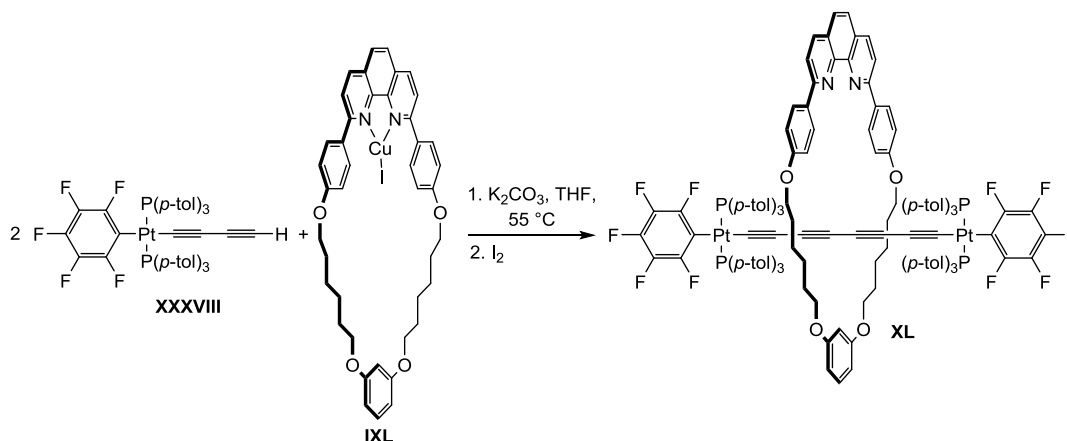
Scheme 1.7 Preorganization effects in binding of Li^+ to cyclic polyether hosts.

In syntheses, *in situ* preorganization has been studied and exploited. It has been used to realize synthetically demanding structures or enhanced selectivities. These are often called template-directed syntheses.⁴⁴ Stoddart has utilized π - π interactions to template the formation of various macrocycles of specific shape and sizes.^{44a,b,45} The reactants are otherwise prone to polymerize (by products) under the reaction conditions. Scheme 1.8 depicts one of many examples in which a pyrene molecule has been used as a template, in this case affording the box-like tetracationic salt **XXXVII**.⁴⁵ Increased yield as compared to the non-template reaction (42% vs. 19%) clearly demonstrates the utility of template-directed syntheses.



Scheme 1.8 Example of a template synthesis by Stoddart.

The Gladysz group had also explored the metal template synthesis of molecular gyroscopes, in which three fold intramolecular ring closing metatheses of alkenes is the key step.⁴⁶ In particular, trigonal planar metal fragments preorganize the alkenes in a favorable conformation for metathesis leading to the desired product over others. Recently, Fujita has shown how TiO₂ nanoparticles with a narrow polydispersity index (PDI = 1.02) can be realized with the aid of a macrocyclic cage he called a spherical coordination template.⁴⁷ He also prepared hollow silica nanoparticles of precise size utilizing a core as a template.⁴⁸ Gladysz, Leigh, and others have shown a metal template approach for synthesizing interlocked molecules better known as rotaxanes and catenanes.⁴⁹ These are designed in such a way that the substrates are forced to react through one another forming the non-covalently interlocked molecule. Scheme 1.9 shows a reaction developed by the Gladysz group in which they couple the axle (**XXXVIII**) through the macrocycle (**IXL**) to form the interlocked molecule, **XL**.



Scheme 1.9 Synthesis of a rotaxane by the Gladysz group.

1.3.2 Preorganization in hydrogen bonding

Both hydrogen bonding and preorganization have been utilized to mutual benefit. Hydrogen bonding has been used to preorganize a compound for a specific purpose^{5b,15,42c,50} while preorganization of a molecule enhances its hydrogen bonding capabilities.^{3a,g,6,51,52} For binding anions, detailed studies have shown that with preorganization, even carbon-hydrogen linkages can efficiently hydrogen bond to anions.^{50e,52}

The Meggers group has made important contributions to the area of preorganized metal containing hydrogen bond donor catalysts, as exemplified by **XLI** in Figure 1.9 (left).⁵³ This chiral-at-metal octahedral iridium(III) cation has been used to chelate a ligand containing a $\text{NH}(\text{C}=\text{CHR})\text{NH}$ moiety (Figure 1.9, middle). The metal has been used to install two additional chelate ligands with hydrogen bond donors in an appropriate orientation to promote the catalytic transformations. One of the chelated ligands acts as the hydrogen bond donor for one of the substrates (Figure 1.9, middle). The other is designed to achieve a compact transition state by bringing the other

substrate in close proximity via hydrogen bonding (Figure 1.9, right). This represents a bifunctional hydrogen bond donor.

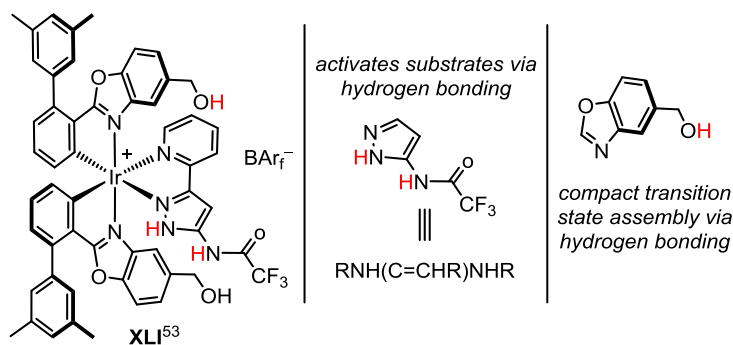
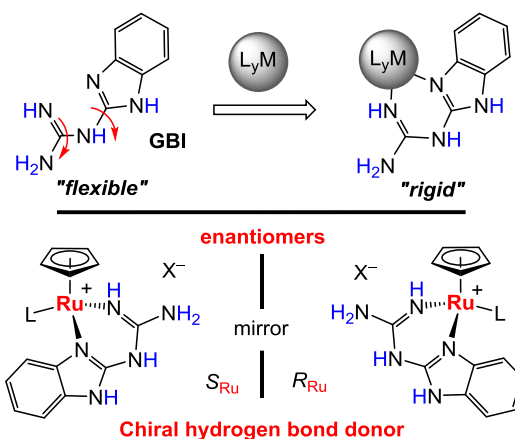


Figure 1.9 Left: preorganization of hydrogen bond donors to promote dual functionality (hydrogen bonding atoms highlighted in red). Middle: fragment that activates substrate via hydrogen bonding (hydrogen bonding atoms highlighted in red). Right: fragment that creates a compact transition state via hydrogen bonding (hydrogen bonding atom highlighted in red).

1.4 Purpose of second coordination sphere promoted catalysis with GBI

Based on the above evidence, **GBI** can be a potent hydrogen bond donor and should be exploitable as a catalyst for simple organic transformations. Towards this end, several questions can be put forward:

- (1) Is **GBI** itself a good hydrogen bond donor catalyst or does one need to preorganize (modify) it (Scheme 1.10, top)?
- (2) Is **GBI** a better catalyst with chelation and second coordination sphere interactions (Scheme 1.10, top)?
- (3) Can one achieve a chiral hydrogen bond donor derived from **GBI** for enantioselective catalysis (Scheme 1.10, bottom)?



Scheme 1.10 Top: preorganizing **GBI** through chelation. Bottom: enantiomers derived by bonding to a metal fragment with two different ligands.

Each of these questions is systematically answered in the following chapters. The results include the syntheses of organometallic and non-metallic **GBI** derivatives and probes of their hydrogen bonding capabilities with organic acceptors. This will be followed by an investigation of their potential as hydrogen bond donor catalysts. Furthermore, enantiopure **GBI** derivatives will be targeted and used as catalysts for highly enantioselective organic transformations. Finally, the concept of second coordination sphere promoted catalysis will be established.

2. MODIFICATION AND APPLICATION OF 2-GUANIDINOBENZIMIDAZOLE FOR SECOND COORDINATION SPHERE PROMOTED CATALYSIS*

2.1 Introduction

2.1.1 Inspiration

The pioneering solid state studies on urea by Etter (see Figure 1.1, chapter 1, and below)¹⁰ laid the foundation for the thiourea based hydrogen bond donor organocatalysis.^{13,54} Similarly, numerous hydrogen bonding interactions of 2-guanidinobenzimidazole (**GBI**) and its derivatives in the solid state (see section 1.2.2, chapter 1)³⁵⁻⁴⁰ inspired me to explore **GBI** as a similar catalyst for hydrogen bond mediated organic transformations.

In this chapter, the capability of **GBI** as a hydrogen bond donor catalyst was initially investigated. Later, problems associated with the system were identified and solutions to the problems were sought. Towards this end, **GBI** was modified. Then, evidence was provided for second coordination sphere hydrogen bonding interactions between organic molecules and the modified compounds. Afterwards, these new compounds were successfully employed as catalysts for hydrogen bond mediated orga-

* Reproduced in part with permission from Scherer, A.; Mukherjee, T.; Hampel, F.; Gladysz, J. A. *Organometallics* **2014**, *33*, 6709-6722. Copyright 2014 American Chemical Society.

nic transformations. The chapter concludes by establishing that these complexes promote organic transformations by second coordination sphere promoted catalysis (SCSPC).

2.1.2 Preorganization and NH acidities

Solid state studies by Etter involving numerous hydrogen bonded 1:1 urea (derivatives) and carbonyl/nitro compound adducts show some interesting features.¹⁰ For example, in the 1:1 urea (derivative)-carbonyl adduct **XLII** (Figure 2.1), the NH protons from urea and the carbonyl oxygen atom are hydrogen bonded to each other. Hydrogen bonding is an interaction between two complementary partners, where one is a donor (D) while the other is an acceptor (A). Here, the NH protons act as hydrogen bond donors (D) and the carbonyl oxygen atom as the acceptor (A). In most of the adducts studied by Etter, two of the NH donor (D) sites in urea attain a *synperiplanar* DD dyad sequence.¹⁰

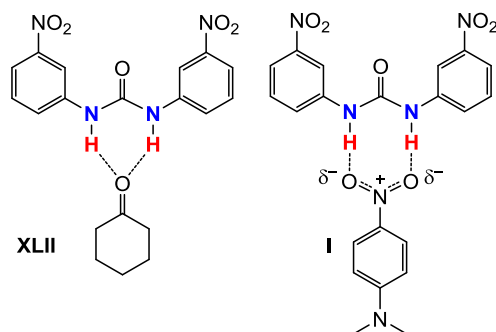
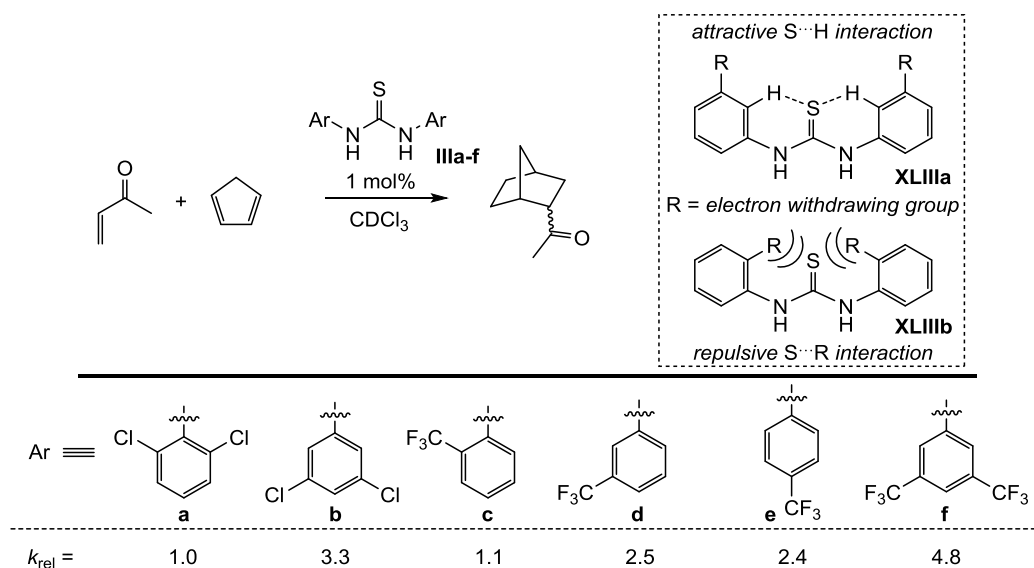


Figure 2.1 Representative crystallographically characterized adducts of urea hydrogen bond donors and Lewis bases.

A similar *synperiplanar* DD dyad sequence is also present in thioureas, and is

responsible for their success as hydrogen bond donor catalysts.^{8e,13a} A modest amount of energy (ca. 7 kcal mol⁻¹) is associated in hydrogen bonding adduct formation between thioureas and carbonyl compounds.^{55,56} On this basis Schreiner predicted that entropic effects could dominate the association constants over the binding enthalpies.⁵⁷ Later, he showed that the strength of this hydrogen bonding interaction depends upon the rigidity of the donor molecule. Finally, he supported the hypothesis by demonstrating that enhanced rigidity increases the efficacy of the catalyst in hydrogen bond donor catalyzed Diels-Alder reaction (Scheme 2.1).⁵⁷

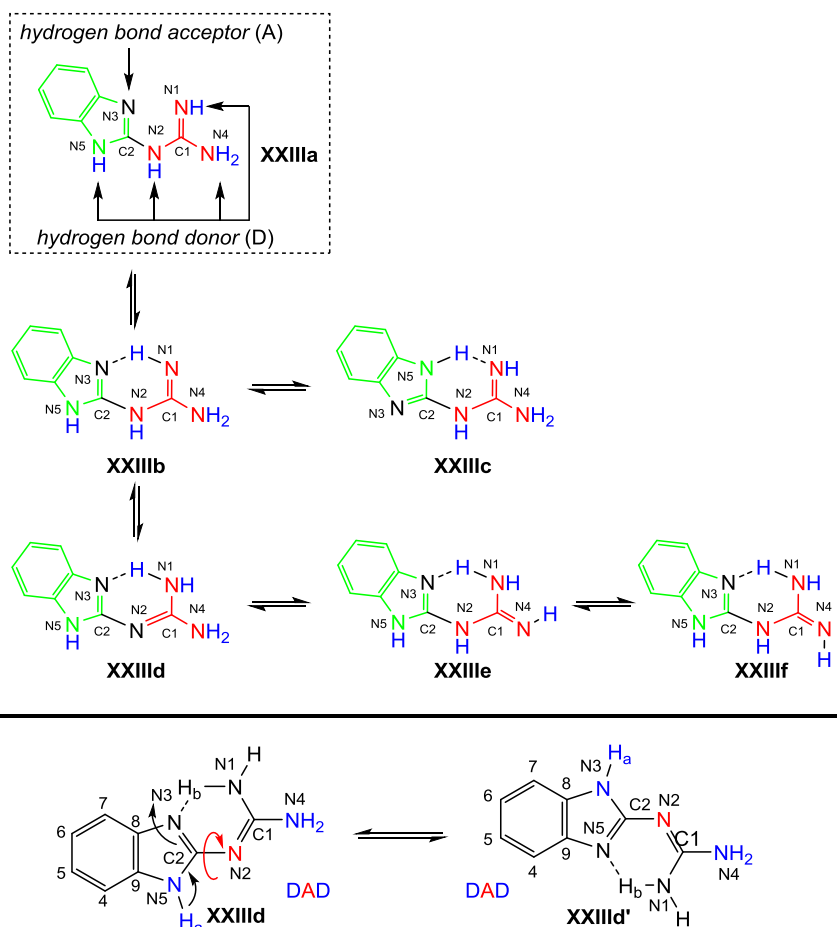
The effect of S...H attractive/S...R repulsive interactions, **XLIIIa** and **XLIIIb** (Scheme 2.1), is evident in the relative rates of **IIIa** and **IIIb**. The two interactions influence the rotations of the aryl groups and thereby catalytic activity. The rigid structure obtainable in **IIIb** accounts for the lesser entropic loss in the process of binding to the acceptor. Similar rate trends with **IIIc,d,e** and **IIIf** support the model mentioned above. In **IIIf**, the two CF₃ group generate the most positively polarized *ortho* H atoms of the series. This leads to the most rigid structure and provides the fastest rate.⁵⁷ At the other extreme, **IIIa** fails to attain a rigid structure and corresponds to the slowest rate. A similar beneficial effect of preorganization with respect to hydrogen bonding to anions is a well-known phenomenon and is well studied (see section 1.3, chapter 1).^{6,51,52}



Scheme 2.1 Diels-Alder reactions catalyzed by thiourea derivatives, their relative rates, and proposed models (**XLIIIa,b**).

As explained in the previous chapter, **GBI** is a flexible molecule that is composed of two rigid units, guanidine and 2-aminobenzimidazole, as shown in Scheme 2.2 (top). These are each capable of achieving a *synperiplanar* DD dyad sequence. When combined into **GBI**, in principle, a DDD triad should be obtained.

On the contrary, **GBI** has numerous tautomeric structures as shown in Scheme 2.2 (top). Structures **XXIIIa,b** and **XXIIIf** achieve this DDD triad while the others achieve ADD (**XXIIIc**), DAD (**XXIII d**), and DDA (**XXIIIe**) sequences. The tautomer **XXIII d** (DAD) and its degenerate structure **XXIII d'** (DAD), as shown in scheme 2.2 (bottom), is believed to be dominant in solution.^{35c} Even crystal structures of **GBI**/crown ether adducts^{37a} (Figure 1.7, left, chapter 1) and aza crown ether adducts^{37b} demonstrate a DAD triad.



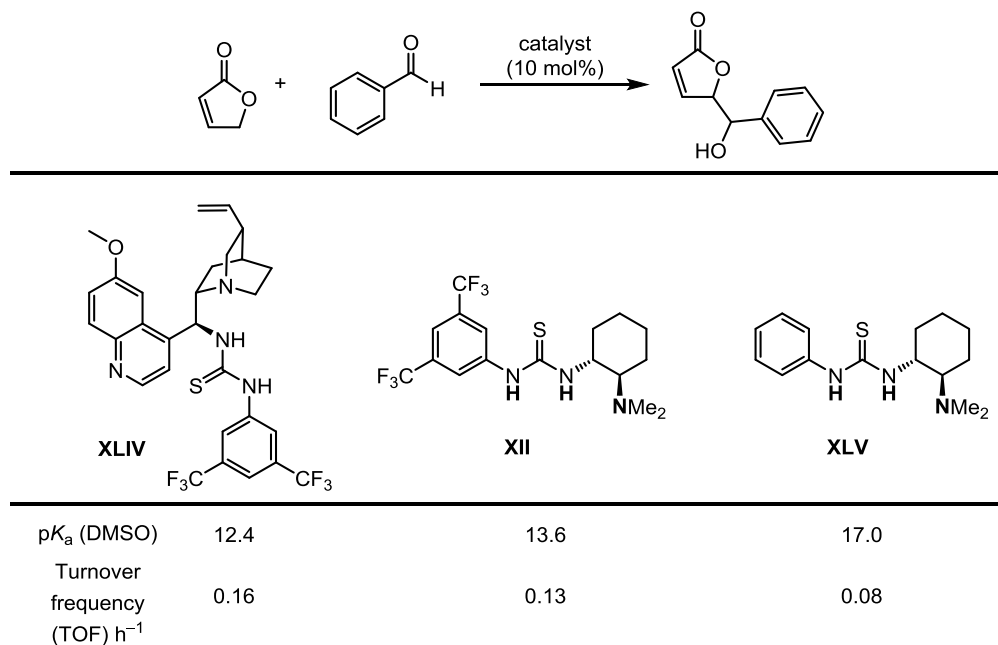
Scheme 2.2 Top: possible tautomers of **GBI**. Potential hydrogen bond donors (highlighted in blue) and hydrogen bond acceptors (highlighted in black). The benzimidazole and guanidine moieties are depicted in green and red. Bottom: degenerate tautomeric (HN3/HN5) and conformational (C2-N2) equilibrium transposing the DAD triad of **GBI**.

In order to efficiently hydrogen bond to complementary acceptors, **GBI** needs to be preorganized into a DDD, ADD, DDA or DAD triad sequence. The first three sequences contain two donor sites (D) next to each other, similar to thioureas. In contrast, the DAD triad contains an acceptor (A) next to each donor (D).

Similar to thioureas, preorganization would reduce the conformational degrees of freedom and thereby increase the hydrogen bonding capabilities of **GBI**. As mentioned before, the beneficial effect of preorganization is well known.^{6,42,43,51,52} Upon

preorganization of **GBI**, there would presumably be analogous effects on its reaction rates and catalytic activities.

Furthermore, the NH acidities in the **GBI** molecule can also contribute to its catalytic activity. As reported by the Schreiner group, in the vinylogous aldol addition of γ -butenolide to benzaldehyde, the catalytic activity can be correlated with the pK_a value of the thiourea catalyst employed (Scheme 2.3).⁵⁸ However, the same series of catalysts fails to correlate to the pK_a values in another reaction.⁵⁸ Although the preorganization of **GBI** is important for enhancing its hydrogen bonding capabilities, the tuning of NH acidities cannot be ignored.



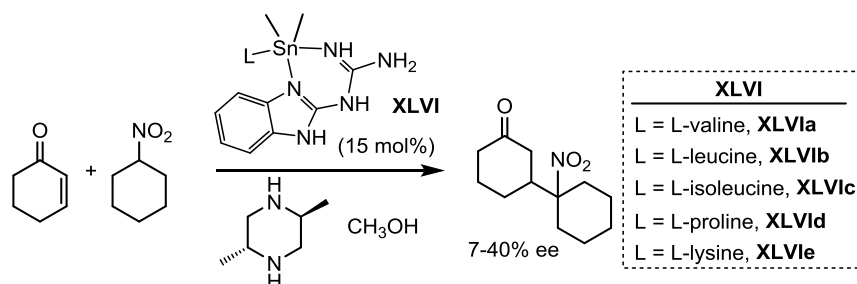
Scheme 2.3 Correlation of catalytic activity and pK_a for a few thiourea based hydrogen bond donor catalysts.

To understand the benefits of preorganization and increased NH acidities, **GBI** and its two constituent fragments (Scheme 2.2) were modified to cationic salts with

BARf^- ²⁶ as the anion. In each case, BARf^- was chosen because it is a weakly coordinating anion⁵⁹ and also cannot participate in hydrogen bonding with the cation.⁶⁰ Finally, the catalytic activities of these salts were compared. These results are presented below. Based on these conclusions, ruthenium-**GBI** complexes were subsequently targeted.

2.1.3 Preorganization of **GBI** by ruthenium

Chelated complexes of **GBI** with boron and tin Lewis acid fragments have been described in the literature.^{40b,c} Solid state studies of transition metal adducts show hydrogen bonding interactions in the second coordination sphere with anions and solvents.^{35b,40a} Inspired by these facts, the Gladysz group has already shown that neutral tin complexes can be active catalysts for hydrogen bond promoted organic transformations (Scheme 2.4).⁶¹ The substrates were activated by hydrogen bonding in the second coordination sphere. Additionally, some of the chelated compounds with an enantiopure ligand attached to tin provided moderate enantioselectivities in the addition of nitrocyclohexane to 2-cyclohexen-1-one (**XLVa-e**, Scheme 2.4).⁶¹



Scheme 2.4 Chiral tin-**GBI** chelate complex catalyzed addition of nitrocyclohexane to 2-cyclohexen-1-one.

Like tin, any chelate susceptible metal should also preorganize **GBI**, as shown in Figure 2.2 (top). Additionally, based on the nature and oxidation state of the metal, the N-H acidities can be further tuned. For example, more electron rich metal fragments will generally decrease X-H bond acidities, and more electron withdrawing metal fragments will generally increase X-H bond acidities. Moreover, an appropriate ligand arrangement around the metal would yield a chiral-at-metal complex as shown in Figure 2.2 (middle). Thus, the metal will serve three functions: (i) preorganization of **GBI**, (ii) tuning N-H acidities, and (iii) transforming achiral **GBI** to a chiral molecule. Furthermore, the solubility of ionic compounds can be optimized for various media by modifying the counter ion. Lastly, successful resolutions of the enantiomers lead to a catalyst that could be applied to enantioselective second coordination sphere promoted catalysis (SCSPC).

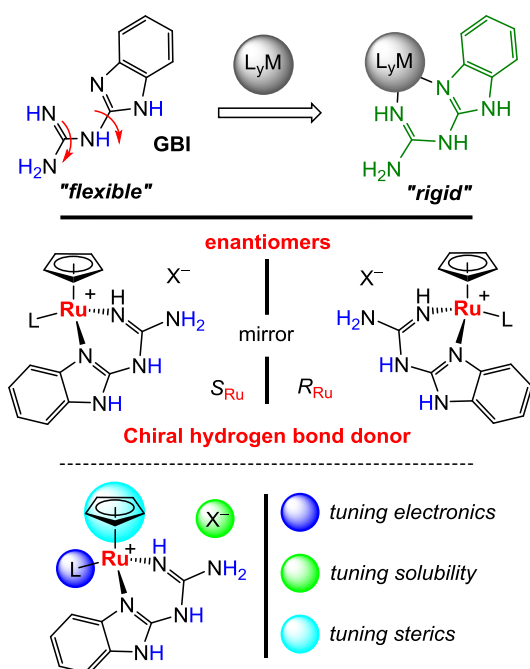


Figure 2.2 Top: preorganization of **GBI** through chelation. Middle: enantiomers derived by bonding to a ruthenium fragment with two different ligands. Bottom: modularity of the catalyst.

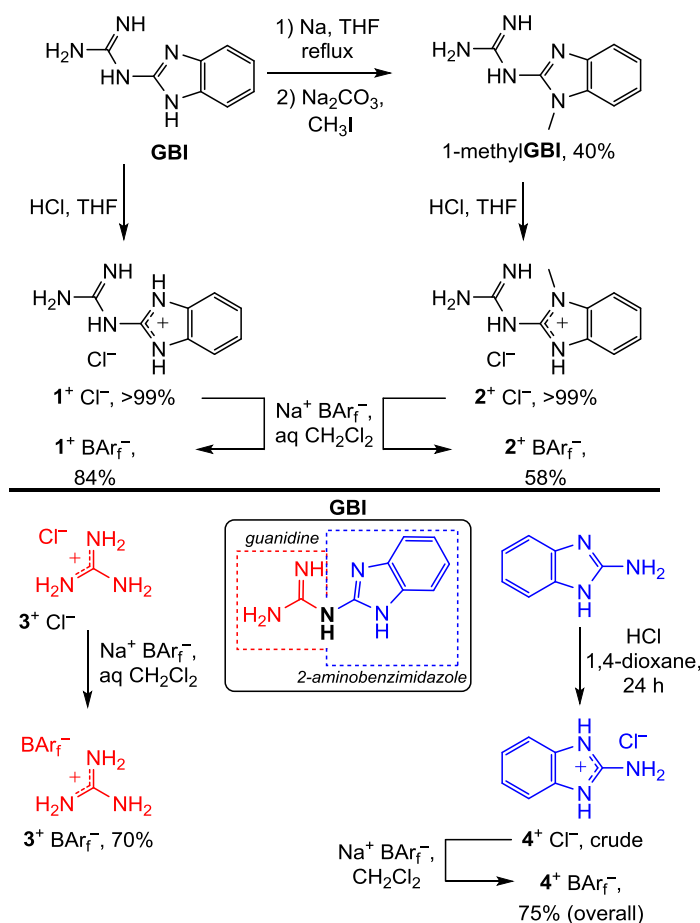
Here, ruthenium was chosen as an initial contender for this purpose. Ruthenium based piano stool complexes are well studied.⁶² These complexes are formally octahedral and with suitable ligand sets are chiral-at-metal.⁶²⁻⁶⁴ Half-sandwich ruthenium complexes similar to $[(\eta^5\text{-C}_5\text{R}_5)\text{RuL}_1\text{L}_2\text{L}_3]$ (R = H or Me) have seen numerous application in catalysis.⁶²

Upon attaching **GBI** to a $[(\eta^5\text{-C}_5\text{R}_5)\text{RuL}]$ fragment, the ruthenium would attain a formally octahedral arrangement with the C_5R_5 ligand occupying three sites. This would be a racemic, chiral-at-metal complex. A cyclopentadienyl ($\eta^5\text{-C}_5\text{H}_5$) variant was chosen because enantiopure chiral-at-metal ($\eta^5\text{-C}_5\text{H}_5$) $\text{RuL}_1\text{L}_2\text{L}_3$ cationic systems have been prepared before.^{62,63d,f,g,64d} Further, the modular catalyst system shown in Figure 2.2 (bottom) can be tuned in terms of electronics, solubilities, and sterics. Each parameter serves different purposes.

2.2 Results

2.2.1 Syntheses of cationic 2-guanidinobenzimidazolium, 2-aminobenzimidazolium, and guanidinium salts

Two cationic species were prepared from **GBI** according to Scheme 2.5 (top). In one, **GBI** was protonated with HCl to form the salt $\mathbf{1}^+ \text{Cl}^-$ according to literature.^{35a} Subsequent anion metathesis with $\text{Na}^+ \text{BARf}^-$ ^{26,65} led to the new salt $\mathbf{1}^+ \text{BARf}^-$ as pale brown solid in 84% yield. Following a literature method, the methylated **GBI** salt $\mathbf{2}^+ \text{Cl}^-$ was prepared.^{35a} Similarly, anion exchange with $\text{Na}^+ \text{BARf}^-$ led to the new salt $\mathbf{2}^+ \text{BARf}^-$ as a dirty white solid in 58% yield.



Scheme 2.5 Top: syntheses of cationic **GBI** derivatives **1⁺ BAr_f⁻** and **2⁺ BAr_f⁻**. Bottom: other relevant derivatives; cationic guanidine derivative, **3⁺ BAr_f⁻** (red), cationic 2-aminobenzimidazole derivative, **4⁺ BAr_f⁻** (blue).

Two other types of salts were also targeted as shown in Scheme 2.5 (bottom). First, the known guanidinium chloride **3⁺ Cl⁻** underwent anion exchange when treated with **Na⁺ BAr_f⁻** under biphasic conditions ($\text{CH}_2\text{Cl}_2/\text{H}_2\text{O}$) to give the new salt **3⁺ BAr_f⁻** in 77% yield. Second, 2-aminobenzimidazolium was protonated with HCl to give the salt **4⁺ Cl⁻** in 50% crude yield. However, the crude sample was directly treated with **Na⁺ BAr_f⁻** to give the new salt **4⁺ BAr_f⁻** as a white powder in 75% overall yield. All of the above **BAr_f⁻** salts were characterized by NMR (^1H and ^{13}C) and IR spectroscopy, and microanalysis, as summarized in the experimental section. They exhibited good

solubilities in CH₂Cl₂, CHCl₃, MeOH, and DMSO.

Due to the application of biphasic CH₂Cl₂/H₂O conditions for the preparation of salt **1**⁺ BAr_f⁻ and **3**⁺ BAr_f⁻ by anion exchange, they were isolated as hydrates (2.0-0.2 H₂O). Crystals of **3**⁺ BAr_f⁻ and **4**⁺ BAr_f⁻ were obtained (see below). In another sequence, crystals of a dicationic bromide salt derived from **GBI** were accidentally obtained (below and experimental section). All of them showed hydrogen bonding to H₂O and are discussed below.

2.2.2 Crystallographic characterization

Crystal structures of guanidinium salts are common, and a search in Cambridge Crystallographic Data Centre (surveyed on March 2015) for "guanidinium" resulted in 1153 crystal structures.⁶⁶ However, none with a BAr_f⁻ counter anion has ever been published. During the course of the above syntheses, single crystals of **3**⁺ BAr_f⁻·H₂O were obtained from a CH₂Cl₂ solution. X-ray data were collected and refined as described in Table 2.1 and the experimental section. The resulting structure is shown in Figure 2.3 (top). Key metrical parameters are summarized in Table 2.2. Several of the CF₃ groups and the C(NH₂)₃ groups were disordered, and modeled as described in the experimental section.

The C-N bond lengths were similar to each other (1.33(3), 1.32(3), and 1.32(2) Å). The cation was hydrogen bonded to a H₂O molecule by two NH units in a dual hydrogen bonding fashion common to urea and thiourea systems (chapter 1, Figure 1.1).^{8e,13a} From the H-N-N-H torsion angles (0.08°, 0.36°, 2.82°) it was evident that the cation contains three pairs of *synperiplanar* NH protons (DD dyad). The NH...O and N...O distances, which are summarized in Table 2.2, were in typical ranges for hydrogen

Table 2.1 Summary of crystallographic data.^a

	$3^+ \text{BAr}_f^- \cdot \text{H}_2\text{O}$	$4^+ \text{BAr}_f^- \cdot \text{H}_2\text{O} \cdot (\text{CH}_2\text{Cl}_2)_{0.5}$	$[\text{1-H}]^{2+} 2\text{Br}^- \cdot \text{H}_2\text{O}$
Molecular formula	$\text{C}_{33}\text{H}_{20}\text{BF}_{24}\text{N}_3\text{O}$	$\text{C}_{39.5}\text{H}_{23}\text{BClF}_{24}\text{N}_3\text{O}_2$	$\text{C}_8\text{H}_{13}\text{Br}_2\text{N}_5\text{O}$
Formula weight	941.33	1057.87	355.05
Crystal system	Tetragonal	Triclinic	Monoclinic
Space group	$P4_1$	$P-1$	$P2_1/c$
Diffractometer	Bruker GADDS	Bruker GADDS	Bruker GADDS
Wavelength [Å]	1.54178	1.54178	1.54178
Unit cell dimensions:			
a [Å]	16.6073(5)	12.9532(6)	8.5710(4)
b [Å]	16.6073(5)	17.0601(8)	11.8259(5)
c [Å]	13.5055(6)	19.5110(9)	12.6300(6)
α [°]	90	97.766(3)	90
β [°]	90	101.549(3)	93.913(3)
γ [°]	90	92.339(3)	90
V [Å ³]	3724.8(3)	4175.4(3)	127.19(10)
Z	4	4 ($Z' = 2$)	4
ρ_{calc} [Mgm ⁻³]	1.679	1.683	1.846
μ [mm ⁻¹]	1.696	2.167	7.985
F (000)	1872	2108	696
Crystal size [mm ³]	0.05 × 0.03 × 0.01	0.12 × 0.08 × 0.06	0.07 × 0.04 × 0.03
Θ range [°]	2.66 to 50.99	2.34 to 60.80	5.13 to 60.92
Index ranges (h,k,l)	-15,16;-16,16;-13,13	-14,14;-19,19;-21,21	-9,9;-13,13;-14,14
Reflections collected	38897	100574	28147
Independent reflections	3971	12367	1936
Completeness to Θ ($\Theta =$)	59.6% (67.68)	81.8% (67.68)	83.5 (67.68)
Data/restraints/parameter	3971/206/566	12367/0/1259	1936/0/149
Goodness-of-fit on F^2	1.043	1.122	1.051
R indices (final) [$I > 2\sigma(I)$]			
R_1	0.0799	0.0914	0.0280
wR_2	0.2029	0.2610	0.0695
R indices (all data)			
R_1	0.0873	0.1132	0.0310
wR_2	0.2096	0.2784	0.0706
Largest diff. peak and hole [eÅ ⁻³]	0.736/-0.499	1.951/-1.114	0.403/-0.695

^a Data common for all structures: T = 173(2) K.

bonds as observed by Etter.^{10b}

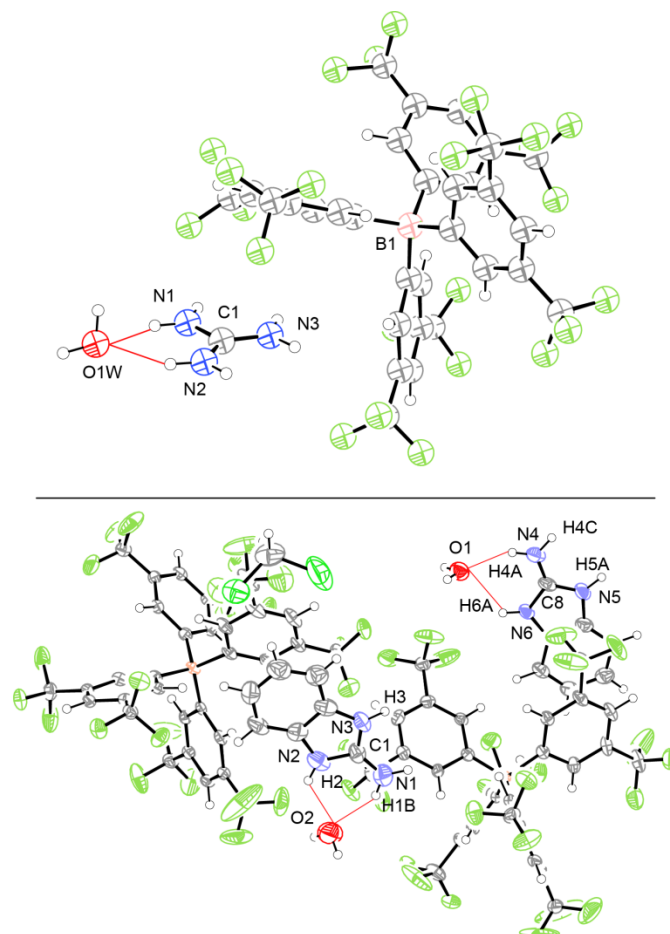


Figure 2.3 Top: thermal ellipsoid diagram (50% probability level) of the molecular structure of 3⁺ BAR_f⁻·H₂O and hydrogen bonding between the cation and H₂O molecule (highlighted in red). Bottom: thermal ellipsoid diagram (50% probability level) showing the structure of two independent molecules of 4⁺ BAR_f⁻·H₂O·(CH₂Cl₂)_{0.5} and hydrogen bonding between the cations and H₂O molecules (highlighted in red) .

Crystal structures of 2-aminobenzimidazolium salts have also been reported in the literature, but none with BAR_f⁻ as the counter anion.⁶⁷ Similarly to the guanidinium salt mentioned above, colorless blocks of 4⁺ BAR_f⁻·H₂O·(CH₂Cl₂)_{0.5} were obtained from a

wet CH₂Cl₂ solution. X-ray data were collected and refined as described in Table 2.1 and the experimental section. The resulting structure is shown in Figure 2.3 (bottom). Key metrical parameters are summarized in Table 2.3. Several of the CF₃ groups and C(NH) groups were disordered. Efforts to model the disorder did not improve the R factor. For the final refinement, some of the CF₃ groups were left with elongated thermal ellipsoids. The asymmetric unit contained two unique 4⁺ BAr_f⁻ salts, two molecules of H₂O and one molecule of CH₂Cl₂. There were two asymmetric units in the unit cell ($Z = 4$; $Z' = 2$).

Table 2.2 Key bond lengths [Å], bond angles [°], and torsion angles [°] for 3⁺ BAr_f⁻·H₂O.^a

N(1)-C(1)	1.324(2)	N(1)-C(1)-N(2)	116.86(2)
N(2)-C(1)	1.321(3)	N(1)-C(1)-N(3)	126.27(2)
N(3)-C(1)	1.330(3)	N(2)-C(1)-N(3)	116.83(2)
H(3B)-O(1W)	2.076	H(1A)-N(1)-N(2)-H(2A)	0.08
H(2B)-O(1W)	2.109	H(2B)-N(2)-N(3)-H(3B)	0.36
N(2)-O(1W)	2.897(2)	H(3A)-N(3)-N(1)-H(1A)	2.82
N(3)-O(1W)	2.871(3)		

^a For atom numbers see Figure 2.3 (top).

The cations differed slightly in C1-N(1/2/3) bond lengths (1.316(9) vs. 1.317(9) Å, 1.332(9) vs. 1.363(9) Å, and 1.353(7) vs. 1.303(9) Å). Each of the cations was hydrogen bonded to a H₂O molecule by a DD type NH dyad. The cation with the shortest C-N bond length (1.303(9) Å) gave the shortest average hydrogen bonding contacts (2.097 Å and 2.174 Å vs. 2.119 Å and 2.293 Å, see Table 2.3).

Table 2.3 Key bond lengths [\AA], bond angles [$^\circ$], and torsion angles [$^\circ$] for 4^+ $\text{BAr}_f^- \cdot \text{H}_2\text{O} \cdot (\text{CH}_2\text{Cl}_2)_{0.5}$.^a

4^+ (cation 1)			
N(1)-C(1)	1.317(9)	N(1)-C(1)-N(2)	121.96(6)
N(2)-C(1)	1.363(9)	N(1)-C(1)-N(3)	129.41(2)
N(3)-C(1)	1.303(9)	N(2)-C(1)-N(3)	108.59(6)
H(1B)-O(2)	2.097	H(1A)-N(1)-N(3)-H(3)	1.50
H(2)-O(2)	2.174	H(1B)-N(1)-N(2)-H(2)	0.69
N(1)-O(2)	2.853(1)	H(2)-N(2)-N(3)-H(3)	0.02
N(2)-O(2)	2.864(9)		
4^+ (cation 2)			
N(4)-C(8)	1.316(9)	N(4)-C(8)-N(6)	125.87(6)
N(6)-C(8)	1.332(9)	N(4)-C(8)-N(5)	125.60(6)
N(5)-C(8)	1.353(7)	N(6)-C(8)-N(5)	108.52(6)(2)
H(4A)-O(1)	2.119	H(4A)-N(4)-N(6)-H(6A)	1.43
H(6A)-O(1)	2.293	H(4C)-N(4)-N(5)-H(5A)	0.22
N(4)-O(1)	2.874(7)	H(5A)-N(5)-N(6)-H(6A)	0.82
N(6)-O(1)	2.961(7)		

^a For atom numbers see Figure 2.3 (bottom).

In a fortuitous event, a bromide salt of diprotonated **GBI**, $[\mathbf{1-H}]^{2+} 2\text{Br}^-$, was accidentally obtained when **GBI** was refluxed in EtOH with $(\eta^5\text{-C}_5\text{H}_5)\text{Fe}(\text{CO})_2(\text{Br})$ and $\text{Na}^+ \text{PF}_6^-$. Details are described in the experimental section. Brown column shaped crystals of $[\mathbf{1-H}]^{2+} 2\text{Br}^- \cdot \text{H}_2\text{O}$ were obtained when a CH_2Cl_2 solution of the crude mixture was concentrated. X-ray data were collected and refined as described in Table 2.1 and the experimental section. The resulting structure is shown in Figure 2.4. Key metrical parameters are summarized in Table 2.4.

The dication was hydrogen bonded through the N1-H1 unit to the H_2O molecule and through the N2-H2 unit to one of the bromide counter anions. The N3-H3 and N4-H4A units hydrogen bonded to the other bromide counter anion in a dual NH motif

similar to thioureas.^{8e,13a} From the H-N-N-H torsion angles, it was evident that each cation contained two pairs of *synperiplanar* NH protons (DD dyad).

The N1-C7 and N2-C7 bond lengths (1.328(4) vs. 1.331(4) Å) were essentially identical, consistent with the positive charge being distributed equally between both imidazolium nitrogen atoms, and appreciable double bond character. The N4-C8 and N5-C8 bonds exhibited comparable double bond character (1.309(4) and 1.321(4) Å), while the N3-C7 and N3-C8 bond lengths (1.375(4) and 1.356(4) Å) were closer to those of single bonds.

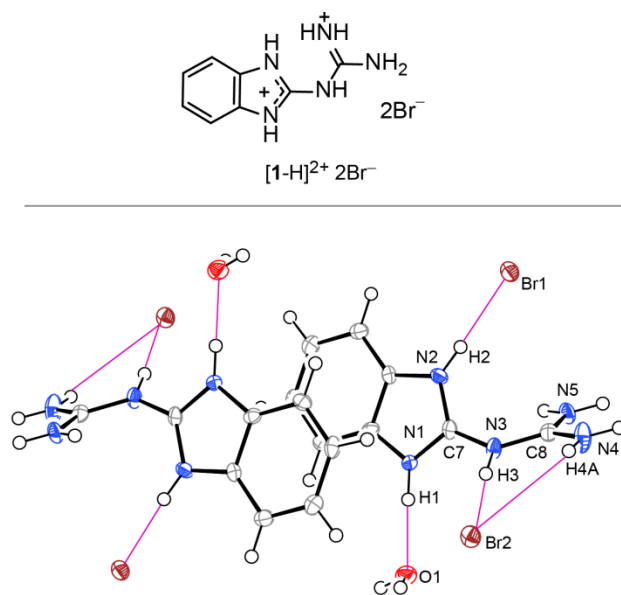


Figure 2.4 Top: a bromide salt of diprotonated **GBI**. Bottom: thermal ellipsoid (50% probability level) of two molecules of [1-H]²⁺ 2Br⁻·H₂O. Key distances involving hydrogen bonds (Å): H1-O1 1.813, N1-O1 2.693(3), H2-Br1 2.415, N2-Br1 3.265(3), H3-Br2 2.331, N3-Br2 3.207(3), H4A-Br2 3.081, N4-Br2 3.759(3).

The N1-C7-N3-C8 and N2-C7-N3-C8 torsion angles, 138.6(3)° and -46.6(5)°, clearly indicated that the plane of the protonated guanidinium fragment was *not parallel* to

the plane of the 2-aminobenzimidazolium unit. The H3-N3-C8-N5, H4A-N4-C8-N5, and H4B-N4-C8-N5 torsion angles, 155.11°, -179.99°, and -0.10°, indicated N5 to be *anti* to H(3) and H(4A). The NH protons of N3-H3 and N4-H4A or N4-H4B and N5-H5A displayed a *syn* relationship to each other (torsion angles 22.05° and 0.04°) while N1-H1 and N3-H3 or N1-H1 and N4-H4A avoided *synperiplanar* orientations, as reflected by torsion angles of 40.61° and 63.42°.

Table 2.4. Key bond lengths [Å], bond angles [°], and torsion angles [°] for [1-H]²⁺ 2Br⁻·2H₂O.^a

N(1)-C(7)	1.328(4)	N(1)-C(7)-N(3)-C(8)	138.6(3)
N(2)-C(7)	1.331(4)	N(2)-C(7)-N(3)-C(8)	-46.6(5)
N(3)-C(7)	1.375(4)	H(1)-N(1)-N(3)-H(3)	40.61
N(3)-C(8)	1.356(4)	H(1)-N(1)-N(4)-H(4A)	63.42
N(4)-C(8)	1.309(4)	H(3)-N(3)-N(4)-H(4A)	22.05
N(5)-C(8)	1.321(4)	H(3)-N(3)-C(8)-N(5)	155.11
N(1)-C(7)-N(2)	110.5(3)	H(4A)-N(4)-C(8)-N(5)	-179.99
N(1)-C(7)-N(3)	123.3(3)	H(4B)-N(4)-C(8)-N(5)	-0.10
N(2)-C(7)-N(3)	125.9(3)	H(4B)-N(4)-N(5)-H(5A)	0.04
N(3)-C(8)-N(5)	120.2(3)		
N(4)-C(8)-N(3)	117.4(3)		
N(4)-C(8)-N(5)	122.3(3)		

^a For atom numbering and distances involving hydrogen bonds, see Figure 2.4.

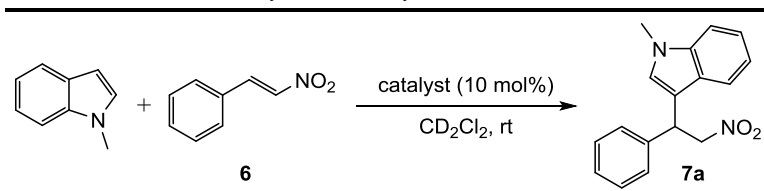
2.2.3 Catalysis with organic hydrogen bond donors

The preceding data establish the hydrogen bonding capabilities of **GBI** and related cationic compounds. This set the stage to investigate their efficacies as catalysts in reactions catalyzed by hydrogen bond donors. As an additional reference point, a neutral molecule with two NH donor groups, *N,N'*-diphenylthiourea (**DPT**), was

simultaneously investigated. This molecule was randomly selected for no obvious reason.

The Friedel-Crafts alkylation of 1-methylindole (**5a**) by *trans*- β -nitrostyrene (**6**) is a benchmark reaction promoted by many hydrogen bond donor catalysts.⁶⁸ Hence, this reaction was investigated with the aforementioned compounds. As shown in Table 2.5, **5a** (2.0 equiv) and **6** (1.0 equiv) were combined in CD₂Cl₂ at room temperature in the presence of 10 mol% of the hydrogen bond donor under aerobic conditions. The reaction was monitored by ¹H NMR against an internal standard, Ph₂SiMe₂. The condensation product 1-methyl-3-(2-nitro-1-phenylethyl)-1*H*-indole (**7a**) has been prepared before and is well characterized.^{68a} The yield of **7a** was used to compare the reactivities of the catalyst.

Table 2.5 Friedel-Crafts alkylation of **5a** by **6**.^a



entry	catalyst	time (h)	yield (%) ^b
1	none	48	0
2	GBI	48	0
3	DPT	48	2
4	1⁺ BAr_f⁻	1	95
5	2⁺ BAr_f⁻	1	25
6	2⁺ BAr_f⁻	3	40
7	3⁺ BAr_f⁻	1	44
8	3⁺ BAr_f⁻	3	76
9	4⁺ BAr_f⁻	1	90

^a Reaction conditions: **6** (2.0 equiv), **5a** (1.0 equiv), and catalyst (10 mol%) in CD₂Cl₂ (0.5 mL). ^b The yields were determined by ¹H NMR against the internal standard Ph₂SiMe₂.

In the absence of the catalyst or in the presence of **GBI**, no **7a** could be detected after 48 h (Table 2.5, entries 1-2). In the case of **DPT**, **7a** was present in 2% yield after 48 h (entry 3). Similar reactions were carried out under identical conditions with the salts **1-4**⁺ BAr_f⁻ (Table 2.5, entries 4-9). In all of the cases, the condensations were clean and **7a** formed as the only product.

In terms of activity, **1**⁺ BAr_f⁻ was superior to **2**⁺ BAr_f⁻ (entries 4 and 5, yield 97% in 1 h vs. 25% in 1 h). The salts **3**⁺ BAr_f⁻ and **4**⁺ BAr_f⁻ were active catalysts and were superior to **2**⁺ BAr_f⁻ (Table 2.5, entries 5-10). Interestingly, **1**⁺ BAr_f⁻ and **4**⁺ BAr_f⁻ showed similar activities, giving **7a** in 95% and 90% yields, respectively, in 1 h. In contrast, **3**⁺ BAr_f⁻ formed **7a** in 44% yield in 1 h. With **2**⁺ BAr_f⁻, a comparable yield of **7a** (40%) was attained after 3 h. Thus, **2**⁺ BAr_f⁻ was the least active of all the salts tested.

2.2.4 Syntheses of ruthenium complexes

The ruthenium bis(phosphine) complex (η^5 -C₅H₅)Ru(PPh₃)₂(Cl) was synthesized by a literature method.⁶⁹ As shown in Scheme 2.6, (η^5 -C₅H₅)Ru(PPh₃)₂(Cl) and **GBI** were reacted in refluxing toluene. Workup gave the racemic "chiral-at-metal" cationic monophosphine complex [(η^5 -C₅H₅)Ru(PPh₃)(**GBI**)]⁺ Cl⁻ (**8**⁺ Cl⁻) as a yellow powder in 96% yield.^{70,71} The salt was insoluble in benzene and toluene, slightly soluble in CHCl₃ or CH₂Cl₂, and soluble in polar solvents such as MeOH, EtOH, and DMSO.

Like most complexes below, **8**⁺ Cl⁻ was characterized by NMR (¹H, ¹³C, ³¹P), IR, and UV-visible spectroscopy, as summarized in Tables 2.6-2.8. Based upon detailed literature ¹H and ¹³C NMR studies, all proton and carbon signals could be

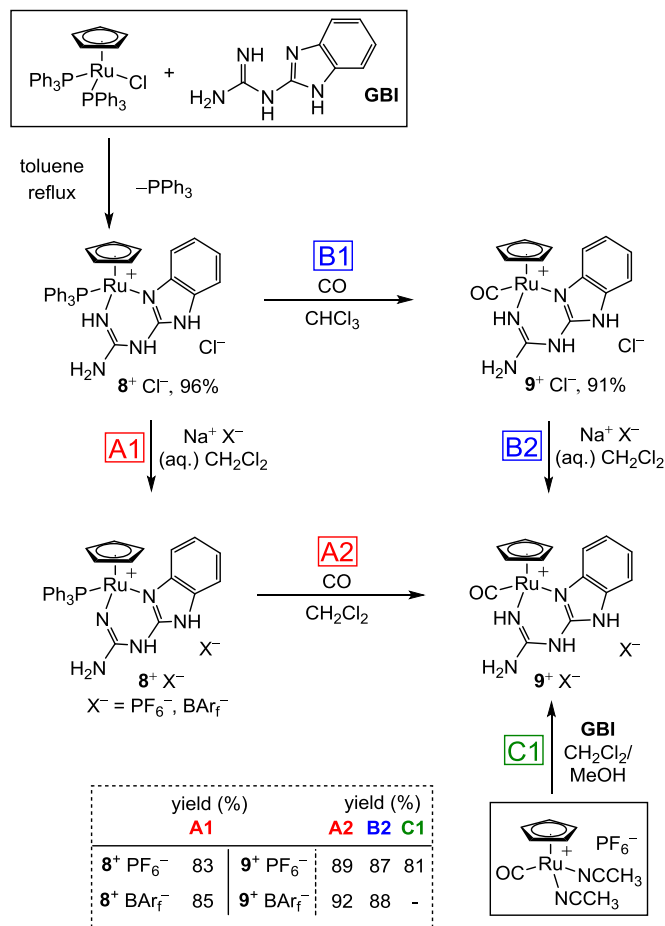
unambiguously assigned.^{35a,b,40b,c} All data supported the coordination of the benzimidazole C=NAr and guanidine C=NH groups.

Next, as shown in Scheme 2.6 (step A1), simple metatheses allowed the chloride anion of $\mathbf{8}^+ \text{Cl}^-$ to be replaced by the weakly coordinating anions PF_6^- and BARf^- .^{59,70,71} The new salts $\mathbf{8}^+ \text{X}^-$ were isolated in 83-85% yields as slightly air-sensitive yellow powders with increased solubility in CH_2Cl_2 . They were characterized similarly to $\mathbf{8}^+ \text{Cl}^-$, including ^{19}F NMR spectra. The cyclopentadienyl ^1H NMR signals exhibited progressively downfield chemical shifts (Table 2.6), suggesting the ruthenium center in $\mathbf{8}^+ \text{BARf}^-$ to have a more cationic character than that in $\mathbf{8}^+ \text{Cl}^-$.⁷²

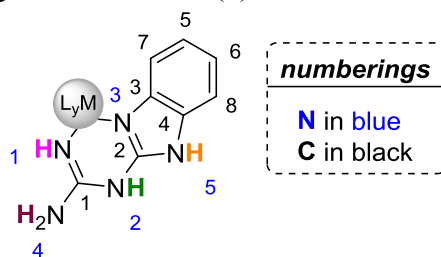
In general, electron withdrawing substituents lead to stronger hydrogen bond donors. Thus, to fine tune catalyst activity, it was sought to replace the PPh_3 ligand by a more weakly donating or stronger π -accepting ligand. As shown in Scheme 2.6 (step B1), a solution of $\mathbf{8}^+ \text{Cl}^-$ was stirred under a static CO atmosphere. Workups gave the substitution product $[(\eta^5\text{-C}_5\text{H}_5)\text{Ru}(\text{CO})(\mathbf{GBI})]^+ \text{Cl}^-$ ($\mathbf{9}^+ \text{Cl}^-$) as an off white powder in 91% yield.^{70,71} Analogous carbonylations were conducted with $\mathbf{8}^+ \text{PF}_6^-$, and $\mathbf{8}^+ \text{BARf}^-$ (step A2).^{70,71} These afforded the corresponding salts $\mathbf{9}^+ \text{X}^-$ as yellow powders in 87-92% yields.

Alternatively, $\mathbf{9}^+ \text{PF}_6^-$ and $\mathbf{9}^+ \text{BARf}^-$ could be accessed in 87-88% yields by exchange of the chloride ion of $\mathbf{9}^+ \text{Cl}^-$, as shown in Scheme 2.6 (step B2). Both overall routes from $\mathbf{8}^+ \text{Cl}^-$ to $\mathbf{9}^+ \text{X}^-$, "A" and "B" (Scheme 2.6), have been repeated several times, and "B" has been found to be the most easily reproducible.⁷³ Another refinement involves an alternative starting material, the cationic bis(acetonitrile) complex $[(\eta^5\text{-C}_5\text{H}_5)\text{Ru}(\text{CO})(\text{NCCH}_3)_2]^+ \text{PF}_6^-$ employed in Scheme 2.6, step C1. As with the starting material $(\eta^5\text{-C}_5\text{H}_5)\text{Ru}(\text{PPh}_3)_2(\text{Cl})$, this educt is easily prepared in one step from a commercially available precursor.⁷⁴ Addition of **GBI** directly affords the

hexafluorophosphate salt $9^+ PF_6^-$ in 81% yield, saving two steps. The aforementioned ruthenium salts were originally prepared by Dr. A. Scherer, but were repeated as part of this work.⁷⁰



Scheme 2.6 Syntheses of cyclopentadienyl ruthenium GBI complexes.

Table 2.6 NH ^1H NMR signals of **8-9** $^+$ X $^-$ (δ).^a

Complex ^a	NH(5)	NH(2)	NH(1)	NH ₂ (4)
8 $^+$ Cl $^-$	11.83	10.19	6.12	6.28
8 $^+$ PF ₆ $^-$	12.13	10.82	6.45	6.63
8 $^+$ BAr _f $^-$	11.75	9.68	6.12	6.03
9 $^+$ Cl $^-$	11.42 ^b	11.42 ^b	6.39	6.72
9 $^+$ PF ₆ $^-$	12.48	10.43	6.34	6.46
9 $^+$ BAr _f $^-$	12.02 ^b	12.02 ^b	6.45	6.63

^a Spectra were recorded in DMSO-*d*₆ (500 or 300 MHz). The δ values are given in ppm. ^b These two NH signals overlap.

Table 2.7 $^{13}\text{C}\{^1\text{H}\}$ NMR signals of the **GBI** ligand in **8-9** $^+$ X $^-$ (δ).^a

Complex	C(1)	C(2)	C(3)	C(4)	C(5)	C(6)	C(7)	C(8)
GBI ^b	159.8	158.9	142.6	132.5	119.9	119.9	114.8	109.1
8 $^+$ Cl $^-$ ^b	154.1	144.7	142.4	131.6	121.6	121.2	117.2	110.5
8 $^+$ PF ₆ $^-$ ^b	152.7	145.3	143.5	132.3	123.4	122.8	118.9	111.4
8 $^+$ BAr _f $^-$ ^b	152.6	145.3	143.9	132.3	123.3	122.7	118.8	111.5
9 $^+$ Cl $^-$ ^d	153.6	145.4	142.5	131.6	123.0	122.5	116.9	111.5
9 $^+$ PF ₆ $^-$ ^c	152.9	144.7	142.7	131.2	124.3	123.8	117.9	111.6
9 $^+$ BAr _f $^-$ ^c	152.4	144.1	142.6	130.8	124.9	124.5	118.4	111.4

^a Spectra were recorded at 100 MHz. The δ values are given in ppm. For the atom numbering scheme, see Table 2.6. ^b In DMSO-*d*₆. ^c In CD₂Cl₂. ^d In CDCl₃.

Table 2.8 C₅H₅ ¹H NMR signals of **8-9**⁺ X⁻,^a and IR ν_{CO} values (brackets)^b for **9**⁺ X⁻.

Anion	Cation	
	8 ⁺	9 ⁺
Cl ⁻	4.41	5.19 (1938)
PF ₆ ⁻	4.61	5.20 ^c (1942) ^c
BAr _f ⁻	5.02	5.30 (1961)

^a δ, DMSO-*d*₆, 300 or 500 MHz, ppm. ^b cm⁻¹. ^c Data for **9**⁺ (*P*)-Phos⁻: 4.85/4.80 ppm in CD₂Cl₂ and 1938 cm⁻¹.

The cyclopentadienyl ¹H NMR chemical shifts of **9**⁺ X⁻ were downfield of those of **8**⁺ X⁻ (δ 5.19-5.30 vs. 4.41-5.02; Table 2.8), suggesting reduced electron density at ruthenium.⁷² Accordingly, **9**⁺ X⁻ exhibited good air stability both in solution and the solid state; powders showed no noticeable decomposition after five years. Curiously, microanalyses gave consistently low nitrogen values, as summarized in the experimental section.

2.2.5 Hydration, hydrogen bonding in the second coordination sphere, H/D exchange, and nonracemic ruthenium complexes

2.2.5.1 Hydration, hydrogen bonding in the second coordination sphere

As Na⁺ BAr_f⁻ is commonly obtained as a hydrate,⁶⁵ **8-9**⁺ BAr_f⁻ all contained low levels of H₂O (2.0-1.0 H₂O). The H₂O could be removed by crystallization, as reported in the full paper associated with this chapter.⁷⁵

In the same paper, the addition of **6** to **9**⁺ BAr_f⁻ has been probed by ¹H NMR. Due to NH...O interactions between **6** and the cation, three NH units of the ruthenium complex shifted downfield (Δδ = 0.02-0.09 ppm) while the other NH unit was

unaffected. Sequential addition of dimethyl malonate ester (**10a**), a dual acceptor (AA type) molecule, to $9^+ \text{BAr}_f^- \cdot 2\text{H}_2\text{O}$ was probed by ^1H NMR (Figure 2.5). A gradual shift of the NH and H_2O protons was observed.

The proton signals of three of the four types of NH units (H5 (orange) /H2 (green) /H4 (purple)) shifted further and further downfield with addition of **10a** (0.5 and 1.0 equiv). At 1.0 equiv of **10a** the $\Delta\delta$ values (ppm) were 0.89, 0.50, and 0.27, respectively. On the other hand, one NH unit (H1 (magenta)) and the H_2O signal (H (red)) shifted upfield and at 1.0 equiv of **10a** the $\Delta\delta$ (ppm) values were 0.11 and 0.24.

Based on the $\Delta\delta$ (ppm) data, the two most possible host-guest adducts would be **XLVIIa** and **XLVIIb**, as shown in Figure 2.5 (top). Out of these two, **XLVIIa** is most likely the dominant form as NH5 signal is shifted to a greater extent than the NH4 signal. However, it should be kept in mind that there are two protons on N4, as opposed only one on N5. These two remain in rapid equilibrium on the NMR time scale in the presence of **10a**, as evidenced by a single signal. Hence, adduct formation will have an intrinsically greater effect on the NH5 signal.

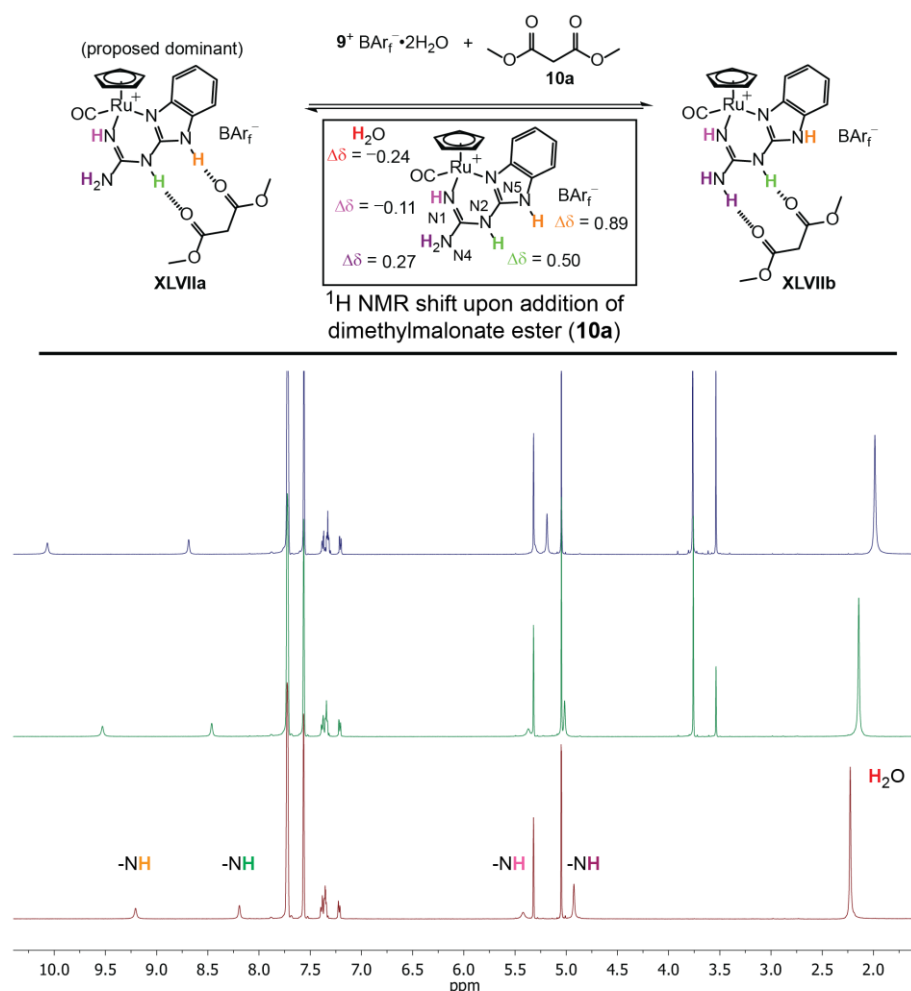


Figure 2.5 ^1H NMR spectra (rt, 500 Hz, CD_2Cl_2): $9^+ \text{BAR}_f^- \cdot 2\text{H}_2\text{O}$ (bottom); after addition of 0.5 equiv of **10a** (middle); after addition of 1.0 equiv of **10a** (top). Key downfield shifted NMR signals (δ , bottom, middle, top, $\Delta(\delta_{\text{top}} - \delta_{\text{bottom}})$): -NH 9.21, 9.53, 10.10, 0.89; -NH 8.19, 8.46, 8.69, 0.50; -NH 4.92, 5.02, 5.19, 0.27. Key upfield shifted NMR signals (δ , bottom, middle, top, $\Delta(\delta_{\text{top}} - \delta_{\text{bottom}})$): -NH 5.41, 5.37, 5.30, -0.11; H_2O 2.23, 2.14, 1.99, -0.24.

2.2.5.2 H/D exchange with ruthenium complexes

When $\text{DMSO-}d_6$ or CDCl_3 solutions of 9^+BAR_f^- were treated with CD_3OD (6 equiv), the NH protons underwent rapid H/D exchange. As shown in Figure 2.6, the NH signals disappeared.⁷⁵ A variety of cationic coordination compounds of **GBI** have been

quantitatively deprotonated by weak bases such as pyridine, NaOMe, and Na_2CO_3 .^{40c,70,75} Hence, it is not surprising that rapid exchange can be observed in the absence of added base. Also, the **GBI** ligand is in principle capable of numerous prototropic equilibria, some of which entail formal 1,3-shifts of protons from the non-coordinating NH/NH₂ moieties to the coordinating C=NAr/C=NH moieties. These may participate in the exchange process, and examples are illustrated in Scheme 2.7.

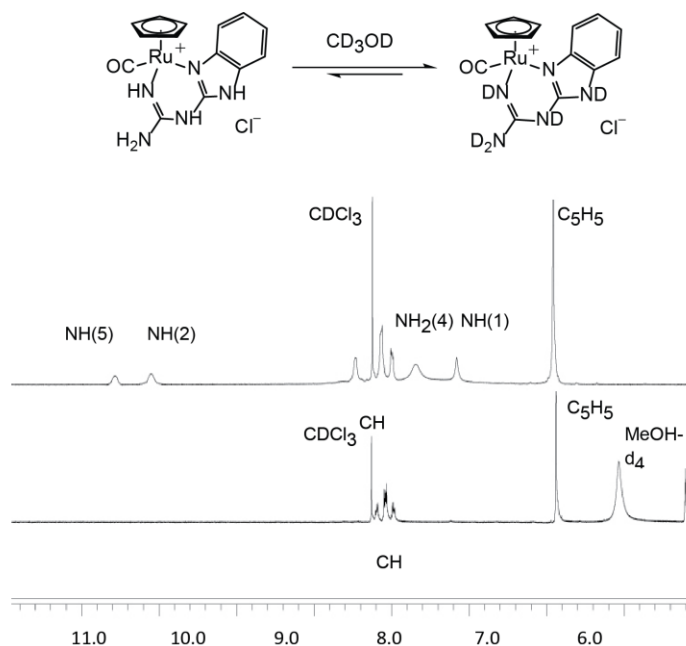
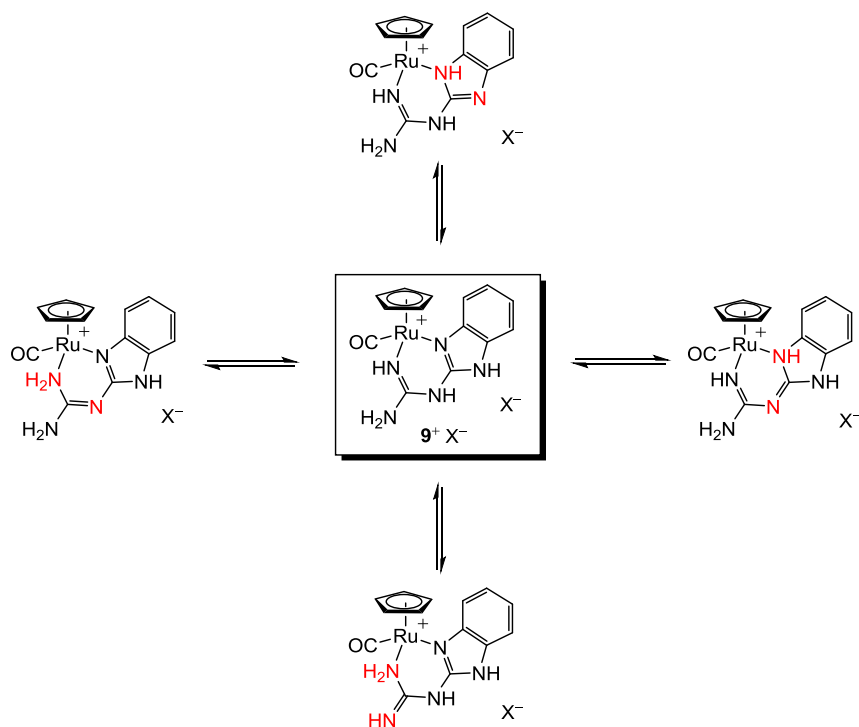


Figure 2.6 ¹H NMR spectra of **9**⁺ Cl⁻ (300 MHz, CDCl₃) before (top) and after (below) the addition of CD₃OD (6 equiv).



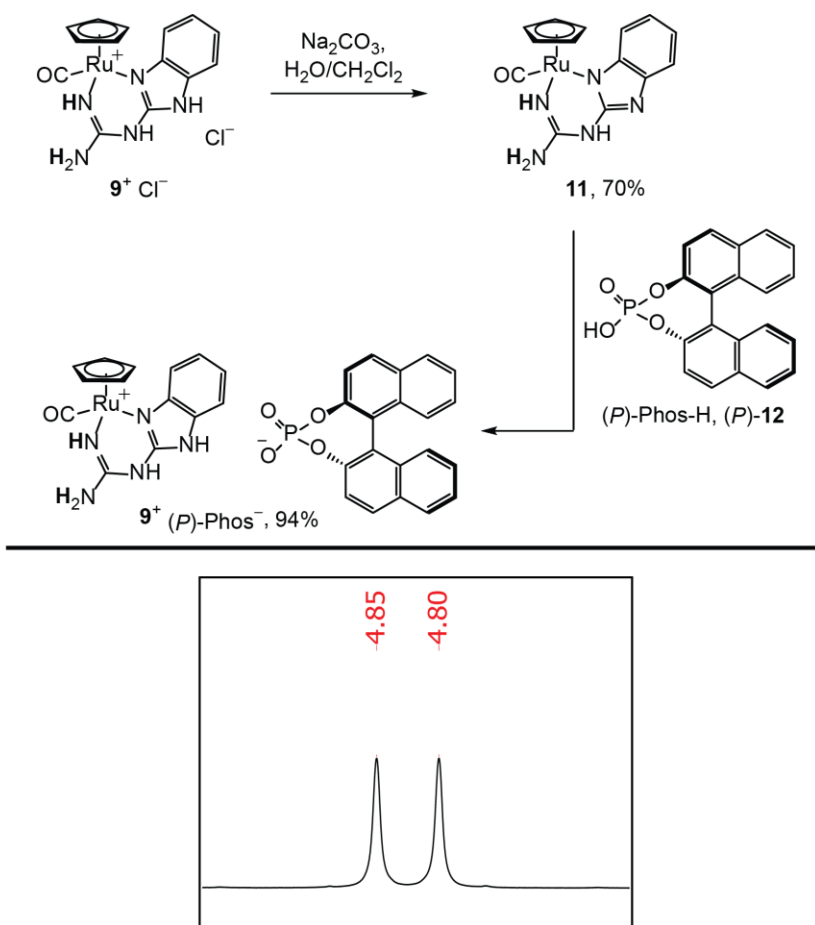
Scheme 2.7 Representative prototropic equilibria involving the **GBI** ligand of the chelate complex $9^+ X^-$.

2.2.5.3 Nonracemic ruthenium complexes

In order to apply the preceding chiral-at-ruthenium complexes as enantioselective catalysis, nonracemic variants would be required. One possible route to enantiopure complexes is by forming diastereomeric salts with chiral anions. Towards this end, $9^+ Cl^-$ was treated with Na_2CO_3 to form the neutral complex, **11**, as shown in Scheme 2.8. This was subsequently protonated with the commercially available enantiopure axially chiral phosphoric acid (*P*)-**12** ((*P*)-Phos-H),²⁶ to form a mixture of diastereomeric salts in 94% yield. The 1H NMR spectrum showed two distinct signals for the cyclopentadienyl ligand due to the formation of two diastereomeric salts (R_{Ru})- 9^+ (*P*)-Phos $^-$ and (S_{Ru})- 9^+ (*P*)-Phos $^-$). This is depicted in Scheme 2.8 (bottom). Two

cyclopentadienyl ^{13}C NMR signals were also observed (δ (ppm) 82.2 and 82.1).

To apply these salts in enantioselective organic transformations, they need to be resolved first. However, all attempts to separate the diastereomers of 9^+ (*P*)-Phos $^-$ by crystallization or precipitation were unsuccessful. The successful resolution and application of related enantiopure catalysts are mentioned in the next chapters.

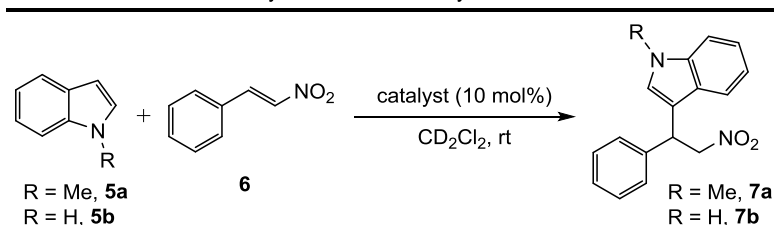


Scheme 2.8 Top: two step exchange of the achiral anion in 9^+Cl^- by a chiral anion. Bottom: the cyclopentadienyl ^1H NMR signal of $9^+ (\text{P})\text{-Phos}^-$ (CD_2Cl_2 , 500 MHz).

2.2.6 Application of racemic chiral-at-ruthenium complexes in second coordination sphere promoted catalysis

The Friedel-Crafts reactions in Table 2.5 were now extended to the **GBI** containing ruthenium salts $\mathbf{8-9}^+ X^-$, and the substrate indole (**5b**). The indoles **5a** or **5b** (2.0 equiv) and **6** (1.0 equiv) were combined in CD_2Cl_2 in NMR tubes in the presence of a salt (0.10 equiv; 10 mol%) along with the internal standard Ph_2SiMe_2 . Reactions of **5b** were stopped after 48 h, irrespective of the state of completion. Results are summarized in Table 2.9, and selected rate profiles are given in Figure 2.7.

Table 2.9 Friedel-Crafts alkylation of **5a** or **5b** by **6**.^a



entry	catalyst	7a		7b	
		time (h)	yield (%) ^b	time (h)	yield (%)
1	none	48	0	48	0
2	GBI	48	0	48	0
3	$\mathbf{8}^+ Cl^-$	48	0	48	0 ^c
4	$\mathbf{8}^+ PF_6^-$	25	30	48	9 ^c
5	$\mathbf{8}^+ BAr_f^-$	8	53	48	46
6	$\mathbf{9}^+ Cl^-$	60	4	48	0 ^c
7	$\mathbf{9}^+ PF_6^-$	10	55	48	27
8	$\mathbf{9}^+ BAr_f^-$	1	97	48	94

^a Reaction conditions: **6** (2.0 equiv), **5a** or **5b** (1.0 equiv), and catalyst (10 mol%) in CD_2Cl_2 (0.5 mL). ^b The yields were determined by 1H NMR against the internal standard Ph_2SiMe_2 . ^c These yields were determined by Dr. A. Scherer.⁷⁰

With many salts, the 3-substituted indoles **7a,b** (Table 2.9) were cleanly formed.

In all cases, **7a** was produced faster, consistent with an electron donating effect of the N-methyl group. However, the slower rate profiles with **7b** are illustrated in Figure 2.7, for better reactivity comparisons.⁷⁵ As shown in entries 1 and 2 of Table 2.9, no reactions were observed without catalyst, or in the presence of **GBI** alone. However, **GBI** is poorly soluble in CH₂Cl₂. Two soluble ruthenium-free systems comparable to **8-9**⁺ X⁻ are described above (Table 2.5, **1**⁺ BAr_f⁻ and **2**⁺ BAr_f⁻).

The rates showed strong dependencies upon the counter anions of the salts. The chloride salts **8-9**⁺ Cl⁻ (entries 3 and 6) did not exhibit any significant activity. The best results were obtained with **8-9**⁺ BAr_f⁻, which gave yields of 46-97% (entries 5 and 8). Less productive were the hexafluorophosphate salts **8-9**⁺ PF₆⁻ (entries 4 and 7), which afforded **7b** in yields up to 27%. Within each counter anion series, rates increased as the cations were varied in the order **8**⁺ < **9**⁺. Although these data are further interpreted in the Discussion section, note that the poorer hydrogen bond accepting anions⁶⁰ and the less electron rich cations give faster rates.

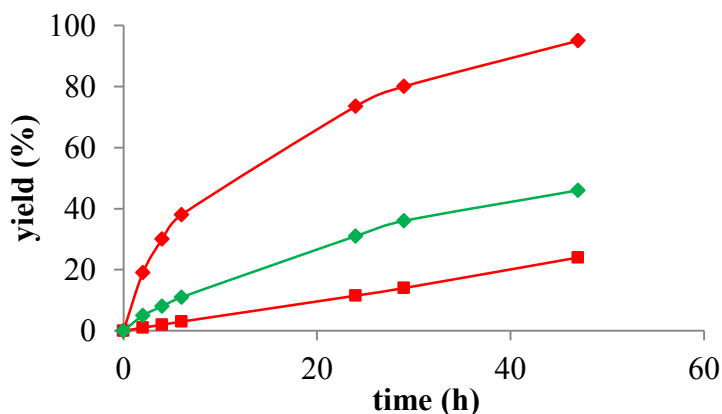


Figure 2.7 Rate profiles for the condensation of **5b** (2.0 equiv) and **6** (1.0 equiv) with different catalysts (10 mol%, rt, selected reactions from Table 2.9): (♦) **9**⁺ BAr_f⁻ (■) **9**⁺ PF₆⁻ (◆) **8**⁺ BAr_f⁻.

2.3 Discussion

2.3.1 Importance of preorganization

In order to understand the contribution of preorganization and NH acidities on the performance of **GBI** as hydrogen bond donor catalyst, the salts **1-4**⁺ BAr_f⁻, **GBI**, and **DPT** were tested as catalysts (Table 2.5). The p*K*_a of *N,N*-diphenylthiourea (**DPT**) is 13.9.⁷⁶ As noted above, 2-aminobenzimidazole and guanidine represent the two halves of **GBI** (Scheme 2.1), and have p*K*_a values of 7.18⁷⁷ and 13.4⁷⁷ respectively. The p*K*_a of **GBI** is 6.97.⁷⁸ Based solely on NH acidities, **GBI** should have been an efficient catalyst but **GBI** was catalytically inactive whereas **DPT** was active to a very slight extent (entry 3 vs. entry 2).

The salts **3,4**⁺ BAr_f⁻ are formed by protonation of 2-aminobenzimidazole and guanidine. These are expected to have lower p*K*_a values and higher NH acidities than their parent compounds. Similarly, cationic species derived from **GBI** (**1,2**⁺ BAr_f⁻) would also possess NH protons with increased acidities. The difference between **1,2**⁺ BAr_f⁻ and **3,4**⁺ BAr_f⁻ is that the first two retain the flexibility of **GBI** whereas the last two are rigid.

The comparable catalytic activity of **1**⁺ BAr_f⁻ and **4**⁺ BAr_f⁻ (Table 2.5, entries 4 vs. 9) may indicate a similar functional group array in the catalytically active site. In contrast, the significantly different reactivity of **1**⁺ BAr_f⁻ and **2**⁺ BAr_f⁻ (Table 2.5, entries 4 vs. 5) suggests a dissimilar functional group array. The somewhat similar catalytic activity of **2**⁺ BAr_f⁻ and **3**⁺ BAr_f⁻ is again suggestive of a similar catalytically active site.

The salt **1**⁺ BAr_f⁻ might preorganize through intramolecular hydrogen bonding.

A proposed structure is shown in Figure 2.8 (left). In doing so, it attains a DDD triad retaining both the DD dyads from guanidine and 2-aminobenzimidazole. In contrast, 2^+ BAr_f^- cannot attain this triad (right). It can retain the existing guanidine DD dyad with or without intramolecular hydrogen bonding similar to 1^+ BAr_f^- . The poorer activity of 2^+ BAr_f^- compared to 3^+ BAr_f^- may be a consequence of the rigidity proposed by Schreiner in thiourea systems.⁵⁷ Moreover, both of the salts 3^+ and 4^+ BAr_f^- do not possess the flexibility of **GBI** or 2^+ BAr_f^- and show better catalytic activity than 2^+ BAr_f^- . (Table 2.5, entries 5-9). This suggests that preorganization is more important than NH acidities in turning **GBI** to an active catalyst.

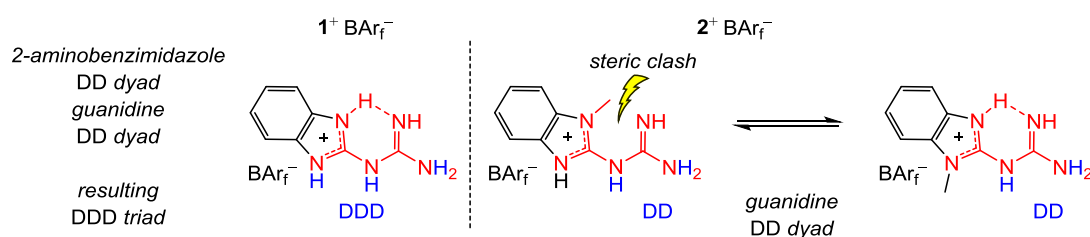


Figure 2.8 Left: proposed preorganization of 1^+ BAr_f^- (red), *synperiplanar* NH donor sites (D) (blue). Right: equilibrium involving 2^+ BAr_f^- .

However, increased acidity of the NH protons due to generation of charge by protonation or methylation of **GBI** cannot be ignored. Both 1^+ BAr_f^- and 2^+ BAr_f^- are much more active catalysts than **GBI** (Table 2.5, entry 2 vs. entries 4 and 5).

Successful catalysis with both 3^+ BAr_f^- and 4^+ BAr_f^- suggests that a dicationic **GBI** derivative might be an even better catalyst. To date, the successful preparation of a dicationic salt with a BAr_f^- counter anion has not been achieved. The crystal structure of a similar bromide salt, $[\mathbf{1-H}]^{2+} 2\text{Br}^-$ (Figure 2.4), reveals that the hydrogen bond that

restricts conformational degrees of freedom in 1^+BARf^- has been disrupted, and bromide anions, which are good hydrogen bond acceptors,⁶⁰ interact with three NH moieties. The guanidinium fragment retains the dyad of *syn* NH units whereas the 2-aminobenzimidazolium fragment is *twisted* (Table 2.4; torsion angles H1-N1-N3-H3, H3-N3-N4-H4A, and H1-N1-N4-H4A; 40.61°, 22.05°, and 63.42°) and the DD dyad from it is lost. Of course, many additional structures would be possible in solution, or with BARf^- counter anions.

Hence, synthesizing metal chelated complexes of **GBI** was envisioned as an alternative and conformationally more "rigid" way of generating a cationic DDD unit from **GBI**, as opposed to the 1^+BARf^- as depicted in Figure 2.8. The superior preorganization offered by this approach is evident in the crystal structures of the ruthenium adducts $8^+ X^-$ ($X^- = \text{BARf}^-, \text{PF}_6^-$).⁷⁵ The crystal structure of the former is shown below in Figure 2.7.

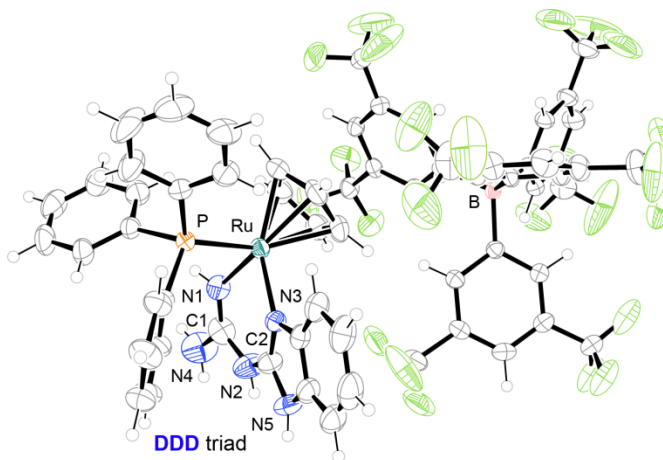


Figure 2.9 Thermal ellipsoid diagram (50% probability level) of the molecular structure of $8^+ \text{BARf}^- \cdot \text{CH}_2\text{Cl}_2$ with the solvate molecule omitted.

2.3.2 Ramification of chiral-at-metal systems

Scheme 2.8 depicts an alternative deprotonation/acidification strategy for counter anion metathesis that differs from the more conventional strategies in Scheme 2.6. The resulting salt $\mathbf{9}^+$ (*P*)-Phos $^-$ features a chiral anion. Accordingly, the ^1H NMR spectrum in CD_2Cl_2 shows two cyclopentadienyl signals of equal intensities ($\Delta\delta = 0.05$ ppm or 25 Hz). These are attributed to the diastereomeric salts (R_{Ru})- $\mathbf{9}^+$ (*P*)-Phos $^-$ and (S_{Ru})- $\mathbf{9}^+$ (*P*)-Phos $^-$. This rather large chemical shift difference suggests a substantial degree of association between the anion and cation, presumably involving hydrogen bonding.

The corresponding salt with an alternative enantiopure chiral anion, TRISPHAT,²⁶ has also been prepared, as reported in the full paper associated with this chapter.⁷⁵ This anion is a poorer hydrogen bond acceptor. Thus, only a single cyclopentadienyl ^1H NMR signal was observed in $\text{DMSO-}d_6$. However, in C_6D_6 a small signal splitting could be detected ($\Delta\delta = 0.01$ ppm or 3 Hz).

A similar conclusion can be reached with the indenyl complex **XLVIII**⁷⁹ and **IL**^{70,75} shown in Figure 2.10. The former is prochiral and the latter is chiral-at-metal. The ^1H NMR signals of the three η^5 protons of the indenyl ligand can be analyzed. In the parent compound **XLVIII**, two are enantiotopic to each other as shown in blue in Figure 2.10 (left), while both of these are heterotopic with respect to the third (shown in red). Upon replacement of one PPh_3 and the chloride ligands by the chelating ligand **GBI**, a racemic complex **IL** is formed, which is chiral-at-metal. Because of the metal chirality, all of the three protons are inequivalent, with those shown in green and blue being diastereotopic.

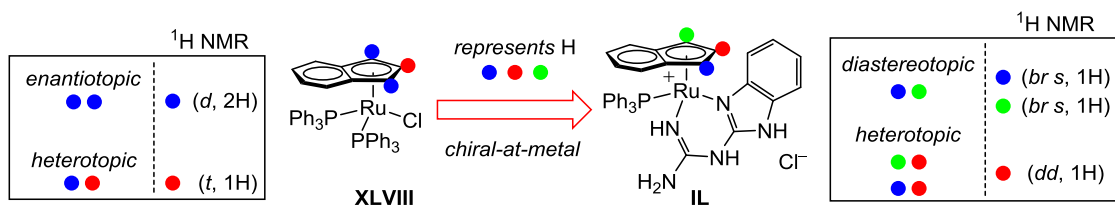


Figure 2.10 Topicities of indenyl protons in **XLVIII** and **IL**, and consequences for ^1H NMR spectra.

This difference is clearly evident from the cyclopentadienyl ^1H NMR signals. In **XLVIII**, the inner proton appeared as a triplet (1H, red) and the outer protons as a doublet (2H, blue). In contrast, in **IL** the external protons exhibit different chemical shifts, each as broad singlet ($2 \times 1\text{H}$, blue and green) while the internal proton signal is a doublet of doublets (1H, red).

To apply these chiral-at-metal complexes in enantioselective organic transformations they need to be resolved first. The resolution and application of closely related catalysts are described in the next chapters.

2.3.3 Support for mechanisms involving second coordination sphere promoted catalysis

Interactions between the malonate ester **10a** and $\mathbf{9}^+ \text{BAR}_f^-$ were documented by ^1H NMR in Figure 2.5. Analogous experiments with the nitroalkene **6** have been reported in a full paper that incorporates much of this chapter.⁷⁵ Thus, spectra of equimolar mixtures of **6** and $\mathbf{9}^+ \text{BAR}_f^-$ were recorded in CD_2Cl_2 and compared to that of $\mathbf{9}^+ \text{BAR}_f^-$ under identical conditions. Of the four NH/NH₂ signals of the **GBI** ligand that can be assigned (Table 2.6), only three shifted downfield. This is illustrated in Figure 2.11; the shifts ranged from 0.09 to 0.02 ppm (top vs. bottom spectrum).

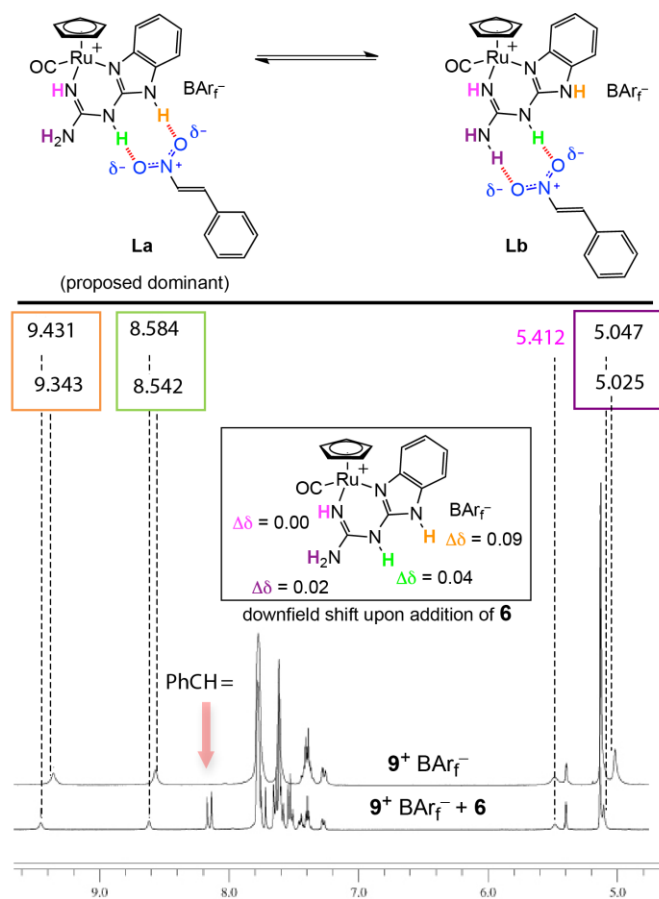


Figure 2.11 ^1H NMR spectra (rt, 300 MHz, CD_2Cl_2) of 9^+BArf^- before (above) after addition of 1 equiv. of **6** (below), and some possible structures of the adduct 9^+BArf^- .

Similarly, the $\text{CH}=\text{CHNO}_2$ proton of **6** shifted slightly downfield. Based upon the magnitudes of the NH shifts (Figure 2.10, box), it was proposed that **6** binds to the cation 9^+ predominantly as shown in **La**. This agrees with the proposed dominant structure shown in Figure 2.5 (structure **XLVIIa**). Downfield shifts of NH signals have also been observed when carbonyl compounds have been added to urea based catalysts.⁸⁰ The data in Table 2.5 and 2.9 and Figures 2.5 and 2.9 validate the underlying hypothesis of this study, namely that by chelation induced preorganization of the conformationally flexible **GBI** ligand by "spectator" transition metal fragments, an

otherwise unreactive species can be rendered an effective hydrogen bond donor catalyst.

By analogy to ureas and thioureas (Figure 2.12), substrate activation would most likely involve two *synperiplanar* NH units. As illustrated by the crystal structures in the literature,⁷⁵ chelation leads to a triad of three *synperiplanar* NH units, and an orthogonal dyad of two *synperiplanar* NH units (Figure 2.9). However, there remains a residual conformational degree of freedom about the NH₂ group (Scheme 2.7). The NMR data in Figure 2.11 suggest that **6** preferentially binds to the two *synperiplanar* NH units *not* associated with the NH₂ group, as depicted in **La**. Note that these two NH groups could adopt any number of conformations in the free ligand, including one in which they would be approximately *anti*.

All of the above mentioned results support the hypothesis of host-guest interactions in the second coordination sphere, which thereby promote the organic transformation. Thus, the catalytic process can be termed second coordination sphere promoted catalysis (SCSPC).

In any event, preorganization can be an important aspect of second coordination sphere binding to coordinated ligands. However, since the ruthenium fragment is cationic, there remains a question as to the effect of positive charge alone, as this should also enhance NH acidities and hydrogen bond donor strengths – even though evidence was provided to show preorganization has greater influence (Table 2.5 and 2.9).

The counter anion also greatly affects the activities of the ruthenium catalysts **8-9**⁺ X⁻. In each case, the same trend is observed, Cl⁻ < PF₆⁻ < BAr_f⁻ (Table 2.9). This parallels the diminishing hydrogen bond accepting properties of the anions.⁵⁹ In particular, chloride is an excellent hydrogen bond acceptor,⁸¹ and a single such anion effectively "poisons" the catalyst. Accordingly, I suggest that (1) there is only one productive substrate binding site that leads to turnover, and (2) chloride preferentially

binds to the same two NH groups as the *trans*- β -nitrostyrene in **La**.

Finally, there is also a marked dependence of catalyst activities upon the cation (Table 2.9 and Figure 2.7). Since CO ligands are weaker donors and stronger π -acceptors than PPh₃ ligands, the ruthenium should be less electron rich in $\mathbf{9}^+ X^-$ as compared to $\mathbf{8}^+ X^-$. This is reflected by the downfield shift of the cyclopentadienyl ¹H NMR signals noted above (Table 2.8).⁷² It also increases the acidities of the NH units, and likewise their hydrogen bond donor strengths, ultimately leading to improved catalytic activities.

2.4 Conclusion

The preceding results and related studies^{70,75} have established that cationic transition metal chelates of **GBI** are effective hydrogen bond donors that can catalyze a variety of organic transformations. Chelation preorganizes **GBI** into a conformation with *synperiplanar* NH units. Unlike most transition metal catalyzed reactions, there is no direct interaction of the substrate with the ruthenium; rather, hydrogen bonds derived from NH groups remote from the metal center are involved. The hydrogen bonding interactions and the activation of the substrates occurs in the second coordination sphere. Hence, the catalysis can rightly be termed as second coordination sphere promoted catalysis.

2.5 Experimental section

2.5.1 General data

All reactions and workups were carried out under nitrogen atmospheres. ^1H , $^{13}\text{C}\{^1\text{H}\}$, $^{31}\text{P}\{^1\text{H}\}$ and $^{19}\text{F}\{^1\text{H}\}$ NMR spectra were recorded on standard 300-500 MHz spectrometers at ambient probe temperature (24 °C) and referenced as follows (δ , ppm): ^1H , residual internal CHCl_3 (7.26), acetone- d_5 (2.05), DMSO- d_5 (2.49), or CHD_2OD (3.30); $^{13}\text{C}\{^1\text{H}\}$, internal CDCl_3 (77.0), acetone- d_6 (29.9), DMSO- d_6 (39.6), or CD_3OD (49.1); $^{19}\text{F}\{^1\text{H}\}$, internal C_6F_6 , (-162.0); $^{31}\text{P}\{^1\text{H}\}$, external H_3PO_4 (0.0). IR spectra were recorded using a Shimadzu IRAffinity-1 spectrophotometer with a Pike MIRacle ATR system (diamond/ZnSe crystal). UV-visible spectra were measured using a Shimadzu UV-1800 UV spectrophotometer. Melting points were recorded with a Stanford Research Systems (SRS) MPA100 (Opti-Melt) automated device. Microanalyses were conducted by Atlantic Microlab.

Solvents were treated as follows: toluene, hexanes, Et_2O , and CH_2Cl_2 were dried and degassed using a Glass Contour solvent purification system; CHCl_3 and CH_3CN were distilled from CaH_2 ; cyclopentadiene (Merck), freshly distilled; pentane (99.7%, J. T. Baker), MeOH (99.8%, BDH), 1,4-dioxane (97%, Alfa Aesar), and EtOH (99.9%, Alfa Aesar) were used as received; CDCl_3 , CD_2Cl_2 , acetone- d_6 , DMSO- d_6 , and CD_3OD (6 \times Cambridge Isotope Laboratories) were used as received. The $\text{Na}^+ \text{PF}_6^-$ (98.5%, Acros), $\text{NH}_4^+ \text{PF}_6^-$ (99.9%, Alfa Aesar), $\text{RuCl}_3 \cdot x\text{H}_2\text{O}$ (30-40% Ru, Acros), 2-guanidinobenzimidazole (**GBI**; 95%, Acros), guanidinium hydrochloride (3^+Cl^- ; 98%, Alfa Aesar), 2-aminobenzimidazole (95%, TCI), *trans*- β -nitrostyrene (**6**; 99%, Alfa Aesar), 1-methylindole (**5a**; 98%, Acros), indole (**5b**; >99%, Aldrich), 1,1'-binaphthyl-

2,2'-diyl hydrogen phosphate (**12**; >99%, Alfa Aesar),²⁶ and other chemicals were used as received from common commercial sources.

2.5.2 Syntheses of GBI derivatives and catalysis

1⁺ BAr_F⁻ (Scheme 2.5).²⁶ A round bottom flask was charged with **1⁺ Cl⁻** ^{35a} (0.021 g, 0.10 mmol), Na⁺ BAr_F⁻ (0.089 g, 0.10 mmol),⁶⁵ CH₂Cl₂ (3 mL), and H₂O (2 mL) with stirring. After 0.5 h, the organic layer was separated and washed with H₂O (3 × 1 mL). The solvent was removed by rotary evaporation. The residue was chromatographed on a silica gel column (5 × 1 cm; 98:2 v/v CH₂Cl₂/MeOH). The solvent was removed from the product containing fractions by oil pump vacuum to give **1⁺ BAr_F⁻·(H₂O)_{0.2}** as a pale brown powder (0.084 g, 0.084 mmol, 84%), mp 172-174 °C (capillary). Anal. Calcd for C₄₀H₂₂BF₂₄N₅·(H₂O)_{0.2}: C 46.06, H 2.16, N 6.71. Found C 45.90, H 2.45, N 6.61.

NMR (δ , CD₂Cl₂): ¹H (500 MHz) 7.73 (s, 8H, *o*-B(C₆H₃(CF₃)₂)₄), 7.56 (s, 4H, *p*-B(C₆H₃(CF₃)₂)₄), 7.43-7.37 (m, 4H, HNCCH(CH)₂CHCNH), 5.65 (br s, 6H, NH), 2.19 (s, 0.4H, H₂O); ¹³C{¹H} (125 MHz) 162.0 (q, ¹J_{CB} = 49.8 Hz, *i*-C₆H₃(CF₃)₂), 158.6 (s, NH=CNH₂), 150.0 (s, N=C(NH)₂), 135.1 (s, *o*-C₆H₃(CF₃)₂), 129.2 (q, ²J_{CF} = 31.6 Hz, *m*-C₆H₃(CF₃)₂), 125.7 (s, HNCCHCHCHCHCNH), 124.9 (q, ¹J_{CF} = 273.7 Hz, C₆H₃(CF₃)₂), 117.9 (s, *p*-C₆H₃(CF₃)₂), 112.3 (s, HNCCHCHCHCHCNH); ¹⁹F{¹H} (470 MHz) -62.9 (s).

IR (cm⁻¹, powder film): 3500 (w), 3425 (w), 1631 (m), 1602 (m), 1543 (s), 1354 (s), 1273 (s), 1138 (m), 1107 (s), 1083 (s), 858 (m), 837 (m).

2⁺ BAr_f⁻ (Scheme 2.5). A round bottom flask was charged with **2⁺ Cl⁻** (0.022 g, 0.10 mmol),^{35a} Na⁺ BAr_f⁻ (0.089 g, 0.10 mmol),⁶⁵ CH₂Cl₂ (2 mL) and H₂O (1 mL) with stirring. After 2 h, the organic layer was separated and washed with H₂O (3 × 1 mL). The solvent was removed by rotary evaporation. The residue was chromatographed on a silica gel column (5 × 1 cm; 98:2 v/v CH₂Cl₂/MeOH). The solvent was removed from the product containing fractions by oil pump vacuum to give **2⁺ BAr_f⁻** as a pale pink powder (0.060 g, 0.058 mmol, 58%), mp 110-113 °C (capillary). Anal. Calcd for C₄₁H₂₄BF₂₄N₅: C 46.75, H 2.30, N 6.65. Found C 47.28, H 2.41, N 6.66.

NMR (δ, CD₂Cl₂): ¹H (500 MHz) 7.71 (s, 8H, *o*-B(C₆H₃(CF₃)₂)₄), 7.55 (s, 4H, *p*-B(C₆H₃(CF₃)₂)₄), 7.11-7.04 (m, 4H, $\overline{\text{NCCH}(\text{CH})_2\text{CHCNCH}_3}$), 5.49 (br s, 4H, NH),⁸² 3.62 (s, 3H, $\overline{\text{NCCH}(\text{CH})_2\text{CHCNCH}_3}$); ¹³C{¹H} (125 MHz) 162.0 (q, ¹J_{CB} = 49.8 Hz, *i*-C₆H₃(CF₃)₂), 158.4 (s, NH=CNH₂), 149.7 (s, N=C(NH)₂), 135.1 (s, *o*-C₆H₃(CF₃)₂), 130.8 and 128.1 (2 s, $\overline{\text{NCCHCHCHCHCNCH}_3}$), 129.1 (q, ²J_{CF} = 31.5 Hz, *m*-C₆H₃(CF₃)₂), 124.9 (q, ¹J_{CF} = 272.3 Hz, C₆H₃(CF₃)₂), 125.6 and 125.5 (2 s, $\overline{\text{NCCHCHCHCHCNCH}_3}$), 117.9 (s, *p*-C₆H₃(CF₃)₂), 112.0 and 111.0 (s, $\overline{\text{NCCHCHCHCHCNCH}_3}$), 39.6 (s, $\overline{\text{NCCHCHCHCHCNCH}_3}$).

IR (cm⁻¹, powder film): 3520 (w), 3444 (w), 3419 (w), 1625 (m), 1585 (s), 1556 (m), 1490 (m), 1456 (w), 1413 (w), 1354 (s), 1315 (w), 1273 (s), 1109 (s), 1097 (s), 931 (w), 885 (s), 835 (s), 746 (s), 709 (s), 680 (s).

3⁺ BAr_f⁻ (Scheme 2.5). A round bottom flask was charged with **3⁺ Cl⁻** (0.038 g, 0.40 mmol), Na⁺ BAr_f⁻ (0.354 g, 0.400 mmol),⁶⁵ CH₂Cl₂ (4 mL) and H₂O (4 mL) with

stirring. After 0.5 h, the organic layer was separated and washed with H₂O (3 × 1.0 mL). The solvent was removed by rotary evaporation. The residue was chromatographed on a silica gel column (5 × 1 cm; 98:2 v/v CH₂Cl₂/MeOH). The solvent was removed from the product containing fractions by oil pump vacuum to give **3**⁺ BAr_f⁻·H₂O as a white powder (0.295 g, 0.307 mmol, 77%), mp 217-219 °C (capillary). Anal. Calcd for C₃₃H₁₈BF₂₄N₃·H₂O: C 42.11, H 2.14, N 4.46. Found C 42.00, H 1.96, N 4.52.

NMR (δ , CD₂Cl₂): ¹H (500 MHz) 7.76 (s, 8H, *o*-B(C₆H₃(CF₃)₂)₄), 7.61 (s, 4H, *p*-B(C₆H₃(CF₃)₂)₄), 5.74 (br s, 6H, NH), 2.45 (s, 2H, H₂O); ¹³C{¹H} (125 MHz) 162.1 (q, ¹J_{CB} = 50.1 Hz, *i*-C₆H₃(CF₃)₂), 156.8 (s, H₂N=CNH₂), 135.2 (s, *o*-C₆H₃(CF₃)₂), 129.3 (q, ²J_{CF} = 30.9 Hz, *m*-C₆H₃(CF₃)₂), 125.0 (q, ¹J_{CF} = 272.8 Hz, C₆H₃(CF₃)₂), 117.9 (s, *p*-C₆H₃(CF₃)₂); ¹⁹F{¹H} (470 MHz) -62.9 (s).

IR (cm⁻¹, powder film): 3518 (w), 1664 (m), 1606 (m), 1354 (s), 1273 (s), 1103 (s), 887 (s), 837 (s), 711 (s), 680 (s), 667 (s).

4⁺ Cl⁻ (Scheme 2.5). A round bottom flask was charged with 2-aminobenzimidazole (0.133 g, 1.00 mmol) and 1,4-dioxane (5 mL). Then HCl (2.0 M in Et₂O; 2.5 mL, 5.0 mmol) was added dropwise with stirring. After 14 h, the solvent was evaporated by oil pump vacuum. The residue was washed with CH₂Cl₂ (3 × 5 mL), and dried by an oil pump vacuum to give crude **4**⁺ Cl⁻ as a yellow-orange oil (0.085 g, 0.50 mmol, ca. 50%). This oily residue was used for the preparation of **4**⁺ BAr_f⁻ without further purification.

4⁺ BAr_f⁻ (Scheme 2.5). A round bottom flask was charged with **4**⁺ Cl⁻ (0.085 g,

ca. 0.50 mmol), Na⁺ BAr_f⁻ (0.443 g, 0.500 mmol),⁶⁵ and CH₂Cl₂ (5 mL). The mixture was sonicated for 15 min, and filtered through a plug of celite (1 × 1 cm), which was rinsed with CH₂Cl₂ (5 mL). The solvent was removed from the filtrate by rotary evaporation and the residue was then chromatographed on a silica gel column (5 × 1 cm; 98:2 v/v CH₂Cl₂/MeOH). The solvent was removed from the product containing fractions by oil pump vacuum to give 4⁺ BAr_f⁻ as a white powder (0.373 g, 0.375 mmol, ca. 75%), mp 151-153 °C (capillary). Anal. Calcd for C₃₉H₂₀BF₂₄N₃: C 46.97, H 2.02, N 4.21. Found C 46.53, H 2.26, N 4.15.

NMR (δ , CD₂Cl₂): ¹H (500 MHz) 7.75 (s, 8H, *o*-B(C₆H₃(CF₃)₂)₄), 7.58 (s, 4H, *p*-B(C₆H₃(CF₃)₂)₄), 7.40 (m, 4H, HNCCH(CH)₂CHCNH), 6.17 (br s, 3H, NH);⁸³ ¹³C {¹H} (125 MHz) 162.2 (q, ¹J_{CB} = 49.9 Hz, *i*-C₆H₃(CF₃)₂), 149.1 (s, H₂N=C(NH)₂), 135.2 (s, *o*-C₆H₃(CF₃)₂), 129.3 (q, ²J_{CF} = 31.3 Hz, *m*-C₆H₃(CF₃)₂), 128.1 (s, HNCCHCHCHCHCNH), 126.1 (s, HNCCHCHCHCHCNH), 125.0 (q, ¹J_{CF} = 276.0 Hz, C₆H₃(CF₃)₂), 117.9 (s, *p*-C₆H₃(CF₃)₂), 112.4 (s, HNCCHCHCHCHCNH; ¹⁹F {¹H} (470 MHz) -63.0 (s).

IR (cm⁻¹, powder film): 3700 (w), 3400 (w), 1638 (m), 1585 (s), 1354 (s), 1273 (s), 1112 (s), 1097 (s), 889 (s), 837 (s), 746 (s), 713 (s), 709 (s), 680 (s), 667 (s).

(η^5 -C₅H₅)Ru(PPh₃)₂(Cl).^{69-71,84} A three necked flask was charged with PPh₃ (14.458 g, 55.182 mmol) and EtOH (100 mL). The mixture was refluxed with stirring. After 15 min, RuCl₃·xH₂O (3.581 g, 17.26 mmol for x = 0; 30-40% Ru) in EtOH (40 mL) and then cyclopentadiene (18 mL) were added. The brown solution was refluxed for 16 h, cooled to room temperature, and stored in a freezer. After 24 h, an orange

precipitate was collected by filtration, washed with cold EtOH (2 × 5 mL), H₂O (2 × 10 mL), cold EtOH (1 × 5 mL), and hexanes (2 × 15 mL), and dried by oil pump vacuum to give the product as a bright orange solid (8.105 g, 11.16 mmol, ca. 65%),⁸⁵ mp 131-132 °C (capillary).

$[(\eta^5\text{-C}_5\text{H}_5)\text{Ru}(\text{CO})(\text{NCCH}_3)_2]^+ \text{PF}_6^-$.⁷⁴ A round bottom flask was charged with $[(\eta^5\text{-C}_5\text{H}_5)\text{Ru}(\text{NCCH}_3)_3]^+ \text{PF}_6^-$ (0.504 g, 1.16 mmol)⁸⁶ and CH₃CN (25 mL). A stream of CO was passed through the brown orange solution. After 40 min, the solvent was removed by oil pump vacuum. The residue was chromatographed on a silica gel column (1 × 20 cm, 3:1 v/v CH₂Cl₂/CH₃CN). The solvent was removed from the product containing fractions to give the product as a golden yellow solid (0.346 g, 0.823 mmol, 71%).

$[(\eta^5\text{-C}_5\text{H}_5)\text{Ru}(\text{PPh}_3)(\text{GBI})]^+ \text{Cl}^-$ (**8**⁺ Cl⁻).^{70,71,75} A Schlenk flask was charged with $(\eta^5\text{-C}_5\text{H}_5)\text{Ru}(\text{PPh}_3)_2(\text{Cl})$ (3.326 g, 4.580 mmol), **GBI** (0.842 g, 4.80 mmol), and toluene (15 mL). The mixture was refluxed with stirring. After 24 h, the mixture was cooled to room temperature. The solvent was decanted from a precipitate, which was washed with toluene (4 × 5 mL) and hexanes (2 × 15 mL) and dried by oil pump vacuum to give **8**⁺ Cl⁻ as a yellow powder (2.798 g, 4.378 mmol, 96%).

NMR (δ , DMSO-*d*₆):^{70,75} ¹H (500 MHz) 11.83 (br s, 1H, **NH**), 10.19 (br s, 1H, **NH**), 7.32-7.09 (m, 17H, P(C₆H₅)₃ and $\overline{\text{NCCH}(\text{CH})_2\text{CHCN}}$), 7.00-6.99 (m, 2H, $\overline{\text{NCCH}(\text{CH})_2\text{CHCN}}$), 6.28 (s, 2H, **NH**₂), 6.12 (s, 1H, **NH**), 4.41 (s, 5H, C₅H₅); ¹³C {¹H} (100 MHz) 154.1 (s, **NH**=**CNH**₂), 144.7 (s, **N**=**C**(**NH**)₂), 142.4 (s, $\overline{\text{NCCHCHCHCHCN}}$), 136.6 (d, ¹J_{CP} = 42.9 Hz, *i*-C₆H₅), 132.7 (d, ²J_{CP} = 13.2 Hz, *o*-C₆H₅), 131.6 (s,

$\overline{\text{NCCHCHCHCHCN}}$, 129.0 (s, *p*-C₆H₅), 127.8 (d, ³J_{CP} = 9.9 Hz, *m*-C₆H₅), 121.6 (s, $\overline{\text{NCCHCHCHCHCN}}$), 121.2 (s, $\overline{\text{NCCHCHCHCHCN}}$), 117.2 (s, $\overline{\text{NCCHCHCHCHCN}}$), 110.5 (s, $\overline{\text{NCCHCHCHCHCN}}$), 74.1 (s, C₅H₅); ³¹P{¹H} (161 MHz) 55.9 (s).

IR (cm⁻¹, powder film.): 3347 (m), 3254 (m), 3200 (w), 3103 (w), 3080 (w), 2798 (m), 2764 (m), 2729 (m), 1679 (s), 1640 (w), 1617 (m), 1590 (m), 1559 (s), 1463 (m), 1436 (m), 1417 (m), 1274 (w), 1251 (m), 1096 (m), 833 (m), 791 (m), 749 (s), 695 (s).

$[(\eta^5\text{-C}_5\text{H}_5)\text{Ru}(\text{PPh}_3)(\text{GBI})]^+ \text{PF}_6^-$ (**8**⁺ PF₆⁻).^{70,71,75} A Schlenk flask was charged with **8**⁺ Cl⁻ (0.224 g, 0.350 mmol), Na⁺ PF₆⁻ (0.295 g, 1.76 mmol), and CH₂Cl₂ (5 mL). The mixture was stirred for 12 h, and filtered through a plug of celite (1 × 1 cm), which was rinsed with CH₂Cl₂ (3 × 5 mL). The filtrate was concentrated by oil pump vacuum (ca. 5 mL). Hexanes (25 mL) was added, and the CH₂Cl₂ was removed by oil pump vacuum. The solvent was decanted from the precipitate, which was dissolved in CH₂Cl₂ (5 mL). The solution was added dropwise to stirred hexanes (25 mL), and the CH₂Cl₂ was removed by oil pump vacuum. The solvent was decanted from the precipitate, which was dried by oil pump vacuum to give **8**⁺ PF₆⁻ as a yellow powder (0.218 g, 0.291 mmol, 83%).⁷³

NMR (δ, DMSO-*d*₆):^{70,75} ¹H (300 MHz) 12.13 (s, 1H, NH), 10.82 (s, 1H, NH), 7.53-7.20 (m, 19H, P(C₆H₅)₃ and $\overline{\text{NCCH}(\text{CH})_2\text{CHCN}}$), 6.63 (s, 2H, NH₂), 6.45 (s, 1H, NH), 4.61 (s, 5H, C₅H₅); ¹³C{¹H} (75 MHz) 152.7 (s, NH=C(NH₂)), 145.3 (s, N=C(NH₂)), 143.5 (s, $\overline{\text{NCCHCHCHCHCN}}$), 136.8 (d, ¹J_{CP} = 39.2 Hz, *i*-C₆H₅), 133.8 (s, *o*-C₆H₅), 132.3 (s, $\overline{\text{NCCHCHCHCHCN}}$), 130.1 (s, *p*-C₆H₅), 128.7 (s, *m*-C₆H₅),

123.4 (s, $\overline{\text{NCCHCHCHCHCN}}$), 122.8 (s, $\overline{\text{NCCHCHCHCHCN}}$), 118.9 (s, $\overline{\text{NCCHCHCHCHCN}}$), 111.4 (s, $\overline{\text{NCCHCHCHCHCN}}$), 75.2 (s, C_5H_5); $^{31}\text{P}\{\text{H}\}$ (161 MHz) 56.3 (s, PPh_3), -142.9 (sep, $^1J_{\text{PF}} = 703.6$ Hz, PF_6^-); $^{19}\text{F}\{\text{H}\}$ (282 MHz) -71.6 (d, $^1J_{\text{FP}} = 707.3$ Hz).

IR (cm^{-1} , powder film): 3505 (w), 3435 (w), 3412 (w), 3377 (w), 1687 (s), 1637 (w), 1586 (m), 1567 (s), 1478 (w), 1436 (m), 1401 (w), 1254 (m), 1092 (m), 880 (s), 862 (s), 841 (s), 741 (s), 698 (s).

$[(\eta^5\text{-C}_5\text{H}_5)\text{Ru}(\text{PPh}_3)(\text{GBI})]^+ \text{BAr}_f^-$ ($\mathbf{8}^+ \text{BAr}_f^-$).^{70,71,75} A Schlenk flask was charged with $\mathbf{8}^+ \text{Cl}^-$ (0.273 g, 0.427 mmol), $\text{Na}^+ \text{BAr}_f^-$ (0.415 g, 0.469 mmol),⁶⁵ and CH_2Cl_2 (5 mL). The mixture was stirred for 12 h, and filtered through a plug of celite (1 \times 2.5 cm), which was rinsed with CH_2Cl_2 (15 mL). The filtrate was concentrated by oil pump vacuum (ca. 5 mL). Hexanes (25 mL) was added, and the solvent was decanted from the precipitate, which was dissolved in CH_2Cl_2 (5 mL). The solution was added dropwise to stirred hexanes (25 mL), and the CH_2Cl_2 was removed by rotary evaporation. The solvent was decanted from the precipitate, which was dried by oil pump vacuum to give $\mathbf{8}^+ \text{BAr}_f^-(\text{H}_2\text{O})_2$ as a yellow powder (0.545 g, 0.363 mmol, 85%).⁷³

NMR (δ , $\text{DMSO-}d_6$):^{70,75} ^1H (300 MHz) 11.75 (s, 1H, **NH**), 9.68 (s, 1H, **NH**), 8.31-8.03 (m, 31H, $\text{B}(\text{C}_6\text{H}_3(\text{CF}_3)_2)_4$, $\text{P}(\text{C}_6\text{H}_5)_3$, and $\overline{\text{NCCH}(\text{CH})_2\text{CHCN}}$), 6.12 (s, 1H, **NH**), 6.03 (s, 2H, NH_2), 5.02 (s, 5H, C_5H_5), 3.35 (s, 4H, H_2O); $^{13}\text{C}\{\text{H}\}$ (75 MHz) 163.1 (q, $^1J_{\text{CB}} = 49.6$ Hz, $i\text{-C}_6\text{H}_3(\text{CF}_3)_2$), 152.6 (s, $\text{NH}=\text{CNH}_2$), 145.3 (s, $\text{N}=\text{C}(\text{NH})_2$), 143.9 (s, $\overline{\text{NCCHCHCHCHCN}}$), 137.1 (d, $^1J_{\text{CP}} = 27.9$ Hz, $i\text{-C}_6\text{H}_5$), 135.2 (s, $o\text{-}$

$\text{C}_6\text{H}_3(\text{CF}_3)_2$, 134.9 (s, *o*- C_6H_5), 132.3 (s, $\overline{\text{NCCHCHCHCHCN}}$), 130.1 (s, *p*- C_6H_5),
 128.8 (s, *m*- C_6H_5), 129.5 (q, $^2J_{\text{CF}} = 31.2$ Hz, *m*- $\text{C}_6\text{H}_3(\text{CF}_3)_2$), 126.7 (q, $^1J_{\text{CF}} = 270.7$
 Hz, $\text{C}_6\text{H}_3(\text{CF}_3)_2$), 123.3 (s, $\overline{\text{NCCHCHCHCHCN}}$), 122.7 (s, $\overline{\text{NCCHCHCHCHCN}}$), 118.8
 (s, $\overline{\text{NCCHCHCHCHCN}}$), 117.9 (s, *p*- $\text{C}_6\text{H}_3(\text{CF}_3)_2$), 111.5 (s, $\overline{\text{NCCHCHCHCHCN}}$), 74.7
 (s, C_5H_5); $^{31}\text{P}\{\text{H}\}$ (161 MHz) 56.4 (s); $^{19}\text{F}\{\text{H}\}$ (282 MHz) -63.7 (s).

IR (cm^{-1} , powder film): 3443 (w), 3405 (w), 1679 (m), 1586 (m), 1563 (m),
 1459 (m), 1355 (s), 1274 (s), 1170 (s), 1119 (s), 1011 (w), 887 (m), 837 (m), 810 (m),
 737 (m), 714 (m), 683 (m).

$[(\eta^5\text{-C}_5\text{H}_5)\text{Ru}(\text{CO})(\text{GBI})]^+ \text{Cl}^-$ (9^+Cl^-).^{70,71,75} A Schlenk flask was charged
 with 8^+Cl^- (0.314 g, 0.491 mmol) and CHCl_3 (25 mL). The sample was saturated with
 CO, fitted with a balloon filled with CO, and stirred. After 12 h, the solution was
 concentrated by rotary evaporation (5 mL), and filtered through a plug of celite (5×1
 cm), which was rinsed with CHCl_3 (30 mL).⁸⁷ The filtrate was concentrated by rotary
 evaporation (ca. 25 mL), and added dropwise to stirred pentane (150 mL). The solvent
 was decanted from the precipitate, which was dissolved in CHCl_3 (25 mL). The solution
 was added dropwise to stirred hexanes (100 mL), and the solvent was decanted from the
 precipitate. This sequence was repeated twice. The residue was triturated with benzene
 and dried by oil pump vacuum to give 9^+Cl^- as an off white powder (0.181 g, 0.447
 mmol, 91%).

NMR (δ):^{70,75} ^1H ($\text{CDCl}_3/\text{CD}_3\text{OD}$, 500 MHz) 7.21-7.18 (m, 1H,
 $\overline{\text{NCCH}(\text{CH})_2\text{CHCN}}$), 7.09-7.06 (m, 2H, $\overline{\text{NCCH}(\text{CH})_2\text{CHCN}}$), 6.99-6.96 (m, 1H,
 $\overline{\text{NCCH}(\text{CH})_2\text{CHCN}}$), 4.87 (s, 5H, C_5H_5); ^1H ($\text{DMSO-}d_6$, 400 MHz) 11.42 (br s, 2H,
 NH),⁸⁸ 7.40-7.38 (m, 1H, $\overline{\text{NCCH}(\text{CH})_2\text{CHCN}}$), 7.20-7.13 (m, 3H, $\overline{\text{NCCH}(\text{CH})_2\text{CHCN}}$),

6.72 (br s, 2H, NH₂), 6.39 (s, 1H, NH), 5.19 (s, 5H, C₅H₅); ¹³C{¹H} (CDCl₃, 100 MHz) 204.1 (s, CO), 153.6 (s, NH=CNH₂), 145.4 (s, N=C(NH)₂), 142.5 (s, $\overbrace{\text{NCCHCHCHCHCN}}$), 131.6 (s, $\overbrace{\text{NCCHCHCHCHCN}}$), 123.0 (s, $\overbrace{\text{NCCHCHCHCHCN}}$), 122.5 (s, $\overbrace{\text{NCCHCHCHCHCN}}$), 116.9 (s, $\overbrace{\text{NCCHCHCHCHCN}}$), 111.5 (s, $\overbrace{\text{NCCHCHCHCHCN}}$), 81.7 (s, C₅H₅).

IR (cm⁻¹, powder film.): 3331 (w), 3266 (w), 3208 (m), 3138 (m), 3111 (w), 1938 (s, ν_{CO}), 1683 (s), 1652 (w), 1567 (s), 1494 (w), 1463 (m), 1420 (w), 1262 (m), 1220 (w), 1092 (w), 1015 (m), 972 (w), 934 (w), 806 (m), 741 (m), 694 (s), 667 (m).

[(η⁵-C₅H₅)Ru(CO)(GBI)]⁺ PF₆⁻ (9**⁺ PF₆⁻).^{70,71,75} **Route A.** A Schlenk flask was charged with **8**⁺ PF₆⁻ (0.172 g, 0.229 mmol) and CH₂Cl₂ (5 mL). The sample was saturated with CO, fitted with a balloon filled with CO, and stirred. After 12 h, the mixture was filtered through a plug of celite (1 × 1 cm), which was rinsed with CH₂Cl₂ (3 × 5 mL).⁸⁷ The filtrate was concentrated by rotary evaporation (ca. 5 mL). Hexanes (25 mL) was added, and the CH₂Cl₂ was removed by rotary evaporation. The solvent was decanted from the precipitate, which was dissolved in CH₂Cl₂ (5 mL). The solution was added dropwise to stirred hexanes (25 mL), and the CH₂Cl₂ was removed by rotary evaporation. The solvent was decanted from the precipitate, which was dried by oil pump vacuum to give **9**⁺ PF₆⁻ as a yellow powder (0.105 g, 0.204 mmol, 89%).⁷³ **Route B.** A Schlenk flask was charged with **9**⁺ Cl⁻ (0.218 g, 0.538 mmol), Na⁺ PF₆⁻ (0.452 g, 2.69 mmol), and CH₂Cl₂ (5 mL). The mixture was stirred for 12 h, and filtered through a plug of celite (1 × 1 cm), which was rinsed with CH₂Cl₂ (3 × 5 mL).⁸⁷ The filtrate was concentrated by rotary evaporation (ca. 5 mL). Hexanes (25 mL) was added, and the CH₂Cl₂ was removed by rotary evaporation. The solvent was decanted from the precipitate, which was dissolved in CH₂Cl₂ (5 mL). The solution was added dropwise to**

stirred hexanes (25 mL), and the CH₂Cl₂ was removed by rotary evaporation. The solvent was decanted from the precipitate, which was dried by oil pump vacuum to give **9**⁺ PF₆⁻ as a yellow powder (0.241 g, 0.468 mmol, 87%).

NMR (δ , DMSO-*d*₆):^{70,75} ¹H (300 MHz) 12.48 (s, 1H, NH), 10.43 (s, 1H, NH), 7.43-7.39 (m, 1H, NCCH(CH)₂CHCN), 7.24-7.16 (m, 3H, NCCH(CH)₂CHCN), 6.46 (s, 2H, NH₂), 6.34 (s, 1H, NH), 5.20 (s, 5H, C₅H₅); ¹³C {¹H} (75 MHz) 203.9 (s, CO), 152.9 (s, NH=CNH₂), 144.7 (s, N=C(NH)₂), 142.7 (s, NCCHCHCHCHCN), 131.2 (s, NCCHCHCHCHCN), 124.3 (s, NCCHCHCHCHCN), 123.8 (s, NCCHCHCHCHCN), 117.9 (s, NCCHCHCHCHCN), 111.6 (s, NCCHCHCHCHCN), 82.0 (s, C₅H₅); ³¹P {¹H} (121 MHz) -142.7 (sep, ¹J_{PF} = 710.3 Hz); ¹⁹F {¹H} (282 MHz) -69.8 (d, ¹J_{FP} = 712.3 Hz).

IR (cm⁻¹, powder film): 2347 (m), 1942 (s, ν_{CO}), 1683 (m), 1652 (w), 1590 (m), 1567 (m), 1521 (w), 1494 (w), 1463 (m), 1243 (m), 1104 (m), 1061 (w), 1015 (w), 837 (s), 741 (m), 660 (w).

Route C. A round bottom flask was charged with [(η^5 -C₅H₅)Ru(CO)(NCCH₃)₂]⁺ PF₆⁻ (0.040 g, 0.095 mmol; see above), **GBI** (0.016 g, 0.095 mmol), CH₂Cl₂ (2 mL), and MeOH (1 mL) with stirring. After 2 d at room temperature, the solvent was removed by oil pump vacuum and the residue was chromatographed on a silica gel column (0.5 × 15 cm, 3:1 v/v CH₂Cl₂/CH₃CN). The solvent was removed from the product containing fractions to give a sticky yellow solid. This was dissolved in CH₂Cl₂ (5 mL) and pentane was added until a precipitate formed. The solvent was removed by oil pump vacuum. More pentane (5 mL) was added and removed by oil

pump vacuum ($2 \times$) to give 9^+PF_6^- as a yellow powder (0.039 g, 0.076 mmol, 81%).

$[(\eta^5\text{-C}_5\text{H}_5)\text{Ru}(\text{CO})(\text{GBI})]^+ \text{BARf}^-$ (9^+BARf^-).^{70,71,75} **Route A.** A Schlenk flask was charged with $8^+ \text{BARf}^- \cdot (\text{H}_2\text{O})_2$ (0.257 g, 0.171 mmol) and CH_2Cl_2 (5 mL). The sample was saturated with CO, fitted with a balloon filled with CO, and stirred. After 24 h, the mixture was filtered through a plug of celite (1×2.5 cm), which was rinsed with CH_2Cl_2 (2×10 mL).⁸⁷ The filtrate was concentrated by rotary evaporation (ca. 5 mL). Hexanes (25 mL) was added, and the CH_2Cl_2 was removed by rotary evaporation. The solvent was decanted from the precipitate, which was dissolved in CH_2Cl_2 (5 mL). The solution was added dropwise to stirred hexanes (25 mL), and the CH_2Cl_2 was removed by rotary evaporation. The solvent was decanted from the precipitate, which was dried by oil pump vacuum to give 9^+BARf^- as a yellow powder (0.194 g, 0.157 mmol, 92%). **Route B.** A Schlenk flask was charged with 9^+Cl^- (0.154 g, 0.381 mmol), $\text{Na}^+ \text{BARf}^-$ (0.354 g, 0.401 mmol),⁶⁵ and CH_2Cl_2 (5 mL). The mixture was stirred for 12 h, and filtered through a plug of celite (1×2.5 cm), which was rinsed with CH_2Cl_2 (2×25 mL).⁸⁷ The filtrate was concentrated by rotary evaporation (ca. 5 mL). Hexanes (25 mL) was added, and the CH_2Cl_2 was removed by rotary evaporation. The solvent was decanted from the precipitate, which was dissolved in CH_2Cl_2 (5 mL). The solution was added dropwise to stirred hexanes (25 mL), and the CH_2Cl_2 was removed by rotary evaporation. The solvent was decanted from the precipitate, which was dried by oil pump vacuum to give $9^+ \text{BARf}^- \cdot (\text{H}_2\text{O})_{1.5}$ ⁷⁵ as a yellow powder (0.420 g, 0.333 mmol, 88%).

NMR (δ):^{70,75} ^1H (DMSO- d_6 , 400 MHz) 12.02 (br s, 2H, NH), 7.78 (s 8H, *o*-B(C₆H₃(CF₃)₂)₄), 7.71 (s, 4H, *p*-B(C₆H₃(CF₃)₂)₄), 7.52-7.49 (m, 1H,

$\overline{\text{NCCH}(\text{CH})_2\text{CHCN}}$, 7.32-7.27 (m, 3H, $\overline{\text{NCCH}(\text{CH})_2\text{CHCN}}$), 6.63 (s, 2H, NH_2), 6.45 (s, 1H, NH), 5.30 (s, 5H, C_5H_5), 3.31 (s, H_2O); $^{13}\text{C}\{^1\text{H}\}$ (CD_2Cl_2 , 75 MHz) 203.3 (s, CO), 163.1 (q, $^1J_{\text{CB}} = 49.6$ Hz, *i*- $\text{C}_6\text{H}_3(\text{CF}_3)_2$), 152.4 (s, $\text{NH}=\text{CNH}_2$), 144.1 (s, $\text{N}=\text{C}(\text{NH})_2$), 142.6 (s, $\overline{\text{NCCHCHCHCHCN}}$), 135.2 (s, *o*- $\text{C}_6\text{H}_3(\text{CF}_3)_2$), 130.8 (s, $\overline{\text{NCCHCHCHCHCN}}$), 129.5 (q, $^2J_{\text{CF}} = 31.2$ Hz, *m*- $\text{C}_6\text{H}_3(\text{CF}_3)_2$), 126.7 (q, $^1J_{\text{CF}} = 270.7$ Hz, $\text{C}_6\text{H}_3(\text{CF}_3)_2$), 124.9 (s, $\overline{\text{NCCHCHCHCHCN}}$), 124.5 (s, $\overline{\text{NCCHCHCHCHCN}}$), 118.4 (s, $\overline{\text{NCCHCHCHCHCN}}$), 117.9 (s, *p*- $\text{C}_6\text{H}_3(\text{CF}_3)_2$), 111.4 (s, $\overline{\text{NCCHCHCHCHCN}}$), 81.9 (s, C_5H_5); $^{19}\text{F}\{^1\text{H}\}$ (CD_2Cl_2 , 282 MHz) -63.2 (s).

IR (cm^{-1} , powder film): 3713 (w), 3652 (w), 2362 (w), 2343 (w), 1961 (s, ν_{CO}), 1718 (m), 1687 (m), 1629 (w), 1575 (m), 1355 (s), 1278 (s), 1116 (s), 1061 (m), 934 (w), 887 (w), 837 (w), 745 (m), 710 (m), 671 (m).

$(\eta^5\text{-C}_5\text{H}_5)\text{Ru}(\text{CO})(\text{GBI-H})$ (11).^{26,70,71} A round bottom flask was charged with 9^+Cl^- (0.248 g, 0.612 mmol), Na_2CO_3 (0.211 g, 1.94 mmol), and $\text{CH}_2\text{Cl}_2/\text{H}_2\text{O}$ (6 mL, 1.5:1 v/v). The mixture was stirred for 30 min. The aqueous phase was separated and extracted with CH_2Cl_2 (3×5 mL). The combined organic phases were dried (Na_2SO_4), filtered, and concentrated by rotary evaporation (ca. 5 mL). Hexanes (25 mL) was added, and the CH_2Cl_2 was removed by rotary evaporation. The solvent was decanted from the precipitate, which was dissolved in CH_2Cl_2 (5 mL). The solution was added dropwise to stirred hexanes (25 mL), and the CH_2Cl_2 was removed by rotary evaporation. The solvent was decanted from the precipitate, which was dried by oil pump vacuum to give **11**· $(\text{CH}_2\text{Cl}_2)_{0.33}$ as a brown powder (0.173 g, 0.435 mmol, 71%), dec. pt. 247°C (capillary). Anal. Calcd for $\text{C}_{14}\text{H}_{13}\text{N}_5\text{ORu}\cdot(\text{CH}_2\text{Cl}_2)_{0.33}$: C 43.40, H 3.47, N 17.66. Found C 43.80, H 3.68, N 17.05.⁸⁹

NMR (δ , DMSO- d_6):⁷⁰ ^1H (400 MHz) 10.15 (s, 1H, NH), 7.06-7.04 (m, 1H, $\overline{\text{NCCH}(\text{CH})_2\text{CHCN}}$), 6.85-6.81 (m, 3H, $\overline{\text{NCCH}(\text{CH})_2\text{CHCN}}$), 5.70 (s, 2H, NH₂), 5.32 (s, CH₂Cl₂), 5.17 (s, 1H, NH), 5.10 (s, 5H, C₅H₅); $^{13}\text{C}\{^1\text{H}\}$ (100 MHz) 207.5 (s, CO), 157.5 (s, NH=CNH₂), 154.6 (s, N=C(NH)₂), 146.1 (s, $\overline{\text{NCCHCHCHCHCN}}$), 139.9 (s, $\overline{\text{NCCHCHCHCHCN}}$), 118.7 (s, $\overline{\text{NCCHCHCHCHCN}}$), 118.5 (s, $\overline{\text{NCCHCHCHCHCN}}$), 114.2 (s, $\overline{\text{NCCHCHCHCHCN}}$), 111.8 (s, $\overline{\text{NCCHCHCHCHCN}}$), 83.0 (s, C₅H₅), 54.9 (s, CH₂Cl₂).

$[(\eta^5\text{-C}_5\text{H}_5)\text{Ru}(\text{CO})(\text{GBI})]^+ (\text{P})\text{-Phos}^-$ ($\mathbf{9}^+$ (P)-Phos⁻).²⁶ A round bottom flask was charged with **11** (0.025 g, 0.05 mmol), **12** (0.020 g, 0.05 mmol), and CH₂Cl₂ (2 mL) with stirring. After 0.5 h, the mixture was filtered through a plug of celite (1 × 2.5 cm), which was rinsed with CH₂Cl₂ (5 mL). Hexanes (20 mL) was added, and the CH₂Cl₂ was removed by rotary evaporation. The solvent was decanted from the precipitate, which was dissolved in CH₂Cl₂ (2 mL). The solution was added dropwise to stirred hexanes (25 mL), and the CH₂Cl₂ was removed by rotary evaporation. The solvent was decanted from the precipitate, which was dried by oil pump vacuum to give $\mathbf{9}^+$ (P)-Phos⁻ as a dirty white powder (0.035 g, 0.050 mmol, >99%), dec. pt. 215 °C (capillary). Anal. Calcd for C₃₄H₂₆N₅O₅PRu: C 56.98, H 3.66, N 9.77. Found C 55.08, H 4.09, N 10.00.⁸⁹

NMR (δ , CD₂Cl₂, diastereomers separated by "/"): ⁹⁰ ^1H (500 MHz) 8.05-8.03 (d, 2H, $^2J_{\text{CH}} = 9.0$ Hz, $\mathbf{H}_{(P)\text{-Phos}}$), 7.95 (d, 2H, $^2J_{\text{CH}} = 8.2$ Hz, $\mathbf{H}_{(P)\text{-Phos}}$), 7.66-7.47, 7.41-7.36, 7.25-7.18, 7.15-7.06, and 7.02-6.99 (5 × m, 2H, 4H, 3H, 2H, and 1H, remaining $\mathbf{H}_{(P)\text{-Phos}}$ and $\overline{\text{NCCH}(\text{CH})_2\text{CHCN}}$), 6.14 (br s, 2H, NH), 5.82 (s, 2H, NH), 5.18/5.07 (2

\times s, 1H/1H, NH), 4.85/4.80 (2 \times s, 5H/5H, C₅H₅); ¹³C{¹H} (125 MHz) 204.8/204.7 (2 \times s, CO), 154.6/152.3 (2 \times s, NH=CNH₂), 149.3/149.2 (2 \times s, C_(P)-Phos), 147.3/147.2 (2 \times s, N=C(NH)₂), 143.3/143.2 (2 \times s, NCCHCHCHCHCN), 135.6/134.7 (2 \times C_(P)-Phos), 131.7/131.6 (2 \times s, NCCHCHCHCHCN), 131.0, 130.9, 128.8, 128.7, 127.3, 127.2, 126.6, 126.5, 125.5, 125.4, (10 \times s, remaining C_(P)-Phos), 122.4/121.9 (s, NCCHCHCHCHCN), 121.8 (s, NCCHCHCHCHCN), 117.0, 116.9 (2 \times s, NCCHCHCHCHCN), 111.6/111.5 (2 \times s, NCCHCHCHCHCN), 82.2/82.1 (2 \times s, C₅H₅).

IR (cm⁻¹, powder film): 3375 (w), 1938 (s, ν_{CO}), 1680 (m), 1566 (m), 1563 (s), 1463 (w), 1354 (w), 1409 (w), 1261 (w), 1240 (w), 1215 (w), 1091 (s), 1068 (s), 960 (s), 837 (m), 810 (m), 749 (m), 700 (m).

Friedel-Crafts Alkylations (Table 2.5 and 2.9). An NMR tube was charged with catalyst (0.010 mmol), an indole (**5a,b**; 0.20 mmol), **6** (0.015 g, 0.10 mmol), an internal standard (Ph₂SiMe₂), and CD₂Cl₂ (0.5 mL). The tube was capped and ¹H NMR spectra were periodically recorded. The CH=CH signals of **6** and the product CH₂NO₂ signals at ca. 5 ppm were integrated versus those of the standards.

1-methyl-3-(2-nitro-1-phenylethyl)-1H-indole (7a). NMR (δ, CDCl₃): ¹H (500 MHz): 7.47 (d, 1H, ³J_{HH} = 7.6 Hz), 7.38–7.23 (m, 7H), 7.10 (m, 1H), 6.88 (s, 1H), 5.21 (t, 1H, ³J_{HH} = 8.0 Hz, CHCH₂NO₂), 5.06 (dd, 1H, ³J_{HH} = 12.4, ²J_{HH} = 8.0 Hz, CHH'NO₂), 4.95 (dd, 1H, ³J_{HH} = 12.4, ²J_{HH} = 8.0 Hz, CHH'NO₂), 3.75 (s, 3H, NCH₃); Literature chemical shift values (CDCl₃) agree within 0.01 ppm.^{68a}

3-(2-nitro-1-phenylethyl)-1*H*-indole (7b).^{70,75} NMR (δ , CDCl₃): ¹H (500 MHz): 8.08 (br s, 1H, C₈H₅NH), 7.55-6.96 (m, 10H, C₈H₅NH and C₆H₅), 5.19 (t, 1H, ³J_{HH} = 8.2 Hz, CHCH₂NO₂), 5.07 (dd, 1H, ²J_{HH} = 12.4 Hz, ³J_{HH} = 7.2 Hz, CHH'NO₂), 4.95 (dd, 1H, ²J_{HH} = 12.4 Hz, ³J_{HH} = 8.2 Hz, CHH'NO₂). Literature values (CDCl₃)⁹¹ agree within 0.01 ppm, and data in CD₂Cl₂ are supplied elsewhere.⁷⁰

Crystallography A. A CH₂Cl₂ (5 mL) solution of **3**⁺ BAr_f⁻·H₂O (ca. 0.03 g) in an NMR tube was allowed to concentrate for 7 d. Grey blocks of **3**⁺ BAr_f⁻·H₂O with well defined faces formed.

Data were collected as outlined in Table 2.1. The integrated intensity information for each reflection was obtained by reduction of the data frames with the program APEX2.⁹² Cell parameters were obtained from 180 frames using a 0.5° scan. Data were corrected for Lorentz and polarization factors, and using SADABS,⁹³ absorption and crystal decay effects. The structure was solved by direct methods using SHELXTL (SHELXS).⁹⁴ All non-hydrogen atoms were refined with anisotropic thermal parameters. Hydrogen atoms were placed in idealized positions using a riding model. Elongated thermal ellipsoids on several CF₃ groups and the C(NH₂)₃ groups indicated disorder, which was modeled. A number of restraints and constraints were applied to the bond distances, angles, and thermal ellipsoids. The parameters were refined by weighted least squares refinement on F^2 to convergence.⁹⁴

B. A wet CH₂Cl₂ (5 mL) solution of **4**⁺ BAr_f⁻ (ca. 0.03 g) in an NMR tube was allowed to concentrate for 7 d. Colorless blocks of **4**⁺ BAr_f⁻·H₂O·(CH₂Cl₂)_{0.5} with well defined faces formed.

Data were collected as outlined in Table 2.1. The integrated intensity information

for each reflection was obtained by reduction of the data frames with the program APEX2.⁹² Cell parameters were obtained from 180 frames using a 0.5° scan. Data were corrected for Lorentz and polarization factors, and using SADABS,⁹³ absorption and crystal decay effects. The structure was solved by direct methods using SHELXTL (SHELXS).⁹⁴ The asymmetric unit contained two unique 4^+ BAr_f^- salts, two molecules of H_2O and one molecule of CH_2Cl_2 . There were two asymmetric units in the unit cell ($Z = 4$; $Z' = 2$). All non-hydrogen atoms were refined with anisotropic thermal parameters. Hydrogen atoms were placed in idealized positions using a riding model. Several of the CF_3 and $\text{C}(\text{NH})$ groups were disordered. Efforts to model the disorder did not improve the R value. For the final refinement, some of the CF_3 groups were left with elongated thermal ellipsoids. The parameters were refined by weighted least squares refinement on F^2 to convergence.⁹⁴

C. A round bottom flask was charged with $(\eta^5\text{-C}_5\text{H}_5)\text{Fe}(\text{CO})_2(\text{Br})$ (0.0510 g, 0.200 mmol), **GBI** (0.0386 g, 0.200 mmol), $\text{NH}_4^+ \text{PF}_6^-$ (0.068 g, 0.400 mmol), and EtOH (10 mL). The mixture was refluxed with stirring. After 14 h, the mixture was cooled to room temperature and the solvent was removed by oil pump vacuum. Then CH_2Cl_2 was added to the residue, and the sample was stirred. The solution was filtered through a short plug of celite.

A portion was allowed to concentrate in an NMR tube. After 1 d, brown column shaped crystals of $[\text{1-H}]^{2+} 2\text{Br}^- \cdot \text{H}_2\text{O}$ were obtained.

Data were collected as outlined in Table 2.1. The integrated intensity information for each reflection was obtained by reduction of the data frames with the program APEX2.⁹² Cell parameters were obtained from 180 frames using a 0.5° scan. Data were corrected for Lorentz and polarization factors and using SADABS⁹³ absorption and

crystal decay effects. The structure was solved by direct methods using SHELXTL (SHELXS).⁹⁴ All non-hydrogen atoms were refined with anisotropic thermal parameters. Hydrogen atoms were placed in idealized positions using a riding model. The parameters were refined by weighted least squares refinement on F^2 to convergence.⁹⁴

3. EPIMERIC CHIRAL-AT-METAL RUTHENIUM COMPLEXES: SEPARATION AND APPLICATIONS*

3.1 Introduction

3.1.1 Modification of GBI to facilitate isolation of enantiopure ruthenium complexes

Encouraged by the rich literature on the formation and separation of diastereomers of chiral-at-metal⁹⁵⁻¹⁰⁰ (specially ruthenium)^{62b,63a-h,96} piano stool complexes, a series of substituted **GBI** complexes was targeted (Figure 1.1, top). Some examples would involve achiral **GBI** derivatives that may afford more readily resolvable enantiomers, and others would involve chiral enantiopure **GBI** derivatives that would lead to mixtures of Ru,C configurational diastereomers. These would potentially be easier to separate, providing an alternative route to enantiopure catalysts. Considering the immense popularity and success of Takemoto's very effective and widely applied dimethylamino containing thiourea catalyst **XII** (Figure 3.1, bottom (left)),^{21a,d} similar bifunctional systems were also sought (Figure 3.1, bottom (right)).

* Reproduced in part with permission from Mukherjee, T.; Ganzmann, C.; Bhuvanesh, N.; Gladysz, J. A. *Organometallics* **2014**, *33*, 6723-6737. Copyright 2014 American Chemical Society.

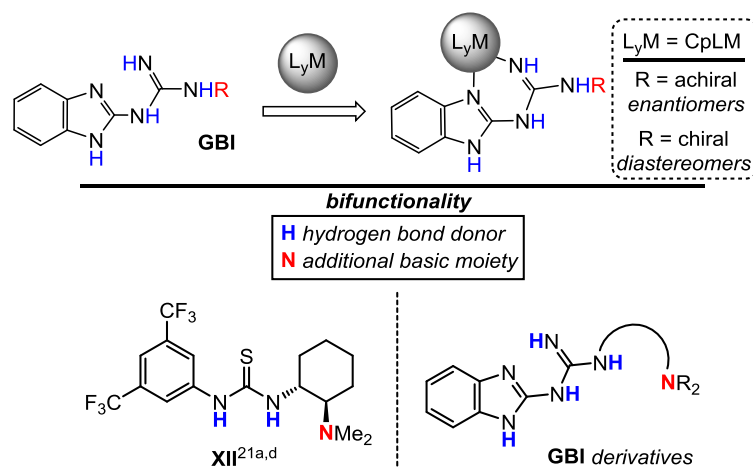


Figure 3.1 Top: **GBI** derivatives and their metal complexes. Bottom: Takemoto's famous thiourea based dual hydrogen bond donor bifunctional catalyst (left), conceptually analogous bifunctional **GBI** (right).

3.2 Results

3.2.1 Syntheses of substituted **GBI** derivatives

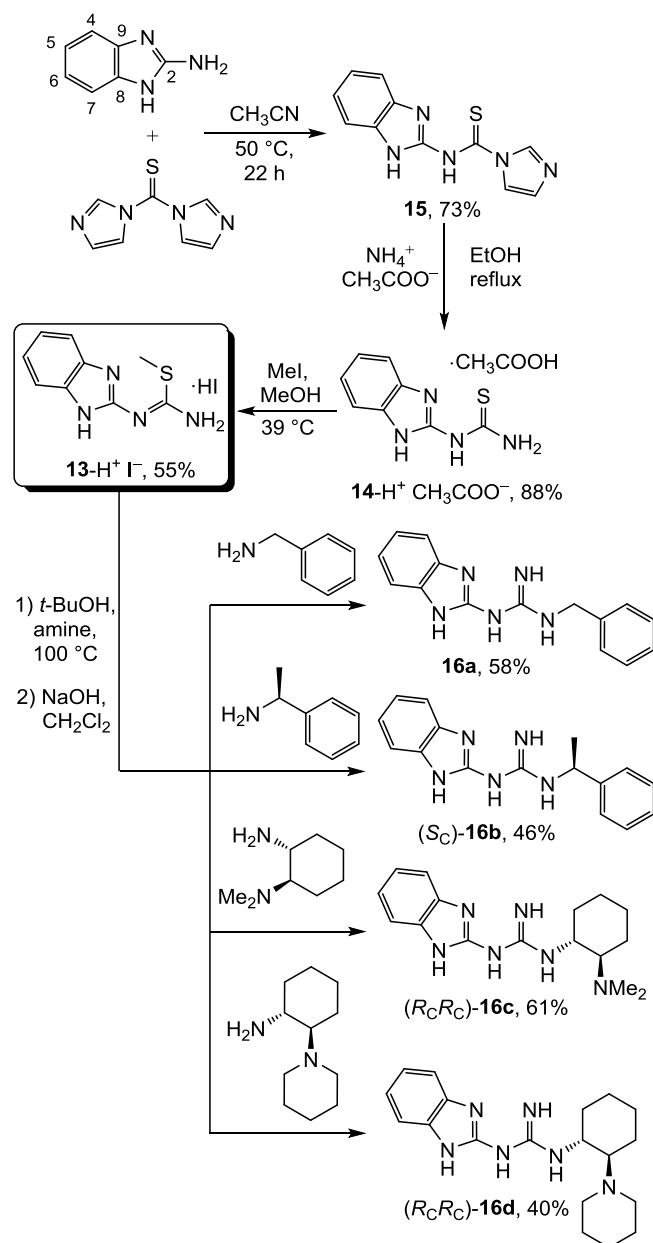
It was first sought to replace the NH_2 group of the **GBI** ligand by alkylated NHR groups, and then obtain enantiopure complexes. Towards this intention, a patent describing a reaction sequence involving the protonated methyl isothiourea $\mathbf{13}\text{-H}^+ \text{I}^-$ shown in Scheme 3.1 and *o*-methoxybenzylamine¹⁰¹ appeared promising. This afforded a **GBI** ligand with a NHCH_2Ar group. Analogous reactions with other primary amines could easily be envisioned. According to the patent, $\mathbf{13}\text{-H}^+ \text{I}^-$ can be obtained by reacting the protonated thiourea $\mathbf{14}\text{-H}^+ \text{CH}_3\text{COO}^-$ and methyl iodide. Compound $\mathbf{14}\text{-H}^+ \text{CH}_3\text{COO}^-$ was in turn accessed from the ammonolysis of the known imidazole derivative **15** (Scheme 3.1).

As a starting point for this work, **15** was prepared by combining aspects of two existing literature procedures involving 2-aminobenzimidazole and 1,1-thiocarbonyl

diimidazole, as depicted in Scheme 3.1 and detailed in the experimental section.^{102,103} Workup gave **15** as a light yellow solid in 73% yield. Subsequent reactions as mentioned in the patent gave **14**-H⁺ CH₃COO⁻ as a pale yellow powder in 88% yield and **13**-H⁺ I⁻ as a white solid in 55% yield. Given the variable degrees of detail and peer review associated with patent preparations, full procedures for both of these steps are given in the experimental section and in the full paper associated with this chapter.¹⁰⁴

As shown in Scheme 3.1, **13**-H⁺ I⁻ was treated with benzyl amine and three other enantiopure chiral primary amines. In the first two cases, the amines were commercially available and excesses were employed. The other two amines, which furthermore incorporated pendant tertiary amines, had to be synthesized, and therefore were utilized in near stoichiometric quantities. Comparable conversions could be obtained by employing longer reaction times. Basic workups afforded the **GBI** derivatives **16a**,^{105,106} (*S_C*)-**16b**,^{105,107} (*R_CR_C*)-**16c**,^{105,107} and (*R_CR_C*)-**16d** as white or pale yellow air stable solids in 40-61% yields. The first two chiral derivatives were originally prepared by Dr. C. Ganzmann, but were repeated as part of this work.¹⁰⁵

Compound **16a** had previously been prepared in 28% yield from the reaction of 2-cyanoaminobenzimidazole and benzyl amine in refluxing DMF.¹⁰⁸ Here, the new route in Scheme 3.1 represents a distinct improvement. All of the above compounds were characterized by NMR (¹H, ¹³C) and IR spectroscopy, and microanalysis, as summarized in the experimental section.



Scheme 3.1 Synthesis of intermediate **13-H⁺ I⁻** and its use towards the syntheses of achiral/chiral substituted **GBI** ligands.

3.2.2 Syntheses of substituted **GBI** complexes

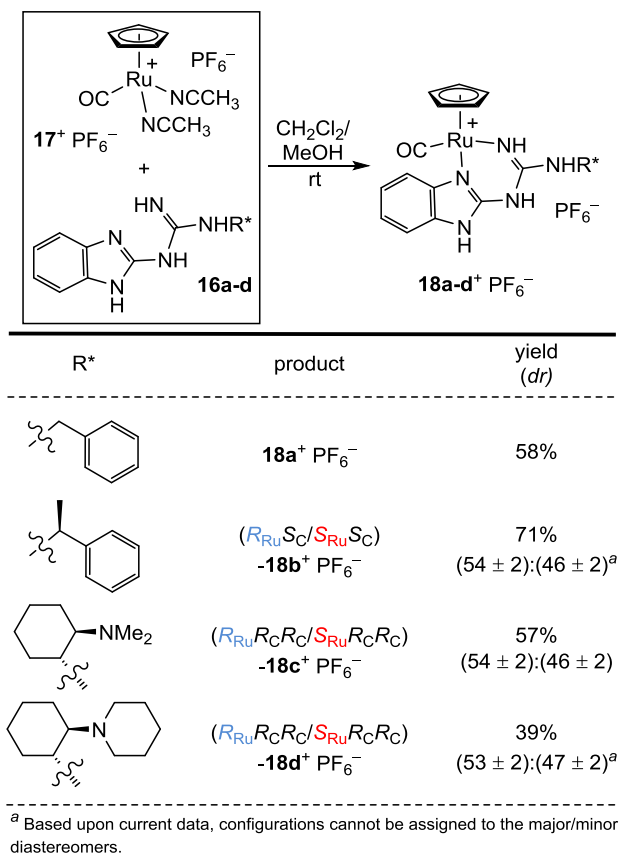
The ligands **16a-d** were complexed to the cyclopentadienyl carbonyl ruthenium

fragment by one of the methods established for **GBI** in the preceding chapter.⁷⁵ As shown in Scheme 3.2, the readily available cationic bis(acetonitrile) complex $[(\eta^5\text{-C}_5\text{H}_5)\text{Ru}(\text{CO})(\text{NCCH}_3)_2]^+ \text{PF}_6^-$ (**17**⁺ PF_6^-)^{74,104} was treated with 1.1-1.3 equiv of the ligands in $\text{CH}_2\text{Cl}_2/\text{MeOH}$ to afford the crude chelates $[(\eta^5\text{-C}_5\text{H}_5)\text{Ru}(\text{CO})(\mathbf{16a-d})]^+ \text{PF}_6^-$ (**18a-d**⁺ PF_6^-).¹⁰⁴ These and all other reactions involving ruthenium species below were conducted under aerobic conditions. As seen in chapter 2, the CO ancillary ligand in **18a-d**⁺ PF_6^- makes for a stronger hydrogen bond donor than a PPh_3 ligand (see Table 2.9).⁷⁵

In the case of the achiral ligand **16a**, the crude sample was chromatographed on silica gel ($\text{CH}_2\text{Cl}_2/\text{CH}_3\text{CN}$) to give **18a**⁺ PF_6^- as a yellow solid in 58% yield.¹⁰⁴⁻¹⁰⁶ This and all new ruthenium complexes were characterized as described for the ligands above. NMR spectra showed only a single cyclopentadienyl ^1H and ^{13}C signal (δ 4.88 and 83.0).¹⁰⁴⁻¹⁰⁶ As noted in the preceding chapter, the cyclopentadienyl carbonyl complexes commonly gave low microanalytical values for nitrogen.

With the chiral enantiopure ligand (*S*_C)-**16b**, the product was either chromatographed on silica gel using $\text{CH}_2\text{Cl}_2/\text{CH}_3\text{CN}$ or on alumina using a $\text{CH}_2\text{Cl}_2/\text{MeOH}$ gradient.^{104,107} In the latter case, nearly all of the PF_6^- counter anion underwent exchange with alumina derived entities to give a material represented as **18b**⁺ X^- . Hence, aliquots were taken to dryness and treated with a CH_2Cl_2 solution of $\text{Na}^+ \text{PF}_6^-$ to regenerate **18b**⁺ PF_6^- .^{104,107} The silica gel based workup directly afforded **18b**⁺ PF_6^- as a greenish-brown solid in 71% yield.^{104,107} The ^1H NMR spectrum exhibited two well separated cyclopentadienyl ^1H NMR signals (δ 5.05 and 4.60, area ratio (54 ± 2):(46 ± 2)), consistent with a mixture of Ru,C configurational diastereomers. The ratio did not change upon further silica gel chromatography, but alumina afforded a more enriched mixture. However, nothing approaching a preparatively useful separation could

be achieved.

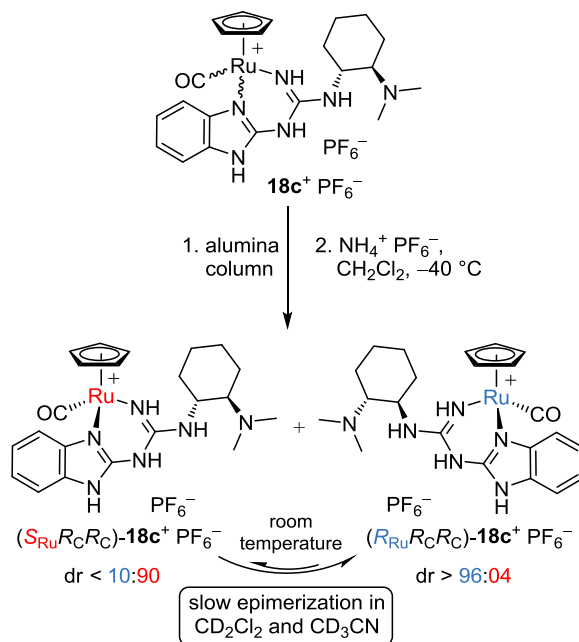


Scheme 3.2 Syntheses of ruthenium chelate complexes of substituted **GBI** ligands.

Similar protocols with the enantiopure ligands (*R*_C*R*_C)-**16c,d** provided salts **18c⁺** PF₆⁻ ¹⁰⁹ and **18d⁺** PF₆⁻ as (54 ± 2):(46 ± 2) and (53 ± 2):(47 ± 2) as mixtures of diastereomers, as assayed by ¹H NMR of the crude samples. Silica gel chromatography led to decomposition, likely connected in some manner to the tertiary amine groups. However, alumina chromatography (CH₂Cl₂/MeOH gradient) afforded the intact cations, but with concomitant anion exchange to give **18c,d⁺** X⁻. Subsequent treatments

with $\text{Na}^+ \text{PF}_6^-$ gave $\mathbf{18c,d}^+ \text{PF}_6^-$ as greenish-brown solids in 57% and 39% yields, with the diastereomer ratios (dr) (always close to 50:50) depending somewhat on the column conditions.

It would be preferable to separately assay the enantioselectivity achievable with each diastereomeric catalyst. Hence, the alumina chromatography conditions were varied. It was found that when higher loadings of $\mathbf{18c}^+ \text{PF}_6^-$ were employed, together with an extended $\text{CH}_2\text{Cl}_2/\text{MeOH}$ gradient, significant diastereomer separation could be achieved, as diagrammed in Scheme 3.3. Three cuts of fractions were collected: an initial series containing predominantly one diastereomer of $\mathbf{18c}^+ \text{X}^-$ (>96:<4), an intermediate series containing both diastereomers (the least in terms of mass), and a final series containing predominantly the other diastereomer (<10:>90).

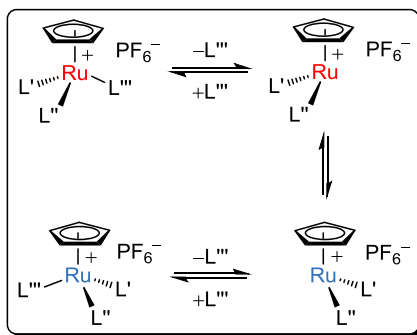


Scheme 3.3 Separation and epimerization of the diastereomers of $\mathbf{18c}^+ \text{PF}_6^-$.

Now the anion exchange was conducted at $-40\text{ }^{\circ}\text{C}$ using CH_2Cl_2 solutions of $\mathbf{18c}^+ \text{X}^-$ (initial and final fractions) and the ammonium salt $\text{NH}_4^+ \text{PF}_6^-$. For the faster eluting diastereomer, assigned as $R_{\text{Ru}}R_{\text{C}}R_{\text{C}}$ based upon data provided below, the dr ranged from $>99:<1$ to $96:04$ (best and worst cases). For the slower moving $S_{\text{Ru}}R_{\text{C}}R_{\text{C}}$ diastereomer, ratios ranged from $02:98$ to $10:90$. The masses recovered were $>60\%$ of the initial $\mathbf{18c}^+ \text{X}^-$ charges. A similar approach with $\mathbf{18d}^+ \text{PF}_6^-$ led to partial separation, with the best dr value for each diastereomer being 80:20. Extensive efforts to crystallize any of the salts $\mathbf{18b-d}^+ \text{PF}_6^-$ were unsuccessful.

3.2.3 Epimerization of GBI complexes, assignment of diastereomer configurations

Complexes $\mathbf{18c,d}^+ \text{PF}_6^-$ were configurationally stable as solids, but underwent slow epimerization in solution as sketched in Scheme 3.3. A number of other chiral-at-metal d^6 cyclopentadienyl adducts have also been observed to undergo epimerization, and detailed mechanistic studies have established ligand dissociation followed by inversion of the resulting pyramidal coordinatively unsaturated species, as shown in Scheme 3.4.^{110,111} Some of the data for $\mathbf{18c}^+ \text{PF}_6^-$ are summarized in Table 3.1, and show that (1) rates are slightly faster in CD_3CN than CD_2Cl_2 , and (2) only moderate losses of diastereomeric purities occur over 24 h at room temperature.



Scheme 3.4 Plausible pathway for the inversion of the ruthenium center in Scheme 3.3.

It was thought that other counter anions might yield salts that could crystallize and aid in the assignment of configurations. When crude $(R_{Ru}R_C R_C)\text{-18c}^+ X^-$ was treated with the salt $\text{Na}^+ \text{BAr}_f^-$ ²⁶ under metathesis conditions similar to those used in the preceding chapter, it proved difficult to remove the excess tetraarylborate anion. Equimolar quantities did not give complete metatheses. However, workup of the reaction of $(R_{Ru}R_C R_C)\text{-18c}^+ X^-$ and ca. 1.0 equiv of the enantiopure chiral phosphate salt $\text{Na}^+ (\Delta)\text{-TRISPHAT}^-$ ^{26,112} gave $(R_{Ru}R_C R_C)\text{-18c}^+ (\Delta)\text{-TRISPHAT}^-$ as a pale yellow powder of ca. 95% purity. This complex underwent slow epimerization in CD_2Cl_2 at room temperature, analogously to $(R_{Ru}R_C R_C)\text{-18c}^+ \text{PF}_6^-$.

Table 3.1 Epimerization data for the diastereomers of $18c^+ PF_6^-$.^a

%de (dr) of ($R_{Ru}R_C R_C$)- $18c^+ PF_6^-$					
time (d)	Solid	Solution			
	-35 °C	CD ₂ Cl ₂		CD ₃ CN	
		-35 °C	rt	-35 °C	Rt
0.0	95.0 (97.5:2.5)	98.0 (99.0:1.0)	96.0 (98.0:2.0)	98.0 (99.0:1.0)	92.4 (96.2:3.8)
1.0	-	-	85.2 (92.6:7.4)	-	80.2 (90.1:9.9)
2.0	-	-	75.4 (87.7:12.3)	-	69.6 (84.8:15.2)
3.0	-	-	66.8 (83.4:16.6)	-	60.0 (80.0:20.0)
4.0	-	-	60.0 (80.0:20.0)	-	51.6 (75.8:24.2)
5.0	95.0 (97.5:2.5)	98.0 (99.0:1.0)	-	98.0 (99.0:1.0)	-

%de (dr) of ($S_{Ru}R_C R_C$)- $18c^+ PF_6^-$					
time (d)	Solid	Solution			
	-35 °C	CD ₂ Cl ₂		CD ₃ CN	
		-35 °C	rt	-35 °C	Rt
0.0	88.0 (6.0:94.0)	90.0 (10.0:90.0)	88.0 (6.0:94.0)	90.0 (10.0:90.0)	45.8 (27.1:72.9)
1.0	-	-	75.4 (12.3:87.7)	-	36.0 (32.0:68.0)
2.0	-	-	64.0 (18.0:82.0)	-	29.8 (35.1:64.9)
3.0	-	-	55.2 (22.4:77.6)	-	24.2 (37.9:62.1)
4.0	-	-	47.4 (26.3:73.7)	-	20.2 (39.9:60.1)
5.0	88.0 (6.0:94.0)	90.0 (10.0:90.0)	-	90.0 (10.0:90.0)	-

^a Measured by ¹H NMR. The C₅H₅ or NMe₂ signals were integrated against the internal standard Ph₂SiMe₂ and the values were averaged.

Small colorless blocks of a CHCl_3 monosolvate of $(R_{\text{Ru}}R_{\text{C}}R_{\text{C}})\text{-18c}^+$ (Δ)- TRISPHAT^- could be grown from $\text{CHCl}_3/\text{C}_6\text{F}_6$. A correct microanalysis was obtained, and the crystal structure was determined using synchrotron radiation as summarized in the experimental section and Appendix B (Table b1). Key metrical parameters are given in Table 3.2. Figure 3.2 shows the structures of the salt (top) and the cation (bottom). These confirm the configurational assignment given above.

Hydrogen bonding is evident between the N10-H10 and N13-H13 linkages of the cation and two oxygen atoms of the (Δ)- TRISPHAT^- anion (Figure 3.2, top; see caption for distances). The structure of the anion is very similar to those found in other TRISPHAT^- salts.^{113,114} These include two ammonium salts that exhibit $\text{NH}\cdots\text{O}$ hydrogen bonding interactions, with distances comparable to those shown in Figure 3.2.¹¹⁴

As with the structures of the two ruthenium **GBI** complexes in the full paper associated with the previous chapter,⁷⁵ the bond lengths of the coordinated $\text{C}=\text{NH}$ and $\text{C}=\text{NAr}$ linkages (1.298(5) and 1.321(5) Å) are shorter than the other four carbon-nitrogen bonds about C2 and C11 (1.345(5)-1.386(5) Å). This provides further support for the ligand tautomer shown in Scheme 3.2 and 3.3 (see Figure 2.2 and Scheme 2.2, chapter 2). Alternative tautomers of the **GBI** would afford different bond length patterns (Scheme 2.3, chapter 2).

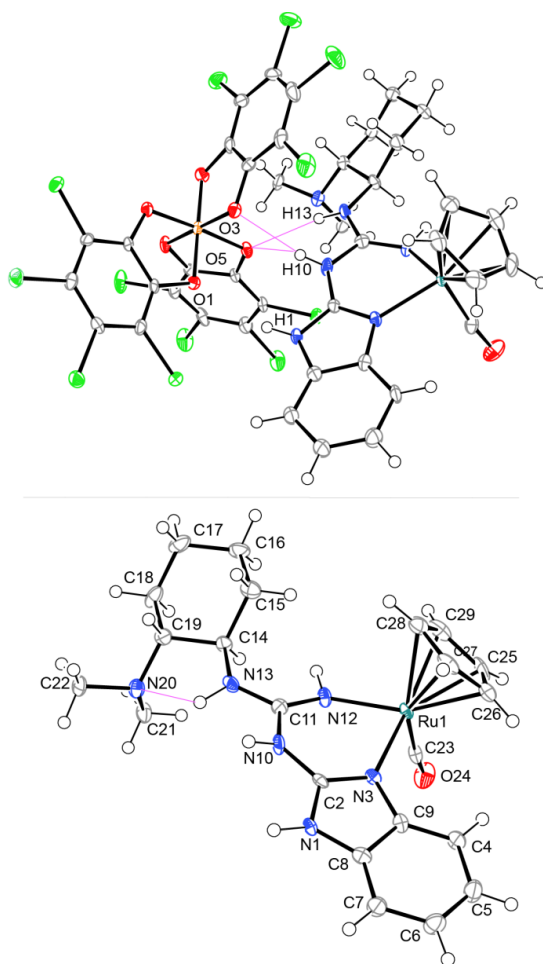


Figure 3.2 Top: thermal ellipsoid diagram (50% probability level) of the molecular structure of $(R_{Ru}R_C R_C)\text{-18c}^+$ (Δ)-TRISPHAT $^- \cdot \text{CHCl}_3$ with the solvate molecule omitted. Bottom: alternative view of the cation. Key distances involving hydrogen bonds (Å): H10-O3 2.23, N10-O3 3.030(6), H10-O5 2.40, N10-O5 3.078(6), H13-O5 2.29, N13-O5 3.072(6), N20-H13 2.21, N20-N13 2.721.

An approximately *synperiplanar* NH triad (N10-H10, N13-H13, N1-H1) is apparent, as reflected by H-N-N-H torsion angles close to 0° (-38.9° , 13.0° , -24.3°). However, the N13-H13 group, which as noted above hydrogen bonds to (Δ)-TRISPHAT, similarly interacts with the nitrogen atom of the dimethylamino group (N20), as indicated in Figure 3.2 (bottom).

Table 3.2 Key bond lengths [Å], bond angles [°], and torsion angles [°] for $(R_{Ru}R_C R_C)-18c^+$ (Δ)-TRISPHAT⁻·CHCl₃ and $(R_{Ru}R_C R_C/S_{Ru}R_C R_C)-18c^+$ (Δ/Λ)-TRISPHAT⁻·(Et₂O)₂.^a

	$(R_{Ru}R_C R_C)-18c^+$ (Δ)- TRISPHAT ⁻ ·CHCl ₃	$(R_{Ru}R_C R_C/S_{Ru}R_C R_C)-18c^+$ (Δ/Λ)- TRISPHAT ⁻ ·(Et ₂ O) ₂	
		$(R_{Ru}R_C R_C)-18c^+$	$(S_{Ru}R_C R_C)-18c^+$
Ru(1)-N(3)	2.119(3)	2.086(6)	2.083(6)
Ru(1)-N(12)	2.094(3)	2.093(6)	2.069(6)
Ru(1)-C(23)	1.861(4)	1.831(7)	1.862(8)
C(2)-N(3)	1.321(5)	1.342(8)	1.320(9)
C(2)-N(1)	1.350(5)	1.348(9)	1.379(9)
C(2)-N(10)	1.360(5)	1.357(9)	1.340(9)
C(11)-N(10)	1.386(5)	1.355(9)	1.370(10)
C(11)-N(12)	1.298(5)	1.296(8)	1.280(9)
C(11)-N(13)	1.345(5)	1.363(9)	1.395(9)
C(14)-N(13)	1.455(5)	1.486(8)	1.480(8)
C(23)-Ru(1)-N(3)	93.92(15)	92.6(3)	92.5(3)
C(23)-Ru(1)-N(12)	92.17(15)	93.6(3)	94.0(3)
N(3)-Ru(1)-N(12)	83.00(12)	82.5(2)	83.4(2)
Ru(1)-N(3)-C(2)	125.0(3)	126.4(5)	124.8(5)
N(3)-C(2)-N(1)	112.7(3)	111.1(6)	111.0(6)
N(3)-C(2)-N(10)	126.8(3)	127.6(6)	130.3(7)
N(1)-C(2)-N(10)	120.4(3)	121.3(6)	118.7(6)
Ru(1)-N(12)-C(11)	130.6(3)	129.4(5)	130.3(5)
N(12)-C(11)-N(10)	120.4(3)	124.1(7)	124.9(7)
N(12)-C(11)-N(13)	125.8(4)	119.8(7)	119.9(7)
N(10)-C(11)-N(13)	113.8(3)	116.1(6)	115.0(6)
C(11)-N(13)-C(14)	123.0(3)	127.3(6)	129.6(6)
C(23)-Ru(1)-N(3)-C(2)	-111.6(3)	-108.8(2)	109.4(2)
C(23)-Ru(1)-N(12)-C(11)	122.3(4)	120.0(2)	-114.4(3)
Ru(1)-N(3)-C(2)-N(10)	3.6(5)	-1.3(10)	-1.8(11)
Ru(1)-N(12)-C(11)-N(10)	-18.7(5)	-23.0(10)	13.7(11)
Ru(1)-N(12)-C(11)-N(13)	160.8(3)	153.5(5)	-172.3(5)
N(3)-C(2)-N(10)-C(11)	19.0(6)	17.6(11)	-15.9(12)
N(12)-C(11)-N(10)-C(2)	-11.4(6)	-5.0(11)	9.7(11)
N(13)-C(14)-C(19)-N(20)	49.4(4)	-65.4(7)	-66.0(8)
N(12)-C(11)-N(13)-C(14)	-1.47(5)	150.4(6)	140.8(7)
H(10)-N(10)-N(13)-H(13)	-38.9	-165.8	130.2
H(10)-N(10)-N(1)-H(1)	13.0	13.6	-11.2
H(1)-N(1)-N(13)-H(13)	-24.3	-144.9	112.5
C(11)-N(13)-C(14)-C(15)	-69.5(8)	-154.8(6)	166.5(7)
C(11)-N(13)-C(14)-C(19)	-166.3(2)	86.7(8)	73.5(9)

^a For distances involving hydrogen bonds, see the captions to Figures 3.2 and 3.3.

The analogous salt with the racemic TRISPHAT anion, ($R_{\text{Ru}}R_{\text{C}}R_{\text{C}}$)-**18c**⁺ (Δ/Λ)-TRISPHAT⁻, was similarly prepared. Two diastereomeric ion pairs are possible, but a ¹H NMR spectrum (CD₂Cl₂) showed only a single cyclopentadienyl signal, in contrast to the example with **9**⁺ (*P*)-Phos⁻ (Scheme 2.8) in the previous chapter. Crystals were obtained over a three week period from Et₂O/CH₃CN, and the structure was determined by X-ray crystallography. As illustrated in Figure 3.3, the salt consisted of a 50:50 mixture of both diastereomers of the ruthenium cation ($R_{\text{Ru}}R_{\text{C}}R_{\text{C}}/S_{\text{Ru}}R_{\text{C}}R_{\text{C}}$) and both enantiomers of the TRISPHAT⁻ anion (Δ/Λ), together with two Et₂O solvate molecules per ruthenium. Consistent with the data in Table 3.1, the ruthenium center epimerized on the time scale of the crystallization. Curiously, the cocrystallization of diastereomeric chiral-at-metal d⁶ cyclopentadienyl complexes has abundant precedent.¹¹⁵

While this mixed salt does not aid in the assignment of configuration, it does provide a structure for the diastereomeric $S_{\text{Ru}}R_{\text{C}}R_{\text{C}}$ cation, as well as a probe of the conformational flexibility of the $R_{\text{Ru}}R_{\text{C}}R_{\text{C}}$ cation. As can be seen in Table 3.2, the bond lengths and angles are quite similar for all three cations in Figures 3.2 and 3.3; those involving ruthenium are very close to other ($\eta^5\text{-C}_5\text{R}_5$)Ru(CO) adducts (R = H or Me) of nitrogen chelate ligands.^{75,116}

However, the $R_{\text{Ru}}R_{\text{C}}R_{\text{C}}$ cation in Figure 3.3 adopts a different conformation about the C11-N13 bond from that in Figure 3.2, as reflected by the N12-C11-N13-C14 torsion angles (150.4° vs. -1.47°). This reduces the number of *synperiplanar* NH linkages to two, as evidenced by a single H-N-N-H torsion angle close to 0° (H10-N10-N1-H1, 13.0°; those involving H13-N13 are -165.8° and -144.9°). Interestingly, the $S_{\text{Ru}}R_{\text{C}}R_{\text{C}}$ cation in Figure 3.3 exhibits a comparable N12-C11-N13-C14 torsion angle (140.8°), similarly leading to only two *synperiplanar* NH linkages.

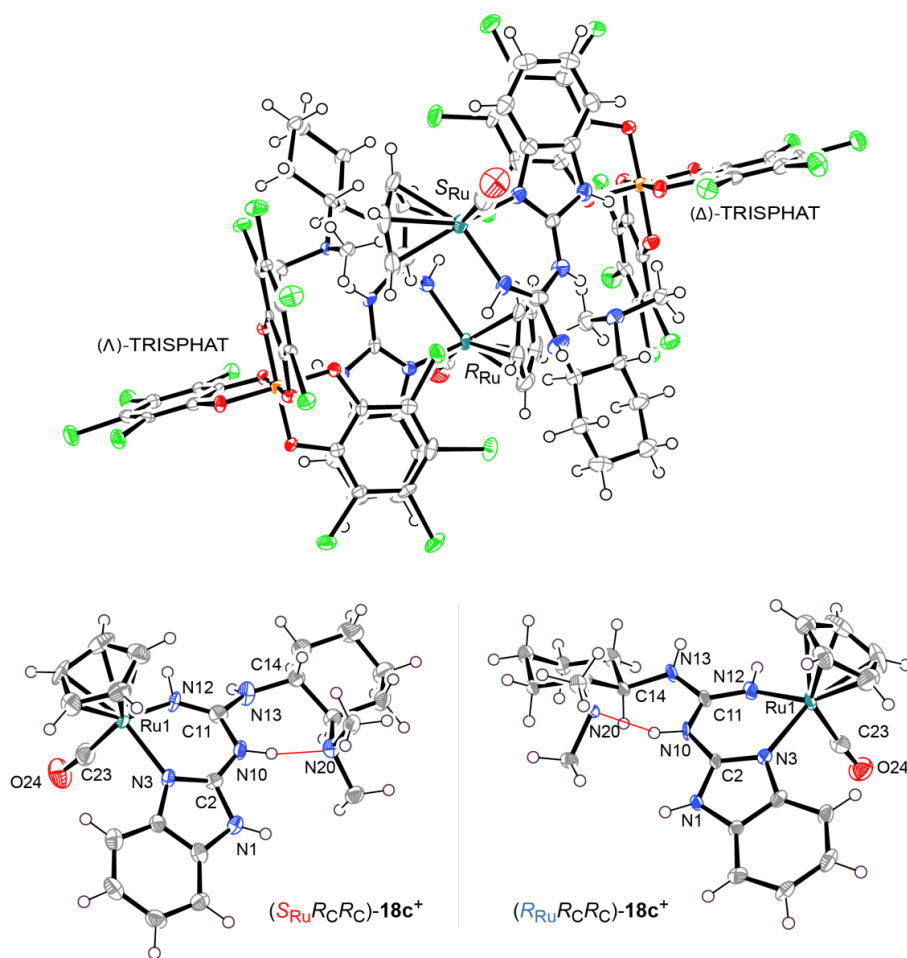


Figure 3.3 Top: thermal ellipsoid diagram (50% probability level) of the molecular structure of $(R_{Ru}R_C R_C/S_{Ru}R_C R_C)-18c^+$ (Δ/Λ)-TRISPHAT $^- \cdot (Et_2O)_2$ with solvate molecules omitted. Bottom: alternative views of each diastereomeric cation. Key distances involving hydrogen bonds (Å): $(S_{Ru}R_C R_C)-18c^+$, H10-N20 1.72, N10-N20, 2.584; $(R_{Ru}R_C R_C)-18c^+$, H10-N20 1.77, N10-N20, 2.609.

The N12-C11-N13-C14 torsion angles in the cations in Figure 3.3 have another consequence. Namely, when coupled with appropriate conformations about the N13-C14 bonds (i.e., C11-N13-C14-C19 torsion angles of 73.5°-86.7°), the dimethylamino nitrogen atoms (N20) are able to intramolecularly hydrogen bond to the H10-N10 moieties (see caption for distances). Hence, under catalytic conditions in solution, equilibrium quantities of at least two distinct intramolecular hydrogen bonding motifs

would also be expected with $(R_{Ru}R_C R_C)\text{-18c}^+$ (Δ)-TRISPHAT⁻ and other salts (N13-H13···N20 and N10-H10···N20). Proportions would decrease with counter anions that are stronger hydrogen bond acceptors.

Prior to obtaining the crystal structure of $(R_{Ru}R_C R_C)\text{-18c}^+$ (Δ)-TRISPHAT⁻, other approaches to assigning configurations were investigated. Thus, CD spectra of $(R_{Ru}R_C R_C)\text{-18c}^+$ PF₆⁻ and $(S_{Ru}R_C R_C)\text{-18c}^+$ PF₆⁻ were recorded, as depicted in Figure 3.4.¹¹⁶ These featured, as commonly seen for diastereomeric chiral-at-metal complexes with opposite metal configurations,^{98,117} two long wavelength absorptions of opposite signs (408, 406 nm). However, the positive band of $(S_{Ru}R_C R_C)\text{-18c}^+$ PF₆⁻ was more than twice as intense. Together with additional positive absorptions or shoulders at 369-372 nm, this suggested the superposition of metal-centered transitions upon a common spectrum derived from the enantiopure ligand (matched absorptions for $(S_{Ru}R_C R_C)\text{-18c}^+$ PF₆⁻, mismatched for $(R_{Ru}R_C R_C)\text{-18c}^+$ PF₆⁻). A computational study (DFT), the results of which are presented in the Appendix B, was carried out to simulate these spectra.¹¹⁸ This led to the same assignments as made crystallographically.

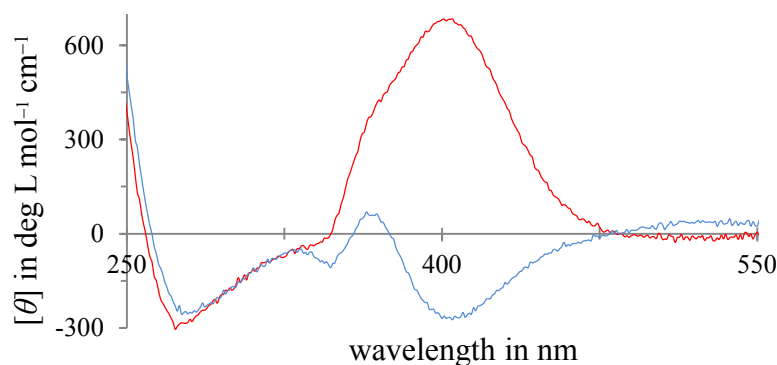


Figure 3.4 CD spectra of $(R_{Ru}R_C R_C)\text{-18c}^+$ PF₆⁻ (blue trace) and $(S_{Ru}R_C R_C)\text{-18c}^+$ PF₆⁻ (red trace) in CH₃CN.

3.2.4 Catalytic reactions

3.2.4.1 Enantioselective second coordination sphere promoted catalysis

With the successful separation of the diastereomers ($R_{Ru}R_C R_C$)-**18c**⁺ PF₆⁻ and ($S_{Ru}R_C R_C$)-**18c**⁺ PF₆⁻ shown in Scheme 3.3 and the configurational assignments established in Figures 3.2 and 3.4, the stage was set for their application as enantioselective catalysts. Accordingly, reactions of indoles (**5a,b**) and *trans*-β-nitrostyrene (**6**) in the presence of ($S_{Ru}R_C R_C$)-**18c**⁺ PF₆⁻ were initially investigated using conditions similar to those described in the preceding chapter. This is a benchmark reaction that can be effected with many hydrogen bond donor catalysts.^{68,119} In all cases, the dr of the catalyst was at least >95:<5. The enantioselectivities were assayed by chiral HPLC as tabulated below and per the traces reproduced in the Appendix B. The absolute configurations were assigned according to previously reported relative retention times.

First, 1-methylindole (**5a**; 2.0 equiv) was treated with **6** (1.0 equiv) in the presence of 10 mol% of ($S_{Ru}R_C R_C$)-**18c**⁺ PF₆⁻ in CD₂Cl₂ at room temperature under aerobic conditions (Table 3.3, entry 1). The reaction was clean and after 24 h, workup gave 1-methyl-3-(2-nitro-1-phenylethyl)-1*H*-indole (**7a**)^{68a} in 60% yield. However, chiral HPLC analysis indicated an ee value of only 2%. Similarly, reaction of indole (**5b**) and **6** under analogous conditions gave, after 48 h, 3-(2-nitro-1-phenylethyl)-1*H*-indole (**7b**)^{119c} in 70% yield with only 1% ee (Table 3.3, entry 2). As represented in the full paper associated with the previous chapter,⁷⁵ the racemic complex [(η⁵-C₅H₅)Ru(CO)(**GBI**)]⁺ PF₆⁻ (**9**⁺ PF₆⁻) also catalyzed the reactions of **5a,b** and **6** under identical conditions.⁷⁵ In all cases the reaction of **5a** was again considerably faster,

consistent with the electron releasing N-methyl group.

Table 3.3 Friedel-Crafts alkylation of **5a** or **5b** with **6** catalyzed by $(S_{Ru}R_C R_C)-\mathbf{18c}^+ PF_6^-$.^{a,b}

entry	R	time (h)	yield (%) ^c	ee (%) ^{d,e,f} (R:S)
1	Me	24	60	2 (49.0:51.0)
2	H	48	70	1 (49.5:50.5)

R = Me, **5a**
R = H, **5b**

6

$(S_{Ru}R_C R_C)-\mathbf{18c}^+ PF_6^-$
(10 mol%)
CD₂Cl₂, rt

7a,b

^a Reaction conditions: **5a** or **5b** (2.0 equiv), **6** (1.0 equiv), and catalyst (10 mol%) in CD₂Cl₂ (0.3 mL). ^b For the workup conditions and other details, see the experimental section. ^c Isolated yields. ^d Enantiomeric excesses (ee) were determined by chiral HPLC. ^e Enantiomer ratios are given in parentheses. ^f Absolute configurations were assigned according to previously reported relative retention times.

Interestingly, the reaction of **5b** and **6** was somewhat faster when catalyzed by $(S_{Ru}R_C R_C)-\mathbf{18c}^+ PF_6^-$ than $\mathbf{9}^+ PF_6^-$ (70% vs. 27% yield after 48 h). One possible explanation is that the $-NMe_2$ moiety participates somehow in the reaction coordinate, rendering $\mathbf{18c}^+ PF_6^-$ not only a hydrogen bond donor but also a bifunctional catalyst similar to Takemoto's system.^{21a,d}

As indicated in chapter 2, these ruthenium complexes interact with dimethyl malonate (**10a**) and **6** through second coordination sphere hydrogen bonding. Based on these results it was next sought to assay $(S_{Ru}R_C R_C)-\mathbf{18c}^+ PF_6^-$ and $(R_{Ru}R_C R_C)-\mathbf{18c}^+ PF_6^-$ as catalysts for carbon-carbon bond forming reactions involving these substrates. Michael additions of diethyl malonate (**10b**) to **6** are commonly used as benchmark reactions for chiral hydrogen bond donor catalysts, particularly those that incorporate tertiary amines.^{21a,d,120} Hence, reactions involving dialkyl malonates and nitroalkenes were investigated (Table 3.4).

First, **10b** (2.0 equiv) was treated with **6** (1.0 equiv) in the presence of 10 mol% of (*S*_{Ru}*R*_C*R*_C)-**18c**⁺ PF₆⁻ or (*R*_{Ru}*R*_C*R*_C)-**18c**⁺ PF₆⁻ in CD₂Cl₂ at room temperature under aerobic conditions (Table 3.4, entry 1). In all cases, the catalyst dr was at least >95:<5. Similar reactions were monitored by ¹H NMR (ca. 25% more dilute, 1.8 equiv malonate ester), and clean conversions to the addition product, ethyl-2-carboethoxy-4-nitro-3-phenylbutyrate (**19a**),¹²¹ were observed over the course of 1-2 d, as represented by the rate profiles in Figure 3.5 (red and blue triangles). With all substrates, (*S*_{Ru}*R*_C*R*_C)-**18c**⁺ PF₆⁻ was the more reactive catalyst.

After the time indicated in Table 3.4, **19a** was isolated by column chromatography. The enantioselectivities (ee) were assayed by chiral HPLC as tabulated below and per the traces reproduced in the Appendix B. The absolute configurations were assigned according to previously reported relative retention times. Both catalyst diastereomers afforded **19a** in high enantiomer excesses (93% and 91%) and isolated yields (95% and 92%).

The free ligand (*R*_C*R*_C)-**16c** was also evaluated as a catalyst. As shown in Table 3.4, entry 1, after 5 d, **19a** was obtained in 65% yield and 41% ee. Hence, (*R*_C*R*_C)-**16c** is a less reactive catalyst, as further evidenced by the rate profile in Figure 3.5 (green triangles), and much less enantioselective. The lower reactivity is consistent with chelate mediated preorganization of the substituted **GBI** ligand in (*S*_{Ru}*R*_C*R*_C)-**18c**⁺ PF₆⁻ and (*R*_{Ru}*R*_C*R*_C)-**18c**⁺ PF₆⁻, and other factors as analyzed in the discussion section. For all three catalysts in entry 1, the same enantiomer of **19a** dominates (*R*_C). This indicates that the ligand based carbon stereocenter, and not the ruthenium, controls the configuration of the new carbon stereocenter in the product, with very little "matched" or "mismatched" sense with the Ru,C diastereomers.

Analogous reactions were carried out with (*S*_{Ru}*R*_C*R*_C)-**18c**⁺ PF₆⁻ or (*R*_{Ru}*R*_C*R*_C)-

18c⁺ PF₆⁻ and three additional aryl substituted nitroalkenes, as summarized in Table 3.3, entries 2-4. The two substrates with substituted phenyl groups (entries 2 and 3) gave rates and product enantioselectivities comparable to entry 1. The furyl substituted alkene used in entry 4 afforded the highest enantioselectivity (>99% ee) of all the reactions studied.

The steric bulk of the malonate ester was varied (ethyl (**10b**)/isopropyl (**10c**)/methyl (**10a**), entries 1, 5, 6). With the smaller **10a**, reactions were distinctly faster, per the rate profiles in Figure 3.5 (red and blue squares). Conversely, the larger **10c** gave slower rates (Figure 3.5, red and blue diamonds) and lower isolated yields. However, the ee values were essentially unchanged. In all of entries 2-6, the free ligand (*R_CR_C*)-**16c** exhibited greatly reduced activity (see also Figure 3.5, green diamonds), but there were no obvious trends other than that associated with the bulk of the malonate ester. The ee values also varied considerably, but not in any systematic manner.

Finally, three synthesized nitroalkenes¹²² with aliphatic substituents were also investigated (Table 3.4, entries 7-9). With (*E*)-1-nitropent-1-ene^{122a} and (*E*)-1-nitrohept-1-ene^{122b} (entries 8,7), clean additions occurred, but they required 6 d to go to ca. 50% completion. For many catalytic reactions, higher temperatures would be employed with less reactive substrates. However, this would increase the catalyst epimerization rates. In any event, the products **19g,h** were obtained in 72-87% ee, enantioselectivities only slightly lower than with the aryl substituted substrates. The free ligand (*R_CR_C*)-**16c** was essentially ineffective. As shown in entry 9, the sterically more congested *t*-butyl substituted nitroalkene was nearly unreactive.

Table 3.4 Yields and ee values for the additions of dialkyl malonates to nitroalkenes catalyzed by the diastereomers of **18c**⁺ PF₆⁻^{a,b}

$R_1 = \text{Me, 10a}$
 $R_1 = \text{Et, 10b}$
 $R_1 = i\text{Pr, 10c}$

entry	<i>(S_{Ru}R_CR_C)-18c</i> ⁺ PF ₆ ⁻ (dr > 95:05)			<i>(R_{Ru}R_CR_C)-18c</i> ⁺ PF ₆ ⁻ (dr > 95:05)			<i>(R_CR_C)-16c</i>		
	time (d)	yield (%)	ee (%) ^{c,d} (R:S)	time (d)	yield (%)	ee (%) ^{c,d} (R:S)	time (d)	yield (%)	ee (%) ^{c,d} (R:S)
1	1	95	93 (96.5:3.5)	2	92	91 (95.5:4.5)	5	65	41 (70.5:20.5)
2	1	>99	93 (96.5:3.5)	2	96	98 (99.0:1.0)	5	47	68 (84.0:16.0)
3	1	83	91 (95.5:4.5)	2	84	89 (94.5:5.5)	5	40	45 (72.5:27.5)
4	1	85	>99 (<0.5:>99.5)	1	74	>99 (<0.5:>99.5)	5	40	18 (41.0:59.0)
5	2	75	88 (94.0:6.0)	3	70	90 (95.0:5.0)	5	30	45 (72.5:27.5)
6	1	97	91 (95.5:4.5)	2	95	88 (94.0:6.0)	5	70	59 (79.5:20.5)
7	6	49	83 (8.5:91.5)	6	41	87 (6.5:93.5)	12	30	10 (45.0:55.0)
8	6	48	84 (8.0:92.0)	6	44	72 (14.0:86.0)			
9	6	12 ^g	—	6	10 ^g	—			

^a Reaction conditions: dialkyl malonate ester (2.0 equiv), nitroalkene (1.0 equiv), and catalyst (10 mol%) in CD₂Cl₂ (0.5 mL). ^b For the workup conditions and other details, see the experimental section. ^c Enantiomeric excesses (ee) were determined by chiral HPLC. ^d Enantiomer ratios are given in parentheses. ^e The configuration of this known compound has not been previously established, but is tentatively assigned by analogy to the known product configurations in entries 1 and 4-6. ^f The configuration of this known compound has not been previously established, but is tentatively assigned by analogy to the known product configuration in entry 7. ^g Yields were measured by ¹H NMR relative to Ph₂SiMe₂ internal standard.

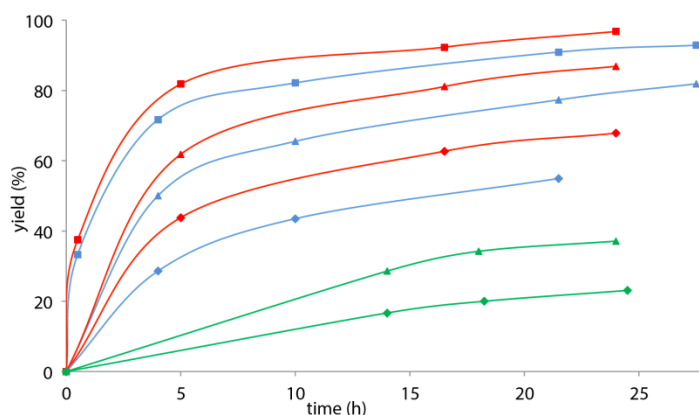


Figure 3.5 Rate profiles for condensations of malonate esters (1.8 equiv) and **6** (1.0 equiv) with different catalysts under conditions similar to Table 3.4 (10 mol%, rt, ca. 25% more dilute). Data for dimethyl malonate: (■) ($S_{Ru}R_C R_C$)-**18c**⁺ PF₆⁻; (□) ($R_{Ru}R_C R_C$)-**18c**⁺ PF₆⁻. Data for diethyl malonate: (▲) ($S_{Ru}R_C R_C$)-**18c**⁺ PF₆⁻; (△) ($R_{Ru}R_C R_C$)-**18c**⁺ PF₆⁻; (▲) ($R_C R_C$)-**16c**. Data for diisopropyl malonate: (◆) ($S_{Ru}R_C R_C$)-**18c**⁺ PF₆⁻; (◇) ($R_{Ru}R_C R_C$)-**18c**⁺ PF₆⁻; (◆) ($R_C R_C$)-**16c**.

3.2.4.2 Other second coordination sphere promoted enantioselective organic transformations

In order to help define the breadth of applicability of catalysts ($S_{Ru}R_C R_C$)-**18c**⁺ PF₆⁻ and ($R_{Ru}R_C R_C$)-**18c**⁺ PF₆⁻, other reactions known to be catalyzed by thiourea based bifunctional hydrogen bond donor catalysts were investigated.^{8g,13,21b,123-126} First, the additions of other types of 1,3-dicarbonyl compounds, or their equivalents, to **6** were probed (Table 3.5).

As shown in entry 1 of Table 3.5, the addition of 2,4-pentanedione (**20**) to **6** in CD₂Cl₂ using 1 mol% of ($S_{Ru}R_C R_C$)-**18c**⁺ PF₆⁻ or ($R_{Ru}R_C R_C$)-**18c**⁺ PF₆⁻ was investigated. A clean reaction occurred. After 24 h, workups gave 70-75% yields of 3-(2-nitro-1-phenylethyl)pentane-2,4-dione (**21**).¹²³ Gratifyingly, chiral HPLC analysis indicated an extremely high ee value (>99%) for both catalysts.

Table 3.5 Yields and ee values for the additions of Michael donors to **6** catalyzed by **18c**⁺ PF₆⁻.^{a,b}

entry	entry	catalyst	yield (%) ^c	ee (%) ^{d,e,f} (R:S)		
1		a	(S _{Ru} R _C R _C)- 18c ⁺ PF ₆ ⁻	70	>99 (>99.5:<0.5)	
		b	(R _{Ru} R _C R _C)- 18c ⁺ PF ₆ ⁻	75	>99 (>99.5:<0.5)	
2		a	(S _{Ru} R _C R _C)- 18c ⁺ PF ₆ ⁻	90 (88:12)	major/minor ee (%) ^{d,e,f} (2S,3R:2R,3S)/ (2R,3R:2S,3S) 84/92 (92.0:8.0)/ (4.0:96.0)	
		b	(R _{Ru} R _C R _C)- 18c ⁺ PF ₆ ⁻	86 (52:48)	87/37 (6.2:93.8)/ (68.7:31.3)	
3		a	(S _{Ru} R _C R _C)- 18c ⁺ PF ₆ ⁻	86 (52:48)	88/91 (5.8:94.2)/ (95.6:4.4)	
		b	(R _{Ru} R _C R _C)- 18c ⁺ PF ₆ ⁻	82 (55:45)	88/91 (5.8:94.2)/ (95.6:4.4)	
4		a	(R _{Ru} R _C R _C)- 18c ⁺ PF ₆ ⁻	rt	75	42 (71.0:29.0)
		b	(R _{Ru} R _C R _C)- 18c ⁺ PF ₆ ⁻	rt	90	54 (77.0:23.0)
		c	(R _{Ru} R _C R _C)- 18c ⁺ PF ₆ ⁻	-35	40	46 (73.0:27.0)
		d	(S _{Ru} R _C R _C)- 18c ⁺ PF ₆ ⁻	-78	40	11 (55.5:44.5)

^a Reaction conditions: Michael donor (1.0 equiv), **6** (1.0 equiv), and catalyst in CD₂Cl₂ (0.3 mL). ^b For the workup conditions and other details, see the experimental section. ^c Isolated yields. ^d Enantiomeric excesses (ee) were determined by chiral HPLC. ^e Enantiomer ratios are given in parentheses. ^f Absolute configurations were assigned according to previously reported relative retention times. ^g The diastereomer ratios (dr) were determined by ¹H NMR. ^h Absolute configurations could not be assigned.

An analogous reaction with ethyl 2-oxocyclopentanecarboxylate (**22**) and **6** was carried out (Table 3.5, entry 2a). Due to the lower symmetry of **22**, the condensation product **23**^{120f,124} features two stereocenters. This leads to two diastereomeric pairs, (*R_CS_C*)-**23** and enantiomer (*S_CR_C*)-**23**, and (*R_CR_C*)-**23** and enantiomer (*S_CS_C*)-**23**. The dr

can be assigned from the distinct ^1H NMR signals.^{120f} Each of the enantiomers can be assigned according to the previously reported relative retention times obtained by chiral HPLC.^{120f,124a} Numerous bifunctional hydrogen bond donors have catalyzed the above reaction with very high distereoselectivities ($>99:<1$) and enantioselectivities ($>99\%$).^{124b}

After 14 h, workup of the reaction in entry 2a gave a 90% yield of an 88:12 diastereomer mixture. The ^1H NMR data indicated these to be the previously reported ($R_C S_C/S_C R_C$)-**23** and ($R_C R_C/S_C S_C$)-**23** diastereomers, respectively.^{120f,124a} Chiral HPLC analysis indicated 84% ee with the enantiomer ($S_C R_C$)-**23** dominant and 92% ee with the enantiomer ($S_C S_C$)-**23** dominant, for the major and minor diastereomer respectively.^{120f,124a}

Another reaction was carried out with benzyl acetoacetate (**24**) and **6** in CD_2Cl_2 at room temperature, but with a slightly higher catalyst loading of 2 mol% (Table 3.5, entries 3a,b). Similar to **23**, the product **25**¹²⁵ also features two stereocenters and can afford two diastereomers. Although both have been reported in the literature, configurations have not been assigned. Nonetheless, the dr can be determined by ^1H NMR.¹²⁵

After 24 h, workup of the reactions with ($S_{\text{Ru}}R_C R_C$)-**18c**⁺ PF_6^- or ($R_{\text{Ru}}R_C R_C$)-**18c**⁺ PF_6^- gave 82-86% yields of nearly a 1:1 mixture of the diastereomers of **25**. Chiral HPLC analysis provided ee values of 87-88% for the diastereomer in slight excess but 37-91% for the other.

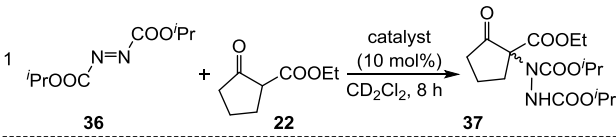
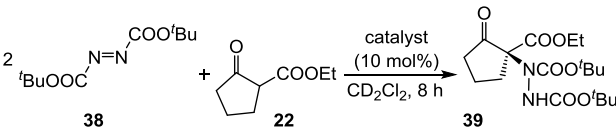
Malononitrile (**26**) and **6** were reacted in the presence of 1-2 mol% ($S_{\text{Ru}}R_C R_C$)-**18c**⁺ PF_6^- or ($R_{\text{Ru}}R_C R_C$)-**18c**⁺ PF_6^- in CD_2Cl_2 at the temperatures specified in Table 3.5, entries 4a-d. A clean reaction occurred in all cases. After 24 h, workups gave 40-90% yields of the product **27**.^{21b} The product was also analyzed by chiral HPLC. Entry

4a, with 1% catalyst loading, gave an ee value of 42%. A higher 2% catalyst loading improved the yield and ee moderately (entry 4a vs. 4b). Lowering the temperature to -35 °C slightly improved the ee values (entry 4a vs. 4c). When $(S_{Ru}R_C R_C)\text{-18c}^+ \text{PF}_6^-$ was employed as catalyst (2 mol%) at -78 °C, **27** was isolated in 40% yield with only 11% ee. Thus, the highest ee, 54% was achieved utilizing 2 mol% of $(R_{Ru}R_C R_C)\text{-18c}^+ \text{PF}_6^-$ as the catalyst at room temperature.

Next, additions of 1,3-dicarbonyl compounds to dialkyl azodicarboxylates were investigated as shown in Table 3.6. The reaction of **22** and diisopropyl azodicarboxylate (**36**) in CD_2Cl_2 was carried out with 10 mol% of $(S_{Ru}R_C R_C)\text{-18c}^+ \text{PF}_6^-$ or $(R_{Ru}R_C R_C)\text{-18c}^+ \text{PF}_6^-$ at -78 °C, as shown in Table 3.6 (entries 1a,b). The addition was monitored by TLC. A clean reaction occurred in all the cases. After 8 h, workup gave >99% yields of diisopropyl 1-(1-(ethoxycarbonyl)-2-oxocyclopentyl)hydrazine-1,2-dicarboxylate (**37**).¹²⁶ Chiral HPLC analysis indicated moderate ee values (33-35%). Although this compound has been prepared earlier in nonracemic form,¹²⁶ the absolute configuration of the major enantiomer was not assigned.

Interestingly, with $(S_{Ru}R_C R_C)\text{-18c}^+ \text{PF}_6^-$, the major enantiomer of **37** corresponded to the first chiral HPLC peak, whereas with $(R_{Ru}R_C R_C)\text{-18c}^+ \text{PF}_6^-$, the major enantiomer corresponded to the second HPLC peak. Unlike the results shown in Tables 3.3 and 3.4, the chiral ruthenium center, and not the ligand based carbon stereocenter, controls the favored product configuration (S_{Ru} vs. R_{Ru} , entry 1a vs. 1b).

Table 3.6 Yields and ee values for the additions of **22** to dialkyl azodicarboxylates catalyzed by **18c**⁺ PF₆⁻.^{a,b}

entry	entry	catalyst	temp (°C)	yield (%) ^c	ee (%) ^{d,e,f}	
1		a	(<i>S</i> _{Ru} <i>R</i> _C <i>R</i> _C)- 18c ⁺ PF ₆ ⁻	-78	>99	35 (67.5:0:32.5)
		b	(<i>R</i> _{Ru} <i>R</i> _C <i>R</i> _C)- 18c ⁺ PF ₆ ⁻	-78	>99	33 (33.5:66.5)
2		a	(<i>S</i> _{Ru} <i>R</i> _C <i>R</i> _C)- 18c ⁺ PF ₆ ⁻	-78	90	82 (9.0:91.0)
		b	(<i>R</i> _{Ru} <i>R</i> _C <i>R</i> _C)- 18c ⁺ PF ₆ ⁻	-78	- ^h	-
		c	(<i>R</i> _{Ru} <i>R</i> _C <i>R</i> _C)- 18c ⁺ PF ₆ ⁻	-35	80 ⁱ	88 (6.0:94.0)

^a Reaction conditions: cyclic β-keto ester (2.0 equiv), dialkyl azodicarboxylate (1.0 equiv), and catalyst (10 mol%) in CD₂Cl₂ (0.3 mL). ^b For the workup conditions and other details, see the experimental section. ^c Isolated yields. ^d Enantiomeric excesses (ee) were determined by chiral HPLC. ^e Enantiomer ratios are given in parentheses. ^f Absolute configurations could not be assigned. ^g Absolute configurations were assigned according to previously reported relative retention times. ^h No conversion to product was detected. ⁱ Reaction was conducted for 16 h.

Intrigued by the results, an analogous reaction was carried out with the bulkier azo compound di-*t*-butyl azodicarboxylate (**38**) and **22** in CD₂Cl₂ at -78 °C (entries 2a-c). After 8 h, workup of the reaction with (*S*_{Ru}*R*_C*R*_C)-**18c**⁺ PF₆⁻ gave the product **39**¹²⁶ in 90% yield and 82% ee (entry 2a). Interestingly, (*R*_{Ru}*R*_C*R*_C)-**18c**⁺ PF₆⁻ under similar conditions did not promote the reaction (entry 2b). At higher temperature and after a longer reaction time, **39** was isolated in 80% yield and 88% ee (entry 2c). In contrast to entries 1a,b, both catalysts gave predominantly the same enantiomer of **39** (*S*_C), which could be assigned from previously reported relative retention times.¹²⁶

3.3 Discussion

3.3.1 Ruthenium catalysts

This study has demonstrated the efficacy of a new class of hydrogen bond donor catalysts for Friedel-Crafts alkylations and highly enantioselective Michael addition reactions (Tables 3.4-3.6). They are indefinitely stable in the solid state, persist for weeks in non-degassed solutions, and can be utilized under aerobic conditions.

As discussed in the previous chapter, chelate complexes of **GBI** attain conformationally more rigid and organized structures. This is exemplified by the crystal structures of the ruthenium adducts $[(\eta^5\text{-C}_5\text{H}_5)\text{Ru}(\text{PPh}_3)(\text{GBI})]^+ \text{X}^-$ (**8**⁺ **X**⁻; **X**⁻ = **BAr_f**⁻, **PF₆**⁻),⁷⁵ the first of which is depicted in Figure 2.9 (chapter 2), and the diastereomers of **18c**⁺ **TRISPHAT**⁻ depicted in Figures 3.2 and 3.3. In the cases of **8**⁺ **X**⁻ and (*R*_{Ru}*R*_C*R*_C)-**18c**⁺ (Δ)-**TRISPHAT**⁻, DDD triads are obtained, although the N13-H13 unit can engage in hydrogen bonding in the latter (Figure 3.2).^{42c,127,128} With the other diastereomers of **18c**⁺ **X**⁻, the N13-H13 terminus rotates so as to direct a N13-C linkage *syn* to the N10-H10 unit, resulting in a DD dyad. This allows the N10-H10 unit to hydrogen bond to the pendant NMe₂ group. Nonetheless, this would be an equilibrium interaction in solution. In any case, ¹H NMR data for samples in which **6** or **10a** was added to **9**⁺ **BAr_f**⁻ in chapter 2 (Figures 2.5 and 2.11) suggest that binding preferentially occurs to the N1-H1 and N10-H10 linkages. These are *synperiplanar* in all of these structures, as depicted in the transition state models proposed below.

The advantages of preorganization with respect to both thermodynamic and kinetic phenomena are well established.^{42c,43,129} Accordingly, the conformationally flexible free ligand (*R*_C*R*_C)-**16c** is a much less active catalyst than the chelates

$(R_{Ru}R_C R_C)-18c^+$ PF_6^- and $(S_{Ru}R_C R_C)-18c^+$ PF_6^- . However, the ruthenium also introduces positive charge, which should enhance NH acidities and therefore hydrogen bond donor strengths. Hence, a cationic derivative of $(R_C R_C)-16c$ would provide a more informative comparison. In the preceding chapter it was shown that a cationic methylated derivative of **GBI**, 2^+ $BARf^-$, remained a much less active catalyst than $[(\eta^5-C_5H_5)Ru(PPh_3)(GBI)]^+ BARf^-$ (8^+ $BARf^-$) and $[(\eta^5-C_5H_5)Ru(CO)(GBI)]^+ BARf^-$ (9^+ $BARf^-$) for the condensation of **5a** and **6**. Unfortunately, an expedient synthesis of a similar derivative of $(R_C R_C)-16c$ was not achieved, due in part to the pendant dimethylamino group.

The effect of the counteranion upon the activity of the ruthenium catalyst was studied in the preceding chapter. In all cases, $BARf^-$ salts were considerably more reactive than hexafluorophosphate salts. This was ascribed to the residual hydrogen bond accepting properties of the PF_6^- anion and competition with the substrate for the DD active site. Although as described above the synthesis of $(R_{Ru}R_C R_C)-18c^+$ $BARf^-$ has proved problematic, samples of ca. 85% purity have been obtained. These proved to be much more active catalysts, pointing the way to possible future enhancements. Using an activated substrate (pK_a values lower than **10b**^{130,131}) can be another way of improving the catalytic efficiencies as demonstrated in Table 3.5. Here, catalyst loadings as low as 1-2 mol% efficiently catalyze Michael additions of 1,3 dicarbonyl equivalents (**20**,¹³⁰ **22**,^{131a} **24**^{131b} or **26**^{131c}) to **6** in reasonable yields and enantioselectivities.

The above analyses of the DD dyad and DDD triads in crystalline $(R_{Ru}R_C R_C/S_{Ru}R_C R_C)-18c^+$ (Δ/Λ) -TRISPHAT $^- \cdot (Et_2O)_2$ and $(R_{Ru}R_C R_C)-18c^+$ (Δ) -TRISPHAT $^- \cdot CHCl_3$ provide a conceptual bridge to a subtle design flaw in catalysts $(S_{Ru}R_C R_C)-18c^+$ PF_6^- and $(R_{Ru}R_C R_C)-18c^+$ PF_6^- . Specifically, Figures 3.2 and 3.3 show that intramolecular hydrogen bonding is possible between the dimethylamino

nitrogen atom (N20) and the H13-N13 and H10-N10 linkages. The latter equilibrium lowers the concentration of the DD site thought to activate the electrophile, and both tie up a dimethylamino group that is intended to activate the nucleophile (see below). In principle, these interactions might be inhibited with a conformationally restricted ligand or perhaps a bulkier tertiary amine. However, such modifications may also adversely affect interactions with the reactants, and thus can only be empirically investigated.

The epimeric catalysts ($S_{Ru}R_C R_C$)-**18c**⁺ PF₆⁻ and ($R_{Ru}R_C R_C$)-**18c**⁺ PF₆⁻ give essentially the same ee values for the reactions in Table 3.4, implying as noted above that the ligand based stereocenters essentially control the product configurations. However, in entries 3 and 4 of Table 3.5, and 1a,b of Table 3.6, the ruthenium configuration can make a difference. This suggests fundamentally different types of transition state assemblies, possibly connected to the change in the type of educts.

Catalysts that would epimerize more slowly are desirable. It has been shown that d⁶ pentamethylcyclopentadienyl complexes are much less configurationally stable than cyclopentadienyl analogs.¹³² To the extent that this represents an electronic effect, cyclopentadienyl ligands that bear electronegative substituents could be helpful. Also, one might consider expanding the steric influence of the ruthenium center with several large cyclopentadienyl substituents, such as phenyl or pentafluorophenyl.

3.3.2 Literature catalysts and mechanisms

The condensations in Table 3.4 compare favorably to those previously effected with other types of hydrogen bond donor catalysts. The best ee values that I am aware of for additions of **10b** to **6** have been obtained with catalysts **LXIII** and **LXIV-LXVII** as summarized Figure 3.6 (85-96% ee vs. 91-93% ee for Table 3, entry 1). Nearly all of

these contain an NH based DD dyad and a tertiary amine. They furthermore catalyze a broad spectrum of additional reactions,^{8g,13,21d} suggesting much yet untapped potential for (*S*_{Ru}*R*_C*R*_C)-**18c**⁺ PF₆⁻ and (*R*_{Ru}*R*_C*R*_C)-**18c**⁺ PF₆⁻.

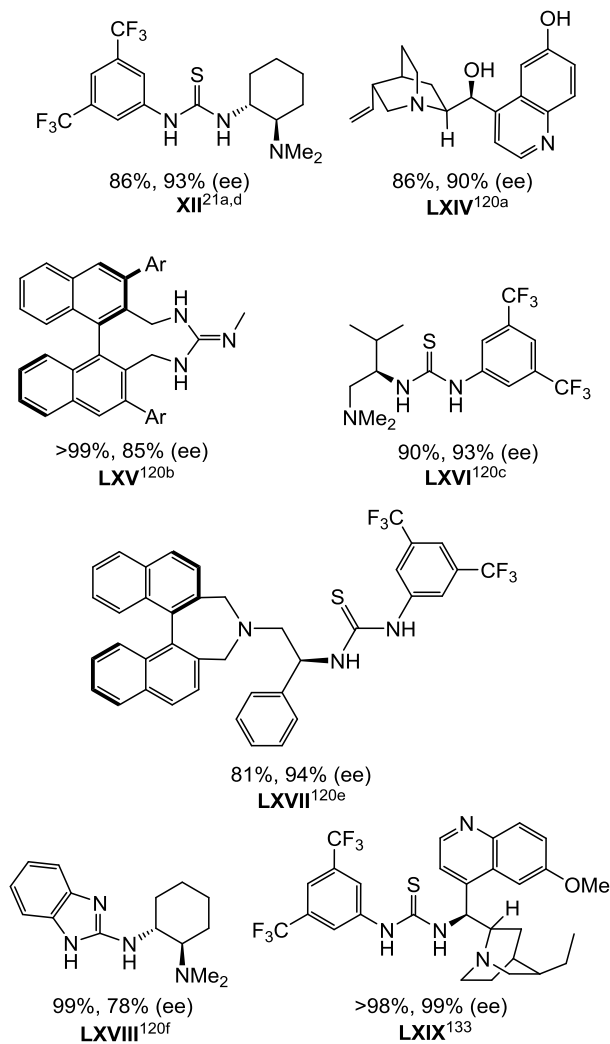


Figure 3.6 Other chiral hydrogen bond donors that catalyze highly enantioselective additions to **6** by **10b** (**XII**, **LXVI**-**LXVIII**) or **10a** (**LXIX**).

A somewhat less enantioselective catalyst, **LXIII**, is also included in Figure 3.6.

Compound **LXIII** can be viewed as a stripped down version of ligand ($R_C R_C$)-**16c** that retains the benzimidazole and dimethylated *trans*-1,2-cyclohexanediamine termini. By itself, **LXIII** (10 mol%) catalyzes the addition of **10b** to **6** over the course of 24 h in 78% ee (toluene solvent) or 70% ee (CH_2Cl_2). Hence, the rate – but not the enantioselectivity – is similar to that of ($S_{\text{Ru}} R_C R_C$)-**18c**⁺ PF_6^- in the absence any conformational preorganization. However, there are too many differences for **LXIII**, ($R_C R_C$)-**16c**, and the ruthenium adducts to be regarded as rigorously comparable systems.

Although these examples are not "stacked" to put the systems reported herein in an undeservedly favorable light, the catalyst **LXIX** has been added to round out the presentation.¹³³ This species, as well as an epimer of **LXIV**,^{120a} catalyze the addition of the alternative educt **10a** to **6** in 98-93% yields and 99% ee, enantioselectivities that beat the other examples in Figure 3.6.¹³³ To my knowledge, no data for **10b** have been reported.

The mechanism of addition of malonate esters to **6** with dimethylamino containing thiourea hydrogen bond donor catalysts (e.g., **XII**) has been investigated both experimentally and computationally.^{21b,c} Takemoto has suggested transition state assemblies of the type **LXX** shown in Figure 3.7.^{21b} These feature the "conventional" activation of the nitroalkene by the *synperiplanar* thiourea NH linkages, and the malonate ester by the tertiary amine, and rationalize the dominant product configuration. However, it has also been proposed that the roles could be reversed, as in **LXXI**.^{21c} Analogous transition state assemblies can be formulated for the ruthenium containing catalysts, as shown by **LXXII** and **LXXIII** (Figure 3.6). In both cases, I suggest that the additional NH linkage acts in concert with the dimethylamino group. There are additional nuances in all of these assemblies, such as the conformation of the $\text{C}=\text{CPh}$

moiety with respect to the nitro group.

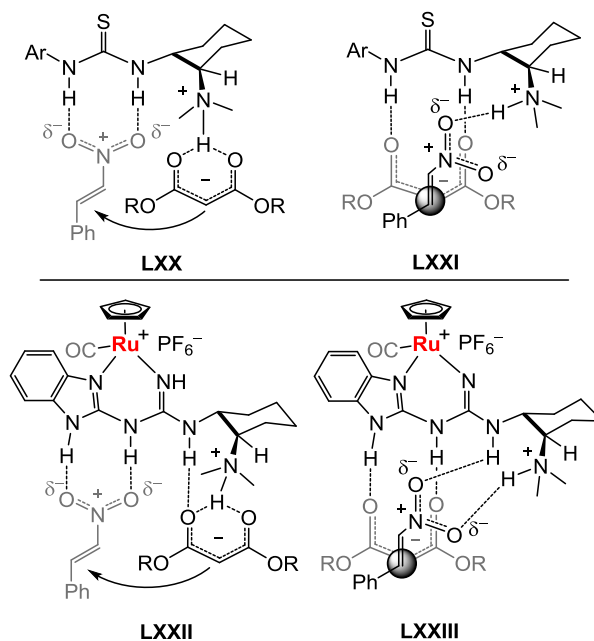


Figure 3.7 Transition state assemblies. Top: proposed models for additions of malonate esters to **6** catalyzed by the bifunctional thiourea **XII**. Bottom: analogous models for the bifunctional ruthenium catalysts used in this chapter.

3.4 Conclusion

This study has established the viability of using chiral enantiopure transition metal complexes containing ligand based NH hydrogen bond donors to catalyze condensations of organic molecules in high yields and enantioselectivities. In this work, the hydrogen bond donors are remote from the metal, part of a bidentate ligand, and thought to be preorganized and thus activated toward substrate binding upon chelation.

3.5 Experimental section

3.5.1 General data

^1H , $^{13}\text{C}\{^1\text{H}\}$, $^{31}\text{P}\{^1\text{H}\}$ and $^{19}\text{F}\{^1\text{H}\}$ NMR spectra were recorded on standard 300-500 MHz spectrometers at ambient probe temperature (24 °C) and referenced as follows (δ , ppm): ^1H , residual internal CHCl_3 (7.26), acetone- d_5 (2.05), DMSO- d_5 (2.49), CHD_2OD (3.30), or CHD_2CN (1.94); ^{13}C , internal CDCl_3 (77.0), acetone- d_6 (29.9), DMSO- d_6 (39.6), CD_3OD (49.1), or CD_3CN (1.3); $^{19}\text{F}\{^1\text{H}\}$, internal 1-bromo-3,5-bis(trifluoromethyl)benzene (-63.56). IR spectra were recorded using a Shimadzu IRAffinity-1 spectrophotometer with a Pike MIRacle ATR system (diamond/ZnSe crystal). UV-visible spectra were measured using an Shimadzu UV-1800 UV spectrophotometer. Circular dichroism spectra were obtained using a Chirascan CD Spectrometer (Applied Photophysics). Melting points were recorded with a Stanford Research Systems (SRS) MPA100 (Opti-Melt) automated device. Microanalyses were conducted by Atlantic Microlab. HPLC analyses were conducted with a Shimadzu instrument package (pump/autosampler/detector LC-20AD/SIL-20A/SPD-M20A; columns Chiralpak AD, Chiralpak AD-H, Chiralpak AS-H, Chiralcel OD, Chiralcel OD-H).

Solvents were treated as follows: THF, toluene, hexanes, Et_2O , and CH_2Cl_2 were dried and degassed using a Glass Contour solvent purification system; CH_3CN was distilled from CaH_2 ; pentane (99.7%, J. T. Baker), MeOH (99.8%, BDH), and *t*-BuOH (99.5%, Acros) were used as received; CDCl_3 , CD_3CN , CD_2Cl_2 , acetone- d_6 , DMSO- d_6 , and CD_3OD (6 \times Cambridge Isotope Laboratories) were used as received. The 2-guanidinobenzimidazole (**GBI**; 95%, Aldrich), 1,1-thiocarbonyldiimidazole (90%, Alfa

Aesar), 2-aminobenzimidazole (99+%, Acros), methyl iodide (99%, Alfa Aesar), $[(\eta^5\text{-C}_5\text{H}_5)\text{Ru}(\text{NCCH}_3)_3]^+ \text{PF}_6^-$ (98%, Acros), benzylamine (99+%, Merck), (S_C)-1-phenylethylamine (98%, Aldrich), Ph_2SiMe_2 (97%, Aldrich), 1-bromo-3,5-bis(trifluoromethyl)benzene (98%, Alfa Aesar), 1-methylindole (**5a**; 98%, Acros), indole (**5b**; >99%, Aldrich), *trans*- β -nitrostyrene (**6**; 99%, Alfa Aesar), 3,4-methylenedioxy- β -nitrostyrene (98%, Alfa Aesar), 3,4-dichloro- β -nitrostyrene (98+%, Alfa Aesar), 1-(2-furyl)-2-nitroethylene (98%, Alfa Aesar), dimethyl malonate (**10a**; 98+%, Alfa Aesar), diethyl malonate (**10b**; 99%, Alfa Aesar), diisopropyl malonate (**10c**; 99%, TCI), 2,4-pentanedione (**20**; 99%, Aldrich), ethyl 2-oxocyclopentanecarboxylate (**22**; >95%, Aldrich), $\text{NH}_4^+ \text{PF}_6^-$ (99.5%, Alfa Aesar), benzyl acetoacetate (**24**; 97%, Aldrich), malononitrile (**26**; 98%, TCI), diisopropyl azodicarboxylate (**36**; 98%, Aldrich), di-*t*-butyl azodicarboxylate (**38**; $\geq 98\%$, Aldrich), NEt_3 (99%, Alfa Aesar), silica gel (SiliFlash F60, Silicycle), neutral alumina (Brockmann I, 50-200 μm , Acros), and Celite were used as received.

All reactions and workups were carried out under air unless noted. Other chemicals were used as received. (*E*)-1-nitropent-1-ene and (*E*)-3,3-dimethyl-1-nitrobut-1-ene were prepared according to literature procedures;^{122a} (*E*)-1-nitrohept-1-ene^{122b} was prepared analogously.

3.5.2 Syntheses of GBI derivatives and catalysis

***N*-(1*H*-Benzimidazol-2-yl)-1*H*-imidazole-1-carbothioamide (**15**).**¹⁰² **Method A.**^{105,107} A round bottom flask was charged with 1,1-thiocarbonyldiimidazole (3.00 g, 16.8 mmol) and dry THF (30 mL), and 2-aminobenzimidazole (2.24 g, 16.8 mmol) was added with stirring. A yellow precipitate formed, which after 14 h was collected by

filtration, washed with THF (20 mL), and dried by oil pump vacuum to give **10** as a light yellow solid (2.24 g, 9.24 mmol, 55%). **Method B.**^{102,103} A round bottom flask was charged with 1,1-thiocarbonyldiimidazole (6.94 g, 39.0 mmol) and CH₃CN (30 mL), and 2-aminobenzimidazole (3.99 g, 30.0 mmol) was added with stirring. The flask was protected from light using a black cloth¹⁰² and placed in a 50 °C oil bath.¹⁰³ A precipitate rapidly formed. After 22 h, the mixture was cooled to room temperature. The precipitate was collected by filtration, washed with CH₃CN (4 × 80 mL), transferred to a flask using EtOAc (20 mL), and dried by oil pump vacuum (40 °C, 1 h and then rt overnight) to give **15** as a light yellow solid (6.91 g, 28.4 mmol, 73%).

NMR (δ , DMSO-d₆):^{102,104,105} ¹H (300 MHz) 13.35 (br s, 1H, **NH**), 8.55 (s, 1H, (C=S)**NCHN**), 7.93 (s, 1H, (C=S)**NCHNCHCH**), 7.62-7.59 (m, 2H, **CH4/7**), 7.35-7.32 (m, 2H, **CH5/6**), 6.99 (s, 1H, (C=S)**NCHNCHCH**), 3.29 (br s, 1H, **NH**); ¹³C {¹H} (125 MHz) 179.0 (s, **C=S**), 152.2 (s, **N(C=N)N**), 136.1, 129.4, 128.9 (3 × s, (C=S)**NCHNCHCH** and **C8/9**), 124.0 (s, **C5/6**), 117.9 (s, (C=S)**NCHNCHCH**), 112.6 (s, **C4/7**).

IR (cm⁻¹, powder film): 1625 (m), 1583 (s), 1509 (m), 1451 (m), 1208 (s), 1050 (s), 741 (vs).

***N*-(1*H*-Benzimidazol-2-yl)thiourea acetate (14-H⁺ CH₃COO⁻).**¹⁰¹ A round bottom flask was charged with *N*-(1*H*-benzimidazol-2-yl)-1*H*-imidazole-1-carbothioamide (**15**; 5.75 g, 23.6 mmol) and EtOH (180 mL), and NH₄⁺ CH₃COO⁻ (18.2 g, 236 mmol) was added with stirring. The mixture was heated at 90 °C, and after 1.5 h cooled to room temperature. The solvent was removed by rotary evaporation to

give an orange oil. Water (300 mL) was added and a white precipitate formed. Addition of ethyl acetate (200 mL) gave two clear phases, which were separated. The aqueous phase was extracted with ethyl acetate (5×200 mL) and the combined organic phases were dried (Na_2SO_4). The solvent was removed by oil pump vacuum to give **14-H⁺ CH₃COO⁻** as a pale yellow powder (5.24 g, 20.7 mmol, 88%).

NMR (δ , acetone- d_6):^{104,134} ¹H (500 MHz) 10.3 (br s, 1H, **NH** or **COOH**), 8.17 (br s, 1 **NH**), 7.47-7.44 (m, 2H, **CH4/7**), 7.17-7.14 (m, 2H, **CH5/6**), 1.97 (s, 3H, **CH₃COO**); ¹³C {¹H} (DMSO- d_6 , 75.5 MHz) 179.7 (s, **C=S**), 172.2 (s, **CH₃COO**), 147.9 (s, **N(C=N)N**), 122.7 (s, **C5/6**), 21.2 (s, **CH₃COO**).¹³⁵

IR (cm^{-1} , powder film): 3401 (m), 3289 (w), 3165 (w), 1706 (m), 1625 (s), 1598 (m), 1409 (m), 1054 (m), 749 (vs).

***N*-(1*H*-Benzimidazol-2-yl)methylisothiourea iodide (13-H⁺ I⁻)**.¹⁰¹ A round bottom flask was charged with **14-H⁺ CH₃COO⁻** (2.34 g, 9.20 mmol) and MeOH (80 mL). The flask was placed in a 39 °C oil bath and methyl iodide (1.43 g, 10.1 mmol) was added dropwise with stirring. After 4 h, the oil bath was removed. The solvent was removed by oil pump vacuum and the residue washed with Et₂O (3×150 mL) to give **13-H⁺ I⁻** as a white solid (1.68 g, 5.60 mmol, 55%).

NMR (δ , CD₃OD):¹⁰⁴ ¹H (500 MHz) 7.49-7.46 (m, 2H, **CH4/7**), 7.38-7.34 (m, 2H, **CH5/6**), 2.55 (s, 3H, **CH₃**); ¹³C {¹H} (125 MHz) 170.3 (s, **CSMe**), 151.2 (s, **N(C=N)N**), 130.7 (s, **C8/9**), 124.3 (s, **C5/6**), 112.7 (s, **C4/7**), 14.7 (s, **SCH₃**).

IR (cm⁻¹, powder film): 3240 (w), 3077 (m), 1615 (m), 1581 (s), 1495 (m), 1405 (m), 750 (vs); UV-visible (nm, 2.94 × 10⁻⁵ M in MeOH (ε, M⁻¹cm⁻¹)): 250 (9570), 307 (20000).

***N*-(1*H*-Benzimidazol-2-yl)-*N'*-(phenylmethyl)guanidine (16a).**^{105,106} A round bottom flask was charged with **13**-H⁺ I⁻ (0.900 g, 2.69 mmol), benzylamine (1.24 mL, 1.22 g, 11.4 mmol), and *t*-BuOH (8 mL), and fitted with a condenser. The mixture was heated at 100 °C for 14 h with stirring and cooled to 50 °C. The solvent was removed by oil pump vacuum to give a sticky yellow residue, and 3% aqueous NaOH (30 mL) was added. The sample was extracted with 95:5 v/v CH₂Cl₂/MeOH (3 × 30 mL). The combined organic phases were dried (Na₂SO₄). The solvent was removed by rotary evaporation and the oily residue was chromatographed on a silica gel column (1.5 × 20 cm, 95:5 → 90:10 v/v CH₂Cl₂/MeOH). The solvent was removed from the product containing fractions by oil pump vacuum to give **16a** as a white solid (0.413 g, 1.56 mmol, 58%), mp 140 °C (capillary). Anal. Calcd for C₁₅H₁₅N₅: C 67.90, H 5.70, N 26.40. Found: C 67.90, H 5.67, N 25.54.¹³⁶

NMR (δ, DMSO-*d*₆):^{104,105,134} ¹H (300 MHz) 7.35-7.21 (m, 6H, NH and C₆H₅), 7.20-7.17 (m, 2H, CH₄/7), 6.96-6.92 (m, 2H, CH₅/6), 4.50 (d, 2H, ³J_{HH} = 5.4 Hz, CH₂);¹³⁷ ¹³C {¹H} (75 MHz) 158.5 and 157.8 (2 × s, 2 N(C=N)N), 137.0 (s, C₈/9), 140.1 (s, *i*-C₆H₅), 129.8 and 127.3 (2 × s, *o*- and *m*-C₆H₅), 126.9 (s, *p*-C₆H₅), 119.8 (s, C₅/6), 111.9 (s, C₄/7), 43.9 (s, CH₂).

IR (cm⁻¹, powder film): 3396 (w), 3052 (w), 1608 (m), 1515 (s), 1453 (s), 1268 (s), 732 (vs); UV-visible (nm, 3.82 × 10⁻⁵ M in MeOH (ε, M⁻¹cm⁻¹)): 243 (12300), 300

(21500).

***N*-(1*H*-Benzimidazol-2-yl)-*N'*-((*S*)-1-phenylethyl)guanidine** ((*S*)-**16b**).^{104,105,107} A round bottom flask was charged with **13**-H⁺ I⁻ (0.900 g, 2.69 mmol), (*S*)-1-phenylethylamine (1.72 mL, 1.63 g, 13.5 mmol), and *t*-BuOH (8 mL), and fitted with a condenser. The mixture was heated at 100 °C for 2 d with stirring and cooled to 50 °C. The solvent was removed by oil pump vacuum to give a sticky yellow residue, and 3% aqueous NaOH (30 mL) was added. The sample was extracted with 95:5 v/v CH₂Cl₂/MeOH (3 × 30 mL). The combined organic phases were dried (Na₂SO₄). The solvent was removed by rotary evaporation and the oily residue was chromatographed on a silica gel column (1.5 × 28 cm, 95:5 v/v CH₂Cl₂/MeOH). The solvent was removed from the product containing fractions by oil pump vacuum to give (*S*)-**16b** as a white solid (0.345 g, 1.23 mmol, 46%), mp 103 °C (capillary). Anal. Calcd for C₁₆H₁₇N₅: C 68.79, H 6.13, N 25.07. Found C 68.72, H 6.15, N 24.83.

NMR (δ , CDCl₃):^{104,105,134} ¹H (500 MHz) 7.33-7.26 (m, 7H, C₆H₅ and CH₄/7), 7.07-7.04 (m, 2H, CH₅/6), 4.59 (q, ¹H, ³J_{HH} = 6.8 Hz, CH), 1.54 (d, 3H, ³J_{HH} = 6.8 Hz, CH₃);¹³⁷ ¹³C {¹H} (125 MHz) 157.0 and 156.4 (2 × s, 2 N(C=N)N), 137.0 (C₈/9), 142.7 (s, *i*-C₆H₅), 129.2 (s, *m*-C₆H₅),¹³⁸ 125.6 (s, *o*-C₆H₅), 127.9 (s, *p*-C₆H₅); 120.8 (s, C₅/6), 112.8 (s, C₄/7), 52.4 (s, CH), 24.3 (s, CH₃).

IR (cm⁻¹, powder film): 3398 (w), 3054 (w), 1597 (m), 1514 (s), 1454 (s), 1282 (s), 737 (s); UV-visible (nm, 2.65 × 10⁻⁵ M in MeOH (ϵ , M⁻¹cm⁻¹)): 245 (6910), 300 (16200); [α]₂₄⁵⁸⁹ = 17.3° ± 0.2° (2.82 mg mL⁻¹, MeOH).

***N*-(1*H*-Benzimidazol-2-yl)-*N'*-((1*R*,2*R*)-*N''*,*N''*-dimethyl-1,2-diaminocyclohexyl)guanidine ((*R_CR_C*)-**16c**).**^{104,105,107} A round bottom flask was charged with **13**-H⁺ I⁻ (0.473 g, 1.42 mmol), (*R_CR_C*)-*N''*,*N''*-dimethyl-1,2-diaminocyclohexane (0.222 g, 1.56 mmol),¹³⁹ and *t*-BuOH (10 mL), and fitted with a condenser. The mixture was heated at 100 °C for 2 d with stirring and cooled to 50 °C. The solvent was removed by oil pump vacuum to give a beige solid, and 3% aqueous NaOH (30 mL) was added. The sample was extracted with 95:5 v/v CH₂Cl₂/MeOH (3 × 30 mL). The combined organic phases were dried (Na₂SO₄). The solvent was removed by rotary evaporation and the oily residue was chromatographed on a silica gel column (1.5 × 25 cm, 8.0:2.0:0.05 → 8.0:2.0:0.10 v/v/v CH₂Cl₂/MeOH/NEt₃). The solvent was removed from the product containing fractions by oil pump vacuum to give (*R_CR_C*)-**16c** as a white solid (0.255 g, 0.850 mmol, 61%). An analytical sample was further purified by precipitation from CH₂Cl₂/pentane and subsequent recrystallization from Et₂O, mp 186 °C (capillary). Anal. Calcd for C₁₆H₂₄N₆: C 63.97, H 8.05, N 27.98. Found C 62.78, H 8.06, N 27.10.¹³⁶

NMR (δ , CDCl₃):^{104,105,134} ¹H (400 MHz) 7.30-7.27 (m, 2H, CH4/7), 7.04-7.01 (m, 2H, CH5/6), 3.44 (td, 1H, ³J_{HH} = 10.4 Hz, ³J_{HH} = 3.6 Hz, CHNH), 2.38-2.33 (m, 2H), 2.24 (s, 6H, N(CH₃)₂), 1.83-1.77, 1.75-1.68, 1.63-1.57, 1.25-1.05 (4 × m, 1H, 1H, 1H, 4H, remaining aliphatic CH);¹³⁷ ¹³C{¹H} (100 MHz) 158.5 and 158.1 (2 × s, 2 N(C=N)N), 137.3 (s, C8/9), 120.2 (s, C5/6), 112.6 (s, C4/7), 67.2 (s, CHN(CH₃)₂), 52.8 (s, CHNH), 39.9 (s, N(CH₃)₂), 33.7, 24.8, 24.4, 21.9 (4 × s, remaining CH₂).

IR (cm⁻¹, powder film): 3398 (w), 2931 (m), 2858 (m), 1603(m), 1518 (vs), 1454 (s), 1261 (s), 734 (s); UV-visible (nm, 2.77 × 10⁻⁵ M in MeOH (ϵ , M⁻¹cm⁻¹)): 245

(5860), 300 (15100); $[\alpha]_{24}^{589} = -35.4^\circ \pm 0.4^\circ$ (2.78 mg mL⁻¹, MeOH).

***N*-(1*H*-benzimidazol-2-yl)-*N'*-((1*R*,2*R*)-*N''*-piperidinyl-1,2-diaminocyclohexyl)guanidine ((*R*_C*R*_C)-**16d**).** A round bottom flask was charged with **13-H⁺ I⁻** (0.781 g, 2.34 mmol), (*R*_C*R*_C)-*N''*-piperidinyl-1,2-diaminocyclohexane (0.468 g, 2.57 mmol),¹⁴⁰ and *t*-BuOH (16 mL), and fitted with a condenser. The mixture was heated at 100 °C for 3 d with stirring and cooled to 50 °C. The solvent was removed by oil pump vacuum to give a beige solid, and 3% aqueous NaOH (30 mL) was added. The sample was extracted with 95:5 v/v CH₂Cl₂/MeOH (3 × 30 mL). The combined organic phases were dried (Na₂SO₄). The solvent was removed by rotary evaporation and the oily residue was chromatographed on a silica gel column (1.5 × 25 cm, 8.0:2.0:0.05 → 8.0:2.0:0.10 v/v/v CH₂Cl₂/MeOH/NEt₃). The solvent was removed from the product containing fractions by oil pump vacuum to give (*R*_C*R*_C)-**16d** as a pale yellow solid (0.318 g, 0.936 mmol, 40%), mp 283 °C (capillary). Anal. Calcd for C₁₉H₂₈N₆: C 67.03, H 8.29, N 24.68. Found C 66.90, H 8.38, N 24.60.

NMR (δ , CD₃OD):¹³⁴ ¹H (500 MHz) 7.27-7.25 (m, 2H, CH4/7), 7.02-7.00 (m, 2H, CH5/6), 3.73-3.68 (m, 1H, CHNH), 2.90 (br s, 2H), 2.59 (br s, 2H), 2.52-2.48, 2.31-2.29, 2.01-1.99, 1.85-1.83, 1.74-1.72, 1.65-1.50, 1.44-1.24 (7 x m, 3H, 1H, 1H, 1H, 1H, 5H, 7H, remaining aliphatic CH);¹³⁷ ¹³C{¹H} (125 MHz) 159.4 and 158.9 (2 × s, 2 N(C=N)N), 133.7 (s, C8/9), 121.5 (s, C5/6), 113.3 (s, C4/7), 70.6 (s, CHNCH₂(CH₂)₃CH₂), 52.8, 51.1 (2 × s, CH₂NCH₂ and CHNH), 34.5, 27.0, 26.3, 25.8, 25.2 (5 × s, CH₂CH₂CH₂CH₂ and CH₂CH₂NCH₂CH₂). The NCH₂CH₂CH₂ signal was not observed and the remaining signals were of approximately equal intensity, although that for CH₂CH₂NCH₂CH₂ should be doubled.

IR (cm⁻¹, powder film): 3273 (w), 2929 (m), 2854 (m), 1610 (m), 1517 (vs), 1456 (s), 1271 (s), 734 (s).

$[(\eta^5\text{-C}_5\text{H}_5)\text{Ru}(\text{CO})(\mathbf{16a})]^+ \text{PF}_6^- (\mathbf{18a}^+ \text{PF}_6^-)$.^{105,106} A round bottom flask was charged with $[(\eta^5\text{-C}_5\text{H}_5)\text{Ru}(\text{CO})(\text{NCCH}_3)_2]^+ \text{PF}_6^- (\mathbf{17}^+ \text{PF}_6^-)$;^{74,104} 0.100 g, 0.237 mmol), **16a** (0.063 g, 0.24 mmol), CH₂Cl₂ (2 mL), and MeOH (1 mL) with stirring. After 2 d, the solvent was removed by oil pump vacuum and the residue was chromatographed on a silica gel column (1 × 15 cm, 3:1 v/v CH₂Cl₂/CH₃CN). The solvent was removed from the product containing fractions. The sticky yellow solid was dissolved in CH₂Cl₂ (5 mL), and pentane was added until a precipitate formed. The solvent was removed by oil pump vacuum. More pentane (5 mL) was added and removed by oil pump vacuum (2 ×) to give **18a**⁺ PF₆⁻ as a yellow powder (0.082 g, 0.136 mmol, 58%). Anal. Calcd for C₂₁H₂₀F₆N₅OPRu: C 41.73, H 3.34, N 11.59. Found C 41.48, H 3.64, N 10.72.¹³⁶

NMR (δ , CD₃CN):^{104,105,134} ¹H (300 MHz) 7.43-7.35, 7.26-7.19 (2 × m, 6H, 3H, CH₄₋₇ and C₆H₅), 6.38 (br s, 1H, NH), 5.34 (br s, 1H, NH), 4.88 (s, 5H, C₅H₅), 4.44 (d, 2H, ³J_{HH} = 6.0 Hz, CH₂);¹³⁷ ¹³C {¹H} (75 MHz) 205.9 (s, CO), 153.5 (s, C11), 146.5 (s, C2), 143.5 (s, C9), 132.5 (s, C8), 138.0 (s, *i*-C₆H₅), 128.5 and 128.2 (2 × s, *o*- and *m*-C₆H₅), 128.8 (s, *p*-C₆H₅), 124.4 and 123.9 (2 × s, C5 and C6), 118.5 (s, C4), 112.1 (s, C7), 83.0 (s, C₅H₅), 45.6 (s, CH₂); ³¹P {¹H} (121 MHz) -143.3 (sep, ¹J_{PF} = 706.5 Hz).

IR (cm⁻¹, powder film): 3391 (m), 1940 (s, ν_{CO}), 1671 (s), 1570 (s), 1536 (s),

1463 (s), 1230 (m), 831 (vs), 736 (s), 556 (vs); UV-visible (nm, 1.99×10^{-5} M in MeOH (ϵ , $\text{M}^{-1}\text{cm}^{-1}$)): 292 (8150).

$(R_{\text{Ru}}S_{\text{C}}/S_{\text{Ru}}S_{\text{C}})-[(\eta^5\text{-C}_5\text{H}_5)\text{Ru}(\text{CO})(\mathbf{16b})]^+ \text{PF}_6^-$ ($(R_{\text{Ru}}S_{\text{C}}/S_{\text{Ru}}S_{\text{C}})-\mathbf{18b}^+ \text{PF}_6^-$).^{104,105,107} A round bottom flask was charged with $\mathbf{17}^+ \text{PF}_6^-$ (0.100 g, 0.237 mmol), (S_{C})- $\mathbf{16b}$ (0.066 g, 0.24 mmol), CH_2Cl_2 (2 mL), and MeOH (1 mL) with stirring. After 2 d, the solvent was removed by oil pump vacuum and the residue was chromatographed on a silica gel column (1 \times 15 cm, 3:1 v/v $\text{CH}_2\text{Cl}_2/\text{CH}_3\text{CN}$). The solvent was removed from the product containing fractions. The sticky yellow solid was dissolved in CH_2Cl_2 (5 mL), and pentane was added until a precipitate formed. The solvent was removed by oil pump vacuum. More pentane (5 mL) was added and removed by oil pump vacuum (2 \times) to give $(R_{\text{Ru}}S_{\text{C}}/S_{\text{Ru}}S_{\text{C}})-\mathbf{18b}^+ \text{PF}_6^-$ as a yellow powder (0.103 g, 0.168 mmol, 71%) and a 54:46 mixture of Ru,C configurational diastereomers. Anal. Calcd for $\text{C}_{22}\text{H}_{22}\text{F}_6\text{N}_5\text{OPRu}$: C 42.72, H 3.59, N 11.32. Found C 43.00, H 4.19, N 10.38.¹³⁶

NMR (δ , CD_3CN ; signals for diastereomers are separated by slashes):^{104,105,134} ^1H (300 MHz) 7.47-7.18 (m, 9H, CH_4 -7 and C_6H_5), 6.26 (br m, 1H, NH), 5.11 (br s, 1H, NH), 5.05/4.60 (2 \times s, 54:46, 5H, C_5H_5), 4.77-4.66 (m, 1H, CH), 1.51/1.49 (2 \times d, 3H, $^3J_{\text{HH}} = 4.8/4.8$ Hz, CH_3);¹³⁷ $^{13}\text{C}\{^1\text{H}\}$ (75 MHz) 205.9/205.4 (2 \times s, CO), 152.9/152.7 (2 \times s, C_{11}), 146.2/146.0 (2 \times s, C_2), 143.8, 143.35, 143.31, 143.26 (4 \times s, C_9 and $i\text{-C}_6\text{H}_5$ diastereomers), 132.4/132.3 (2 \times s, C_8), 129.90/129.87 (2 \times s, $m\text{-C}_6\text{H}_5$),¹³⁸ 126.9/126.8 (2 \times s, $o\text{-C}_6\text{H}_5$), 128.9/128.8 (2 \times s, $p\text{-C}_6\text{H}_5$), 124.47/124.45, 124.03/124.00 (4 \times s, C_5 and C_6), 118.60/118.53 (2 \times s, C_4), 112.1 (s, C_7), 83.1/82.8 (2 \times s, C_5H_5), 52.7/52.5 (2 \times s, CH), 23.7/23.6 (2 \times s, CH_3); $^{31}\text{P}\{^1\text{H}\}$ (121 MHz) -143.2 (sep, $^1J_{\text{PF}} = 706.6$ Hz).

IR (cm⁻¹, powder film): 3402 (m), 1943 (s, ν_{CO}), 1670 (s), 1570 (s), 1537 (s), 1463 (s), 1229 (m), 833 (vs), 738 (s), 556 (vs); UV-visible (nm, 1.88×10^{-5} M in MeOH (ϵ , M⁻¹cm⁻¹)): 295 (8050), 322 (4480); $[\alpha]_{24}^{589} = -15.4^\circ \pm 0.4^\circ$ (1.94 mg mL⁻¹, MeOH).

(*R*_{Ru}*R*_C*R*_C/*S*_{Ru}*R*_C*R*_C)-[(η^5 -C₅H₅)Ru(CO)(16c)]⁺ PF₆⁻ (*R*_{Ru}*R*_C*R*_C/*S*_{Ru}*R*_C*R*_C)-18c**⁺ PF₆⁻).**^{104,109} A round bottom flask was charged with **17**⁺ PF₆⁻ (0.090 g, 0.21 mmol), (*R*_C*R*_C)-**16c** (0.064 g, 0.21 mmol), CH₂Cl₂ (2 mL), and MeOH (1 mL) with stirring. After 2 d, the solvent was removed by oil pump vacuum and the residue was chromatographed on an alumina column (1 × 10 cm, 100:1 → 95:5 v/v CH₂Cl₂/MeOH). An impurity eluted first, followed by impurity/product fractions, and then product containing fractions. The solvent was removed from the last set to give a yellow brown solid. The solid was dissolved in CH₂Cl₂ (5 mL) and added to a suspension of Na⁺ PF₆⁻ (0.143 g, 0.851 mmol) in CH₂Cl₂ (5 mL). The mixture was stirred overnight, and filtered through a plug of Celite (1 × 5 cm), which was washed with CH₂Cl₂ (150 mL). The solvent was removed from the filtrate by rotary evaporation. The sticky yellow solid was dissolved in CH₂Cl₂ (5 mL), and pentane was added until a precipitate formed. The solvent was removed by oil pump vacuum. More pentane (5 mL) was added and removed by oil pump vacuum (2 ×) to give (*R*_{Ru}*R*_C*R*_C/*S*_{Ru}*R*_C*R*_C)-**18c**⁺ PF₆⁻ as a green brown powder (0.078 g, 0.119 mmol, 57%) as a mixture of Ru,C configurational diastereomers.¹⁴¹

NMR (δ , CD₃CN; signals for diastereomers are separated by slashes):^{104,134} ¹H (300 MHz) 7.36-7.25 (m, 1H, CH4/7), 7.19-7.05 (m, 3H, CH7/4, CH5, and CH6), 5.17-5.12 (br m, 1H, NH), 5.08/5.05 (2 × s, 5H, C₅H₅), 3.71-3.53 (two overlapping br m, 1H,

CHNH), 3.07-2.84 (m, 1H, CHN(CH₃)₂), 2.77/2.75 (2 × s, 6H, N(CH₃)₂), 2.09-2.00, 1.92-1.81, 1.80-1.70, 1.55-1.23 (4 × m, 2H, 1H, 1H, 4H, remaining aliphatic CH);¹³⁷ ¹³C{¹H} (125 MHz) 207.7/207.1 (2 × s, CO), 157.0 (br s, C11), 151.0 (br s, C2), 144.6/144.5 (2 × s, C9), 132.92/132.85 (2 × s, C8), 123.1/123.0¹⁴²/122.9 (3 × s, C5 and C6), 117.63/117.59 (2 × s, C4), 111.0/110.8 (2 × s, C7), 83.6/83.5 (2 × s, C₅H₅), 72.0/70.9 (2 × s, CHN(CH₃)₂), 53.0/52.0 (2 × s, CHNH), 41.2/41.0 (2 × br s, N(CH₃)₂), 33.3/33.2 (2 × s, CH₂), 24.90, 24.87, 24.52, 24.46, 24.42, 24.00 (6 × s, remaining 3 CH₂).

IR (cm⁻¹, powder film): 3395 (m), 2948 (m), 2866 (w), 1927 (s, ν_{CO}), 1673 (m), 1588 (m), 1535 (s), 1464 (s), 1256 (m), 823 (vs), 738 (s), 555 (vs); UV-visible (nm, 2.20 × 10⁻⁵ M in MeOH (ε, M⁻¹cm⁻¹)): 296 (4480), 318 (4180).

Separation of diastereomers of 18c⁺ PF₆⁻. A round bottom flask was charged with 17⁺ PF₆⁻ (0.545 g, 1.29 mmol), (R_CR_C)-16c (0.510 g, 1.70 mmol), CH₂Cl₂ (12 mL), and MeOH (6 mL) with stirring. After 3 d, the solvent was removed by oil pump vacuum and the residue was chromatographed on alumina column (3 × 20 cm with CH₂Cl₂/MeOH, 100:2.5 v/v (1000 mL) → 100:3.0 v/v (500 mL) → 100:3.5 v/v (500 mL) → 100:4.0 v/v (500 mL) → 100:6.0 v/v (500 mL) → 100:10.0 v/v (500 mL)). Three fractions, the first and the third containing one diastereomer and the second a mixture, were collected. The solvents were removed from the first and third fractions by rotary evaporation to give (R_{Ru}R_CR_C)-18c⁺ X⁻ (0.290 g) and (S_{Ru}R_CR_C)-18c⁺ X⁻ (0.220 g) as pale yellow brown and pale brown solids, respectively, where X⁻ is principally derived from the alumina (<10% PF₆⁻).

(*R*_{Ru}*R*_C*R*_C)-**18c**⁺ X⁻. NMR (δ , CD₃CN):¹³⁴ ¹H (500 MHz) 7.24-7.22 (m, 1H, CH4/7), 7.07-6.98 (m, 3H, CH5, CH6, and CH4/7), 6.42 (br s, 2H, NH), 6.14 (br s, 1H, NH), 5.22 (br s, 1H, NH), 5.04 (s, 5H, C₅H₅), 3.33-3.31 (m, 1H, CHNH), 2.31-2.27 (m, 1H, CHN(CH₃)₂), 2.23-2.19 (m, 1H), 2.08 (s, 6H, N(CH₃)₂), 1.80-1.74, 1.67-1.65, 1.32-1.13 (3 \times m, 1H, 1H 4H, remaining aliphatic CH); ¹³C{¹H} (125 MHz) 207.6 (s, CO), 157.0 (s, C11), 153.2 (s, C2), 146.0 (s, C9), 138.4 (s, C8), 121.3, 121.0 (2 \times s, C5 and C6), 116.5 (s, C4), 112.9 (s, C7), 83.4 (s, C₅H₅), 67.9 (s, CHN(CH₃)₂), 52.9 (s, CHNH), 40.3 (s, N(CH₃)₂), 33.5 (s, CH₂), 25.6, 25.1, 22.7 (3 \times s, remaining 3 CH₂).

(*S*_{Ru}*R*_C*R*_C)-**18c**⁺ X⁻. NMR (δ , CD₃CN):¹³⁴ ¹H (500 MHz) 7.19-7.18 (m, 1H, CH4/7), 7.05-6.98 (m, 2H, CH5 and CH6), 5.92 (br s, 1H, NH), 5.27 (br s, 2H, NH), 5.07 (s, 5H, C₅H₅), 4.89 (br s, 1H, NH), 3.41-3.28 (m, 1H, CHNH), 2.39-2.33 (m, 1H, CHN(CH₃)₂), 2.26 (s, 6H, N(CH₃)₂), 2.09-2.05, 1.86-1.84, 1.77-1.74, 1.65-1.62, 1.34-1.10 (5 \times m, 1H, 1H, 1H, 1H, 4H, remaining aliphatic CH);¹³⁷ ¹³C{¹H} (125 MHz) 207.6 (s, CO), 157.7 (s, C11), 153.4 (s, C2), 145.8 (s, C9), 136.8 (s, C8), 121.4, 121.3 (2 \times s, C5 and C6), 116.4 (s, C4), 112.0 (s, C7), 83.7 (s, C₅H₅), 68.1 (s, CHN(CH₃)₂), 53.0 (s, CHNH), 40.5 (s, N(CH₃)₂), 34.4 (s, CH₂), 25.5, 25.2, 22.9 (3 \times s, remaining 3 CH₂).

A round bottom flask was charged with (*R*_{Ru}*R*_C*R*_C)-**18c**⁺ X⁻ (0.049 g, ca. 0.1 mmol if the mass is considered to represent the cation) and CH₂Cl₂ (5 mL) and was placed in a -40 °C cold bath. Then NH₄⁺ PF₆⁻ (0.143 g, 0.851 mmol) was added with stirring. After 17 h, the mixture was filtered through a plug of Celite (0.1 \times 3 cm), which was washed with additional CH₂Cl₂ (2 mL). The solvent was removed from the filtrate by rotary evaporation. The sticky yellow brown solid was dissolved in CH₂Cl₂ (1 mL), and pentane was added until a precipitate formed. The solvent was removed by oil pump

vacuum. More pentane (5 mL) was added and removed by oil pump vacuum (2 ×) to give ($R_{Ru}R_C R_C$)-**18c**⁺ PF₆⁻ as a yellow brown powder (0.032 g, 0.050 mmol; 99:01 $R_{Ru}R_C R_C/S_{Ru}R_C R_C$, configurations assigned crystallographically). Anal. Calcd for C₂₂H₂₉F₆N₆OPRu: C 41.32, H 4.57, F 17.82, N 13.14. Found C 40.92, H 4.92, F 16.24, N 12.19.¹³⁶

NMR (δ , CD₃CN):¹³⁴ ¹H (500 MHz) 7.22 (d, 1H, ³J_{HH} = 7.7 Hz, CH_{4/7}), 7.12-7.05 (m, 3H, CH₅, CH₆, and CH_{4/7}), 5.04 (s, 5H, C₅H₅), 4.97 (br s, 1H, NH) 4.65 (br s, 1H, NH), 3.59-3.55 (m, 1H, CHNH), 2.82-2.74 (m, 1H, CHN(CH₃)₂), 2.74 (s, 6H, N(CH₃)₂), 2.05-2.03, 1.86-1.83, 1.75-1.77, 1.48-1.40, 1.36-1.24 (5 × m, 2H, 1H, 1H, 1H, 3H, remaining aliphatic CH);¹³⁷ ¹³C {¹H} (125 MHz) 208.1 (s, CO), 160.2 (s, C11), 153.7 (s, C2), 144.9 (s, C9), 133.1 (2 × s, C8), 122.5, 122.4 (2 × s, C5 and C6), 117.3 (s, C4), 110.4 (s, C7), 83.6 (s, C₅H₅), 72.8 (s, CHN(CH₃)₂), 53.4 (s, CHNH), 41.3 (s, N(CH₃)₂), 33.1, 24.9, 24.6, 24.6 (4 × s, remaining 4 CH₂); ¹⁹F {¹H} (470 MHz) -72.89 (d, ¹J_{FP} = 706.41 Hz).

IR (cm⁻¹, powder film): 3412 (m), 2937 (m), 2866 (w), 1923 (s, ν_{CO}), 1680 (m), 1589 (m), 1535 (s), 1463 (s), 1255 (m), 1222 (m), 833 (vs), 740 (s); UV-visible (nm, 2.20 × 10⁻⁵ M in MeOH (ϵ , M⁻¹cm⁻¹)): 294 (11923), 314 (10384); CD (nm, 2.6 × 10⁻³ M in CH₃CN ([θ], deg·L·mol⁻¹cm⁻¹ and $\Delta\epsilon$, L·mol⁻¹cm⁻¹): 408 (-268 and -0.089), 368 (+58.0 and +0.019).

A round bottom flask was charged with ($S_{Ru}R_C R_C$)-**18c**⁺ X⁻ (0.049 g, 0.1 mmol if the mass is considered to represent the cation) and CH₂Cl₂ (5 mL) and was placed in a -40 °C cold bath. Then NH₄⁺ PF₆⁻ (0.143 g, 0.851 mmol) was added with stirring. After

17 h, mixture was filtered through a plug of Celite (0.1 × 3 cm), which was washed with additional CH₂Cl₂ (2 mL). The solvent was removed from the filtrate by rotary evaporation. The sticky yellow brown solid was dissolved in CH₂Cl₂ (1 mL), and pentane was added until a precipitate formed. The solvent was removed by oil pump vacuum. More pentane (5 mL) was added and removed by oil pump vacuum (2 ×) to give (*S*_{Ru}*R*_C*R*_C)-**18c**⁺ PF₆⁻ as a green brown powder (0.028 g, 0.045 mmol; 02:98 *R*_{Ru}*R*_C*R*_C/*S*_{Ru}*R*_C*R*_C, configurations assigned crystallographically). Anal. Calcd for C₂₂-H₂₉N₆F₆PORu: C 41.32, H 4.57, F 17.82, N 13.14. Found C 40.90, H 4.88, F 17.16, N 12.40.¹³⁶

NMR (δ , CD₃CN):¹³⁴ ¹H (500 MHz) 7.19 (d, 1H, ³*J*_{HH} = 7.2 Hz, CH4/7), 7.11-7.05 (m, 2H, CH5 and CH6), 6.99 (d, 1H, ³*J*_{HH} = 7.3 Hz, CH4/7), 5.08 (s, 5H, C₅H₅), 4.84 (br s, 1H, NH) 4.68 (br s, 1H, NH); 3.74-3.70 (m, 1H, CHNH), 2.86-2.81 (m, 1H, CHN(CH₃)₂), 2.75 (s, 6H, N(CH₃)₂), 2.04-2.02, 1.87-1.84, 1.76-1.75, 1.50-1.24 (4 × m, 2H, 1H, 1H, 4H, remaining aliphatic CH);¹³⁷ ¹³C{¹H} (125 MHz) 208.1 (s, CO), 159.7 (s, C11), 154.0 (s, C2), 145.2 (s, C9), 133.0 (s, C8), 122.3, 122.1 (2 × s, C5 and C6), 117.0 (s, C4), 110.1 (s, C7), 83.9 (s, C₅H₅), 72.4 (s, CHN(CH₃)₂), 52.6 (s, CHNH), 41.2 (s, N(CH₃)₂), 33.4 (s, CH₂), 25.0, 24.6, 24.1 (3 × s, remaining 3 CH₂); ¹⁹F{¹H}(470 MHz) -72.88 (d, ¹*J*_{FP} = 706.37 Hz).

IR (cm⁻¹, powder film): 3392 (m), 2937 (m), 2864 (w), 1925 (s, ν _{CO}), 1672 (m), 1589 (m), 1535 (s), 1463 (s), 1255 (m), 1220 (m), 833 (vs), 738 (s); UV-visible (nm, 2.20 × 10⁻⁵ M in MeOH (ϵ , M⁻¹cm⁻¹)): 294 (10400), 315 (8400); CD (nm, 2.7 × 10⁻³ M in CH₃CN ([θ], deg·L·mol⁻¹cm⁻¹ and $\Delta\epsilon$, L·mol⁻¹cm⁻¹)): 406 (+672 and +0.204), 372 (sh, +441 and +0.133).

(*R*_{Ru}*R*_C*R*_C)-18c⁺ (Δ)-TRISPHAT⁻. A round bottom flask was charged with (*R*_{Ru}*R*_C*R*_C)-18c⁺ X⁻ (0.010 g, ca. 0.2 mmol based upon cation mass), CH₂Cl₂ (1.0 mL), and water (0.5 mL). Then Na⁺ (Δ)-TRISPHAT⁻ (0.015 g, 0.019 mmol; ca. 95% purity by ¹H NMR)²⁶ was added with stirring. After 1.5 h, the organic layer was washed with water (2 × 0.5 mL). The organic layer was dried (Na₂SO₄) and filtered through a plug of Celite. The solvent was removed from the filtrate by rotary evaporation. The sticky yellow brown solid was dissolved in CH₂Cl₂ (1 mL), and hexane was added until a precipitate formed. The solvent was removed by oil pump vacuum. More hexane (1 mL) was added and removed by oil pump vacuum (2 ×) to give (*R*_{Ru}*R*_C*R*_C)-18c⁺ (Δ)-TRISPHAT⁻ as a yellow powder (0.015 g, >99% *R*_{Ru}*R*_C*R*_C/*S*_{Ru}*R*_C*R*_C) of ca. 95% purity. For a microanalysis, see the sample used for crystallography below.

NMR (δ, CDCl₃):¹³⁴ ¹H (500 MHz) 9.56 (br s, 1H, NH) 7.32-7.29 (m, 1H, CH4/7), 7.26-7.21 (m, 2H, CH5, CH6), 7.17-7.15 (m, 1H CH7/4), 5.85 (br s, 1H, NH), 5.03 (s, 5H, C₅H₅), 4.81 (s, 1H, NH), 2.95-2.90 (m, 1H, CHNH), 2.00 (s, 6H, N(CH₃)₂), 1.98-1.91, 1.88-1.70, 1.68-1.55, 1.22-1.09 (4 × m, 1H, 3H, 3H, 4H, CHN(CH₃)₂, NH, and remaining aliphatic CH); ¹³C {¹H} (125 MHz) 203.8 (s, CO), 153.4 (s, C11), 145.7 (s, C2), 142.3 (s, C9), 141.1 (d, ²J_{CP} = 6.4 Hz, P(O₂C₆Cl₄), 130.9 (s, C8), 123.6 (s, C5/C6), 123.5 (s, P(O₂C₆Cl₄), 123.3 (s, C5/C6), 117.2 (s, C4), 114.5 (d, ²J_{CP} = 19.2 Hz, P(O₂C₆Cl₄), 111.4 (s, C7), 81.8 (s, C₅H₅), 66.8 (s, CHN(CH₃)₂), 51.4 (s, CHNH), 39.9 (s, N(CH₃)₂), 34.7 (s, CH₂), 25.3, 24.7, 24.1, (3 × s, remaining 3 CH₂); ³¹P {¹H} (202 MHz) -81.2 (s, P(O₂C₆Cl₄)).

IR (cm⁻¹, powder film): 3383 (m), 2958 (m), 2864 (w), 1940 (s, ν_{CO}), 1668 (m), 1591 (m), 1537 (m), 1446 (s), 1390 (m), 1236 (m), 989 (s), 821 (vs), 740 (m), 719 (m),

671 (s).

(*R*_{Ru}*R*_C*R*_C)-18c⁺ (Δ/Λ)-TRISPHAT⁻. A round bottom flask was charged with **(*R*_{Ru}*R*_C*R*_C)-18c⁺ X⁻** (0.010 g, ca. 0.02 mmol based upon cation mass) and CH₂Cl₂ (0.5 mL). Then (*n*-Bu)₃NH⁺ (±)-TRISPHAT⁻ (0.057 g, 0.059 mmol)¹⁴³ was added with stirring. After 10 min, the mixture was filtered and the filtrate was cooled to -35 °C. After a few hours, white crystals began to form. After 48 h, the mixture was filtered and the solvent was removed from the filtrate by rotary evaporation to give a pale white solid containing a 1:2 mixture of the cations (*R*_{Ru}*R*_C*R*_C)-18c⁺ and (*n*-Bu)₃NH⁺, as assayed by ¹H and ¹³C NMR, together with X⁻ and (±)-TRISPHAT⁻ anions. The NMR signals for (*R*_{Ru}*R*_C*R*_C)-13c⁺ were very similar to those from the preceding preparation. A crystal structure of a complex derived from this sample is described below.

(*R*_{Ru}*R*_C*R*_C/*S*_{Ru}*R*_C*R*_C)-[(η⁵-C₅H₅)Ru(CO)(16d)]⁺ PF₆⁻ (*R*_{Ru}*R*_C*R*_C/*S*_{Ru}*R*_C*R*_C)-18d⁺ PF₆⁻. A round bottom flask was charged with **17⁺ PF₆⁻** (0.090 g, 0.21 mmol), (*R*_C*R*_C)-16d (0.064 g, 0.21 mmol), CH₂Cl₂ (2 mL), and MeOH (1 mL). The mixture was stirred for 2 d at room temperature. The solvent was removed by oil pump vacuum and the residue was chromatographed on an alumina column (1 × 10 cm, 100:1 v/v → 95:5 v/v CH₂Cl₂/MeOH). The solvent was removed from the product containing fractions. The yellow brown solid was dissolved in CH₂Cl₂ (5 mL) and added to a suspension of Na⁺ PF₆⁻ (0.143 g, 0.851 mmol) in CH₂Cl₂ (5 mL). The mixture was stirred overnight, and filtered through a plug of Celite (1 × 5 cm), which was washed with CH₂Cl₂ (150 mL). The solvent was removed from the filtrate by rotary evaporation. The sticky yellow solid was dissolved in CH₂Cl₂ (5 mL), and pentane was added until a precipitate formed. The solvent was removed by oil pump vacuum. More pentane (5 mL) was added and

removed by oil pump vacuum (2 ×) to give (*R*_{Ru}*R*_C*R*_C/*S*_{Ru}*R*_C*R*_C)-**18d**⁺ PF₆⁻ as a green brown powder (0.055 g, 0.082 mmol, 39%) as a mixture of Ru,C configurational diastereomers.¹⁴¹ Anal. Calcd for C₂₅H₃₃F₆N₆PORu: C 44.18, H 4.89, F 16.77, N 12.37. Found C 43.90, H 4.88, F 16.56, N 11.70.¹³⁶

NMR (δ , CD₂Cl₂; signals for diastereomers are separated by slashes):¹³⁴ ¹H (500 MHz) 8.24 (br s, 2H, NH), 7.28-7.75 (m, 1H, CH4/7), 7.15-7.03 (m, 3H, CH5, CH6, and CH7/4), 6.52-6.18 (2 × br s, 1.5H, NH), 5.08/5.05 (2 × s, 5H, C₅H₅), 4.80 (s, 0.5H, NH), 3.44-3.38, 3.22-3.16 (2 × m, 1H, CHNH), 2.65-2.67, 2.59-2.51, 2.47-2.37, 2.32-2.07, 1.95-1.84, 1.82-1.10 (6 × m, 1H, 1H, 3H, 1H, 4H, 11H, remaining aliphatic CH); ¹³C{¹H} (125 MHz) 205.8/205.4 (2 × s, CO), 156.1/156.0 (2 × s, C11), 150.0/149.7 (2 × s, C2), 143.9 (s, C9), 134.1/133.8 (2 × s, C8), 122.2/122.0/121.9/121.7 (4 × s, C5 and C6), 116.7/116.1 (2 × s, C4), 112.4/111.7 (2 × s, C7), 82.6 (s, C₅H₅), 69.8/68.7 (2 × s, CHNCH₂(CH₂)₃CH₂), 53.2/50.2 (2 × s, CHNH), 34.3/33.4 (2 × s, CHNCH₂(CH₂)₃CH₂), 30.1 (s, CH₂), 26.8/26.6, 25.7/25.6, 25.2/25.1, 25.0/24.9, 24.3/24.2 (5 × s, remaining CH₂).

Friedel-Crafts alkylation of indoles with *trans*- β -nitrostyrene (Table 3.3). An NMR tube was charged with catalyst (0.0013 g, 0.0020 mmol), an indole (**5a,b**; 0.040 mmol), **6** (0.0029 g, 0.020 mmol), an internal standard (Ph₂SiMe₂), and CD₂Cl₂ (0.3 mL). The tube was capped and ¹H NMR spectra were periodically recorded. The CH=CH signals of **6** and the product CH₂NO₂ signals at ca. 5 ppm were integrated versus those of the standard. After the specified time (Table 3.3), the solvent was removed. The residue was taken up in hexane/ethyl acetate (30:70 v/v) and passed through a short silica gel column, which was washed with additional hexane/ethyl

acetate (50:50 v/v, 5 mL). The solvent was removed, and a second silica gel chromatography step was carried out (column length substrate dependent). The solvent was removed from the product containing fractions (yields, Table 3.3).

1-Methyl-3-(2-nitro-1-phenylethyl)-1*H*-indole (7a, entry 1). NMR (δ , CDCl₃) ¹H (500 MHz): 7.47 (d, 1H, ³*J*_{HH} = 7.6 Hz), 7.38–7.23 (m, 7H), 7.10 (m, 1H), 6.88 (s, 1H), 5.21 (t, 1H, ³*J*_{HH} = 8.0 Hz, CHCH₂NO₂), 5.06 (dd, 1H, ³*J*_{HH} = 12.4, ²*J*_{HH} = 8.0 Hz, CHH'NO₂), 4.95 (dd, 1H, ³*J*_{HH} = 12.4, ²*J*_{HH} = 8.0 Hz, CHH'NO₂), 3.75 (s, 3H, NCH₃); Literature chemical shift values (CDCl₃) agree within 0.01 ppm.^{68a}

The enantiomeric excess was determined by HPLC with a Chiralpak AS-H column, hexane/2-PrOH (90:10 v/v), 1.0 mL/min, λ = 210 nm; *t*_R = 14.6 min (minor, *R*), 18.6 min (major, *S*).^{144,145}

3-(2-Nitro-1-phenylethyl)-1*H*-indole (7b, entry 2). NMR (δ , CDCl₃) ¹H (500 MHz): 8.08 (br s, 1H, C₈H₅NH), 7.55-6.96 (m, 10H, C₈H₅NH and C₆H₅), 5.19 (t, 1H, ³*J*_{HH} = 8.2 Hz, CHCH₂NO₂), 5.07 (dd, 1H, ²*J*_{HH} = 12.4 Hz, ³*J*_{HH} = 7.2 Hz, CHH'NO₂), 4.95 (dd, 1H, ²*J*_{HH} = 12.4 Hz, ³*J*_{HH} = 8.2 Hz, CHH'NO₂). Literature values (CDCl₃)^{119b} agree within 0.01 ppm, and data in CD₂Cl₂ are supplied elsewhere.⁷⁰

The enantiomeric excess was determined by HPLC with a Chiralcel AD column, hexane/2-PrOH (70:30 v/v), 0.9 mL/min, λ = 210 nm; *t*_R = 18.2 min (minor, *R*), 19.6 min (major, *S*).^{145,146}

Additions of dialkyl malonates to nitroalkenes (Table 3.4, Figure 3.5). A J. Young NMR tube was charged with **6** (e.g. Table 3.4, entry 1 or Figure 3.5, red/blue triangles: 0.0149 g, 0.100 mmol), catalyst (0.010 mmol, 10 mol%), Ph₂SiMe₂ (ca. 0.050 mmol; internal standard), and CD₂Cl₂ (0.5 mL, Table 3.4; 0.7 mL, Figure 3.5). Then the malonate ester (**10a-c**; 0.200 mmol, Table 3.4; 0.180 mmol, Figure 3.5) was added and the tube was capped. Product formation was monitored vs. the standard by ¹H NMR (Figure 3.5). After the specified time (Table 3.4), the solvent was removed. The residue was taken up in hexane/ethyl acetate (30:70 v/v) and passed through a short silica gel column, which was washed with additional hexane/ethyl acetate (30:70 v/v, 5 mL). The solvent was removed, and a second silica gel chromatography step was carried out (column length substrate dependent). The solvent was removed from the product containing fractions (yields, Table 3.4).

Ethyl-2-carboethoxy-4-nitro-3-phenylbutyrate (19a, entry 1).^{121,147} NMR (δ , CDCl₃): ¹H (500 MHz) 7.32-7.23 (m, 5H), 4.92 (dd, 1H, J = 13.2, 4.7 Hz), 4.86 (dd, 1H, J = 13.2, 9.5 Hz), 4.26-4.17 (m, 3H), 4.00 (q, 2H, J = 7.1 Hz), 3.82 (d, 1H, J = 9.3 Hz), 1.25 (t, 3H, J = 7.1 Hz), 1.03 (t, 3H, J = 7.1 Hz); ¹³C{¹H} (125 MHz) 167.4, 166.7, 136.2, 128.8, 128.3, 127.9, 77.6, 62.1, 61.8, 55.0, 42.9, 13.9, 13.6.

The enantiomeric excess was determined by HPLC with a Chiralpak AS-H column, hexane/2-PrOH (90:10 v/v), 1.0 mL/min, λ = 220 nm; t_R = 11.8 min (minor, *S*), 13.4 min (major, *R*).^{145,148}

Ethyl-2-carboethoxy-4-nitro-3-(3,4-dichlorophenyl)butyrate (19b, entry 2).^{147,149} NMR (δ , CDCl₃): ¹H (500 MHz) 7.40 (d, 1H, J = 8.3 Hz), 7.36 (d, 1H, J = 2.0

Hz), 7.11 (dd, 1H, $J = 2.0, 8.3$ Hz), 4.87 (m, 2H), 4.22 (m, 3H), 4.08 (q, 2H, $J = 7.3$ Hz), 3.76 (d, 1H, $J = 8.8$ Hz), 1.27 (t, 3H, $J = 7.1$ Hz), 1.13 (t, 3H, $J = 7.1$ Hz); $^{13}\text{C}\{^1\text{H}\}$ (125 MHz) 167.2, 166.6, 136.8, 133.3, 132.9, 131.0, 130.4, 127.6, 77.2, 62.5, 62.3, 54.8, 42.2, 14.1, 13.9.

The enantiomeric excess was determined by HPLC with a Chiralcel OD column, hexane/2-PrOH (94:06 v/v), 1.0 mL/min, $\lambda = 215$ nm; $t_{\text{R}} = 20.3$ min (major), 22.8 min (minor).¹⁵⁰

Ethyl-2-carboethoxy-4-nitro-3-(3,4-methylenedioxyphenyl)butyrate (19c, entry 3).^{121,147} NMR (δ , CDCl_3): ^1H (500 MHz) 6.73-6.67 (m, 3H), 5.93 (s, 2H), 4.87 (dd, 1H, $J = 13.2, 4.6$ Hz), 4.78 (dd, 1H, $J = 13.2, 9.4$ Hz), 4.27-4.17 (m, 2H), 4.14 (ddd, 1H, $J = 9.4, 9.4, 4.6$ Hz), 4.04 (q, 2H, $J = 7.1$ Hz), 3.74 (d, 1H, $J = 9.4$ Hz), 1.26 (t, 3H, $J = 7.1$ Hz), 1.10 (t, 3H, $J = 7.1$ Hz); $^{13}\text{C}\{^1\text{H}\}$ (125 MHz) 167.4, 166.7, 147.9, 147.5, 129.7, 121.5, 108.5, 108.2, 101.2, 77.8, 62.1, 61.8, 55.0, 42.7, 13.9, 13.8.

The enantiomeric excess was determined by HPLC with a Chiralpak AS-H column, hexane/2-PrOH (90:10 v/v), 1.0 mL/min, $\lambda = 215$ nm; $t_{\text{R}} = 29.6$ min (major, *R*), 34.3 min (minor, *S*).^{121,145,151}

Ethyl-2-carboethoxy-4-nitro-3-(2-furyl)butyrate (19d, entry 4).^{147,149} NMR (δ , CDCl_3): ^1H (500 MHz) 7.31 (app d, 1H, $J = 2.0$ Hz), 6.26 (app dd, 1H, $J = 2.9, 2.0$ Hz), 6.19 (app d, 1H, $J = 2.9$ Hz), 4.91-4.84 (m, 2H), 4.34 (ddd, 1H, $J = 7.8, 7.8, 5.4$ Hz), 4.19 (dq, 2H, $J = 7.2, 2.0$ Hz), 4.11 (q, 2H, $J = 7.2$ Hz), 3.87 (d, 1H, $J = 7.8$ Hz), 1.23 (t, 3H, $J = 7.1$ Hz), 1.16 (t, 3H, $J = 7.1$ Hz); $^{13}\text{C}\{^1\text{H}\}$ (125 MHz) 167.0, 166.7,

149.5, 142.6, 110.4, 108.3, 75.3, 62.0, 52.9, 36.7, 13.8, 13.7.

The enantiomeric excess was determined by HPLC with a Chiralpak AS-H column, hexane/2-PrOH (99:01 v/v), 1.0 mL/min, $\lambda = 215$ nm; $t_R = 26.3$ min (minor, *R*), 29.0 min (major, *S*).^{145,148,151}

1-Methylethyl-2-(1-methylethoxycarbo)-4-nitro-3-phenylbutyrate (19e, entry 5).^{121,147} NMR (δ , CDCl₃): ¹H (500 MHz) 7.32-7.22 (m, 5H), 5.08 (sep, 1H, *J* = 6.3 Hz), 4.92 (dd, 1H, *J* = 12.9, 4.5 Hz), 4.84 (dd, 1H, *J* = 12.9, 9.7 Hz), 4.83 (sep, 1H, *J* = 6.3 Hz), 4.2 (ddd, 1H, *J* = 9.5, 9.5, 4.4 Hz), 3.67 (d, 1H, *J* = 9.3), 1.24 (d, 3H, *J* = 6.3 Hz), 1.23 (d, 3H, *J* = 6.3 Hz), 1.06 (d, 3H, *J* = 6.3 Hz), 1.01 (d, 3H, *J* = 6.3 Hz); ¹³C{¹H} (125 MHz) 167.0, 166.3, 136.3, 128.8, 128.2, 128.10, 128.08, 77.9, 69.9, 69.5, 55.1, 42.9, 21.5, 21.4, 21.24, 21.20.

The enantiomeric excess was determined by HPLC with a Chiralcel OD column, hexane/2-PrOH (95:05 v/v), 0.75 mL/min, $\lambda = 220$ nm; $t_R = 10.7$ min (minor, *S*), 13.0 min (major, *R*).^{145,148}

Methyl-2-carbomethoxy-4-nitro-3-phenylbutyrate (19f, entry 6).^{121,147} NMR (δ , CDCl₃): ¹H (500 MHz) 7.34-7.26 (m, 3H), 7.24-7.21 (m, 2H), 4.92 (dd, 1H, *J* = 13.2, 4.8 Hz), 4.88 (dd, 1H, *J* = 13.2, 9.2 Hz), 4.24 (ddd, 1H, *J* = 9.0, 9.0, 4.9 Hz), 3.86 (d, 1H, *J* = 8.8 Hz), 3.75 (s, 3H), 3.55 (s, 3H); ¹³C{¹H} (125 MHz) 167.8, 167.2, 136.1, 129.0, 128.4, 127.8, 77.3, 54.7, 53.0, 52.8, 42.9.

The enantiomeric excess was determined by HPLC with a Chiralpak AS-H

column, hexane/2-PrOH (90:10 v/v), 1.0 mL/min, $\lambda = 215$ nm; $t_R = 17.0$ min (minor, *S*), 19.5 min (major, *R*).^{148,151}

Ethyl-2-carboethoxy-3-(1-nitromethyl)nonanoate (19g, entry 7).^{147,152} NMR (δ , CDCl₃): ¹H (300 MHz) 4.72-4.65 (m, 1H), 4.55-4.47 (m, 1H), 4.24-4.16 (m, 4H), 3.60 (d, 1H, $J = 5.9$ Hz), 2.90-2.81 (m, 1H), 1.54 (br s, 2H), 1.45-1.41 (m, 2H), 1.28-1.24 (m, 12H), 0.86 (t, $J = 6.4$ Hz, 3H); ¹³C{¹H} NMR (75): 168.0, 167.8, 77.2, 61.9, 61.8, 52.7, 37.0, 31.5, 30.1, 28.9, 26.6, 22.5, 14.0.

The enantiomeric excess was determined by HPLC with a Chiralcel OD column, hexane/2-PrOH (99:01 v/v), 0.60 mL/min, $\lambda = 215$ nm; $t_R = 11.6$ min (minor, *S*), 18.1 min (major, *R*).^{151,152}

Ethyl-2-carboethoxy-3-(1-nitromethyl)hexanoate (19h, entry 8).^{147,153} NMR (δ , CDCl₃): ¹H (300 MHz) 4.71 (dd, 1H, $J = 8.7, 4.8$ Hz), 4.54 (dd, 1H, $J = 6.9, 6.3$ Hz), 4.19-4.26 (m, 4H), 3.62 (d, 1H, $J = 5.7$ Hz), 2.88-2.94 (m, 1H), 1.35-1.49 (m, 4H), 1.28 (t, 6H, $J = 7.2$ Hz), 0.92 (t, 3H, $J = 6.9$ Hz); ¹³C{¹H} (125 MHz) 168.0, 167.8, 76.7, 61.9, 61.7, 52.6, 36.6, 32.1, 29.6, 19.8, 14.0, 13.7.

The enantiomeric excess was determined by HPLC with a Chiralcel OD column, hexane/2-PrOH (99:01 v/v), 0.60 mL/min, $\lambda = 215$ nm; $t_R = 13.3$ min (major), 22.8 min (minor).¹⁵⁰

Additions of Michael donors to 6 catalyzed by 18c⁺ PF₆⁻ (Table 3.5). A J. Young NMR tube was charged with a Michael donor (e.g. 2,4-pentanedione (entry 1),

0.0184 g, 0.200 mmol), **6** (e.g. entry 1, 0.0298 g, 0.200 mmol), and CD₂Cl₂ (1.0 mL). Then the catalyst (e.g. entry 1, 0.0013 g, 0.0020 mmol, 1 mol%) was added. The tube was capped. Product formation was monitored by TLC. After the specified time (Table 3.5), the solvent was removed. The residue was taken up in hexane/ethyl acetate (30:70 v/v) and passed through a short silica gel column, which was washed with additional hexane/ethyl acetate (50:50 v/v, 5 mL). The solvent was removed, and a second silica gel chromatography step was carried out (column length substrate dependent). The solvent was removed from the product containing fractions (yields, Table 3.5).

3-(2-Nitro-1-phenylethyl)pentane-2,4-dione (21, entry 1).¹²³ NMR (δ , CDCl₃):^{123a,147} ¹H (500 MHz) 7.34-7.25 (m, 3H), 7.19-7.16 (m, 2 H), 4.64-4.61 (m, 2 H), 4.36 (d, 1H, *J* = 10.7 Hz), 4.27-4.20 (m, 1H), 2.28 (s, 3H), 1.93 (s, 3H); ¹³C{¹H} (125 MHz) 201.6, 200.9, 135.9, 129.3, 128.5, 127.9, 78.2, 70.7, 42.9, 30.5, 29.7.

The enantiomeric excess was determined by HPLC with a Chiralpak AS-H column, hexane/2-PrOH (85:15 v/v), 1.0 mL/min, λ = 215 nm; *t*_R = 14.9 min (minor, *S*), 22.6 min (major, *R*).^{123b,145}

Ethyl 1-(2-nitro-1-phenylethyl)-2-oxo-cyclopentanecarboxylate (23, entry 2).¹²⁴ NMR (δ , CDCl₃; signals for diastereomers are separated by slashes):^{120f,124,147} ¹H (300 MHz) 7.21-7.35 (m, 5H); 5.29/5.18 (dd, 1H, *J* = 13.5/13.5, 11.1/3.9 Hz), 5.02/4.83 (dd, 1H, *J* = 13.5/13.5, 11.0/4.0 Hz), 4.15-28 (m, 2H), 4.08 (dd, 1H, *J* = 10.8, 3.9 Hz), 2.30-2.42 (m, 2H), 1.80-2.09 (m, 4H), 1.28 (m, 3H); ¹³C{¹H} (75 MHz) 215.5/212.3, 171.0/169.2, 135.4/135.3, 129.3/129.2, 128.7/128.4, 128.2/128.1, 76.9/76.4, 62.4, 62.1, 47.2/46.1, 39.5/37.8, 33.5/31.0, 19.5/19.3, 14.0/13.9.

The enantiomeric excess was determined by HPLC with a Chiralcel OD column, hexane/2-PrOH (90:10 v/v), 1.0 mL/min, $\lambda = 220$ nm; major diastereomer, $t_R = 8.4$ min (minor, $R_C S_C$), 10.9 min (major, $S_C R_C$);^{124a,145} minor diastereomer, $t_R = 7.3$ min (minor, $R_C R_C$), 9.9 min (major, $S_C S_C$).^{120f,145}

Phenylmethyl 2-acetyl-4-nitro-3-phenyl-butyrate (25, entry 3). NMR (δ , $CDCl_3$; signals for diastereomers are separated by slashes):^{125,147} 1H (300 MHz) 7.28-7.07 (m, 10H), 5.19/4.93 (s, 2H), 4.80-4.73 (m, 2H), 4.28-4.15/4.06-4.03 (m, 2H), 2.25/2.00 (s, 3H); $^{13}C\{^1H\}$ (75 MHz) 200.86/199.92, 167.33/166.68, 136.21, 134.59/134.45, 129.10/128.96, 128.75/128.69, 128.53/128.46, 128.32/128.24, 127.83/127.78, 77.74, 67.82, 67.64, 61.83/61.16, 42.50/42.23, 30.17/30.07.

The enantiomeric excess was determined by HPLC with a Chiralcel AD-H column, hexane/2-PrOH (85:15 v/v), 0.75 mL/min, $\lambda = 230$ nm; $t_R = 13.2$ min (minor), 20.9 min (major), 17.4 min (major), 27.1 min (minor).¹²⁵

2-(2-Nitro-1-phenylethyl)propanedinitrile (27, entry 4). NMR (δ , $CDCl_3$):^{21b,147} 1H (500 MHz) 7.54-7.41 (m, 3H), 7.41-7.29 (m, 2H), 4.99 (dd, 1H, $J = 14.3, 8.2$ Hz), 4.91 (dd, 1H, $J = 14.3, 6.1$ Hz), 4.43 (d, 1H, $J = 5.8$ Hz), 4.15-4.03 (m, 1H); $^{13}C\{^1H\}$ (125 MHz) 131.8, 130.4, 129.4, 127.7, 110.5, 110.4, 74.9, 43.5, 27.5.

The enantiomeric excess was determined by HPLC with a Chiralcel OD column, hexane/2-PrOH (50:50 v/v), 0.50 mL/min, $\lambda = 215$ nm; $t_R = 19.5$ min (major), 54.7 min (minor).^{21b,154}

Additions of 22 to dialkyl azodicarboxylates (Table 3.6). A J. Young NMR tube was charged with **22** (e.g. entry 1, 0.0062 g, 0.040 mmol), dialkyl azodicarboxylate (entry 1, 0.0040 g, 0.020 mmol), and CD₂Cl₂ (0.3 mL) and cooled to the specified temperature. Then the catalyst (0.0013 g, 0.0020 mmol, 10 mol%) was added. The tube was capped. Product formation was monitored by TLC. After the specified time (Table 3.6), the solvent was removed. The residue was taken up in hexane/ethyl acetate (30:70 v/v) and passed through a short silica gel column, which was washed with additional hexane/ethyl acetate (50:50 v/v, 5 mL). The solvent was removed, and a second silica gel chromatography step was carried out (column length substrate dependent). The solvent was removed from the product containing fractions (yields, Table 3.6).

Diisopropyl 1-(1-(ethoxycarbonyl)-2-oxocyclopentyl)hydrazine-1,2-dicarboxylate (37, entry 1). NMR (δ , CDCl₃):^{126,147} ¹H (500 MHz) 6.64 (m, 1H), 4.90 (septet, 2H, $J = 5.9$ Hz), 4.21 (q, 2H, $J = 6.8$ Hz), 1.68-2.63 (m, 6H), 1.21-1.29 (m, 15H); ¹³C{¹H} (125 MHz) 206.3, 167.5, 155.8, 155.1, 70.0, 63.8, 62.4, 36.7, 31.8, 21.8, 18.5, 14.0.

The enantiomeric excess was determined by HPLC with a Chiralcel AD column, hexane/2-PrOH (95:05 v/v), 1.0 mL/min, $\lambda = 215$ nm; $t_R = 9.0$ min, 11.5 min.^{126,154}

Di(*t*-butyl) 1-(1-(ethoxycarbonyl)-2-oxocyclopentyl)hydrazine-1,2-dicarboxylate (39, entry 2). NMR (δ , CDCl₃):^{126,147} ¹H (500 MHz) 6.51 (s, 1H), 4.21 (m, 2H), 2.60-1.73 (6H, m), 1.60-1.40 (m, 18H), 1.28 (t, 3H, $J = 7.0$ Hz); ¹³C{¹H} (125 MHz) 205.3, 167.8, 155.0, 154.1, 82.4, 81.1, 63.8, 61.9, 36.1, 32.5, 27.8, 27.7, 25.0, 18.4, 13.8.

The enantiomeric excess was determined by HPLC with a Chiralcel AD column, hexane/2-PrOH (98:02 v/v), 1.0 mL/min, $\lambda = 215$ nm; $t_R = 13.7$ min (minor, *R*), 18.0 min (major, *S*).^{126,151}

Crystallography A. A CHCl₃/C₆F₆ (0.50/0.05 mL) solution of (*R*_{Ru}*R*_C*R*_C)-**18c**⁺ Δ-TRISPHAT⁻ (ca. 0.03 g, >99:01 *R*_{Ru}*R*_C*R*_C/*S*_{Ru}*R*_C*R*_C) in an NMR tube was allowed to concentrate (6 h). Colorless blocks of (*R*_{Ru}*R*_C*R*_C)-**18c**⁺ (Δ)-TRISPHAT⁻·CHCl₃ with well defined faces formed. Anal. Calcd for C₄₀H₂₉Cl₁₂N₆O₇PRu·CHCl₃: C 35.62, H 2.19, Cl 38.49, N 6.08. Found: C 35.04, H 2.05, Cl 38.24, N 5.84. The blocks were too small to analyze with in-house facilities. Thus, synchrotron radiation (Advanced Light Source, Lawrence Berkeley National Laboratory, beamline 11.3.1) was employed for unit cell determination and data collection on a D8 goniostat equipped with a CCD detector.

The integrated intensity information for each reflection was obtained by reduction of the data frames with the program APEX2.⁹² Cell parameters were obtained from 60 frames using a 0.5° scan. Data were corrected for Lorentz and polarization factors, and using SADABS,⁹³ absorption and crystal decay effects. The structure was solved by direct methods using SHELXTL (SHELXS).⁹⁴ All non-hydrogen atoms were refined with anisotropic thermal parameters. Hydrogen atoms were placed in idealized positions using a riding model. One chlorine atom and the hydrogen atom of the CHCl₃ molecule showed displacement disorder (Cl53:Cl54, H50:H50A), which was refined to a 72:28 occupancy ratio. The parameters were refined by weighted least squares refinement on F^2 to convergence.⁹⁴ The absolute configuration was confirmed using the Flack parameter.¹⁵⁵

B. Et₂O vapor was allowed to slowly diffuse into a CH₃CN solution of the ca. 1:2 mixture of (*R*_{Ru}*R*_C*R*_C)-**18c**⁺ X and (*n*-Bu)₃NH⁺ (Δ/Λ)-TRISPHAT⁻ generated above. After 3 weeks, colorless needles of (*R*_{Ru}*R*_C*R*_C/*S*_{Ru}*R*_C*R*_C)-**18c**⁺ (Δ/Λ)-TRISPHAT⁻·(Et₂O)₂ (a 1:1 mixture of two diastereomers of **18c**⁺ and two enantiomers of TRISPHAT⁻, with two Et₂O molecules per ruthenium) with well defined faces were obtained. A Bruker GADDS diffractometer was employed for unit cell determination and data collection.

The integrated intensity information for each reflection was obtained by reduction of the data frames with the program APEX2.⁹² Cell parameters were obtained from 180 frames using a 0.5° scan. Data were corrected for Lorentz and polarization factors, and using SADABS⁹³ absorption and crystal decay effects. The structure was solved by direct methods using SHELXTL (SHELXS) (*Z* = 4; *Z'* = 2).⁹⁴

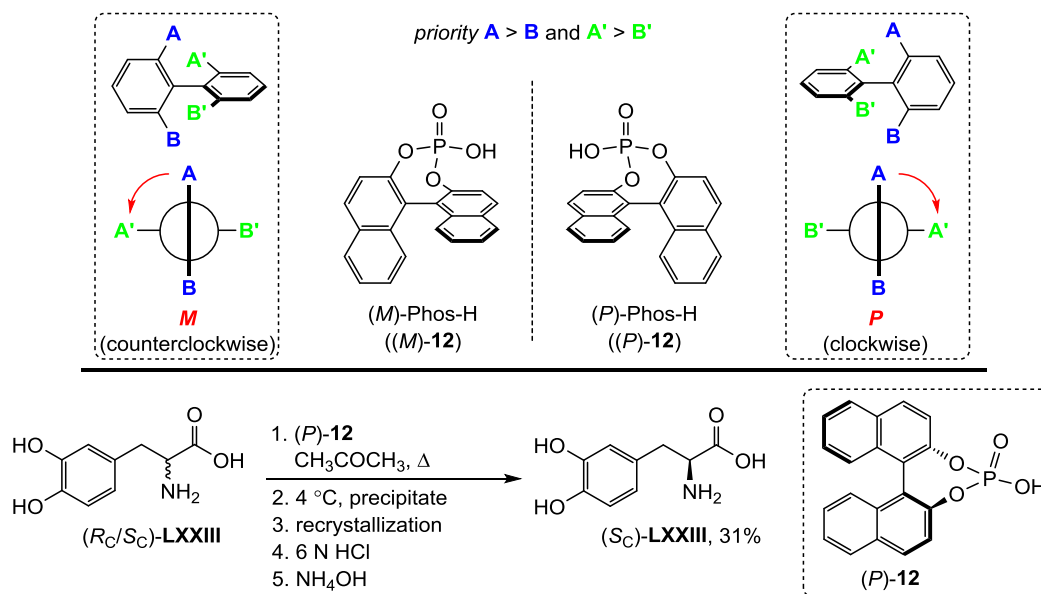
All non-hydrogen atoms were refined with anisotropic thermal parameters. Hydrogen atoms were placed in idealized positions using a riding model. The oxygen atom and a carbon atom of one of the four Et₂O molecules in the unit cell showed displacement disorder (O3D:O3E, C1D:C2D), which was refined to a 60:40 occupancy ratio. The parameters were refined by weighted least squares refinement on *F*² to convergence.⁹⁴ The absolute configuration was confirmed using the Flack parameter.¹⁵⁵

4. ENANTIOPURE CHIRAL-AT-METAL RUTHENIUM COMPLEXES: SYNTHESSES, RESOLUTION, AND APPLICATIONS IN SECOND COORDINATION SPHERE PROMOTED CATALYSIS

4.1 Introduction

4.1.1 Applications of chiral phosphoric acid derivatives in literature

Chiral phosphoric acids have seen immense uses in catalytic organic transformations.¹⁵⁶ Out of many, those with a biphenyl based axial chiral core have been at the heart of this chemistry.¹⁵⁶ Chiral biphenyl systems are atropisomers.¹⁵⁷ By analyzing the Newman projection along the biaryl axis, the absolute axial configuration can be deduced as *P* or *M*, as shown in Scheme 4.1, top (box).¹⁵⁷ The concept has been illustrated with two enantiomers, (*M*)-Phos-H (*(M)*-**12**) and (*P*)-Phos-H (*(P)*-**12**),²⁶ of a chiral phosphoric acid.

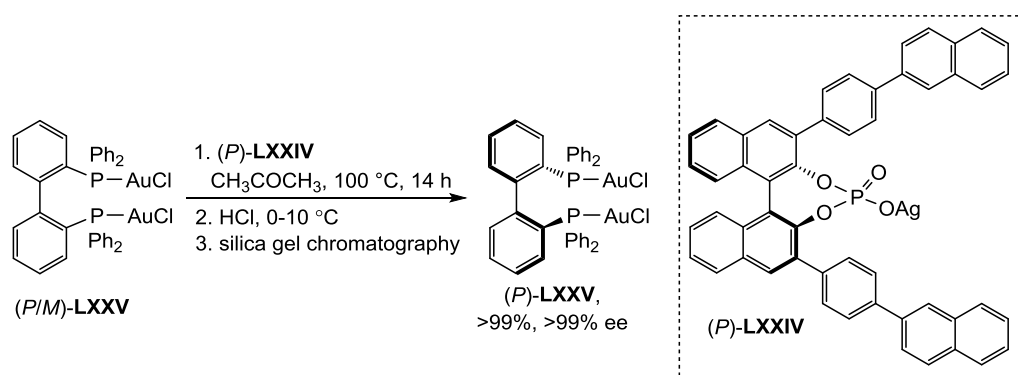


Scheme 4.1 Top: *P* and *M* descriptors for an axial chiral phosphoric acid. Bottom: resolution of a chiral amino acid using an enantiopure phosphoric acid.

Recently, atropisomers of phosphoric acid derivatives have been used as chiral anions, Brønsted acids, Lewis acids, and Lewis bases.^{156h} One typical application has been for the resolution of chiral amines and amino acids with enantiopure phosphoric acids (Scheme 4.1, bottom).¹⁵⁸ Compound *(S_C)-LXXIII* is a potent neurotransmitter and has been used to treat Parkinson's disease.¹⁵⁹ The absolute configuration of this enantiopure amine is well established in literature.¹⁶⁰ The acid *(P)-12* has been used with this racemic amino acid, *(R_C/S_C)-LXXIII*, to form a pair of diastereomeric salts. These salts were separated by recrystallization from MeOH/CH₃COCH₃. The recrystallized product was diastereomerically pure and its neutralization afforded the enantiopure amino acid *(S_C)-LXXIII*.^{158,160}

The anions derived from chiral phosphoric acids have also been applied in numerous enantioselective organic transformations.^{156f} One example from the Mikami group is illustrated in Scheme 4.2. A silver salt derived from a chiral phosphoric acid

((*P*)-LXXIV) was used to abstract a chloride ligand from a neutral gold complex (LXXV) to form a cationic gold species (Scheme 4.2).¹⁶¹ Concomitant loss of silver chloride led to the formation of a single diastereomeric salt. Temperature controlled treatment of the product with HCl and subsequent silica gel chromatography led to the resolved neutral gold species in quantitative yield.



Scheme 4.2 Resolution of neutral gold species using a silver salt of an enantiopure phosphoric acid ((*P*)-LXXIV).

4.1.2 Utilization of chiral phosphoric acid with chiral-at-metal ruthenium complexes

As mentioned in chapter 2 (Scheme 2.8), when commercially available enantiopure chiral phosphoric acid (*P*)-**12** was used to protonate the ruthenium complex (η^5 -C₅H₅)Ru(CO)(**GBI-H**) (**11**),²⁶ a cationic **GBI** complex [(η^5 -C₅H₅)Ru(CO)(**GBI**)]⁺ (*P*)-Phos⁻ (**9**⁺ (*P*)-Phos⁻)²⁶ was isolated. Here, (*P*)-Phos⁻ is the conjugate base of (*P*)-**12** and acts as the chiral anion for the cationic chiral-at-metal ruthenium complex. The ¹H NMR spectrum showed two distinct signals for the cyclopentadienyl ligand due to the formation of two diastereomeric salts, (*R*_{Ru})-**9**⁺ (*P*)-Phos⁻ and (*S*_{Ru})-**9**⁺ (*P*)-Phos⁻. This

is depicted in Scheme 2.8 (bottom). Any attempt to separate these ionic species led only to partial enrichment.

In this chapter, this concept has been extended to modified ruthenium systems to achieve better resolution of chiral-at-metal ruthenium **GBI** complexes (Figure 4.1). This modification includes substituting the parent cyclopentadienyl (C_5H_5) ligand to give a bulky and electron withdrawing pentaphenylcyclopentadienyl (C_5Ph_5) ligand.¹⁶² The bulkier substituent would be expected to create a bigger difference between matched and mismatched ion pairs. This might result in greater differences in solubilities and chromatographic retention times.

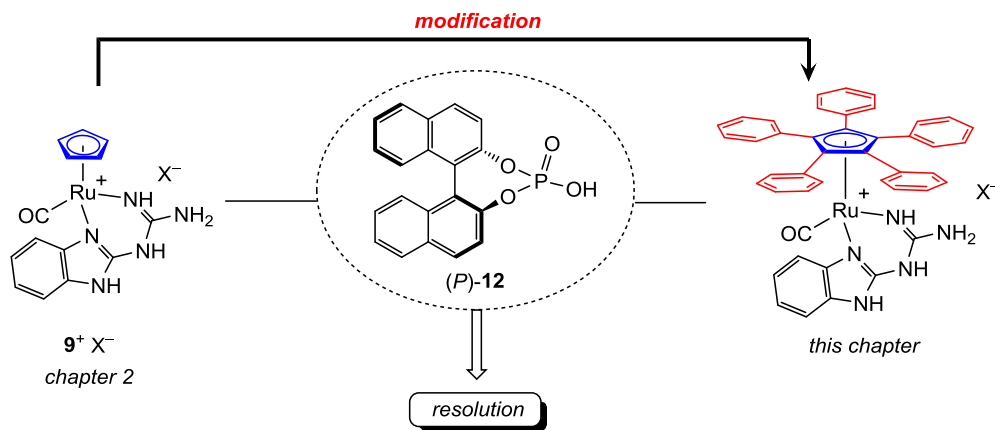


Figure 4.1 Specific aim of this chapter: does modification of the cyclopentadienyl ligand of $9^+ X^-$ to a pentaphenylcyclopentadienyl ligand lead to a more easily resolved cation and an effective enantioselective catalyst?

As described below, this approach has allowed diastereomerically pure salts to be isolated. The chiral (*P*)-Phos⁻ counter anion has been subsequently metathesized to an achiral BAr_f⁻²⁶ counter anion, which is also a very poor hydrogen bond acceptor. This sets the stage for probing the catalytic ability of the enantiopure complex in enantioselective second coordination sphere promoted catalysis (SCSPC).

4.2 Results

4.2.1 Synthesis and resolution of modified ruthenium GBI complexes

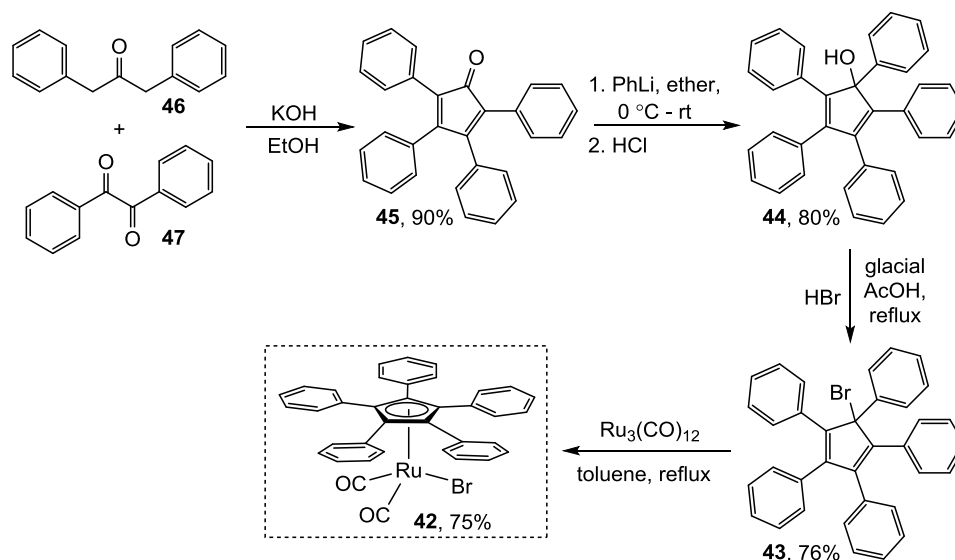
4.2.1.1 Synthesis of ruthenium precursor

The pentaphenylcyclopentadienyl ruthenium complex $(\eta^5\text{-C}_5\text{Ph}_5)\text{Ru}(\text{CO})_2(\text{Br})$ (**42**) has been reported in the literature.¹⁶³ A number of derivatives have also been prepared.^{163c,164} Hence, **42** was investigated for the syntheses of ruthenium **GBI** complexes that can act as hydrogen bond donor catalysts similar to $[(\eta^5\text{-C}_5\text{H}_5)\text{Ru}(\text{CO})(\text{GBI})]^+ \text{X}^-$ (**9**⁺ **X**⁻, Chapter 2) and the bifunctional analog **18c**⁺ **PF**₆⁻ (Scheme 3.2, Chapter 3). Complexes **9**⁺ **X**⁻ and **18c**⁺ **PF**₆⁻ have been previously prepared via different methods as described in chapter 2 and 3 as well as in the full papers associated with these chapters.^{75,104}

Complex **42** was prepared by refluxing $\text{Ru}_3(\text{CO})_{12}$ and 5-bromo-1,2,3,4,5-pentaphenyl-1,3-cyclopentadiene (**43**) in toluene (Scheme 4.3). A chromatographic workup (experimental section) gave **42** as a greenish yellow solid in better yields than reported in the literature (75% vs. 68%¹⁶³).

Compound **43** was in turn synthesized by brominating 1,2,3,4,5-pentaphenylcyclopenta-2,4-dien-1-ol (**44**), following a literature procedure (Scheme 4.3).¹⁶⁵ Workup gave **43** as an orange-yellow solid in 76% yield. Similarly, **44** was prepared in 80% yield according to a literature procedure starting from 2,3,4,5-tetraphenylcyclopentadienone (**45**).¹⁶⁵ Compound **45** can in turn be easily prepared by a two fold aldol condensation of 1,3-diphenyl acetone (**46**) and benzil (**47**). This is a very popular experiment and is conducted in the undergraduate organic laboratory

program.¹⁶⁶



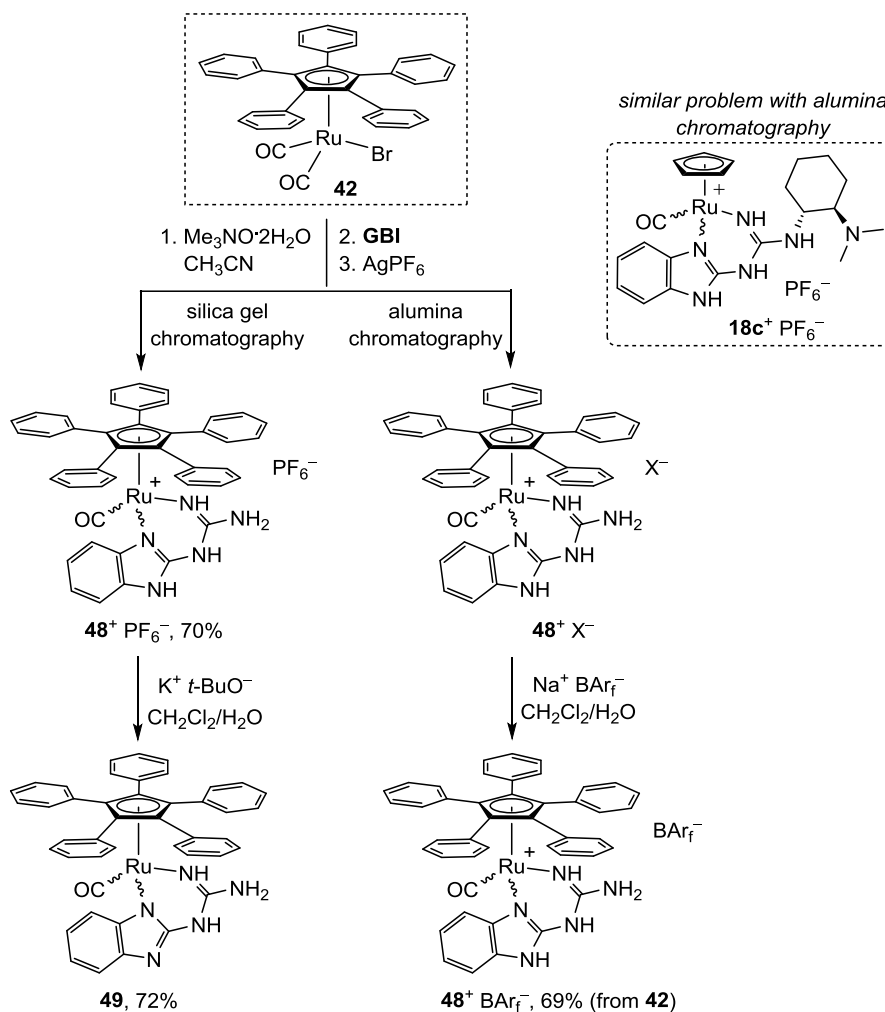
Scheme 4.3 Synthesis of a ruthenium pentaphenylcyclopentadienyl complex (**42**) from 2,3,4,5-tetraphenylcyclopentadienone (**45**).

4.2.1.2 Synthesis of ruthenium GBI complexes

In order to synthesize ruthenium **GBI** complexes, a paper used for preparing (η^5 -C₅Ph₅)Ru(CO)(PEt₃)(Br) and [(η^5 -C₅Ph₅)Ru(CO)(PEt₃)(MeC≡CMe)]⁺ PF₆⁻ starting from **42** was considered.^{163a} According to that study, **42** was treated with Me₃NO·2H₂O in the presence of excess PEt₃ to remove the CO ligand as CO₂ and form (η^5 -C₅Ph₅)Ru(CO)(PEt₃)(Br) and the byproduct Me₃N.^{163a} Treatment of the isolated product (η^5 -C₅Ph₅)Ru(PEt₃)(CO)(Br) with Ag⁺ PF₆⁻ in the presence of excess but-2-yne provided the bromide ligand substitution product [(η^5 -C₅Ph₅)Ru(CO)(PEt₃)(MeC≡CMe)]⁺ PF₆⁻.^{163a} Thus, two of the monodentate ligands in

42 are easily replaced via a two step sequence.

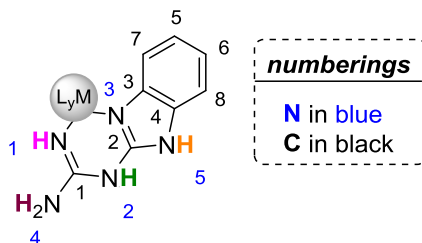
As shown in Schemes 2.6 (chapter 2) and 3.2 (chapter 3), the **GBI** or substituted **GBI** ligands can displace chloride, PPh_3 , and CH_3CN ligands from cyclopentadienyl ruthenium complexes. Towards a similar end with **42**, a CH_3CN suspension was treated with $\text{Me}_3\text{NO}\cdot 2\text{H}_2\text{O}$, **GBI**, and $\text{Ag}^+ \text{PF}_6^-$ (Scheme 4.4). After solvent removal the residue was further purified by chromatography, either using silica gel or alumina.



Scheme 4.4 Syntheses of pentaphenylcyclopentadienyl ruthenium **GBI** complexes.

Silica gel chromatography provided racemic chiral-at-metal $[(\eta^5\text{-C}_5\text{Ph}_5)\text{Ru}(\text{CO})(\text{GBI})]^+ \text{PF}_6^-$ (**48**⁺ PF_6^-) as a bright green powder in 70% yield. The salt was soluble in CH_2Cl_2 , CHCl_3 , CH_3CN , DMSO, and MeOH but insoluble in toluene. Like all of the new complexes mentioned below, **48**⁺ PF_6^- was characterized by NMR (^1H , ^{13}C) and IR spectroscopy as summarized in Tables 4.1-4.4 and the experimental section. Based upon the ^1H and ^{13}C NMR studies for a similar compound $[(\eta^5\text{-C}_5\text{H}_5)\text{Ru}(\text{CO})(\text{GBI})]^+ \text{PF}_6^-$ (**9**⁺ PF_6^-) mentioned in chapter 2 (Tables 2.6-2.8) including 2D NMR experiments (see Appendix C), all proton and carbon signals could be unambiguously assigned. These and other data supported the coordination of the benzimidazole $\text{C}=\text{NAr}$ and guanidine $\text{C}=\text{NH}$ groups, as verified by crystallography below.

Table 4.1 NH ^1H NMR signals of **48**⁺ X^- and **49** (δ).^a



Complex ^a	NH(5)	NH(2)	NH(1)	NH ₂ (4)
48 ⁺ PF_6^-	<i>_b</i>	<i>_b</i>	4.77	5.48
48 ⁺ BAr_f^-	9.47	8.36	5.13	5.03
$(R_{\text{Ru}}/S_{\text{Ru}})$ - 48 ⁺ (<i>P</i>)-Phos ^{-c}	13.67/13.16	12.03/10.81	4.45/4.92	5.56/6.12
(S_{Ru}) - 48 ⁺ (<i>P</i>)-Phos ⁻	13.77	12.33	4.48	5.70
49 ^d	<i>_b</i>	<i>_b</i>	<i>_b</i>	<i>_b</i>
9 ⁺ BAr_f^-	9.21	8.19	5.41	4.92

^a Spectra were recorded in CD_2Cl_2 (500 MHz). The δ values are given in ppm. ^b These NH signals were not observed. ^c Signals for diastereomers are separated by a "/"; the first entry is for (S_{Ru}) -**48**⁺ (*P*)-Phos⁻. ^d Spectra were recorded in $\text{CD}_2\text{Cl}_2/\text{CD}_3\text{OD}$ (500 MHz).

However, as shown in Scheme 4.4, chromatography over alumina led to $48^+ X^-$ as a pale green powder. Here X^- denotes an unknown alumina derived anion, with a PF_6^- content of <5%. Similar problems were encountered with $18c^+ PF_6^-$ (Scheme 4.4, box) as described in chapter 3 and the full paper associated with it.¹⁰⁴ Similar to $18c^+ PF_6^-$, anion metathesis of $48^+ X^-$ with either $Na^+ PF_6^-$ or $NH_4^+ PF_6^-$ did not lead to complete exchange of the unknown anion. In contrast, treatment of $48^+ X^-$ with $Na^+ BAr_f^-$ ^{26,65} under biphasic conditions (CH_2Cl_2/H_2O) led to pure $48^+ BAr_f^-$ in 69% yield. Given the aqueous conditions, $48^+ BAr_f^-$ was isolated as a hydrate (2.0-4.0 H_2O). This new salt was characterized similarly to the hexafluorophosphate salt (Tables 4.1-4.4). A satisfactory microanalysis was obtained. Compound $48^+ BAr_f^-$ was soluble in toluene, along with CH_2Cl_2 , $CHCl_3$, CH_3CN , DMSO, and MeOH.

Table 4.2 $^{13}C\{^1H\}$ NMR signals of the **GBI** ligand in $48^+ X^-$ and **49** (δ).^a

Complex	C(1)	C(2)	C(3)	C(4)	C(5)	C(6)	C(7)	C(8)
GBI ^b	159.8	158.9	142.6	132.5	119.9	119.9	114.8	109.1
$48^+ PF_6^-$	154.3	146.0	141.2	132.3	124.1	122.9	118.9	111.8
$48^+ BAr_f^-$	152.9	144.0	140.9	132.4	125.3	124.1	119.6	111.5
$(R_{Ru}/S_{Ru})-48^+ (P)-Phos^-$ ^c	155.02/ 154.71	147.08/ 146.75	141.46/ 141.42	132.78/ 132.72	123.36/ 122.98	122.14/ 121.88	118.36/ 117.84	111.92/ 111.73
$(S_{Ru})-48^+ (P)-Phos^-$	155.1	147.2	141.5	132.8	123.3	122.1	118.4	111.9
49 ^d	158.9	154.4	143.9	137.9	120.7	119.9	117.3	111.7
$9^+ BAr_f^-$	152.4	144.1	142.6	130.8	124.9	124.5	117.9	111.4

^a Spectra were recorded in CD_2Cl_2 (125 MHz) unless noted. The δ values are given in ppm. ^b Spectra were recorded in $DMSO-d_6$ (100 MHz). ^c Signals for diastereomers are separated by a "/"; the first entry is for $(S_{Ru})-48^+ (P)-Phos^-$. ^d Spectra were recorded in CD_2Cl_2/CD_3OD (125 MHz).

When a CH₂Cl₂ solution of **48**⁺ PF₆⁻ and a H₂O solution of K⁺ *t*-BuO⁻ were combined, a biphasic yellow suspension was obtained. Workup gave the neutral chiral-at-metal ruthenium complex (η^5 -C₅Ph₅)Ru(CO)(**GBI**_{-H}) (**49**) as a bright yellow powder in 72% yield (Scheme 4.4). The complex was characterized similarly to the salts mentioned above (Tables 4.1-4.4). An analogous deprotonation of [(η^5 -C₅H₅)Ru(CO)(**GBI**)]⁺ Cl⁻ (**9**⁺ Cl⁻) was described in chapter 2 (Scheme 2.8). Similar transformations have been described in the literature.⁷⁰ Here, **GBI**_{-H} is the conjugate base of **GBI**, which acts as an anionic ligand for the [(η^5 -C₅Ph₅)Ru(CO)]⁺ fragment. Compound **49** was partially soluble in CH₂Cl₂ and CH₃CN, and completely soluble in MeOH and DMSO.

Table 4.3 ¹³C {¹H} NMR chemical shifts of the CO and pentaphenylcyclopentadienyl ligands (δ) of **48**⁺ X⁻ and **49**.^a

Complex	CO	<i>o</i> -C _{Ph}	<i>i</i> -C _{Ph}	<i>m</i> -C _{Ph}	<i>p</i> -C _{Ph}	C ₅ Ph ₅
48 ⁺ PF ₆ ⁻	205.3	132.3	131.9	128.1	128.1	100.6
48 ⁺ BAr _f ⁻	204.5	132.2	131.5	128.4	128.2	100.4
<i>(R</i> _{Ru} / <i>S</i> _{Ru})- 48 ⁺ (<i>P</i>)-Phos ⁻	205.5	132.28/	132.11/	127.97/	127.90/	100.64/
		132.17	132.03	127.76	127.67	100.32
<i>(S</i> _{Ru})- 48 ⁺ (<i>P</i>)-Phos ⁻	205.5	132.3	132.1	128.0	127.9	100.7
49 ^b	207.8	133.0	132.6	127.7	127.4	101.6

^a Spectra were recorded in CD₂Cl₂ (125 MHz). The δ values are given in ppm. ^b Spectra were recorded in CD₂Cl₂/CD₃OD (125 MHz).

Table 4.4 $^{13}\text{C}\{^1\text{H}\}$ NMR chemical shifts of the CO ligand (δ) and IR ν_{CO} values (cm^{-1}) for **48**⁺ X⁻, **49**, **9**⁺ X⁻, and **11**.^a

	48 ⁺ BAr _f ⁻	9 ⁺ BAr _f ⁻	48 ⁺ PF ₆ ⁻	9 ⁺ PF ₆ ⁻	49	11
CO	204.5	203.3	205.3	203.9 ^b	207.8 ^c	207.5 ^b
ν_{CO}	1977	1961 ⁷⁵	1948	1942 ⁷⁵	1934	1926 ⁷⁰

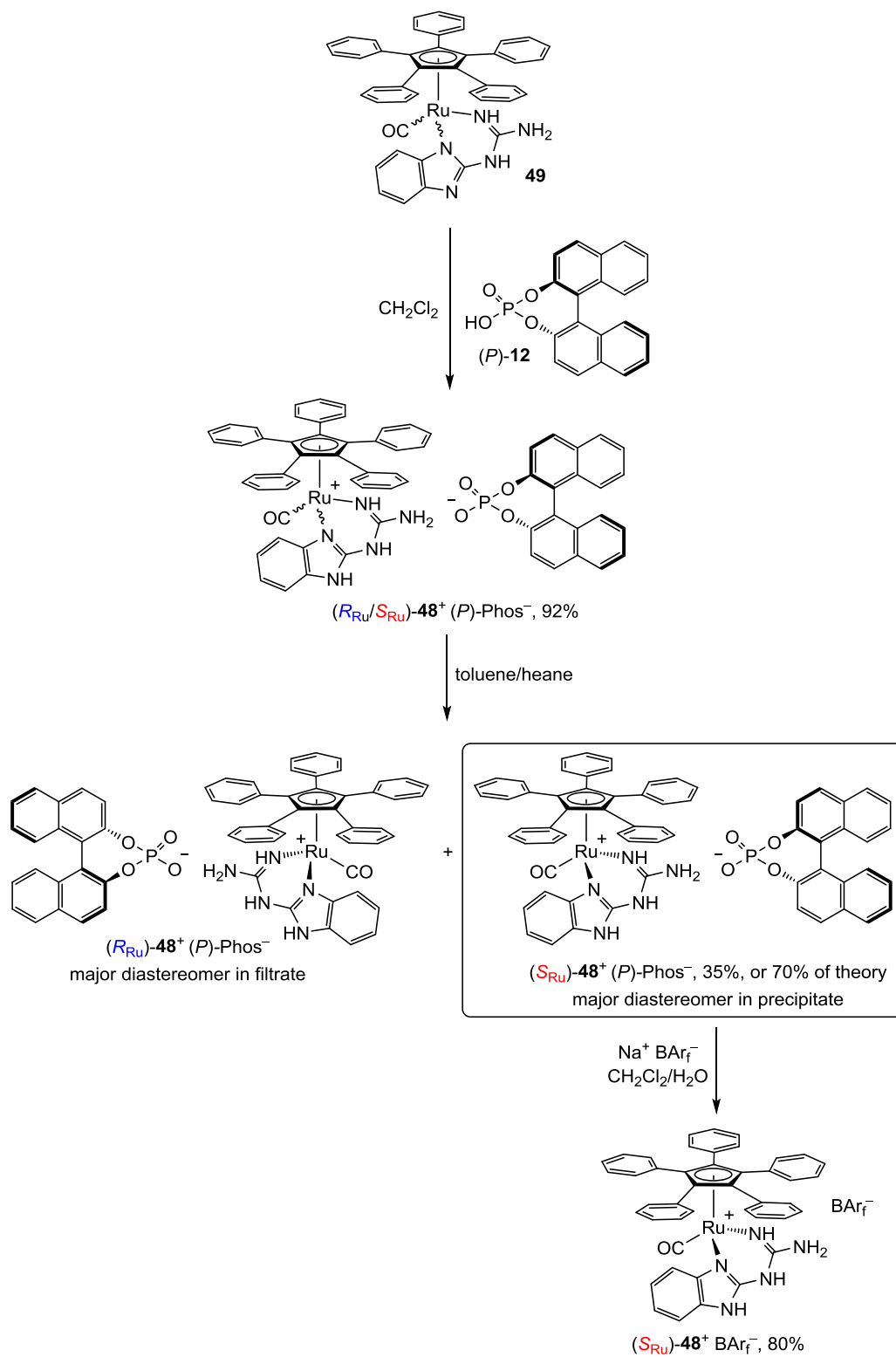
^a Spectra were recorded in CD₂Cl₂ (125 MHz). The δ values are given in ppm. ^b Spectra were recorded in DMSO-*d*₆ (100 MHz). ^c Spectra were recorded in CD₂Cl₂/CD₃OD (125 MHz).

4.2.1.3 Resolution of ruthenium GBI complexes

As shown in chapter 2 (Scheme 2.8) and noted above, the neutral complex (η^5 -C₅H₅)Ru(CO)(GBI_{-H}) (**11**) was subsequently protonated with the enantiopure axially chiral phosphoric acid (*P*)-**12** to form a mixture of diastereomeric salts, (*R*_{Ru})-**9**⁺ (*P*)-Phos⁻ and (*S*_{Ru})-**9**⁺ (*P*)-Phos⁻. With the racemic chiral-at-metal neutral ruthenium complex **49** in hand, a similar strategy was investigated. Thus, **49** was treated with equimolar amounts of (*P*)-**12** in CH₂Cl₂ to generate a pair of diastereomeric salts with (*P*)-Phos⁻ as the counter anion (Scheme 4.5). Filtration through celite and evaporation of the solvent gave a pale green powder of (*R*_{Ru}/*S*_{Ru})-**48**⁺ (*P*)-Phos⁻ in 92% yield.

The ¹H NMR spectrum exhibited two sets of well separated NH proton signals (δ 13.67/13.16, 12.03/10.81, 5.56/6.12, and 4.45/4.92; area ratios 50±2:50±2). The cations gave two sets of ¹³C NMR signals for most of the carbon atoms. These data are consistent with a mixture of diastereomeric salts, (*R*_{Ru})-**48**⁺ (*P*)-Phos⁻ and (*S*_{Ru})-**48**⁺ (*P*)-Phos⁻.

Attempted separation of the salts by silica gel or neutral alumina chromatography was unsuccessful. However, an appreciable solubility difference in cold toluene/hexane



Scheme 4.5 Resolution of a chiral-at-metal ruthenium complex with enantiopure (*P*)-12.

was noted. When (R_{Ru}/S_{Ru})-**48**⁺ (*P*)-Phos⁻ was dissolved in 90:10 v/v toluene/hexane and kept at -35 °C, a greenish black supernatant and a yellow precipitate formed (Scheme 4.5). Workup gave (S_{Ru})-**48**⁺ (*P*)-Phos⁻ in 35% yield, or 70% of theory. The greenish black filtrate provided a mixture of diastereomers, (R_{Ru}/S_{Ru})-**48**⁺ (*P*)-Phos⁻, with the R_{Ru} configuration predominating, as a pale green salt in 60% yield.

As shown in Figure 4.2, NMR (¹H and ¹³C) spectroscopy was employed to assay the diastereomer ratio (dr). Based on the NH proton and carbon signals from the cation, the dr was determined. The ¹H NMR spectrum of the mixture (Figure 4.2, bottom, red) and separated diastereomer (bottom, cyan) indicates that the latter contains only one set of NH signals; the other set is below the limits of detection. The ¹³C NMR spectrum of the separated diastereomer contained only one set of carbon signals for the cation (Tables 4.2 and 4.3 and Figure 4.2, top, cyan). In contrast, the diastereomeric mixture exhibited two signals for each of the carbon atoms (Tables 4.2 and 4.3 and Figure 4.2, top, red). The ¹H and ¹³C NMR spectrum together indicated that the resolved compound has a high dr. Since the NH signals do not exchange in CD₂Cl₂, the ¹H NMR spectrum in Figure 4.2(b) suggests a minimum dr of >98:<02, when the peak at 4.48 ppm was integrated against a peak introduced at 4.92 ppm as an upper bound for the residual signal of the other diastereomer.

The salt (S_{Ru})-**48**⁺ (*P*)-Phos⁻ was characterized similarly to the aforementioned complexes. Microanalysis and ¹H NMR (experimental section) showed that the isolated salt is a toluene monosolvate. Complex (S_{Ru})-**48**⁺ (*P*)-Phos⁻ was highly soluble in CH₂Cl₂ and CHCl₃ but not in CH₃CN. The salt obtained from the greenish black filtrate had a dr of 80:20 (R_{Ru}/S_{Ru}) as similarly assayed by ¹H NMR spectroscopy.

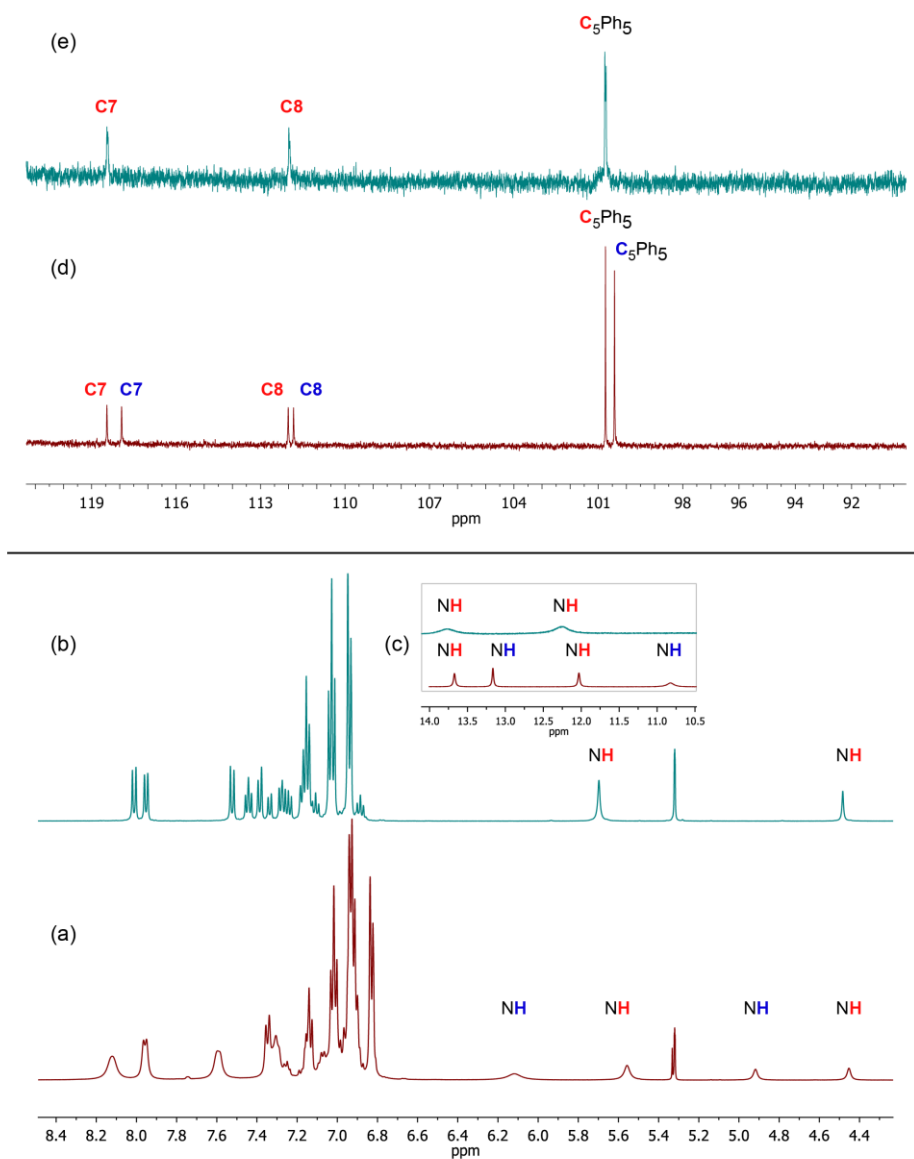


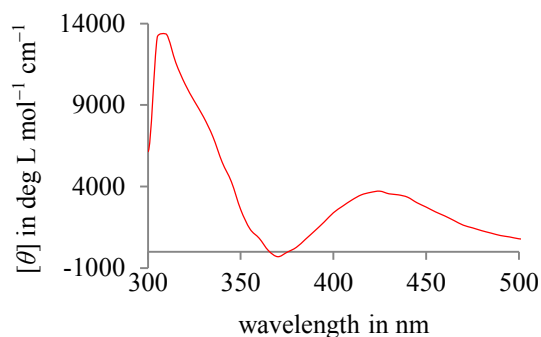
Figure 4.2 Partial NMR spectra (CD_2Cl_2): (a) ^1H (500 MHz), mixture of $(R_{\text{Ru}})\text{-48}^+$ (P)- Phos^- and $(S_{\text{Ru}})\text{-48}^+$ (P)- Phos^- ; (b) ^1H (500 MHz), $(S_{\text{Ru}})\text{-48}^+$ (P)- Phos^- as a toluene solvate per text and experimental section; (c) (inset) downfield NH signals for (a) and (b); (d) $^{13}\text{C}\{^1\text{H}\}$ (125 MHz), mixture of $(R_{\text{Ru}})\text{-48}^+$ (P)- Phos^- and $(S_{\text{Ru}})\text{-48}^+$ (P)- Phos^- ; (e) $(S_{\text{Ru}})\text{-48}^+$ (P)- Phos^- as a toluene solvate per text and experimental section.

Next, $(S_{\text{Ru}})\text{-48}^+$ (P)- Phos^- was treated with $\text{Na}^+ \text{BARf}^-$ under biphasic

(CH₂Cl₂/H₂O) conditions to give $[(\eta^5\text{-C}_5\text{Ph}_5)\text{Ru}(\text{CO})(\text{GBI})]^+ \text{BAr}_f^-$ ($(S_{\text{Ru}})\text{-48}^+ \text{BAr}_f^-$) in 80% yield (Scheme 4.5). As the anion exchange employed aqueous conditions, the salt was isolated as a hydrate (1.0-2.0 H₂O). It was characterized analogously to the other new salts above, as well as CD spectroscopy (Figure 4.3a).

As shown in Figure 4.3b and in chapter 3 (Figure 3.4), the cyclopentadienyl complex $(S_{\text{Ru}}R_C R_C)\text{-18c}^+ \text{PF}_6^-$ gives a positive long wavelength absorption (red trace, 408 nm). Accordingly, the enantiomer of 48^+BAr_f^- with a positive long wavelength adsorption (red trace, Figure 4.3a; 425 nm with additional shoulders at 400 and 435 nm) was tentatively assigned an S_{Ru} ruthenium configuration.

(a)



(b)

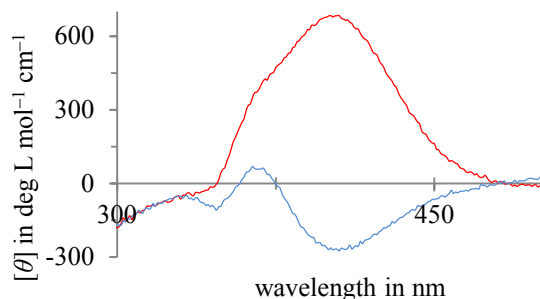


Figure 4.3 (a) CD spectrum of $(S_{\text{Ru}})\text{-48}^+ \text{BAr}_f^-$ (red trace) in CH₃CN. (b) CD spectra of $(R_{\text{Ru}}R_C R_C)\text{-18c}^+ \text{PF}_6^-$ (blue trace) and $(S_{\text{Ru}}R_C R_C)\text{-18c}^+ \text{PF}_6^-$ (red trace) in CH₃CN.

4.2.2 Physical characterization of ruthenium complexes and its precursors

4.2.2.1 Spectroscopic characterization of ruthenium complexes

Selected ^1H and $^{13}\text{C}\{^1\text{H}\}$ NMR and IR data for the ruthenium complexes $\mathbf{48}^+ \text{X}^-$ are presented in Tables 4.1-4.4 and Figure 4.4. The spectroscopic properties are similar to those of $\mathbf{9}^+ \text{X}^-$ in chapter 2. The ^1H NMR spectrum of $\mathbf{48}^+ \text{BAr}_f^-$ shows the NH protons to be 0.26-0.11 ppm downfield of those in $[(\eta^5\text{-C}_5\text{H}_5)\text{Ru}(\text{CO})(\text{GBI})]^+ \text{BAr}_f^-$ ($\mathbf{9}^+ \text{BAr}_f^-$, Table 4.1). This may be a consequence of the shielding anisotropy of the five phenyl rings, which have a radial disposition about the cyclopentadienyl ligand. To the extent that this might also reflect enhanced NH acidities, $\mathbf{48}^+ \text{X}^-$ might also be a superior hydrogen bond donor. The IR ν_{CO} values of $\mathbf{48}^+ \text{X}^-$ are 16-6 cm^{-1} higher in frequency than those of $\mathbf{9}^+ \text{X}^-$, consistent with the pentaphenylcyclopentadienyl ligand being more electron withdrawing than cyclopentadienyl, in accordance with past observations.¹⁶²

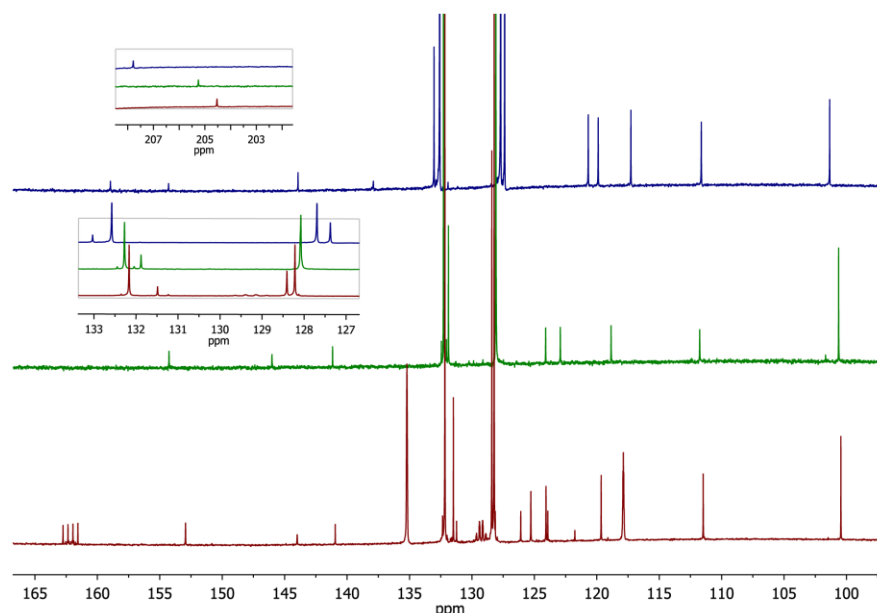


Figure 4.4 $^{13}\text{C}\{^1\text{H}\}$ NMR spectra (125 MHz): 48^+ BAR_f^- in CD_2Cl_2 (bottom, red), 48^+ PF_6^- in CD_2Cl_2 (middle, green), **49** in $\text{CDCl}_3/\text{CD}_3\text{OD}$ (top, blue), and insets showing the *i*- C_{Ph} , *o*- C_{Ph} , *m*- C_{Ph} , *p*- C_{Ph} , and CO signals.

The ^1H NMR signals of the **GBI** protons in the neutral complex **49** are 0.27-0.21 ppm upfield of those of the cationic complex 48^+ BAR_f^- (7.16, 7.03, and 6.72 ppm vs. 7.37, 7.26, and 6.99 ppm). The $^{13}\text{C}\{^1\text{H}\}$ **GBI** signals also exhibit shifts (Tables 4.2, 4.3 and Figure 4.4, top). The C1-C4 **GBI** carbon signals of **49** are shifted 10.4-3.9 ppm downfield from those in 48^+ BAR_f^- . The relatively low ν_{CO} value of **49** (1934 cm^{-1}) indicates a more electron rich ruthenium center than in 48^+ X^- ($\text{X}^- = \text{BAR}_f^-/\text{PF}_6^-$, $1977/1948\text{ cm}^{-1}$).⁷²

4.2.2.2 Crystallographic characterization of ruthenium complexes

During the course of the synthesis described above, single crystals of 48^+ $\text{PF}_6^- \cdot (\text{C}_5\text{H}_{12})_{1.5}$ were obtained. X-ray data were collected and refined as described in

the experimental section and Table 4.3. The resulting structure is shown in Figure 4.5 and the key metrical parameters are summarized in Tables 4.5-4.7.

The cation is formally octahedral, with the pentaphenylcyclopentadienyl ligand occupying three coordinating sites, as evident from the OC-Ru-N and N-Ru-N bond angles of ca. 90°. The **GBI** ligand is slightly puckered as reflected by the many torsion angles with values near 0° or ±180°. The average differences from 0° and 180° are 16.6(13)° and 19.1(15)°, respectively. The bond lengths of the coordinated C=NH (C1-N1) and C=NAr (C2-N3) linkages (1.284(7) and 1.320(7) Å) are shorter than the other four carbon-nitrogen bonds about C1 and C2 (1.337(7)-1.374(7) Å). An alternative tautomer of the **GBI** ligand would afford different carbon-nitrogen bond length patterns as mentioned in the previous chapter and the two full papers associated with chapters 2 and 3.^{75,104} The ruthenium-nitrogen bond lengths are similar to those in literature.^{75,104,116}

The three NH units on the nitrogen atoms remote from the ruthenium atom, N5-H5, N2-H2, and N4-H4B, exhibit an approximately *synperiplanar* NH triad, as evidenced by H-N-N-H torsion angles that are reasonably close to 0° (-24.7°, -24.4°, -51.2°; average difference from 0°, 33.5(15)°). The two other NH units, N1-H1 and N4-H4A, exhibit an approximately *synperiplanar* NH dyad with a torsion angle of 25.2°.

Table 4.5 Summary of crystallographic data.^a

	48⁺ PF ₆ ⁻ ·(C ₅ H ₁₂) _{1.5}	48⁺ BAr _f ⁻ ·H ₂ O	49
Molecular formula	C _{51.5} H ₅₂ F ₆ N ₅ OPRu	C ₇₆ H ₄₈ BF ₂₄ N ₅ O ₂ Ru	C ₄₄ H ₃₃ N ₅ ORu
Formula weight	1003.02	1631.07	748.82
Crystal system	Monoclinic	Triclinic	Tetragonal
Space group	<i>P</i> 2 ₁ / <i>c</i>	<i>P</i> -1	<i>I</i> 4 ₁ / <i>a</i>
Diffractometer	Bruker GADDS	Bruker APEX 2	Bruker GADDS
Wavelength [Å]	1.54178	0.71073	1.54178
Unit cell dimensions:			
<i>a</i> [Å]	16.961(2)	12.9707(17)	34.0508(9)
<i>b</i> [Å]	19.556(3)	14.5334(19)	34.0508(9)
<i>c</i> [Å]	15.9890(19)	21.518(3)	13.84405(5)
<i>α</i> [°]	90	76.628(2)	90
<i>β</i> [°]	117.211(8)	82.008(2)	90
<i>γ</i> [°]	90	78.719(2)	90
<i>V</i> [Å ³]	4716.3(10)	3851.4(9)	16051.5(8)
<i>Z</i>	4	2	16
<i>ρ</i> _{calc} [Mgm ⁻³]	1.413	1.406	1.239
<i>μ</i> [mm ⁻¹]	3.579	0.309	3.454
F (000)	2068	1640	6144
Crystal size [mm ³]	0.25 × 0.08 × 0.08	0.38 × 0.11 × 0.09	0.13 × 0.08 × 0.06
<i>θ</i> range [°]	2.93 to 60.00	1.58 to 27.58	2.60 to 60.00
Index ranges (<i>h,k,l</i>)	-16,18;-21,21;-17,17	-16,16;-18,18;-27,27	-38,38;-38,38;-1 5,15
Reflections collected	90436	86052	169554
Independent reflections	6958	17616	5959
Completeness to <i>θ</i> (<i>θ</i> =)	99.6% (60.0)	99.8% (25.2)	100% (60.0)
Data/restraints/parameter	6958/4/601	17616/868/1170	5959/37/450
Goodness-of-fit on F ²	1.058	1.020	1.068
<i>R</i> indices (final) [<i>I</i> >2 σ (<i>I</i>)]			
<i>R</i> ₁	0.0479	0.0519	0.0365
<i>wR</i> ₂	0.1208	0.1193	0.0783
<i>R</i> indices (all data)			
<i>R</i> ₁	0.0656	0.0808	0.0404
<i>wR</i> ₂	0.1456	0.1354	0.0798
Largest diff. peak and hole [eÅ ⁻³]	0.844/-1.132	1.61/-0.728	0.450/-0.443

^a Data common for all structures: T = 173(2) K.

As illustrated in Figure 4.5, each PF_6^- anion exhibits numerous hydrogen bonds to each of the two neighboring cations. The $\text{F}\cdots\text{H}$, $\text{F}\cdots\text{N}$, and $\text{P}\cdots\text{N}$ distances, summarized in Table 4.7, are in typical ranges for hydrogen bonds.¹⁶⁷ All of the NH linkages participate in hydrogen bonding with the anion. In the cyclopentadienyl variant, $[(\eta^5\text{-C}_5\text{H}_5)\text{Ru}(\text{PPh}_3)(\text{GBI})]^+ \text{PF}_6^-$ ($\mathbf{8}^+ \text{PF}_6^- \cdot \text{CH}_2\text{Cl}_2$), the Ru-NH protons were not involved in hydrogen bonding interactions, but the other NH groups were.⁷⁵ Although it is unlikely of any special significance, some of the hydrogen bonding distances in $\mathbf{48}^+ \text{PF}_6^- \cdot (\text{C}_5\text{H}_{12})_{1.5}$ are shorter than those in $\mathbf{8}^+ \text{PF}_6^- \cdot \text{CH}_2\text{Cl}_2$ ($\text{F}\cdots\text{H}$: 2.029, 2.052, 2.082, and 2.108 Å vs. 2.195 Å; $\text{P}\cdots\text{N}$: 3.781(6) Å vs. 3.802(3) Å; $\text{F}\cdots\text{N}$: 2.907(7) and 2.855(7) Å vs. 2.939(4) Å). Interestingly, the shortest $\text{F}\cdots\text{H}$ contact in $\mathbf{48}^+ \text{PF}_6^- \cdot (\text{C}_5\text{H}_{12})_{1.5}$ is that associated with the Ru-NH moiety (2.029 Å).

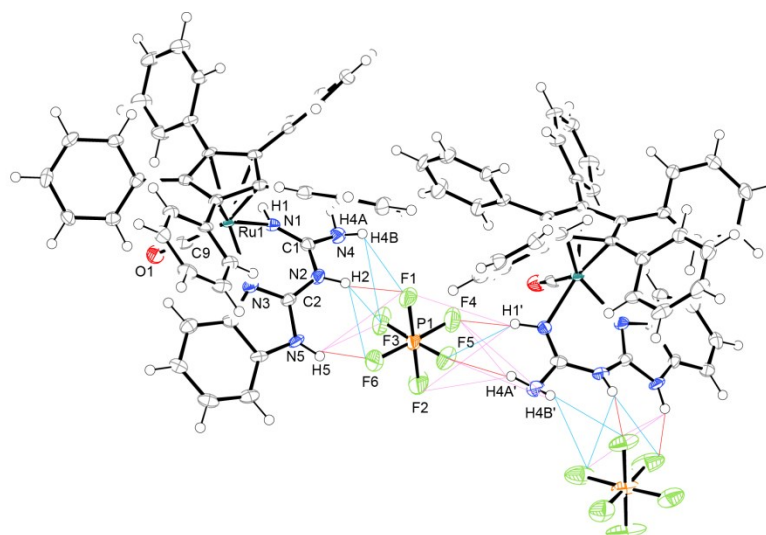


Figure 4.5 Thermal ellipsoid diagram (50% probability level) showing the structure of two molecules of $\mathbf{48}^+ \text{PF}_6^- \cdot (\text{C}_5\text{H}_{12})_{1.5}$ with solvent molecules omitted and hydrogen bonding between cations and anions. Hydrogen bonding distances of < 2.5 Å (in red), 2.5 - 3.2 Å (in cyan), and 3.2 - 4.0 Å (in magenta).

Table 4.6 Key bond lengths [Å], bond angles [°], and torsion angles [°] for **48⁺** PF₆⁻·(C₅H₁₂)_{1.5}, **48⁺** BAr_f⁻·H₂O, and **49**.^{a,b}

	48⁺ PF ₆ ⁻ ·(C ₅ H ₁₂) _{1.5}	48⁺ BAr _f ⁻ ·H ₂ O	49
Ru(1)-N(1)	2.097(4)	2.105(2)	2.104(3)
Ru(1)-N(3)	2.134(4)	2.108(2)	2.107(2)
Ru(1)-C(9)	1.860(6)	1.868(4)	1.839(4)
C(1)-N(1)	1.284(7)	1.278(4)	1.295(4)
C(1)-N(2)	1.374(7)	1.386(4)	1.365(4)
C(1)-N(4)	1.337(7)	1.362(4)	1.354(4)
C(2)-N(2)	1.354(7)	1.372(4)	1.389(4)
C(2)-N(3)	1.320(7)	1.303(4)	1.348(4)
C(2)-N(5)	1.352(7)	1.347(4)	1.339(4)
C(9)-Ru(1)-N(1)	92.5(2)	93.05(12)	92.73
C(9)-Ru(1)-N(3)	89.4(2)	89.22(12)	91.90
N(1)-Ru(1)-N(3)	81.54(16)	80.71(9)	80.56(10)
N(1)-C(1)-N(2)	120.7(5)	121.2(2)	121.9(3)
N(1)-C(1)-N(4)	124.5(5)	125.4(3)	123.9(3)
Ru(1)-N(1)-C(1)	129.5(4)	130.3(2)	126.6(2)
Ru(1)-N(3)-C(2)	123.5(4)	124.5(2)	124.4(2)
C(2)-N(2)-C(1)	123.9(4)	122.2(2)	120.9(3)
N(3)-C(2)-N(2)	126.5(5)	126.6(3)	122.9(3)
N(3)-C(2)-N(5)	112.1(5)	113.0(3)	116.6(3)
C(9)-Ru(1)-N(3)-C(2)	-118.5(5)	-124.8(3)	-122.9(3)
C(9)-Ru(1)-N(1)-C(1)	-123.5(5)	-120.4(3)	133.5(3)
N(1)-C(1)-N(4)-H(4B)	-132.8	-162.8	139.4
Ru(1)-N(1)-C(1)-N(4)	160.9(4)	-167.0(2)	157.8(2)
Ru(1)-N(3)-C(2)-N(5)	176.9(3)	168.2(2)	179.4(2)
N(4)-C(1)-N(2)-C(2)	-159.1(5)	-157.2(3)	153.1(3)
N(5)-C(2)-N(2)-C(1)	150.2(5)	154.7(3)	-138.4(3)
C(3)-N(3)-C(2)-N(2)	176.7(5)	173.7(3)	-173.5(3)
C(8)-N(5)-C(2)-N(2)	-178.0(5)	-176.2(3)	174.8(3)
N(3)-C(2)-C(1)-N(4)	-173.3(7)	-165.5(3)	172.3(3)
N(1)-C(1)-C(2)-N(5)	152.5(7)	160.8(4)	143.7(3)
N(4)-C(1)-C(8)-C(3)	-169.1(7)	-165.6(3)	166.5(3)
N(1)-C(1)-C(8)-C(4)	140.0(2)	143.0(9)	-116.2(7)
Average	160.9(15)	163.1(9)	155.9(19)

Table 4.6 Continued

	48^+ PF ₆ ⁻ ·(C ₅ H ₁₂) _{1.5}	48^+ BAr _f ⁻ ·H ₂ O	49
Average difference from 180°	19.1(15)	16.9(9)	24.1(19)
Ru(1)-N(3)-C(2)-N(2)	3.6(8)	-14.0(4)	2.6(4)
Ru(1)-N(1)-C(1)-N(2)	-17.9(8)	10.9(4)	-19.2(4)
N(1)-C(1)-N(2)-C(2)	-21.9(8)	24.7(4)	-29.6(4)
N(3)-C(2)-N(2)-C(1)	29.2(9)	-22.9(4)	38.3(4)
H(5)-N(5)-C(2)-N(2)	2.0	3.7	
H(2)-N(2)-C(2)-N(5)	-29.8	-25.5	13.0
H(2)-N(2)-C(1)-N(4)	20.8	23.0	2.2
H(4B)-N(4)-C(1)-N(2)	-46.2	19.2	-43.4
H(1)-N(1)-C(1)-N(4)	14.9	6.4	-7.4
H(4A)-N(4)-C(1)-N(1)	12.8	-43.9	20.0
C(3)-N(3)-C(2)-N(5)	-2.7(6)	-4.1(3)	3.3(3)
N(4)-C(1)-C(2)-N(5)	-16.0(1)	-7.4(6)	21.7(5)
N(1)-C(1)-C(2)-N(3)	-4.8(5)	2.6(3)	6.9(3)
N(1)-C(1)-C(8)-C(3)	-9.8(5)	-0.5(2)	13.9(2)
Average difference from 0°	16.6(13)	14.9(12)	17.0(14)
<i>synperiplanar DD dyads</i>			
H(4A)-N(4)-N(1)-H(1)	25.2	-35.0	11.5
H(2)-N(2)-N(4)-H(4B)	-24.7	38.4	-38.0
H(2)-N(2)-N(5)-H(5)	-24.4	-19.1	
H(5)-N(5)-N(4)-H(4B)	-51.2	14.9	
Average difference from 0°	33.5(15)	24.1(12)	38.0(0)

^a For distances involving hydrogen bonds, see Table 4.5. ^b For atom numbers, see Figures 4.6-4.8.

The salt 48^+ BAr_f⁻·H₂O could also be characterized crystallographically. X-ray data were collected and refined as described in the experimental section and Table 4.3.

The resulting structure is shown in Figure 4.6. Several of the CF₃ groups were disordered and modeled. Key metrical data are summarized in Tables 4.5, 4.6, and 4.8. In this case the **GBI** ligand is more planar than **48**⁺ PF₆⁻·(C₅H₁₂)_{1.5} with torsion angles closer to 0° or ± 180°. The average differences from 0° and 180° are 14.9(12)° and 16.9(9)°, respectively. The carbon-nitrogen bond lengths exhibit similar patterns as in **48**⁺ PF₆⁻·(C₅H₁₂)_{1.5}. The H₂O molecule in the lattice exhibits hydrogen bonding with three of the five NH units (N2-H2, N4-H4B, and N5-H5). However, in contrast to **48**⁺ PF₆⁻·(C₅H₁₂)_{1.5}, there are no hydrogen bonding interactions involving the BAr_f⁻ anion, consistent with its poor hydrogen bond acceptor properties.⁶⁰

Table 4.7 Selected F···H, P···N, and F···N distances [Å] in **48**⁺ PF₆⁻·(C₅H₁₂)_{1.5}.^{a,b}

F1···H4B	2.717	P1···N4	4.156(7)
F1···H2	2.052 ^b	P1···N5	4.258(5)
F1···H5	3.492	P1···N1'	4.151(5)
F1···H1'	3.665	P1···N4'	4.218(7)
F2···H4A'	3.562	F1···N2	2.907(7) ^b
F2···H1'	3.595	F1···N4	3.331(8)
F3···H4B	2.932	F1···N5	3.965(6)
F3···H2	2.820	F2···N1'	4.365(6)
F3···H5	3.783	F2···N4'	4.113(7)
F4···H1'	2.029 ^b	F3···N2	3.275(8)
F4···H4A'	3.234	F3···N4	3.073(9)
F4···H4B'	3.958	F3···N5	4.241(7)
F5···H1'	2.825	F4···N1'	2.959(6)
F5···H4A'	2.108 ^b	F4···N4'	3.825(8)
F5···H4B'	3.485	F5···N1'	3.525(6)
F6···H2	2.621	F5···N4'	2.953(8)
F6···H5	2.082 ^b	F6···N2	3.175(9)
P1···N2	3.781(6) ^b	F6···N5	2.855(7) ^b

^a For atom numbers, see Figures 4.6-4.8. ^b Shortest F···H, P···N and F···N distances [Å] in **8**⁺ PF₆⁻·CH₂Cl₂: 2.195; 3.802(3); and 2.939(4).⁷⁵

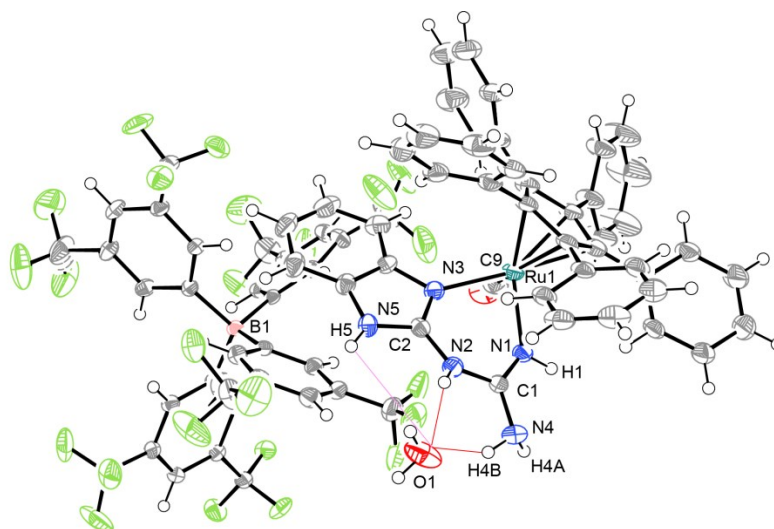


Figure 4.6 Thermal ellipsoid diagram (50% probability level) showing the structure of 48^+ $\text{BARf}^- \cdot \text{H}_2\text{O}$ and hydrogen bonding between cation and solvent. Hydrogen bonding distances of < 2.5 Å (in red) and 3.2 - 4.0 Å (in magenta).

The three NH units on the nitrogen atoms remote from the ruthenium atom, N5-H5, N2-H2, and N4-H4B, exhibit an approximately *synperiplanar* NH triad as evidenced by H-N-N-H torsion angles that are reasonably close to 0° (38.4° , -19.1° , 14.9° ; average difference from 0° , $24.1(12)^\circ$). The other two NH units, N1-H1 and N4-H4A, exhibit an approximately *synperiplanar* NH dyad with a torsion angle of -35.0° . The NH units in 48^+ $\text{BARf}^- \cdot \text{H}_2\text{O}$ more closely resemble a *synperiplanar* NH triad than they do in 48^+ $\text{PF}_6^- \cdot (\text{C}_5\text{H}_{12})_{1.5}$ (average difference from 0° , $24.1(12)^\circ$ vs. $33.5(15)^\circ$). This is clear from Figure 4.7, which shows the overlaid structures of both the cations.

Table 4.8 Selected $\text{O} \cdots \text{H}$ and $\text{O} \cdots \text{N}$ distances [Å] in 48^+ $\text{BARf}^- \cdot \text{H}_2\text{O}$.^{a,b}

$\text{O1} \cdots \text{H2}$	2.046 ^b	$\text{O1} \cdots \text{N2}$	2.796 ^b
$\text{O1} \cdots \text{H4B}$	2.281	$\text{O1} \cdots \text{N4}$	3.043
$\text{O1} \cdots \text{H5}$	3.434	$\text{O1} \cdots \text{N5}$	3.903

^a For atom numbers, see Figure 4.7. ^b Shortest $\text{F} \cdots \text{H}$ and $\text{F} \cdots \text{N}$ distances [Å] in 48^+ $\text{PF}_6^- \cdot (\text{C}_5\text{H}_{12})_{1.5}$: 2.029 and 2.855(7).

According to the full paper associated with chapter 2,⁷⁵ the Ru-P distance in the hexafluorophosphate salt $\mathbf{8}^+ \text{PF}_6^- \cdot \text{CH}_2\text{Cl}_2$ is slightly shorter than that in $\mathbf{8}^+ \text{BAr}_f^- \cdot \text{CH}_2\text{Cl}_2$ salt (2.302(3) Å vs 2.3154(10) Å). The former cation is hydrogen bonded to the anion while no such interactions are present in the latter. Hydrogen bonding with the anion increases electron density on ruthenium and enhances back bonding.⁷⁵ This leads to a slightly shorter Ru-P bond in the former salt as PF_6^- is a better hydrogen bond acceptor.⁶⁰ However in contrast, the Ru-CO distance in the salt $\mathbf{48}^+ \text{BAr}_f^- \cdot \text{H}_2\text{O}$ (1.868(4) Å) is similar to that in $\mathbf{48}^+ \text{PF}_6^- \cdot (\text{C}_5\text{H}_{12})_{1.5}$ (1.860(6) Å). Due to the solvate in the former, both the cations now have hydrogen bonding opportunities.

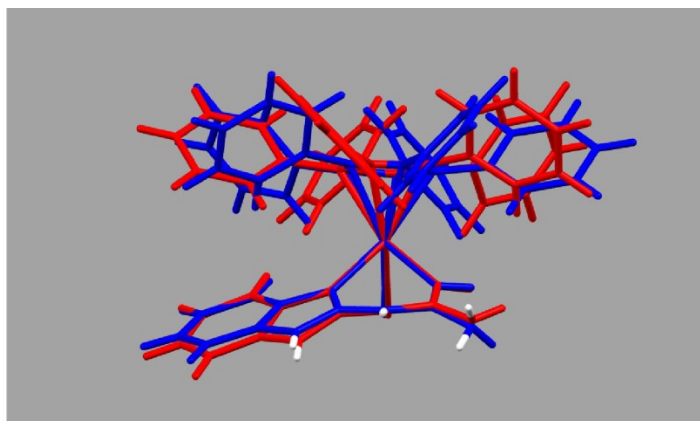


Figure 4.7 Overlay of the cations of $\mathbf{48}^+ \text{PF}_6^- \cdot (\text{C}_5\text{H}_{12})_{1.5}$ (in red), and $\mathbf{48}^+ \text{BAr}_f^- \cdot \text{H}_2\text{O}$ (in blue); key -NH groups are shown in white.

The deprotonated **GBI** complex **49** was also characterized by X-ray crystallography. X-ray data were collected and refined as described in the experimental section and Table 4.3. The resulting structure is shown in Figure 4.8. Key metrical data are summarized Table 4.4.

The cation is formally octahedral, with the pentaphenylcyclopentadienyl ligand

occupying three coordinating sites, as evident from the OC-Ru-N and N-Ru-N bond angles of ca. 90°. The ruthenium-nitrogen bond lengths are similar to those in literature.^{75,104,116} The **GBI** ligand is slightly puckered. As one approach to quantifying this, consider the many torsion angles with values near 0° or ±180°. The average differences from 0° and 180° are 17.0(14)° and 24.1(19)°, respectively.

The carbon nitrogen bond length of the coordinated CNH (C1-N1) linkage is considerably shorter than that of the coordinated CNAr (C2-N3) linkage (1.295(4) vs. 1.348(4) Å). At the same time, the non-coordinated C2-N5 linkage is shorter than the C2-N2, C1-N2, and C1-N4 linkages (1.339(4) vs. 1.389(4), 1.365(4), and 1.354(4) Å). For reference, typical carbon nitrogen double bond lengths are 1.279 Å¹⁶⁸ (Ph(H)C=NR (R = Ph, 1.286(8) Å; R = Me, 1.284(10) Å))¹⁶⁹ and single bond lengths (C_{sp2}-N) range from 1.355 Å (C_{sp2}-N_{sp2}) to 1.416 Å (C_{sp2}-N_{sp3}).¹⁶⁸ These data are best modeled by a tautomer of **49** that has been deprotonated at N5 and exhibits the dominant resonance form shown in Scheme 4.4 (C=NH for C1-N1, C-NAr for C2-N3, and C=NAr for C2-N5).

Two NH units on the nitrogen atoms remote from the ruthenium atom, N2-H2 and N4-H4B, exhibit a roughly *synperiplanar* NH dyad, as reflected by a H-N-N-H torsion angle reasonably close to 0° (38.0°). The other two NH units, N1-H1 and N4-H4A, exhibit a more *synperiplanar* NH dyad, as evidenced by a torsion angle of 11.5°.

In **49**, the **GBI** ligand is even more puckered than it is in **48**⁺ PF₆⁻·(C₅H₁₂)_{1.5}. The average differences of ligand-based torsion angles from 0° or ±180° now increases to 17.0(14)° and 24.1(19)° as opposed to 16.6(13)° and 19.1(15)°. This is clearly illustrated in Figures 4.7 and 4.9.

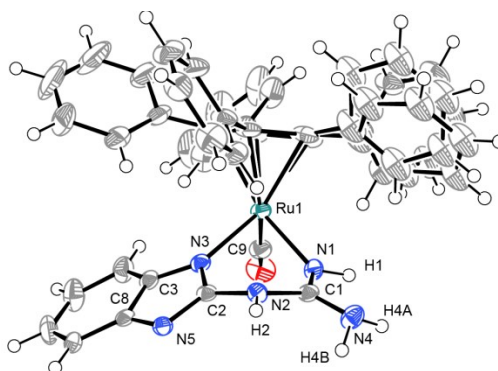


Figure 4.8 Thermal ellipsoid diagram (50% probability level) showing the structure of **49**.

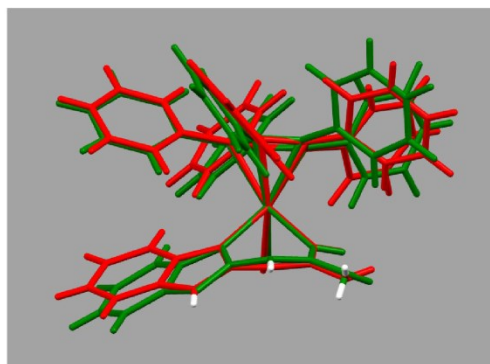


Figure 4.9 Overlay of the cation of **48**⁺ PF₆⁻·(C₅H₁₂)_{1.5} (in red), and the neutral complex **49** (in green); key -NH groups are shown in white.

4.2.3 Hydrogen bonding and catalysis in the second coordination sphere

4.2.3.1 Hydrogen bonding in the second coordination sphere

As shown in chapter 2 (Figure 2.5), the addition of dimethyl malonate (**10a**) to **9**⁺ BA_rf⁻·2H₂O has been probed by ¹H NMR. Due to NH···O interactions between **10a** and the cation, three NH units of the ruthenium complex shifted downfield (at 1.0 equiv of **10a**; Δδ (ppm) = 0.89, 0.50, and 0.27; Δν (Hz) = 445, 250, and 135), while the Ru-NH

unit shifted upfield. Thus, a similar experiment with **10a** and the hydrate $48^+ \text{BAr}_f^- \cdot 4\text{H}_2\text{O}$ was conducted.

As shown in Figure 4.10, **10a** was added to $48^+ \text{BAr}_f^- \cdot 4\text{H}_2\text{O}$. The ^1H NMR signals of three of the four types of NH units (H5 (orange)/H2 (green)/H4 (purple)) shifted progressively downfield with the addition of increasing amounts of **10a** (0.5 and 1.0 equiv). At 1.0 equiv of **10a**, the $\Delta\delta$ values (ppm) were 1.08, 0.52, and 0.32 ($\Delta\nu$ (Hz) = 540, 260, and 160), respectively. On the other hand, one NH unit (H1 (magenta)) and the H_2O signal shifted upfield and at 1.0 equiv of **10a** the $\Delta\delta$ (ppm) values were 0.15 and 0.16.

Based on the $\Delta\delta$ (ppm) data, the two most probable host-guest adducts would be **LXXVa** and **LXXVb**, as shown in Figure 4.11 (top). Out of these two, **LXXVa** is most likely the dominant form as the NH5 signal is shifted to a greater extent than the NH4 signal. However, it should be kept in mind that there are two protons on N4, as opposed only one on N5. These two remain in rapid equilibrium on the NMR time scale in the presence of **10a**, as evidenced by a single signal. Hence, adduct formation will have an intrinsically greater effect on the NH5 signal.

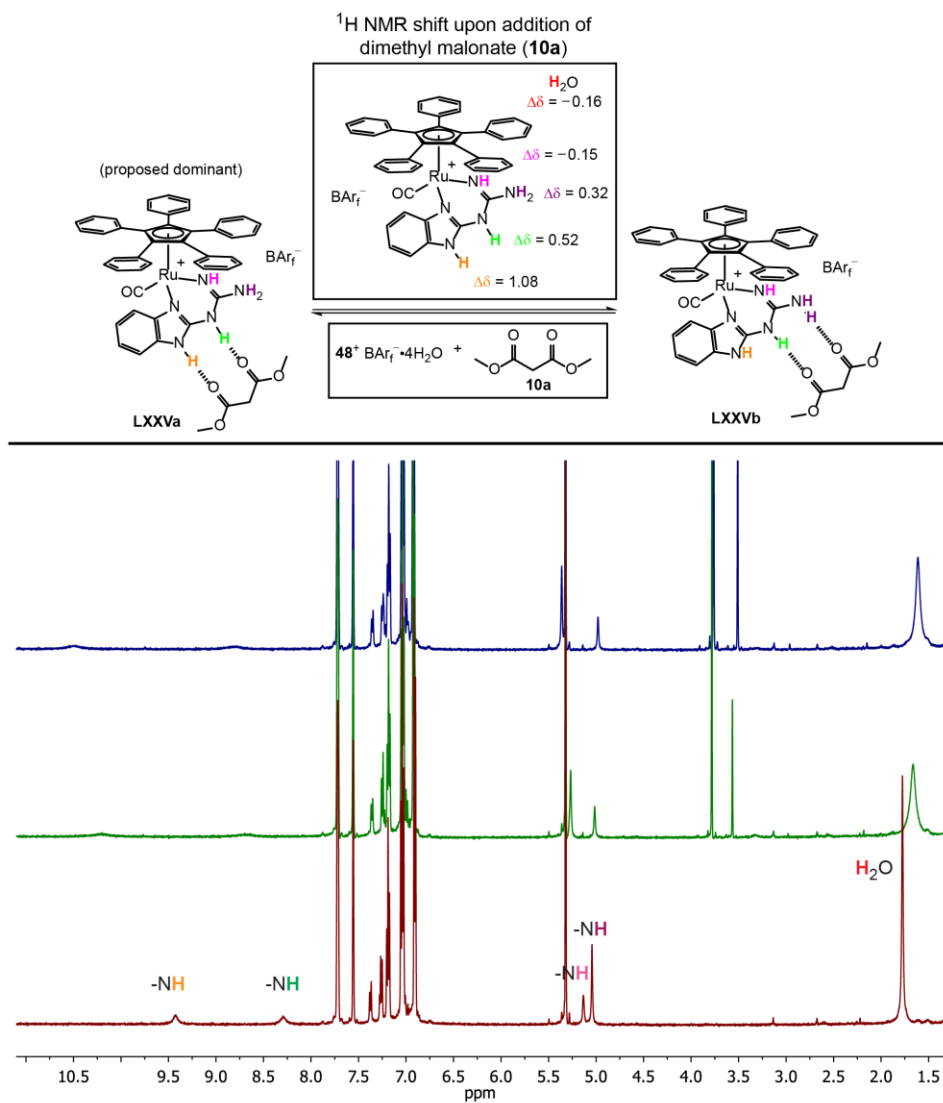


Figure 4.10 ¹H NMR spectra (rt, 500 Hz, CD₂Cl₂): **48**⁺ BARf⁻·4H₂O (bottom); after addition of 0.5 equiv of **10a** (middle); after addition of 1.0 equiv of **10a** (top). Key downfield shifted NMR signals (δ , bottom, middle, top, $\Delta(\delta_{\text{top}} - \delta_{\text{bottom}})$): -NH 9.42, 10.20, 10.50, 1.08; -NH 8.29, 8.67, 8.81, 0.52; -NH 5.04, 5.27, 5.36, 0.32. Key upfield shifted NMR signals (δ , bottom, middle, top, $\Delta(\delta_{\text{top}} - \delta_{\text{bottom}})$): -NH 5.13, 5.01, 4.98, -0.15; H₂O 1.77, 1.66, 1.61, -0.16.

Comparing the relative downfield shifts in the cases of **48**⁺ BARf⁻·4H₂O and **9**⁺ BARf⁻·2H₂O with 1.0 equiv of **10a**, the host guest interaction with **10a** appears to be slightly stronger in the former ($\Delta\delta$ (ppm) = 1.08 vs. 0.89, 0.52 vs. 0.50, and 0.32 vs.

0.27; $\Delta\nu$ (Hz) = 540 vs. 445, 260 vs. 250, and 160 vs. 135).

4.2.3.2 Catalysis in the second coordination sphere

Once enantiopure (S_{Ru})-**48**⁺ BAr_f⁻ was obtained (Scheme 4.5), the stage was set for employing this hydrogen bond donor as a catalyst. The condensation of 1-methylindole (**5a**) and *trans*- β -nitrostyrene (**6**) to give 3-substituted indoles (**7a**) was studied first, using conditions identical to those mentioned in chapters 2 (Table 2.9) and chapter 3 (Table 3.3). This is a benchmark reaction that can be effected with many hydrogen bond donor catalysts.⁶⁸ The enantioselectivities were assayed by chiral HPLC as tabulated below.

Thus, 1-methylindole (**5a**; 2.0 equiv) was treated with **6** (1.0 equiv) in the presence of 5-10 mol% of (S_{Ru})-**48**⁺ BAr_f⁻ in CD₂Cl₂ at room temperature under aerobic conditions (Table 4.9, entries 1a,b). The reactions were clean and after 1-3 h, workups gave 1-methyl-3-(2-nitro-1-phenylethyl)-1*H*-indole (**7a**)^{68a} in $\geq 95\%$ yields. However, chiral HPLC analyses indicated racemic products.

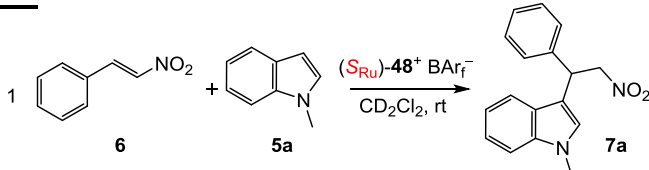
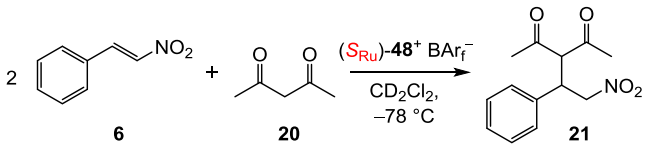
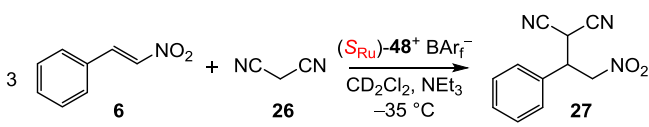
Next, a Michael addition reaction mentioned in chapter 3 was chosen for further screening. The addition of 2,4-pentanedione (**20**) to **6** was efficiently catalyzed in the presence of ($R_{Ru}R_C R_C$)-**18c**⁺ PF₆⁻ or ($S_{Ru}R_C R_C$)-**18c**⁺ PF₆⁻ at room temperature (see Table 3.5, entry 1). As both the diastereomers of **18c**⁺ PF₆⁻ contain a NMe₂ moiety, no external base was added. After 24 h, workups gave 70-75% yields of 3-(2-nitro-1-phenylethyl)pentane-2,4-dione (**21**).¹²³ Chiral HPLC analysis indicated an extremely high ee (>99%).

As shown in Table 4.9 (entries 2), the addition of **20** to **6** in CD₂Cl₂ using 10 mol% of (S_{Ru})-**48**⁺ BAr_f⁻ in CD₂Cl₂ at -78 °C under aerobic conditions was

investigated. The reaction was monitored by TLC. The formation of product **21** was only observed in the presence of 10 mol% of both (S_{Ru})-**48**⁺ BArf⁻ and NEt₃ (entries 2a,b vs. entry 2c). After 24 h, workup gave **21** in >99% yield. However, chiral HPLC analysis indicated a racemic product.

Analogously, malononitrile (**26**) and **6** were reacted in the presence of 10 mol% of both (S_{Ru})-**48**⁺ BArf⁻ and NEt₃ in CD₂Cl₂ at -35 °C (Table 3.5, entry 3a). The reaction was also monitored by TLC. After 1 h, workup gave the product **27** in 80% yield.^{21a} However, chiral HPLC analysis again indicated a racemic product.

Table 4.9 Yields and ee values for Friedel-Crafts alkylations^a and Michael addition reactions^b catalyzed by (S_{Ru})-**48**⁺ BArf⁻.^c

entry	entry	catalyst (mol%)	time (h)	yield (%) ^d	ee (%) ^{e,f}
	a	10	1	>99	0 (50.0:50.0)
	b	5	3	95	0 (50.0:50.0)
	a	10	-	24	-
	b	-	10	24	-
	c	10	10	24	>99
	a	10	1	80	0 (50.0:50.0)

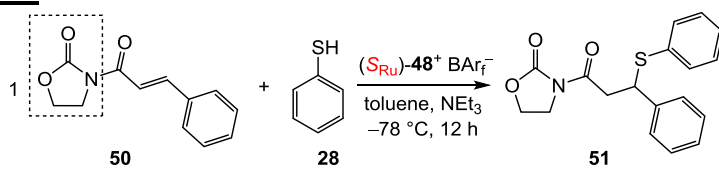
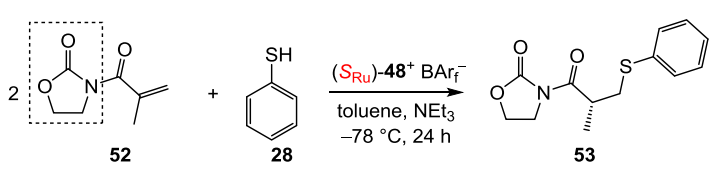
^a Reaction conditions: **5a** (2.0 equiv), **6** (1.0 equiv), catalyst (10 mol%), CD₂Cl₂ (0.3 mL). ^b Reaction conditions: **20** or **26** (1.0 equiv), **6** (1.0 equiv), catalyst (10 mol%), and NEt₃ (10 mol%) in CD₂Cl₂ (0.3 mL). ^c For the workup conditions and other details, see the experimental section. ^d Isolated yields. ^e Enantiomeric excesses (ee) were determined by chiral HPLC. ^f Enantiomer ratios are given in parentheses.

4.2.3.3 Enantioselective catalysis in the second coordination sphere

Next the focus was shifted to a different kind of hydrogen bond acceptor, *trans*-3-cinnamoyloxazolidin-2-one (**50**; Table 4.10, entry 1), based on a 2-oxazolidinone core (Table 4.10, box). This core is immensely popular in chemistry related to the Evans chiral auxiliary.¹⁷⁰ Compound **50** recently has been utilized as a substrate in organocatalyzed tandem Michael addition reactions.¹⁷¹ Some derivatives of **50** have also been used in organocatalyzed Michael additions of thiols. Many hafnium based Lewis acids have also been found to catalyze the addition of thiols to the Michael acceptor **50** in moderate yields (10-70%), but the enantioselectivities with the enantiopure catalyst have been poor (43-59% ee).¹⁷² Hence, this reaction was investigated (Table 4.10, entry 1).

Initially, **50** (2.0 equiv) was treated with thiophenol (**28**, 1.0 equiv) in the presence of NEt₃ (1.0 equiv) and 10 mol% of (*S*_{Ru})-**48**⁺ BAR_F⁻ in toluene at -78 °C (Table 4.10, entry 1a). After 12 h, workup gave only a 25% yield of the product, 3-(3-phenyl-3-(phenylthio)propanoyl)oxazolidin-2-one (**51**).¹⁷² Gratifyingly, chiral HPLC analysis indicated an extremely high ee value (>99%). Although this compound has been prepared earlier in enantioenriched form, the absolute configuration of the enantiomer was not assigned.¹⁷² Compound **50** was not highly soluble under the reaction condition and crashed out of the solution. This might be the reason for low yield. An analogous reaction under more dilute conditions and using a longer reaction time gave **51** in 60% yield and in >99% ee (entry 1b).

Table 4.10 Yields and ee values for the additions of **28** to **50** or **52** catalyzed by $(S_{Ru})\text{-48}^+ \text{BARf}^-$.^{a,b}

entry	entry	catalyst (mol%)	yield (%) ^c	ee (%) ^{d,e,f}
	a	10	25	>99 (0.2:99.8)
	b ^g	10	60	>99 (0.2:99.8)
		10	70	7 (46.5:53.5)

^a Reaction conditions: **28** (1.0 equiv), **50** or **52** (2.0 equiv), catalyst (10 mol%), and NEt_3 (1.0 equiv) in toluene (0.3 mL). ^b For the workup conditions and other details, see the experimental section. ^c Isolated yields. ^d Enantiomeric excesses (ee) were determined by chiral HPLC. ^e Enantiomer ratios are given in parentheses. ^f The absolute configurations could not be assigned. ^g The reaction was conducted in toluene (0.6 mL) for 48 h. ^h The absolute configuration was assigned according to previously reported relative retention times.

Similarly, 3-(2-methyl-2-propenoyl)oxazolidin-2-one (**52**) and **28** were reacted in the presence of NEt_3 (1.0 equiv) and 10 mol% of $(S_{Ru})\text{-48}^+ \text{BARf}^-$ in toluene at -78°C (Table 4.10, entry 2). After 24 h, workup gave a 70% yield of the product **53**, for which the configuration of the enantiomers had been previously assigned.¹⁷³ Chiral HPLC analysis of the product indicated a 7% ee.

4.2.3.4 Multifunctional catalysis in the second coordination sphere

Complex **49** contains a benzimidazolic nitrogen that has been deprotonated, as shown in Figure 4.8 and Table 4.6. The reprotonation of this nitrogen is vital in the resolution of the chiral-at-metal ruthenium complex, as shown in Scheme 4.5. This indicates that **49** can act as a base and raises the possibility that it could participate in base catalyzed reactions. Importantly, reattachment of the proton transforms the

ruthenium fragment into a hydrogen bond donor with a *synperiplanar* DDD triad (Figures 4.6-4.9 and Table 4.6). As demonstrated in chapters 2 and 3 and Tables 4.9 and 4.10, this motif promotes reaction via second coordination sphere hydrogen bonding. To investigate the possibilities of **49** acting as a catalyst, Michael addition reactions between 1,3-dicarbonyl equivalents and **6** were investigated (Table 4.11). These are benchmark reactions for hydrogen bond donor catalysts that incorporate bases for additional functionality.¹²⁰

Table 4.11 Isolated yields for the addition of Michael donors to **6** catalyzed by **49**.^{a,b}

entry		yield (%)
1		75
2		90

^a Reaction conditions: Michael donor (2.0 equiv), **6** (1.0 equiv), catalyst (10 mol%) in CD₂Cl₂ (0.5 mL). ^b For the workup conditions and other details, see the experimental section.

First, diethyl malonate (**10b**; 2.0 equiv) was treated with **6** (1.0 equiv) in the presence of 10 mol% of **49** and the internal standard Ph₂SiMe₂ in CD₂Cl₂ at room temperature under aerobic conditions (Table 4.11, entry 1). The reaction was monitored by ¹H NMR. A clean conversion to the addition product, ethyl-2-carboethoxy-4-nitro-3-phenylbutyrate (**19a**),^{120a} was observed. After 24 h, workup gave **19a** in 75% yield.

To extend the scope of this strategy, **26** and **6** were reacted in the presence of 10 mol% of **49** in CD₂Cl₂ (Table 4.11, entry 2). After 1 h, workup gave the product **27** in 90% yield.^{21a}

4.3 Discussion

4.3.1 Second coordination sphere promoted catalysis

The successful syntheses of the salts **48**⁺ X⁻ containing bulky cyclopentadienyl ligands were achieved in this chapter (Table 4.1-4.4 and Scheme 4.4). These were extended to the formation of a neutral complex **49** by treatment with K⁺ *t*-BuO⁻ (Scheme 4.4). Protonation of this neutral compound with an enantiopure acid, separation of the diastereomers, and subsequent anion metathesis afforded the resolved catalyst (*S*_{Ru})-**48**⁺ BAr_f⁻ (Scheme 4.5 and Figure 4.2). This differs from the chiral catalysts in chapter 3 in the absence of a conventional carbon stereocenter.

The facility with which **48**⁺ X⁻ can enter into hydrogen bonding interactions is evidenced by the NMR data in Figure 4.10 and the crystal structures in Figures 4.5 and 4.6. The results presented in Tables 4.9 and 4.10 clearly indicate that **48**⁺ BAr_f⁻ acts as a hydrogen bond donor catalyst and promotes simple organic transformations. Based on the evidence provided above, it is clear that the catalyst activates the substrate through hydrogen bonding in the second coordination sphere and hence these catalyzed reactions are examples of second coordination sphere promoted catalysis (SCSPC).

4.3.2 Transition state assemblies for Table 4.10

In an effort to overcome the poor enantioselectivity with **6** (Table 4.9), a hydrogen bond acceptor based on a 2-oxazolidinone backbone, **50**, was considered (Table 4.10). It was hypothesized that the electronically differentiated carbonyl groups (Figure 4.11, blue and red) would preferentially direct the binding of the catalyst to one regiochemical form over the other (Figure 4.11, top). Furthermore, the C=C-C=O single bond in **50** can adopt either a *s-cis* or *s-trans* conformation (**50a/b**). The two conformers present opposite C=C enantiofaces with respect to either side of the approximately planar Ph-C=C-C=O assembly. However, the *s-trans* conformation encounters A^{1,3} strain between the vinyl (C=CHPh) and NCH₂ protons and thus the *s-cis* conformation is favored by approximately 4.5 kcal/mol.¹⁷⁴

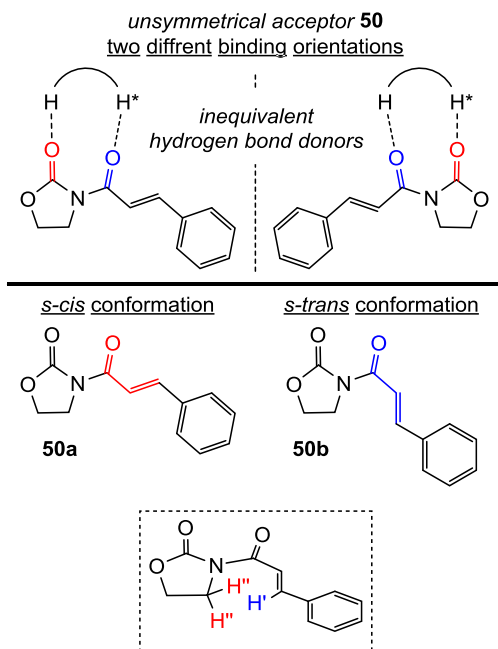


Figure 4.11 Rationale behind choosing **50** as the hydrogen bond acceptor (top); two conformations around the C=C-C=O single bond are shown (middle); the *s-trans* conformation results in A^{1,3} strain with a strain energy of ca. 4.5 kcal/mol (bottom, box).¹⁷⁴

As shown in Figure 4.12, the electronically differentiated C=O groups are suggested to promote regioselective dyad binding, and the A^{1,3} strain an *s-cis* C=C-C=O conformation. The enhanced radial extension of the pentaphenylcyclopentadienyl ligand blocks the approach of the nucleophile to the *re, re* C=C face, so that the nucleophile must approach the *si, si* C=C face from the bottom as in Figure 4.12. Importantly, the absolute configuration of the major enantiomer from the reaction of **50** and **28** has not been established. Thus, it may prove necessary to switch the regioselectivity with which **28** binds to the dyad in this model.

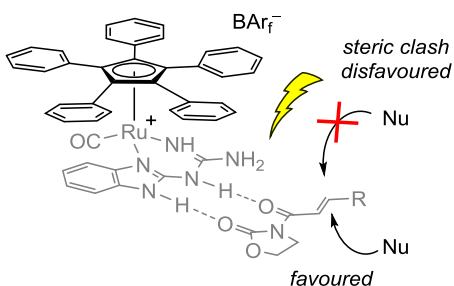


Figure 4.12 Transition state model for rationalizing the extremely high enantioselectivity.

With respect to the substrate **52**, which features a methyl substituent α to the amide carbonyl group and a terminal alkene, the relevant *s-cis* and *s-trans* conformations are depicted in Figure 4.13. Now both are destabilised by $A^{1,3}$ strain, and no clear $C=C-C=O$ conformational preference is expected, either in the free ligand or a hydrogen bonded assembly. Accordingly, the product **53** is nearly racemic.

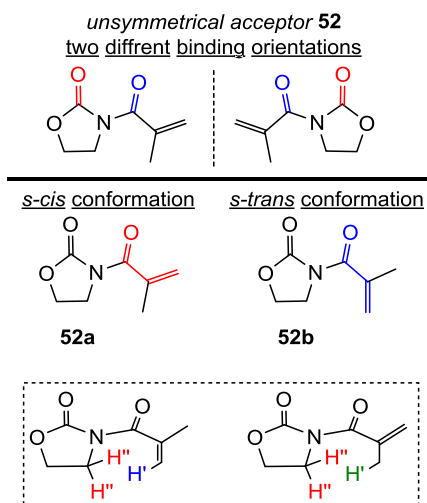


Figure 4.13 Representation of **52** as the hydrogen bond acceptor (top); two conformations around the $C=C-C=O$ single bond are shown (middle); *s-trans* and *s-cis* conformations both encounter $A^{1,3}$ strain (bottom, box).

4.3.3 Multiple role of the metal

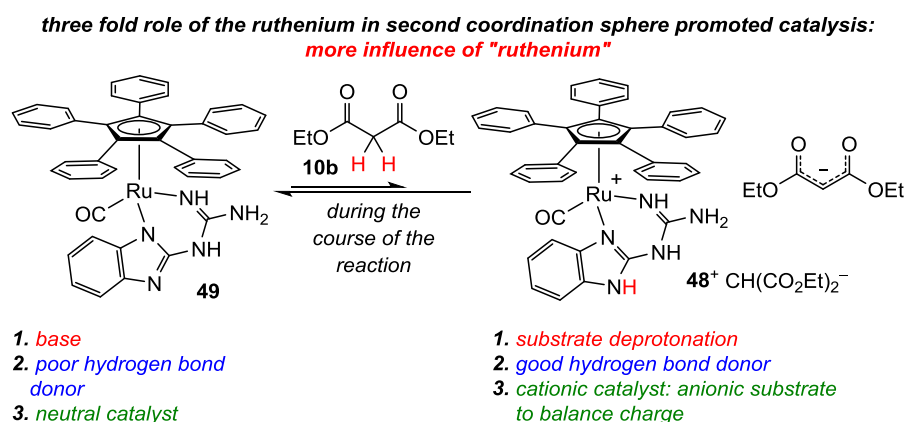
Attaching ruthenium to **GBI** primarily creates a second coordination sphere where the substrate can bind with the *synperiplanar* NH DDD triad. In the case of C=C conjugated carbonyl and nitro substrates, this will polarize the π -system. This activates the substrate towards nucleophiles. The ruthenium complex can also provide the necessary chiral atmosphere for enantioselective product formation, as seen in Table 4.10 (entries 1a and 1b).

The scope of this system can be further expanded where the ligand can have additional functionality. Initially, **49** is a neutral compound due to the combination of the anionic **GBI_H** ligand and a $[(\eta^5\text{-C}_5\text{Ph}_5)\text{Ru}(\text{CO})]^+$ fragment. Compound **49** is devoid of the DDD triad and the remaining NH protons distort from *synperiplanarity* as evident from the crystal structure (Figures 4.7-4.9). This *syn* arrangement is an important feature of the immensely popular thiourea based hydrogen bond donors.^{8f,13a}

When the deprotonated benzimidazolic nitrogen regains the proton by deprotonating a substrate, the complex turns cationic. The conjugate base has to pair with the substrate derived counter anion as there is no other anion to compete. In the process, the cationic species has regained its DDD triad and can activate either the conjugate base further or any other substrate by hydrogen bonding. Thus, in theory, **49** would be a multifunctional catalyst: (1) acting as a base to activate one substrate, (2) serving as a hydrogen bond donor to activate the other substrate, and (3) ion pairing with the conjugate base of the more acidic substrate.

The successful catalytic reactions shown in Table 4.11 clearly reflect this multifunctionality of **49**. Scheme 4.6 illustrates the possible activation modus. When diethyl malonate ester (**10b**) is added to **49**, an equilibrium will be reached between **49**

and $48^+ \text{CH}(\text{CO}_2\text{Et})_2^-$. Complex $48^+ \text{CH}(\text{CO}_2\text{Et})_2^-$ is depicted as a cationic ruthenium species with the conjugate base of **10b** as the counter anion. The conjugate base can react further with any other reactant. Finally, the initial anionic addition intermediate can deprotonate the benzimidazolic proton of the cation in $48^+ \text{CH}(\text{CO}_2\text{Et})_2^-$ and complete the reaction. In doing so, the neutral ruthenium complex **49** is reformed. This can activate another substrate and carry on the catalytic cycle. This model nicely fits with the results (Table 4.11) as a catalytic amount (10 mol%) of **49** was enough to effect reactions in 75-90% yields without any external base.



Scheme 4.6 Strategic aspects of the application of the neutral ruthenium complex **49** in catalysis.

Similar concepts have recently been explored by Meggers with the iridium complex **LXXIX** (Figure 4.17).¹⁷⁵ In the same vein, here also a neutral iridium complex is transformed to a cationic species during the course of the catalytic cycle. It activates one of the substrates by deprotonating and the other by hydrogen bonding. Finally, high enantioselectivities were also observed for the products. The entire process of substrate activation, deprotonation, and condensation happens in the second coordination sphere

and broadens the scope of second coordination sphere promoted catalysis.

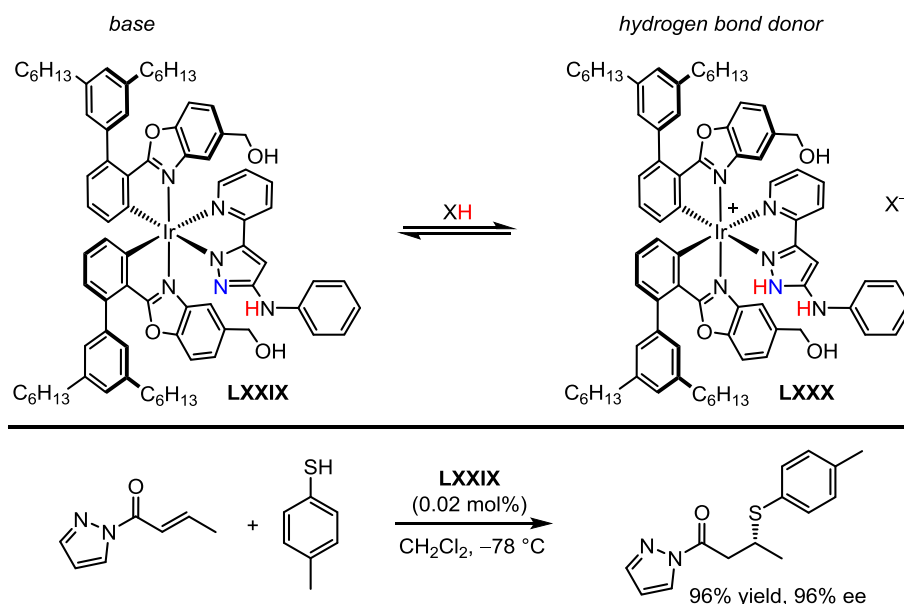


Figure 4.17 Deprotonated neutral complex (**LXXIX**) capable of acting as a base and hydrogen bond donor.

4.4 Conclusion

The elaboration of the chiral cationic cyclopentadienyl ruthenium **GBI** complexes to pentaphenylcyclopentadienyl ruthenium **GBI** complexes enables the facile resolution of the enantiomers and provides a new set of catalysts to be applied in hydrogen bond donor promoted enantioselective organic transformations. The chelation of **GBI** preorganizes the NH moieties of the ligand into *synperiplanar* arrays, and their acidities are increased relative to cyclopentadienyl analogs.

Unlike most transition metal catalyzed reactions, there is no direct interaction of the substrate with the ruthenium; rather, hydrogen bonds derived from NH groups

remote from the metal center are involved. These chiral-at-metal complexes contains no additional ligand chirality, contrary to the catalysts in chapter 3, and hence enantioselection is a sole function of the metal chirality. As the hydrogen bonding interactions, activation of the substrates, and promotion of the enantioselective transformations occur in the second coordination sphere, these results extend the horizon of second coordination sphere promoted catalysis (SCSPC). However, unless special features are built into the substrate, the enantioselectivities generally appear to be lower than with the catalyst in chapter 3.

Finally, it has been shown that deprotonated variants, which are neutral, can function as bases, thereby further activating substrates in what can be viewed as multifunctional second coordination sphere promoted catalysis. This constitute yet another promising direction for future investigation.

4.5 Experimental Section

4.5.1 General data

^1H , $^{13}\text{C}\{^1\text{H}\}$, and $^{31}\text{P}\{^1\text{H}\}$ NMR spectra were recorded on standard 500 MHz spectrometers at ambient probe temperature (24 °C) and referenced as follows (δ , ppm): ^1H , residual internal CHCl_3 (7.26), CHD_2OD (3.30), or CHDCl_2 (5.32); ^{13}C , internal CDCl_3 (77.0), CD_3OD (49.1), or CD_2Cl_2 (53.9); $^{31}\text{P}\{^1\text{H}\}$, external H_3PO_4 (0.0). IR spectra were recorded using a Shimadzu IRAffinity-1 spectrophotometer with a Pike MIRacle ATR system (diamond/ZnSe crystal). Circular dichroism spectra were obtained using a Chirascan CD Spectrometer (Applied Photophysics). Melting points were recorded with a Stanford Research Systems (SRS) MPA100 (Opti-Melt) automated device. Microanalyses were conducted by Atlantic Microlab. HPLC analyses were conducted with a Shimadzu instrument package (pump/autosampler/detector LC-20AD/SIL-20A/SPD-M20A; columns Chiralpak AD, Chiralpak AD-H, Chiralpak AS-H, Chiralcel OD, Chiralcel OD-H).

Solvents were treated as follows: toluene, hexanes, Et_2O , and CH_2Cl_2 were dried and degassed using a Glass Contour solvent purification system; CH_3CN (99.5% BDH); pentane (99.7%, J. T. Baker), MeOH (99.8%, BDH), CDCl_3 , CD_2Cl_2 , and CD_3OD (3 \times Cambridge Isotope Laboratories) were used as received. The 2-guanidinobenzimidazole (**GBI**; 95%, Aldrich), 1-methylindole (**5a**; 98%, Acros Organics), *trans*- β -nitrostyrene (**6**; 99%, Alfa Aesar), (*S*)-1,1'-binaphthyl-2,2'-diyl hydrogen phosphate or (*P*)-1,1'-binaphthyl-2,2'-diyl hydrogen phosphate ((*P*)-**12**; 98%, Alfa Aesar), 2,4-pentanedione (**20**; 99%, Aldrich), malononitrile (**26**; 98%, TCI), thiophenol (**28**; 97%, Aldrich), NEt_3 (99%, Alfa Aesar), $\text{Ag}^+ \text{PF}_6^-$ (99%, Alfa Aesar), $\text{Me}_3\text{NO}\cdot 2\text{H}_2\text{O}$ (98%, TCI), $\text{Ru}_3(\text{CO})_{12}$

(99%, Aldrich), CH₃COOH (≥99.7%, Aldrich), K⁺ *t*-BuO⁻ (97%, Alfa Aesar), PhLi (2.0 M in Bu₂O, Aldrich), HBr (45% w/v in CH₃COOH, Alfa Aesar), silica gel (SiliFlash F60, Silicycle), neutral alumina (Brockmann I, 50-200 μm, Acros Organics), and celite were used as received.

Compounds *trans*-3-cinnamoyloxazolidin-2-one (**50**) and 3-(2-methyl-2-propenoyl)oxazolidin-2-one (**52**) were prepared following literature procedures.^{176,177} Reactions in Schlenk flasks were carried under nitrogen atmospheres. Other reactions and workups were carried out under air.

4.5.2 Syntheses and catalysis

1,2,3,4,5-pentaphenylcyclopenta-2,4-dien-1-ol (44).¹⁶⁵ A Schlenk flask was charged with tetraphenylcyclopentadienone (**45**, 2.50 g, 6.56 mmol)¹⁶⁶ and Et₂O (50 mL) with stirring. The mixture was cooled to 0 °C and PhLi (2.0 M in Bu₂O; 5.00 mL, 10.0 mmol) was added dropwise with vigorous stirring. The ice bath was removed and the grey-yellow suspension was stirred. After 2 h, the mixture was cooled to 0 °C and HCl (1.0 M in H₂O) was added slowly, followed by H₂O (5 mL). A pale brown precipitate formed. Then CH₂Cl₂ (30 mL) was added, giving an organic/aqueous liquid/liquid biphasic system. The organic layer was separated, washed with H₂O (3 × 5 mL), and dried (Na₂SO₄). The solvent was removed by oil pump vacuum (rt, then 40 °C) to give **44** as a pale yellow solid (2.43 g, 5.25 mmol, 80%).

NMR (δ, CDCl₃):¹⁶⁵ ¹H (500 MHz) 7.57 (d, 2H, ³J_{HH} = 7.1 Hz), 7.27 (t, 1H, ³J_{HH} = 7.8 Hz), 7.19-7.10 (m, 7H), 7.08-6.97 (m, 14H), 2.46 (s, 1H); ¹³C{¹H} (125 MHz) 147.9, 142.5 (2 × s, *i*-C_{Ph}CCOH and *i*-C_{Ph}C=CCOH), 140.1 (s, *i*-C_{Ph}COH),

135.0, 133.8 (2 × s, C=CCOH and C=CCOH), 129.9, 129.5, 127.9, 127.7, 127.0, 127.1 (6 × s, *o*- and *m*-C_{Ph}CCOH, *o*- and *m*-C_{Ph}C=CCOH, and *o*- and *m*-C_{Ph}COH), 128.4 (s, *p*-C_{Ph}CCOH or *p*-C_{Ph}C=CCOH), 126.9 (s, *p*-C_{Ph}COH), 125.0 (s, *p*-C_{Ph}C=CCOH or *p*-C_{Ph}CCOH), 90.2 (s, COH).

5-Bromo-1,2,3,4,5-pentaphenyl-1,3-cyclopentadiene (43).¹⁶⁵ A round bottom flask was charged with **44** (1.50 g, 3.20 mmol) and CH₃COOH (12 mL) with stirring. The mixture was refluxed and cooled to room temperature, giving an orange solution. Then HBr (0.60 mL) was added. The resulting suspension was refluxed. After 30 min, the oil bath was allowed to cool to room temperature. After 4 h, the orange precipitate was isolated by filtration, washed with H₂O (3 × 10 mL), and dried by oil pump vacuum (60 °C, 12 h) to give crude **43**. The residue was then chromatographed on a silica gel column (3 × 15 cm, 80:20 v/v hexanes/CH₂Cl₂) to give **43** as orange yellow solid (1.27 g, 2.43 mmol, 76%), which was light sensitive and stored in the dark.

NMR (δ , CDCl₃):¹⁶⁵ ¹H (500 MHz) 7.58-7.52 (m, 3H), 7.30-7.26 (m, 5H), 7.18-6.89 (m, 17H); ¹³C {¹H} (125 MHz) 148.2, 141.8 (2 × s, *i*-C_{Ph}CCBr and *i*-C_{Ph}C=CCBr), 135.8 (s, *i*-C_{Ph}CBr), 134.6, 134.1 (2 × s, C=CCBr and C=CCBr), 130.4, 130.0 (2 × s, *o*- and *m*-C_{Ph}CCBr), 128.3 (s, *p*-C_{Ph}CCBr), 127.8 (s, *p*-C_{Ph}CBr or *p*-C_{Ph}C=CCBr), 127.7 (s, *o*/*m*-C_{Ph}C=CCBr), 127.4 (s, *p*-C_{Ph}C=CCBr or *p*-C_{Ph}CBr), 127.4 (s, *m*/*o*-C_{Ph}C=CCBr), 127.1, 127.0 (2 × s, *o*- and *m*-C_{Ph}CBr), 76.6 (s, CBr).

(η^5 -C₅Ph₅)Ru(CO)₂Br (42).¹⁶³ A Schlenk flask was charged with **43** (0.247 g, 0.470 mmol), Ru₃(CO)₁₂ (0.100 g, 0.156 mmol), and toluene (6 mL) with stirring. The mixture was refluxed. After 4 h, the oil bath was removed. After 4 h, the solvent was

removed by rotary evaporation and the residue was chromatographed on a silica gel column (3 × 20 cm, 80:20 → 20:80 v/v hexanes/CH₂Cl₂). The solvent was removed from the product containing fractions by oil pump vacuum to give **42** as a greenish yellow solid (0.240 g, 0.352 mmol, 75%).

NMR (δ , CD₂Cl₂):¹⁷⁸ ¹H (500 MHz) 7.23 (tt, 5H, ³J_{HH} = 7.2 Hz, ⁴J_{HH} = 1.5 Hz, *p*-C_{Ph}H), 7.11 (tt, 10H, ³J_{HH} = 8.1 Hz, ⁴J_{HH} = 2.2 Hz, *o*-C_{Ph}H), 7.07-7.05 (m, 10H, *m*-C_{Ph}H); ¹³C {¹H} (125 MHz) 197.2 (s, CO), 132.7 (s, *o*-C_{Ph}), 130.0 (s, *i*-C_{Ph}), 128.7 (s, *p*-C_{Ph}), 128.10 (s, *m*-C_{Ph}), 107.1 (s, C₅Ph₅).

[(η^5 -C₅Ph₅)Ru(CO)(GBI)]⁺ PF₆⁻ (48**⁺ PF₆⁻). A Schlenk flask was charged with **42** (0.200 g, 0.293 mmol), CH₃CN (10 mL), and (after 2 min) Me₃NO·2H₂O (0.032 g, 0.29 mmol) with stirring. Within 5 min, the suspension became an orange solution. Then **GBI** (0.051 g, 0.29 mmol) was added. After 15 min, Ag⁺ PF₆⁻ (0.074 g, 0.29 mmol) was added. After 16 h, the solvent was removed by rotary evaporation. Then CH₂Cl₂ (10 mL) was added. The suspension was passed through celite, which was washed with CH₂Cl₂ (3 × 10 mL). The solvent was removed from the combined filtrates by rotary evaporation. The residue was chromatographed on a silica gel column (3 × 25 cm, 100:2 v/v CH₂Cl₂/MeOH). The solvent was removed from the product containing fractions by rotary evaporation. The residue was washed with 50:50 v/v CH₂Cl₂/hexane (3 × 30 mL) and dried by oil pump vacuum to give **48**⁺ PF₆⁻ as a bright green solid (0.199 g, 0.204 mmol, 70%), dec. pt. 156 °C (capillary). Anal. Calcd for C₄₄H₃₄F₆N₅OPRu·C₆H₁₄: C 61.22, H 4.93, N 7.14. Found C 61.29, H 4.67, N 7.93.⁸⁹**

NMR (δ , CD₂Cl₂):¹⁷⁹ ¹H (500 MHz) 7.35 (d, 1H, ³J_{HH} = 8.0 Hz, CH_{7/8}), 7.20-

7.14 (m, 7H, *p*-C_{Ph}H, CH5/6, and CH8/7), 7.02 (t, 10H, ³J_{HH} = 7.2 Hz, *m*-C_{Ph}H),¹⁸⁰ 6.95-6.90 (m, 11H, *o*-C_{Ph}H and CH6/5), 5.48 (br s, 2H, H₂NC=NH), 4.77 (s, 1H, RuNH), 1.27 (m, C₆H₁₄), 0.98-0.82 (m, C₆H₁₄);¹⁸¹ ¹³C{¹H} (125 MHz) 205.3 (s, CO), 154.3 (s, C1), 146.0 (s, C2), 141.1 (s, C3), 141.5 (s, C4), 132.3 (s, *o*-C_{Ph}), 131.9 (s, *i*-C_{Ph}), 128.1 (s, *m*-C_{Ph} and *p*-C_{Ph}),¹⁸² 124.1 (s, C5), 122.3 (s, C6), 118.9 (s, C7), 111.8 (s, C8), 100.6 (s, C₅Ph₅), 30.2, 24.1, 14.3 (3 × s, C₆H₁₄).

IR (cm⁻¹, powder film): 3367 (m), 3057 (m), 2960 (w), 2924 (w), 1948 (s, ν_{CO}), 1674 (s), 1558 (m), 1500 (s), 1462 (w), 1444 (m), 1398 (m), 1259 (w), 1076 (m), 1028 (s), 1014 (m), 840 (s), 800 (s), 738 (s), 698 (s)

[(η⁵-C₅Ph₅)Ru(CO)(GBI)]⁺ BAr_f⁻ (48**⁺ BAr_f⁻).**²⁶ A Schlenk flask was charged with **42** (0.0200 g, 0.0293 mmol), CH₃CN (1 mL), and (after 1 min) Me₃NO·2H₂O (0.0032 g, 0.029 mmol) with stirring. Within 5 min, the suspension became an orange solution. Then **GBI** (0.0051 g, 0.029 mmol) was added. After 15 min, Ag⁺ PF₆⁻ (0.0074 g, 0.029 mmol) was added. After 16 h, the solvent was removed by rotary evaporation. Then CH₂Cl₂ (1 mL) was added. The suspension was passed through celite, which was washed with CH₂Cl₂ (3 × 1 mL). The solvent was removed from the combined filtrates by rotary evaporation. The residue was chromatographed on a alumina column (3 × 15 cm, 95:5 → 75/25 v/v CH₂Cl₂/MeOH). The solvent was removed from the product containing fractions by oil pump vacuum to give **48**⁺ X⁻ where X⁻ is principally derived from the alumina (<5% PF₆⁻).¹⁰⁴

A round bottom flask was charged with **48**⁺ X⁻ (0.025 g, ca. 0.033 mmol if the mass is considered to represent the cation), CH₂Cl₂ (2 mL), H₂O (1 mL), and Na⁺ BAr_f⁻ (0.029 g, 0.033 mmol)^{26,65} with stirring. After 30 min, the organic layer was separated,

washed with H₂O (3 × 3 mL), and dried (Na₂SO₄). The evaporation of the solvent by rotary evaporation led to partial decomposition of the compound. Therefore, the solvent was removed by purging N₂ through the solution. Then 30:70 v/v CH₂Cl₂/hexane (4 mL) was added and the mixture was passed through a short plug of celite. The solvent was removed by purging N₂ through the filtrate. Hexanes (2 mL) was added to give a suspension. The solvent was removed by purging N₂ through the mixture. This hexane/purge cycle was repeated to give **48**⁺ BAr_F⁻·4H₂O (0.040 g, 0.023 mmol, 69%) as a dirty green solid, dec. pt. 105 °C (capillary). The sample appeared to partially decompose under oil pump vacuum. Hence, it was dried in air for one week. Anal. Calcd for C₇₆H₄₆BF₂₄N₅ORu·(H₂O)₂: C 55.57, H 3.21, N 4.21. Found C 55.76, H 3.37, N 3.95. Calcd for C₇₆H₄₆BF₂₄N₅ORu·(H₂O)₄ (per the integration of the H₂O peak in the undried sample used for ¹H NMR): C 54.40, H 3.38, N 4.12.

NMR (δ, CD₂Cl₂):¹⁷⁹ ¹H (500 MHz) 9.47 (br s, 1H, NH), 8.36 (br s, 1H, NH), 7.72 (s, 8H, *o*-B(C₆H₃(CF₃)₂)₄), 7.56 (s, 4H, *p*-B(C₆H₃(CF₃)₂)₄), 7.37 (d, 1H, ³J_{HH} = 7.8 Hz, CH7/8), 7.27-7.25 (m, 2H, CH5/6 and CH8/7), 7.19 (t, 5H, ³J_{HH} = 7.6 Hz, *p*-C_{Ph}H), 7.04 (t, 10H, ³J_{HH} = 8.7 Hz, *m*-C_{Ph}H),¹⁸⁰ 7.02-6.95 (m, 1H, CH6/5), 6.92 (t, 10H, ³J_{HH} = 7.6 Hz, *o*-C_{Ph}H), 5.13 (s, 1H, RuNH), 5.05 (br s, 2H, H₂NC=NH), 1.80 (br s, 8H, H₂O); ¹³C{¹H} (125 MHz) 204.5 (s, CO), 162.5 (q, ¹J_{CB} = 50.7 Hz, *i*-C₆H₃(CF₃)₂), 152.9 (s, C1), 144.0 (s, C2), 140.9 (s, C3), 135.2 (s, *o*-C₆H₃(CF₃)₂), 132.4 (s, C4), 132.3 (s, *o*-C_{Ph}), 131.5 (s, *i*-C_{Ph}), 129.2 (q, ²J_{CF} = 29.1 Hz, *m*-C₆H₃(CF₃)₂), 128.4 (s, *p*-C_{Ph}),¹⁸⁰ 128.2 (s, *m*-C_{Ph}),¹⁸⁰ 125.3 (s, C5), 124.9 (q, ¹J_{CF} = 271.7 Hz, C₆H₃(CF₃)₂), 124.1 (s, C6), 119.6 (s, C7), 117.9 (s, *p*-C₆H₃(CF₃)₂), 111.5 (s, C8), 100.4 (s, C₅Ph₅).

IR (cm⁻¹, powder film): 3689 (w), 3649 (w), 3450 (w), 3401 (w), 1977 (m, ν_{CO}), 1681 (m), 1608 (w), 1564 (m), 1354 (s), 1274 (s), 1163 (s), 1114 (s), 1091 (m), 1029 (w), 927 (w), 889 (w), 839 (w), 742 (s), 700 (s), 680 (s), 669 (s).

(η^5 -C₅Ph₅)Ru(CO)(GBI-H) (49).²⁶ A round bottom flask was charged with **48**⁺ PF₆⁻ (0.462 g, 0.459 mmol), K⁺ *t*-BuO⁻ (0.360 g, 3.21 mmol), CH₂Cl₂ (100 mL), and H₂O (30 mL) with stirring. A yellow suspension began to form within a few minutes. After 2 h, MeOH (10 mL) was added to the organic/aqueous liquid/liquid biphasic system. The organic layer was separated, washed with H₂O (3 × 4 mL), and dried (Na₂SO₄). The solvent was removed by rotary evaporation. The residue was washed with CH₂Cl₂ (3 × 10 mL) and dried by oil pump vacuum to give **49** as a bright yellow powder (0.250 g, 0.334 mmol, 73%), dec. pt. 160 °C (capillary). Anal. Calcd for C₄₄H₃₅N₅ORu: C 70.57, H 4.44, N 9.35. Found C 71.00, H 4.65, N 9.01.

NMR (δ , CD₂Cl₂/CD₃OD):^{179,183} ¹H (500 MHz) 7.16 (d, 1H, ³J_{HH} = 7.7 Hz, CH8),¹⁸⁰ 7.09 (t, 5H, ³J_{HH} = 7.3 Hz, *p*-C_{Ph}H), 7.03 (d, 1H, ³J_{HH} = 7.9 Hz, CH7),¹⁸⁰ 6.99-6.88 (m, 21H, *m*-C_{Ph}H, *o*-C_{Ph}H, and CH6), 6.72 (t, 1H, ³J_{HH} = 7.7 Hz, CH5);¹⁸⁰ ¹³C{¹H} (125 MHz) 207.8 (s, CO), 159.0 (s, C1), 154.4 (s, C2), 143.9 (s, C3), 137.9 (s, C4), 133.0 (s, *i*-C_{Ph}), 132.6 (s, *o*-C_{Ph}), 127.7 (s, *m*-C_{Ph}),¹⁸⁰ 127.4 (s, *p*-C_{Ph}),¹⁸⁰ 120.7 (s, C5), 119.9 (s, C6), 117.3 (s, C7), 111.7 (s, C8), 101.4 (s, C₅Ph₅).

IR (cm⁻¹, powder film): 3479 (w), 3369 (w), 3059 (w), 2956 (w), 2922 (w), 2852 (w), 1934 (s, ν_{CO}), 1668 (m), 1622 (w), 1602 (w), 1566 (m), 1502 (w), 1444 (w), 1375 (s), 1261 (w), 1240 (s), 1074 (m), 1028 (w), 920 (w), 864 (w), 844 (w), 800 (w), 783 (w), 740 (s), 700 (s).

(*R*_{Ru}/*S*_{Ru})-48⁺ (*P*)-Phos⁻.²⁶ A round bottom flask was charged with CD₂Cl₂ (2 mL), **49** (0.075 g, 0.10 mmol), and **12** (0.035 g, 0.10 mmol) with stirring. Within 2 min, a clear solution was obtained. After 10 min, the solution was filtered through a short plug of celite. The filtrate was added dropwise to hexanes (5 mL) with stirring. A pale green precipitate formed. The solvent was removed by oil pump vacuum to give (*R*_{Ru}/*S*_{Ru})-48⁺ (*P*)-Phos⁻ as a pale green solid (0.10 g, 0.092 mmol, 92%) as a 50±2:50±2 mixture of Ru,Axial configurational diastereomers, as assayed by ¹H NMR using the NH protons at 4.45 and 4.92 ppm.

NMR (δ , CD₂Cl₂; signals for diastereomers are separated by "/"): ¹H (500 MHz) 13.67/13.16 (br s, 1H, NH), 12.30/10.81 (br s, 1H, NH), 8.12 (br s, 2H, **H**_{(*P*)-Phos}), 7.95 (d, 2H, ³J_{HH} = 7.3 Hz, **H**_{(*P*)-Phos}), 7.59 (br s, 2H, **H**_{(*P*)-Phos}), 7.36-7.23, 7.19-7.13, 7.08-6.98, 6.97-6.90, 6.84-6.82 (5 × m, 6H, 3H, 8H, 13H, and 5H, remaining **H**_{(*P*)-Phos}, C_{Ph}**H**, and CH5-8), 6.12/5.56 (br s, 1H, NH), 4.92/4.45 (br s, 1H, NH); ¹³C {¹H} (125 MHz) 205.55 (s, CO), 155.02/154.71 (s, C1), 149.05/148.98 (s, C_{(*P*)-Phos}), 147.08/146.75 (s, C2), 141.46/141.42 (s, C3), 132.78/132.72 (s, C4), 132.28/132.17 (s, *o*-C_{Ph}), 132.11/132.03 (s, *i*-C_{Ph}), 131.59, 130.90, 129.31, 128.70, 128.50 (5 × s, C_{(*P*)-Phos}) 127.97/127.76 (s, *m*-C_{Ph}), 127.90/127.67 (s, *p*-C_{Ph}), 127.31, 126.35, 125.35 (3 × s, C_{(*P*)-Phos}), 123.36/122.98 (s, C5), 122.68 (s, C_{(*P*)-Phos}), 122.14/121.88 (s, C6), 121.63 (s, C_{(*P*)-Phos}), 118.36/117.84 (s, C7), 111.92/111.73 (s, C8), 100.64/100.32 (s, C₅Ph₅); ³¹P {¹H} (CD₂Cl₂, 202 MHz) 6.2 (s, **P**_{(*P*)-Phos}).

(*S*_{Ru})-48⁺ (*P*)-Phos⁻. A round bottom flask was charged with (*R*_{Ru}/*S*_{Ru})-48⁺ (*P*)-Phos⁻ (0.100 g, 0.100 mmol) and 90:10 v/v toluene/hexane (5 mL) with stirring. After 2 min, the solution was kept at -35 °C for 24 h. This gave a yellow solid

suspended in a dirty green supernatant. The solid was isolated by filtration, washed with 70:30 v/v toluene/hexane (3×2 mL), and dried by rotary evaporation. The solvent was removed from the combined filtrates by rotary evaporation. Then 90:10 v/v toluene/hexane (3 mL) was added. The sample was kept at -35 °C for 24 h. Again a yellow solid suspended in a dirty green supernatant formed. The yellow solid was isolated by filtration and washed with 70:30 v/v toluene/hexane (3×1 mL). The two crops of solid were combined and dried by oil pump vacuum to give (S_{Ru})-**48**⁺ (*P*)-Phos⁻·CH₃C₆H₅ (0.042 g, 0.035 mmol, 35% or 70% of theory, $>98:<02$ S_{Ru}/R_{Ru} as assayed by ¹H NMR using the NH protons at 4.48 and 4.92 ppm; the ¹³C NMR signals for the cation are consistent with a high diastereomer ratio) as a bright yellow powder, dec. pt. 105 °C (capillary). Anal. Calcd for C₇₁H₅₄N₅O₅PRu·C₆H₅CH₃: C 71.71, H 4.58, N 5.89. Found C 72.06, H 4.78, N 5.66. The configuration was assigned by analogy to that of (S_{Ru})-**48**⁺ BARf⁻, which was assigned by CD spectroscopy (Figure 4.3(a)).

NMR (δ , CD₂Cl₂):^{179,184} ¹H (500 MHz) 13.77 (br s, 1H, NH), 12.33 (br s, 1H, NH), 8.01 (d, 2H, ³J_{HH} = 8.9 Hz, **H**_{(*P*)-Phos}), 7.95 (d, 2H, ³J_{HH} = 8.9 Hz, **H**_{(*P*)-Phos}), 7.52 (d, 2H, ³J_{HH} = 8.2 Hz, **H**_{(*P*)-Phos}), 7.44 (t, 2H, ³J_{HH} = 8.2 Hz, **H**_{(*P*)-Phos}), 7.38 (d, 2H, ³J_{HH} = 8.2 Hz, **H**_{(*P*)-Phos}), 7.33 (d, 1H, ³J_{HH} = 7.7 Hz, **CH**_{7/8}), 7.29-7.23 (m, 4H, **H**_{(*P*)-Phos}, **CH**_{8/7}, and **CH**_{5/6}), 7.18-7.10 (m, 10H, *p*-C_{Ph}**H** and CH₃C₆**H**₅), 7.04-6.99 (t, 10H, ³J_{HH} = 7.8 Hz, *m*-C_{Ph}**H**), 6.97-6.91 (d, 10H, ³J_{HH} = 7.6 Hz, *o*-C_{Ph}**H**), 6.88 (t, 1H, ³J_{HH} = 7.7 Hz, **CH**_{6/5}), 5.70 (s, 2H, NH₂), 4.48 (s, 1H, RuNH), 2.34 (s, 3H, CH₃C₆**H**₅); ¹³C{¹H} (CD₂Cl₂, 125 MHz) 205.5 (s, CO), 155.1 (s, C1), 149.3 (s, C_{(*P*)-Phos}), 147.2 (s, C2), 141.5 (s, C3), 138.6 (s, *i*-C₆**H**₅CH₃), 132.8 (s, C4), 132.3 (s, *o*-C_{Ph}), 132.1 (s, *i*-C_{Ph}), 131.3 (s, *o*-C₆**H**₅CH₃), 131.6, 130.7, 129.3, 128.7, 128.5 (5 × s, C_{(*P*)-Phos} and *m*-

$\text{C}_6\text{H}_5\text{CH}_3$) 128.0 (s, *m*- C_{Ph}),¹⁸⁰ 127.9 (s, *p*- C_{Ph}),¹⁸⁰ 127.2, 126.5 (2 × s, $\text{C}_{(P)\text{-Phos}}$), 125.7 (s, *p*- $\text{C}_6\text{H}_5\text{CH}_3$), 125.3 (s, $\text{C}_{(P)\text{-Phos}}$), 123.3 (s, C5), 122.5 (s, $\text{C}_{(P)\text{-Phos}}$), 122.1 (s, C6), 121.9 (s, $\text{C}_{(P)\text{-Phos}}$), 118.4 (s, C7), 111.9 (s, C8), 100.7 (s, C_5Ph_5) 21.6 (s, $\text{C}_6\text{H}_5\text{CH}_3$); ³¹P{¹H} (CD₂Cl₂, 202 MHz) 6.2 (s, $\text{P}_{(P)\text{-Phos}}$).

The solvent was removed from the combined filtrates by oil pump vacuum to give ($R_{\text{Ru}}/S_{\text{Ru}}$)-**48**⁺ (*P*)-Phos⁻ (0.064 g, 0.060 mmol, 60%, 80:20 $R_{\text{Ru}}/S_{\text{Ru}}$ as assayed by ¹H NMR vs. the NH protons at 4.45 and 4.92 ppm) as a pale green solid.

(S_{Ru})-**48**⁺ BAr_f^- . A round bottom flask was charged with (S_{Ru})-**48**⁺ (*P*)-Phos⁻ (0.050 g, 0.050 mmol), Na⁺ BAr_f^- (0.044 g, 0.050 mmol), CH₂Cl₂ (3 mL), and H₂O (2 mL) with stirring. After 5 min, the organic layer turned dirty green. After 30 min, it was separated, washed with H₂O (3 × 3 mL), and dried (Na₂SO₄). The evaporation of the solvent by rotary evaporation led to partial decomposition of the compound. Therefore, the solvent was removed by purging N₂ through the solution. Then 30:70 v/v CH₂Cl₂/hexane (4 mL) was added and the mixture was passed through a short plug of celite. The solvent was removed by purging N₂ through the filtrate. Hexanes (2 mL) was added to give a suspension. The solvent was removed by purging N₂ through the mixture. This hexane/purge cycle was repeated to give (S_{Ru})-**48**⁺ $\text{BAr}_f^- \cdot 2\text{H}_2\text{O}$ as a dirty green solid (0.064 g, 0.040 mmol, 80%), dec. pt. 105 °C (capillary). The sample appeared to partially decompose under oil pump vacuum. Hence, it was dried in air for one week. Anal. Calcd for C₇₆H₄₆BF₂₄N₅ORu·H₂O: C 55.96, H 2.97, N 4.29. Found C 56.38, H 3.29, N 4.50. Calcd for C₇₆H₄₆BF₂₄N₅ORu·(H₂O)₂ (per the integration of the H₂O peak in the undried sample used for ¹H NMR): C 55.57, H 3.21, N 4.21. The configuration was tentatively assigned by the CD spectra (Figure 4.3; see additional details in text).

NMR (δ , CD₂Cl₂):^{26,179} ¹H (500 MHz) 9.45 (br s, 1H, NH), 8.33 (br s, 1H, NH), 7.72 (s, 8H, *o*-B(C₆H₃(CF₃)₂)₄), 7.56 (s, 4H, *p*-B(C₆H₃(CF₃)₂)₄), 7.37 (d, 1H, ³J_{HH} = 7.8 Hz, CH7/8), 7.27-7.25 (m, 2H, CH5/6 and CH8/7), 7.19 (t, 5H, ³J_{HH} = 7.6 Hz, *p*-C_{Ph}H), 7.04 (t, 10H, ³J_{HH} = 8.7 Hz, *m*-C_{Ph}H), 7.02-6.95 (m, 1H, CH6/5), 6.92 (d, 10H, ³J_{HH} = 7.6 Hz, *o*-C_{Ph}H), 5.13 (s, 1H, RuNH), 5.06 (br s, 2H, NH₂), 1.73 (br s, 4H, H₂O); ¹³C{¹H} (125 MHz) 204.5 (s, CO), 162.55 (q, ¹J_{CB} = 50.7 Hz, *i*-C₆H₃(CF₃)₂), 152.9 (s, C1), 144.0 (s, C2), 140.9 (s, C3), 135.2 (s, *o*-C₆H₃(CF₃)₂), 132.4 (s, C4), 132.3 (s, *o*-C_{Ph}), 131.5 (s, *i*-C_{Ph}), 129.2 (q, ²J_{CF} = 30.9 Hz, *m*-C₆H₃(CF₃)₂), 128.4 (s, *p*-C_{Ph}), ¹⁸⁰ 128.2 (s, *m*-C_{Ph}), ¹⁸⁰ 125.3 (s, C5), 124.9 (q, ¹J_{CF} = 271.7 Hz, C₆H₃(CF₃)₂), 124.1 (s, C6), 119.6 (s, C7), 117.9 (s, *p*-C₆H₃(CF₃)₂), 111.5 (s, C8), 100.4 (s, C₅Ph₅).

CD (nm, 1.2 × 10⁻³ M in CH₃CN ([θ], deg·L·mol⁻¹cm⁻¹ and $\Delta\epsilon$, L·mol⁻¹cm⁻¹): 310 (+13336 and +4.04), 330 (sh, +828 and +2.50), 345 (sh, +4288 and +1.30), 360 (sh, +8262 and +0.25), 370 (-299 and -0.09), 400 (sh, +2396 and +0.73), 425 (+3714 and +1.12), 435 (sh, +3498 and +1.07).

Friedel-Crafts alkylations catalyzed by (*S*_{Ru})-48⁺ BAr_f⁻ (Table 4.9, entry 1).

1-methyl-3-(2-nitro-1-phenylethyl)-1*H*-indole (7a).⁶⁸ An NMR tube was charged with (*S*_{Ru})-48⁺ BAr_f⁻ (entry 1a, 0.0034 g, 0.0020 mmol, 10 mol%), **5a** (0.0052 g, 0.040 mmol), **6** (0.0030 g, 0.020 mmol), an internal standard (Ph₂SiMe₂, 0.0021 g, 0.010 mmol) and CD₂Cl₂ (0.5 mL). The tube was capped. Product formation was monitored vs. the standard by ¹H NMR. After specified time, the solvent was removed by rotary evaporation. The residue was taken up in hexane/ethyl acetate (30:70 v/v) and passed through a short silica gel column, which was washed with additional hexane/ethyl

acetate (50:50 v/v, 5 mL). The solvent was removed from the combined filtrates by rotary evaporation, and a second silica gel chromatography step was carried out (1 × 10 cm, 90:10 v/v hexane/ethyl acetate). The solvent was removed from the product containing fractions by oil pump vacuum to give **7a** (0.0056 g, 0.020 mmol, >99%) as a colorless oil.

NMR (δ , CDCl₃): ¹H (500 MHz) 7.47 (d, 1H, J = 7.6 Hz), 7.38-7.23 (m, 7H), 7.10 (m, 1H), 6.88 (s, 1H), 5.21 (t, 1H, J = 8.0 Hz), 5.06 (dd, 1H, J = 12.4, 8.0 Hz), 4.95 (dd, 1H, J = 12.4, 8.0 Hz), 3.75 (s, 3H); Literature chemical shift values (CDCl₃) agree within 0.01 ppm.^{68a}

The enantiomeric excess was determined by HPLC with a Chiralpak AS-H column, hexane/2-PrOH (90:10 v/v), 1.0 mL/min, λ = 210 nm; t_R = 14.6 min, 18.6 min.¹⁸⁵

Michael addition reactions catalyzed by (*S*_{Ru})-48**⁺ BAr_f⁻ (Table 4.9).**

3-(2-nitro-1-phenylethyl)pentane-2,4-dione (21, entry 2c). A J. Young NMR tube was charged with **20** (0.0020 g, 0.020 mmol), **6** (0.0030 g, 0.020 mmol), and CD₂Cl₂ (0.5 mL) and cooled to -78 °C. Then (*S*_{Ru})-**48**⁺ BAr_f⁻ (0.0034 g, 0.0020 mmol, 10 mol%) and NEt₃ (0.0002 g, delivered by syringe, mass corresponds to weight of NMR tube before/after; 0.002 mmol, 10 mol%) were added and the tube was capped. Product formation was monitored by TLC. After 24 h, the solvent was removed by rotary evaporation. The residue was taken up in hexane/ethyl acetate (30:70 v/v) and passed through a short silica gel column, which was washed with additional hexane/ethyl acetate (50:50 v/v, 5 mL). The solvent was removed from the combined filtrates by

rotary evaporation, and a second silica gel chromatography step was carried out (1 × 10 cm, 80:20 v/v hexane/ethyl acetate). The solvent was removed from the product containing fractions by oil pump vacuum to give **21** (0.0025 g, 0.020 mmol, >99%) as a colorless oil.

NMR (δ , CDCl₃):^{123a,147} ¹H (500 MHz) 7.34-7.25 (m, 3H), 7.19-7.16 (m, 2H), 4.64-4.61 (m, 2H), 4.36 (d, 1H, J = 10.7 Hz), 4.27-4.20 (m, 1H), 2.28 (s, 3H), 1.93 (s, 3H); ¹³C{¹H} (125 MHz) 201.6, 200.9, 135.9, 129.3, 128.5, 127.9, 78.2, 70.7, 42.9, 30.5, 29.7.

The enantiomeric excess was determined by HPLC with a Chiralpak AS-H column, hexane/2-PrOH (85:15 v/v), 1.0 mL/min, λ = 215 nm; t_R = 14.9 min, 22.6 min.^{123b}

2-(2-nitro-1-phenylethyl)propanedinitrile (27, entry 3c). A J. Young NMR tube was charged with **26** (0.0013 g, 0.020 mmol), **6** (0.0029 g, 0.020 mmol), and CD₂Cl₂ (0.5 mL) and cooled to -35 °C. Then (*S*_{Ru})-**48**⁺ BAr_f⁻ (0.0034 g, 0.0020 mmol, 10 mol%) and NEt₃ (0.0002 g, delivered by syringe, mass corresponds to weight of NMR tube before/after; 0.002 mmol, 10 mol%) were added and the tube was capped. Product formation was monitored by TLC. After 1 h, the solvent was removed by rotary evaporation. The residue was taken up in hexane/ethyl acetate (30:70 v/v) and passed through a short silica gel column, which was washed with additional hexane/ethyl acetate (50:50 v/v, 5 mL). The solvent was removed from the combined filtrates by rotary evaporation, and a second silica gel chromatography step was carried out (1 × 10 cm, 60:40 v/v hexane/ethyl acetate). The solvent was removed from the product

containing fractions by oil pump vacuum to give **27** (0.0034 g, 0.016 mmol, 80%) as a pale yellow oil.

NMR (δ , CDCl_3):^{21a,147} ^1H (500 MHz) 7.54-7.41 (m, 3H), 7.41-7.29 (m, 2H), 4.99 (dd, 1H, $J = 14.3, 8.2$ Hz), 4.91 (dd, 1H, $J = 14.3, 6.1$ Hz), 4.43 (d, 1H, $J = 5.8$ Hz), 4.15-4.03 (m, 1H); $^{13}\text{C}\{^1\text{H}\}$ (125 MHz) 131.8, 130.4, 129.4, 127.7, 110.5, 110.4, 74.9, 43.5, 27.5.

The enantiomeric excess was determined by HPLC with a Chiralcel OD column, hexane/2-PrOH (50:50 v/v), 0.50 mL/min, $\lambda = 215$ nm; $t_{\text{R}} = 19.5$ min, 54.7 min.^{21a,186}

Additions of 28 to 50 or 52 catalyzed by (S_{Ru})-48⁺ BARf^- (Table 4.10). A J. Young NMR tube was charged with the Michael acceptor (**50** or **52**, 0.040 mmol), **28** (0.0022 g, 0.020 mmol), and CD_2Cl_2 (0.3 mL) and cooled to -78 °C. Then (S_{Ru})-48⁺ BARf^- (0.0034 g, 0.0020 mmol, 10 mol%) and NEt_3 (0.0022 g, delivered by syringe, mass corresponds to weight of NMR tube before/after; 0.020 mmol) were added and the tube was capped. Product formation was monitored by TLC. After the specified time, the solvent was removed by rotary evaporation. The residue was taken up in hexane/ethyl acetate (30:70 v/v) and passed through a short silica gel column, which was washed with additional hexane/ethyl acetate (50:50 v/v, 5 mL). The solvent was removed from the combined filtrates by rotary evaporation, and a second silica gel chromatography step was carried out (1 \times 10 cm, CH_2Cl_2). The solvent was removed from the product containing fractions by rotary evaporation (yields, Table 4.10).

3-[1-oxo-3-phenyl-3-(phenylthio)propyl]oxazolidin-2-one (51, entry 1). NMR

(δ , CDCl₃):^{147,172} ¹H (500 MHz) 7.35-7.37 (m, 2H), 7.25-7.29 (m, 2H), 7.18 (t, 1H, J = 7.3 Hz), 4.30-4.40 (m, 2H), 4.02-4.07 (m, 1H), 3.87-3.98 (m, 2H), 3.30 (dd, 1H, J = 13.4, 8.0 Hz), 3.01 (dd, 1H, J = 13.4, 5.7 Hz), 1.28 (d, 3H, J = 8.5 Hz); ¹³C{¹H} (125 MHz) 175.5, 153.1, 135.9, 130.3, 129.0, 126.6, 62.0, 42.8, 38.3, 37.4, 17.4.

The enantiomeric excess was determined by HPLC with a Chiralpak AS-H column, hexane/2-PrOH (90:10 v/v), 1.0 mL/min, λ = 210 nm; t_R = 32.5 min (major), 34.4 min (minor).¹⁸⁷

3-[(2-methyl-1-oxo-3-(phenylthio)propyl]oxazolidin-2-one (53, entry 2).
NMR (δ , CDCl₃):^{147,173} ¹H (500 MHz) 7.35-7.37 (m, 2H), 7.25-7.29 (m, 2H), 7.18 (t, 1H, J = 7.3 Hz), 4.30-4.40 (m, 2H), 4.02-4.07 (m, 1H), 3.87-3.98 (m, 2H), 3.30 (dd, 1H, J = 13.4, 8.0 Hz), 3.01 (dd, 1H, J = 13.4, 5.7 Hz), 1.28 (d, 3H, J = 8.5 Hz); ¹³C{¹H} (125 MHz) 175.5, 153.1, 135.9, 130.3, 129.0, 126.6, 62.0, 42.8, 38.3, 37.4, 17.4.

The enantiomeric excess was determined by HPLC with a Chiralcel OD column, hexane/2-PrOH (70:30 v/v), 1.0 mL/min, λ = 254 nm; t_R = 22.7 min (major, *S*), 25.5 min (minor, *R*).^{151,173}

Addition of Michael donors to 6 catalyzed by 49 (Table 4.11).

Ethyl-2-carboethoxy-4-nitro-3-phenylbutyrate (19a, entry 1). A J. Young NMR tube was charged with **10b** (0.0320 g, 0.200 mmol), Ph₂SiMe₂ (~0.0500 mmol; internal standard), **6** (0.0150 g, 0.100 mmol), and CD₂Cl₂ (0.5 mL). Then **49** (0.0075 g, 0.010 mmol, 10 mol%) was added and the tube was capped. Product formation was monitored vs. the standard by ¹H NMR. After 24 h, the solvent was removed by rotary

evaporation. The residue was taken up in hexane/ethyl acetate (30:70 v/v) and passed through a short silica gel column, which was washed with additional hexane/ethyl acetate (50:50 v/v, 5 mL). The solvent was removed from the combined filtrates by rotary evaporation, and a second silica gel chromatography step was carried out (1 × 10 cm, 80:20 v/v hexane/ethyl acetate). The solvent was removed from the product containing fractions by oil pump vacuum to give **19a** (0.0306 g, 0.0750 mmol, 75%) as a colorless oil.

NMR (δ , CDCl₃):^{120a,147} ¹H (500 MHz) 7.32-7.23 (m, 5H), 4.92 (dd, 1H, J = 13.2, 4.7 Hz), 4.86 (dd, 1H, J = 13.2, 9.5 Hz), 4.26-4.17 (m, 3H), 4.00 (q, 2H, J = 7.1 Hz), 3.82 (d, 1H, J = 9.3 Hz), 1.25 (t, 3H, J = 7.1 Hz), 1.03 (t, 3H, J = 7.1 Hz); ¹³C{¹H} (125 MHz) 167.4, 166.7, 136.2, 128.8, 128.3, 127.9, 77.6, 62.1, 61.8, 55.0, 42.9, 13.9, 13.6.

2-(2-nitro-1-phenylethyl)propanedinitrile (27, entry 2). A J. Young NMR tube was charged with **26** (0.0660 g, 0.100 mmol), Ph₂SiMe₂ (~0.050 mmol; internal standard), **6** (0.0149 g, 0.100 mmol), and CD₂Cl₂ (0.5 mL). Then **49** (0.0075 g, 0.010 mmol, 10 mol%) was added and the tube was capped. Product formation was monitored vs. the standard by ¹H NMR. After 1 h, the solvent was removed by rotary evaporation. The residue was taken up in hexane/ethyl acetate (30:70 v/v) and passed through a short silica gel column, which was washed with additional hexane/ethyl acetate (50:50 v/v, 5 mL). The solvent was removed from the combined filtrates by rotary evaporation, and a second silica gel chromatography step was carried out (1 × 10 cm, 60:40 v/v hexane/ethyl acetate). The solvent was removed from the product containing fractions by oil pump vacuum to give **27** (0.0161 g, 0.0750 mmol, 80%) as a pale yellow oil.

NMR (δ , CDCl_3):^{21a,147} ^1H (500 MHz) 7.54-7.41 (m, 3H), 7.41-7.29 (m, 2H), 4.99 (dd, 1H, $J = 14.3, 8.2$ Hz), 4.91 (dd, 1H, $J = 14.3, 6.1$ Hz), 4.43 (d, 1H, $J = 5.8$ Hz), 4.15-4.03 (m, 1H); $^{13}\text{C}\{^1\text{H}\}$ (125 MHz) 131.8, 130.4, 129.4, 127.7, 110.5, 110.4, 74.9, 43.5, 27.5.

Crystallography A. A CH_2Cl_2 /pentane solution of 48^+PF_6^- was kept in an NMR tube. After 24 h, yellow blocks of $48^+ \text{PF}_6^-(\text{C}_5\text{H}_{12})_{1.5}$ with well defined faces had formed.

Data were collected as outlined in Table 4.5. The integrated intensity information for each reflection was obtained by reduction of the data frames with the program APEX2.⁹² Cell parameters were obtained from 180 frames using a 0.5° scan. Data were corrected for Lorentz and polarization factors, and using SADABS,⁹³ absorption and crystal decay effects. The structure was solved by direct methods using SHELXTL (SHELXS).⁹⁴ Hydrogen atoms were placed in idealized positions and were refined using a riding model. All non-hydrogen atoms were refined with anisotropic thermal parameters. The parameters were refined by weighted least squares refinement on F^2 to convergence.⁹⁴

B. A CH_2Cl_2 /hexane solution of $48^+ \text{BARf}^- \cdot 4\text{H}_2\text{O}$ was kept in an NMR tube. After 1 week, colorless blocks of $48^+ \text{BARf}^- \cdot \text{H}_2\text{O}$ with well defined faces had formed.

Data were collected as outlined in Table 4.5. The integrated intensity information for each reflection was obtained by reduction of the data frames with the program APEX2.⁹² Cell parameters were obtained from 60 frames using a 0.5° scan. Data were corrected for Lorentz and polarization factors, and using SADABS,⁹³ absorption and

crystal decay effects. The structure was solved by direct methods using SHELXTL (SHELXS).⁹⁴ Several of the CF₃ groups were disordered and were modeled. Residual electron density peaks close to the fluorine atoms of the CF₃ groups indicated further disorder, but modeling efforts were not successful. Additional residual electron densities were observed, and tentatively assigned to a disordered and/or partially occupied hexane. This electron density contribution was extracted with the program PLATON/SQUEEZE.¹⁸⁸ Hydrogen atoms were placed in idealized positions and were refined using a riding model. All non-hydrogen atoms were refined with anisotropic thermal parameters. The parameters were refined by weighted least squares refinement on F^2 to convergence.⁹⁴

C. A CHCl₃/MeOH solution (10:1 v/v) of **49** was kept in an NMR tube. After 1 week, colorless needles of **49** with well defined faces had formed.

Data were collected as outlined in Table 4.5. The integrated intensity information for each reflection was obtained by reduction of the data frames with the program APEX2.⁹² Cell parameters were obtained from 180 frames using a 0.5° scan. Data were corrected for Lorentz and polarization factors, and using SADABS,⁹³ absorption and crystal decay effects. The structure was solved by direct methods using SHELXTL (SHELXS).⁹⁴ The phenyl ring C39 to C33 was disordered between two positions and was modeled with a 53:47 occupancy ratio. Larger thermal ellipsoids on C21 to C26 suggested disorder, but modeling efforts were not successful. Additional residual electron densities were observed, and tentatively assigned to disordered and/or partially occupied H₂O or MeOH molecule sites. Thus, the electron density contribution was extracted with the program PLATON/SQUEEZE.¹⁸⁸ Hydrogen atoms were placed in idealized positions and were refined using a riding model. All non-hydrogen atoms were

refined with anisotropic thermal parameters. The parameters were refined by weighted least squares refinement on F^2 to convergence.⁹⁴

5. SUMMARY AND CONCLUSION

5.1 Conclusion from this study

This dissertation for the first time describes the development of new chiral-at-metal ruthenium based organometallic hydrogen bond donors derived from 2-guanidinobenzimidazole (**GBI**) and their application in enantioselective catalysis. Unlike most transition metal catalyzed reactions, there is no direct interaction of the substrate with the ruthenium; rather, association involves hydrogen bonding derived from NH groups which are remote from the metal center (Figure 5.1). The hydrogen bonding interactions and the activation of the substrates occurs solely in the second coordination sphere, and thereby promote the reactions (Figure 5.1). Thus, these systems successfully justify the term second coordination sphere promoted catalysis.

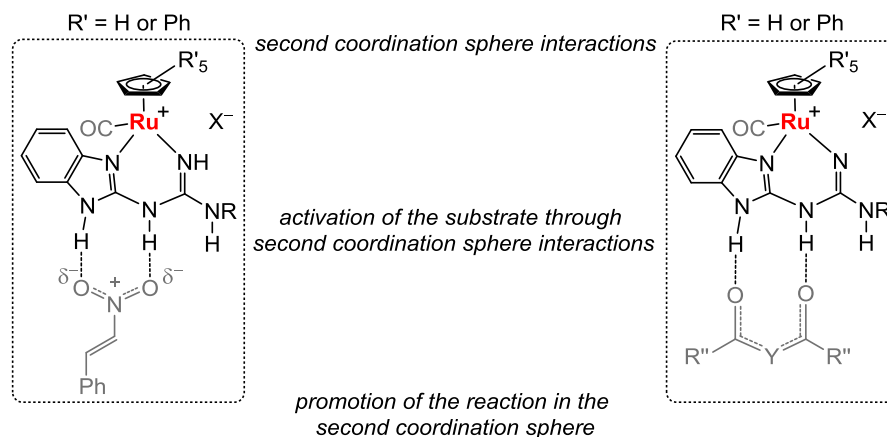


Figure 5.1 Transition state assemblies. Activation models for ruthenium based organometallic hydrogen bond donor catalysts described in this thesis.

GBI is a chelating ligand with NH protons that can act as potent hydrogen bond donors (D). Chelating to ruthenium preorganizes the NH protons in a *synperiplanar* conformation. Comparisons of catalytic efficacies of **GBI** and its derivatives (chapters 1-4) lead to the conclusion that preorganization is vital in turning **GBI** into an active catalyst. However, increasing the NH proton acidities by protonation, methylation, or chelation cannot be completely ignored.

Furthermore, chiral substituted **GBI** ligands (**GBI-R**) afford ruthenium complexes as mixtures of Ru,C configurational diastereomers ($[(\eta^5\text{-C}_5\text{H}_5)\text{Ru}(\text{CO})(\text{GBI-R})]^+ \text{PF}_6^-$ (**18a-d**⁺ PF_6^-)). Using an enantiopure ligand bearing an additional basic NMe₂ moiety, the diastereomers could be easily separated ($(R_{\text{Ru}}R_{\text{C}}R_{\text{C}})\text{-18c}^+ \text{PF}_6^-$ and $(S_{\text{Ru}}R_{\text{C}}R_{\text{C}})\text{-18c}^+ \text{PF}_6^-$). These efficiently catalyze Friedel-Crafts alkylations of indoles, Michael addition reactions of 1,3-dicarbonyl equivalents to nitroalkenes, and additions of cyclic-β-keto esters to dialkyl azodicarboxylates. In all of these reactions, products are obtained in high yields even in the absence of any external base, showing that the bifunctional capability of the ligand is retained. Most of the reactions are also highly enantioselective (90-99% ee). When compared, the free ligand performs poorly in catalytic efficacies and enantioselectivities, establishing the importance of the metal in tuning the properties of the attached ligand, influencing any interactions happening in the second coordination sphere, and thereby enhancing the catalytic abilities. The configuration of the product is usually controlled by the carbon as opposed to the ruthenium stereocenter.

Similarly, enantiopure chiral-at-metal ruthenium **GBI** complex ($[(\eta^5\text{-C}_5\text{Ph}_5)\text{Ru}(\text{CO})\text{GBI}]^+ \text{BARf}^-$ ($(S_{\text{Ru}})\text{-48}^+ \text{BARf}^-$) bearing a bulky electron withdrawing pentaphenylcyclopentadienyl ligand could also be synthesized. The metal complex is also an efficient catalyst for Friedel-Crafts alkylations and Michael addition reactions

under aerobic conditions. Importantly, the addition of thiophenol (**28**) to *trans*-3-cinnamoyloxazolidin-2-one (**50**) is highly enantioselective (>99%). Here, the ruthenium atom is the only stereocenter in the molecule, contrary to complexes mentioned previously. This indicates that the metal stereocenter alone can influence the second coordination sphere interaction to such an extent that enantioselectivities as high as >99% can be achieved.

Isolation of these aforementioned enantiopure ruthenium complexes followed by their successful application in catalysis establishes the viability of using these enantiopure transition metal complexes containing ligand based NH hydrogen bond donors to catalyze enantioselective organic transformations in high yields and enantioselectivities. Furthermore, the neutral complex $(\eta^5\text{-C}_5\text{Ph}_5)\text{Ru}(\text{CO})(\text{GBI-H})$ (**49**), which features a deprotonated **GBI** ligand, is capable of acting as a multifunctional catalyst and promotes Michael addition reactions in the absence of any external base. This new system provides a promising direction for future developments of a multifunctional catalyst system. In these reactions, **49** acts as a base to activate one substrate, hydrogen bonds to the other, and ion pairs with the conjugate base of the first substrate. Each of these represents a second coordination sphere interaction, and expands the horizon of SCSPC.

5.2 Beyond this study

The above studies should inspire chemist to explore numerous other metal complexes that could be potential hydrogen bond donor catalysts and participate in SCSPC. Furthermore, these overlooked hydrogen bond donors could easily be fine-tuned

for a plethora of additional functionalities and thereby promoting numerous other enantioselective organic transformations.

REFERENCES

- (1) (a) Jeffrey, G. A. *An Introduction to Hydrogen Bonding*; Oxford University Press: New York, 1997. (b) Steiner, T. *Angew. Chem., Int. Ed.* **2002**, *41*, 48-76; *Angew. Chem.* **2002**, *114*, 50-80. (c) Arunan, E.; Desiraju, G. R.; Klein, R. A.; Sadlej, J.; Scheiner, S.; Alkorta, I.; Clary, D. C.; Crabtree, R. H.; Dannenberg, J. J.; Hobza, P.; Kjaergaard, H. G.; Legon, A. C.; Mennucci, B.; Nesbitt, D. J. *Pure Appl. Chem.* **2011**, *83*, 1637-1641.
- (2) Siden, R. R. *DNA Structure and Function*; Academic Press: San Diego, CA, 1994.
- (3) (a) White, A. J.; Wharton, C. W. *Biochem. J.* **1990**, *270*, 627-637. (b) Gerlt, J. A.; Kreevoy, M. M.; Cleland, W. W.; Frey, P. A. *Chem. Biol.* **1997**, *4*, 259-267. (c) Perrin, C. L.; Nielson, J. B. *Annu. Rev. Phys. Chem.* **1997**, *48*, 511-544. (d) Cleland, W. W.; Frey, P. A. Gerlt, J. A. *J. Biol. Chem.* **1998**, *273*, 25529-25532. (e) Guo, H.; Salahub, D. R. *Angew. Chem., Int. Ed.* **1998**, *37*, 2985-2990; *Angew. Chem.* **1998**, *110*, 3155-3160. (f) Tuchscherer, G.; Lehmann, C.; Mathieu, M. *Angew. Chem., Int. Ed.* **1998**, *37*, 2990-2993; *Angew. Chem.* **1998**, *110*, 3160-3164. (g) Schowen, K. B.; Limbach, H.-H.; Denisov, G. S.; Schowen, R. L. *Biochim. Biophys. Acta* **2000**, *1458*, 43-62. (h) Simón, L.; Goodman, J. M. *J. Org. Chem.* **2010**, *75*, 1831-1840.
- (4) Moore, T. S.; Winmill, T. F. *J. Chem. Soc., Trans.* **1912**, *101*, 1635-1676.
- (5) (a) Whitesides, G. M.; Simanek, E. E.; Mathias, J. P.; Seto, C. T.; Chin, D. N.; Mammen, M.; Gordon, D. M. *Acc. Chem. Res.* **1995**, *28*, 37-44. (b) Sherrington, D. C.; Taskinen, K. A. *Chem. Soc. Rev.* **2001**, *30*, 83-93.
- (6) Amendola, V.; Fabbrizzi, L.; Mosca, L. *Chem. Soc. Rev.* **2010**, *39*, 3889-3915.

- (7) Brammer, L.; Swearingen, J. K.; Bruton, E. A.; Sherwood, P. *Proc. Natl. Acad. Sci. U.S.A.* **2002**, *99*, 4956-4961.
- (8) (a) Kirby, A. J. *Angew. Chem., Int. Ed.* **1996**, *35*, 706-724; *Angew. Chem.* **1996**, *108*, 770-790. (b) Zhao, Y.; Rodrigo, J.; Hoveyda, A. H.; Snapper, M. L. *Nature* **2006**, *443*, 67-70. (c) Davie, E. A. C.; Mennen, S. M.; Xu, Y.; Miller, S. J. *Chem. Rev.* **2007**, *107*, 5759-5812. (d) Knowles, R. R.; Jacobsen, E. N. *Proc. Natl. Acad. Sci. U.S.A.* **2010**, *107*, 20678-20685. (e) Wennemers, H. *Chem. Comm.* **2011**, *47*, 12036-12041. (f) Parmar, D.; Sugiono, E.; Raja, S.; Rueping, M. *Chem. Rev.* **2014**, *114*, 9047-9153. (g) Fang, X.; Wang, C.-J. *Chem. Commun.* **2015**, *51*, 1185-1197.
- (9) Representative reports from 2014-2015: (a) Kim, H. J.; Ajitha, M. J.; Lee, Y.; Ryu, J.; Kim, J.; Lee, Y.; Jung, Y.; Chang, S. *J. Am. Chem. Soc.* **2014**, *136*, 1132-1140. (b) Wang, W.; Kumar, M.; Hammond, G. B.; Xu, B. *Org. Lett.* **2014**, *16*, 636-639. (c) McGuirk, C. M.; Katz, M. J.; Stern, C. L.; Sarjeant, A. A.; Hupp, J. T.; Farha, O. K.; Mirkin, C. A. *J. Am. Chem. Soc.* **2015**, *137*, 919-925.
- (10) (a) Etter, M. C.; Urbańczyk-Lipkowska, Z.; Zia-Ebrahimi, M.; Panunto, T. W. *J. Am. Chem. Soc.* **1990**, *112*, 8415-8426. (b) Etter, M. C. *Acc. Chem. Res.* **1990**, *23*, 120-126.
- (11) Curran, D. P.; Kuo, L. H. *Tetrahedron Lett.* **1995**, *36*, 6647-6650.
- (12) (a) Dalko, P. I.; Moisan, L. *Angew. Chem., Int. Ed.* **2004**, *43*, 5138-5175; *Angew. Chem.* **2004**, *116*, 5248-5286. (b) Berkessel, A.; Gröger, H. *Asymmetric Organocatalysis: From Biomimetic Concepts to Application in Asymmetric Synthesis*; Wiley-VCH: Weinheim, 2005; Chapter 1.
- (13) For reviews, see: (a) Doyle, A. G.; Jacobsen, E. N. *Chem. Rev.* **2007**, *107*, 5713-5743. (b) Yu, X.; Wang, W. *Chem. Asian J.* **2008**, *3*, 516-532. (c) Zhang, Z.;

- Schreiner, P. R. *Chem. Soc. Rev.* **2009**, *38*, 1187-1198. (d) Nakanishi, W. Related Organocatalysts (2): Urea Derivatives. In *Superbases for Organic Synthesis: Guanidines, Amidines, Phosphazenes and Related Organocatalysts*; Ishikawa, T., Ed.; John Wiley & Sons: Great Britain, 2009; Chapter 9. (e) Kotke, M.; Schreiner, P. M. (Thio)urea Organocatalysts. In *Hydrogen Bonding in Organic Synthesis*; Pihko, P. M., Ed.; Wiley-VCH: Weinheim, Germany, 2009; Chapter 6.
- (14) (a) Ishikawa, T. Guanidines in Organic Synthesis In *Superbases for Organic Synthesis: Guanidines, Amidines, Phosphazenes and Related Organocatalysts*; Ishikawa, T., Ed.; John Wiley & Sons: Great Britain, 2009; Chapter 4.3. (b) Selig, P. *Synthesis* **2013**, *45*, 703-718.
- (15) (a) Thadani, A. N.; Stankovic, A. R.; Rawal, V. H. *Proc. Natl. Acad. Sci. U.S.A.* **2004**, *101*, 5846-5850. (b) Etzenbach-Effers, K.; Berkessel, A. Noncovalent Organocatalysis Based on Hydrogen Bonding: Elucidation of Reaction Paths by Computational Methods. In *Asymmetric Organocatalysis*; List, B., Ed.; Topics in Current Chemistry Series, Vol. 291; Springer: Berlin, Germany, 2010; Chapter 1. (c) Gratzer, K.; Gururaja, G. N.; Waser, M. *Eur. J. Org. Chem.* **2013**, 4471-4482.
- (16) (a) Unni, A. K.; Takenaka, N.; Yamamoto, H.; Rawal, V. H. *J. Am. Chem. Soc.* **2005**, *127*, 1336-1337. (b) Shen, J.; Tan, C.-H. *Org. Biomol. Chem.* **2007**, *6*, 3229-3236.
- (17) (a) McDougal, N. T.; Schaus, S. E. *J. Am. Chem. Soc.* **2003**, *125*, 12094-12095. (b) McDougal, N. T.; Trevellini, W. L.; Rodgen, S. A.; Kliman, L. T.; Schaus, S. E. *Adv. Synth. Catal.* **2004**, *346*, 1231-1240. (c) Matsui, K.; Takizawa, S.; Sasai, H. *J. Am. Chem. Soc.* **2005**, *127*, 3680-3681. (d) Tillman, A. L.; Dixon, D. *Org. Biomol. Chem.* **2007**, *5*, 606-609. (e) Shibasaki, M.; Matsunaga, S. BINOL. In *Privileged Chiral Ligands and Catalysts*; Zhou, Q.-L., Ed.; Wiley-VCH:

Weinheim, Germany, 2011; Chapter 8.

- (18) (a) Ishikawa, T.; Kumamoto, T. Amidines in Organic Synthesis. In *Superbases for Organic Synthesis: Guanidines, Amidines, Phosphazenes and Related Organocatalysts*; Ishikawa, T., Ed.; John Wiley & Sons: Great Britain, 2009; Chapter 3. (b) Yamamoto, H.; Payette, J. N. Brønsted Acids, H-Bond Donors, and Combined Acid Systems in Asymmetric Catalysis. In *Hydrogen Bonding in Organic Synthesis*; Pihko, P. M., Ed.; Wiley-VCH: Weinheim, Germany, 2009; Chapter 5.
- (19) (a) Alemán, J.; Parra, A.; Jiang, H.; Jørgensen, K. A. *Chem. Eur. J.* **2011**, *17*, 6890-6899. (b) Lu, T.; Wheeler, S. E. *Chem. Eur. J.* **2013**, *19*, 15141-15147.
- (20) (a) Schafer, A. G.; Wieting, J. M.; Mattson, A. E. *Org. Lett.* **2011**, *13*, 5228-5231. (b) Tran, N. T.; Wilson, S. O.; Franz, A. K. *Org. Lett.* **2012**, *14*, 186-189.
- (21) (a) Okino, T.; Hoashi, Y.; Takemoto, Y. *J. Am. Chem. Soc.* **2003**, *125*, 12672-12673. (b) Okino, T.; Hoashi, Y.; Furukawa, T.; Xu, X.; Takemoto, Y. *J. Am. Chem. Soc.* **2005**, *127*, 119-125. (c) Hamza, A.; Schubert, G.; Soós, T.; Pápai, I. *J. Am. Chem. Soc.* **2006**, *128*, 13151-13160. (d) Takemoto, Y. *Chem. Pharm. Bull.* **2010**, *58*, 593-601.
- (22) Zhu, Y.; Malerich, J. P.; Rawal, V. H. *Angew. Chem., Int. Ed.* **2010**, *49*, 153-156; *Angew. Chem.* **2010**, *122*, 157-160.
- (23) Corey, E. J.; Grogan, M. J. *Org. Lett.* **1999**, *1*, 157-160.
- (24) Epstein, L. M.; Shubina, E. S.; Krylov, A. N.; Kreindlin, A. Z.; Rybinskaya, M. I. *J. Orgmet. Chem.* **1993**, *447*, 277-280.
- (25) Brammer, L.; McCann, M. C.; Bullock, R. M.; McMullan, R. K.; Sherwood, P. *Organometallics* **1992**, *11*, 2339-2341.
- (26) Abbreviations: en = 1,2-ethylenediamine; **GBI_{-H}** = 2-guanidinobenzimidazole

that has been deprotonated at N5 (see Scheme 1.3 for atom numbering); dimethyl**GBI-H** = 5,6-dimethyl-2-guanidinobenzimidazole that has been deprotonated; $\text{BAr}_f = \text{B}(3,5\text{-C}_6\text{H}_3(\text{CF}_3)_2)_4$; TRISPHAT = (tris(tetrachlorobenzenediolato)phosphate(V) or $\text{P}(o\text{-C}_6\text{Cl}_4\text{O}_2)_3$. (*M*)-Phos-H = 1,1'-binaphthyl-2,2'-diyl hydrogen phosphate or $\text{HOP}(=\text{O})(o\text{-C}_{10}\text{H}_6\text{O})_2$ with *M* axial chiral configuration, (*M*)-**12**; (*P*)-Phos-H = 1,1'-binaphthyl-2,2'-diyl hydrogen phosphate or $\text{HOP}(=\text{O})(o\text{-C}_{10}\text{H}_6\text{O})_2$ with *P* axial chiral configuration, (*P*)-**12**; (*P*)-Phos⁻ = 1,1'-binaphthyl-2,2'-diyl phosphate or $^-\text{OP}(=\text{O})(o\text{-C}_{10}\text{H}_6\text{O})_2$ with *P* axial chiral configuration;

- (27) (a) Web based Cambridge Crystallographic Data Centre (WebCSD) search results for text "tris(ethylenediamine)-cobalt". (b) Selected examples of $[\text{Co}(\text{en})_3]^{3+} 3\text{X}^-$ salts from the Cambridge Crystallographic Data Centre (CSD Refcodes): ACHXCO, IRIRAC01, ENCOIH, CIXWUB, BIRSUO.
- (28) (a) Miyoshi, K.; Izumoto, S.; Yoneda, H. *Bull. Chem. Soc. Jpn.* **1986**, *59*, 3475-3482. (b) Mizuta, T.; Tada, T.; Kushi, Y.; Yoneda, H. *Inorg. Chem.* **1988**, *27*, 3836-3841. (c) For substituted 1,2-ethylenediamine systems, see: Mizuta, T.; Toshitani, K.; Miyoshi, K.; Yoneda, H. *Inorg. Chem.* **1990**, *29*, 3020-3026.
- (29) (a) Brammer, L. Hydrogen Bonds in Inorganic Chemistry: Application to Crystal Design. In *Crystal Design: Structure and Function*; Desiraju, G. R., Ed.; Vol. 7; Wiley & Sons: England, 2003; Chapter 1. (b) Brammer, L. *Chem. Soc. Rev.* **2004**, *33*, 476-489.
- (30) (a) Colquhoun, H. M.; Stoddart, J. F.; Williams, D. J. *Angew. Chem., Int. Ed. Engl.* **1986**, *25*, 487-507; *Angew. Chem.* **1986**, *98*, 483-503. (b) Raymo, F. M.; Stoddart, J. F. *Chem. Ber.* **1996**, *129*, 981-990.
- (31) Amoroso, A. J.; Arif, A. M.; Gladysz, J. A. *Organometallics* **1997**, *16*, 6032-

6034.

- (32) (a) B. Breit; Seiche, W. *J. Am. Chem. Soc.* **2003**, *125*, 6608-6609. (b) Breit, B.; Seiche, W. *Angew. Chem., Int. Ed.* **2005**, *44*, 1640-1643; *Angew. Chem.* **2005**, *117*, 1666-1669. (c) Seiche, W.; Schuschkowski, A.; Breit, B. *Adv. Synth. Catal.* **2005**, *347*, 1488-1494. (d) Breit, B. *Angew. Chem., Int. Ed.* **2005**, *44*, 6816-6825; *Angew. Chem.* **2005**, *117*, 6976-6986. (e) Weis, M.; Waloch, C.; Seiche, W.; Breit, B. *J. Am. Chem. Soc.* **2006**, *128*, 4188-4189. (f) Greef, M. D.; Breit, B. *Angew. Chem., Int. Ed.* **2009**, *48*, 551-554; *Angew. Chem.* **2009**, *121*, 559-562. (g) Wieland, J.; Breit, B. *Nat. Chem.* **2010**, *2*, 832-837.
- (33) Meeuwissen, J.; Reek, J. N. H. *Nat. Chem.* **2010**, *2*, 615-621.
- (34) Noyori, R.; Ohkuma, T. *Angew. Chem., Int. Ed.* **2001**, *40*, 40-73; *Angew. Chem.* **2001**, *113*, 40-75.
- (35) (a) Andrade-López, N.; Ariza-Castolo, A.; Contreras, R.; Vázquez-Olmos, A.; Barba-Behrens, N.; Tlahuext, H. *Heteroat. Chem.* **1997**, *8*, 397-410. (b) Cenicerós-Gómez, A. E.; Barba-Behrens, N.; Bernès, S.; Nöth, H.; Castillo-Blum, S. E. *Inorg. Chim. Acta* **2000**, *304*, 230-236. (c) Castillo-Blum, S. E.; Barba-Behrens, N. *Coord. Chem. Rev.* **2000**, *196*, 3-30.
- (36) Steel, P. J. *J. Heterocycl. Chem.* **1991**, *28*, 1817-1818.
- (37) (a) Caira, M. R.; Watson, W. H.; Vögtle, F.; Müller, W. *Acta Cryst.* **1984**, *C40*, 1047-1050. (b) Watson, W. H.; Galloy, J.; Grossie, D. A. *J. Org. Chem.* **1984**, *49*, 347-353.
- (38) Bishop, M. M.; Lindoy, L. F.; Thorn-Seshold, O. T.; Piltz, R. O.; Turner, P. J. *Heterocycl. Chem.* **2001**, *38*, 1377-1382.
- (39) (a) Willis, P. G. Doctoral Thesis, University of Kentucky, 2001. (b) Chen, J.; Willis, P. G.; Parkin, S.; Cammers, A. *Eur. J. Org. Chem.* **2005**, 171-178. (c)

- Bishop, M. M.; Lee, A. H. W.; Lindoy, L. F.; Turner, P. *Polyhedron* **2003**, *22*, 735-743.
- (40) (a) Barba-Behrens, N.; Vázquez-Olmos, A.; Castillo-Blum, S. E.; Höjer, G.; Meza-Höjer, S.; Hernández, R. M.; Rosales-Hoz, M. J.; Vincente, R.; Escuer, A. *Transition Met. Chem.* **1996**, *21*, 31-37. (b) Andrade-López, N.; Cartas-Rosado, R.; García-Baéz, E.; Contreras, R.; Tlahuext, H. *Heteroat. Chem.* **1998**, *9*, 399-409. (c) Fialon, M.-P.; Andrade-López, N.; Barba-Behrens, N.; Contreras, R. *Heteroat. Chem.* **1998**, *9*, 637-641. (d) Sanchez-Guadarrama, O.; Lopez-Sandoval, H.; Sanchez-Bartez, F.; Gracia-Mora, I.; Hopfl, H.; Barba-Behrens, N. *J. Inorg. Biochem.* **2009**, *103*, 1204-1213.
- (41) Arablo, N.; Torabi, S. A. A. A.; Morsali, A.; Skelton, W. B.; White, A. H. *Aust. J. Chem.* **2003**, *56*, 945-947.
- (42) (a) Cram, D. J. *Angew. Chem., Int. Ed. Engl.* **1986**, *25*, 1039-1057; *Angew. Chem.* **1986**, *98*, 1041-1060. (b) Desper, J. M.; Gellman, S. H. *J. Am. Chem. Soc.* **1990**, *112*, 6732-6734. (c) Wittenberg, J. B.; Isaacs, L. Complementarity and Preorganization. In *Supramolecular Chemistry: From Molecules to Nanomaterials*; Gale, P., Steed, J., Eds.; Vol. 1; Wiley & Sons: Hoboken, NJ, 2012.
- (43) Cram, D. J.; Lein, G. M. *J. Am. Chem. Soc.* **1985**, *107*, 3657-3668.
- (44) (a) Meyer, C. D.; Joiner, C. S.; Stoddart, J. F. *Chem. Soc. Rev.* **2007**, *36*, 1705-1723. (b) Griffiths, K. E.; Stoddart, J. F. *Pure Appl. Chem.* **2008**, *80*, 485-506. (c) Breiner, B.; Nitschke, J. R. *Nat. Chem.* **2010**, *2*, 6-7. (d) Stefankiewicz, A. R.; Sambrook, M. R.; Sanders, J. K. M. *Chem. Sci.* **2012**, *3*, 2326-2329. (e) Zhang, Z.; Zaworotko, M. J. *Chem. Soc. Rev.* **2014**, *43*, 5444-5455.
- (45) Barnes, J. C.; Juriček, M.; Strutt, N. L.; Frascioni, M.; Sampath, S.; Giesener, M.

- A.; McGrier, P. L.; Bruns, C. J.; Stern, C. L.; Sarjeant, A. A.; Stoddart, J. F. *J. Am. Chem. Soc.* **2013**, *135*, 183-192.
- (46) (a) Shima, T.; Hampel, F.; Gladysz, J. A. *Angew. Chem., Int. Ed.* **2004**, *43*, 5537-5540; Shima, T.; Hampel, F.; Gladysz, J. A. *Angew. Chem.* **2004**, *116*, 5653-5656. (b) Skopek, K.; Hershberger, M. C.; Gladysz, J. A. *Coord. Chem. Rev.* **2007**, *251*, 1723-1733.
- (47) Ichijo, T.; Sato, S.; Fujita, M. *J. Am. Chem. Soc.* **2013**, *135*, 6786-6789.
- (48) Takao, K.; Suzuki, K.; Ichijo, T.; Sato, S.; Asakura, H.; Teramura, K.; Kato, K.; Ohba, T.; Morita, T.; Fujita, M. *Angew. Chem., Int. Ed.* **2012**, *51*, 5893-5896; *Angew. Chem.* **2012**, *124*, 5995-5998.
- (49) For reviews, see: (a) Crowley, J. D.; Goldup, S. M.; Lee, A.-L.; Leigh, D. A.; McBurney, R. T. *Chem. Soc. Rev.* **2009**, *38*, 1530-1541. (b) Beves, J. E.; Blight, B. A.; Campbell, C. J.; Leigh, D. A.; McBurney, R. T. *Angew. Chem., Int. Ed.* **2011**, *50*, 9260-9327; *Angew. Chem.* **2011**, *123*, 9428-9499.
- (50) (a) Alvarez, J.; Wang, Y.; Gómez-Kaifer, M.; Kaifer, A. E. *Chem. Commun.* **1998**, 1455-1456. (b) Wu, Z.-Q.; Shao, X.-B.; Li, C.; Hou, J.-L.; Wang, K.; Jiang, X.-K.; Li, Z.-T. *J. Am. Chem. Soc.* **2005**, *127*, 17460-17468. (c) Binder, W. H.; Zirbs, R. Supramolecular Polymers and Networks with Hydrogen Bonds in the Main and Side-Chain. In *Hydrogen Bonded Polymers*; Binder, W., Ed.; Advances in Polymer Science, Volume 207; Springer: Heidelberg, Germany, 2007; Chapter 1. (d) Bouteiller, L. Assembly via Hydrogen Bonds of Low Molar Mass Compounds into Supramolecular Polymers. In *Hydrogen Bonded Polymers*; Binder, W., Ed.; Advances in Polymer Science, Volume 207; Springer: Heidelberg, Germany, 2007; Chapter 2. (e) Lee, S.; Hua, Y.; Park, H.; Flood, A. H. *Org. Lett.* **2010**, *12*, 2100-2102.

- (51) Bianchi, A.; García-España, E. Thermodynamic Aspects of Anion Coordination. In *Anion Coordination Chemistry*; Bowman-James, K.; Bianchi, A.; García-España, E., Eds; Wiley-VCH: Weinheim, 2011; Chapter 2.
- (52) Hua, Y.; Ramabhadran, R. O.; Karty, J. A.; Raghavachari, K.; Flood, A. H. *Chem. Commun.* **2011**, 47, 5979-5981.
- (53) (a) Liang-An, C.; Xu, W.; Huang, B.; Ma, J.; Wang, L.; Xi, J.; Harms, K.; Gong, L.; Meggers, E. *J. Am. Chem. Soc.* **2013**, 135, 10598-10601. (b) For similar systems see: Chen, L.-A.; Tang, X.; Xi, J.; Xu, W.; Gong, L.; Meggers, E. *Angew. Chem., Int. Ed.* **2013**, 52, 14021-14025; *Angew. Chem.* **2013**, 125, 14271-14275.
- (54) (a) Dalko, P. I.; Moisan, L. *Angew. Chem., Int. Ed.* **2004**, 43, 5138-5175; *Angew. Chem.* **2004**, 116, 5248-5286. (b) Nakanishi, W. Related Organocatalysts (2): Urea Derivatives. In *Superbases for Organic Synthesis: Guanidines, Amidines, Phosphazenes and Related Organocatalysts*; Ishikawa, T., Ed.; John Wiley & Sons: Great Britain, 2009; Chapter 9. (c) Kotke, M.; Schreiner, P. M. (Thio)urea Organocatalysts. In *Hydrogen Bonding in Organic Synthesis*; Pihko, P. M., Ed.; Wiley-VCH: Weinheim, Germany, 2009; Chapter 6.
- (55) Schreiner, P. R.; Wittkopp, A. *Org. Lett.* **2002**, 4, 217-220.
- (56) Lippert, K. M.; Hof, K.; Gerbig, D.; Ley, D.; Hausmann, H.; Guenther, S.; Schreiner, P. R. *Eur. J. Org. Chem.* **2012**, 5919-5927.
- (57) Wittkopp, A.; Schreiner, P. R. *Chem. Eur. J.* **2003**, 9, 407-414.
- (58) Jakab, G.; Tancon, C.; Zhang, Z.; Lippert, K. M.; Schreiner, P. R. *Org. Lett.* **2012**, 7, 1724-1727.
- (59) (a) Beck, W.; Sünkel, K. *Chem. Rev.* **1988**, 88, 1405-1421. (b) Strauss, S. H. *Chem. Rev.* **1993**, 93, 927-942. (c) Krossing, I.; Raabe, I. *Angew. Chem., Int. Ed.*

- 2004**, *43*, 2066-2090; *Angew. Chem.* **2004**, *116*, 2116-2142. (d) Díaz-Torres, R.; Alvarez, S. *Dalton Trans.* **2011**, *40*, 10742-10750.
- (60) (a) Lungwitz, R.; Spange, S. *New J. Chem.* **2008**, *32*, 392-394. (b) Cláudio, A. F. M.; Swift, L.; Hallett, J. P.; Welton, T.; Coutinho, J. A. P.; Freire, M. G. *Phys. Chem. Chem. Phys.* **2014**, *16*, 6593-6601.
- (61) Wolf, I. M. Doctoral Thesis, Universität Erlangen-Nürnberg, 2010.
- (62) (a) Bauer, E. B. *Chem. Soc. Rev.* **2012**, *41*, 3153-3167. (b) Kumar, P.; Gupta, R. K.; Pandey, D. S. *Chem. Soc. Rev.* **2014**, *43*, 707-733.
- (63) (a) Kataoka, Y.; Saito, Y.; Nagata, K.; Kitamura, K.; Shibahara, A.; Tani, K. *Chem. Lett.* **1995**, *24*, 833-834. (b) Pfister, B.; Stauber, R.; Salzer, A. *J. Organomet. Chem.* **1997**, *533*, 131-141. (c) Therrien, B.; König, A.; Ward, T. R. *Organometallics* **1999**, *18*, 1565-1568. (d) Trost, B. M.; Vidal, B.; Thommen, M. *Chem. Eur. J.* **1999**, *5*, 1055-1069. (e) Faller, J. W.; Fontaine, P. P. *Organometallics* **2005**, *24*, 4132-4138. (f) Bregman, H.; Meggers, E. *Org. Lett.* **2006**, *8*, 5465-5468. (g) Tsuno, T. Doctoral Thesis, Universität Regensburg, 2007; Chapter 3. (h) Ruzziconi, R.; Bellachioma, G.; Ciancaleoni, G.; Lepri, S.; Superchi, S.; Zanasi, R.; Monaco, G. *Dalton Trans.* **2014**, *43*, 1636-1650.
- (64) (a) Therrien, B.; Ward, T. R. *Angew. Chem., Int. Ed.* **1999**, *38*, 405-408; *Angew. Chem.* **1999**, *111*, 418-421. (b) Pinto, P.; Marconi, G.; Heinemann, F. W.; Zenneck, U. *Organometallics* **2004**, *23*, 374-380. (c) Djukic, J.-P.; Berger, A.; Duquenne, M.; Pfeffer, M.; de Cian, A.; Kyritsakas-Gruber, N. *Organometallics* **2004**, *23*, 5757-5767. (d) da Costa, A. P.; Mata, J. A.; Royo, B.; Peris, E. *Organometallics* **2010**, *29*, 1832-1838.
- (65) Yakelis, N. A.; Bergman, R. G. *Organometallics* **2005**, *24*, 3579-3581.
- (66) Selected examples of guanidinium salts from the Cambridge Crystallographic

Data Centre (CSD Refcodes): ABUNOB, BACDIS, GUDPYP, IZIJEH, KEDDEC, LOSCIF.

- (67) All examples of 2-aminobenzimidazolium salts from the Cambridge Crystallographic Data Centre (CSD Refcodes): DOKZEJ, EMIHAJ, HOFJAN, HUZSIE, JEJMUH, SIXYUU, SIXZAB, SIZCOU, UPETOZ.
- (68) The following papers describe hydrogen bond donor catalysts for the Friedel-Crafts alkylation of **5a** by **6**: (a) Zhuang, W.; Hazell, R. G.; Jørgensen, K. A. *Org. Biomol. Chem.* **2005**, *3*, 2566-2571. (b) Fleming, E. M.; McCabe, T.; Connon, S. J. *Tetrahedron Lett.* **2006**, *47*, 7037-7042. (c) Akalay, D.; Dürner, D.; Bats, J. W.; Bolte, M.; Göbel, M. W. *J. Org. Chem.* **2007**, *72*, 5618-5624. (d) Takenaka, N.; Sarangthem, R. S.; Seerla, S. K. *Org. Lett.* **2007**, *15*, 2819-2822. (e) Gu, Y.; Barrault, J.; Jérôme, F. *Adv. Synth. Catal.* **2008**, *350*, 2007-2012. (f) Rodriguez, A. A.; Yoo, H.; Ziller, J. W.; Shea, K. J. *Tetrahedron Lett.* **2009**, *50*, 6830-6833. (g) Marqués-López, E.; Alcaine, A.; Tejero, T.; Herrera, R. P. *Eur. J. Org. Chem.* **2011**, 3700-3705. (h) Niu, F.; Wu, J.; Zhang, L.; Li, P.; Zhu, J.; Wu, Z.; Wang, C.; Song, W. *ACS Catal.* **2011**, *1*, 1158-1161. (i) Tran, N. T.; Wilson, S. O.; Franz, A. K. **2012**, *14*, 186-189. (j) Dong, X.-W.; Liu, T.; Hu, Y.-Z.; Liu, X.-Y.; Che, C.-M. *Chem. Commun.* **2013**, *49*, 7681-7683. (k) Shokri, A.; Wang, X.-B.; Kass, S. R. *J. Am. Chem. Soc.* **2013**, *135*, 9525-9530. (l) Carmona, D.; Lamata, M. P.; Pardo, P.; Rodríguez, R.; Lahoz, F. J.; García-Orduña, P.; Alkorta, I.; Elguero, J.; Oro, L. A. *Organometallics* **2014**, *33*, 616-619.
- (69) Bruce, M. I.; Windsor, N. J. *Aust. J. Chem.* **1977**, *30*, 1601-1604.
- (70) Scherer, A. Doctoral Thesis, Universität Erlangen-Nürnberg, 2009.
- (71) This experiment was originally conducted by Dr. A. Scherer and repeated as part of this work.

- (72) King, R. B. *Inorg. Chim. Acta.* **1968**, *2*, 454-458. These page numbers correspond to those on the PDF file downloaded from the publisher. However, as of March 2015, the publisher's table of contents on the web indicates the page numbers 449-453.
- (73) Multiple attempts were sometimes required to obtain reasonable yields of 8^+ PF_6^- and 8^+ BAr_f^- in the initial step A1.
- (74) Gill, T. P.; Mann, K. R. *Organometallics* **1982**, *1*, 485-488.
- (75) Scherer, A.; Mukherjee, T.; Hampel, F.; Gladysz, J. A. *Organometallics* **2014**, *33*, 6709-6722.
- (76) (a) Bordwell, F. G.; Algrim, D. J.; Harrelson, J. A. *J. Am. Chem. Soc.* **1988**, *110*, 5903-5904. (b) Bordwell, F. G.; Ji, G. Z. *J. Am. Chem. Soc.* **1991**, *113*, 8398-8401. (c) Brown, T. N.; Mora-Diez, N. *J. Phys. Chem. B* **2006**, *110*, 9270-9279.
- (77) Sullivan, J. D.; Giles, R. L.; Looper, R. E. *Curr. Bioact. Compd.* **2009**, *5*, 39-78.
- (78) Taylor, P. J.; Wait, A. R. *J. Chem. Soc., Perkin Trans. 2* **1986**, 1765-1770.
- (79) Oro, L. A.; Ciriano, M. A.; Campo, M.; Foces-Foces, C.; Cano, F. H. *J. Organomet. Chem.* **1985**, *289*, 117-131.
- (80) Berkessel, A.; Cleemann, F.; Mukherjee, S.; Müller, T. N.; Lex, J. *Angew Chem., Int. Ed.* **2005**, *44*, 807-811; *Angew. Chem.* **2005**, *117*, 817-821.
- (81) (a) Lam, S. Y.; Louis, C.; Benoit, R. L. *J. Am. Chem. Soc.* **1976**, *98*, 1156-1160. (b) Meshcheryakov, D.; Arnaud-Neu, F.; Böhmer, V.; Bolte, M.; Hubscher-Bruder, V.; Jobin, E.; Thondorf, I.; Werner, S. *Org. Biomol. Chem.* **2008**, *6*, 1004-10014. (c) Amendola, V.; Bergamaschi, G.; Boiocchi, M.; Fabbrizzi, L.; Milani, M. *Chem. Eur. J.* **2010**, *16*, 4368-4380.
- (82) Only a single signal was observed for the five NH protons, and it integrated to 4H, suggestive of some H/D exchange.

- (83) Only a single signal was observed for the four NH protons, and it integrated to 3H, suggestive of some H/D exchange.
- (84) For an alternative microwave procedure see reference 75.
- (85) An exact yield cannot be calculated due to the indeterminate hydration level of the RuCl₃.
- (86) This complex was purchased from ACROS or prepared by a literature method: Trost, B. M.; Older, C. M. *Organometallics* **2002**, *21*, 2544-2546. The commercial material contained up to 10% of the precursor [(η⁵-C₅H₅)Ru(C₆H₆)]⁺ PF₆⁻, but gave equally good results.
- (87) The workup was carried out under ambient laboratory conditions.
- (88) The very broad signal precluded an accurate integration.
- (89) This sample cannot be represented as analytically pure, but the microanalytical data are provided to illustrate the best result obtained to date.
- (90) **H**_{(P)-Phos}, **C**_{(P)-Phos}, and **P**_{(P)-Phos} denote the proton, carbon, and phosphorous atoms of (P)-Phos,²⁶ respectively.
- (91) Herrera, R. P.; Sgarzani, V.; Bernardi, L.; Ricci, A. *Angew. Chem., Int. Ed.* **2005**, *44*, 6576-6579; *Angew. Chem.* **2005**, *117*, 6734-6737.
- (92) APEX2 "Program for Data Collection on Area Detectors" BRUKER AXS Inc., 5465 East Cheryl Parkway, Madison, WI 53711-5373 USA.
- (93) SADABS, Sheldrick, G. M. "Program for Absorption Correction of Area Detector Frames", BRUKER AXS Inc., 5465 East Cheryl Parkway, Madison, WI 53711-5373 USA.
- (94) Sheldrick, G. M. *Acta Cryst. A* **2008**, *64*, 112-122.
- (95) Brunner, H. *Eur. J. Inorg. Chem.* **2001**, 905-912.
- (96) Ganter, C. *Chem. Soc. Rev.* **2003**, *32*, 130-138.

- (97) Amouri, H., Gruselle, M. Some Examples of Chiral Organometallic Complexes and Asymmetric Catalysis. In *Chirality in Transition Metal Chemistry: Molecules, Supramolecular Assemblies and Materials*; Amouri, H., Gruselle, M., Eds; John Wiley & Sons: Great Britain, 2008, Chapter 3.1.
- (98) Merrifield, J. H.; Strouse, C. E.; Gladysz, J. A. *Organometallics* **1982**, *1*, 1204-1211.
- (99) Mimassi, L.; Cordier, C.; Guyard-Duhayon, C.; Mann, B. E.; Amouri, H. *Organometallics* **2007**, *26*, 860-864.
- (100) Amouri, H., Gruselle, M. Chiral Recognition in Organometallic and Coordination Compounds. In *Chirality in Transition Metal Chemistry: Molecules, Supramolecular Assemblies and Materials*; Amouri, H., Gruselle, M., Eds; John Wiley & Sons: Great Britain, 2008, Chapter 4, Table 4.1.
- (101) Netz, A.; Amberg, W.; Lange, U.; Ochse, M.; Kling, A.; Hutchins, C. W.; Garcia-Ladona, F.-X.; Wernet, W. German Patent 102004008141; *Chem. Abstr.* **2005**, *143*, 266930.
- (102) Ganesh, M; Seidel, D. *J. Am. Chem. Soc.* **2008**, *130*, 16464-16465.
- (103) Cook, J. H., II.; McDonald, I. M.; King, D.; Olson, R. E.; Wang, N.; Iwuagwu, C. I.; Zusi, F. C.; Macor, J. E. U.S. Patent WO 2009131926 A1; *Chem. Abs.* **2009**, *151*, 508582.
- (104) Mukherjee, T.; Ganzmann, C.; Bhuvanesh, N.; Gladysz, J. A. *Organometallics* **2014**, *33*, 6723-6737.
- (105) Ganzmann, C. Doctoral Thesis, Universität Erlangen-Nürnberg, 2010.
- (106) This experiment was conducted by Dr. C. Ganzmann, see also reference 105.
- (107) This experiment was originally conducted by Dr. C. Ganzmann and repeated as part of this work.

- (108) Garratt, P. J.; Hobbs, C. J.; Wrigglesworth, R. *Tetrahedron* **1989**, *45*, 829-834.
- (109) This mixture of diastereomers has been similarly generated previously, but no separation was reported.
- (110) Brunner, H.; Ike, H.; Muschiol, M.; Tsuno, T.; Koyama, k.; Kurosawa, T.; Zabel, M. *Organometallics* **2011**, *30*, 3666-3676.
- (111) Dewey, M. A.; Stark, G. A.; Gladysz, J. A. *Organometallics* **1996**, *15*, 4798-4807.
- (112) Snelders, D. J. M.; Kunna, K.; Müller, C.; Vogt, D.; van Koten, G.; Klein Gebbink, R. J. M. *Tetrahedron: Asymmetry* **2010**, *21*, 1411.
- (113) (a) Amouri, H.; Caspar, R.; Gruselle, M.; Guyard-Duhayon, C.; Boubekeur, K.; Lev, D. A.; Collins, L. S. B.; Grotjahn, D. B. *Organometallics* **2004**, *23*, 4338-4341. (b) Mimassi, L.; Guyard-Duhayon, C.; Rager, M. N.; Amouri, H. *Inorg. Chem.* **2004**, *43*, 6644-6649. (c) Sénéchal-David, K.; Toupet, L.; Maury, O.; Bozec, H. L. *Cryst. Growth Des.* **2006**, *6*, 1493-1496. (d) Correia, I.; Amouri, H.; Cordier, C. *Organometallics* **2007**, *26*, 1150-1156.
- (114) (a) Shevchenko, I. V.; Fischer, A.; Jones, P. G.; Schmutzler, R. *Chem. Ber.* **1992**, *125*, 1325-1332. The shortest N···O distances are 3.13 and 3.00 Å. (b) Lacour, L.; Ginglinger, C.; Grivet, C.; Bernardinelli, G. *Angew. Chem., Int. Ed.* **1997**, *36*, 608-610; *Angew. Chem.* **1997**, *109*, 660-662. The shortest N···O distance is 3.06 Å, and the H···O distance is 2.27 Å.
- (115) (a) Jones, P.; Vagg, R. S.; Williams, P. A. *Inorg. Chem.* **1984**, *23*, 4110-4111. (b) Brunner, H.; Weber, M.; Zabel, M.; Zwack, T. *Angew. Chem., Int. Ed.* **2003**, *42*, 1859-1862; *Angew. Chem.* **2003**, *115*, 1903-1907. (c) Dreos, R.; Mechi, L.; Nardin, G.; Randaccio, L.; Siega, P. *J. Organomet. Chem.* **2005**, *690*, 3815-3821.
- (116) (a) Yamaguchi, Y.; Nagashima, H. *Organometallics* **2000**, *19*, 725-727. (b)

- Standfest-Hauser, C. M.; Mereiter, K.; Schmid, R.; Kirchner, K. *Eur. J. Inorg. Chem.* **2003**, 1883-1892. (c) Bregman, H.; Williams, D. S.; Atilla, G. E.; Carroll, P. J.; Meggers, E. *J. Am. Chem. Soc.* **2004**, *126*, 13594-13595. (d) Takemoto, S.; Oshio, S.; Shiromoto, T.; Matsuzaka, H. *Organometallics* **2005**, *24*, 801-804. (e) Petrovic, D.; Glöge, T.; Bannenberg, T.; Hrib, C. G.; Randoll, S.; Jones, P. G.; Tamm, M. *Eur. J. Inorg. Chem.* **2007**, 3472-3475. (f) Huang, H.; Hughes, R. P.; Rheingold, A. L. *Polyhedron* **2008**, *27*, 734-738.
- (117) (a) Chou, C.-K.; Miles, D. L.; Bau, R.; Flood, T. C. *J. Am. Chem. Soc.* **1978**, *100*, 7271-7278. (b) Brunner, H. *Adv. Organomet. Chem.* **1980**, *18*, 151-206.
- (118) The DFT calculations were carried out in collaboration with Dr. Liza Perez, Department of Chemistry, Texas A&M University, College Station.
- (119) The following papers describe hydrogen bond donor catalysts for the reaction of **5b** and **6**: (a) Dessole, G.; Herrera, R. P.; Ricci, A. *Synlett* **2004**, *13*, 2374-2378. (b) Zhuang, W.; Hazell, R. G.; Jørgensen, K. A. *Org. Biomol. Chem.* **2005**, *3*, 2566-2571. (c) Herrera, R. P.; Sgarzani, V.; Bernardi, L.; Ricci, A. *Angew. Chem., Int. Ed.* **2005**, *44*, 6576-6579; *Angew. Chem.* **2005**, *117*, 6734-6737. (d) Fleming, E. M.; McCabe, T.; Connon, S. J. *Tetrahedron Lett.* **2006**, *47*, 7037-7042. (e) Akalay, D.; Dürner, G.; Bats, J. W.; Bolte, M.; Göbel, M. W. *J. Org. Chem.* **2007**, *72*, 5618-5624. (f) Takenaka, N.; Sarangthem, R. S.; Seerla, S. K. *Org. Lett.* **2007**, *9*, 2819-2822. (g) Rodriguez, A. A.; Yoo, H.; Ziller, J. W.; Shea, K. J. *Tetrahedron Lett.* **2009**, *50*, 6830-6833. (h) Marqués-López, E.; Alcaine, A.; Tejero, T.; Herrera, R. P. *Eur. J. Org. Chem.* **2011**, 3700-3705. (i) Tran, N. T.; Wilson, S. O.; Franz, A. K. *Org. Lett.* **2012**, *14*, 186-189. (j) Shokri, A.; Wang, X.-B.; Kass, S. R. *J. Am. Chem. Soc.* **2013**, *135*, 9525-9530.
- (120) Other chiral hydrogen bond donors that catalyze the addition of **10b** to **6** with

- yields of >60% and ee values of >40%: (a) Li, H.; Wang, Y.; Tang, L.; Deng, L. *J. Am. Chem. Soc.* **2004**, *126*, 9906-9907. (b) Tereda, M.; Ube, H.; Yaguchi, Y. *J. Am. Chem. Soc.* **2006**, *128*, 1454-1455. (c) Andrés, J. M.; Manzano, R.; Pedrosa, R. *Chem. Eur. J.* **2008**, *14*, 5116-5119. (d) McGarraugh, P.; Brenner, S. E. *Tetrahedron* **2009**, *65*, 449-455. (e) Yan, L. J.; Liu, Q. Z.; Wang, X. L. *Chin. Chem. Lett.* **2009**, *20*, 310-313. (f) Almaşi, D.; Alonso, D. A.; Gómez-Bengoa, E.; Nájera, C. *J. Org. Chem.* **2009**, *74*, 6163-6168. (g) Menguy, L.; Couty, F. *Tetrahedron: Asymmetry* **2010**, *21*, 2385-2389. (h) Li, X.; Deng, H.; Zhang, B.; Li, J.; Zhang, L.; Luo, S.; Cheng, J.-P. *Chem. Eur. J.* **2010**, *16*, 450-455. (i) Camps, P.; Galdeano, C.; Muñoz-Torrero, D.; Rull, J.; Calvet, T.; Font-Bardia, M. *Tetrahedron: Asymmetry* **2011**, *22*, 745-751. (j) Inokuma, T.; Furukawa, M.; Uno, T.; Suzuki, Y.; Yoshida, K.; Yano, Y.; Matsuzaki, K.; Takemoto, Y. *Chem. Eur. J.* **2011**, *17*, 10470-10477. (k) Lee, M.; Zhang, L.; Park, Y.; Park, H.-g. *Tetrahedron* **2012**, *68*, 1452-1459. (l) Suez, G.; Bloch, V.; Nisnevich, G.; Gandelman, M. *Eur. J. Org. Chem.* **2012**, 2118-2122. (m) Puglisi, A.; Benaglia, M.; Annunziata, R.; Siegel, J. S. *ChemCatChem* **2012**, *4*, 972-975. (n) Naicker, T.; Arvidsson, P. I.; Kruger, H. G.; Maguire, G. E. M.; Govender, T. *Eur. J. Org. Chem.* **2012**, 3331-3337. (o) Mayans, E.; Gargallo, A.; Álvarez-Larena, Á.; Illa, O.; Ortuño, R. M. *Eur. J. Org. Chem.* **2013**, 1425-1433. (p) Subba Reddy, B. V.; Swain, M.; Reddy, M.; Yadav, J. S. *R. Soc. Chem. Adv.* **2013**, *3*, 8756-8765.
- (121) Evans, D. A.; Seidel, D. *J. Am. Chem. Soc.* **2005**, *127*, 9958-9959.
- (122) (a) Hwu, J. R.; Keh-Loong, C.; Ananthan, S.; Patel, H. V. *Organometallics* **1996**, *15*, 499-505. (b) Lucet, D.; Sabelle, S.; Kostelitz, O.; Gall, T. L.; Mioskowski, C. *Eur. J. Org. Chem.* **1999**, 2583-2591.
- (123) (a) Flock, A. M.; Krebs, A.; Bolm, C. *Synlett* **2010**, 1219-1222. (b) Nemoto, T.;

- Obuchi, K.; Tamura, S.; Fukuyama, T.; Hamada, Y. *Tetrahedron Lett.* **2011**, *52*, 987-991.
- (124) (a) Manzano, R.; Andrés, J. M.; Muruzábal, M. D. Pedrosa R. *Adv. Synth. Catal.* **2010**, *352*, 3364- 3372. (b) Liu, B.; Han, X.; Dong, Z.; Lv, H.; Zhou, H.-B.; Dong, C. *Tetrahedron: Asymmetry* **2013**, *24*, 1276-1280.
- (125) Han, X.; Luo, J.; Liuab, C.; Lu, Y. *Chem. Commun.* **2009**, 2044-2046.
- (126) Terada, M.; Nakano, M.; Ube, H. *J. Am. Soc. Chem.* **2006**, *128*, 16044-16045.
- (127) For overviews of hydrogen bonding motifs involving donor/acceptor dyads, triads, and higher arrays, see Prins, L. J.; Reinhoudt, D. N.; Timmermann, P. *Angew. Chem., Int. Ed.* **2001**, *40*, 2382-2426; *Angew. Chem.* **2001**, *113*, 2446-2492.
- (128) (a) Zimmerman, S. C.; Murray, T. J. *Tetrahedron Lett.* **1994**, *35*, 4077-4080. (b) Bell, D. A.; Anslyn, E. V. *Tetrahedron* **1995**, *51*, 7161-7172. (c) Blight, B. A.; Camara-Campos, A.; Djurdjevic, S.; Kaller, M.; Leigh, D. A.; McMillan, F. M.; McNab, H.; Slawin, A. M. Z. *J. Am. Chem. Soc.* **2009**, *131*, 14116-14122. (d) Wang, H.-B.; Mudraboyina, B. P.; Wisner, J. A. *Chem. Eur. J.* **2012**, *18*, 1322-1327. (e) See also Blight, B A.; Hunter, C. A.; Leigh, D. A.; McNab, H.; Thomson, P. I. T. *Nat. Chem.* **2011**, *3*, 244-248.
- (129) Dydio, P.; Reek, J. N. H. *Chem. Sci.* **2014**, *5*, 2135-2145.
- (130) Olmstead, W. N.; Bordwell, F. G. *J. Org. Chem.* **1980**, *45*, 3299-3305.
- (131) (a) Mori, K.; Oshiba, M.; Hara, T.; Mizugaki, T.; Ebitani, K.; Kaneda, K. *Tetrahedron Lett.* **2005**, *46*, 4283-4286. (b) For pK_a value of a related compound $\text{CH}_3\text{C}(=\text{O})\text{CH}_2\text{C}(=\text{O})\text{OCH}_2\text{Et}$, see: Bordwell, F. G. *Acc. Chem. Res.* **1988**, *21*, 456-463. (c) Matthews, W. S.; Bares, J. E.; Bartmess, J. E.; Bordwell, F. G.; Cornforth, F. J.; Drucker, G. E.; Margolin, Z.; McCallum, R. J.; McCollum, G.

- J.; Vanier, N. R. *J. Am. Chem. Soc.* **1975**, *97*, 7006-7014.
- (132) Peng, T.-S.; Winter, C. H.; Gladysz, J. A. *Inorg. Chem.* **1994**, *33*, 2534-2542.
- (133) (a) McCooney, S. H.; Connon, S. J. *Angew. Chem., Int. Ed.* **2005**, *44*, 6367-6370; *Angew. Chem.* **2005**, *117*, 6525-6528. (b) For some related catalysts, see: Ye, J.; Dixon, D. J.; Hynes, P. S. *Chem. Commun.* **2005**, 4481-4483.
- (134) See the structure of 2-aminobenzimidazole and **GBI** in Scheme 1 for the atom numbering scheme used for the ^1H and ^{13}C NMR spectra. The assignments are based upon literature and 2D NMR data described in the full paper associated with the previous chapter.⁷⁵
- (135) The C4/7 and C8/9 signals were not observed.
- (136) These microanalytical data feature one or more values outside of normally accepted ranges, but are presented nonetheless as the best fit obtained to date. As noted in the preceding chapter,⁷⁵ most of the ruthenium cyclopentadienyl carbonyl complexes give low nitrogen analyses.
- (137) Commonly, not all NH ^1H NMR signals were observed. In some cases, this could be attributed to H/D exchange with the solvent. In other cases, very broad signals between 8 and 2 ppm could be detected.
- (138) The $^{13}\text{C}\{^1\text{H}\}$ NMR signal with the chemical shift closest to benzene is assigned to the meta aryl carbon: Mann, B. E. *J. Chem. Soc., Perkin Trans. 2* **1972**, 30-34.
- (139) (a) Mitchell, J. M.; Finney, N. S. *Tetrahedron Lett.* **2000**, *41*, 8431-8434. The authors did not characterize the diastereomeric or enantiomeric purity of the (*1R,2R*)-*N*¹,*N*¹-dimethyl-1,2-diaminocyclohexane reported in this paper. However, many have utilized their synthesis to prepare diastereomerically and enantiomerically pure derivatives, per the following references. (b) Zhang, W.; Shi, M. *Synlett* **2007**, 19-30. (c) Douglas, A. F.; Patrick, B. O.; Mehrkhodavandi,

- P. Angew. Chem., Int. Ed.* **2008**, *47*, 2290-2293; *Angew. Chem.* **2008**, *120*, 2322-2325. (d) Steurer, M.; Bolm, C. *J. Org. Chem.* **2010**, *75*, 3301-3310.
- (140) Zhu, Y.; Malerich, J. P.; Rawal, V. H. *Angew. Chem., Int. Ed.* **2010**, *49*, 153-156; *Angew. Chem.* **2010**, *122*, 157-160.
- (141) The diastereomer ratio (dr) of the final product varied somewhat, since the chromatography fractions in which the less polar diastereomer co-eluted with a byproduct were discarded.
- (142) Based upon intensity, this signal is attributed to two coinciding resonances.
- (143) Favarger, F.; Goujon-Ginglinger, C.; Monchaud, D.; Lacour, J. *J. Org. Chem.* **2004**, *69*, 8521-8524.
- (144) Huang, W.-g.; Wang, H.-s.; Huang, G.-b.; Wu, Y.-m.; Pan, Y.-m. *Eur. J. Org. Chem.* **2012**, 5839-5843.
- (145) The absolute configuration was assigned by HPLC using conditions similar to those in the literature.
- (146) Wu, J.; Li, X.; Wu, F.; Wan, B. *Org. Lett.* **2011**, *13*, 4834-4837.
- (147) The ¹H and ¹³C NMR spectra agree well with those previously reported.
- (148) Andrés, J. M.; Manzano, R.; Pedrosa, R. *Chem. Eur. J.* **2008**, *14*, 5116-5119.
- (149) McGarraugh, P. G.; Brenner, S. E. *Tetrahedron* **2009**, *65*, 449-455.
- (150) The absolute configurations were not assigned in the earlier study but are presumed to be analogous to the faster/slower eluting enantiomers of **19a,c-g**.
- (151) The chiral column used differs from that in the literature cited but the order of elution of the well separated enantiomers is presumed to be identical.
- (152) Lee, M.; Zhang, L.; Park, Y.; Park, H.-G. *Tetrahedron* **2012**, *68*, 1452-1459.
- (153) Liu, J.-M.; Wang, X.; Ge, Z.-M.; Sun, Q.; Cheng, T.-M.; Li, R.-T. *Tetrahedron* **2011**, *67*, 636-640.

- (154) The separation of these enantiomers by chiral HPLC has been previously reported but the configurations have not yet been assigned.
- (155) Flack, H. D. *Acta Cryst. A* **1983**, *39*, 876-881.
- (156) (a) Kampen, D.; Reisinger, C. M.; List, B. Chiral Brønsted Acids for Asymmetric Organocatalysis. In *Asymmetric Organocatalysis*; List, B., Ed.; Topics in Current Chemistry Series, Vol. 291; Springer: Berlin, Germany, 2010; pp 395-455. (b) Zamfir, A.; Schenker, S.; Freund, M.; Tsogoeva, S. B. *Org. Biomol. Chem.* **2010**, *8*, 5262-5276. (c) Terada, M. *Synthesis* **2010**, *12*, 1929-1982 (d) Terada, M.; Momiyama, N. Enantioselective Synthesis of Amines by Chiral Brønsted Acid Catalysts. In *Chiral Amine Synthesis: Methods, Developments and Applications*; Nugent, T. C., Ed.; Wiley-VCH, Weinheim, Germany, 2010; Chapter 3. (e) Rueping, M.; Kuenkel, A.; Atodiresei, I. *Chem. Soc. Rev.* **2011**, *40*, 4539-4549. (f) Phipps, R. J.; Hamilton, G. L.; Toste, F. D. *Nat. Chem.* **2012**, *4*, 603-614. (g) Yang, Z.-P.; Zhang, W.; You, S.-L. *J. Org. Chem.* **2014**, *79*, 7785-7798. (h) Parmar, D.; Sugiono, E.; Raja, S.; Rueping, M. *Chem. Rev.* **2014**, *114*, 9047-9153. (i) Bhadury, P. S.; Sun, Z. *Curr. Org. Chem.* **2014**, *18*, 127-150.
- (157) Bringmann, G.; Mortimer, A. J. P.; Keller, P. A.; Gresser, M. J.; Garner, J.; Breuning, M. *Angew. Chem., Int. Ed.* **2005**, *44*, 5384-5427; *Angew. Chem.* **2005**, *117*, 5518-5563.
- (158) Jacques, J.; Fouquey, C.; Viterbo, R. *Tetrahedron Lett.* **1971**, *12*, 4617-4620.
- (159) (a) Barbeau, A. *Canad. Med. Assoc. J.* **1969**, *10*, 59-68. (b) Hauser, R. A. *Eur. Neurol.* **2009**, *62*, 1-8.
- (160) Sayyed, I. A.; Sudalai, A. *Tetrahedron: Asymmetry* **2004**, *15*, 3111-3116.
- (161) Aikawa, K.; Kojima, M.; Mikami, K. *Angew. Chem., Int. Ed.* **2009**, *48*, 6073-6077; *Angew. Chem.* **2009**, *121*, 6189-6193.

- (162) (a) Broadley, K.; Lane, G. A.; Connelly, N. G.; Geiger, W. E. *J. Am. Chem. Soc.* **1983**, *105*, 2486-2481. (b) Bruce, M. I. *Adv. Organomet. Chem.* **2001**, *48*, 71-288; see pp 246-250.
- (163) (a) Connelly, N. G.; Manners, I. *J. Chem. Soc., Dalton Trans.* **1989**, 283-288. (b) Adams, H.; Bailey, N. A.; Browning, A. F.; Ramsden, J. A.; White, C. *J. Organomet. Chem.* **1990**, *387*, 305-314. (c) Martin-Matute, B.; Edin, M.; Bogár, K.; Kaynak, F. B.; Bäckvall, J.-E. *J. Am. Chem. Soc.* **2005**, *127*, 8817-8825.
- (164) (a) Vives, G.; Carella, A.; Launay, J.-P.; Rapenne, G. *Coord. Chem. Rev.* **2008**, *252*, 1451-1459. (b) Mavrynsky, D.; Murzin, D. Y.; Leino, R. *ChemCatChem* **2013**, *5*, 2436-2445.
- (165) Janiak, C.; Schumann, H.; Stader, C.; Wrackmeyer, B.; Zuckerman, J. J. *Eur. J. Inorg. Chem.* **1988**, *121*, 1745-1751.
- (166) Harrison, E. A. Jr. *J. Chem. Educ.* **1998**, *75*, 636-637.
- (167) (a) McCrindle, R.; Ferguson, G.; McAlees, A. J.; Massod, P.; Stephenson, D. K. *J. Chem. Soc. Dalton Trans.* **1982**, 1291-1296. (b) Steiner, T. *Angew. Chem., Int. Ed.* **2002**, *41*, 48-76; *Angew. Chem.* **2002**, *114*, 50-80. (c) Husain, A.; Nami, A. A.; Siddiqi, K. S. *Appl. Organometal. Chem.* **2011**, *25*, 761-768.
- (168) Allen, F. H.; Kennard, O.; Watson, D. G.; Brammer, L.; Orpen, A. G.; Taylor, R. *J. Chem. Soc., Perkin Trans. 2* **1987**, S1-S19.
- (169) Callomon, J. H.; Hirota, E.; Iijima, T.; Kuchitau, K.; Lafferty, W. J. In *Landolt-Börnstein Numerical Data and Functional Relationships in Science and Technology*; Madelung, O., Hellwege, K.-H., Hellwege, A. M., Eds.; Springer-Verlag: New York, 1987; Vol. 7 (Structure Data of Free Polyatomic Molecules), pp 938, 1036.
- (170) (a) Evans, D. A.; Bartroli, J.; Shih, T. L. *J. Am. Chem. Soc.* **1981**, *103*, 2127-

2129. (b) Ager, D. J.; Prakash, I.; Schaad, D. R. *Chem. Rev.* **1996**, *96*, 835-875.
- (171) (a) Zu, L.; Wang, J.; Li, H.; Xie, H.; Jiang, W.; Wang, W. *J. Am. Chem. Soc.* **2007**, *129*, 1036-1037. (b) Breman, A. C.; Smits, J. M. M.; de Gelder, R.; van Maarseveen, J. H.; Ingemann, S.; Hiemstra, H. *Synlett* **2012**, 2195-2200. (c) Chen, W.; Jing, Z.; Chin, K. F.; Qiao, B.; Zhao, Y.; Yan, L.; Tan, C.-H.; Jiang, Z. *Adv. Synth. Catal.* **2014**, *356*, 1291-1300.
- (172) (a) Kobayashi, S.; Ogawa, C.; Kawamura, M.; Sugiura, M. *Synlett* **2001**, 983-985. (b) Matsumoto, K.; Watanabe, A.; Uchida, T.; Ogi, K.; Katsuki, T. *Tetrahedron. Lett.* **2004**, *45*, 2385-2388.
- (173) Rana, N. K.; Singh, V. K. *Org. Lett.* **2011**, *13*, 6520-6523.
- (174) (a) Haase, C.; Sarko, C. R.; DiMare, M. *J. Org. Chem.* **1995**, *60*, 1777-1787. (b) Anslyn, E. V.; Dougherty, D. A. *Modern Physical Organic Chemistry*; University Science Books: Sausalito, CA, 2006; pp 104-105.
- (175) Ma, J.; Ding, X.; Hu, Y.; Huang, Y.; Gong, L.; Meggers, E. *Nat. Commun.* **2014**, *5*, 4531-4536.
- (176) Sibi, M. P.; Manyem, S. *Org. Lett.* **2002**, *4*, 2929-2932.
- (177) Bull, S. D.; Davies, S. G.; Garner, A. G.; Kruchinin, D.; Key, M.-S.; Roberts, P. M.; Savory, E. D.; Smith, A. D.; Thomson, J. E. *Org. Biomol. Chem.* **2006**, *4*, 2945-2964.
- (178) Literature chemical shift values (CDCl₃) agree within 0.03 ppm.^{163c}
- (179) See Table 4.1 for atom numbering.
- (180) Assignments were made based upon ¹H-¹H COSY, DEPT-90, ¹H-¹³C HSQC, and ¹H-¹³C HMBC NMR experiments, results from which are in the Appendix C.
- (181) The remaining NH signals were not observed.

- (182) This signal is due to two overlapping resonance. The intensity was almost 1.5 times that of the *o*-C_{ph} signal.
- (183) Due to the poor solubility of **49** in CD₂Cl₂, 1:1 v/v CD₂Cl₂/CD₃OD was used.
- (184) **H**_{(P)-Phos}, **C**_{(P)-Phos}, and **P**_{(P)-Phos} denote proton, carbon, and phosphorous atoms of (P)-Phos,²⁶ respectively.
- (185) Huang, W.-g.; Wang, H.-s.; Huang, G.-b.; Wu, Y.-m.; Pan, Y.-m. *Eur. J. Org. Chem.* **2012**, 5839-5843.
- (186) The separation of these enantiomers by chiral HPLC has been previously reported but the configurations have not yet been assigned.^{21a}
- (187) The separation of these enantiomers by chiral HPLC has been previously reported but the configurations have not yet been assigned.¹⁷²
- (188) Spek, A. L. *J. Appl. Cryst.* **2003**, *36*, 7-13.
- (189) Frisch, M. J.; Trucks, G. W.; Schlegel, H. B.; Scuseria, G. E.; Robb, M. A.; Cheeseman, J. R.; Scalmani, G.; Barone, V.; Mennucci, B.; Petersson, G. A.; Nakatsuji, H.; Caricato, M.; Li, X.; Hratchian, H. P.; Izmaylov, A. F.; Bloino, J.; Zheng, G.; Sonnenberg, J. L.; Hada, M.; Ehara, M.; Toyota, K.; Fukuda, R.; Hasegawa, J.; Ishida, M.; Nakajima, T.; Honda, Y.; Kitao, O.; Nakai, H.; Vreven, T.; Montgomery, J. A., Jr.; Peralta, J. E.; Ogliaro, F.; Bearpark, M.; Heyd, J. J.; Brothers, E.; Kudin, K. N.; Staroverov, V. N.; Kobayashi, R.; Normand, J.; Raghavachari, K.; Rendell, A.; Burant, J. C.; Iyengar, S. S.; Tomasi, J.; Cossi, M.; Rega, N.; Millam, M. J.; Klene, M.; Knox, J. E.; Cross, J. B.; Bakken, V.; Adamo, C.; Jaramillo, J.; Gomperts, R.; Stratmann, R. E.; Yazyev, O.; Austin, A. J.; Cammi, R.; Pomelli, C.; Ochterski, J. W.; Martin, R. L.; Morokuma, K.; Zakrzewski, V. G.; Voth, G. A.; Salvador, P.; Dannenberg, J. J.; Dapprich, S.; Daniels, A. D.; Farkas, Ö.; Foresman, J. B.; Ortiz, J. V.; Cioslowski, J.; Fox, D.

- J. Gaussian 09, Revision D.01, Gaussian, Inc., Wallingford CT, 2009.
- (190) (a) Martin, J. M. L.; Sundermann, A. *J. Chem. Phys.* **2001**, *114*, 3408-3420. (b) Andrae, D.; Häußermann, U.; Dolg, M.; Stoll, H.; Preuss, H. *Theor. Chem. Acc.* **1990**, *77*, 123-141.
- (191) (a) Krishnan, R.; Binkley, J. S.; Seeger, R.; Pople, J. A. *J. Chem. Phys.* **1980**, *72*, 650-654. (b) Clark, T.; Chandrasekhar, J.; Spitznagel, G. W.; Schleyer, P. V. R. *J. Comp. Chem.* **1983**, *4*, 294-301. (c) Frisch, M. J.; Pople, J. A.; Binkley, J. S. *J. Chem. Phys.* **1984**, *80*, 3265-3269.
- (192) Becke, A. D. *J. Chem. Phys.* **1993**, *98*, 5648-5652.
- (193) Lee, C.; Yang, W.; Parr, R. G. *Phys. Rev. B* **1988**, *37*, 785-789.
- (194) (a) Runge, E.; Gross, E. K. U. *Phys. Rev. Lett.* **1984**, *52*, 997-1000. (b) Stratmann, R. E.; Scuseria, G. E.; Frisch, M. J. *J. Chem. Phys.* **1998**, *109*, 8218-8224.
- (195) Tomasi, J.; Mennucci, B.; Cammi, R. *Chem. Rev.* **2005**, *105*, 2999-3093.
- (196) Helgaker, T.; Jørgensen, P. *J. Chem. Phys.* **1991**, *95*, 2595-2601.
- (197) BHandHLYP as implemented in G09: $\text{BHandHLYP} = 0.5 \times E_X^{\text{HF}} + 0.5 \times E_X^{\text{LSDA}} + 0.5 \times \Delta E_X^{\text{Becke88}} + E_C^{\text{LYP}}$ functional.

APPENDIX A

This appendix contains NMR spectra and the checkCIF reports related to chapter 2, titled *Modification and Application of 2-guanidinobenzimidazole for Second Coordination Sphere Promoted Catalysis*.

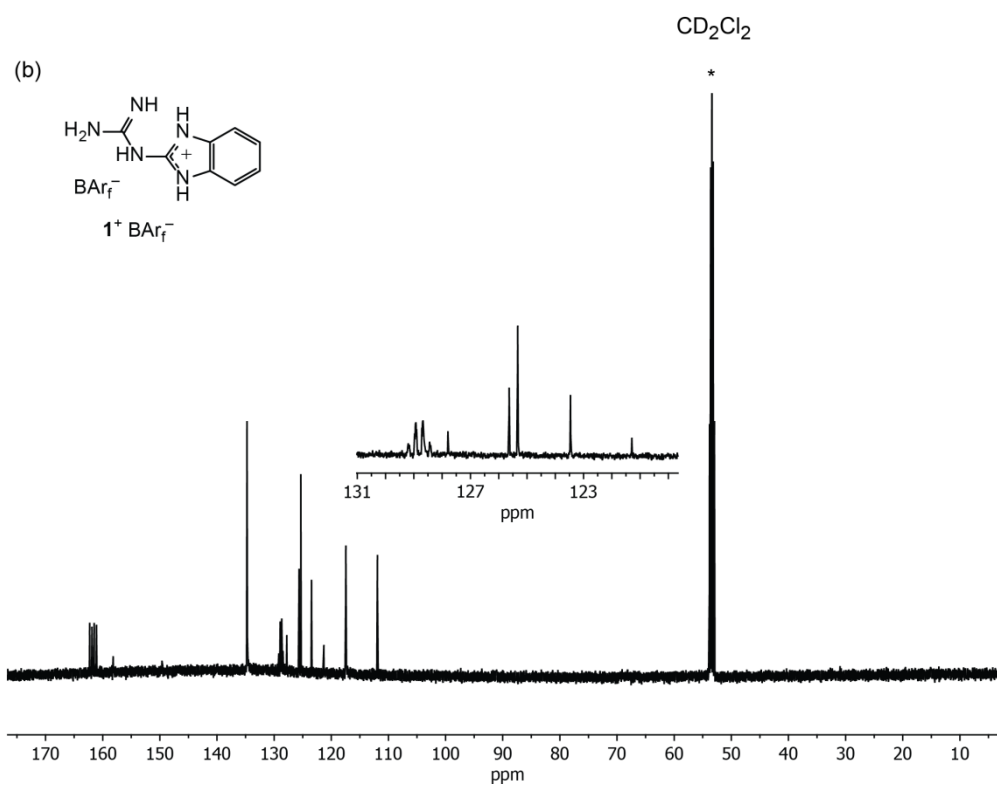
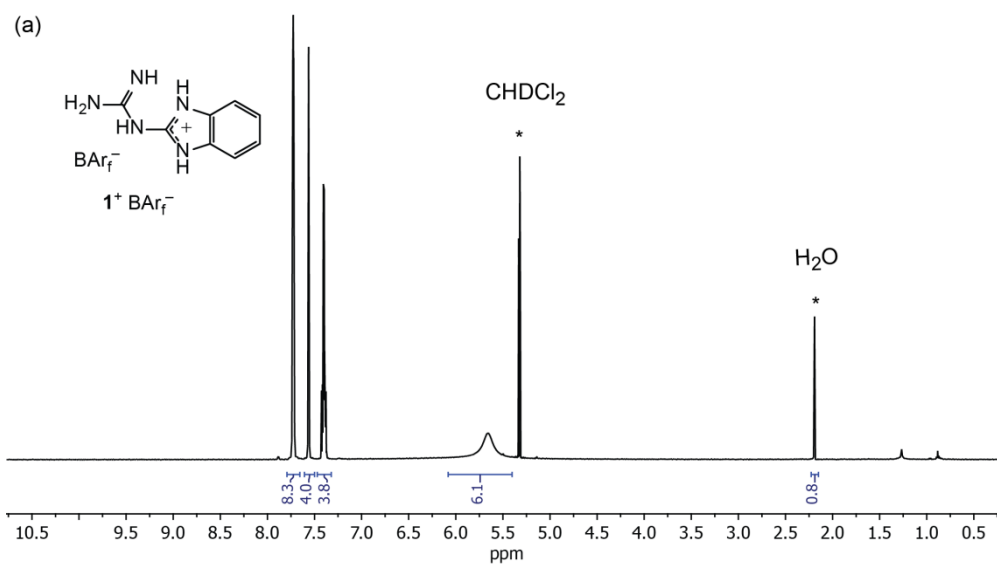


Figure a1 NMR spectra of 1^+BAr_f^- (CD_2Cl_2 ; * = solvent or H_2O): (a) ^1H (500 MHz); (b) $^{13}\text{C}\{^1\text{H}\}$ (125 MHz).

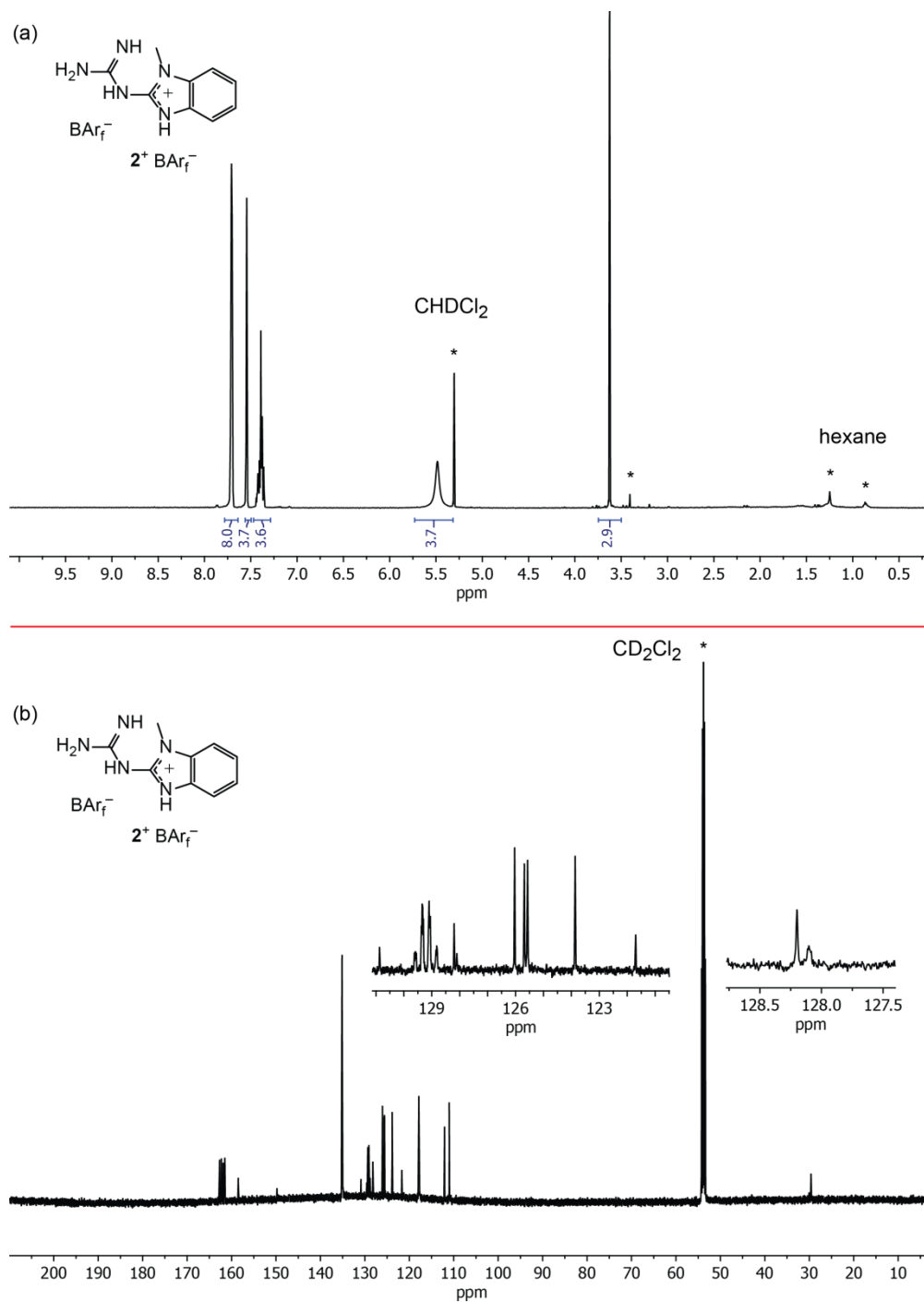


Figure a2 NMR spectra of 2^+BAr_f^- (CD_2Cl_2 ; * = solvent or impurities): (a) ^1H (500 MHz); (b) $^{13}\text{C}\{^1\text{H}\}$ (125 MHz).

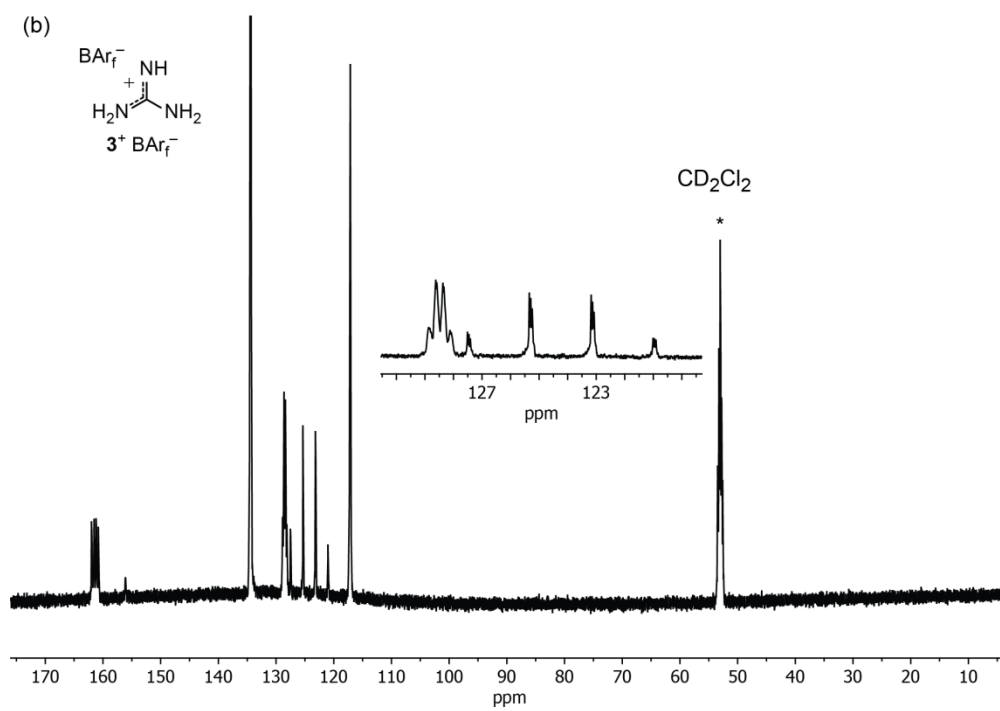
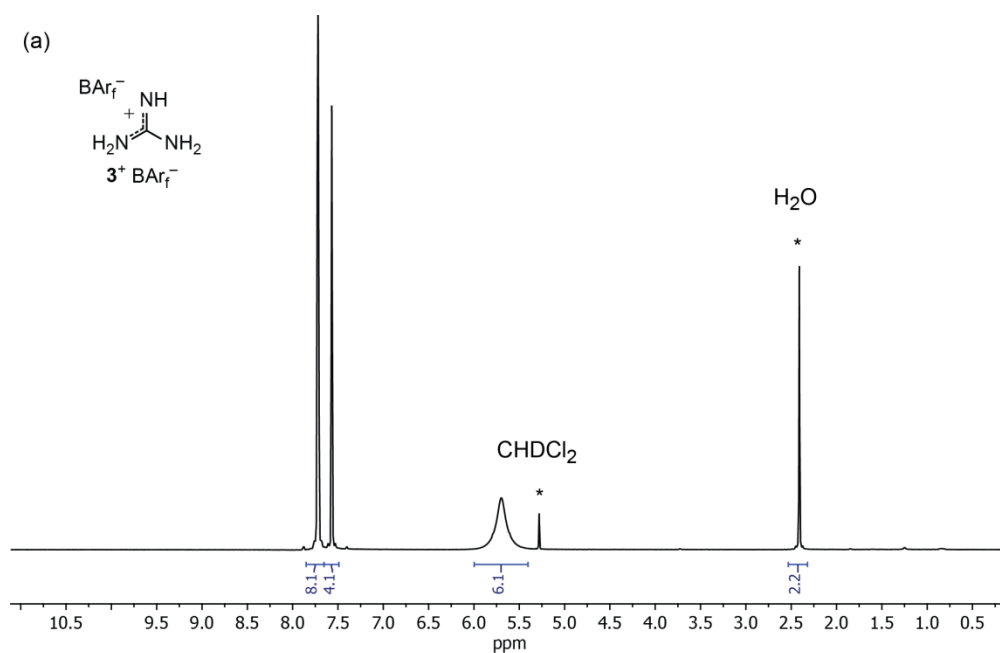


Figure a3 NMR spectra of 3^+BAr_f^- (CD_2Cl_2 ; * = solvent or H_2O): (a) ^1H (500 MHz); (b) $^{13}\text{C}\{^1\text{H}\}$ (125 MHz).

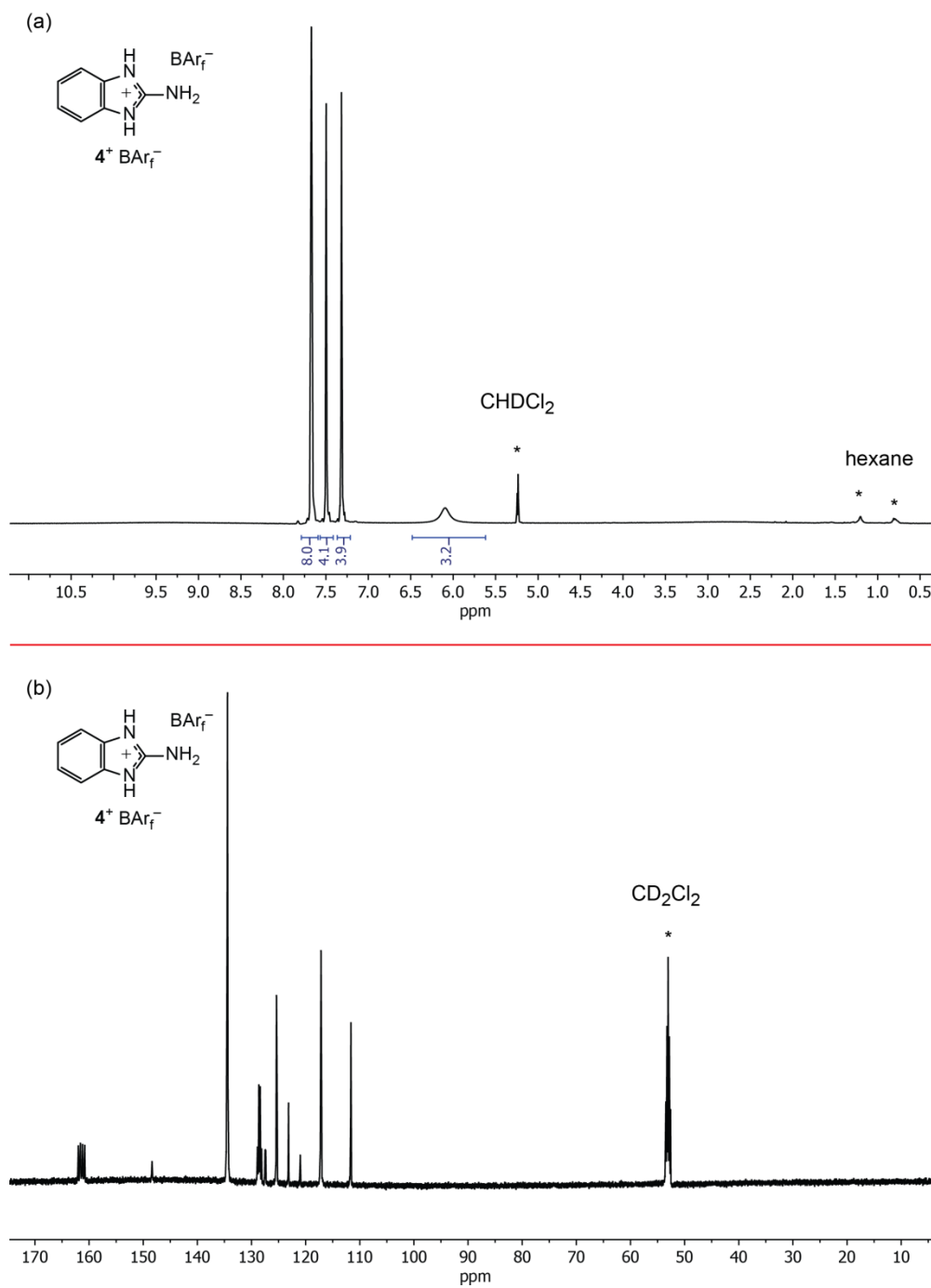


Figure a4 NMR spectra of 4^+ BAr_f^- (CD_2Cl_2 ; * = solvent or impurities): (a) ^1H (500 MHz); (b) $^{13}\text{C}\{^1\text{H}\}$ (125 MHz).

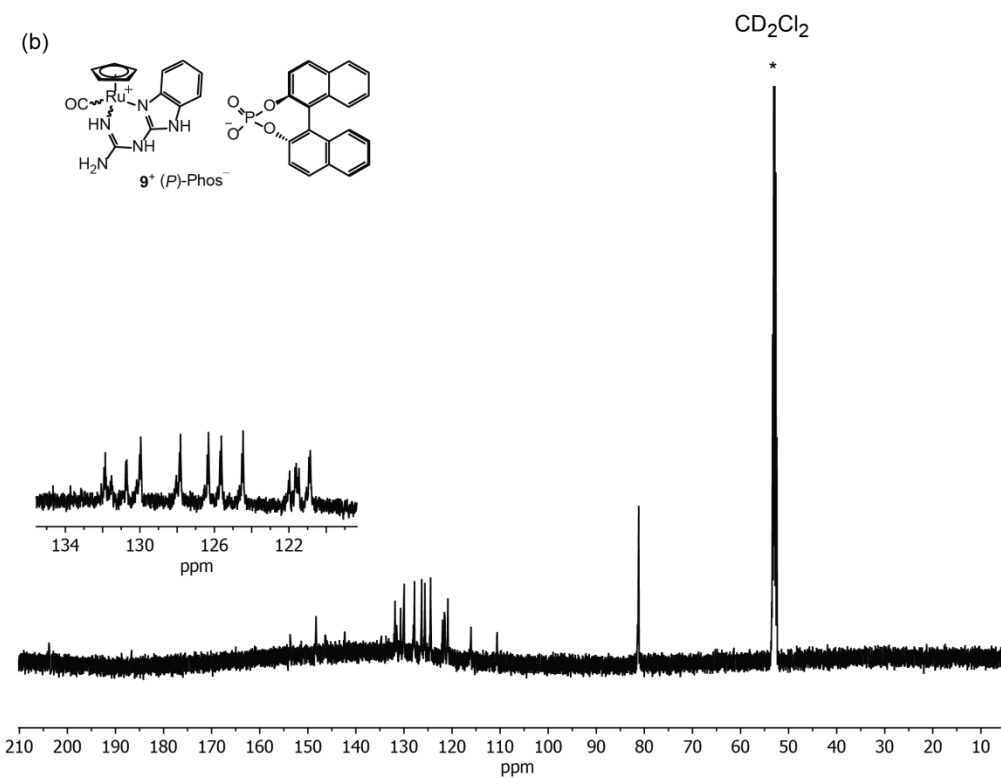
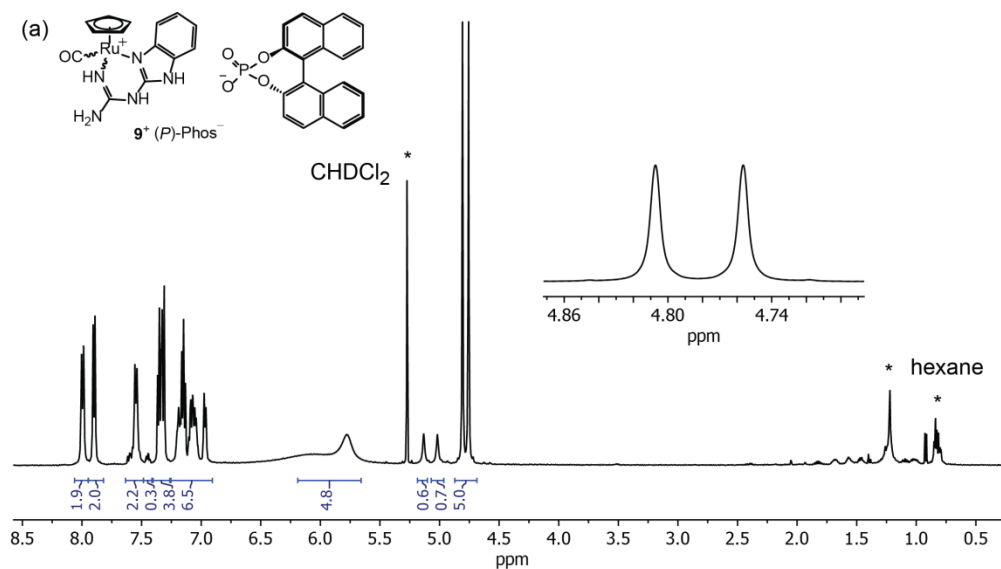


Figure a5 NMR spectra of 9^+ (*P*)-Phos $^-$ (CD₂Cl₂; * = solvent or impurities): (a) ^1H (500 MHz); (b) $^{13}\text{C}\{^1\text{H}\}$ (125 MHz).

CheckCIF report for $3^+ \text{BAr}_f^- \cdot \text{H}_2\text{O}$

The following ALERTS were generated. Each ALERT has the format

test-name_ALERT_alert-type_alert-level.

Alert level A

THETM01_ALERT_3_A The value of $\sin(\theta_{\text{max}})/\text{wavelength}$ is less than 0.550

Calculated $\sin(\theta_{\text{max}})/\text{wavelength} = 0.5040$

Crystallographer's Response: Data was collected on a Bruker GADDS instrument with Cu-source and MWPC (multiwire proportional counter) detector. Under these experimental conditions the maximum angle that can be collected is 120 degrees two-theta. The quality of the crystal used was poor and no reflections were found above 102 degree 2-theta.

PLAT089_ALERT_3_A Poor Data / Parameter Ratio ($Z_{\text{max}} < 18$) 3.72

Crystallographer's Response: Data was collected on a Bruker GADDS instrument with Cu-source and MWPC (multiwire proportional counter) detector. Under these experimental conditions the maximum angle that can be collected is 120 degrees two-theta. The quality of the crystal used was poor and no reflections were found above 102 degree 2-theta.

Alert level B

PLAT019_ALERT_1_B _diffn_measured_fraction_theta_full/_max < 1.0 0.598 Report

Crystallographer's Response: Data was collected on a Bruker GADDS instrument with Cu-source and MWPC (multiwire proportional counter) detector which has geometrical restrictions.

PLAT340_ALERT_3_B Low Bond Precision on C-C Bonds 0.0180 Ang.

Crystallographer's Response: The quality of the crystal used was poor and no reflections were found above 102 degree 2-theta.

PLAT420_ALERT_2_B D-H Without Acceptor O1W - HIWA ...

Crystallographer's Response: Hydrogen atoms on the water could not be located and was placed to satisfy the stoichiometry. No hydrogen bonding was considered for the geometric location due to disorder of the neighboring nitrogen and fluorine atoms.

Alert level C

CRYSC01_ALERT_1_C The word below has not been recognised as a standard identifier. gray

CRYSC01_ALERT_1_C No recognised colour has been given for crystal colour.

DIFMX01_ALERT_2_C The maximum difference density is $> 0.1 * ZMAX * 0.75$

_refine_diff_density_max given = 0.736

Test value = 0.675

DIFMX02_ALERT_1_C The maximum difference density is $> 0.1 * ZMAX * 0.75$

The relevant atom site should be identified.

REFNR01_ALERT_3_C Ratio of reflections to parameters is < 8 for a non-centrosymmetric structure, where $Z_{MAX} < 18 \sin(\theta)/\lambda$ 0.5040 Proportion of unique data used 1.0000 Ratio reflections to parameters 7.0159

PLAT097_ALERT_2_C Large Reported Max. (Positive)

Residual Density 0.74 eA^{-3}

PLAT213_ALERT_2_C Atom F1 has ADP max/min Ratio 3.5 prolat

And 2 other PLAT213 Alerts More ...

PLAT220_ALERT_2_C Large Non-Solvent C Ueq(max)/Ueq(min) Range 3.1 Ratio

PLAT234_ALERT_4_C Large Hirshfeld Difference F4A -- C8N .. 0.21 Ang.

And 13 other PLAT234 Alerts More ...

PLAT243_ALERT_4_C High 'Solvent' Ueq as Compared to Neighbors of N1 Check

PLAT250_ALERT_2_C Large U3/U1 Ratio for Average U(i,j) Tensor 2.7 Note

PLAT417_ALERT_2_C Short Inter D-H..H-D H2B .. H1WB .. 2.10 Ang.

PLAT417_ALERT_2_C Short Inter D-H..H-D H1WB .. H3AB .. 2.11 Ang.

PLAT713_ALERT_1_C TORSION Unknown or Inconsistent Label N2_A

N2_A C1_A N1 C1A_B

Alert level G

PLAT002_ALERT_2_G Number of Distance or Angle Restraints on AtSite 57

PLAT003_ALERT_2_G Number of Uiso or Uij Restrained non-H Atoms ... 3

PLAT007_ALERT_5_G Number of Unrefined Donor-H Atoms 14

PLAT042_ALERT_1_G Calc. and Reported MoietyFormula Strings Differ

PLAT072_ALERT_2_G SHELXL First Parameter in WGHT Unusually Large. 0.12

PLAT083_ALERT_2_G SHELXL Second Parameter in WGHT Unusually Large. 16.99

Why?

PLAT171_ALERT_4_G The CIF-Embedded .res File Contains EADP Records 13

PLAT176_ALERT_4_G The CIF-Embedded .res File Contains SADI Records 16

PLAT178_ALERT_4_G The CIF-Embedded .res File Contains SIMU Records 1

PLAT230_ALERT_2_G Hirshfeld Test Diff for F6A -- C8N .. 7.9 su

And 5 other PLAT230 Alerts More ...

PLAT242_ALERT_2_G Low Ueq as Compared to Neighbors for C7N

And 3 other PLAT242 Alerts More ...

PLAT301_ALERT_3_G Main Residue Disorder Percentage = 39

PLAT302_ALERT_4_G Anion/Solvent Disorder Percentage = 60

PLAT434_ALERT_2_G Short Inter HL..HL Contact F2 .. F17 .2.78 Ang.

PLAT720_ALERT_4_G Number of Unusual/Non-Standard Labels 10

PLAT790_ALERT_4_G Centre of Gravity not Within Unit Cell: Resd. # 3 H2 O

PLAT811_ALERT_5_G No ADDSYM Analysis: Too Many Excluded Atoms

PLAT860_ALERT_3_G Number of Least-Squares Restraints 206

CheckCIF report for $4^+ \text{BAr}_f^- \cdot \text{H}_2\text{O} \cdot (\text{CH}_2\text{Cl}_2)_{0.5}$

The following ALERTS were generated. Each ALERT has the format

test-name_ALERT_alert-type_alert-level.

Alert level A

PLAT213_ALERT_2_A Atom F9C has ADP max/min Ratio 8.2 prolat

Crystallographer's Response: Several terminal CF₃ groups were present in the structure. Some of the F atoms showed elongated thermal ellipsoids indicating disorder. Our efforts to model this disorder, while increasing the number of parameters, restraints and constraints, did not improve the reliability factors. The model also indicated extended disorder as the thermal ellipsoids were still elongated. For the final refinement, a model with no disorder, but with elongated ellipsoids were used.

Alert level B

DIFMX01_ALERT_2_B The maximum difference density is > 0.1*ZMAX*1.00
_refine_diff_density_max given = 1.951 Test value = 1.700

Crystallographer's Response: Several terminal CF₃ groups were present in the structure. Some of the F atoms showed elongated thermal ellipsoids indicating disorder. Our efforts to model this disorder, while increasing the number of parameters, restraints and constraints, did not improve the reliability factors. The model also indicated extended disorder as the thermal ellipsoids were still elongated.

For the final refinement, a model with no disorder, but with elongated ellipsoids were used.

THETM01_ALERT_3_B The value of $\sin(\theta_{\max})/\lambda$ is less than 0.575
Calculated $\sin(\theta_{\max})/\lambda = 0.5661$

Crystallographer's Response: Data was collected on a Bruker GADDS instrument with Cu-source and MWPC (multiwire proportional counter) detector. Under these experimental conditions the maximum angle that can be collected is 120 degrees two-theta.

PLAT019_ALERT_1_B _diffn_measured_fraction_theta_full/_max < 1.0 0.839 Report

Crystallographer's Response: Data was collected on a Bruker GADDS instrument with Cu-source and MWPC (multiwire proportional counter) detector which has geometrical restrictions.

PLAT097_ALERT_2_B Large Reported Max. (Positive) Residual Density 1.95 eA^{-3}

Crystallographer's Response: Several terminal CF₃ groups were present in the structure. Some of the F atoms showed elongated thermal ellipsoids indicating disorder. Our efforts to model this disorder, while increasing the number of parameters, restraints and constraints, did not improve the reliability factors. The model also indicated extended disorder as the thermal ellipsoids were still elongated. For the final refinement, a model with no disorder, but with elongated ellipsoids were used.

PLAT213_ALERT_2_B Atom F16 has ADP max/min Ratio 4.1 prolat

Crystallographer's Response: Several terminal CF₃ groups were present in the structure. Some of the F atoms showed elongated thermal ellipsoids indicating disorder. Our efforts to model this disorder, while increasing the number of parameters, restraints and constraints, did not improve the reliability factors. The model also indicated extended disorder as the thermal ellipsoids were still elongated. For the final refinement, a model with no disorder, but with elongated ellipsoids were used.

PLAT213_ALERT_2_B Atom F18 has ADP max/min Ratio 4.4 prolat

PLAT420_ALERT_2_B D-H Without Acceptor O1 - H1C ...

Crystallographer's Response: We could not locate the hydrogen atoms on the water molecules. Hydrogen atoms were placed only to satisfy the stoichiometry.

Alert level C

DIFMX02_ALERT_1_C The maximum difference density is $> 0.1 * Z_{MAX} * 0.75$ The relevant atom site should be identified.

REFNR01_ALERT_3_C Ratio of reflections to parameters is < 10 for a centrosymmetric structure $\sin(\theta)/\lambda$ 0.5661 Proportion of unique data used 1.0000 Ratio reflections to parameters 9.8229

RFACR01_ALERT_3_C The value of the weighted R factor is > 0.25 Weighted R factor given 0.278

PLAT084_ALERT_3_C High wR2 Value (i.e. > 0.25) 0.28 Report

PLAT213_ALERT_2_C Atom F13 has ADP max/min Ratio 3.2 prolat

Crystallographer's Response: Several terminal CF₃ groups were present in the structure. Some of the F atoms showed elongated thermal ellipsoids indicating disorder. Our efforts to model this disorder, while increasing the number of parameters, restraints and constraints, did not improve the reliability factors. The model also indicated extended disorder as the thermal ellipsoids were still elongated. For the final refinement, a model with no disorder, but with elongated ellipsoids were used.

And 3 other PLAT213 Alerts More ...

PLAT220_ALERT_2_C Large Non-Solvent F Ueq(max)/Ueq(min) Range 4.0 Ratio

PLAT220_ALERT_2_C Large Non-Solvent F Ueq(max)/Ueq(min) Range 5.3 Ratio

PLAT230_ALERT_2_C Hirshfeld Test Diff for F8C -- C32D .. 6.0 su

PLAT234_ALERT_4_C Large Hirshfeld Difference F23 -- C32B .. 0.17 Ang.

PLAT234_ALERT_4_C Large Hirshfeld Difference F7C -- C32D .. 0.18 Ang.

PLAT244_ALERT_4_C Low 'Solvent' Ueq as Compared to Neighbors of C1T

PLAT334_ALERT_2_C Small Average Benzene C-C Dist. C2 -C7 1.36 Ang.

PLAT340_ALERT_3_C Low Bond Precision on C-C Bonds 0.0082 Ang.

PLAT420_ALERT_2_C D-H Without Acceptor N3 - H3 ...

Crystallographer's Response: We could not locate the hydrogen atoms on the water molecules. Hydrogen atoms were placed only to satisfy the stoichiometry.

And 2 other PLAT420 Alerts More ...

PLAT480_ALERT_4_C Long H...A H-Bond Reported H1B .. F13C .. 2.59 Ang.

Alert level G

PLAT007_ALERT_5_G Number of Unrefined Donor-H Atoms 12

PLAT042_ALERT_1_G Calc. and Reported MoietyFormula Strings Differ

PLAT045_ALERT_1_G Calculated and Reported Z Differ by 0.50 Ratio

PLAT072_ALERT_2_G SHELXL First Parameter in WGHT Unusually Large. 0.16
Report

PLAT083_ALERT_2_G SHELXL Second Parameter in WGHT Unusually Large. 9.17
Why?

PLAT154_ALERT_1_G The su's on the Cell Angles are Equal 0.00300 Degree

PLAT242_ALERT_2_G Low Ueq as Compared to Neighbors for C7B

And 15 other PLAT242 Alerts More ...

PLAT434_ALERT_2_G Short Inter HL..HL Contact F15C .. F20 .2.82 Ang.

PLAT434_ALERT_2_G Short Inter HL..HL Contact F24 .. F24 .2.80 Ang.

PLAT720_ALERT_4_G Number of Unusual/Non-Standard Labels2

PLAT790_ALERT_4_G Centre of Gravity not Within Unit Cell: Resd. # 4
C7 H8 N3

PLAT790_ALERT_4_G Centre of Gravity not Within Unit Cell: Resd. # 6
H2 O

CheckCIF report for $[\text{1-H}]^{2+} \cdot 2\text{Br}^- \cdot \text{H}_2\text{O}$

The following ALERTS were generated. Each ALERT has the format

test-name_ALERT_alert-type_alert-level.

Alert level B

Crystal system given = monoclinic

THETM01_ALERT_3_B The value of $\sin(\theta_{\text{max}})/\text{wavelength}$ is less than 0.575

Calculated $\sin(\theta_{\text{max}})/\text{wavelength} = 0.5668$

Crystallographer's Response: Data was collected on a Bruker GADDS instrument with Cu-source and MWPC (multiwire proportional counter) detector. Under these experimental conditions the maximum angle that can be collected is 120 degrees two-theta.

PLAT019_ALERT_1_B Check $\text{diffn_measured_fraction_theta_full}/\text{max}$ 0.845

Crystallographer's Response: Data was collected on a Bruker GADDS instrument with Cu-source and MWPC (multiwire proportional counter) detector which has geometrical restrictions

Alert level C

PLAT480_ALERT_4_C Long H...A H-Bond Reported H4B .. BR2 .. 3.08 Ang.

PLAT911_ALERT_3_C Missing # FCF Refl Between THmin & STh/L= 0.567 24

PLAT913_ALERT_3_C Missing # of Very Strong Reflections in FCF 4

PLAT976_ALERT_2_C Negative Residual Density at 0.91A from N5 -0.42 eA^{-3}

Alert level G

PLAT007_ALERT_5_G Number of Unrefined Donor-H Atoms 9 Why?

PLAT042_ALERT_1_G Calc. and Reported MoietyFormula Strings Differ

PLAT909_ALERT_3_G Percentage of Observed Data at Theta(Max) still 82 %

APPENDIX B

This appendix contains NMR spectra, details of calculated circular dichroism (CD) spectra of $(R_{Ru}R_C R_C)\text{-18c}^+ \text{PF}_6^-$ and $(S_{Ru}R_C R_C)\text{-18c}^+ \text{PF}_6^-$, chiral HPLC traces, and the checkCIF reports related to chapter 3, titled *Epimeric Chiral-at-Metal Ruthenium Complexes: Separation and Applications*.

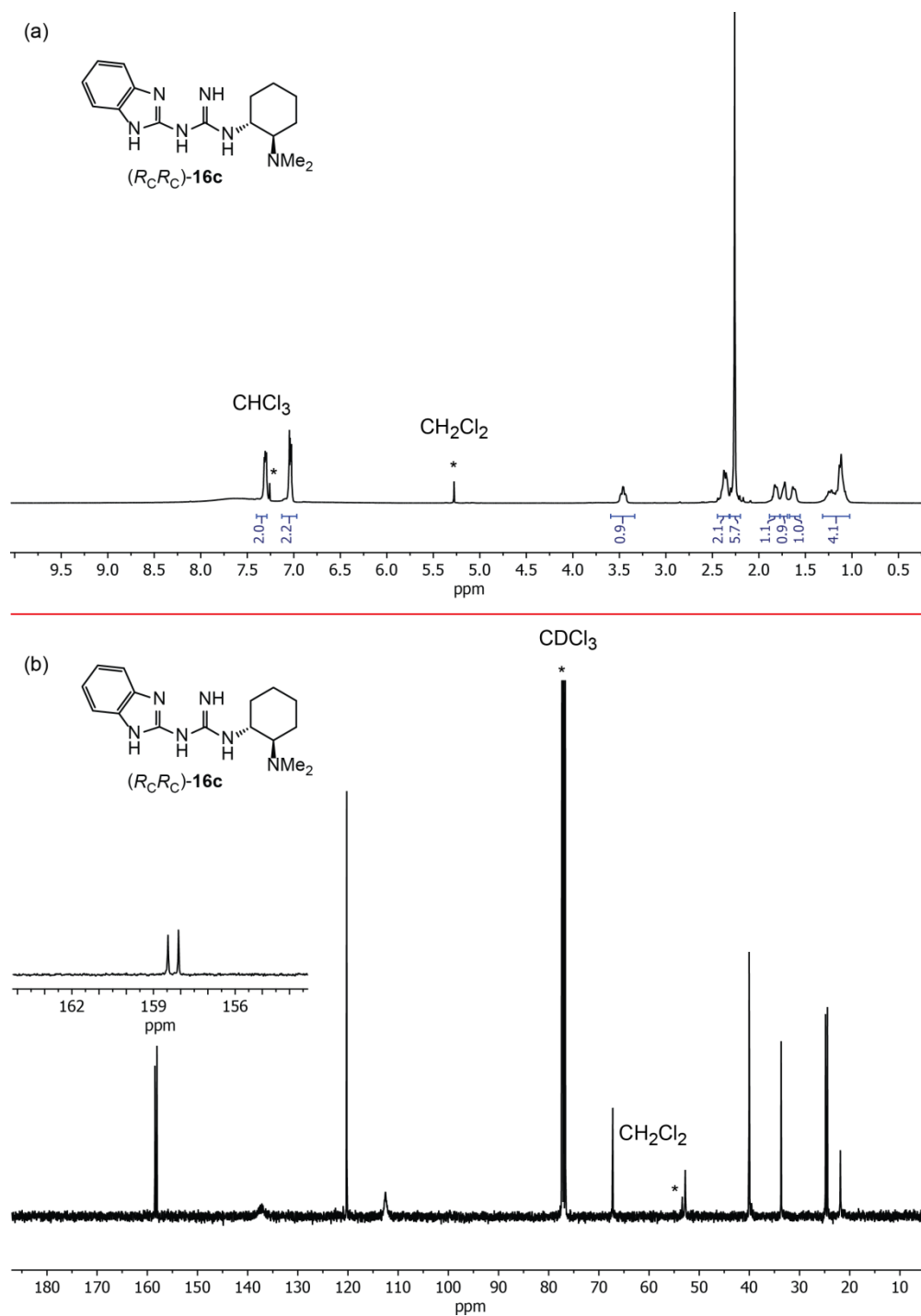


Figure b1 NMR spectra of ($R_C R_C$)-**16c** (CDCl₃; * = solvent or impurities): (a) ¹H (500 MHz); (b) ¹³C{¹H} (125 MHz).

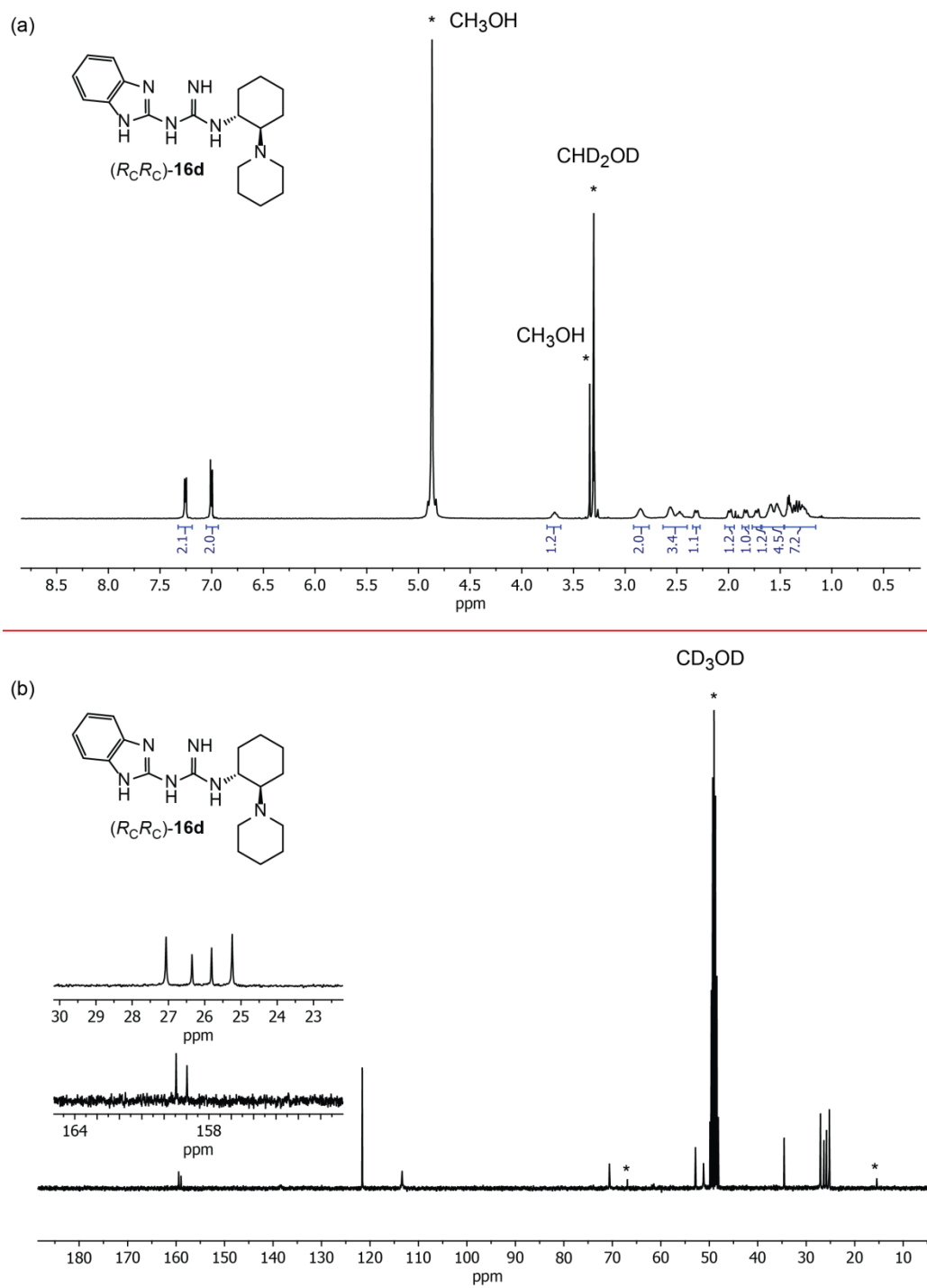


Figure b2 NMR spectra of (*R_CR_C*)-**16d** (CD₃OD; * = solvent or impurities): (a) ¹H (500 MHz); (b) ¹³C{¹H} (125 MHz).

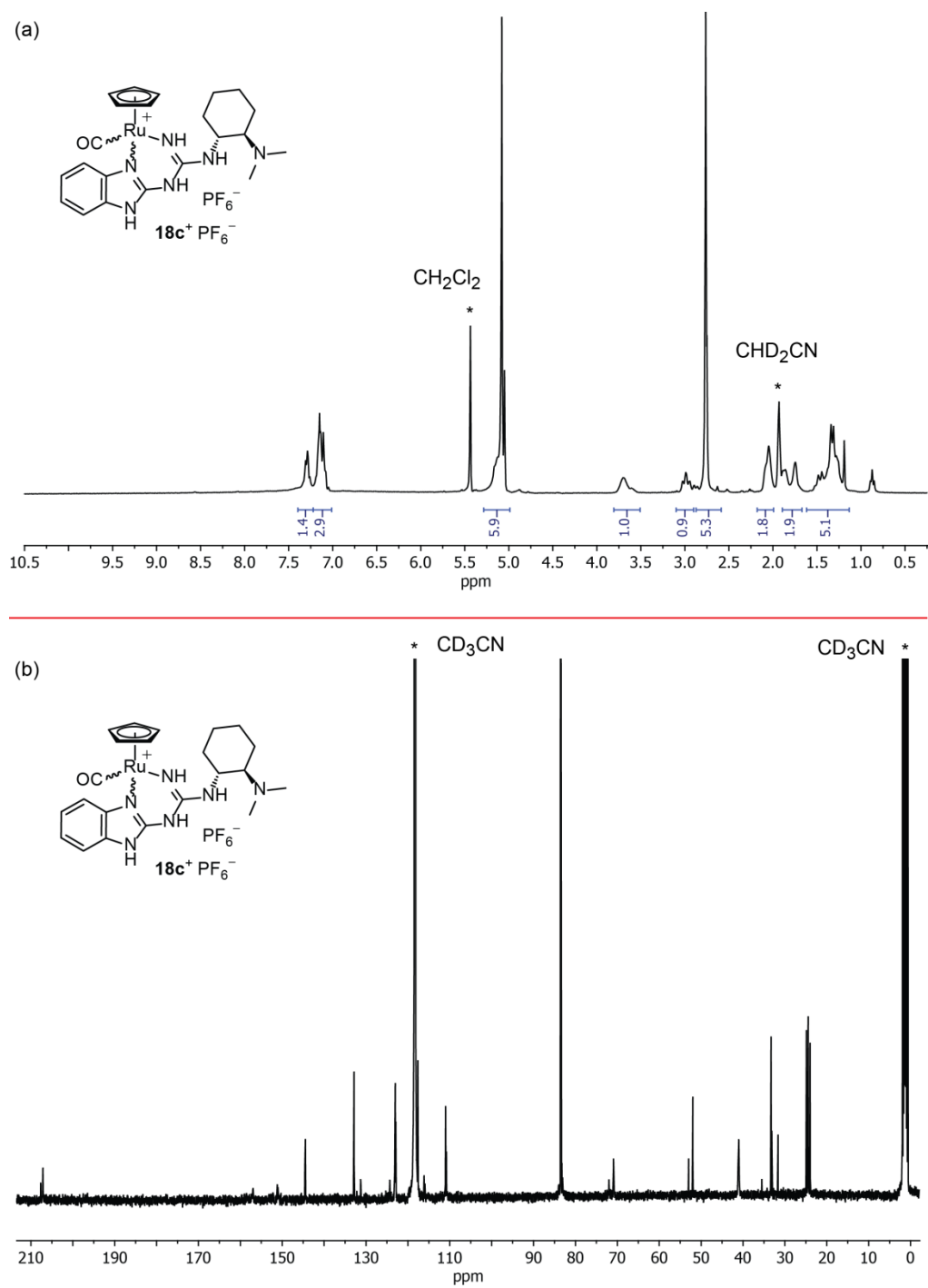


Figure b3 NMR spectra of $(R_{Ru}R_C R_C/S_{Ru}R_C R_C)-18c^+ PF_6^-$ (CD_3CN ; * = solvent or impurities): (a) 1H (500 MHz); (b) $^{13}C\{^1H\}$ (125 MHz).

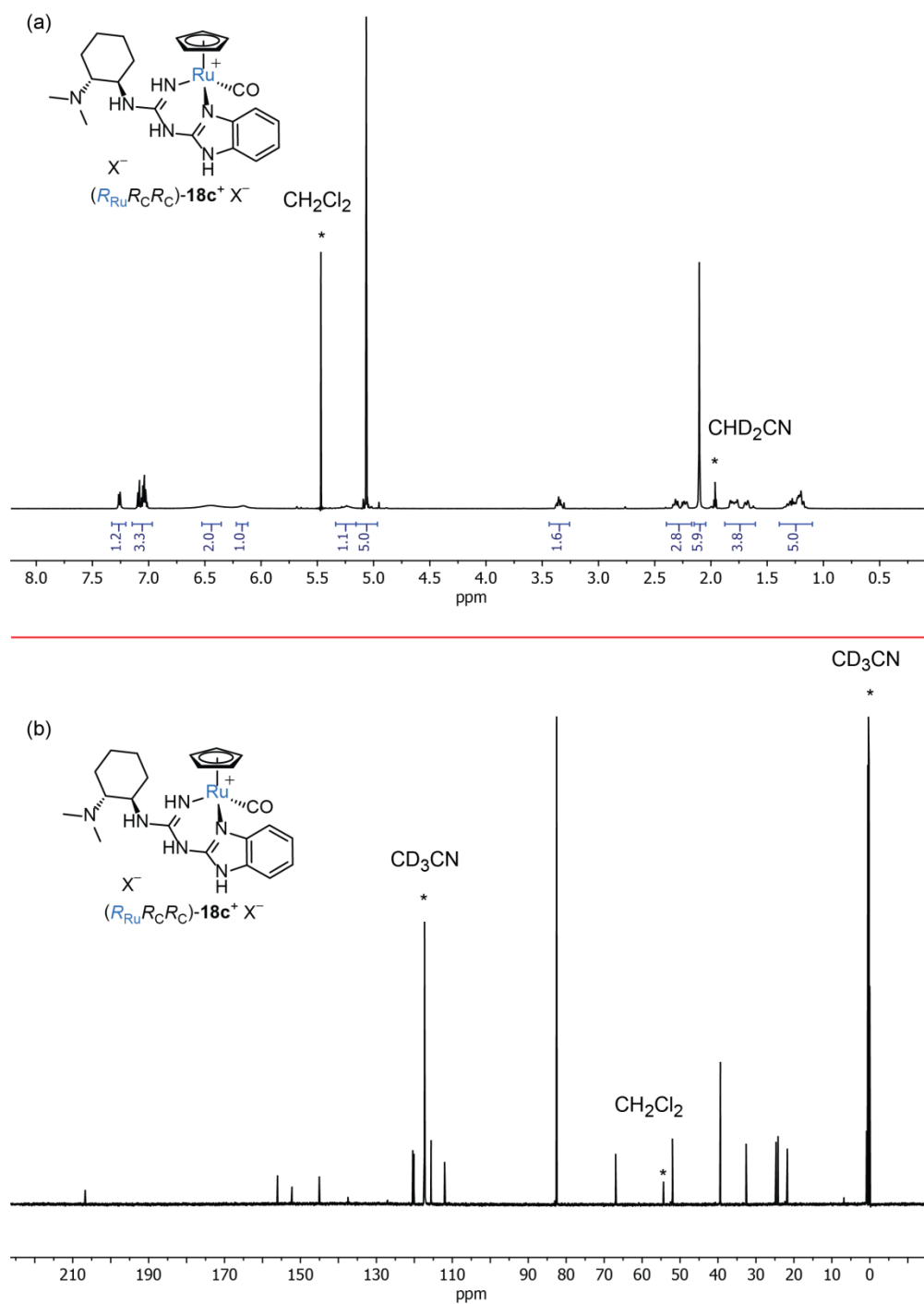


Figure b4 NMR spectra of $(R_{Ru}R_C R_C)\text{-}18\text{c}^+ \text{X}^-$ (CD_3CN ; * = solvent or impurities): (a) ^1H (500 MHz); (b) $^{13}\text{C}\{^1\text{H}\}$ (125 MHz).

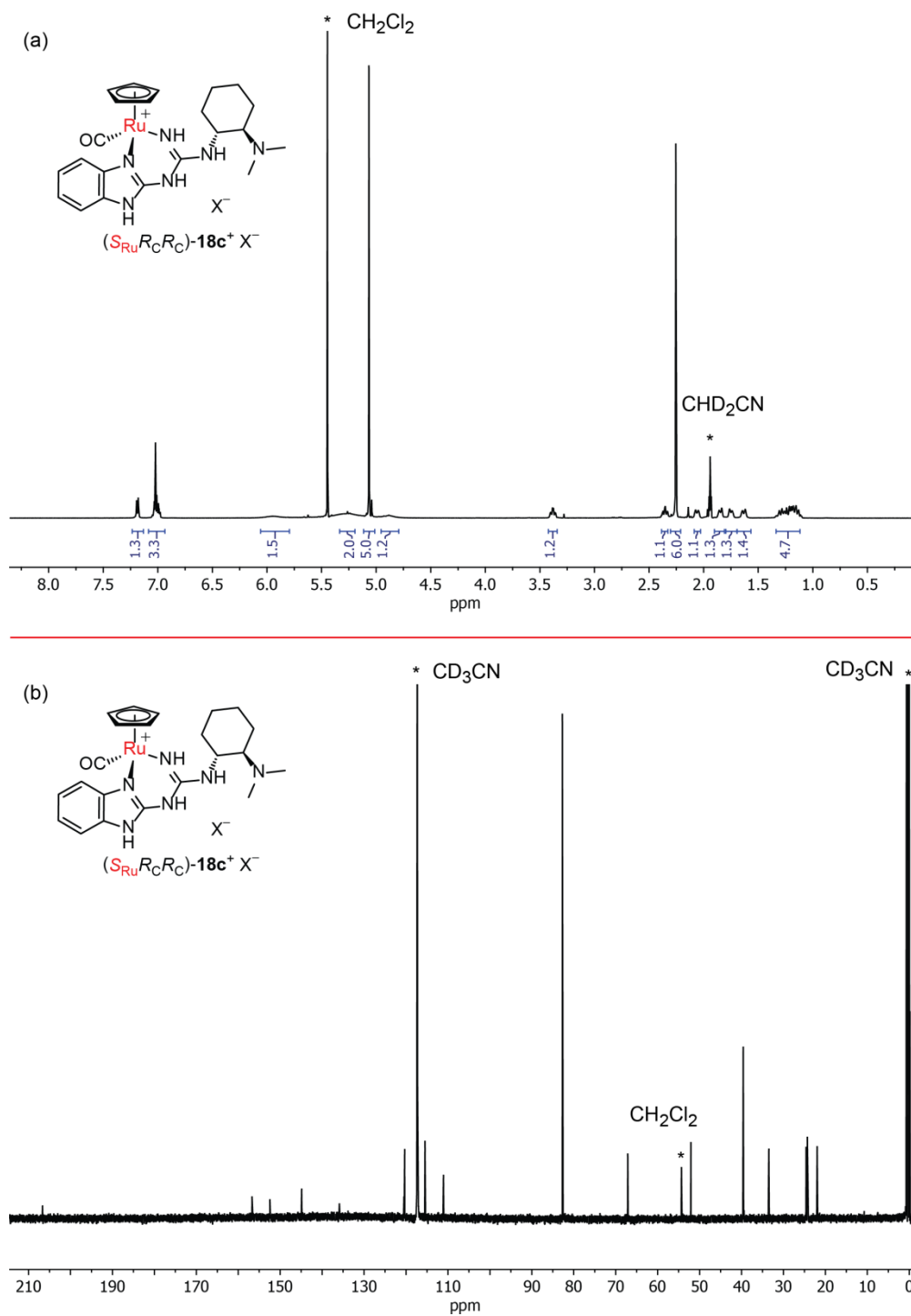


Figure b5 NMR spectra of $(S_{Ru}R_C R_C)\text{-18c}^+ X^-$ (CD_3CN ; * = solvent or impurities): (a) ^1H (500 MHz); (b) $^{13}\text{C}\{^1\text{H}\}$ (125 MHz).

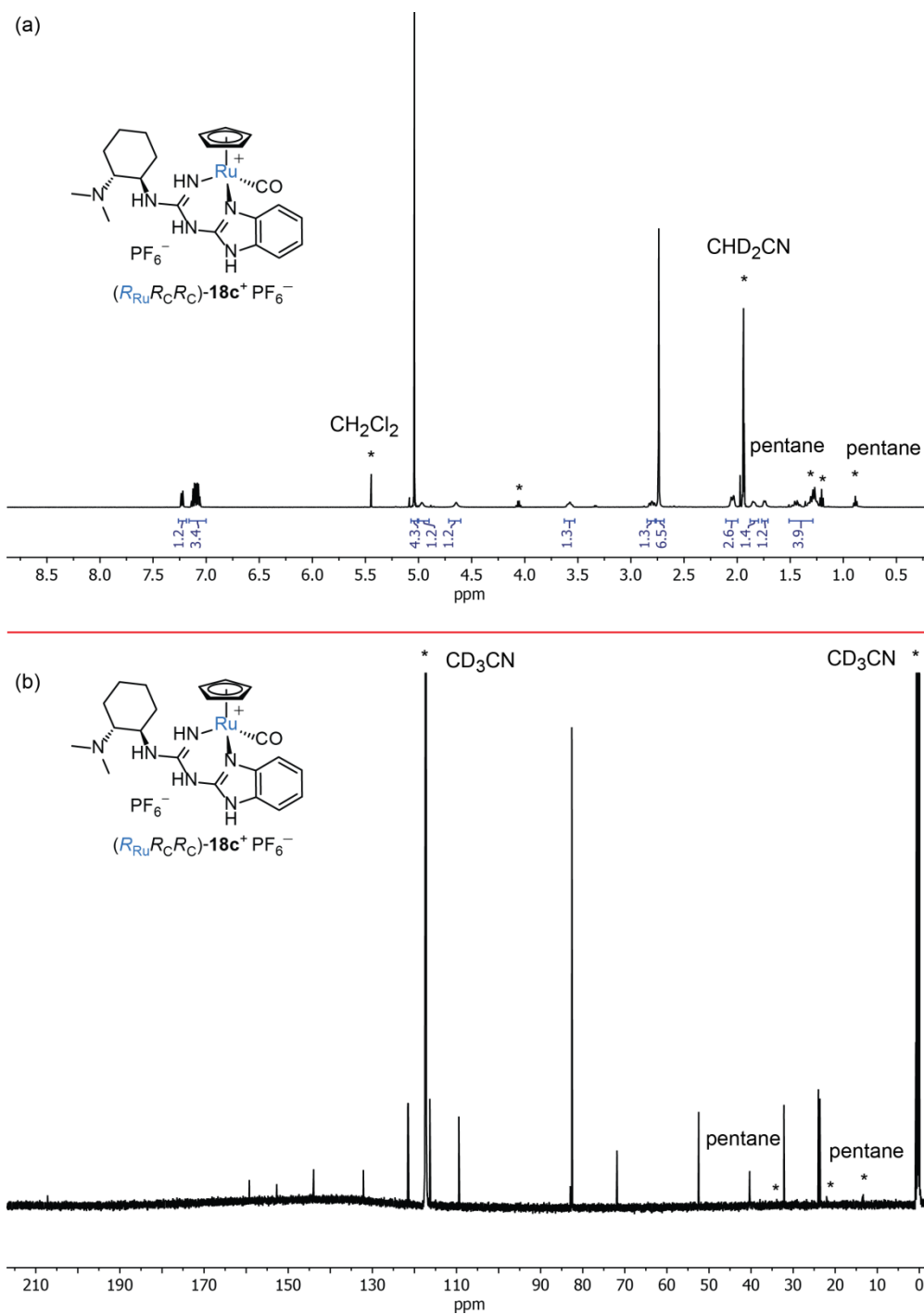


Figure b6 NMR spectra of $(R_{Ru}R_C R_C)\text{-18c}^+ \text{PF}_6^-$ (CD_3CN ; * = solvent or impurities): (a) ^1H (500 MHz); (b) $^{13}\text{C}\{^1\text{H}\}$ (125 MHz).

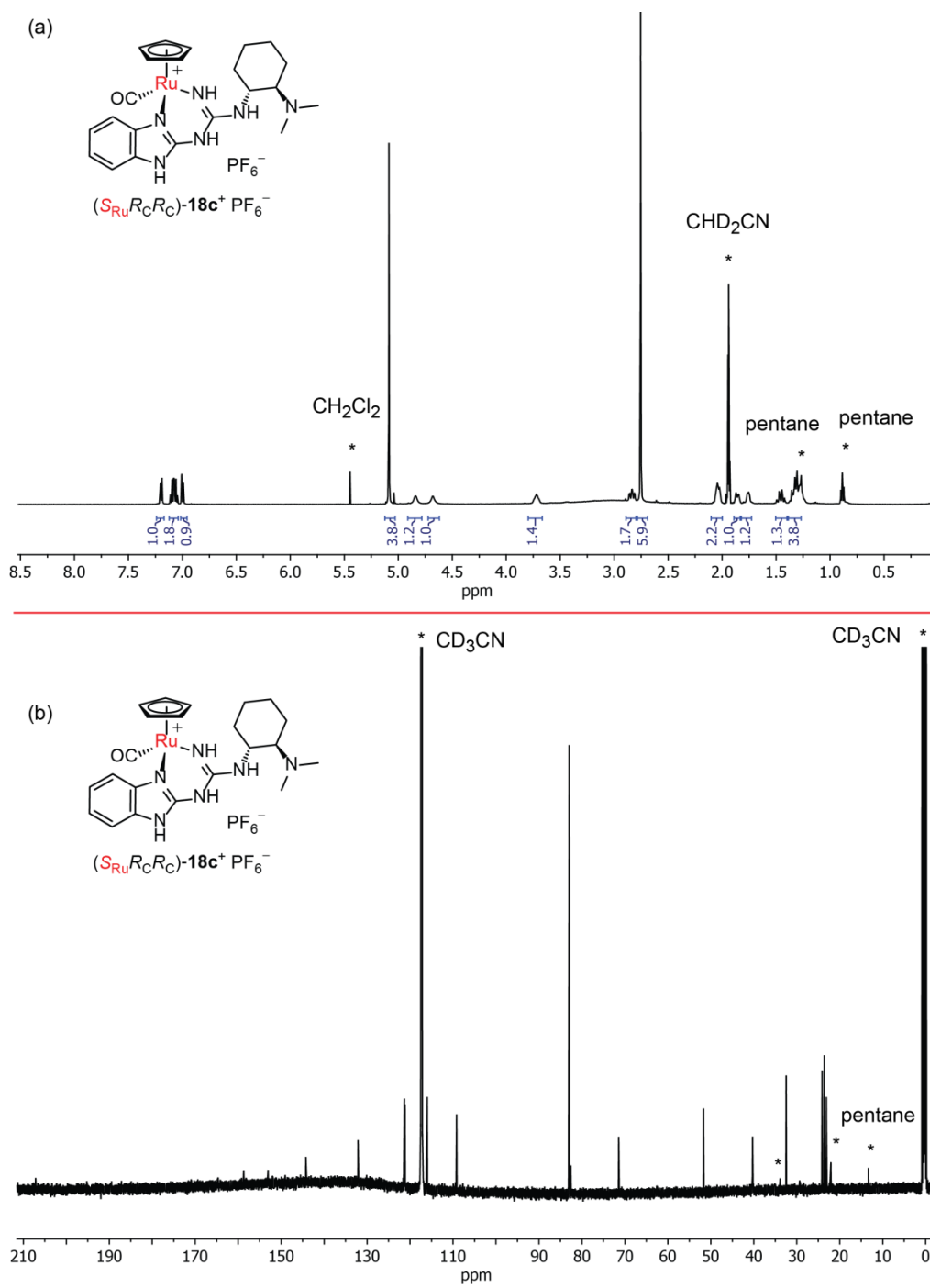


Figure b7 NMR spectra of $(S_{Ru}R_C R_C)\text{-18c}^+ \text{PF}_6^-$ (CD_3CN ; * = solvent or impurities):
 (a) ^1H (500 MHz); (b) $^{13}\text{C}\{^1\text{H}\}$ (125 MHz).

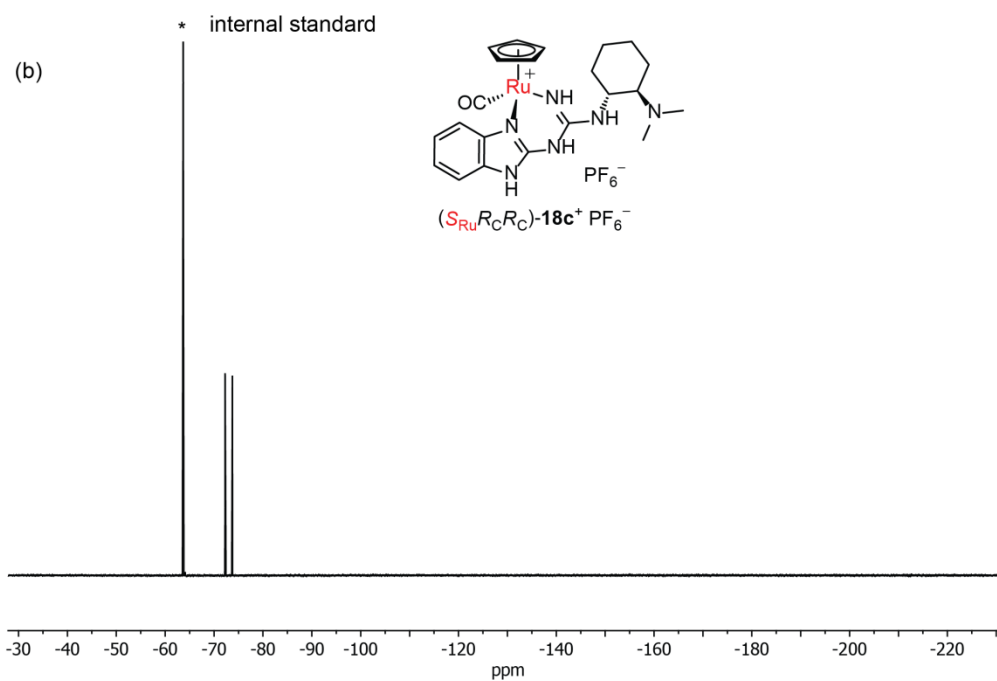
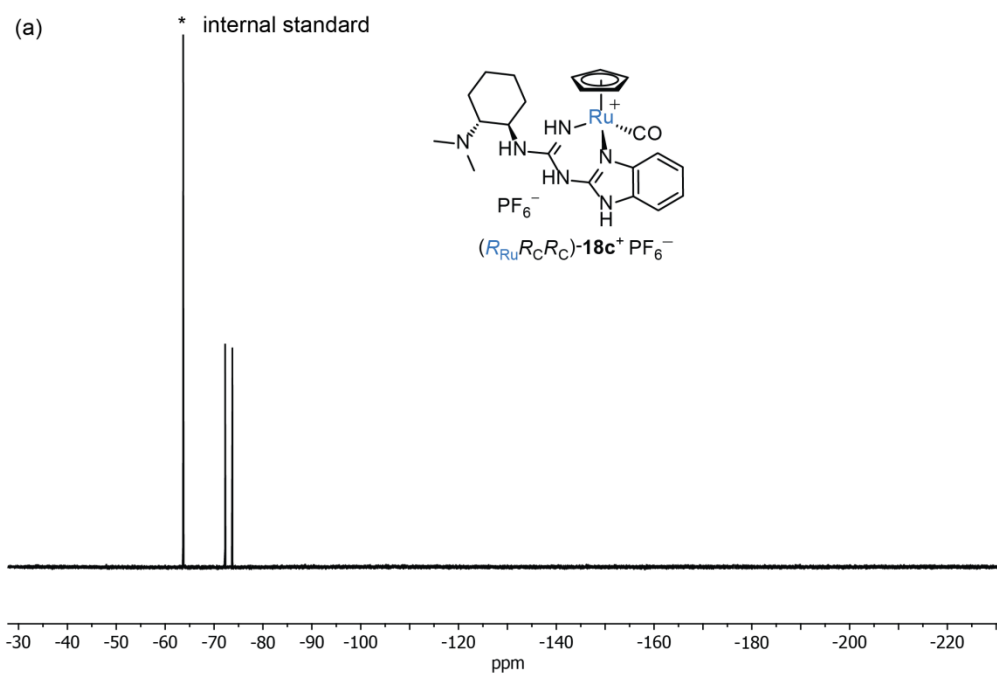


Figure b8 NMR spectra (CD_3CN ; * = internal standard, 1-bromo-3,5-bis(trifluoromethyl)benzene (-63.56 ppm)): (a) $^{19}\text{F}\{^1\text{H}\}$ (470 MHz), $(R_{Ru}R_C R_C)\text{-18c}^+ \text{PF}_6^-$; (b) $^{19}\text{F}\{^1\text{H}\}$ (470 MHz), $(S_{Ru}R_C R_C)\text{-18c}^+ \text{PF}_6^-$.

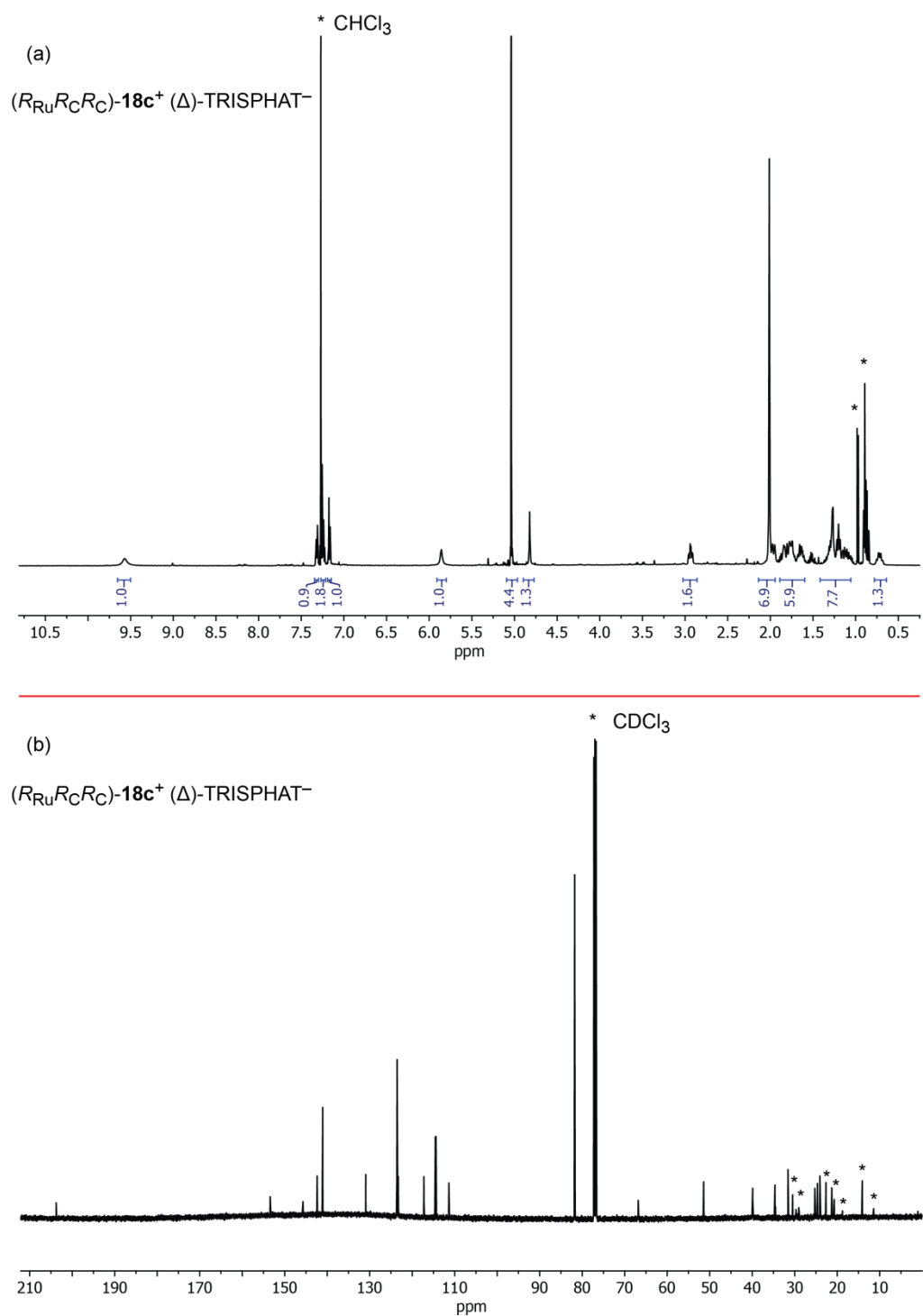


Figure b9 NMR spectra of $(R_{Ru}R_C R_C)\text{-18c}^+ \text{TRISPHAT}^-$ (CDCl_3 ; * = solvent or impurities): (a) ^1H (500 MHz), (b) $^{13}\text{C}\{^1\text{H}\}$ (125 MHz).

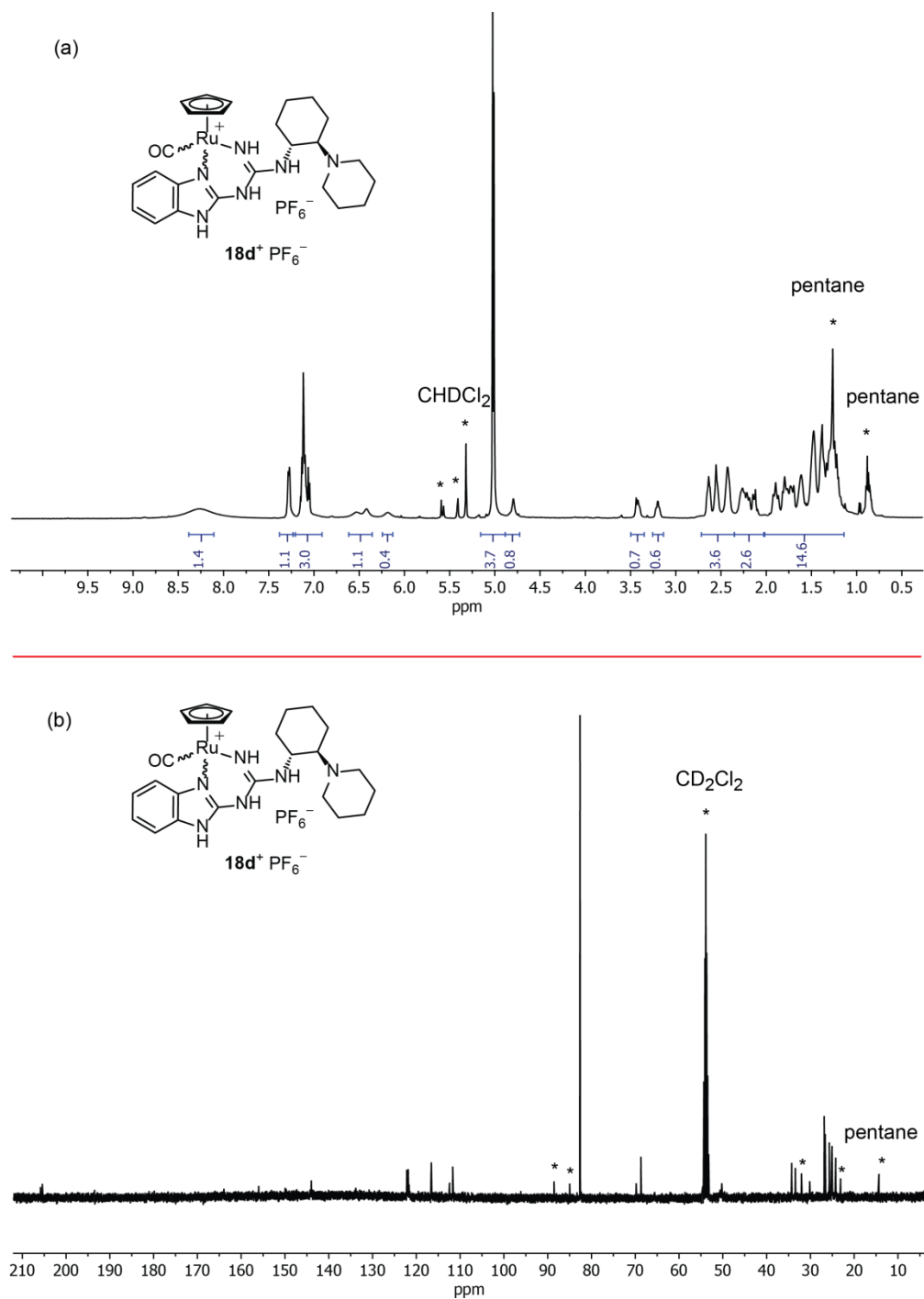


Figure b10 NMR spectra of (*R*_{Ru}*R*_C*R*_C/*S*_{Ru}*R*_C*R*_C)-**18d⁺** PF₆⁻ (CD₂Cl₂; * = solvent or impurities): (a) ¹H (500 MHz); (b) ¹³C{¹H} (125 MHz).

Table b1 Summary of crystallographic data.

	$(R_{Ru}R_C R_C)-18c^+$ (Δ)- TRISPHAT ⁻ ·CHCl ₃	$(R_{Ru}R_C R_C/S_{Ru}R_C R_C)-18c^+$ (Δ/Λ)-TRISPHAT ⁻ ·(Et ₂ O) ₂ ^a
molecular formula	C ₄₁ H ₃₀ Cl ₁₅ N ₆ O ₇ PRu	C ₄₈ H ₄₉ Cl ₁₂ N ₆ O ₉ PRu
formula weight	1382.50	1411.37
temperature (K)	150(2)	110(2)
wavelength (Å)	0.77490	1.54178
crystal system	Monoclinic	Monoclinic
space group	<i>P</i> 2 ₁	<i>P</i> 2 ₁
unit cell dimensions:		
<i>a</i> [Å]	10.286(2)	15.3215(5)
<i>b</i> [Å]	20.552(4)	13.8122(4)
<i>c</i> [Å]	13.183(4)	27.4488(8)
α [°]	90	90
β [°]	111.967(2)	103.025(2)
γ [°]	90	90
<i>V</i> [Å ³]	2584.6(10)	5659.4(3)
<i>Z</i>	2	4
ρ_{calc} [Mgm ⁻³]	1.776	1.656
μ [mm ⁻¹]	1.165	8.226
F (000)	1376	2856
crystal size [mm ³]	0.03 × 0.03 × 0.015	0.08 × 0.04 × 0.03
Θ range [°]	1.82 to 27.50	1.65 to 59.99
index ranges (<i>h,k,l</i>)	-12,12;-24,24;-15,15	-17,17;-15,14;-30,30
reflections collected	24796	73140
independent reflections	9102	15448
completeness to Θ	99.5% (27.50°)	79.8% (67.68°)
data/restraints/parameters	9102/1/652	15448/7/1403
goodness-of-fit on F ²	1.014	1.056
<i>R</i> indices (final) [<i>I</i> >2σ(<i>I</i>)]		
<i>R</i> ₁	0.0367	0.0303
<i>wR</i> ₂	0.0847	0.0697
<i>R</i> indices (all data)		
<i>R</i> ₁	0.0380	0.0361
<i>wR</i> ₂	0.0854	0.0720
absolute structure parameter	0.03(2)	0.006(4)
Largest diff. peak and hole [eÅ ⁻³]	0.451/-0.376	0.657/-0.849

^a a 1:1 mixture of two diastereomers of **18c**⁺ and two enantiomers of TRISPHAT⁻, with two Et₂O molecules per ruthenium.

Calculation of the circular dichroism (CD) excitations of $(R_{Ru}R_C R_C)-18c^+ PF_6^-$ and $(S_{Ru}R_C R_C)-18c^+ PF_6^-$

All calculations were performed using the Gaussian 09 (G09) suite of programs.¹⁸⁹ Full geometry optimizations in the gas phase were performed on the cations of the diastereoisomers, $(R_{Ru}R_C R_C)-18c^+ PF_6^-$ and $(S_{Ru}R_C R_C)-18c^+ PF_6^-$, using Density Functional Theory (DFT) with the Stuttgart/Dresden (SDD) basis set and small-core quasi-relativistic Effective Core Potential (ECP)¹⁹⁰ for ruthenium and the triple- ζ quality Pople basis set on carbon, nitrogen, and hydrogen, including a diffuse and polarization function on carbon and nitrogen (6-311+G(d)).¹⁹¹ The B3LYP functional (Becke-3 hybrid exchange¹⁹² and Lee-Yang-Parr correlation¹⁹³), as implemented in G09, was used for the geometry optimization. Frequency calculations on the B3LYP optimized geometry were performed to confirm that the stationary points were minima (i.e. all real frequencies). Time-Dependent Density Functional Theory (TD-DFT)¹⁹⁴ calculations in implicit CH₃CN (PCM)¹⁹⁵ at the B3LYP gas phase optimized geometries were performed to calculate the CD excitations and rotatory strengths¹⁹⁶ of $(R_{Ru}R_C R_C)-18c^+ PF_6^-$ and $(S_{Ru}R_C R_C)-18c^+ PF_6^-$ using both the B3LYP and BHandHLYP¹⁹⁷ functionals with the SDD basis set and ECP on ruthenium and triple- ζ quality Pople basis set including a diffuse and polarization function on carbon, nitrogen, and hydrogen (6-311+G(d)).¹⁹¹

CD spectra were simulated using the Gaussian function shown in Equation 1

$$\Delta\epsilon(E) = \frac{1}{2.297 \times 10^{-39}} \frac{1}{\sqrt{2\pi\sigma}} \sum_i^A \Delta E_i R_i e^{-\left[\frac{E-\Delta E_i}{2\sigma}\right]^2} \quad \text{Equation 1}$$

where σ is the band width at height $1/e$ ($\sigma = 0.20$ eV), ΔE_i and R_i are the excitation energy (eV) and rotatory strength R (10^{-40} cgs) in dipole length (R_{len}) for excitation i , A is the number of excitations calculations ($A = 33$), and $\Delta\epsilon$ is the molar extinction coefficient ($M^{-1}cm^{-1}$).

The purpose of checking the results with two basis sets was to increase confidence in the conclusions, should they be the same for both methods. The results for all of the above calculations are given in Figures b11 and b12.

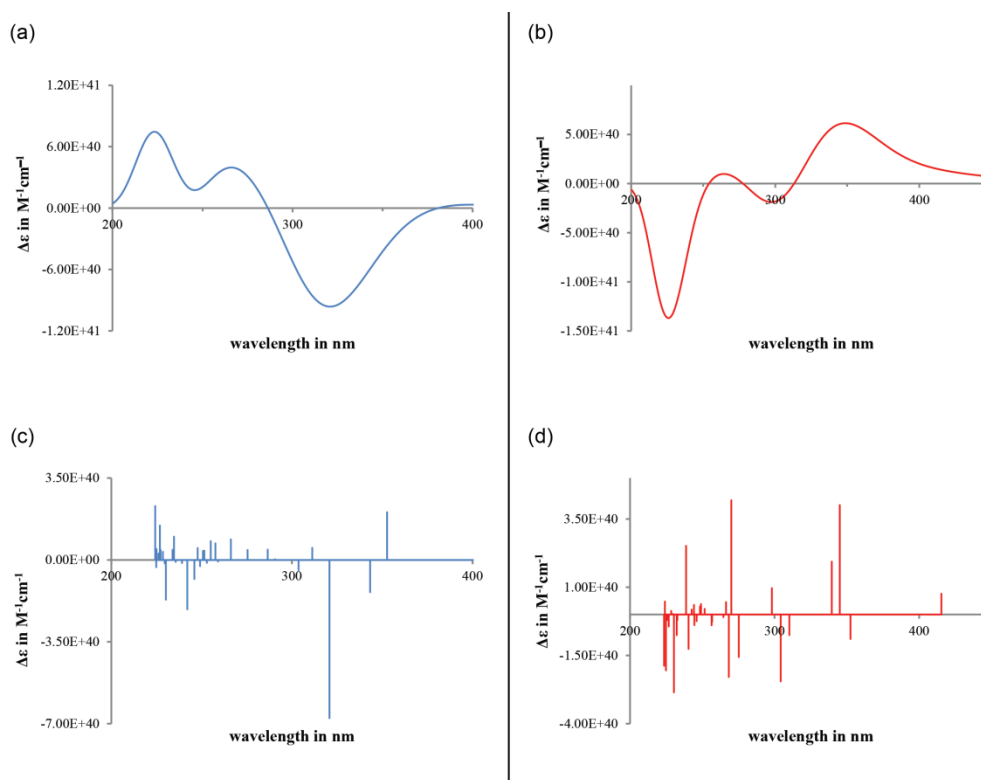


Figure b11 Calculated CD excitations and rotatory strengths using the B3LYP functional: (a) Simulated CD spectrum of $(R_{Ru}R_C R_C)-18c^+ PF_6^-$; (b) Simulated CD spectrum of $(S_{Ru}R_C R_C)-18c^+ PF_6^-$; (c) Plot of calculated CD excitations for $(R_{Ru}R_C R_C)-18c^+ PF_6^-$ versus wavelength; (d) Plot of calculated CD excitations for $(S_{Ru}R_C R_C)-18c^+ PF_6^-$ versus wavelength.

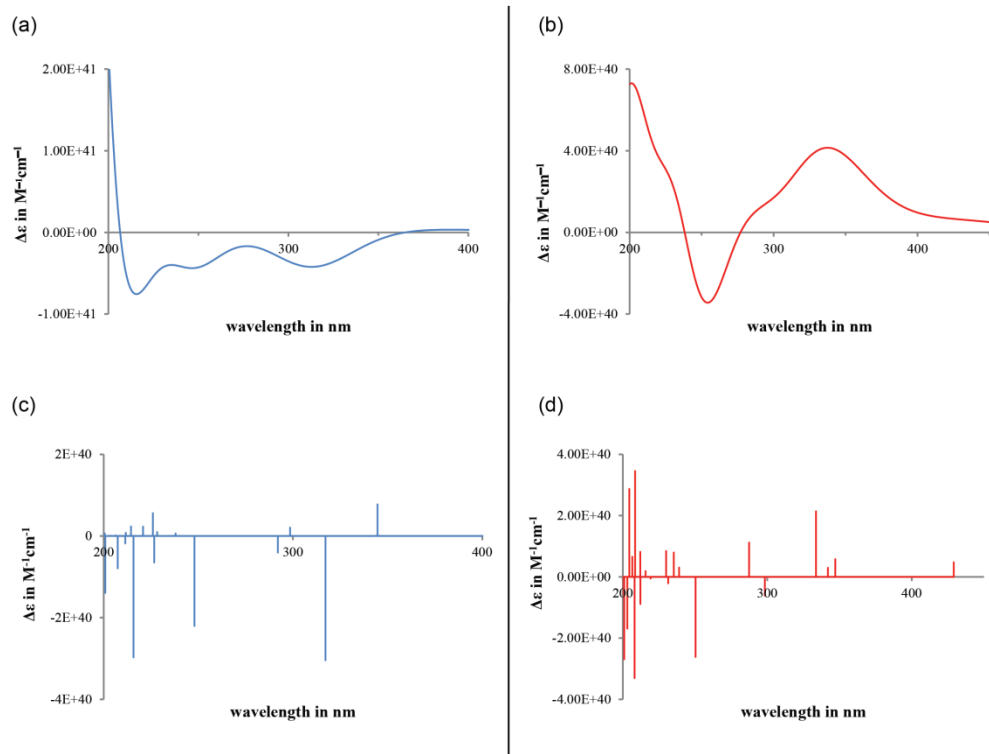
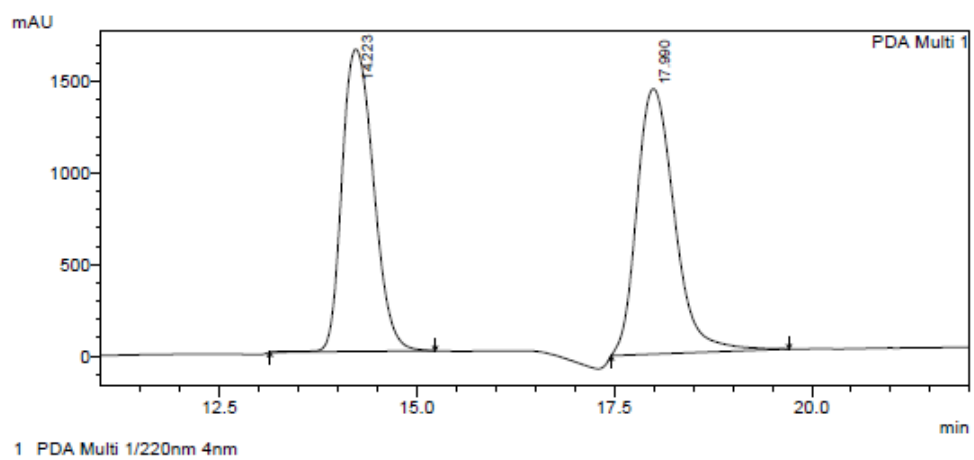


Figure b12 Calculated CD excitations and rotatory strengths using the BHandHLYP functional: (a) Simulated CD spectrum of $(R_{Ru}R_C R_C)\text{-18c}^+ \text{PF}_6^-$; (b) Simulated CD spectrum of $(S_{Ru}R_C R_C)\text{-18c}^+ \text{PF}_6^-$; (c) Plot of calculated CD excitations for $(R_{Ru}R_C R_C)\text{-18c}^+ \text{PF}_6^-$ versus wavelength; (d) Plot of calculated CD excitations for $(S_{Ru}R_C R_C)\text{-18c}^+ \text{PF}_6^-$ versus wavelength.

HPLC traces

Friedel-Crafts alkylation of 5a or 5b with 6 catalyzed by $(S_{Ru}R_C R_C)-18c^+ PF_6^-$

(Table 3.3)



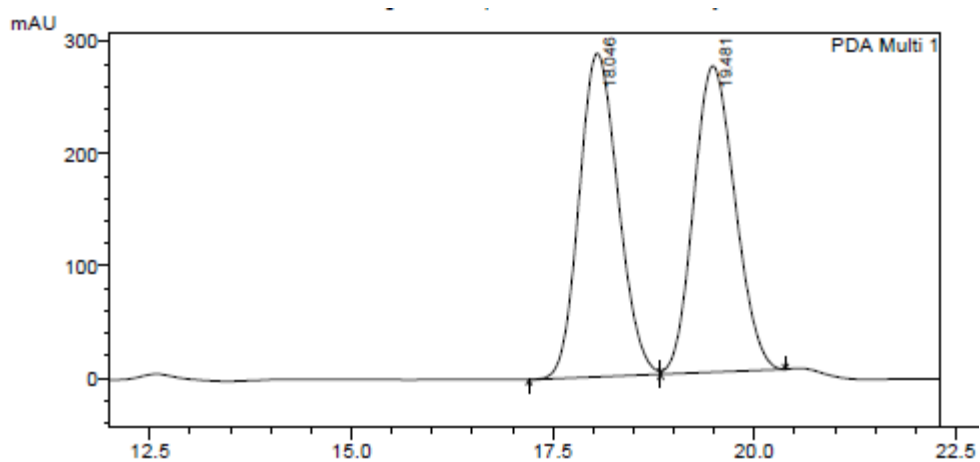
1 PDA Multi 1/220nm 4nm

PeakTable

PDA Ch1 220nm 4nm

Peak#	Ret. Time	Area	Height	Area %	Height %
1	14.223	45956573	1651316	48.826	53.244
2	17.990	48166676	1450118	51.174	46.756
Total		94123249	3101433	100.000	100.000

Figure b13 HPLC trace of 7a (Table 3.3, entry 1): catalyzed by $(S_{Ru}R_C R_C)-18c^+ PF_6^-$.



1 PDA Multi 1/254nm 4nm

PeakTable

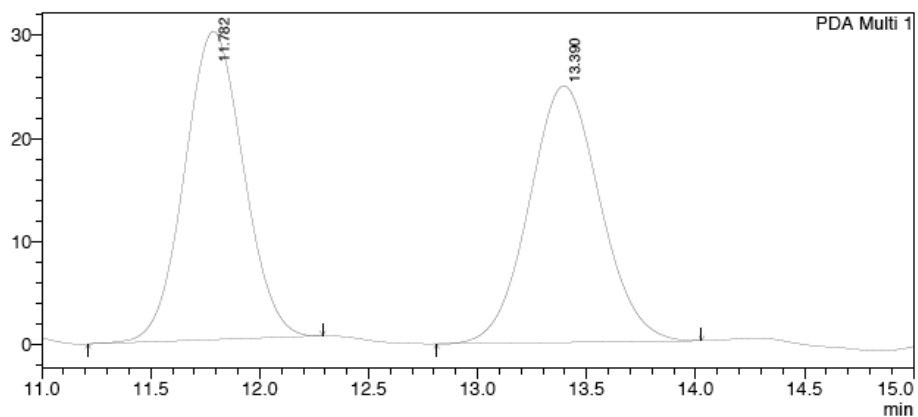
PDA Ch1 254nm 4nm

Peak#	Ret. Time	Area	Height	Area %	Height %
1	18.046	9721277	288697	49.875	51.375
2	19.481	9770018	273242	50.125	48.625
Total		19491294	561939	100.000	100.000

Figure b14 HPLC trace of **7b** (Table 3.3, entry 2): catalyzed by $(S_{Ru}R_C R_C)-18c^+ PF_6^-$.

Addition of dialkyl malonates to nitroalkenes (Table3.4)

(a)
mAU



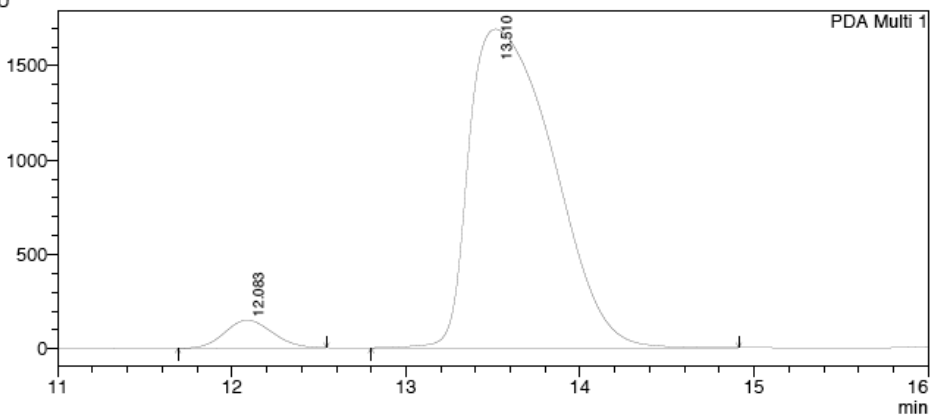
1 PDA Multi 1/215nm 4nm

PeakTable

PDA Ch1 215nm 4nm

Peak#	Ret. Time	Area	Height	Area %	Height %
1	11.782	563981	29978	50.011	54.597
2	13.390	563741	24930	49.989	45.403
Total		1127721	54908	100.000	100.000

(b)
mAU

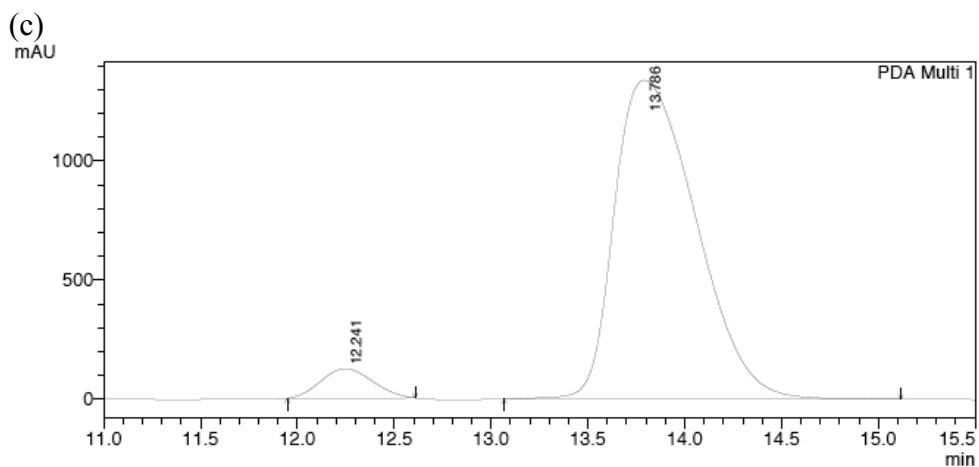


1 PDA Multi 1/215nm 4nm

PeakTable

PDA Ch1 215nm 4nm

Peak#	Ret. Time	Area	Height	Area %	Height %
1	12.083	2812925	147691	4.720	8.040
2	13.510	56777222	1689184	95.280	91.960
Total		59590147	1836875	100.000	100.000

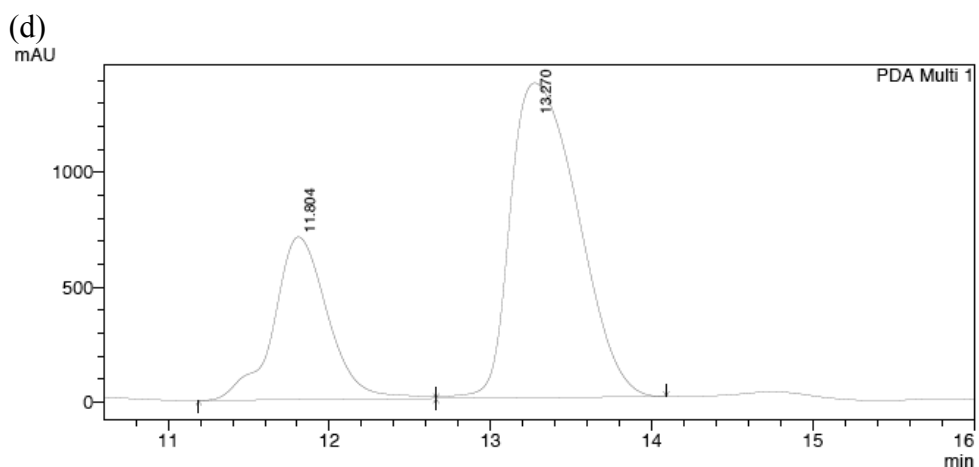


1 PDA Multi 1/215nm 4nm

PeakTable

PDA Ch1 215nm 4nm

Peak#	Ret. Time	Area	Height	Area %	Height %
1	12.241	2301902	124093	5.533	8.475
2	13.786	39297271	1340016	94.465	91.521
3	30.677	638	49	0.002	0.003
Total		41599811	1464158	100.000	100.000



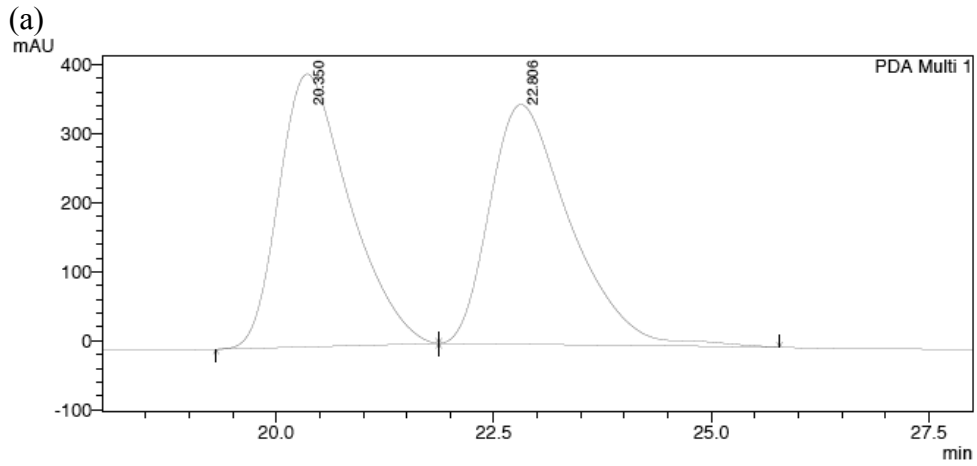
1 PDA Multi 1/215nm 4nm

PeakTable

PDA Ch1 215nm 4nm

Peak#	Ret. Time	Area	Height	Area %	Height %
1	11.804	16655331	708576	29.440	34.094
2	13.270	39919086	1369717	70.560	65.906
Total		56574417	2078293	100.000	100.000

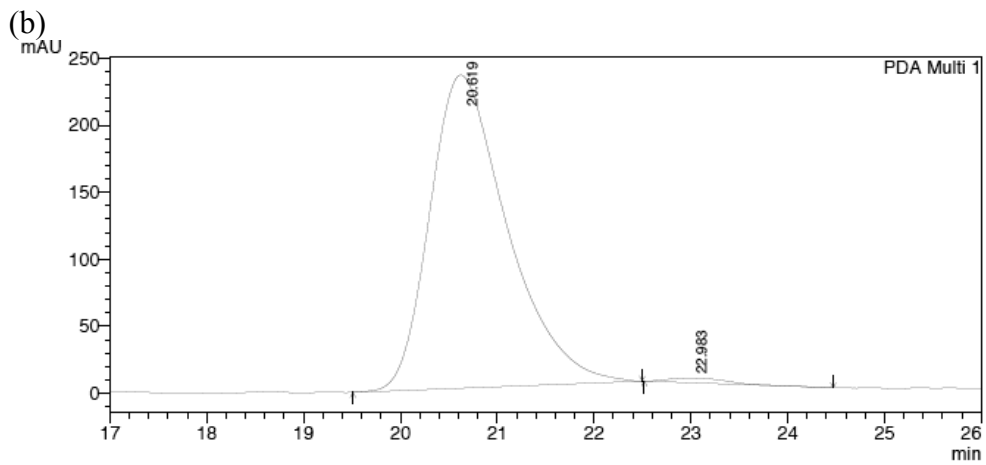
Figure b15 HPLC traces of **19a** (Table 3.4, entry 1): (a) racemic sample; (b) catalyzed by $(S_{Ru}R_C R_C)\text{-18c}^+ \text{PF}_6^-$; (c) catalyzed by $(R_{Ru}R_C R_C)\text{-18c}^+ \text{PF}_6^-$; (d) catalyzed by $(R_C R_C)\text{-16c}$.



PeakTable

PDA Ch1 215nm 4nm

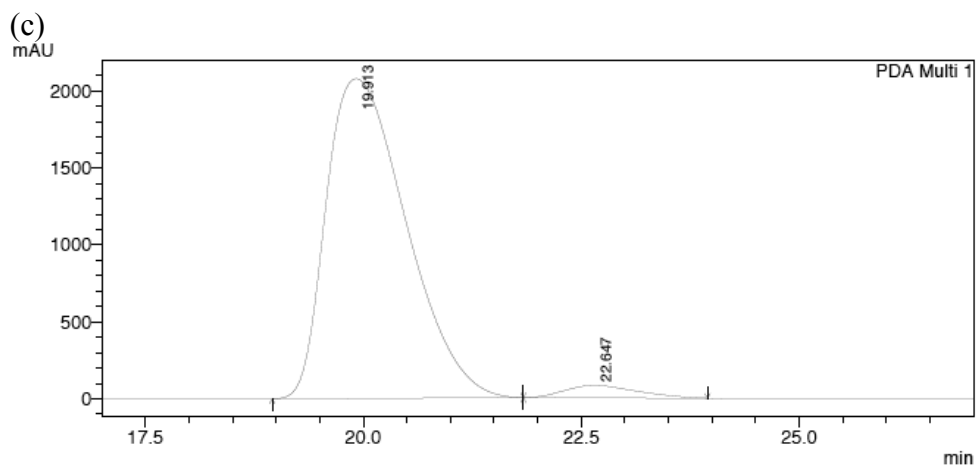
Peak#	Ret. Time	Area	Height	Area %	Height %
1	20.350	22283866	394878	49.925	53.229
2	22.806	22351106	346970	50.075	46.771
Total		44634972	741848	100.000	100.000



PeakTable

PDA Ch1 215nm 4nm

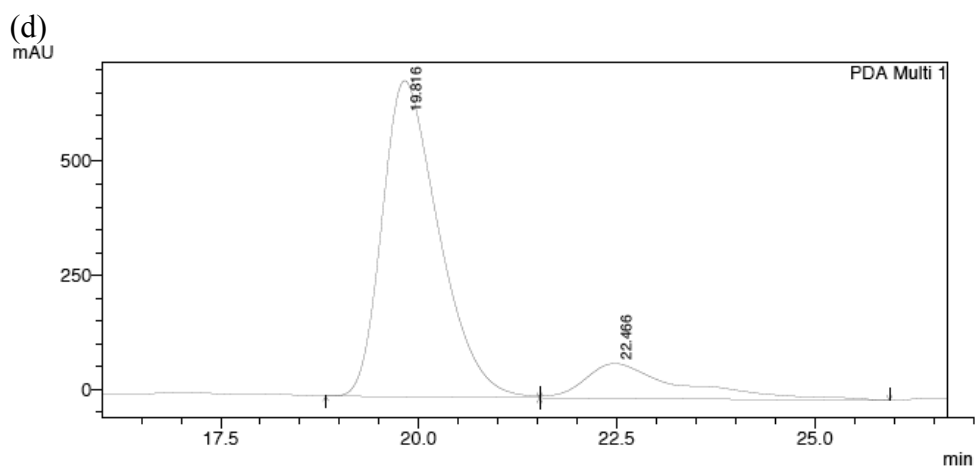
Peak#	Ret. Time	Area	Height	Area %	Height %
1	20.619	13013635	233593	98.843	98.531
2	22.983	152319	3483	1.157	1.469
Total		13165954	237077	100.000	100.000



PDA Ch1 215nm 4nm

PeakTable

Peak#	Ret. Time	Area	Height	Area %	Height %
1	19.913	132598615	2077601	96.618	96.254
2	22.647	4641689	80861	3.382	3.746
Total		137240304	2158462	100.000	100.000

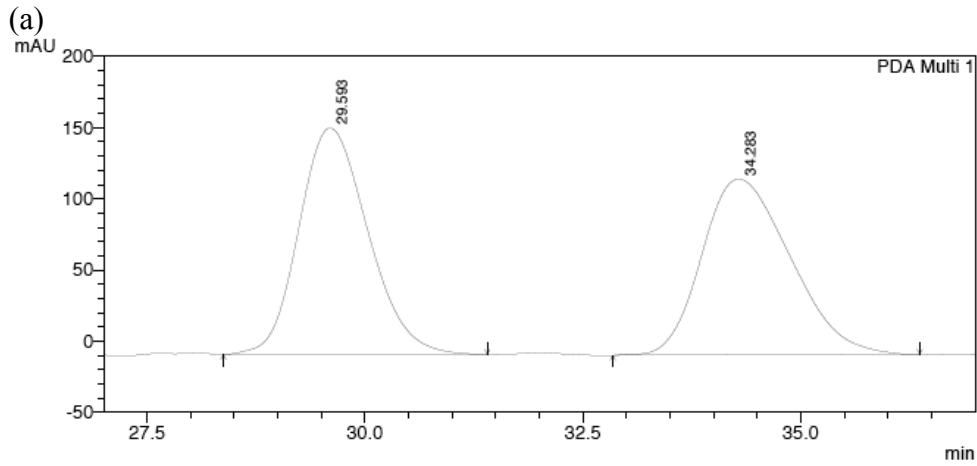


PDA Ch1 215nm 4nm

PeakTable

Peak#	Ret. Time	Area	Height	Area %	Height %
1	19.816	34540964	693355	84.158	90.081
2	22.466	6502010	76347	15.842	9.919
Total		41042973	769702	100.000	100.000

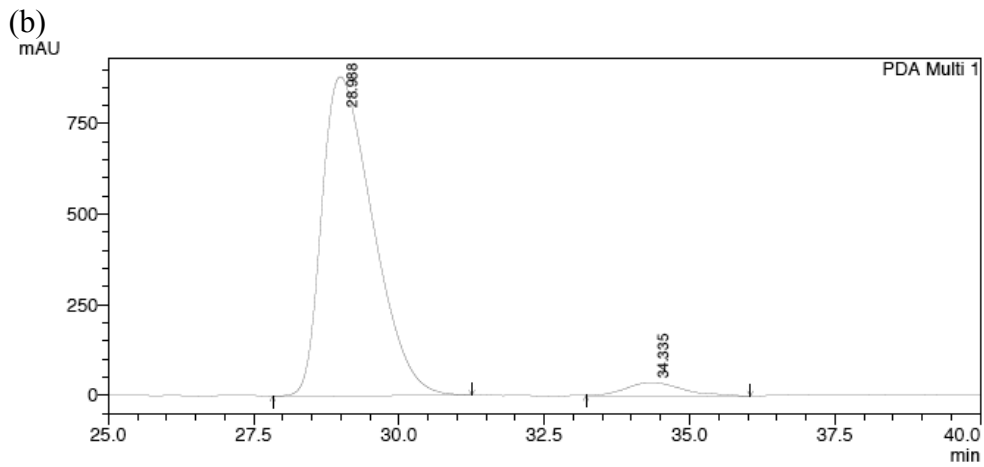
Figure b16 HPLC traces of **19b** (Table 3.4, entry 2): (a) racemic sample; (b) catalyzed by ($S_{Ru}R_C R_C$)-**18c**⁺ PF₆⁻; (c) catalyzed by ($R_{Ru}R_C R_C$)-**18c**⁺ PF₆⁻; (d) catalyzed by ($R_C R_C$)-**16c**.



PeakTable

PDA Ch1 215nm 4nm

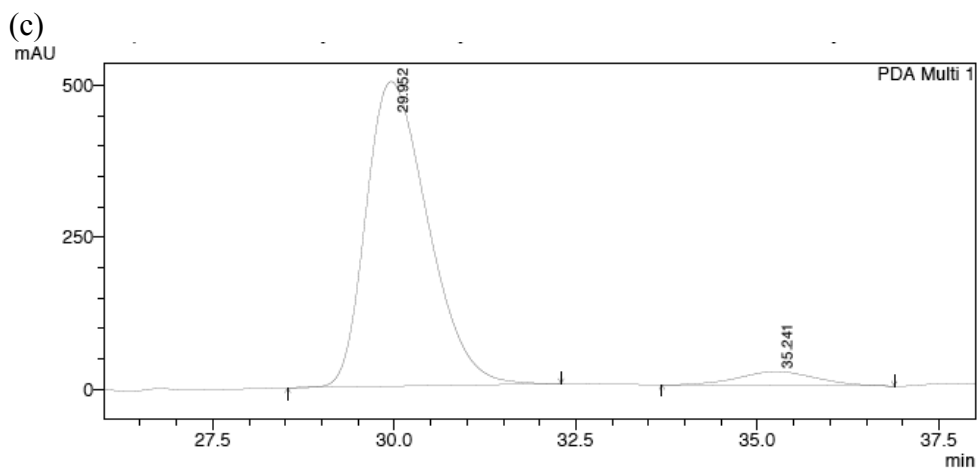
Peak#	Ret. Time	Area	Height	Area %	Height %
1	29.593	8752157	158903	50.187	56.289
2	34.283	8686944	123396	49.813	43.711
Total		17439100	282299	100.000	100.000



PeakTable

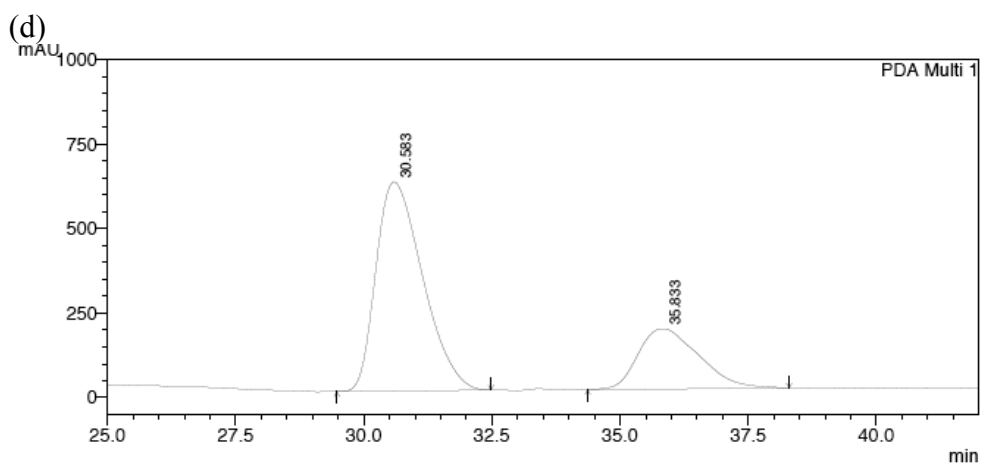
PDA Ch1 215nm 4nm

Peak#	Ret. Time	Area	Height	Area %	Height %
1	28.988	53859955	881649	95.609	95.981
2	34.335	2473853	36915	4.391	4.019
Total		56333808	918564	100.000	100.000



PeakTable

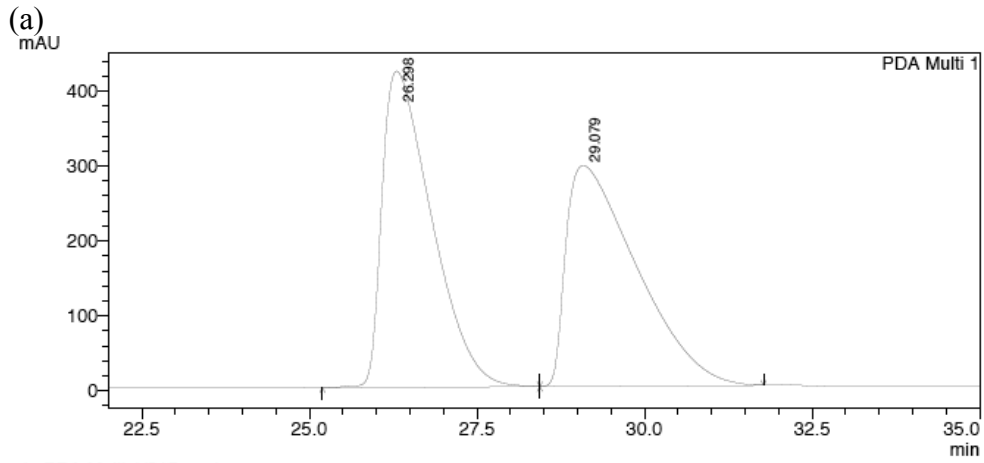
PDA Ch1 215nm 4nm					
Peak#	Ret. Time	Area	Height	Area %	Height %
1	29.952	29754861	501684	94.592	95.698
2	35.241	1701046	22552	5.408	4.302
Total		31455907	524236	100.000	100.000



PeakTable

PDA Ch1 215nm 4nm					
Peak#	Ret. Time	Area	Height	Area %	Height %
1	30.583	39197918	618202	72.670	77.566
2	35.833	14741742	178795	27.330	22.434
Total		53939659	796996	100.000	100.000

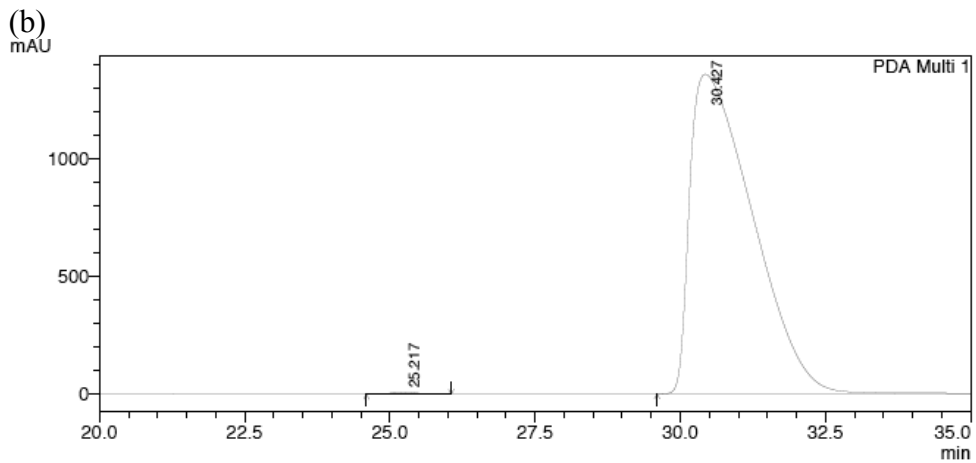
Figure b17 HPLC traces of **19c** (Table 3.4, entry 3): (a) racemic sample; (b) catalyzed by $(S_{Ru}R_C R_C)\text{-18c}^+ \text{PF}_6^-$; (c) catalyzed by $(R_{Ru}R_C R_C)\text{-18c}^+ \text{PF}_6^-$; (d) catalyzed by $(R_C R_C)\text{-16c}$.



PeakTable

PDA Ch1 215nm 4nm

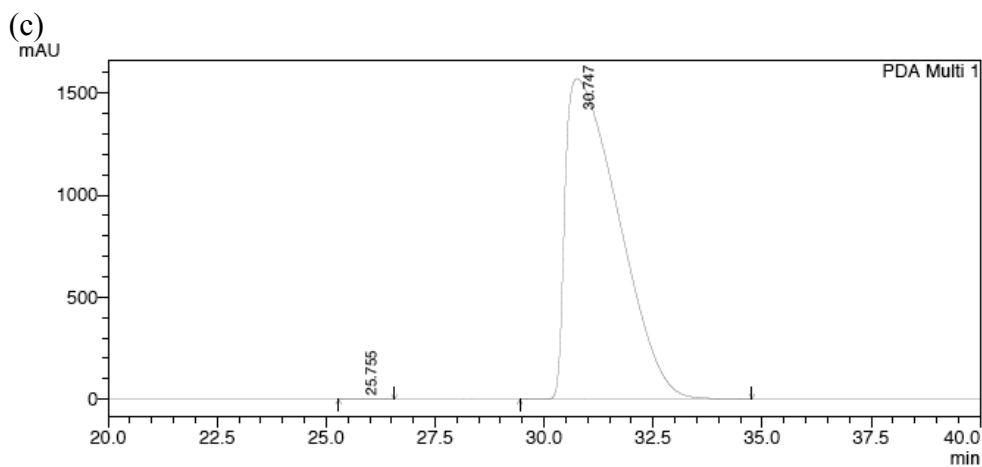
Peak#	Ret. Time	Area	Height	Area %	Height %
1	26.298	21717903	421881	50.132	58.884
2	29.079	21603442	294575	49.868	41.116
Total		43321345	716456	100.000	100.000



PeakTable

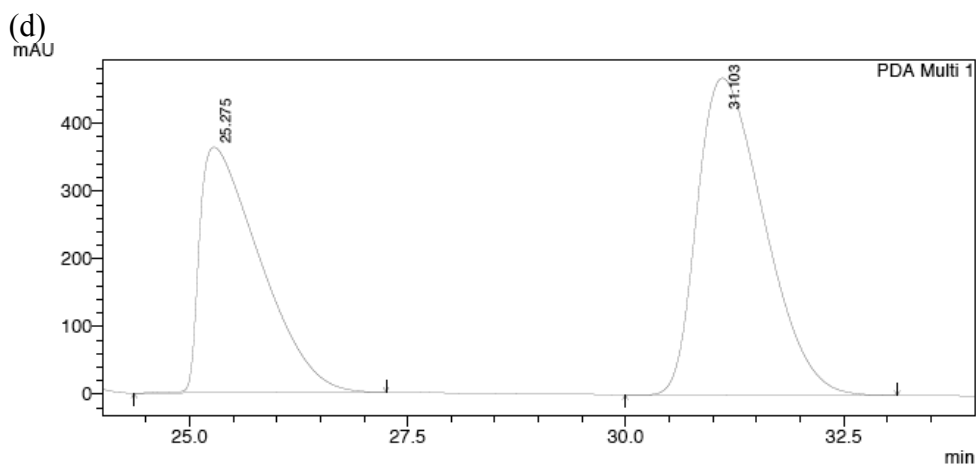
PDA Ch1 215nm 4nm

Peak#	Ret. Time	Area	Height	Area %	Height %
1	25.217	268975	9313	0.263	0.680
2	30.427	101915988	1360432	99.737	99.320
Total		102184963	1369745	100.000	100.000



PeakTable

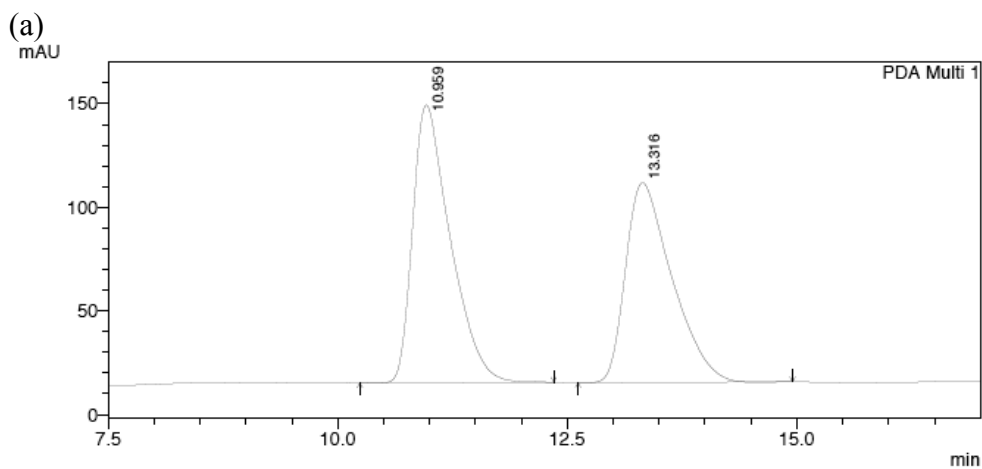
Peak#	Ret. Time	Area	Height	Area %	Height %
1	25.755	55894	1941	0.042	0.123
2	30.747	133011744	1571367	99.958	99.877
Total		133067638	1573308	100.000	100.000



PeakTable

Peak#	Ret. Time	Area	Height	Area %	Height %
1	25.275	17505324	363131	41.100	43.678
2	31.103	25086330	468256	58.900	56.322
Total		42591654	831386	100.000	100.000

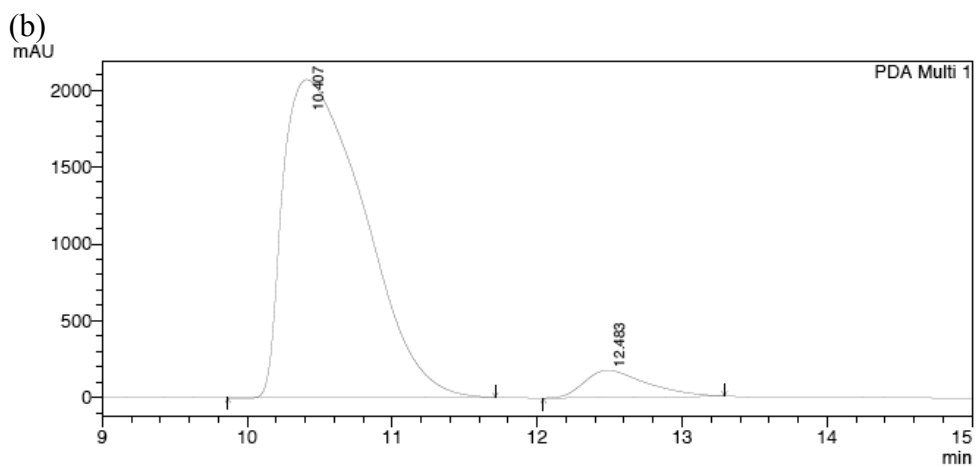
Figure b18 HPLC traces of **19d** (Table 3.4, entry 4): (a) racemic sample; (b) catalyzed by ($S_{Ru}R_C R_C$)-**18c**⁺ PF₆⁻; (c) catalyzed by ($R_{Ru}R_C R_C$)-**18c**⁺ PF₆⁻; (d) catalyzed by ($R_C R_C$)-**16c**.



PeakTable

PDA Ch1 215nm 4nm

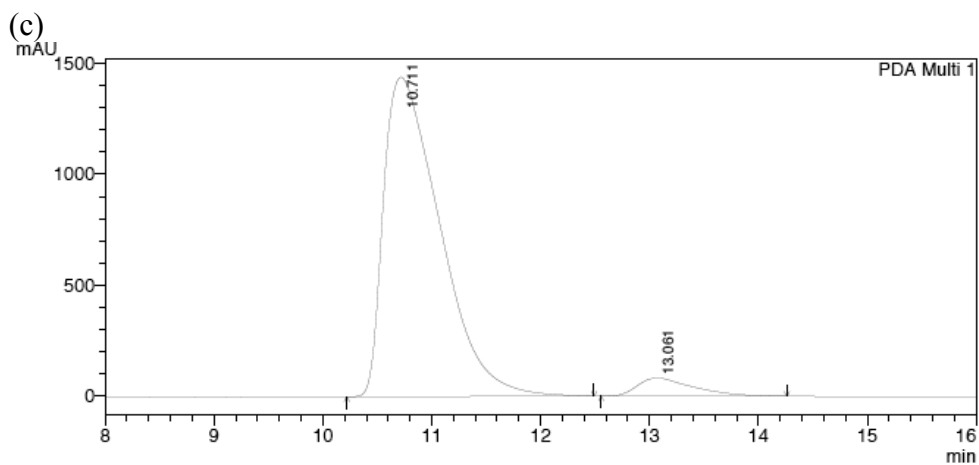
Peak#	Ret. Time	Area	Height	Area %	Height %
1	10.959	3822233	134008	53.077	58.156
2	13.316	3379078	96420	46.923	41.844
Total		7201311	230427	100.000	100.000



PeakTable

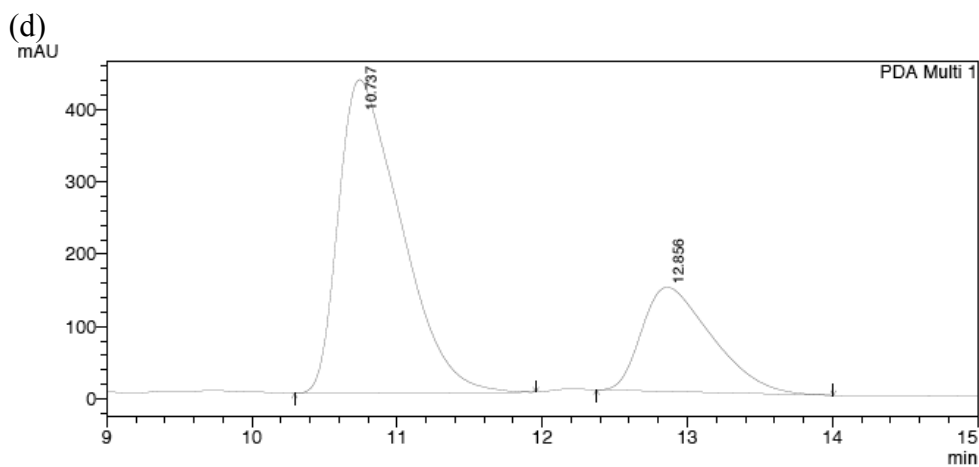
PDA Ch1 215nm 4nm

Peak#	Ret. Time	Area	Height	Area %	Height %
1	10.407	80461754	2069277	93.877	92.164
2	12.483	5247953	175940	6.123	7.836
Total		85709707	2245217	100.000	100.000



PeakTable

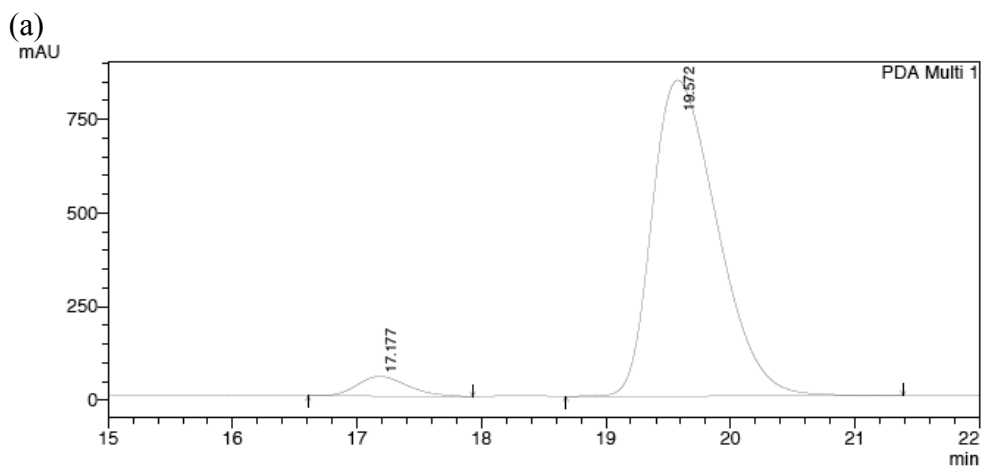
Peak#	Ret. Time	Area	Height	Area %	Height %
1	10.711	51772069	1438106	94.694	94.602
2	13.061	2901231	82057	5.306	5.398
Total		54673300	1520163	100.000	100.000



PeakTable

Peak#	Ret. Time	Area	Height	Area %	Height %
1	10.737	12958035	433532	72.827	75.047
2	12.856	4834850	144147	27.173	24.953
Total		17792885	577679	100.000	100.000

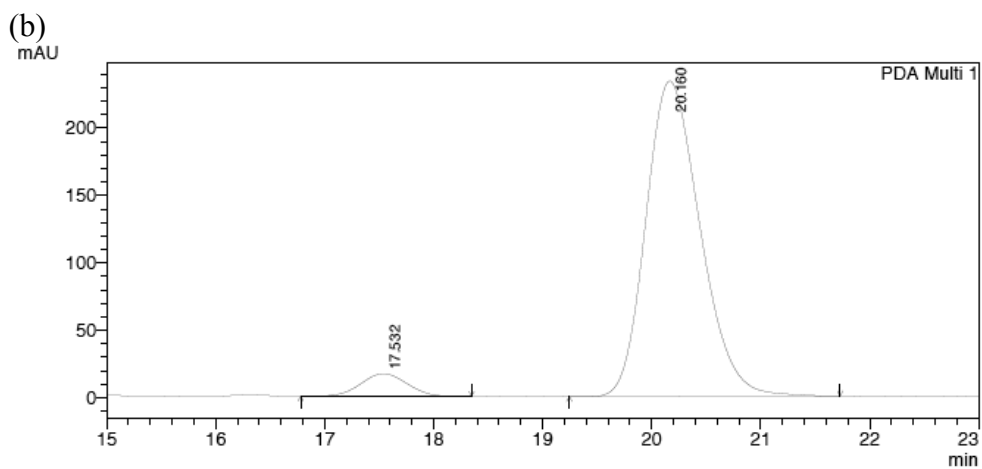
Figure b19 HPLC traces of **19e** (Table 3.4, entry 5): (a) racemic sample; (b) catalyzed by ($S_{Ru}R_C R_C$)-**18c**⁺ PF₆⁻; (c) catalyzed by ($R_{Ru}R_C R_C$)-**18c**⁺ PF₆⁻; (d) catalyzed by ($R_C R_C$)-**16c**.



PeakTable

PDA Ch1 215nm 4nm

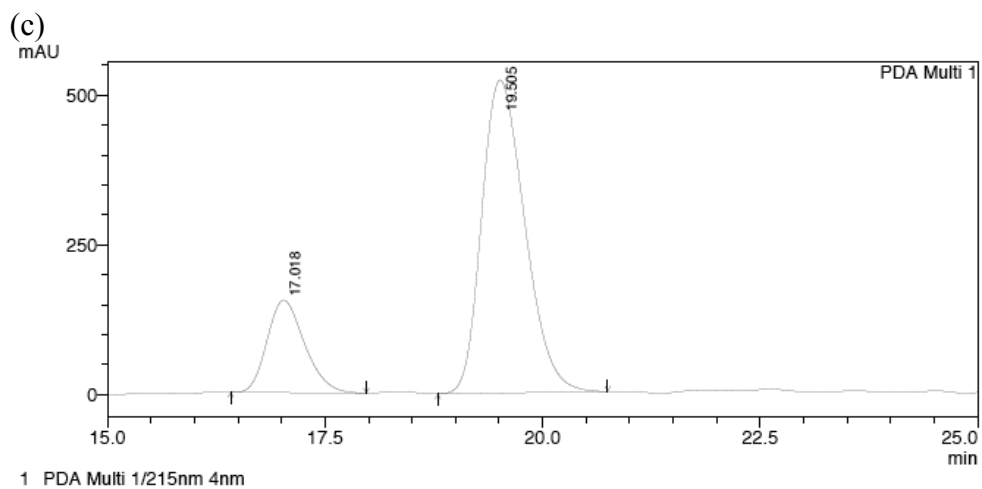
Peak#	Ret. Time	Area	Height	Area %	Height %
1	17.177	1481045	52615	4.611	5.870
2	19.572	30638336	843729	95.389	94.130
Total		32119381	896345	100.000	100.000



PeakTable

PDA Ch1 215nm 4nm

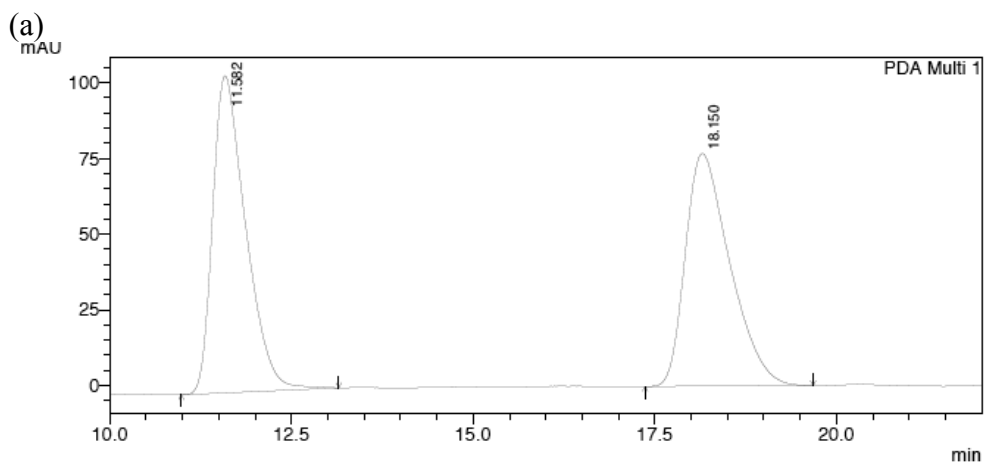
Peak#	Ret. Time	Area	Height	Area %	Height %
1	17.532	491011	16786	5.720	6.696
2	20.160	8092439	233894	94.280	93.304
Total		8583451	250680	100.000	100.000



PeakTable

Peak#	Ret. Time	Area	Height	Area %	Height %
1	17.018	4612790	154270	20.398	22.783
2	19.505	18000702	522849	79.602	77.217
Total		22613492	677120	100.000	100.000

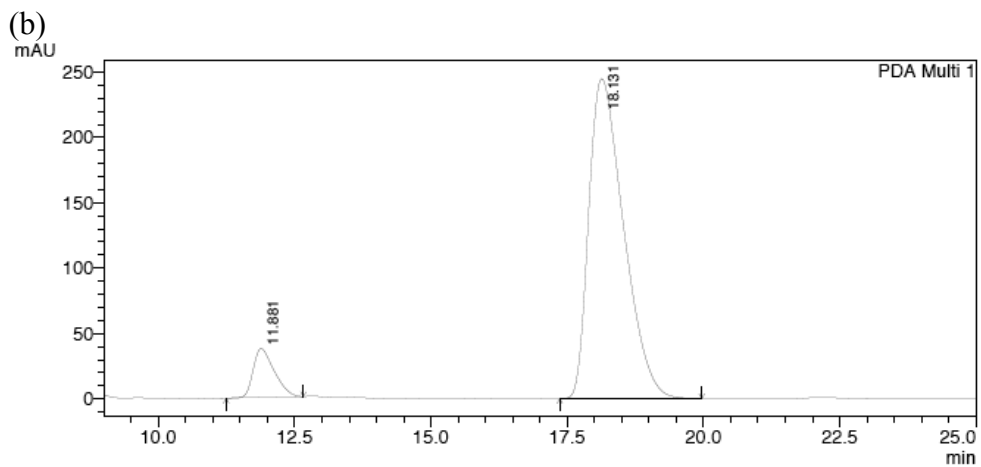
Figure b20 HPLC traces of **19f** (Table 3.4, entry 6): (a) catalyzed by ($S_{Ru}R_C R_C$)-**18c**⁺ PF₆⁻; (b) catalyzed by ($R_{Ru}R_C R_C$)-**18c**⁺ PF₆⁻; (c) catalyzed by ($R_C R_C$)-**16c**.



PeakTable

PDA Ch1 215nm 4nm

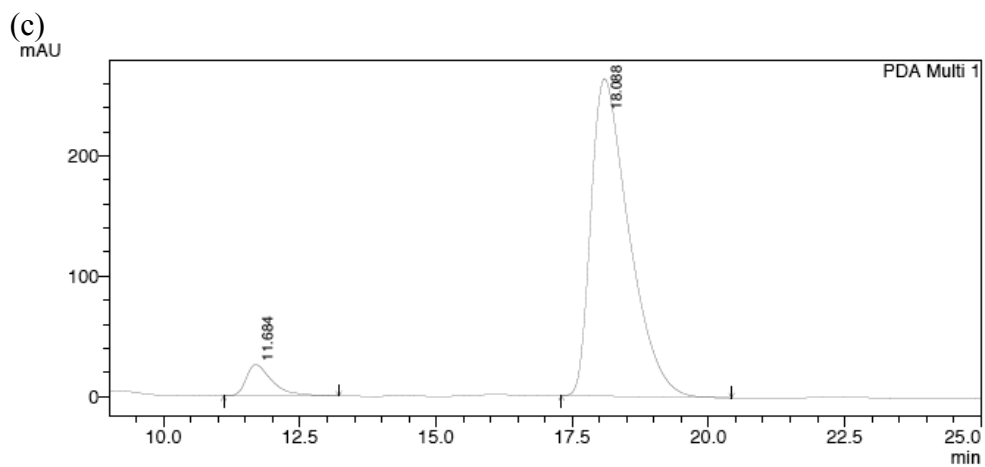
Peak#	Ret. Time	Area	Height	Area %	Height %
1	11.582	3316681	104734	50.327	57.687
2	18.150	3273581	76823	49.673	42.313
Total		6590262	181557	100.000	100.000



PeakTable

PDA Ch1 215nm 4nm

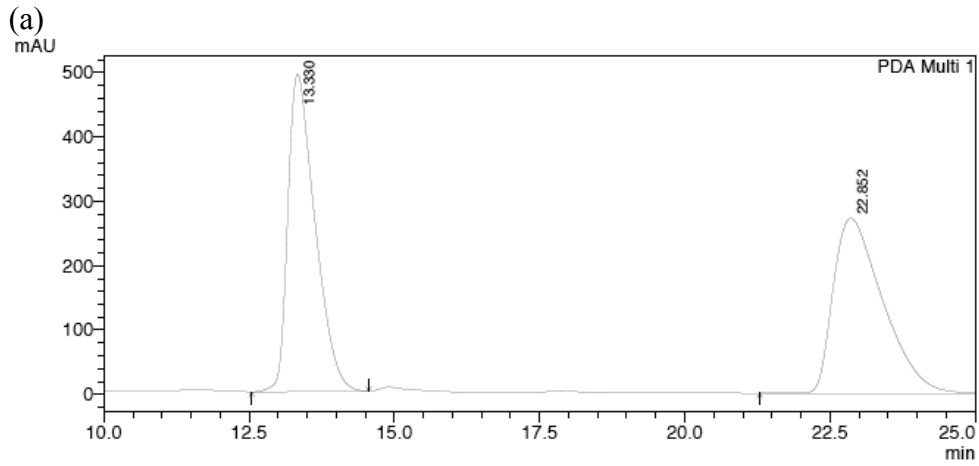
Peak#	Ret. Time	Area	Height	Area %	Height %
1	11.881	1004051	37440	8.444	13.260
2	18.131	10886164	244902	91.556	86.740
Total		11890215	282342	100.000	100.000



PeakTable

Peak#	Ret. Time	Area	Height	Area %	Height %
1	11.684	870372	26101	6.370	9.004
2	18.088	12792408	263785	93.630	90.996
Total		13662780	289886	100.000	100.000

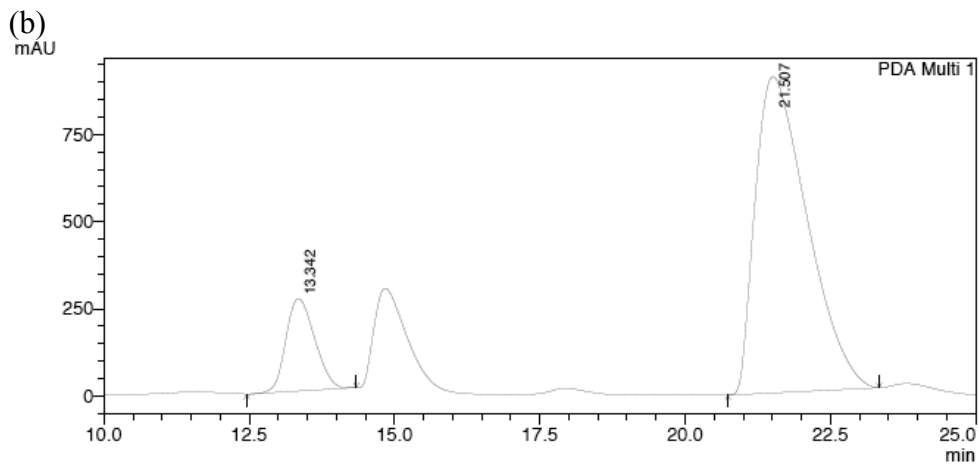
Figure b21 HPLC traces of **19g** (Table 3.4, entry 7): (a) racemic sample; (b) catalyzed by (*S*_{Ru}*R*_C*R*_C)-**18c**⁺ PF₆⁻; (c) catalyzed by (*R*_{Ru}*R*_C*R*_C)-**18c**⁺ PF₆⁻.



PeakTable

PDA Ch1 215nm 4nm

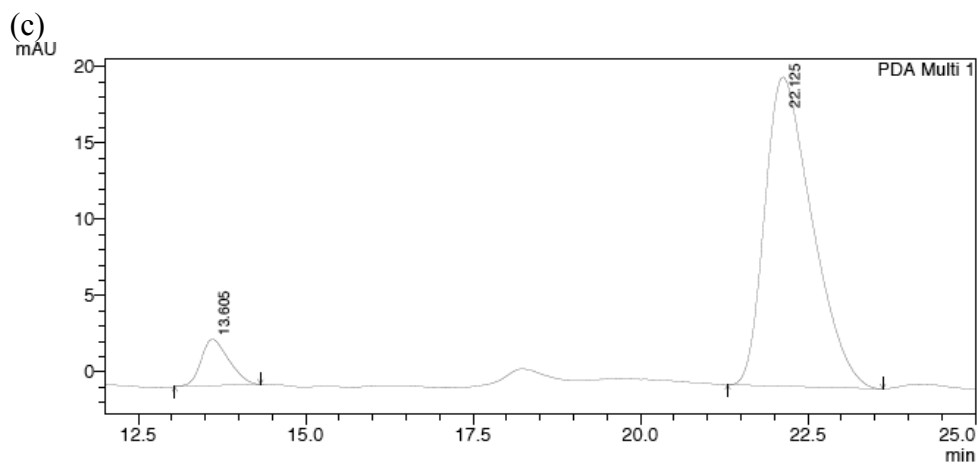
Peak#	Ret. Time	Area	Height	Area %	Height %
1	13.330	16100150	493529	49.876	64.423
2	22.852	16180220	272550	50.124	35.577
Total		32280369	766079	100.000	100.000



PeakTable

PDA Ch1 215nm 4nm

Peak#	Ret. Time	Area	Height	Area %	Height %
1	13.342	9120036	264786	13.899	22.600
2	21.507	56495845	906833	86.101	77.400
Total		65615880	1171619	100.000	100.000



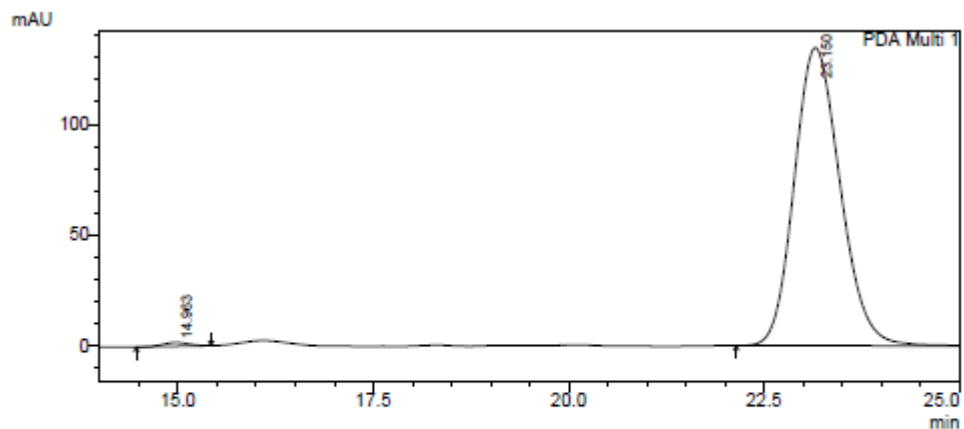
PeakTable

Peak#	Ret. Time	Area	Height	Area %	Height %
1	13.605	87181	3040	8.040	13.058
2	22.125	997218	20238	91.960	86.942
Total		1084400	23278	100.000	100.000

Figure b22 HPLC traces of **19h** (Table 3.4, entry 8): (a) racemic sample; (b) catalyzed by ($S_{Ru}R_C R_C$)-**18c**⁺ PF₆⁻; (c) catalyzed by ($R_{Ru}R_C R_C$)-**18c**⁺ PF₆⁻.

Additions of Michael donors to 6 (Table 3.5).

(a)



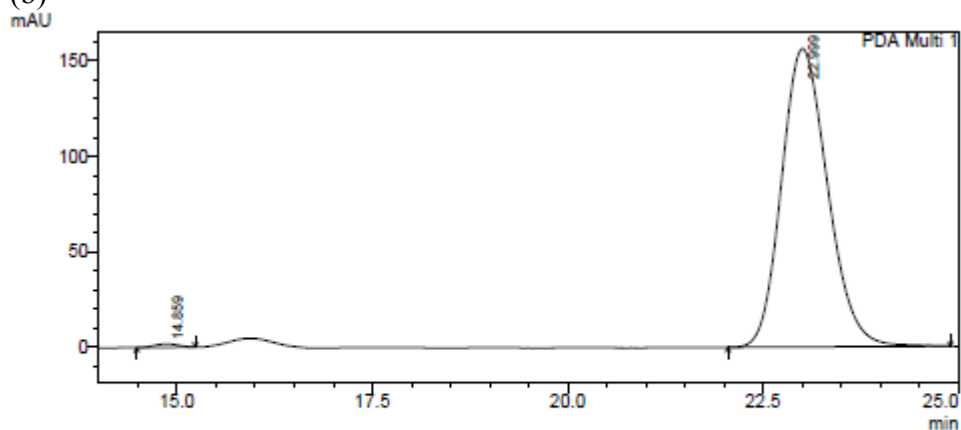
1 PDA Multi 1/210nm 4nm

PeakTable

PDA Ch1 210nm 4nm

Peak#	Ret. Time	Area	Height	Area %	Height %
1	14.963	39208	1692	0.706	1.241
2	23.150	5515031	134643	99.294	98.759
Total		5554239	136335	100.000	100.000

(b)



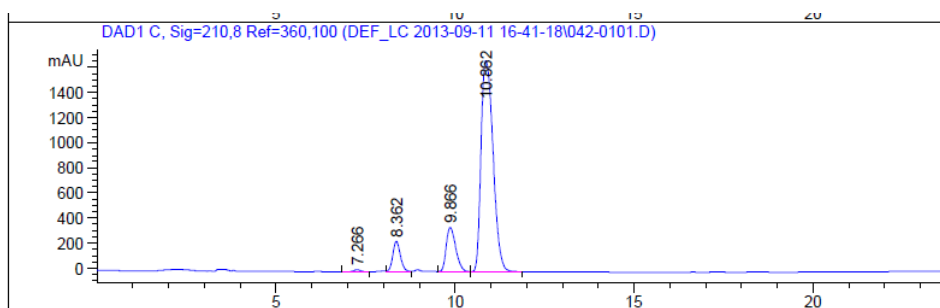
1 PDA Multi 1/210nm 4nm

PeakTable

PDA Ch1 210nm 4nm

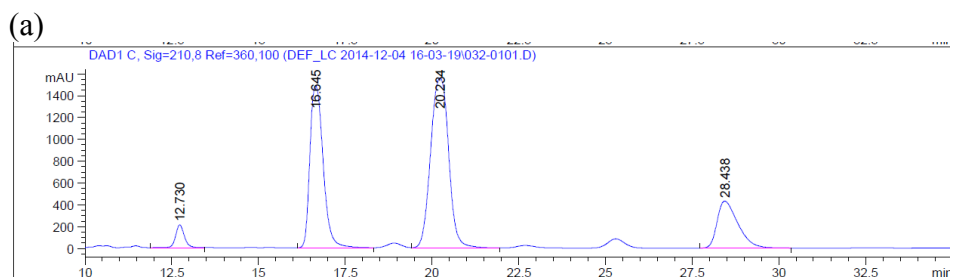
Peak#	Ret. Time	Area	Height	Area %	Height %
1	14.859	39474	1873	0.611	1.185
2	22.999	6421324	156260	99.389	98.815
Total		6460798	158133	100.000	100.000

Figure b23 HPLC traces of **21** (Table 3.5, entry 1): (a) catalyzed by ($S_{Ru}R_C R_C$)-**18c**⁺ PF₆⁻; (b) catalyzed by ($R_{Ru}R_C R_C$)-**18c**⁺ PF₆⁻.

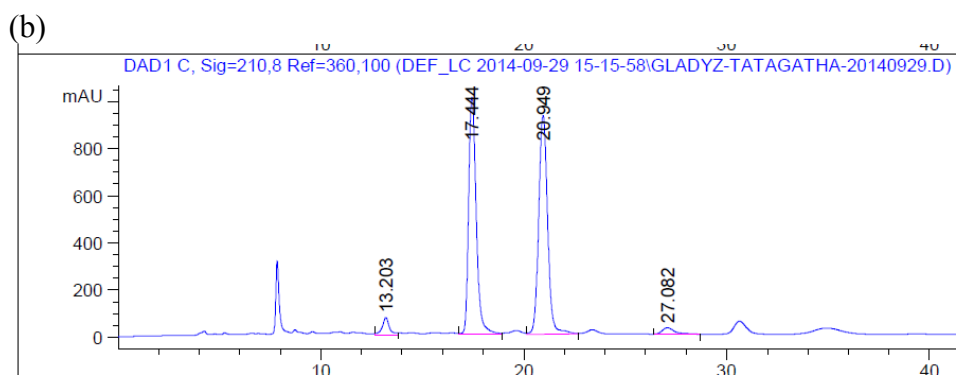


Peak #	RetTime [min]	Type	Width [min]	Area [mAU*s]	Height [mAU]	Area %
1	7.266	VB	0.2140	233.80872	16.83352	0.4709
2	8.362	VV	0.2303	3649.79102	244.35503	7.3504
3	9.866	VV	0.2861	6539.18750	352.96991	13.1694
4	10.862	VB	0.3744	3.92316e4	1680.41602	79.0094

Figure b24 HPLC trace of **23** (Table 3.5, entry 2): catalyzed by $(S_{Ru}R_C R_C)\text{-18c}^+ \text{PF}_6^-$.

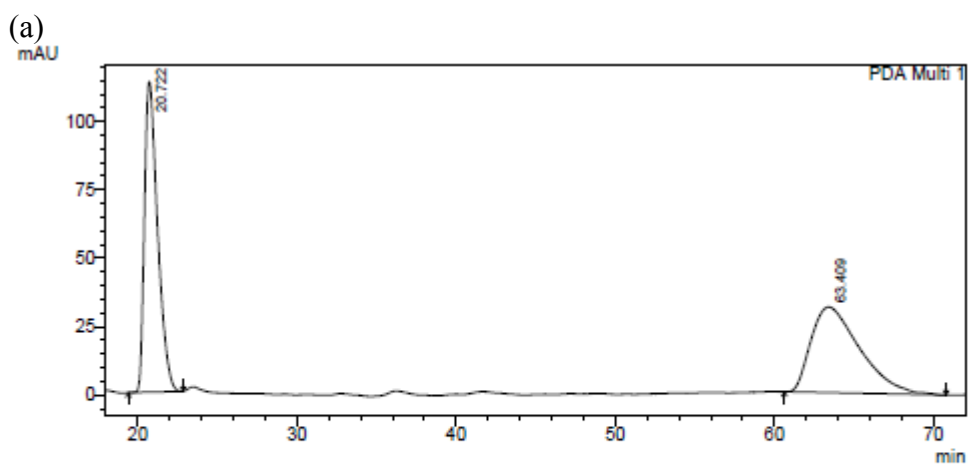


Peak #	RetTime [min]	Type	Width [min]	Area [mAU*s]	Height [mAU]	Area %
1	12.730	VB	0.2733	3755.66431	209.38499	3.1993
2	16.645	BB	0.4174	3.94563e4	1488.01062	33.6111
3	20.234	VB	0.5745	5.61951e4	1558.93457	47.8702
4	28.438	BB	0.6340	1.79836e4	431.71286	15.3194



Peak #	RetTime [min]	Type	Width [min]	Area [mAU*s]	Height [mAU]	Area %
1	13.203	BB	0.3573	1811.13281	73.03262	3.1292
2	17.444	VB	0.4059	2.63954e4	1006.84290	45.6049
3	20.949	VV	0.4774	2.84635e4	929.11578	49.1781
4	27.082	BB	0.6562	1208.36267	27.30770	2.0878

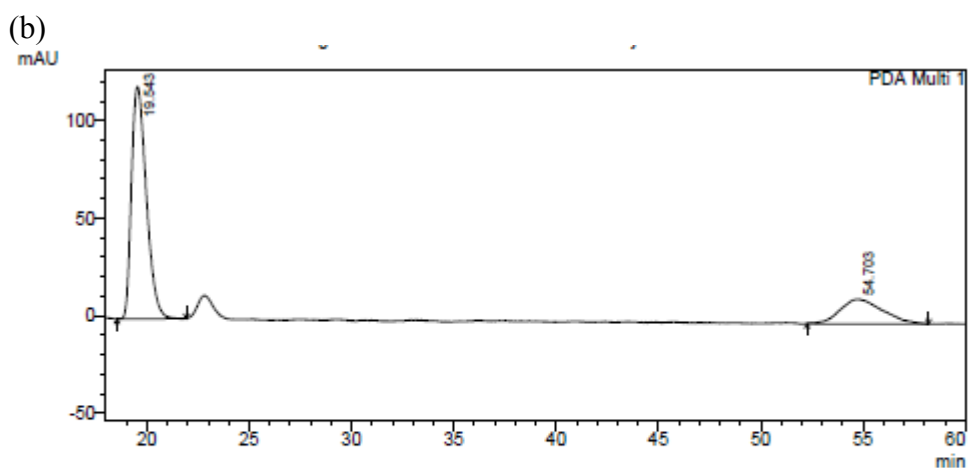
Figure b25 HPLC traces of **25** (Table 3.5, entry 3): (a) catalyzed by ($S_{Ru}R_C R_C$)-**18c**⁺ PF₆⁻; (b) catalyzed by ($R_{Ru}R_C R_C$)-**18c**⁺ PF₆⁻.



1 PDA Multi 1/254nm 4nm

PeakTable

Peak#	Ret. Time	Area	Height	Area %	Height %
1	20.722	6528392	113442	49.511	78.354
2	63.409	6657317	31339	50.489	21.646
Total		13185709	144781	100.000	100.000



1 PDA Multi 1/254nm 4nm

PeakTable

Peak#	Ret. Time	Area	Height	Area %	Height %
1	19.543	5993244	118898	76.810	90.375
2	54.703	1809420	12663	23.190	9.625
Total		7802664	131561	100.000	100.000

(c)

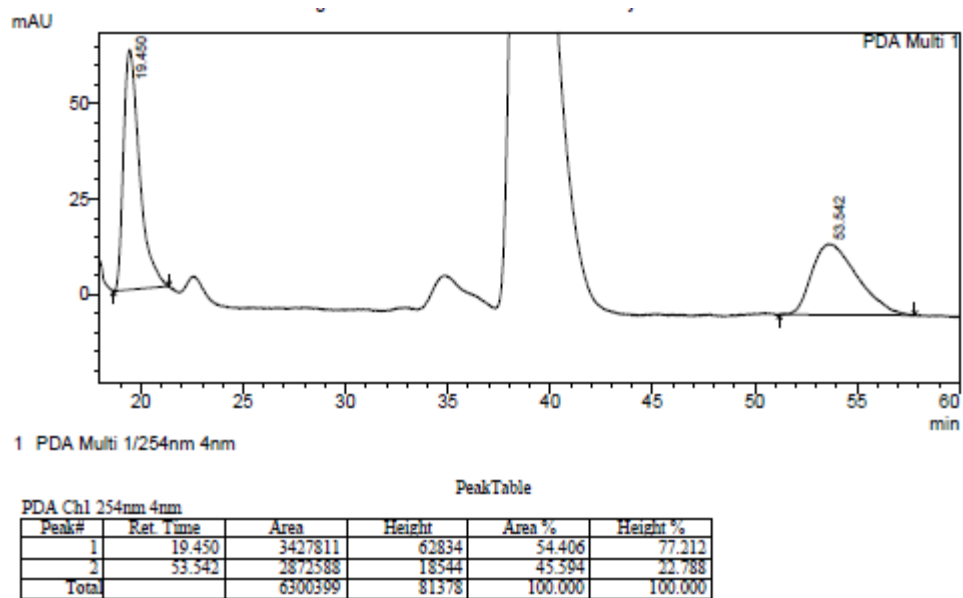
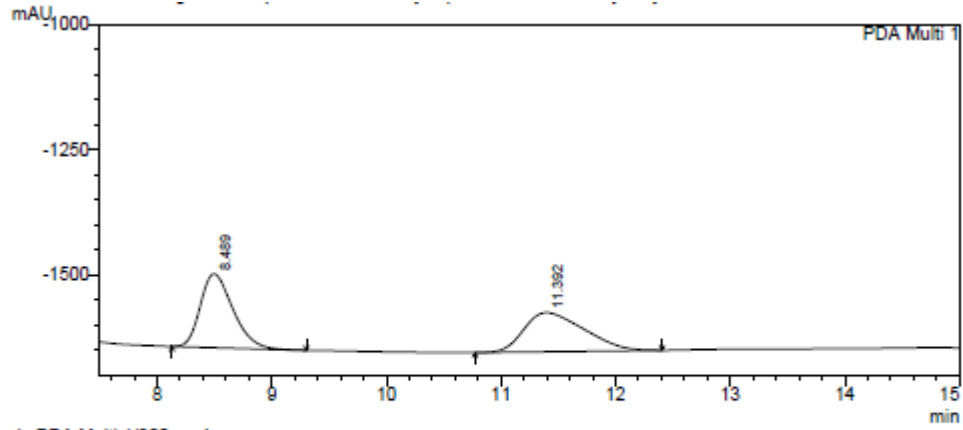


Figure b26 HPLC traces of **27** (Table 3.5, entry 4): (a) racemic sample; (b) catalyzed by $(R_{Ru}R_C R_C)\text{-18c}^+ \text{PF}_6^-$ (entry 4b) ; (c) catalyzed by $(S_{Ru}R_C R_C)\text{-18c}^+ \text{PF}_6^-$ (entry 4d).

Additions of 22 to dialkyl azodicarboxylates (Table 3.6).

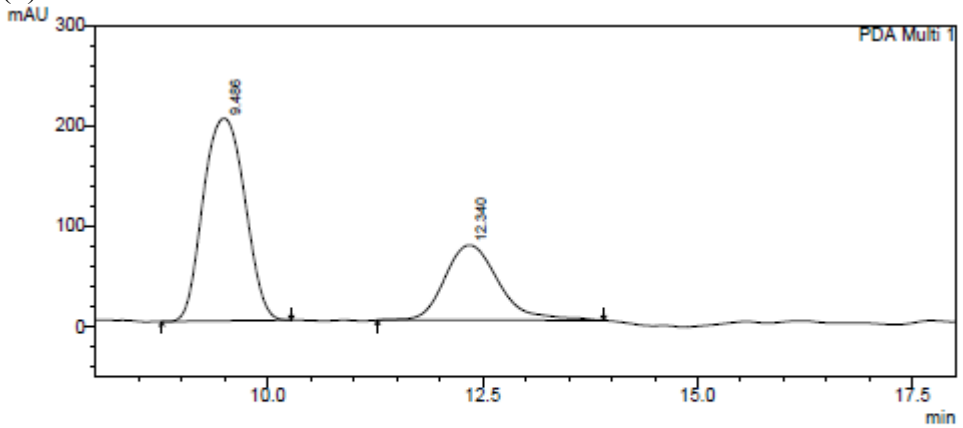
(a)



PeakTable

Peak#	Ret. Time	Area	Height	Area %	Height %
1	8.489	2927632	147052	50.774	65.378
2	11.392	2838360	77873	49.226	34.622
Total		5765992	224924	100.000	100.000

(b)



PeakTable

Peak#	Ret. Time	Area	Height	Area %	Height %
1	9.486	6812931	201869	67.588	71.966
2	12.340	3267203	74794	32.412	27.034
Total		10080133	276663	100.000	100.000

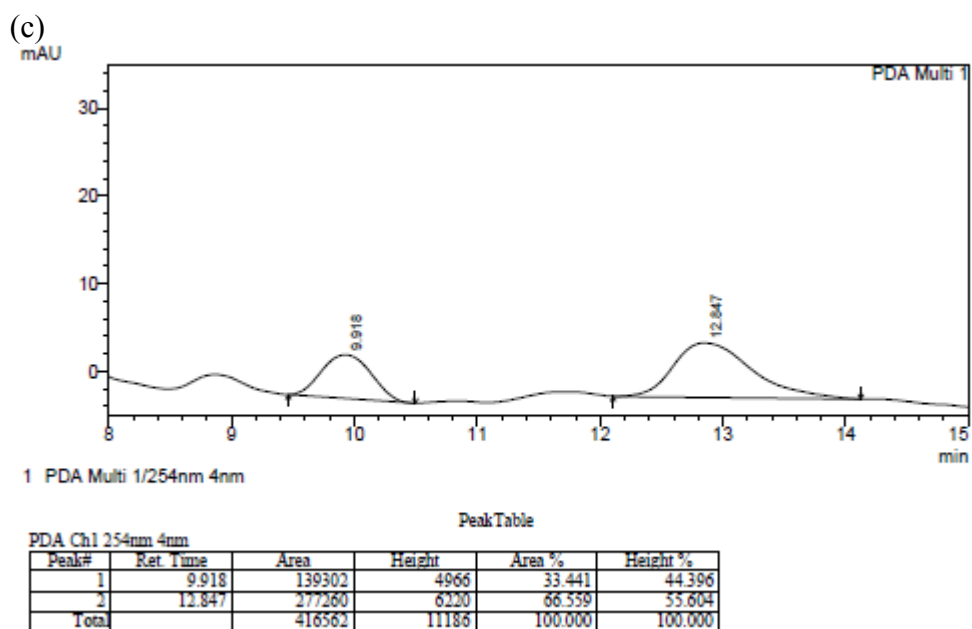
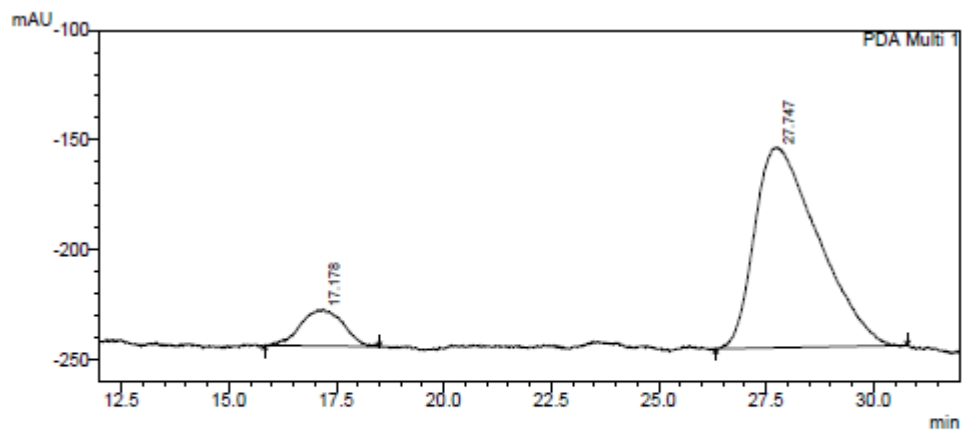


Figure b27 HPLC traces of **37** (Table 3.6, entry 1): (a) racemic sample; (b) catalyzed by ($S_{Ru}R_C R_C$)-**18c**⁺ PF₆⁻ (entry 1a) ; (c) catalyzed by ($R_{Ru}R_C R_C$)-**18c**⁺ PF₆⁻ (entry 1b).

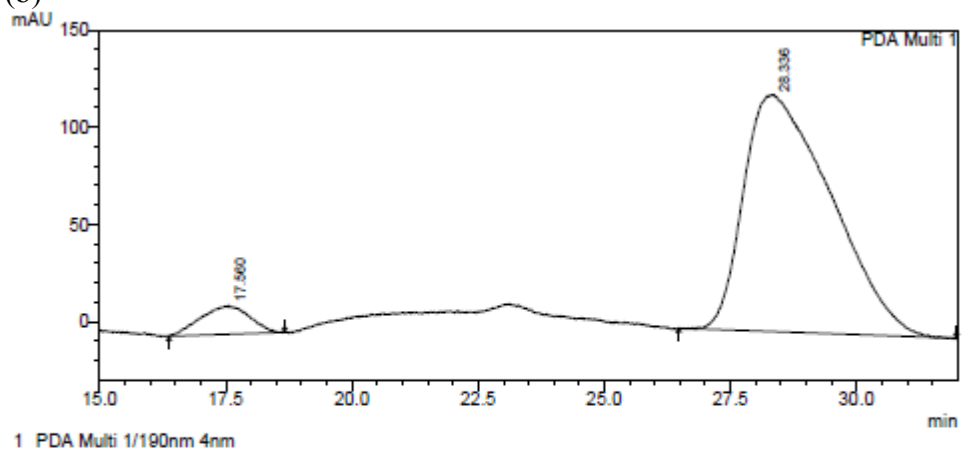
(a)



PeakTable

Peak#	Ret. Time	Area	Height	Area %	Height %
1	17.178	1142369	16798	10.825	15.519
2	27.747	9410844	91444	89.175	84.481
Total		10553214	108242	100.000	100.000

(b)



PeakTable

Peak#	Ret. Time	Area	Height	Area %	Height %
1	17.560	984910	14775	6.288	10.814
2	28.336	14679137	121852	93.712	89.186
Total		15664047	136627	100.000	100.000

Figure b28 HPLC traces of **39** (Table 3.6, entry 2): (a) catalyzed by ($S_{Ru}R_C R_C$)-**18c**⁺ PF₆⁻ (entry 2a); (b) catalyzed by ($R_{Ru}R_C R_C$)-**18c**⁺ PF₆⁻ (entry 2c).

APPENDIX C

This appendix contains the NMR spectra (1D and 2D), chiral HPLC traces, and the checkCIF reports related to chapter 4, titled *Enantiopure Chiral-at-Metal Ruthenium Complexes: Syntheses, Resolution, and Applications in Second Coordination Sphere Promoted Catalysis*.

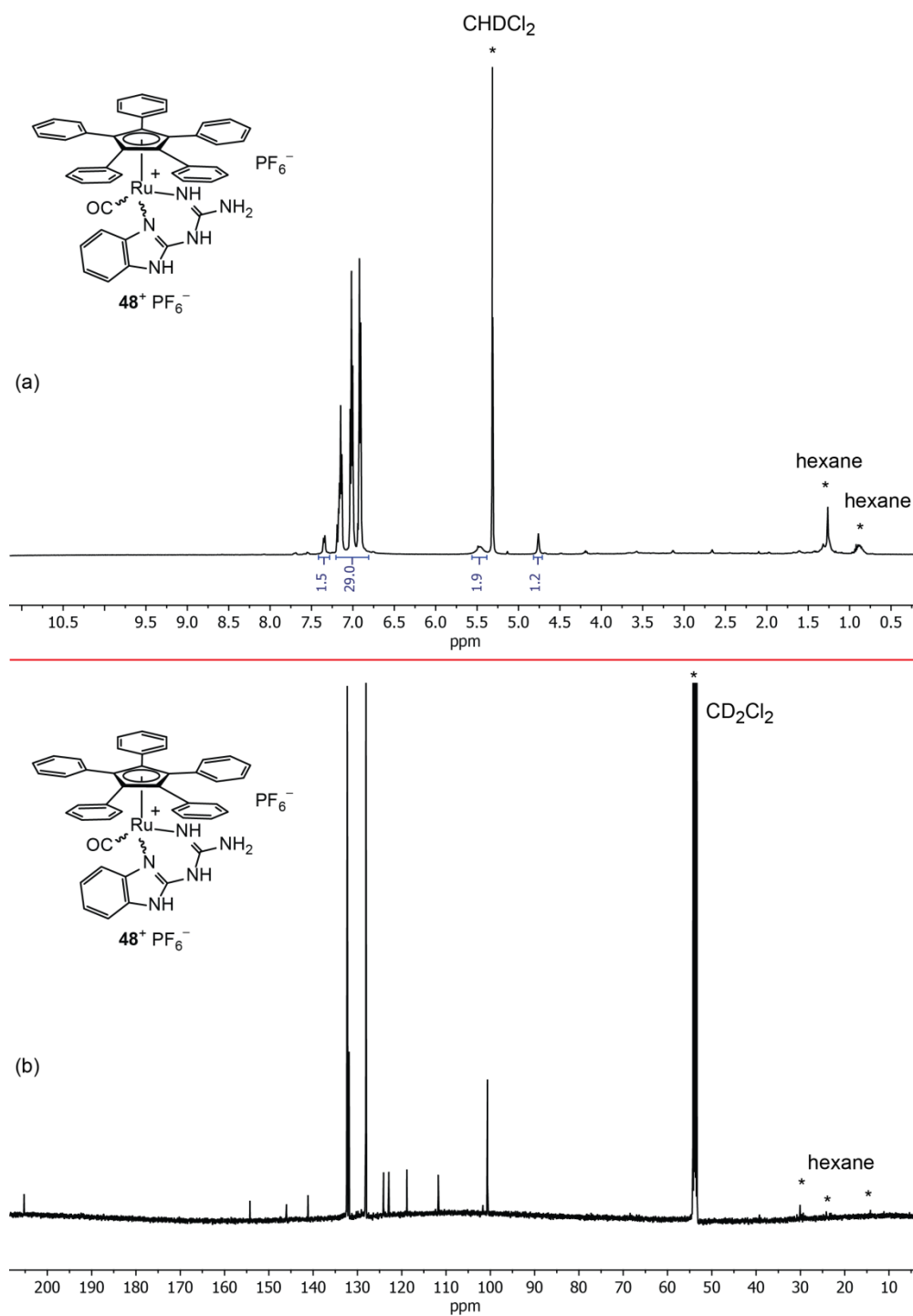


Figure c1 NMR spectra of 48^+PF_6^- (CD_2Cl_2 ; * = solvent or impurities): (a) ^1H (500 MHz); (b) $^{13}\text{C}\{^1\text{H}\}$ (125 MHz).

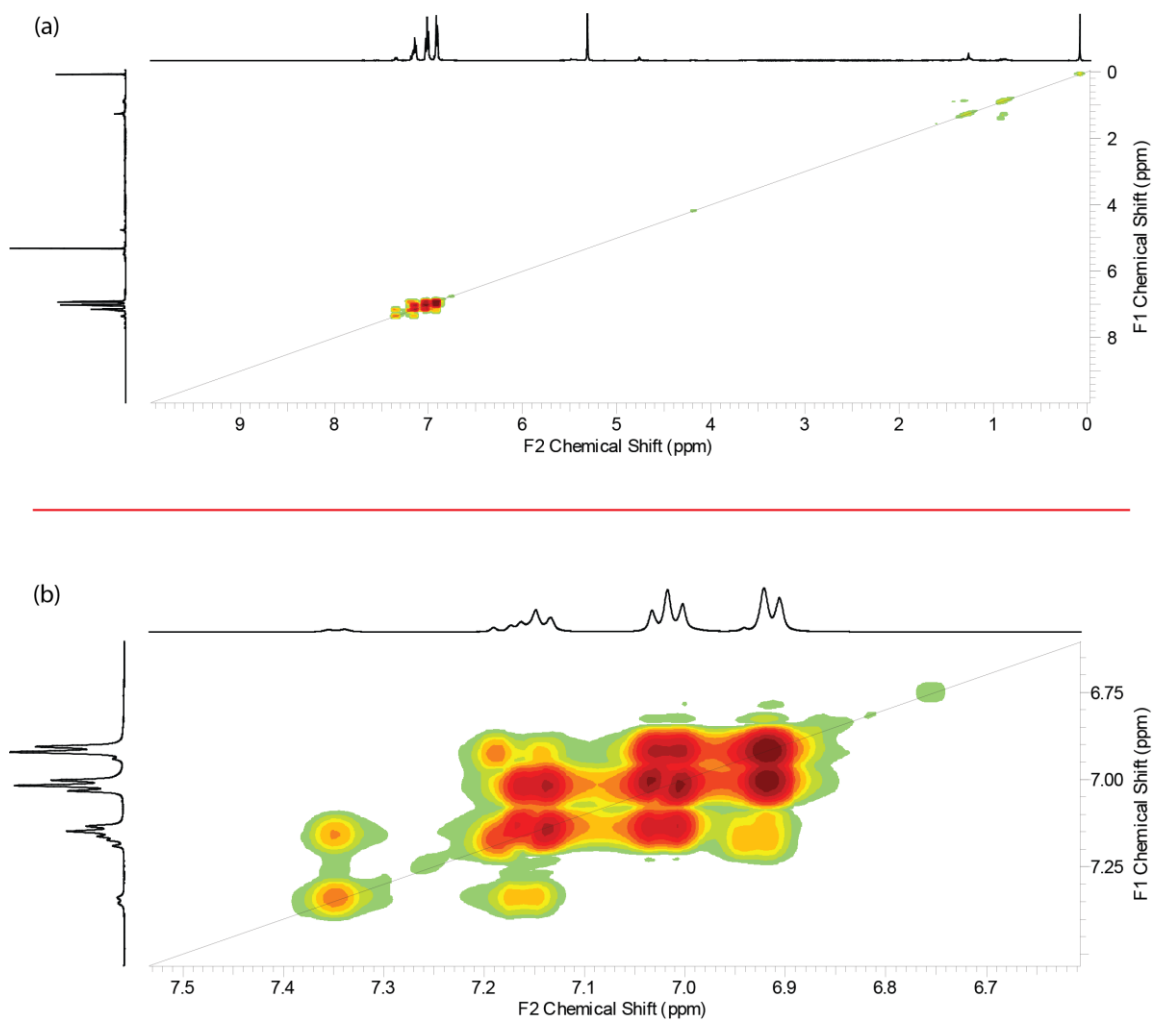


Figure c2 NMR spectra of 48^+ PF_6^- (CD_2Cl_2 , 500 MHz): (a) ^1H - ^1H COSY; (b) Partial ^1H - ^1H COSY for the aromatic region.

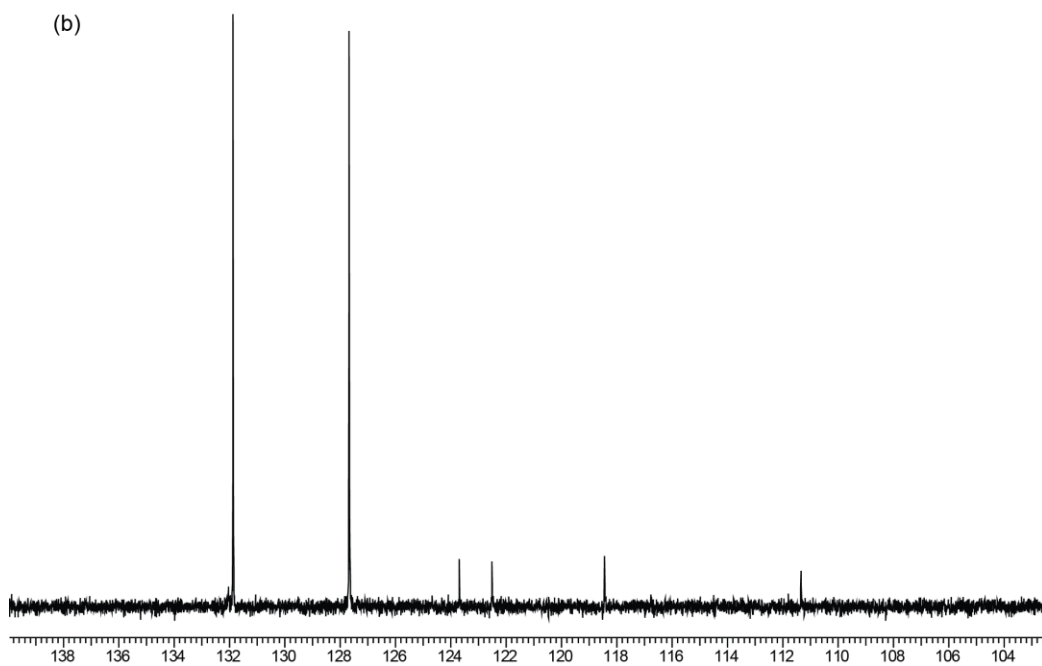
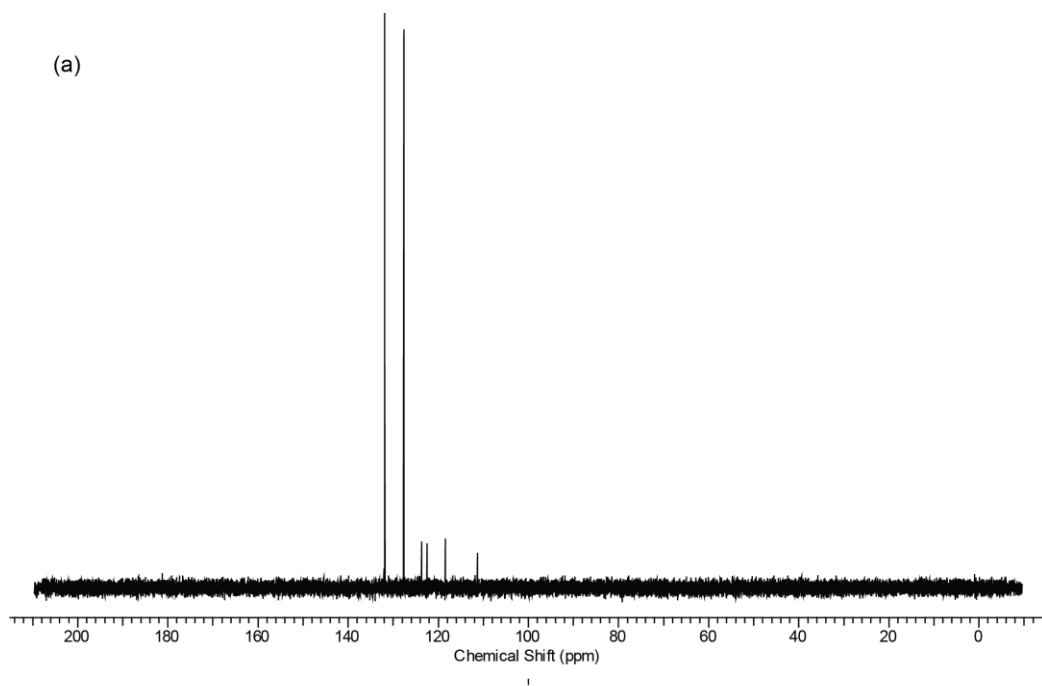


Figure c3 NMR spectra of $48^+ PF_6^-$ (CD_2Cl_2 , 500 MHz): (a) ^{13}C DEPT-90; (b) Partial ^{13}C DEPT-90 for the aromatic region.

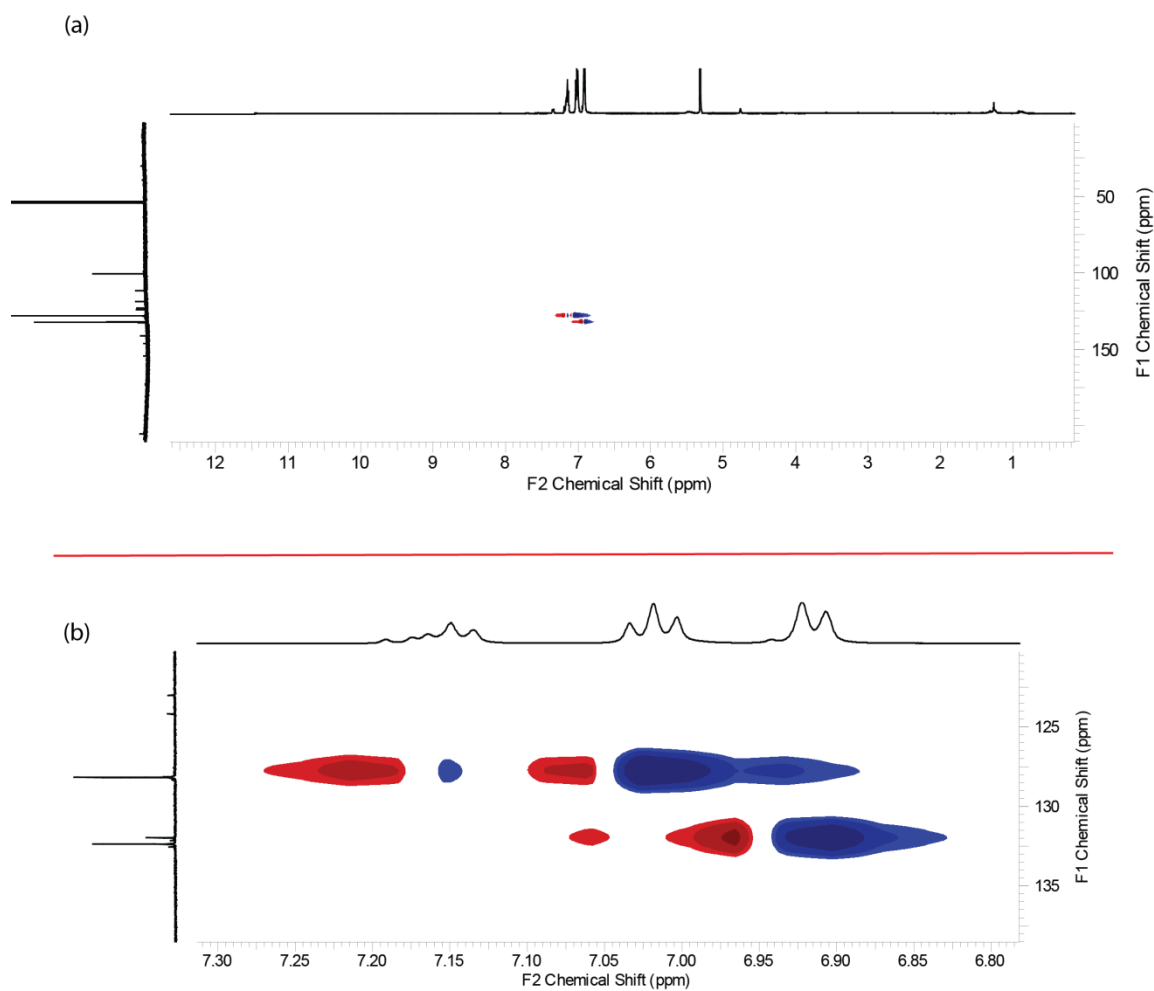


Figure c4 NMR spectra of 48^+PF_6^- (CD_2Cl_2 , 500 MHz): (a) ^1H - ^{13}C HSQC; (b) Partial ^1H - ^{13}C HSQC for the aromatic region.

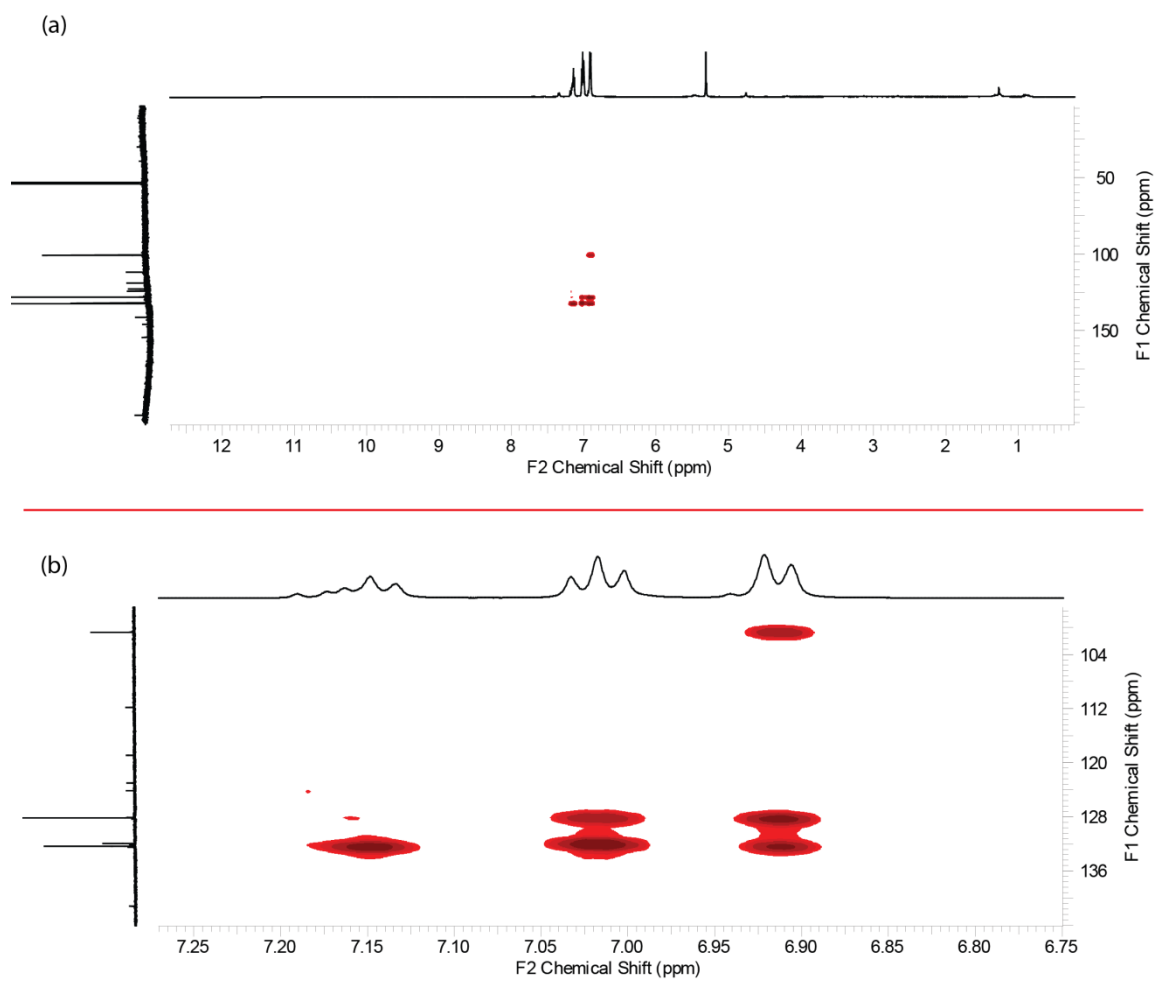


Figure c5 NMR spectra of 48^+ PF_6^- (CD_2Cl_2 , 500 MHz): (a) ^1H - ^{13}C HMBC; (b) Partial ^1H - ^{13}C HMBC for the aromatic region.

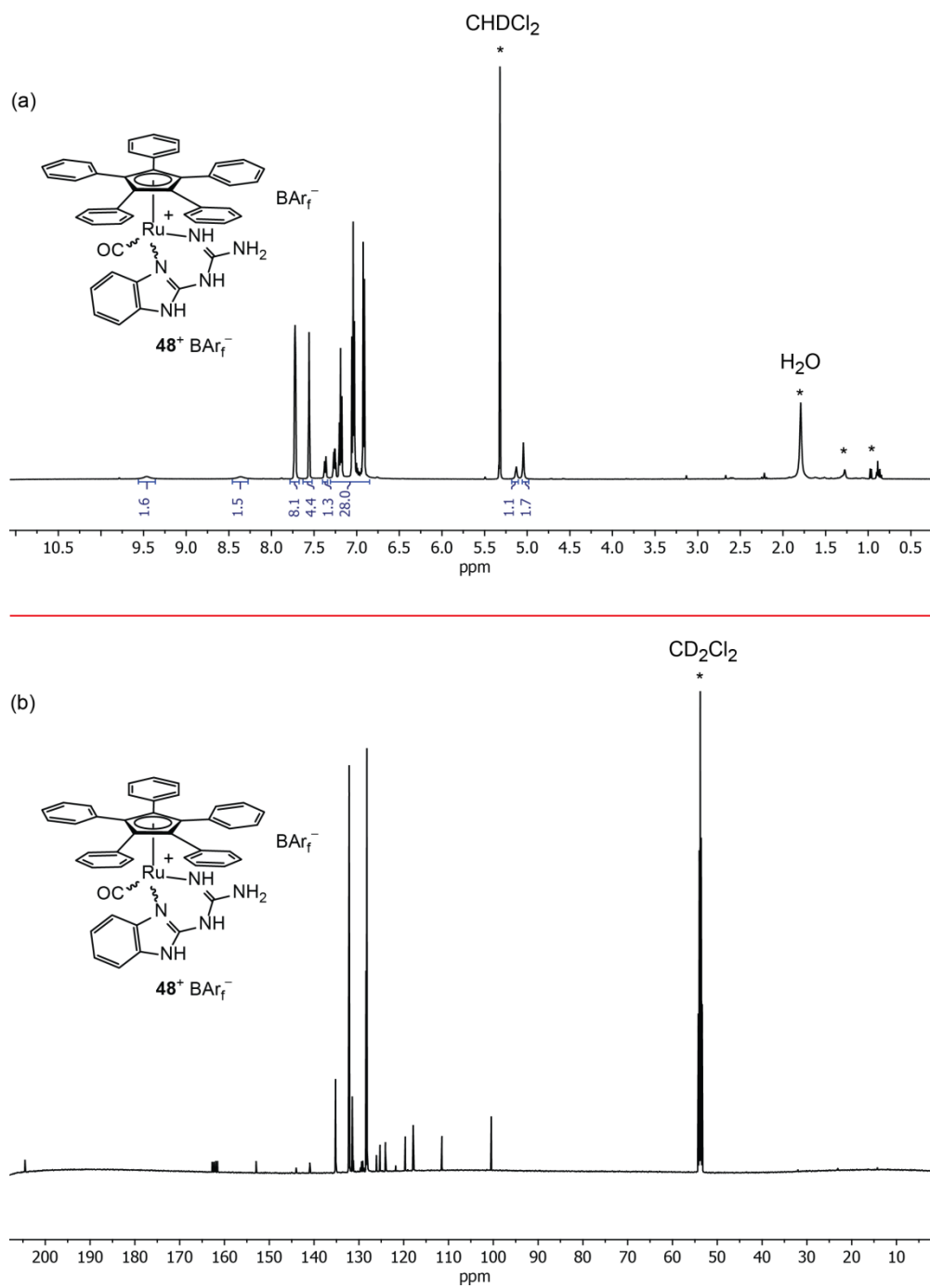


Figure c6 NMR spectra of 48^+BAR_f^- (CD_2Cl_2 ; * = solvent or impurities): (a) ^1H (500 MHz); (b) $^{13}\text{C}\{^1\text{H}\}$ (125 MHz).

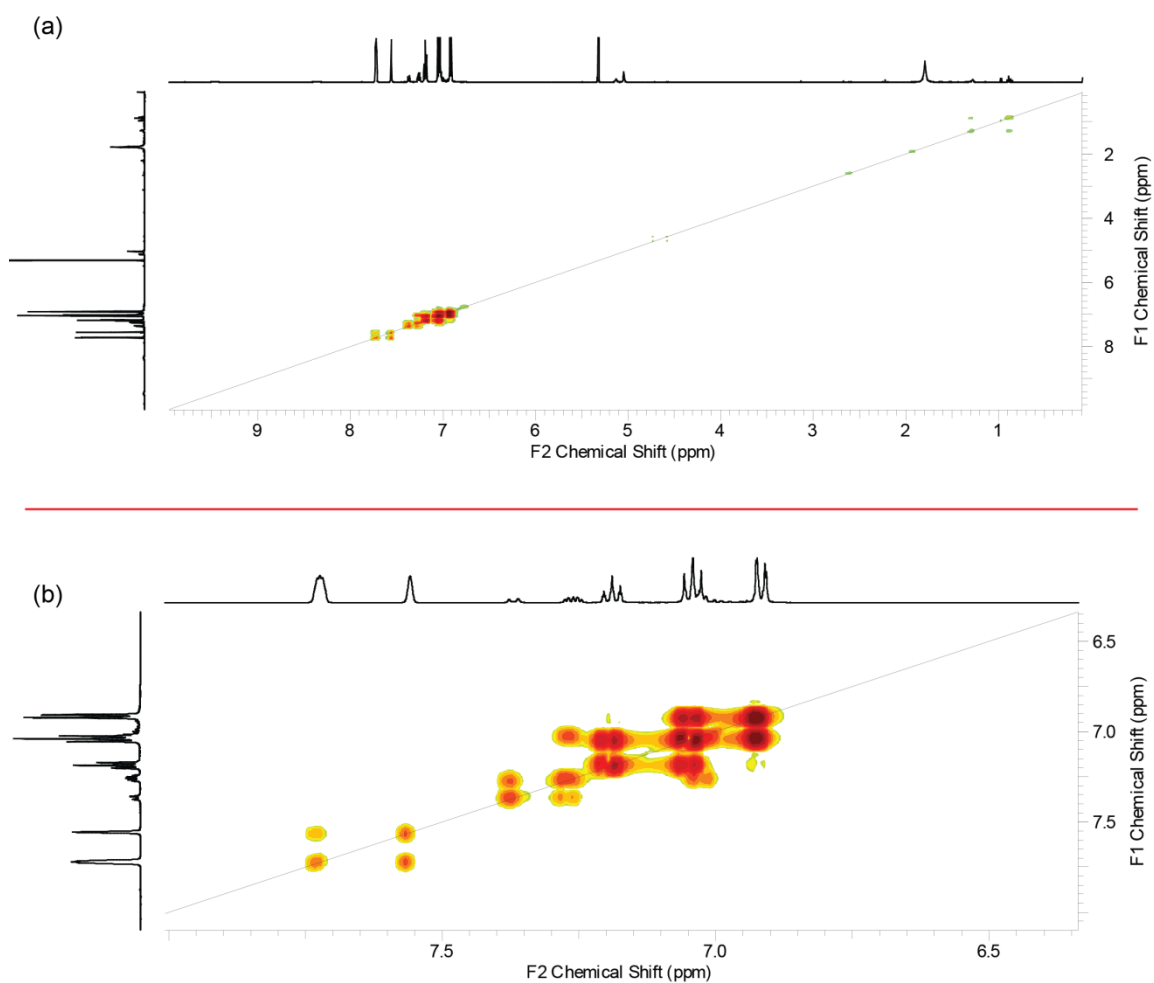


Figure c7 NMR spectra of 48^+ BAr_f^- (CD_2Cl_2 , 500 MHz): (a) 1H - 1H COSY; (b) Partial 1H - 1H COSY for the aromatic region.

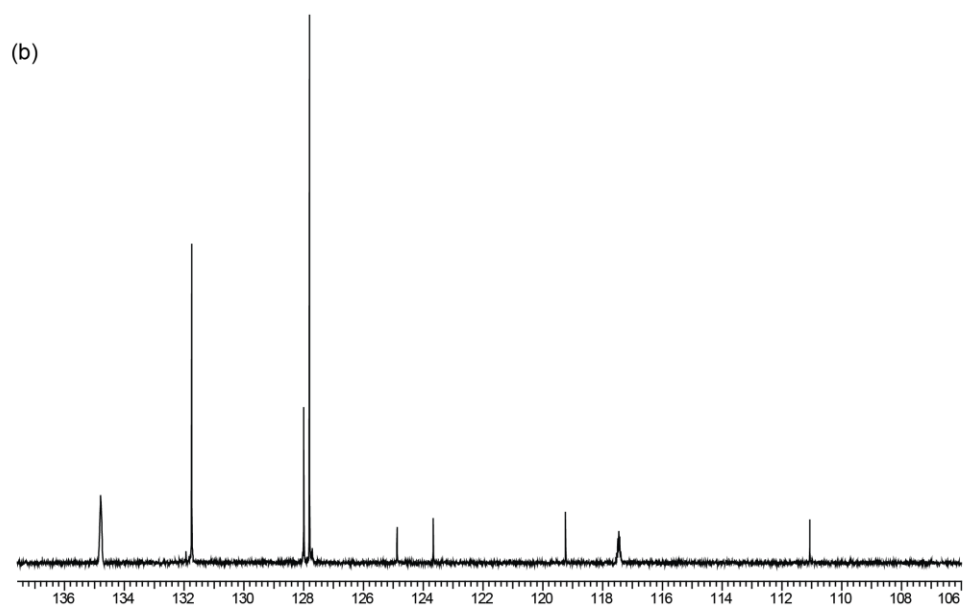
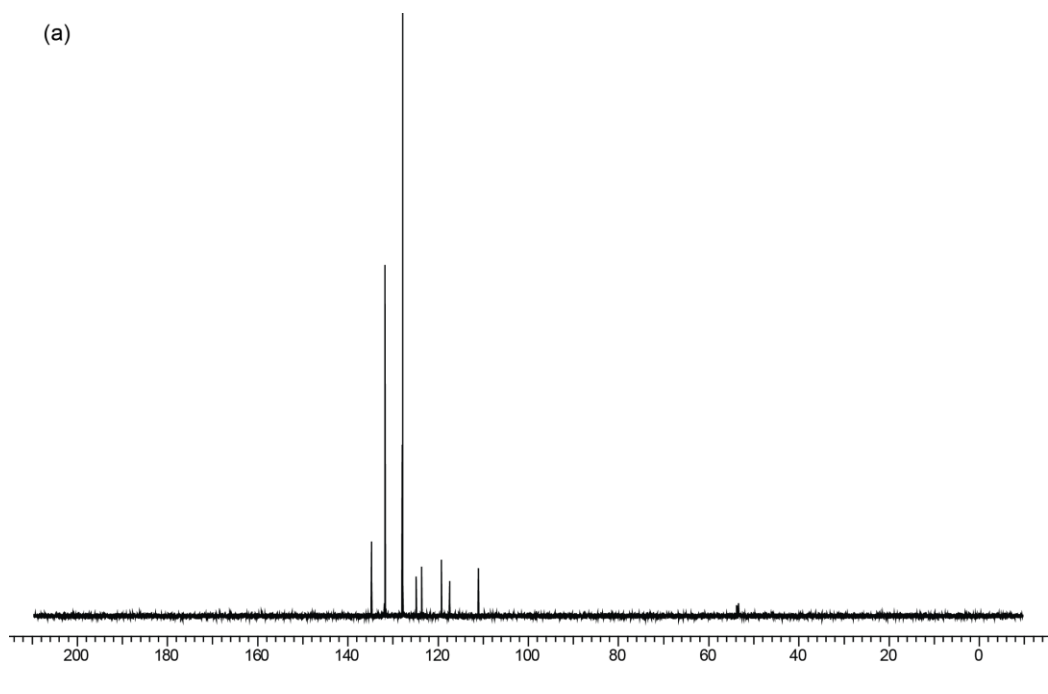


Figure c8 NMR spectra of 48^+ BAr_f^- (CD_2Cl_2 , 500 MHz): (a) ^{13}C DEPT-90; (b) Partial ^{13}C DEPT-90 for the aromatic region.

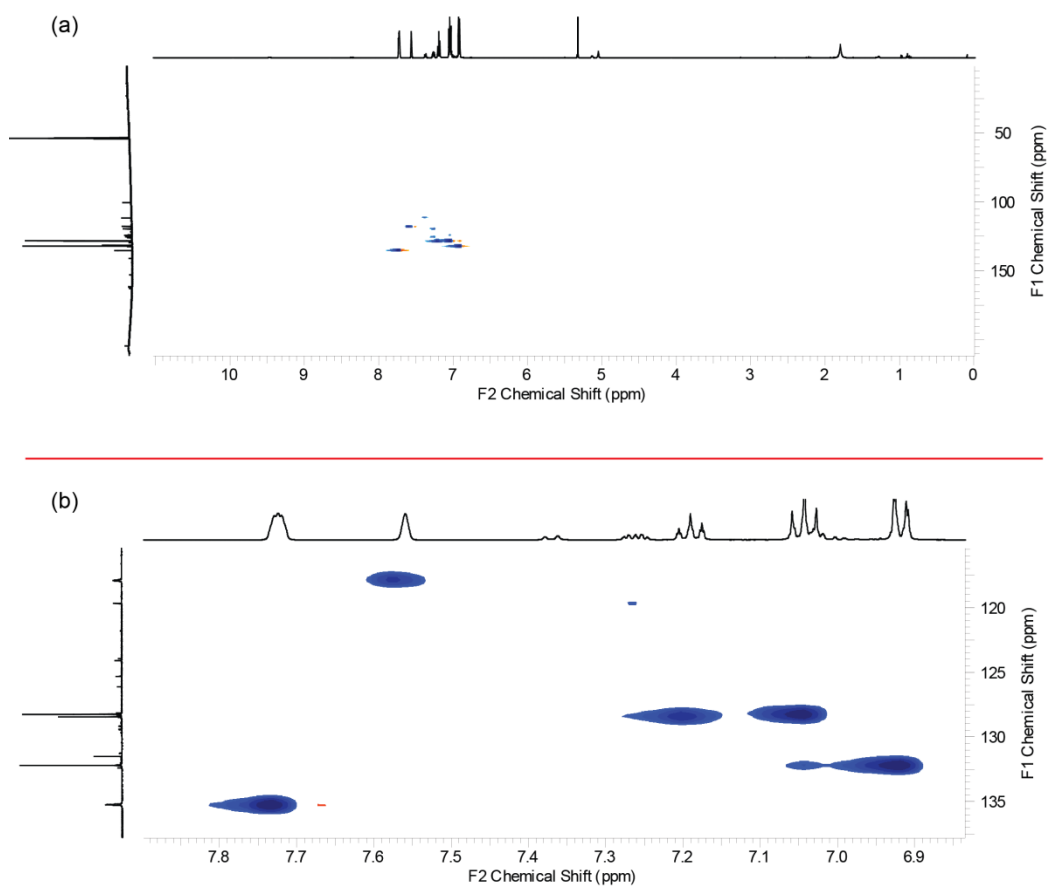


Figure c9 NMR spectra of 48^+ BArf^- (CD_2Cl_2 , 500 MHz): (a) ^1H - ^{13}C HSQC; (b) Partial ^1H - ^{13}C HSQC for the aromatic region.

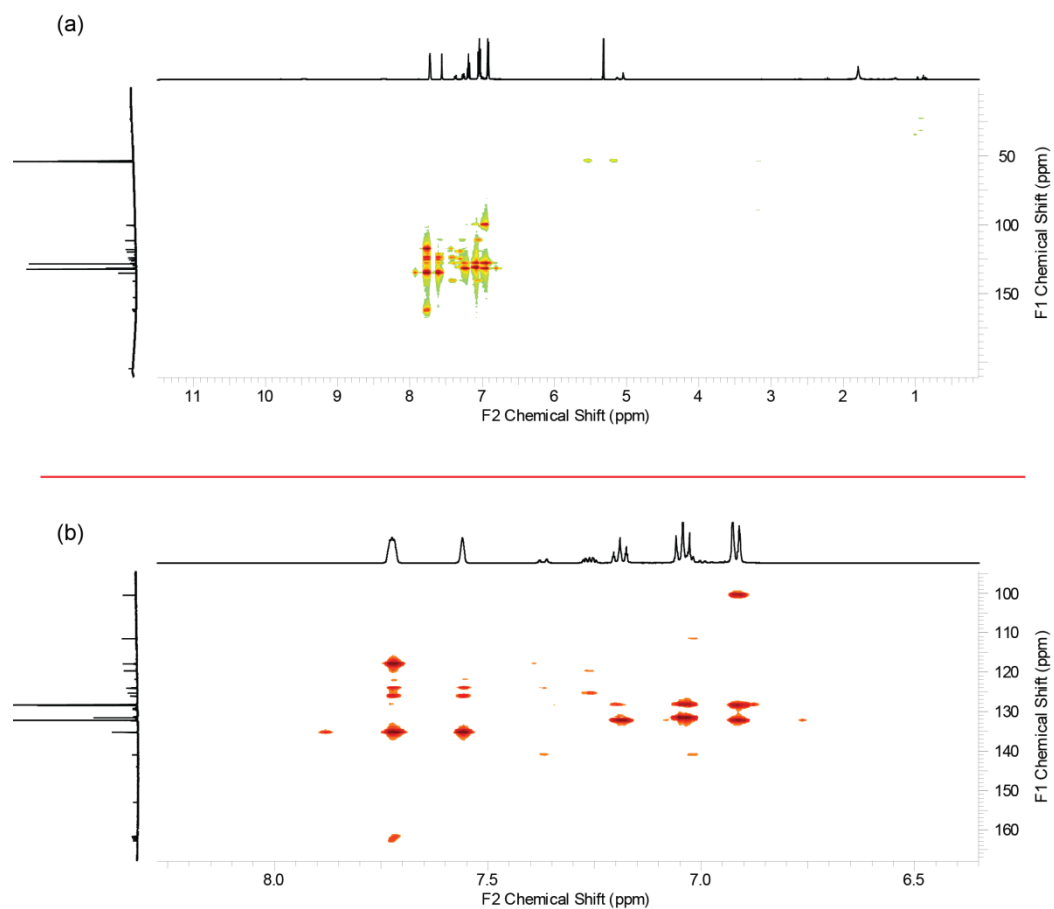


Figure c10 NMR spectra of 48^+BArF^- (CD_2Cl_2 , 500 MHz): (a) ^1H - ^{13}C HMBC; (b) Partial ^1H - ^{13}C HMBC for the aromatic region.

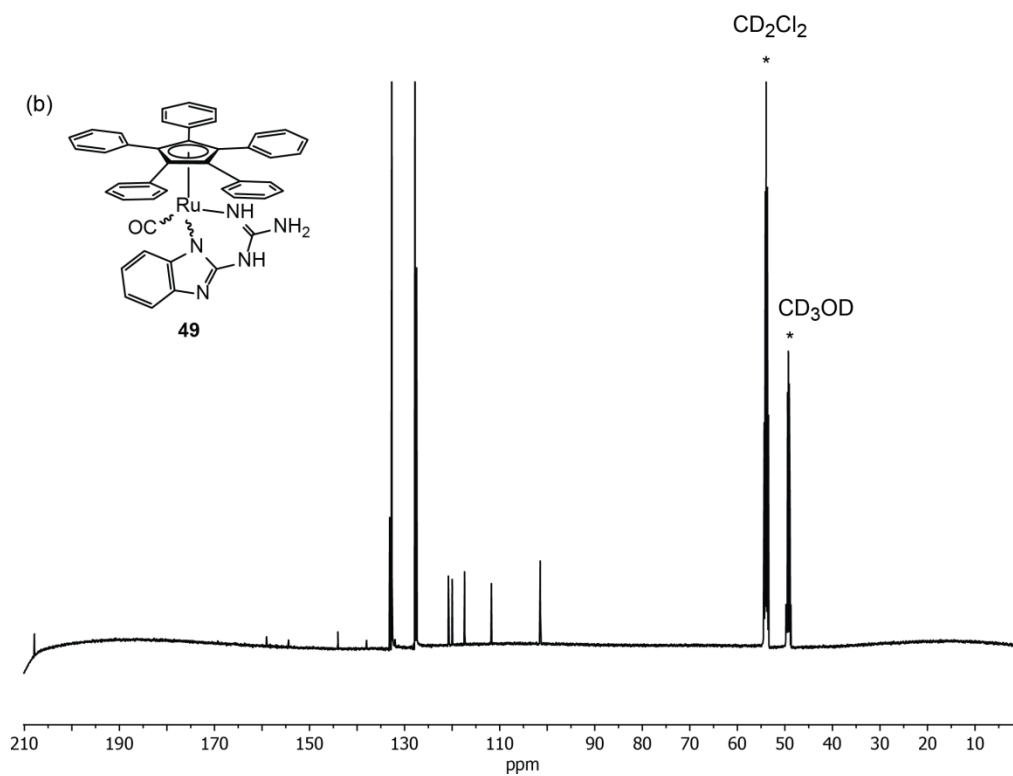
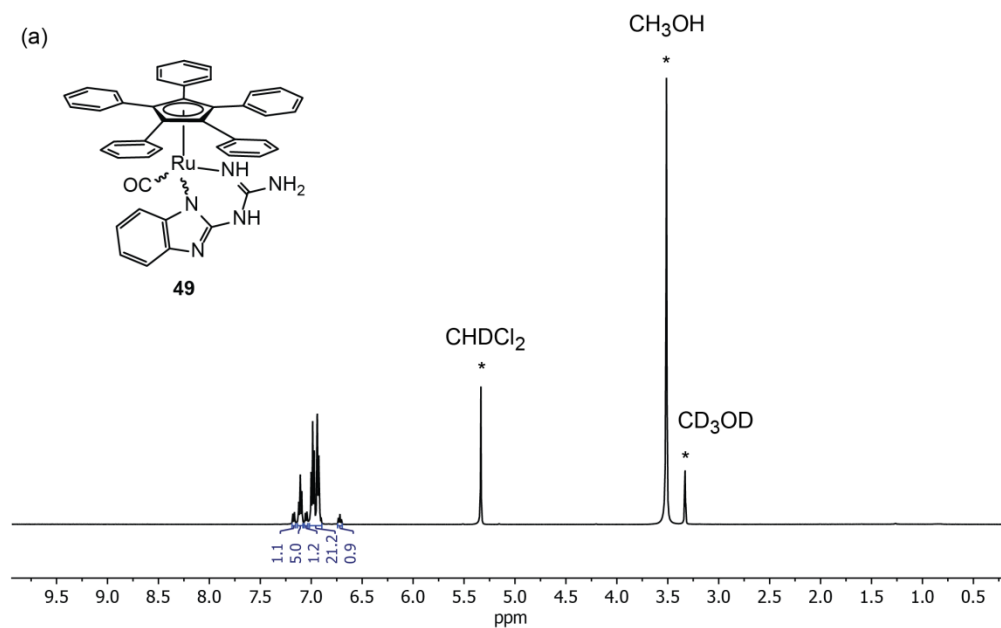


Figure c11 NMR spectra of **49** (1:1 v/v CD₂Cl₂/CD₃OD; * = solvent or impurities): (a) ¹H (500 MHz); (b) ¹³C{¹H} (125 MHz).

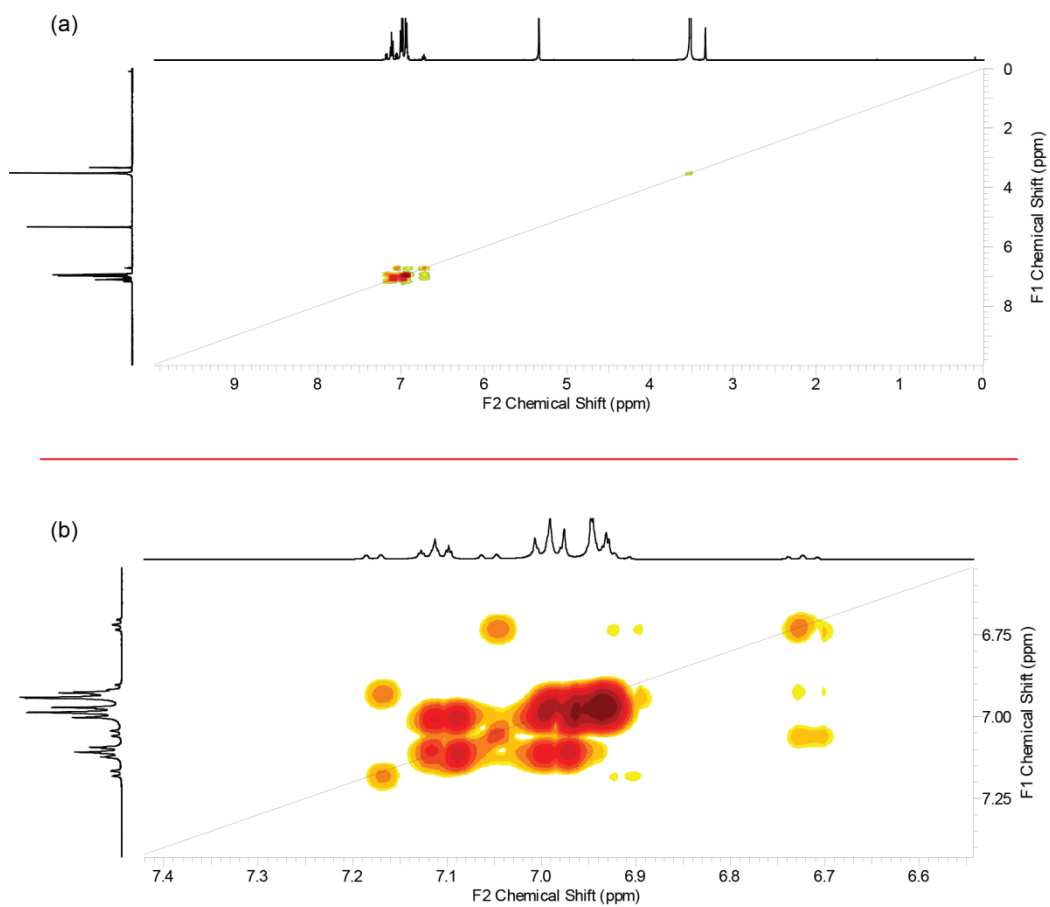


Figure c12 NMR spectra of **49** (1:1 v/v CD₂Cl₂/CD₃OD, 500 MHz): (a) ¹H-¹H COSY; (b) Partial ¹H-¹H COSY for the aromatic region.

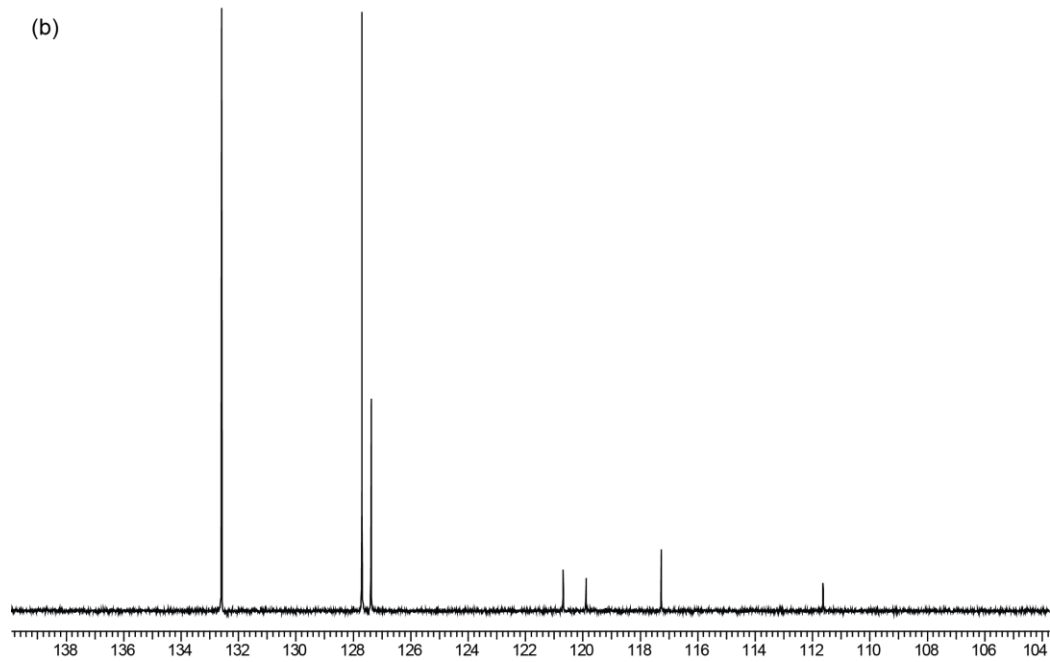
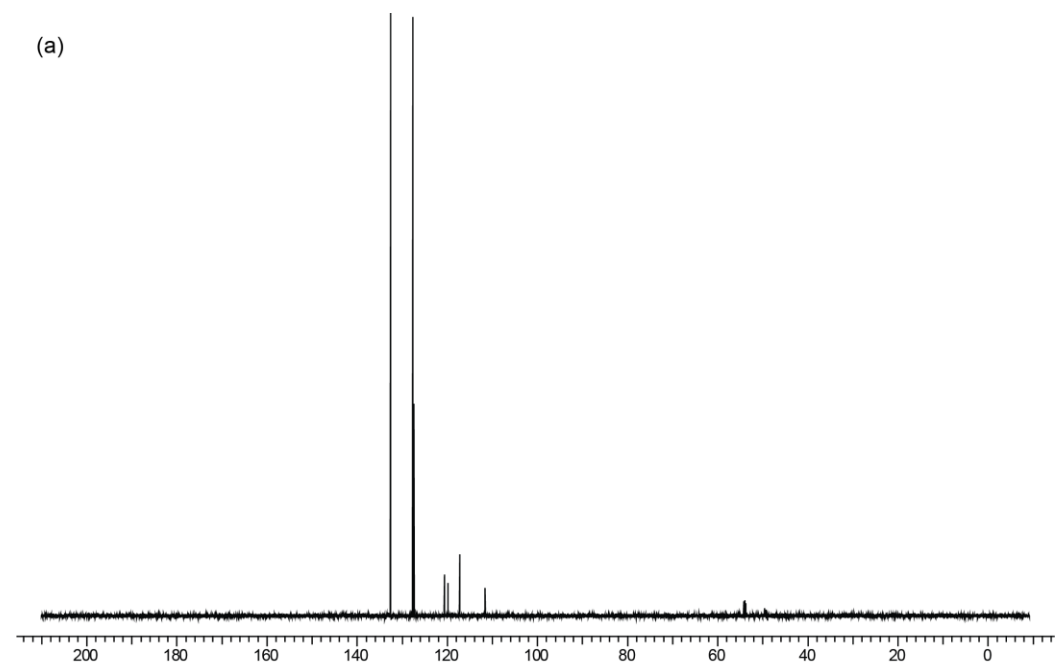


Figure c13 NMR spectra of **49** (1:1 v/v CD₂Cl₂/CD₃OD, 500 MHz): (a) ¹³C DEPT-90; (b) Partial ¹³C DEPT-90 for the aromatic region.

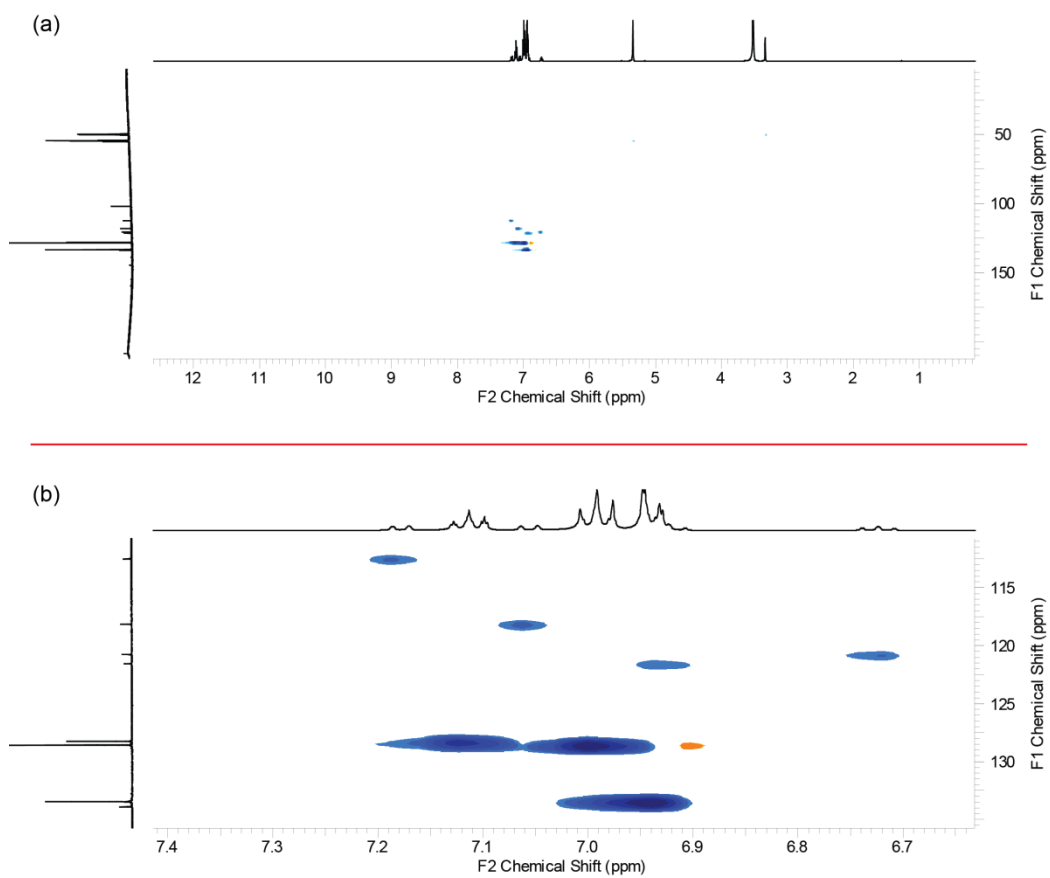


Figure c14 NMR spectra of **49** (1:1 v/v $\text{CD}_2\text{Cl}_2/\text{CD}_3\text{OD}$, 500 MHz): (a) ^1H - ^{13}C HSQC; (b) Partial ^1H - ^{13}C HSQC for the aromatic region.

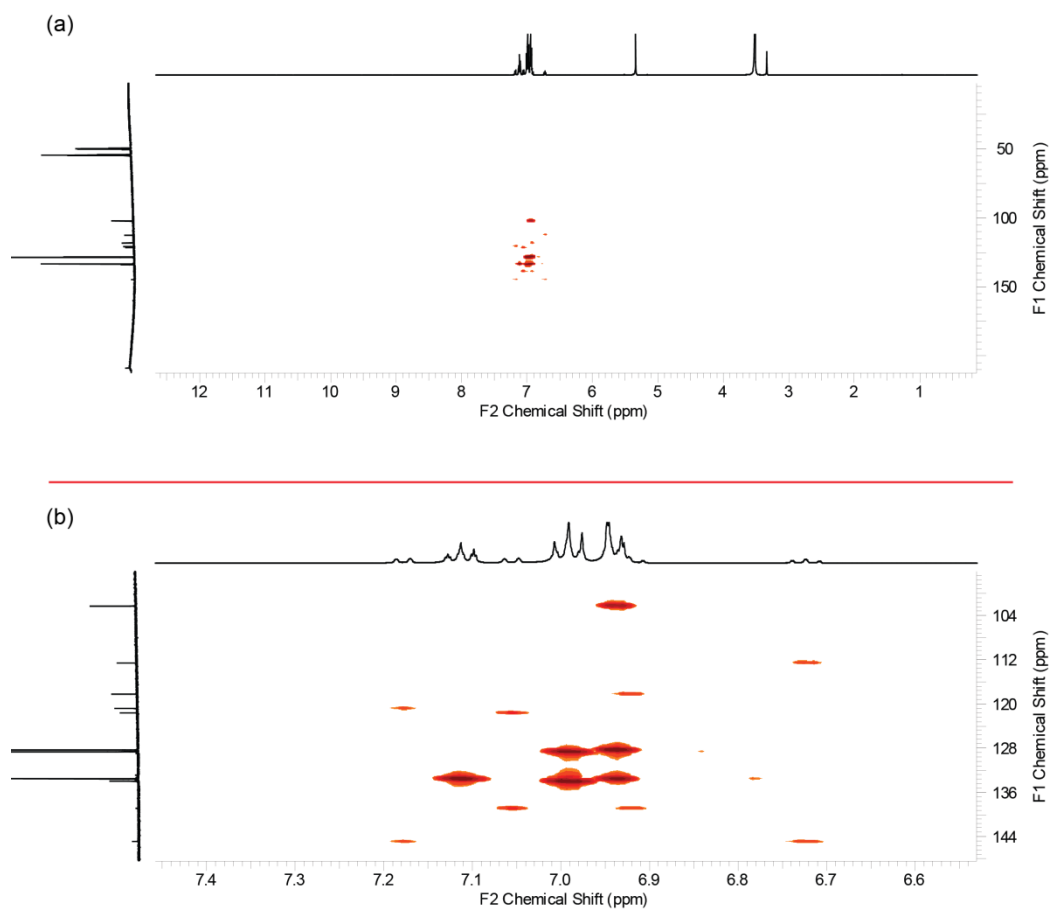


Figure c15 NMR spectra of **49** (1:1 v/v $\text{CD}_2\text{Cl}_2/\text{CD}_3\text{OD}$, 500 MHz): (a) ^1H - ^{13}C HMBC; (b) Partial ^1H - ^{13}C HMBC for the aromatic region.

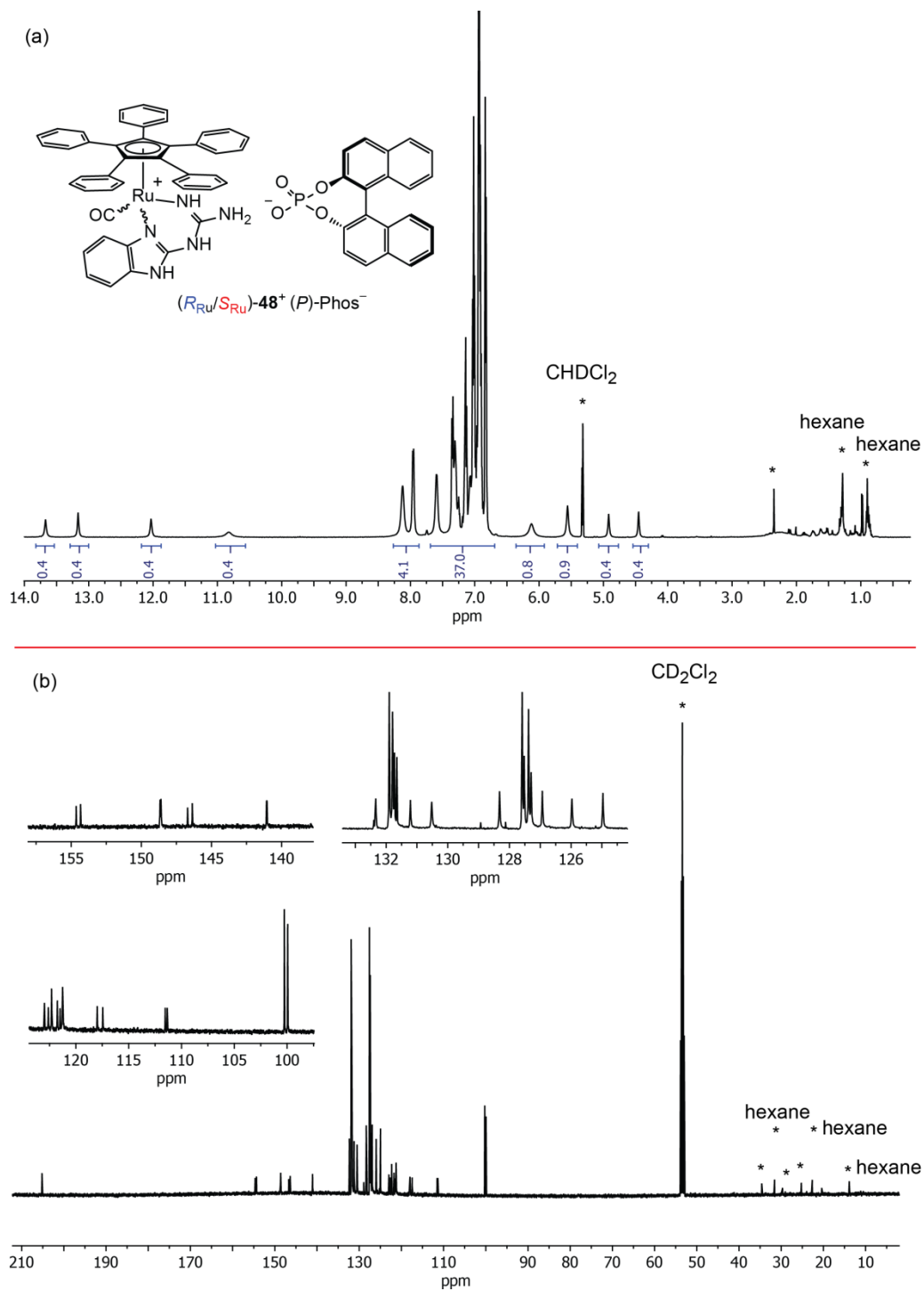


Figure c16 NMR spectra of $(R_{Ru}/S_{Ru})\text{-48}^+ (P)\text{-Phos}^-$ (CD_2Cl_2 ; * = solvent or impurities): (a) ^1H (500 MHz); (b) $^{13}\text{C}\{^1\text{H}\}$ (125 MHz).

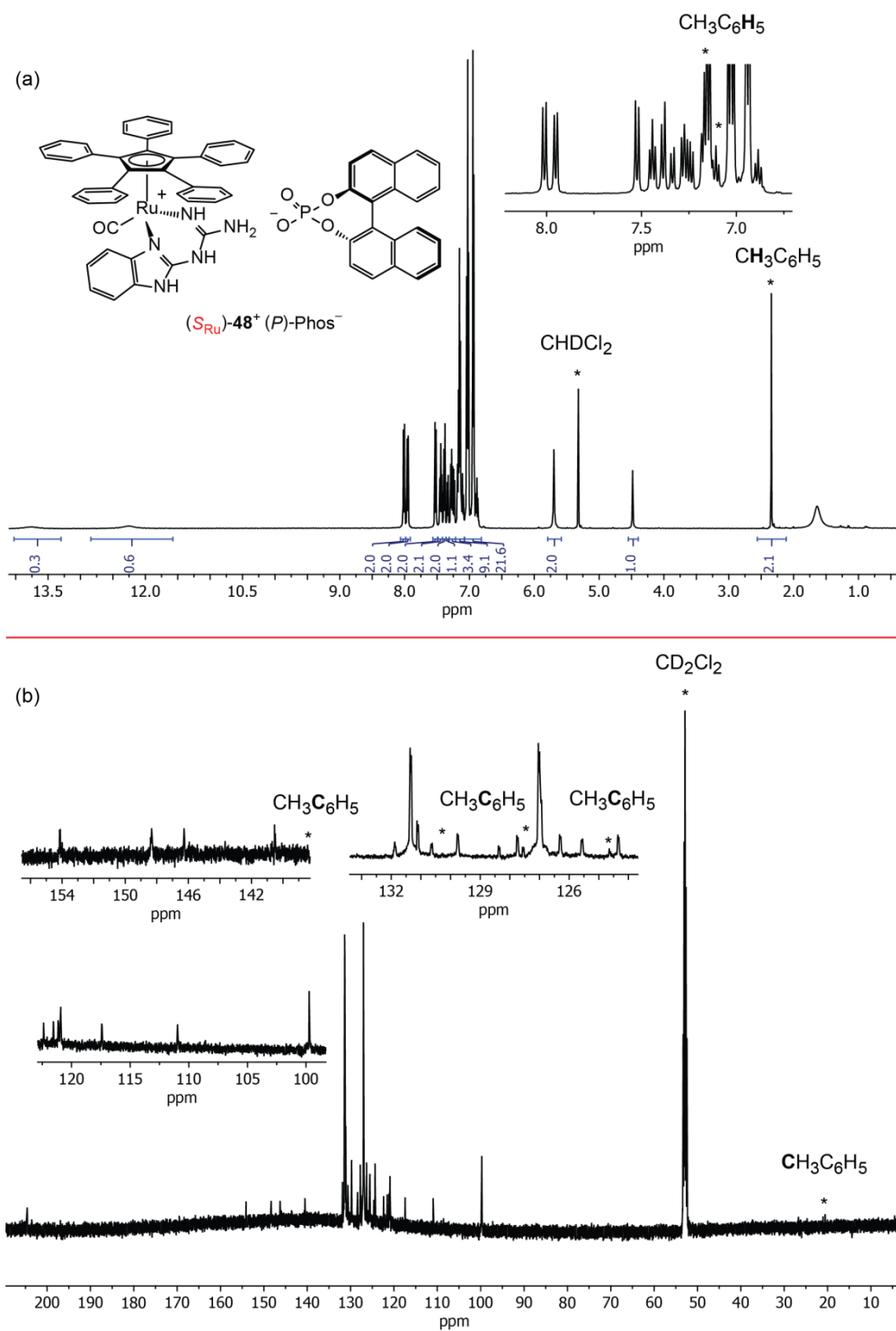
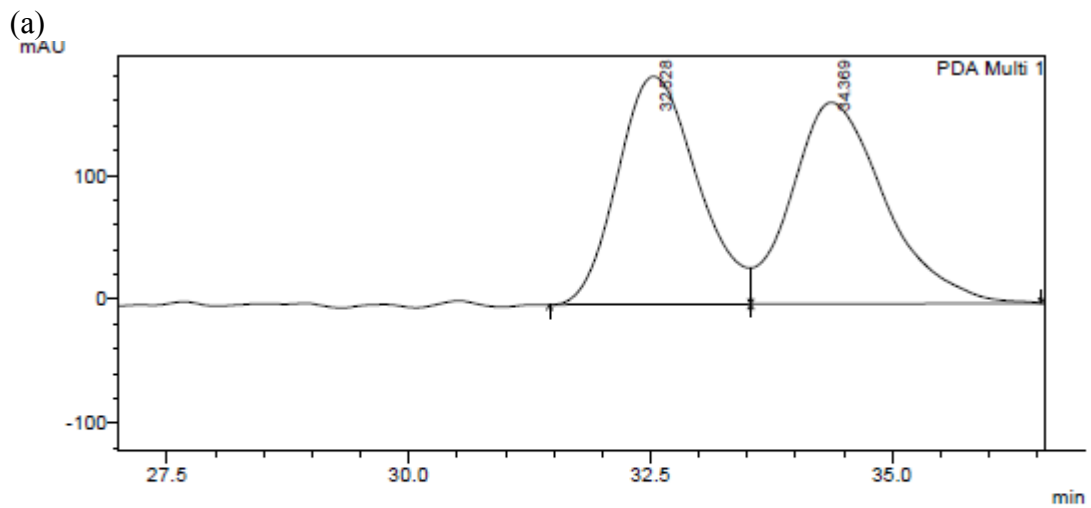


Figure c17 NMR spectra of $(S_{Ru})\text{-}48^+ (P)\text{-Phos}^-$ (CD_2Cl_2 ; * = solvent or impurities):
 (a) ^1H (500 MHz); (b) $^{13}\text{C}\{^1\text{H}\}$ (125 MHz).

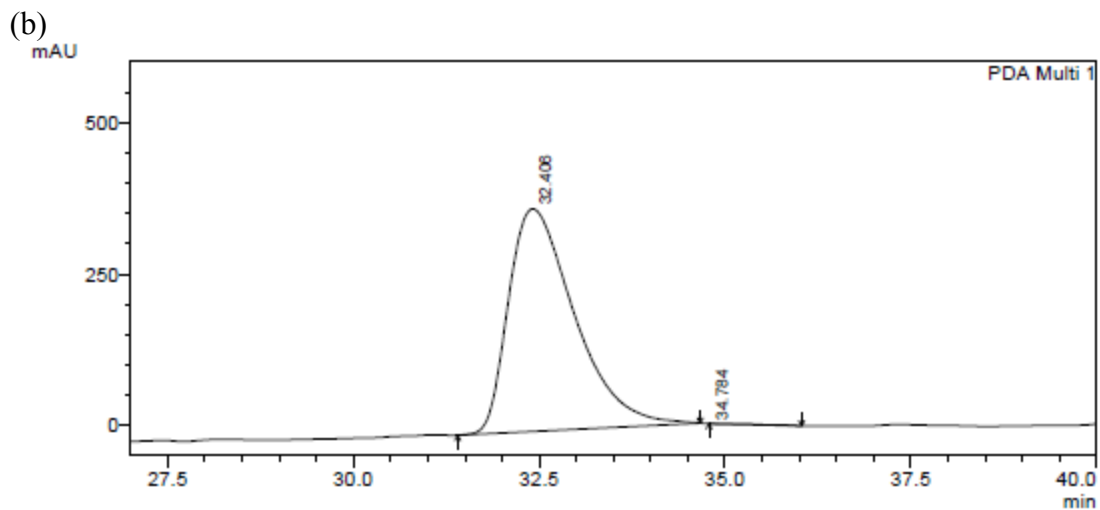
Additions of 28 to 50 or 52 catalyzed by $(S_{Ru})\text{-}48^+ \text{BAr}_f^-$ (Table 4.10).



PeakTable

PDA Chl 210nm 4nm

Peak#	Ret. Time	Area	Height	Area %	Height %
1	32.528	10622947	183852	49.204	53.087
2	34.369	10966636	162471	50.796	46.913
Total		21589582	346323	100.000	100.000

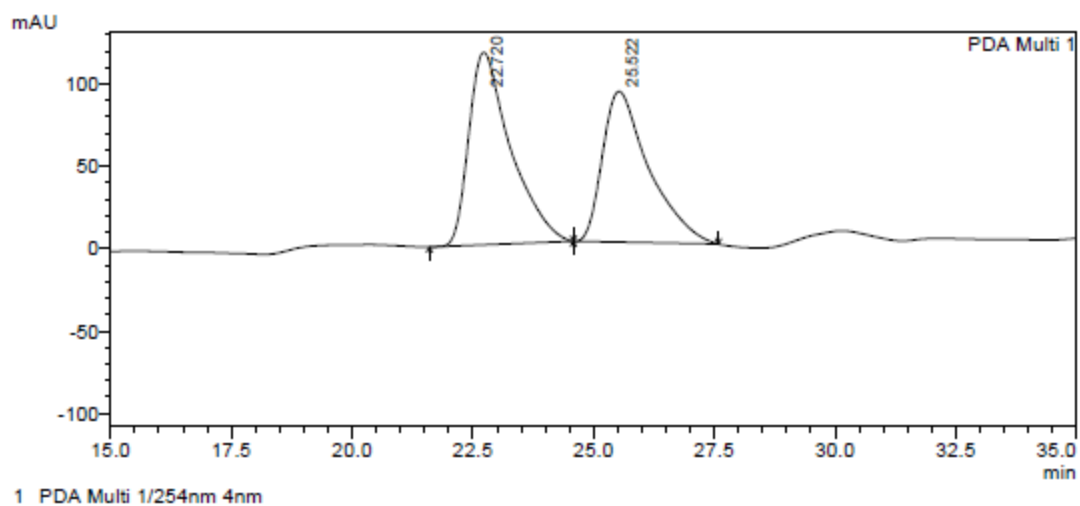


PeakTable

PDA Chl 210nm 4nm

Peak#	Ret. Time	Area	Height	Area %	Height %
1	32.406	22710818	367085	99.860	100.000
2	34.784	31828	0	0.140	0.000
Total		22742645	367085	100.000	100.000

Figure c32. HPLC traces of **51** (Table 4.10, entry 1): (a) racemic sample; (b) catalyzed by $(S_{Ru})\text{-}48^+ \text{BAr}_f^-$.



PeakTable

PDA Ch1 254nm 4nm

Peak#	Ret. Time	Area	Height	Area %	Height %
1	22.720	7037859	116912	53.462	56.069
2	25.522	6126302	91603	46.538	43.931
Total		13164160	208514	100.000	100.000

Figure c33. HPLC trace of **53** (Table 4.10, entry 1): catalyzed by $(S_{Ru})\text{-48}^+ \text{BAr}_f^-$.

CheckCIF report for $48^+ \text{PF}_6^- \cdot (\text{C}_5\text{H}_{12})_{1.5}$

The following ALERTS were generated. Each ALERT has the format

test-name_ALERT_alert-type_alert-level.

Alert level B

THETM01_ALERT_3_B The value of $\sin(\theta_{\text{max}})/\text{wavelength}$ is less than 0.575

Calculated $\sin(\theta_{\text{max}})/\text{wavelength} = 0.5617$

PLAT023_ALERT_3_B Resolution (too) Low [$\sin(\theta)/\text{Lambda} < 0.6$]...60.00 Degree

Alert level C

PLAT048_ALERT_1_C MoietyFormula Not Given a

PLAT125_ALERT_4_C No '_symmetry_space_group_name_Hall' Given

PLAT243_ALERT_4_C High 'Solvent' Ueq as Compared to Neighbors of C60

PLAT250_ALERT_2_C Large U3/U1 Ratio for Average U(i,j) Tensor Low...3.6

PLAT342_ALERT_3_C Bond Precision on C-C Bonds0.0085 Ang.

PLAT420_ALERT_2_C D-H Without Acceptor N4 – H4B

Alert level G

PLAT002_ALERT_2_G Number of Distance or Angle Restraints on AtSite 4

PLAT005_ALERT_5_G No '_iucr_refine_instructions_details' in the CIF

PLAT007_ALERT_5_G Number of Unrefined Donor-H Atoms 5

PLAT045_ALERT_1_G Calculated and Reported Z Differ by0.50 Ratio

PLAT244_ALERT_4_G Low 'Solvent' Ueq as Compared to Neighbors of P1
 PLAT300_ALERT_4_G Atom Site Occupancy of *C61 is Constrained at 0.500
 PLAT300_ALERT_4_G Atom Site Occupancy of *C61A is Constrained at 0.500
 PLAT300_ALERT_4_G Atom Site Occupancy of *C62 is Constrained at 0.500
 PLAT302_ALERT_4_G Anion/Solvent Disorder Percentage = 10
 PLAT304_ALERT_4_G Non-Integer Number of Atoms (8.50) in Resd. # 4
 PLAT432_ALERT_2_G Short Inter X...Y Contact C60 .. C62 .. 2.48 Ang.
 PLAT710_ALERT_4_G Delete 1-2-3 or 2-3-4 Linear Torsion Angle ... # 12
 N1 -RU1 -C9 -O1 -135.00 11.00 1.555 1.555 1.555 1.555
 PLAT710_ALERT_4_G Delete 1-2-3 or 2-3-4 Linear Torsion Angle ... # 13
 N3 -RU1 -C9 -O1 144.00 11.00 1.555 1.555 1.555 1.555
 PLAT710_ALERT_4_G Delete 1-2-3 or 2-3-4 Linear Torsion Angle ... # 14
 C12 -RU1 -C9 -O1 13.00 11.00 1.555 1.555 1.555 1.555
 PLAT710_ALERT_4_G Delete 1-2-3 or 2-3-4 Linear Torsion Angle ... # 15
 C13 -RU1 -C9 -O1 -25.00 11.00 1.555 1.555 1.555 1.555
 PLAT710_ALERT_4_G Delete 1-2-3 or 2-3-4 Linear Torsion Angle ... # 16
 C11 -RU1 -C9 -O1 42.00 11.00 1.555 1.555 1.555 1.555
 PLAT710_ALERT_4_G Delete 1-2-3 or 2-3-4 Linear Torsion Angle ... # 17
 C10 -RU1 -C9 -O1 24.00 11.00 1.555 1.555 1.555 1.555
 PLAT710_ALERT_4_G Delete 1-2-3 or 2-3-4 Linear Torsion Angle ... # 18
 C14 -RU1 -C9 -O1 -39.00 11.00 1.555 1.555 1.555 1.555
 PLAT779_ALERT_4_G Suspect or Irrelevant (Bond) Angle in CIF # 264
 C62 -C61 -C62 3.564 1.555 1.555 17.00 Deg.
 PLAT779_ALERT_4_G Suspect or Irrelevant (Bond) Angle in CIF # 273

C62 -C61 -H62B 3.564 1.555 1.555 43.40 Deg.
PLAT779_ALERT_4_G Suspect or Irrelevant (Bond) Angle in CIF # 274
C62 -C61 -H62B 1.555 1.555 1.555 36.00 Deg.
PLAT779_ALERT_4_G Suspect or Irrelevant (Bond) Angle in CIF # 283
C62 -C62 -C61A 3.564 1.555 1.555 31.00 Deg.
PLAT790_ALERT_4_G Centre of Gravity not Within Unit Cell: Resd. # 2
F6P
PLAT790_ALERT_4_G Centre of Gravity not Within Unit Cell: Resd. # 3
C5 H12
PLAT790_ALERT_4_G Centre of Gravity not Within Unit Cell: Resd. # 4
C2.50 H6
PLAT809_ALERT_1_G Can not Parse the SHELXL Weighting Scheme String
PLAT860_ALERT_3_G Number of Least-Squares Restraints 4
PLAT899_ALERT_4_G SHELXL97 is Deprecated and Succeeded by SHELXL 2014

CheckCIF report for 48^+ $\text{BAr}_f^- \cdot \text{H}_2\text{O}$

The following ALERTS were generated. Each ALERT has the format

test-name_ALERT_alert-type_alert-level.

Alert level B

PLAT417_ALERT_2_B Short Inter D-H..H-D ...H2 H1SB .. 2.06 Ang.

Alert level C

PLAT094_ALERT_2_C Ratio of Maximum / Minimum Residual Density 2.22

PLAT213_ALERT_2_C Atom F4C has ADP max/min Ratio 3.1 prolat

PLAT213_ALERT_2_C Atom F22D has ADP max/min Ratio 3.2 prolat

PLAT220_ALERT_2_C Large Non-Solvent C Ueq(max)/Ueq(min) Range 3.9 Ratio

PLAT241_ALERT_2_C High Ueq as Compared to Neighbors for C31

PLAT250_ALERT_2_C Large U3/U1 Ratio for Average U(i,j) Tensor 2.5

PLAT420_ALERT_2_C D-H Without Acceptor N4 - H4B

PLAT480_ALERT_4_C Long H...A H-Bond Reported H1 . F9C ...2.57 Ang.

PLAT480_ALERT_4_C Long H...A H-Bond Reported H2 .. F21C .. 2.61 Ang.

PLAT480_ALERT_4_C Long H...A H-Bond Reported H5 .. F16C .. 2.58 Ang.

PLAT480_ALERT_4_C Long H...A H-Bond Reported H5 .. F21D .. 2.57 Ang.

PLAT480_ALERT_4_C Long H...A H-Bond Reported H1SB .. F3C .. 2.56 Ang.

Alert level G

PLAT002_ALERT_2_G Number of Distance or Angle Restraints on AtSite 44
PLAT003_ALERT_2_G Number of Uiso or Uij Restrained non-H Atoms ... 40
PLAT007_ALERT_5_G Number of Unrefined Donor-H Atoms 7
PLAT042_ALERT_1_G Calc. and Reported MoietyFormula Strings Differ The
PLAT154_ALERT_1_G su's on the Cell Angles are EqualThe...0.00200 Degree
PLAT176_ALERT_4_G CIF-Embedded .res File Contains SADI Records The 12
PLAT178_ALERT_4_G CIF-Embedded .res File Contains SIMU Records 5
PLAT242_ALERT_2_G Low Ueq as Compared to Neighbors for C7C
PLAT242_ALERT_2_G Low Ueq as Compared to Neighbors for C8C
PLAT242_ALERT_2_G Low Ueq as Compared to Neighbors for C15C
PLAT300_ALERT_4_G Atom Site Occupancy of >F10C is Constrained at 0.505
PLAT300_ALERT_4_G Atom Site Occupancy of >F11C is Constrained at 0.505
PLAT300_ALERT_4_G Atom Site Occupancy of >F12C is Constrained at 0.505
PLAT300_ALERT_4_G Atom Site Occupancy of >F13D is Constrained at 0.540
PLAT300_ALERT_4_G Atom Site Occupancy of >F14D is Constrained at 0.540
PLAT300_ALERT_4_G Atom Site Occupancy of >F15D is Constrained at 0.540
PLAT300_ALERT_4_G Atom Site Occupancy of >F16D is Constrained at 0.600
PLAT300_ALERT_4_G Atom Site Occupancy of >F17D is Constrained at 0.600
PLAT300_ALERT_4_G Atom Site Occupancy of >F18D is Constrained at 0.600
PLAT300_ALERT_4_G Atom Site Occupancy of >F19C is Constrained at 0.707
PLAT300_ALERT_4_G Atom Site Occupancy of >F20C is Constrained at 0.707
PLAT300_ALERT_4_G Atom Site Occupancy of >F21C is Constrained at 0.707
PLAT300_ALERT_4_G Atom Site Occupancy of >F22D is Constrained at 0.511

PLAT300_ALERT_4_G Atom Site Occupancy of >F23D is Constrained at 0.511
PLAT300_ALERT_4_G Atom Site Occupancy of >F24D is Constrained at 0.511
PLAT300_ALERT_4_G Atom Site Occupancy of <F10D is Constrained at 0.495
PLAT300_ALERT_4_G Atom Site Occupancy of <F11D is Constrained at 0.495
PLAT300_ALERT_4_G Atom Site Occupancy of <F12D is Constrained at 0.495
PLAT300_ALERT_4_G Atom Site Occupancy of <F13C is Constrained at 0.460
PLAT300_ALERT_4_G Atom Site Occupancy of <F14C is Constrained at 0.460
PLAT300_ALERT_4_G Atom Site Occupancy of <F15C is Constrained at 0.460
PLAT300_ALERT_4_G Atom Site Occupancy of <F16C is Constrained at 0.400
PLAT300_ALERT_4_G Atom Site Occupancy of <F17C is Constrained at 0.400
PLAT300_ALERT_4_G Atom Site Occupancy of <F18C is Constrained at 0.400
PLAT300_ALERT_4_G Atom Site Occupancy of <F19D is Constrained at 0.293
PLAT300_ALERT_4_G Atom Site Occupancy of <F20D is Constrained at 0.293
PLAT300_ALERT_4_G Atom Site Occupancy of <F21D is Constrained at 0.293
PLAT300_ALERT_4_G Atom Site Occupancy of <F22C is Constrained at 0.489
PLAT300_ALERT_4_G Atom Site Occupancy of <F23C is Constrained at 0.489
PLAT300_ALERT_4_G Atom Site Occupancy of <F24C is Constrained at 0.489
PLAT300_ALERT_4_G Atom Site Occupancy of >C16C is Constrained at 0.505
PLAT300_ALERT_4_G Atom Site Occupancy of >C23D is Constrained at 0.540
PLAT300_ALERT_4_G Atom Site Occupancy of >C24D is Constrained at 0.600
PLAT300_ALERT_4_G Atom Site Occupancy of >C31C is Constrained at 0.707
PLAT300_ALERT_4_G Atom Site Occupancy of >C32D is Constrained at 0.511
PLAT300_ALERT_4_G Atom Site Occupancy of <C16D is Constrained at 0.495
PLAT300_ALERT_4_G Atom Site Occupancy of <C23C is Constrained at 0.460

PLAT300_ALERT_4_G Atom Site Occupancy of <C24C is Constrained at 0.400
PLAT300_ALERT_4_G Atom Site Occupancy of <C31D is Constrained at 0.293
PLAT300_ALERT_4_G Atom Site Occupancy of <C32C is Constrained at 0.489
PLAT301_ALERT_3_G Main Residue Disorder Percentage = 19
PLAT434_ALERT_2_G Short Inter HL..HL Contact F1C .. F10D .. 2.81 Ang.
PLAT434_ALERT_2_G Short Inter HL..HL Contact F2C .. F10C . 2.79 Ang.
PLAT434_ALERT_2_G Short Inter HL..HL Contact F8C .. F18D 2.79 Ang.
PLAT606_ALERT_4_G VERY LARGE Solvent Accessible VOID(S) in Structure
PLAT720_ALERT_4_G Number of Unusual/Non-Standard Labels 2
PLAT860_ALERT_3_G Number of Least-Squares Restraints 868
PLAT869_ALERT_4_G ALERTS Related to the use of SQUEEZE Suppressed

CheckCIF report for **49**

The following ALERTS were generated. Each ALERT has the format

test-name_ALERT_alert-type_alert-level.

Alert level B

THETM01_ALERT_3_B The value of $\sin(\theta_{\max})/\lambda$ is less than 0.575

Calculated $\sin(\theta_{\max})/\lambda = 0.5617$

Alert level C

PLAT220_ALERT_2_C Large Non-Solvent C $U_{\text{eq}}(\max)/U_{\text{eq}}(\min)$ Range 4.7 Ratio

PLAT222_ALERT_3_C Large Non-Solvent H $U_{\text{iso}}(\max)/U_{\text{iso}}(\min)$... 4.3 Ratio

PLAT241_ALERT_2_C High U_{eq} as Compared to Neighbors for C24

PLAT411_ALERT_2_C Short Inter H...H Contact H24 .. H43 .. 2.12 Ang.

PLAT420_ALERT_2_C D-H Without Acceptor N3 -H3 ..

PLAT420_ALERT_2_C D-H Without Acceptor N5 - H5B ..

Alert level G

PLAT002_ALERT_2_G Number of Distance or Angle Restraints on AtSite 19

PLAT005_ALERT_5_G No `_iucr_refine_instructions_details` in the CIF

PLAT007_ALERT_5_G Number of Unrefined Donor-H Atoms4

PLAT083_ALERT_2_G SHELXL Second Parameter in WGHT Unusually Large...81.46

PLAT152_ALERT_1_G The Supplied and Calc. Volume s.u. Differ by ...2 Units

PLAT230_ALERT_2_G Hirshfeld Test Diff for O1 -- C9 .. 5.5 su

PLAT230_ALERT_2_G Hirshfeld Test Diff for C14 -- C39 .. 7.5 su

PLAT230_ALERT_2_G Hirshfeld Test Diff for C14 -- C39A .. 5.5 su

PLAT232_ALERT_2_G Hirshfeld Test Diff (M-X) Ru1 -- C9 .. 5.8 su

PLAT300_ALERT_4_G Atom Site Occupancy of >C39 is Constrained at 0.528

PLAT300_ALERT_4_G Atom Site Occupancy of >C40 is Constrained at 0.528

PLAT300_ALERT_4_G Atom Site Occupancy of >C41 is Constrained at 0.528

PLAT300_ALERT_4_G Atom Site Occupancy of >C42 is Constrained at 0.528

PLAT300_ALERT_4_G Atom Site Occupancy of >C43 is Constrained at 0.528

PLAT300_ALERT_4_G Atom Site Occupancy of >C44 is Constrained at 0.528

PLAT300_ALERT_4_G Atom Site Occupancy of <C39A is Constrained at 0.472

PLAT300_ALERT_4_G Atom Site Occupancy of <C40A is Constrained at 0.472

PLAT300_ALERT_4_G Atom Site Occupancy of <C41A is Constrained at 0.472

PLAT300_ALERT_4_G Atom Site Occupancy of <C42A is Constrained at 0.472

PLAT300_ALERT_4_G Atom Site Occupancy of <C43A is Constrained at 0.472

PLAT300_ALERT_4_G Atom Site Occupancy of <C44A is Constrained at 0.472

PLAT301_ALERT_3_G Main Residue Disorder Percentage = 12

PLAT606_ALERT_4_G VERY LARGE Solvent Accessible VOID(S) in Structure

PLAT710_ALERT_4_G Delete 1-2-3 or 2-3-4 Linear Torsion Angle ... # 51

N3 -RU1 -C9 -O1 133.00 4.00 1.555 1.555 1.555 1.555

PLAT710_ALERT_4_G Delete 1-2-3 or 2-3-4 Linear Torsion Angle ... # 52

N1 -RU1 -C9 -O1 -147.00 4.00 1.555 1.555 1.555 1.555

PLAT710_ALERT_4_G Delete 1-2-3 or 2-3-4 Linear Torsion Angle ... # 53

C12 -RU1 -C9 -O1 -13.00 4.00 1.555 1.555 1.555 1.555

PLAT710_ALERT_4_G Delete 1-2-3 or 2-3-4 Linear Torsion Angle ... # 54
 C13 -RU1 -C9 -O1 24.00 4.00 1.555 1.555 1.555 1.555
 PLAT710_ALERT_4_G Delete 1-2-3 or 2-3-4 Linear Torsion Angle ... # 55
 C11 -RU1 -C9 -O1 -42.00 4.00 1.555 1.555 1.555 1.555
 PLAT710_ALERT_4_G Delete 1-2-3 or 2-3-4 Linear Torsion Angle ... # 56
 C10 -RU1 -C9 -O1 -27.00 4.00 1.555 1.555 1.555 1.555
 PLAT710_ALERT_4_G Delete 1-2-3 or 2-3-4 Linear Torsion Angle ... # 57
 C14 -RU1 -C9 -O1 34.00 4.00 1.555 1.555 1.555 1.555
 PLAT779_ALERT_4_G Suspect or Irrelevant (Bond) Angle in CIF # 96
 C39 -C14 -C39A 1.555 1.555 1.555 10.90 Deg.
 PLAT860_ALERT_3_G Number of Least-Squares Restraints 37
 PLAT869_ALERT_4_G ALERTS Related to the use of SQUEEZE Suppressed
 PLAT899_ALERT_4_G SHELXL97 is Deprecated and Succeeded by SHELXL 2014